



THE UNIVERSITY OF QUEENSLAND
A U S T R A L I A

**Trajectory Optimisation of a Partially-Reusable
Rocket-Scramjet-Rocket Small Satellite Launch System**

Sholto O. Forbes-Spyratos

B.Eng. (Mechanical and Aerospace) (Hons. I) & B.Sc. (Physics)

A thesis submitted for the degree of Doctor of Philosophy at
The University of Queensland in 2018

School of Mechanical Engineering

Centre for Hypersonics

Abstract

The small satellite industry is expanding rapidly, driving a need for dedicated and cost effective small satellite launchers. For this reason, work is ongoing at The University of Queensland to develop a three stage, partially-reusable small satellite launch system. This launch system consists of two rocket stages, along with a scramjet-powered accelerator for cost-efficient reusability and launch flexibility. During the launch of this system, there are complex trade-offs between the performance of each stage that must be accounted for. The rocket stages perform significantly better at high altitudes due to diminished drag losses, while the airbreathing stage will generally perform better at low altitudes due to the high density operation of the scramjet engines. This work develops an optimal trajectory profile for a rocket-scramjet-rocket, three stage launch system, determining the flight path which maximises the payload-to-orbit capabilities of the launch system.

Significant work has previously been carried out on the design of the scramjet-powered accelerator, designated the SPARTAN, as well as the third stage rocket. However, the first stage has not been designed, and the third stage previously used a costly, pump-fed motor. In this study, a first stage rocket is designed, based on a Falcon-1e scaled down lengthwise to 8.5m, and the third stage rocket is redesigned to be powered by a cost effective pressure-fed engine. The aerodynamics of the first stage and the SPARTAN are simulated using computational fluid dynamics, to produce accurate aerodynamic databases. The aerodynamics of the third stage are modelled using Missile Datcom, and propulsion models are developed for all three stages. The aerodynamic and performance models are used to create a trimmed three degree of freedom simulation of the launch system.

A package is developed to calculate the maximum payload-to-orbit trajectory of the rocket-scramjet-rocket launch system, designated LODESTAR, which uses optimal control theory to design flight paths. LODESTAR utilises GPOPS-2, a pseudospectral method optimal control software, configured to calculate maximum payload-to-orbit trajectory profiles. Along with the configuration of GPOPS-2, LODESTAR provides a dynamic simulation of each vehicle, and tools to verify and examine the optimised solutions produced by GPOPS-2.

Launch trajectories are initially simulated assuming that the SPARTAN lands at some position downrange. A launch trajectory is simulated in which the SPARTAN flies at maximum dynamic pressure as a reference and verification case. This trajectory achieves a payload-to-orbit of 98.3kg, launching to sun synchronous orbit. The maximum payload-to-orbit trajectory of the launch system is calculated, and is found to differ significantly from the trajectory in which the SPARTAN is constrained to constant dynamic pressure. The SPARTAN is found to deviate from its maximum dynamic pressure at both stage separation points, and for a segment in the middle of its trajectory. The higher separation points result in the efficiency of the SPARTAN reducing, but increase the efficiency of the rocket stages, improving the overall efficiency of the system. Additionally, an altitude raising manoeuvre is performed in a region where the specific impulse of the scramjet engines is relatively

homogeneous with varied flight conditions, resulting in a very small performance increase. Overall, flying an optimal trajectory increases the payload-to-orbit of the system launching to sun synchronous orbit to 156.4kg, an increase of 19.5% compared to a trajectory in which the SPARTAN flies at maximum dynamic pressure.

The fly-back of the SPARTAN is included within the trajectory optimisation, and a maximum payload-to-orbit flight path to sun synchronous orbit is simulated. It is found that the SPARTAN must ignite its scramjet engines during its return flight, causing the fly-back to become an important consideration in the optimal trajectory design. When the fly-back is included, the first stage pitches easterly, rather than northerly. The SPARTAN banks heavily throughout its acceleration to manoeuvre to polar inclination, decreasing the performance of the SPARTAN, but also reducing the amount of fuel used during fly-back, for a net performance gain. The fly-back is found to exhibit multiple ‘skipping’ manoeuvres, which serve to increase the range of the SPARTAN, minimising the fuel necessary during the return flight. In addition, the scramjet engines are powered on at the troughs of the first three skips, corresponding to the points of highest possible specific impulse. The launch system is able to deliver 132.1kg of payload to sun synchronous orbit while successfully returning the SPARTAN to its initial launch site.

A study is conducted to quantify the sensitivity of the launch system to variations in key design parameters. The behaviour of the maximum payload-to-orbit trajectory is investigated as the physical characteristics of the launch system are modified. The sensitivities of coupled design parameters are compared, to quantify their relative impacts on the performance of the launch system. The magnitudes of these relative impacts are assessed, to indicate the design trade-offs which will produce an increase in the launch system performance.

Declaration by author

This thesis is composed of my original work, and contains no material previously published or written by another person except where due reference has been made in the text. I have clearly stated the contribution by others to jointly-authored works that I have included in my thesis.

I have clearly stated the contribution of others to my thesis as a whole, including statistical assistance, survey design, data analysis, significant technical procedures, professional editorial advice, and any other original research work used or reported in my thesis. The content of my thesis is the result of work I have carried out since the commencement of my research higher degree candidature and does not include a substantial part of work that has been submitted to qualify for the award of any other degree or diploma in any university or other tertiary institution. I have clearly stated which parts of my thesis, if any, have been submitted to qualify for another award.

I acknowledge that an electronic copy of my thesis must be lodged with the University Library and, subject to the policy and procedures of The University of Queensland, the thesis be made available for research and study in accordance with the Copyright Act 1968 unless a period of embargo has been approved by the Dean of the Graduate School.

I acknowledge that copyright of all material contained in my thesis resides with the copyright holder(s) of that material. Where appropriate I have obtained copyright permission from the copyright holder to reproduce material in this thesis.

Publications During Candidature

Journal papers

S. O. Forbes-Spyratos, M. P. Kearney, M. K. Smart, and I. H. Jahn. “Trajectory Design of a Rocket-Scramjet-Rocket Multi-Stage Launch System”. In: *Journal of Spacecraft and Rockets* (2018). DOI: [10.2514/1.A34107](https://doi.org/10.2514/1.A34107)

Conference papers

S. Forbes-Spyratos, M. Kearney, M. Smart, and I. Jahn. “Trajectory design of a rocket-scramjet-rocket multi-stage launch system”. In: *21st AIAA International Space Planes and Hypersonics Technologies Conference, Hypersonics 2017*. Xiamen, China, 2017. ISBN: 9781624104633

S. O. Forbes-Spyratos, M. P. Kearney, M. K. Smart, and I. H. Jahn. “Fly-back of a scramjet-powered accelerator”. In: *AIAA Scitech, 2018*. Orlando, FL, 2018. ISBN: 9781624105241. DOI: [10.2514/6.2018-2177](https://doi.org/10.2514/6.2018-2177)

J. Chai, M. Smart, S. Forbes-Spyratos, and M. Kearney. “Fly Back Booster Design for Mach 5 Scramjet Launch”. In: *68th International Astronautical Congress*. Aelaide, Australia, 2017

Publications Included in This Thesis

This thesis comprises partly of publications, as allowed by University of Queensland Policy PPL 4.60.07. The papers that have been included have all been published in peer reviewed journals at the time of submission.

S. O. Forbes-Spyratos, M. P. Kearney, M. K. Smart, and I. H. Jahn. “Trajectory Design of a Rocket-Scramjet-Rocket Multi-Stage Launch System”. In: *Journal of Spacecraft and Rockets* (2018). DOI: [10.2514/1.A34107](https://doi.org/10.2514/1.A34107)

Contributor	Contribution
Sholto O. Forbes-Spyratos	Conception and Design (85%) Performed simulations (100%) Analysis of results (90%) Wrote and edited paper (85%)
Ingo H. Jahn	Conception and Design (5%) Analysis of results (5%) Wrote and edited paper (7.5%)
Michael P. Kearney	Conception and Design (5%) Wrote and edited paper (7.5%)
Michael K. Smart	Conception and Design (5%) Analysis of results (5%) Wrote and edited paper (5%)

Contributions by Others to the Thesis

The model of the Baseline SPARTAN was provided for this work by Dr. Dawid Preller and Mr. Joseph Chai, including mass properties, dimensions, and CAD models. The CRESTM10 scramjet engine database was provided for this study by Prof. Michael Smart, consisting of tabulated performance data over a range of inlet conditions. The viscous correction incorporated into the SPARTAN's aerodynamic calculations was performed by Mr. Alexander Ward, and provided for this study in the form of a tabulated aerodynamic database.

XXX Put into here for heat analysis (and alex)

Statement of Parts of the Thesis Submitted to Qualify for the Award of Another Degree

None.

For Kaitlin, with love to my family and friends and utmost gratitude to my advisors: Ingo Jahn, Michael Kearney, and Michael Smart.

I'm trying to find a way off this planet.
Rocket Raccoon

Keywords

airbreathing propulsion, scramjets, hypersonics, access-to-space, small satellite launchers, airbreathing launch systems

Australian and New Zealand Standard Research Classification (ANZSRC)

ANZSRC code: 090107 Hypersonic Propulsion and Hypersonic Aerodynamics, 20%

ANZSRC code: 090106 Flight Dynamics, 10%

ANZSRC code: 090108, Satellite, Space Vehicle and Missile Design and Testing, 25%

ANZSRC code: 090104 Aircraft Performance and Flight Control Systems, 15%

ANZSRC code: 010303 Optimisation, 30%

Fields of Research (FoR) Classification

FoR code: 0901, Aerospace Engineering, 100%

CONTENTS

List of figures	xxiv
List of tables	xxvii
1 Introduction	1
1.1 Research aims	4
1.2 Thesis Outline and Contributions	6
2 Background	9
2.1 Small Satellite Launchers	11
2.2 Scramjets	13
2.3 The Launch System Design Process	15
3 Literature review	19
3.1 Hypersonic Airbreathing Launch Systems and Trajectories	20
3.1.1 Single Stage Airbreathing Launch Systems	26
3.1.2 Two-Stage Launch Systems	27
3.1.3 Three-Stage Launch Systems	39
3.2 Hypersonic Vehicle Return and Glide Trajectories	42
3.3 The SPARTAN	44
3.4 Optimal Control	49
3.4.1 Shooting Methods	50
3.4.2 Collocation Methods	52
3.5 Available Optimal Control Solvers	55
3.6 Aerodynamic Analysis	57
3.7 Summary	60

CONTENTS

4 Modelling of Launch System Dynamics	63
4.1 The Second Stage Scramjet Accelerator	65
4.1.1 The Scramjet Accelerator	65
4.1.2 Thermal Protection	66
4.1.3 Propulsion	67
4.1.4 Aerodynamics	71
4.1.5 Trimmed Aerodynamic Database of the Scramjet Accelerator with Engine-On	82
4.1.6 Trimmed Aerodynamic Database of the Scramjet Accelerator with Engine-Off	82
4.2 The First Stage Rocket	84
4.2.1 The Aerodynamics of the First Stage Rocket and Scramjet Accelerator	86
4.3 The Third Stage Rocket	87
4.3.1 Geometry	89
4.3.2 Fuel Tank Sizing	90
4.3.3 Heat Shield Sizing	90
4.3.4 Propulsion	91
4.3.5 Aerodynamics	94
4.3.6 Thrust Vectoring	94
4.4 Summary	96
5 Trajectory Modelling and Optimisation	97
5.1 Mission Definition	98
5.2 Vehicle Simulation	99
5.2.1 Equations of Motion	100
5.3 Optimal Control Problem Structure	101
5.3.1 Trajectory Connection Points	103
5.3.2 I. First Stage Vertical Ascent	104
5.3.3 II. First Stage Pitching Ascent	105
5.3.4 III. Second Stage Ascent Trajectory	106
5.3.5 IV. Second Stage Return Trajectory	108
5.3.6 V. Third Stage Powered Ascent	109
5.3.7 VI. Third Stage Unpowered Ascent	110
5.3.8 VII. Hohmann Transfer	110
5.4 Optimal Solution Analysis	112
5.5 The Optimisation Process in LODESTAR	114
5.6 Trajectory and Performance Analysis	116
5.7 Summary	117

6 Optimised Ascent Trajectory	119
6.1 Case 1: Constant Dynamic Pressure Trajectory	121
6.2 Case 2: Optimised Ascent Trajectory	126
6.3 Energy Usage Analysis	133
6.4 Sensitivity Analysis	135
6.4.1 Case 3: Maximum Dynamic Pressure Sensitivity	137
6.4.2 Case 4: Scramjet Accelerator Drag Sensitivity	138
6.4.3 Case 5: C-REST Specific Impulse Sensitivity	139
6.4.4 Case 6: scramjet accelerator Mass Sensitivity	141
6.4.5 Case 7: Scramjet Accelerator Fuel Mass Sensitivity	142
6.4.6 Case 8: Third Stage Mass Sensitivity	144
6.4.7 Case 9: Third Stage Specific Impulse Sensitivity	145
6.4.8 Case 10: Third Stage Drag Sensitivity	146
6.5 Comparison of Design Parameters	148
6.6 Summary	150
7 Optimised Trajectory Including Fly-Back	153
7.1 Case 11: SPARTAN Trajectory with Scramjet Accelerator Return	154
7.2 Ascent Trajectory	155
7.3 Fly-Back Trajectory	160
7.4 Energy Usage Analysis	162
7.5 Design Sensitivity Analysis	164
7.5.1 Case 12: Maximum Dynamic Pressure Sensitivity with Fly-Back	166
7.5.2 Case 13: Scramjet Accelerator Drag Sensitivity with Fly-Back	167
7.5.3 Case 14: C-REST Specific Impulse Sensitivity with Fly-Back	169
7.5.4 Case 15: Scramjet Accelerator Mass Sensitivity with Fly-Back	170
7.5.5 Case 16: Scramjet Accelerator Fuel Mass Sensitivity with Fly-Back	172
7.5.6 Case 17: Third Stage Mass Sensitivity with Fly-Back	173
7.5.7 Case 18: Third Stage Specific Impulse Sensitivity with Fly-Back	174
7.6 Comparison of Sensitivities with Fly-Back	175
7.7 Summary	177
8 Conclusions	179
9 Recommendations for future work	185
References	187

CONTENTS

A Thermal Analysis	205
A.1 Thermal Analysis of the Standard Trajectory	207
A.2 Heating limited Trajectory	208
A.3 TPS Design Exploration	208
A.4 Scramjet Accelerator	208
A.5 Third Stage	208
B Uncertainties and Simplifications	217
B.1 Modelling and Design Simplifications	218
B.1.1 Control	218
B.1.2 Staging Effects	219
B.1.3 Mass Model Simplifications	220
B.2 Aerodynamic and Propulsion Simulation Uncertainties	221
B.2.1 Aerodynamic Uncertainty	221
B.2.2 Propulsion System Uncertainties	223
B.2.3 Quantification of Aerodynamic and Propulsion Uncertainty Effects	224
B.2.4 Atmospheric Variations	225
C Examples and Verification	227
C.1 Example - Brachistochrone Problem	227
C.2 Example - Space Shuttle Reentry	228
C.2.1 Problem Formulation	229
C.2.2 Unconstrained Result	230
C.2.3 Heating Rate Limited Result	232
C.3 Optimised Trajectory Verification	233
C.4 Optimised Trajectory Analysis	233
C.4.1 Mesh History	233
C.4.2 Verification	235
D Modelling and Simulation	239
D.1 Propulsion Interpolation Scheme	239
D.2 SPARTAN Flow Results	240
D.3 Cart3D Mesh	241
D.4 Performance of the SPARTAN During Fly-Back	243
E Alternate Trajectory Cases	245
E.1 Trajectory With Decreased Third Stage TPS Mass	245
E.2 Trajectory With Variation in Return Drag	245

E.3	Maximum Payload-To-Orbit Trajectory With Dynamic Pressure Constraint	245
E.4	Sonic Boom Ground Effects	246
E.5	Alternate Launch Location	248
F	Trajectory Plot Comparisons	253
F.1	Optimised Ascent Trajectory Comparisons With No Fly-Back	254
F.1.1	Case 3: Maximum Dynamic Pressure Sensitivity Comparison	254
F.1.2	Case 4: SPARTAN Drag Sensitivity Comparison	256
F.1.3	Case 5: SPARTAN Specific Impulse Sensitivity Comparison	258
F.1.4	Case 6: SPARTAN Mass Sensitivity Comparison	260
F.1.5	Case 7: SPARTAN Fuel Mass Sensitivity Comparison	262
F.1.6	Case 8: Third Stage Mass Sensitivity Comparison	264
F.1.7	Case 9: Third Stage Specific Impulse Sensitivity Comparison	266
F.1.8	Case 10: Third Stage Drag Sensitivity Comparison	268
F.2	Optimised Ascent Trajectory Comparisons With Fly-Back	270
F.2.1	Case 12: Dynamic Pressure Sensitivity Comparison	270
F.2.2	Case 13: SPARTAN Drag Sensitivity Comparison	273
F.2.3	Case 14: SPARTAN Specific Impulse Sensitivity Comparison	276
F.2.4	Case 15: SPARTAN Mass Sensitivity Comparison	279
F.2.5	Case 16: SPARTAN Fuel Mass Sensitivity Comparison	282
F.2.6	Case 17: Third Stage Mass Sensitivity Comparison	285
F.2.7	Case 18: Third Stage Specific Impulse Sensitivity Comparison	288
G	Viscous Drag Variation	291

LIST OF FIGURES

1.1	The SPARTAN scramjet-powered accelerator[16].	4
2.1	Comparison of Blue Origin and SpaceX partially-reusable launch systems with existing and historic launch systems[17].	9
2.2	The trajectory of the Falcon Heavy[19].	10
2.3	The trajectory of the Ariane featuring Adeline[24].	11
2.4	A simple schematic of a scramjet engine[47].	14
2.5	Characteristic performance for airbreathing and rocket engines with Mach number[48].	14
2.6	The general design process flow for a launch vehicle, adapted from Blair et al[53] . .	16
3.1	An example airbreathing flight corridor of an airbreathing launch vehicle[49].	21
3.2	An illustration of the optimised maximum range trajectory of a hypersonic vehicle[89].	44
3.3	The elevons of the SPARTAN[12].	45
3.4	The scramjet accelerator of the SPARTAN, as designed by Preller[82].	46
3.5	The flight trajectory of the SPARTAN. a) shows the physical trajectory and b) shows the forces on the vehicle and performance indicators.	47
3.6	The third stage rocket of the rocket-scramjet-rocket launch system[12].	48
3.7	The third stage trajectory of The SPARTAN launch system[82].	48
3.8	A comparison of single shooting and multiple shooting[97].	52
3.9	Examples of h and p collocation methods[97].	53
3.10	Comparison of optimisation techniques[89]. A hypersonic vehicle is optimised for maximum range. The hp-adaptive method can be observed to have produced the most optimal result.	55
3.11	The Skylon spaceplane, simulated using Cart3D at $Mach\ 12.189$, $\alpha = 7.512^\circ$ [150]. Cell distribution produced by mesh adaptation is shown.	59

LIST OF FIGURES

3.12 Comparisons of Cart3D with experimental data and the FUN3D Navier-Stokes CFD solver. P1, P2 and P3 indicate pressure tap locations. Modified from Sagerman et al.[146]. XXX Change this picture to something more relevant	60
4.1 The launch process of the rocket-scramjet-rocket launch system, presented in simplified form.	64
4.2 The SPARTAN launch system, top view, showing the scramjet accelerator and first stage.	65
4.3 The SPARTAN launch system, side view, showing the scramjet accelerator and fuel tanks, along with the third and first stages.	65
4.4 The external features of the scramjet accelerator.	66
4.5 The C-RESTM10 propulsion database, specific impulse.	68
4.6 The locations of conditions relevant to C-REST engine simulation.	69
4.7 Flow conditions after the conical shock generated by the vehicle nose cone as a function of flight Mach number and angle of attack. Figure a) shows the Mach number, b) shows the pressure ratio, and c) shows the temperature ratio following the conical shock, at the engine inlet.	70
4.8 Specific impulse of the C-REST engines with input temperature and Mach number. Available data points are indicated.	71
4.9 Operable equivalence ratio of the C-REST engines with input temperature and Mach number. Available data points are indicated.	72
4.10 The process for generating aerodynamic databases.	73
4.11 Surface triangulation of the scramjet accelerator, generated using Pointwise[157].	74
4.12 The convergence of a Cart3D simulation of the scramjet accelerator at Mach 6, 2° angle of attack.	75
4.13 View of the scramjet accelerator surface triangulation showing engine outlet boundaries.	76
4.14 The total thrust output of the scramjet accelerator, including the CRESTM10 database, and Cart3D nozzle and boat tail simulations.	76
4.15 The specific impulse of the scramjet accelerator, including the C-rest database, and Cart3D nozzle and boat tail simulations.	77
4.16 Centre of gravity positions throughout the flight of the scramjet accelerator.	78
4.17 The forces on the scramjet accelerator during flight.	78
4.18 scramjet accelerator model showing control surfaces.	79
4.19 Flap deflection required for trim of the scramjet accelerator. Negative up.	80
4.20 Viscous drag coefficient across various Mach numbers.	81
4.21 Engine-on Cart3D simulation at Mach 6, 2° angle of attack, and 25km altitude.	82

4.22	The aerodynamic coefficients of the scramjet accelerator with the C-REST engines powered-on at 30km altitude. Coefficients correspond to a reference area of 62.77m^2 and a centre of gravity of 15.24m (full of fuel, with third stage).	83
4.23	Cart3D flow result for the scramjet accelerator, at Mach 6, 2° angle of attack.	84
4.24	Aerodynamic Characteristics of the scramjet accelerator with C-REST engine powered-off at an altitude of 30km. Coefficients correspond to a reference area of 62.77m^2 and a centre of gravity of 15.16m (no third stage, no fuel).	85
4.25	Unstarted scramjet engines at mach 3, 2° angle of attack.	86
4.26	Cart3D result for the scramjet accelerator and first stage vehicles at Mach 2, -1° angle of attack.	87
4.27	The aerodynamic characteristics of the SPARTAN stack. Coefficients correspond to a reference area of 62.77m^2	88
4.28	Thrust vectoring moment balancing of the first stage.	89
4.29	The third stage rocket, showing major internal features.	89
4.30	Variation in coefficient of thrust with area ratio[164].	94
4.31	Aerodynamic characteristics of the third stage rocket, for a reference area of 0.95m^2	95
4.32	Thrust vector moment balancing of the third stage.	96
5.1	Sun synchronous orbit illustration, passing over the equator at the same time each day[173].	98
5.2	Approximate location of the ELA launch site. Image from Google maps.	99
5.3	The Earth-fixed components of the geodetic rotational coordinate system.	101
5.4	Illustration of the phases of the launch profile. Controlled and uncontrolled phases are distinguished.	103
5.5	The Hohmann transfer manoeuvre. ΔV indicates a velocity change due to a burn.	111
5.6	XXX Change 6DOF in this image! also check section no.s The process of the rocket-scramjet-rocket trajectory optimisation. Relevant sections are indicated in square brackets at each process step.	115
6.1	Maximum payload-to-orbit trajectory path with the scramjet accelerator flying at constant dynamic pressure (Case 1). Initial heading angle 91.4°	121
6.2	The first stage trajectory of the launch system, with the scramjet accelerator constrained to flight at constant dynamic pressure (Case 1).	123
6.3	The constant dynamic pressure flight path of the scramjet accelerator (Case 1).	124
6.4	The third stage trajectory of the launch system, with the scramjet accelerator constrained to flight at constant dynamic pressure (Case 1).	125
6.5	The optimised maximum payload-to-orbit trajectory of the launch system (Case 2).	127

LIST OF FIGURES

6.6	The optimised maximum payload-to-orbit trajectory of the launch system under power of the first stage rocket (Case 2)	128
6.7	The optimised maximum payload-to-orbit trajectory of the scramjet accelerator (Case 2)	130
6.8	Net I_{sp} contours for the scramjet accelerator at Mach numbers from 5-9, showing flight conditions for an optimised trajectory with no constraints (Case 2) and a constant dynamic pressure trajectory (Case 1)	131
6.9	The specific impulse of the C-REST engines, plotted for inlet temperature (T_1) and inlet Mach number (M_1). Data points are shown in black.	131
6.10	The third stage trajectory of the launch system flying the maximum payload-to-orbit trajectory (Case 2)	132
6.11	The sensitivity of the key design parameters of the launch system.	148
7.1	Maximum payload-to-orbit trajectory path with the inclusion of scramjet accelerator fly-back (Case 11). Initial heading angle of 3.3°	154
7.2	The first stage of the optimised maximum payload-to-orbit trajectory with scramjet accelerator fly-back (Case 11).	156
7.3	The acceleration of the scramjet accelerator flying an optimised maximum payload-to-orbit trajectory with scramjet accelerator fly-back (Case 11).	157
7.4	Net I_{sp} contours for the scramjet accelerator at Mach numbers between 5.5 and 8.5, showing the optimised trajectory path (Case 11).	158
7.5	The third stage trajectory of an optimised maximum payload-to-orbit trajectory with scramjet accelerator fly-back (Case 11).	159
7.6	The fly-back trajectory of the scramjet accelerator flying an optimised maximum payload-to-orbit trajectory (Case 11).	160
7.7	The sensitivity of the key design parameters of the launch system, including scramjet accelerator fly-back. Red and green coloured areas indicate decreases or increases in the magnitude of sensitivity respectively, compared to the sensitivity study without scramjet accelerator fly-back in Section 6.5.	176
A.1	The points chosen for thermal analysis, selected for the potential of high heat loading.	206
A.2	Temperature time histories on the scramjet accelerator.	209
A.3	Temperature time histories on the third stage rocket with time.	210
A.4	210
A.5	211
A.6	212
A.7	213
A.8	214

A.9	214
A.10	215
B.1	Variation in temperature and density in the 1976 U.S Standard Atmosphere Model[155]. Arrows indicate lowest and highest mean monthly values obtained at any location, and dashed lines indicate one-percent extremes.	226
C.1	The solution to the Brachistochrone problem, solved in GPOPS-2[119].	228
C.2	231
C.3	231
C.4	232
C.5	233
C.6	The mesh history of each phase of the optimised, maximum payload-to-orbit trajectory with SPARTAN fly-back (Case 11). the phases are shown in each subfigure as follows: a) first stage rocket, b) SPARTAN acceleration, c) SPARTAN fly-back and d) third stage.	234
C.7	The Hamiltonian time history of each phase of the maximum payload-to-orbit optimised trajectory, with SPARTAN fly-back (Case 11).	235
C.8	The error between the integrated dynamics of the system, and the solution states of each phase of the maximum payload-to-orbit optimised trajectory, with SPARTAN fly-back (Case 11). Normalised to the range of each state.	236
C.9	The error between the forward simulated states, and the solution states of each phase of the maximum payload-to-orbit optimised trajectory, with SPARTAN fly-back (Case 11). Normalised to the range of each state.	237
D.1	The transformation to a normalised interpolation scheme.	239
D.2	CART3D flow result for the SPARTAN, at Mach 1.1, 6° angle of attack.	240
D.3	CART3D flow result for the SPARTAN, at Mach 3, 6° angle of attack.	241
D.4	Adapted mesh of the SPARTAN at Mach 6 3° angle of attack.	241
D.5	Adapted mesh around the SPARTAN and first stage vehicles, flying at Mach 2, -1° angle of attack.	242
D.6	The performance of the SPARTAN during the boost phase. Light blue indicates that the scramjet engines are turned on.	243
E.1	The optimised maximum payload-to-orbit trajectory of the launch system constrained to 50kPa between Mach numbers 6 to 8, under power of the first stage rocket.	247
E.2	The optimised maximum payload-to-orbit trajectory of the SPARTAN, constrained to 50kPa between Mach numbers 6 to 8.	249

LIST OF FIGURES

E.3	The third stage trajectory of the launch system flying the maximum payload-to-orbit trajectory, constrained to 50kPa between Mach numbers 6 to 8.	250
E.4	The level of population annoyance with increasing overpressure.	251
E.5	The sonic boom overpressure on the ground, for the optimised trajectory path (Case 11).	251
E.6	The optimised maximum payload-to-orbit trajectory of the launch system launching onto a southerly orbit, from Streaky Bay.	252
F.1	Comparison of SPARTAN ascent trajectories with variation in the maximum dynamic pressure of the SPARTAN.	254
F.2	Comparison of third stage rocket ascent trajectories with variation in the maximum dynamic pressure of the SPARTAN.	255
F.3	Comparison of SPARTAN ascent trajectories with variation in the drag of the SPARTAN.	256
F.4	Comparison of third stage rocket ascent trajectories with variation in the drag of the SPARTAN.	257
F.5	Comparison of SPARTAN ascent trajectories with variation in the specific impulse of the SPARTAN.	258
F.6	Comparison of third stage rocket ascent trajectories with variation in the specific impulse of the SPARTAN.	259
F.7	Comparison of SPARTAN ascent trajectories with variation in the mass of the SPARTAN.	260
F.8	Comparison of third stage rocket ascent trajectories with variation in the mass of the SPARTAN.	261
F.9	Comparison of SPARTAN ascent trajectories with variation in the fuel mass of the SPARTAN.	262
F.10	Comparison of third stage rocket ascent trajectories with variation in the fuel mass of the SPARTAN.	263
F.11	Comparison of SPARTAN ascent trajectories with variation in the mass of the third stage.	264
F.12	Comparison of third stage rocket ascent trajectories with variation in the mass of the third stage.	265
F.13	Comparison of SPARTAN ascent trajectories with variation in the specific impulse of the third stage.	266
F.14	Comparison of third stage rocket ascent trajectories with variation in the specific impulse of the third stage.	267
F.15	Comparison of SPARTAN ascent trajectories with variation in the drag of the third stage.	268

F.16 Comparison of third stage rocket ascent trajectories with variation in the drag of the third stage.	269
F.17 Comparison of SPARTAN ascent trajectories with variation in the maximum dynamic pressure of the SPARTAN.	270
F.18 Comparison of third stage rocket ascent trajectories with variation in the maximum dynamic pressure of the SPARTAN.	271
F.19 Comparison of SPARTAN return trajectories with variation in the maximum dynamic pressure of the SPARTAN.	272
F.20 Comparison of SPARTAN ascent trajectories with variation in the drag of the SPARTAN.	273
F.21 Comparison of third stage rocket ascent trajectories with variation in the drag of the SPARTAN.	274
F.22 Comparison of SPARTAN return trajectories with variation in the drag of the SPARTAN.	275
F.23 Comparison of SPARTAN ascent trajectories with variation in the specific impulse of the SPARTAN.	276
F.24 Comparison of third stage rocket ascent trajectories with variation in the specific impulse of the SPARTAN.	277
F.25 Comparison of SPARTAN return trajectories with variation in the specific impulse of the SPARTAN.	278
F.26 Comparison of SPARTAN ascent trajectories with variation in the mass of the SPARTAN.	279
F.27 Comparison of third stage rocket ascent trajectories with variation in the mass of the SPARTAN.	280
F.28 Comparison of SPARTAN return trajectories with variation in the mass of the SPARTAN.	281
F.29 Comparison of SPARTAN ascent trajectories with variation in the fuel mass of the SPARTAN.	282
F.30 Comparison of third stage rocket ascent trajectories with variation in the fuel mass of the SPARTAN.	283
F.31 Comparison of SPARTAN return trajectories with variation in the fuel mass of the SPARTAN.	284
F.32 Comparison of SPARTAN ascent trajectories with variation in the mass of the third stage.	285
F.33 Comparison of third stage rocket ascent trajectories with variation in the mass of the third stage.	286
F.34 Comparison of SPARTAN return trajectories with variation in the mass of the third stage.	287

LIST OF FIGURES

F.35 Comparison of SPARTAN ascent trajectories with variation in the specific impulse of the third stage.	288
F.36 Comparison of third stage rocket ascent trajectories with variation in the specific impulse of the third stage.	289
F.37 Comparison of SPARTAN return trajectories with variation in the specific impulse of the third stage.	290
G.1 Comparison of SPARTAN ascent trajectories with variation in the viscous drag of the SPARTAN.	293
G.2 Comparison of third stage ascent trajectories with variation in the viscous drag of the SPARTAN.	294
G.3 Comparison of SPARTAN return trajectories with variation in the viscous drag of the SPARTAN.	295

LIST OF TABLES

2.1	A selection of the small satellite launchers which are operational or in development	12
3.1	Summary of programs capable of pseudospectral optimisation.	56
4.1	Mass breakdown of the modified scramjet accelerator vehicle.	66
4.2	First Stage Engine Properties[162].	86
4.3	Mass breakdown of the third stage rocket.	89
4.4	Third stage fuel distribution.	90
4.5	Third stage heat shield breakdown.	91
4.6	Comparison of upper stage rocket engines, sourced primarily from the Encyclopedia Astronautica reference website[162].	92
5.1	Segment coupling conditions for combined trajectory optimisation.	105
5.2	Optimisation setup of the first stage phase.	106
5.3	Optimisation setup of the second stage ascent. * This is only used in the constant dynamic pressure simulation. XXX Check these, particularly traj angle	107
5.4	Optimisation setup of the second stage return.	108
5.5	Optimisation setup of the third stage powered ascent.	109
6.1	Summary of the key results from a maximum payload-to-orbit trajectory with the scramjet accelerator constrained to 50kPa (Case 1). XXX about sig figs: the high number of sig figs have been included to highlight trends in the variation section. I should potentially argue that a high number of significant figures are included for this, but make note that the results are still subject to significant sources of error?	122
6.2	A summary of key results from the maximum payload-to-orbit trajectory (Case 2).	129

LIST OF TABLES

6.3	An energy usage breakdown of the ascent trajectories, both with, and without, the scramjet accelerator constrained to constant dynamic pressure (Cases 1 & 2). Blue indicates a 'productive' energy usage, whereas red indicates energy 'wastage'. XXX fix all to be same s.f.	134
6.4	Comparison of key trajectory parameters with variation in the maximum dynamic pressure of the scramjet accelerator (Case 3).	137
6.5	Comparison of key trajectory parameters with variation in the drag of the scramjet accelerator (Case 4).	139
6.6	Comparison of key trajectory parameters with variations in the specific impulse of the C-REST engines (Case 5).	140
6.7	Comparison of key trajectory parameters with variation in the structural mass of the scramjet accelerator (Case 6).	141
6.8	Comparison of key trajectory parameters with variation in the fuel mass of the scramjet accelerator (Case 7).	143
6.9	Comparison of key trajectory parameters with variation in the mass of the third stage (Case 8).	144
6.10	Comparison of key trajectory parameters with variation in the third stage specific impulse (Case 9).	146
6.11	Comparison of key trajectory parameters with variation in the drag of the third stage (Case 10).	147
7.1	Selected trajectory conditions for a maximum payload-to-orbit trajectory including scramjet accelerator fly-back (Case 11).	155
7.2	An energy usage breakdown of the ascent trajectories, both with, and without, scramjet accelerator fly-back (Cases 11 & 2). Blue indicates a 'productive' energy usage, whereas red indicates energy 'wastage'. Negative energy indicates energy being supplied.	163
7.3	Comparison of key trajectory parameters with variation in the maximum dynamic pressure of the scramjet accelerator, with fly-back (Case 12).	166
7.4	Comparison of key trajectory parameters with variation in the drag of the scramjet accelerator, with fly-back (Case 13).	168
7.5	Comparison of key trajectory parameters with variation in the specific impulse of the C-REST engines, with fly-back (Case 14).	169
7.6	Comparison of key trajectory parameters with variation in the structural mass of the scramjet accelerator, with fly-back (Case 15).	171
7.7	Comparison of key trajectory parameters with variation in the fuel mass of the scramjet accelerator, with fly-back (Case 16).	172

7.8	Comparison of key trajectory parameters with variation in the mass of the third stage, with fly-back (Case 17)	173
7.9	Comparison of key trajectory parameters with variation in the specific impulse of the third stage, with fly-back (Case 18)	175
B.1	The uncertainty margins associated with the aerodynamic and propulsive modelling of The SPARTAN.	224
C.1	Optimisation setup of the Brachistochrone problem.	228
E.1	A summary of key results from the maximum payload-to-orbit trajectory, constrained to 50kPa between Mach numbers 6 to 8.	246
E.2	A summary of key trajectory parameters of the maximum payload-to-orbit trajectory launched in a southerly direction.	248
G.1	Summary of key trajectory parameters with SPARTAN viscous drag variation.	292

CHAPTER 1

INTRODUCTION

I need to make it really clear that this work essentially sits before a detailed design optimisation, determining and analysis the mission profile in order to make informed decisions in the next design iterations

I should make a point that the sensitivity analysis is a significant contribution

I should make it very clear that I want to do this without the hard limits of separation point limitations

"This work is intended as a step in the development process of rocket-scramjet-rocket launch systems, informing future design studies by calculating and investigating the maximum payload-to-orbit optimised trajectory of a representative launch system. "

XXX Plug this in this section? This work aims to expand our knowledge on the operation of airbreathing launch systems, by developing a trajectory for a rocket-scramjet-rocket small satellite launch system, of a design based on The SPARTAN launch system under development by The University of Queensland and Hypersonix. This optimal trajectory profile is investigated to give insights into the trade-offs between the rocket and airbreathing stages that are unique to this type of launch system. This manner of optimal trajectory analysis allows for generalities to be made about the nature of the trajectory shape, and for the understanding of the performance of this type of launch system to be improved. This trajectory analysis is intended to both aid in the ongoing design process of multi-stage launchers, by characterising the performance needs of a rocket-scramjet-rocket launch system throughout its trajectory, as well as to stand on its own merit by indicating the best possible trajectory shape for this type of launch system.

In recent years, the space sector has seen a significant shift in the paradigm of space launch system design. The sector has moved towards privatisation, with new and innovative launch systems competing to offer the most cost-efficient and reliable launches. The sector has also seen a split between those who produce large satellite launchers and those who produce small satellite launchers.

CHAPTER 1. INTRODUCTION

For large payload launchers, reusability is a major focus in the design of new launch systems, with the purpose of making a launch system cost efficient over multiple launches[5]. For small payload launchers, reusability is more complex than for large launchers, as the additional systems necessary for reusability add a larger fraction of system mass, and require a proportionally larger fuel mass. Consequently, the focus of small launch system design is currently on producing expendable launch systems as cheaply and efficiently as possible, using state of the art technologies such as 3D printing to expedite the process and minimise cost[6]. However, if reusability is able to be successfully integrated into small launch system design, it has the potential to increase the cost efficiency and launch flexibility, potentially opening up the small satellite market significantly.

A potential candidate for integrating reusability into small satellite launch systems is the use of airbreathing engines[7, 8]. Airbreathing engines produce higher specific impulse than rockets, and do not require oxidiser to be carried on-board a launch vehicle[9]. The higher efficiency and reduced propellant mass of airbreathing vehicles allows the additional mass of the systems necessary for reusability to be mitigated[10]. An airbreathing vehicle can be designed in a similar fashion to a conventional aircraft, with wings, stabilisers and ailerons[11, 12]. A vehicle designed in this fashion has a high lift-to-drag ratio, and good manoeuvrability, allowing for a return flight and landing on a conventional landing strip[12]. This style of return removes the need for transport, enabling a fast turn-around and cost-efficient re-use.

The primary airbreathing engines in consideration for launch vehicles are ramjet and scramjet engines[13]. These engines offer good efficiency and have operational regimes that allow them to effectively accelerate a launch vehicle over a range of Mach numbers. Ramjets and scramjets rely on the high velocity of the aircraft to compress the flow of air entering the engine before combustion. Ramjets slow the air to subsonic speeds before combustion and are limited to operation at low Mach numbers, whereas scramjets keep the flow supersonic throughout, and operate within the hypersonic regime, above Mach 5. These engines have limited operational regimes, and require atmospheric flight in order to take oxidiser from the air. These operational constraints mean that a launch system cannot be solely powered by airbreathing engines. Rocket power is necessary for at least the exoatmospheric portion of the trajectory. As a result, the designs of airbreathing launch systems require rocket stages, usually separated into multiple stages to increase weight efficiency[7]. If a scramjet engine is used as the airbreathing engine of the launch system, rocket power is also desirable for accelerating scramjet accelerator to minimum operational speed, as the alternative is using turbojets and ramjets sequentially[7], which is weight and cost intensive.

Calculating a suitable trajectory for an airbreathing launch system is an integral part of the preliminary vehicle and mission design process. A trajectory must be calculated that allows the launch system to achieve its objective of placing a payload into orbit, while recovering any reusable stages. Ideally, the calculated trajectory will achieve the maximum possible payload-to-orbit, while adhering to the structural, heating and propulsive limitations of the vehicle. The trajectory design for a partially-

airbreathing launch system is complex and requires consideration of each of the individual stages in order to maximise the performance of the launch system, and consequently, its cost efficiency. The airbreathing engines of a ramjet or scramjet-powered stage require high dynamic pressure to operate effectively, and airbreathing stages are generally designed for high lift-to-drag. Conversely, rocket-powered stages operate more efficiently at higher altitude, and are generally designed for weight and cost efficiency. For these launch systems, the various stages and engines involved during launch require trade-offs in engine efficiency and thrust generation, stage mass, and vehicle aerodynamics. These factors require the launch trajectory of the system to be thoroughly simulated and optimised, to ensure that the launch vehicle is operating effectively.

Optimal control theory is a general set of techniques which find a control law to maximise a given metric of a system, subject to a set of constraints[14, 15]. Optimal control theory can be used to calculate the optimised trajectory profile for a launch vehicle in a robust and computationally efficient manner, allowing a trajectory to be calculated in which the flight path of each individual stage is considered simultaneously to produce a maximum-payload trajectory[15]. Optimal control is able to produce an optimised trajectory which satisfies the specific structural and flight constraints of the vehicle being simulated, allowing the physical limitations of the vehicle, such as heating and structural loading limits, to be imposed[15]. These constraints also allow any necessary mission conditions to be established, such as reaching orbital velocity and achieving fly-back. An optimal trajectory calculated for multiple launch vehicle stages simultaneously, without predispositions, can offer valuable insights into the performance of a launch vehicle, and drive future design decisions. This concurrent optimisation of multiple stages is particularly important for launch systems incorporating airbreathing engines, where the performance and operational requirements of each stage are significantly different.

This study applies optimal control theory to a three stage rocket-scramjet-rocket launch system being developed by The University of Queensland. The second stage of this system is a scramjet-powered accelerator, designated the SPARTAN[12]. This launch system is designed to be partially reusable, with at least the second stage scramjet vehicle flying back to the initial launch site, as well as possibly the first stage booster[12] although this is beyond the scope of this study. In previous studies it has been assumed that by maximising the performance of the SPARTAN, that the performance of the launch system is also maximised[12]. The trajectory of the launch system has been designed around the SPARTAN flying at its maximum dynamic pressure, and all other trajectory stages have conformed to this assumption. However, these studies did not consider the interaction between stages, or the fly-back of the SPARTAN. This study will develop trajectory planning tools for partially-airbreathing launch systems, and calculate an optimised launch trajectory for the rocket-scramjet-rocket system incorporating the SPARTAN. This optimised trajectory will be calculated with the aim of producing an optimal trajectory profile which may be applied to any multi-stage rocket-airbreathing-rocket system for delivering small satellites to Earth orbit. The impact of the fly-back of the scramjet stage on the optimised trajectory will be studied, and the ability of the rocket-scramjet-rocket system to effectively

deliver small payloads to orbit and return the scramjet stage to its initial launch site will be assessed.



Figure 1.1: The SPARTAN scramjet-powered accelerator[16].

1.1 Research aims

The aim of this work is to design the trajectory of a rocket-scramjet-rocket small satellite launch system. The purpose of this optimised trajectory is to maximise the payload-to-orbit capabilities of the launch system, thereby also maximising the cost efficiency of the system. The optimal trajectory will be utilised to assess the feasibility of return flight, as well as to determine the impact of key vehicle design parameters on the performance of the launch system.

These aims will be achieved by addressing the following objectives:

1. *Development of a detailed design and aerodynamic simulation for a rocket-scramjet-rocket launch system.*

A detailed launch system design and robust dynamic simulation are required in order for optimal control to be applied to a launch system. The design must be representative of a standard rocket-scramjet-rocket launch system for the optimal trajectory results to be generally applicable. The dynamic simulation must be accurate and robust in order for the optimised trajectory to be meaningful.

2. *Calculation of the maximum payload-to-orbit trajectory for a rocket-scramjet-rocket launch system using optimal control, with and without fly-back.*

The optimal trajectory shape of a multi-stage rocket-scramjet-rocket system is sensitive to the design and aerodynamic characteristics of each stage, and cannot be easily assumed. The use of

optimal control techniques allows a maximum-payload trajectory to be calculated with few assumptions as to the general shape of the trajectory. The inclusion of the fly-back of the scramjet stage in the trajectory optimisation allows the impact of the fly-back to be minimised.

3. *Analysis of the sensitivity of the maximum payload-to-orbit trajectory to variations in key design parameters of the launch system*

The optimal trajectory shape and maximum payload-to-orbit are dependent on the design of the launch system. Assessing the sensitivity of the optimised trajectory shape and payload-to-orbit to key aerodynamic and propulsive properties allows the relative impacts of various design parameters to be calculated and contrasted, and for the optimal trajectory shape to be investigated.

1.2 Thesis Outline and Contributions

XXX Update

Chapter 2 - Literature Review

A review of literature related to the various aspects of this study is presented. The theory behind scramjet propulsion is outlined, followed by a background of reusable and small satellite launch systems. A review of the trajectories of partially-airbreathing launch systems is presented, comparing the optimised trajectories of various conceptual vehicles. An overview of optimal control techniques is presented, with particular emphasis on the pseudospectral method of solving optimal control problems, which is employed within this study. Lastly, an overview of the optimal control and aerodynamic solvers that are used in this study is presented.

Chapter 3 - Launch Vehicle Design and Simulation

The design, aerodynamics and engine models of all three stages are detailed. The SPARTAN scramjet-powered stage is presented first, followed by the first and third stages. The design of each stage is shown, along with sizing and mass breakdowns. The propulsion model used for each stage is detailed, along with the modelling and interpolation schemes used. The aerodynamic characteristics and simulation methodology of each stage is presented, and the process for trimming each vehicle is specified.

Chapter 4 - LODESTAR

The method used for the simulation and optimisation of the trajectory is presented, including the details of the trajectory analysis program, LODESTAR, which has been developed for this study. The specifics of the optimal control methodology are presented. The simulation methodology is detailed, along with the construction of the optimal control simulation for the mission used in this study. The specific set-up of the optimal control program is detailed for each trajectory stage, specifying the costs and constraints which drive the optimal control solver. Finally, the methods for validating the final solutions are specified.

Chapter 5 - Optimised Ascent Trajectory

Optimised trajectories, designed using LODESTAR, are presented. A trajectory is designed in which the SPARTAN flies at a constant dynamic pressure, for comparison purposes. A maximum payload-to-orbit trajectory is created and it is found that an increase in altitude at the stage separation points significantly improves payload-to-orbit. This trajectory is compared and contrasted to the constant dynamic pressure trajectory to determine the sources of the performance increase. Key vehicle design

parameters are varied. The trends in maximised payload-to-orbit and trajectory shape are analysed to study the relative impact of the design parameters on the performance of the launch system.

Chapter 6 - Optimised Trajectory Including Fly-Back

The trajectory of the launch system is optimised for maximum payload-to-orbit, including the fly-back of the SPARTAN to its initial launch location. It is found to be necessary to reignite the scramjet engines during the return flight of the SPARTAN to achieve fly-back. The SPARTAN is found to bank during acceleration to lessen the fuel consumed during the return flight. The trajectories with, and without, fly-back are compared to determine the impact of SPARTAN fly-back on the performance of the launch system. In a similar fashion to Chapter 5, the effects of key vehicle parameters on the optimised trajectory are studied. The sensitivity of the optimised trajectory and payload-to-orbit are analysed, with emphasis on how the fly-back trajectory is affected by the varied vehicle parameters.

Conclusions and Recommendations

The body of this thesis concludes by summarising the most significant findings from this work. Recommendations for future work are made.

CHAPTER 2

BACKGROUND

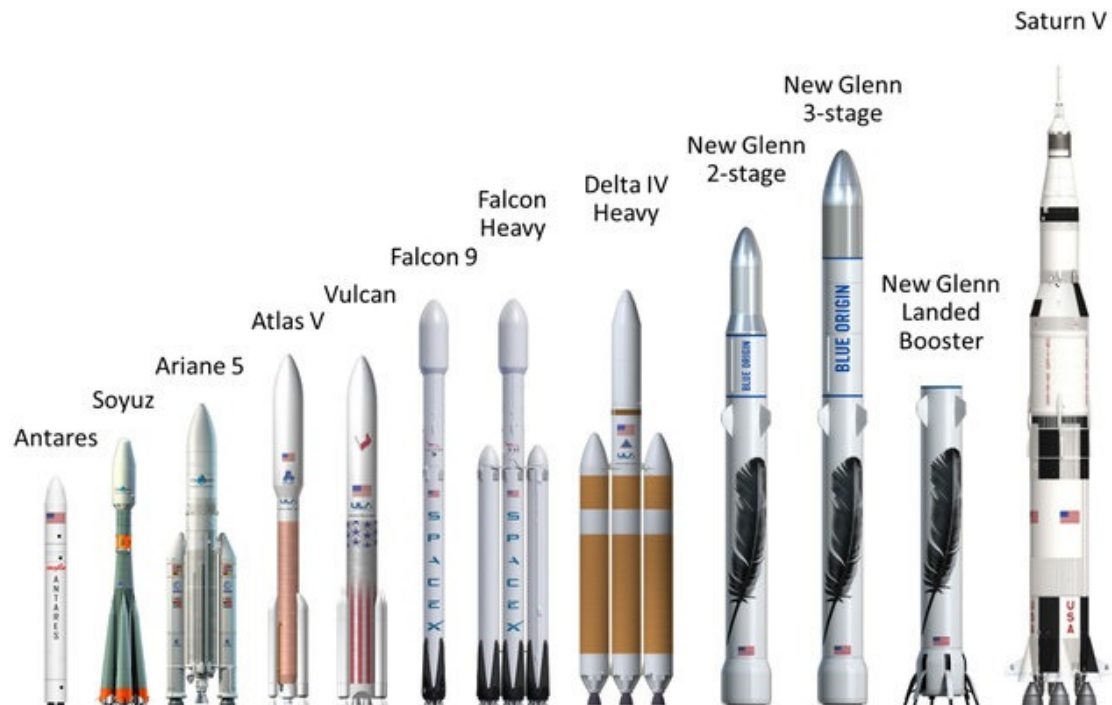


Figure 2.1: Comparison of Blue Origin and SpaceX partially-reusable launch systems with existing and historic launch systems[17].

Launch system technologies have progressed rapidly over the last 60 years. From the early vehicles based on intercontinental ballistic missile technology such as the Thor based launch systems, capable of launching 40-400kg to LEO in the 1960s, to the more modern Atlas V based systems of the 2000s capable of launching 9750-18500kg to LEO[18]. The materials, propulsion technology, aerodynamics and guidance algorithms have all improved significantly, enabling rockets to become

CHAPTER 2. BACKGROUND

more efficient, cheaper to produce, and more reliable. As the demand for satellite launches grows, and the cost of development of launchers becomes cheaper, the potential for profiting from space launches increases. This has driven a large portion of the space flight industry to move towards privatisation, with a heavy focus on reusable technology.

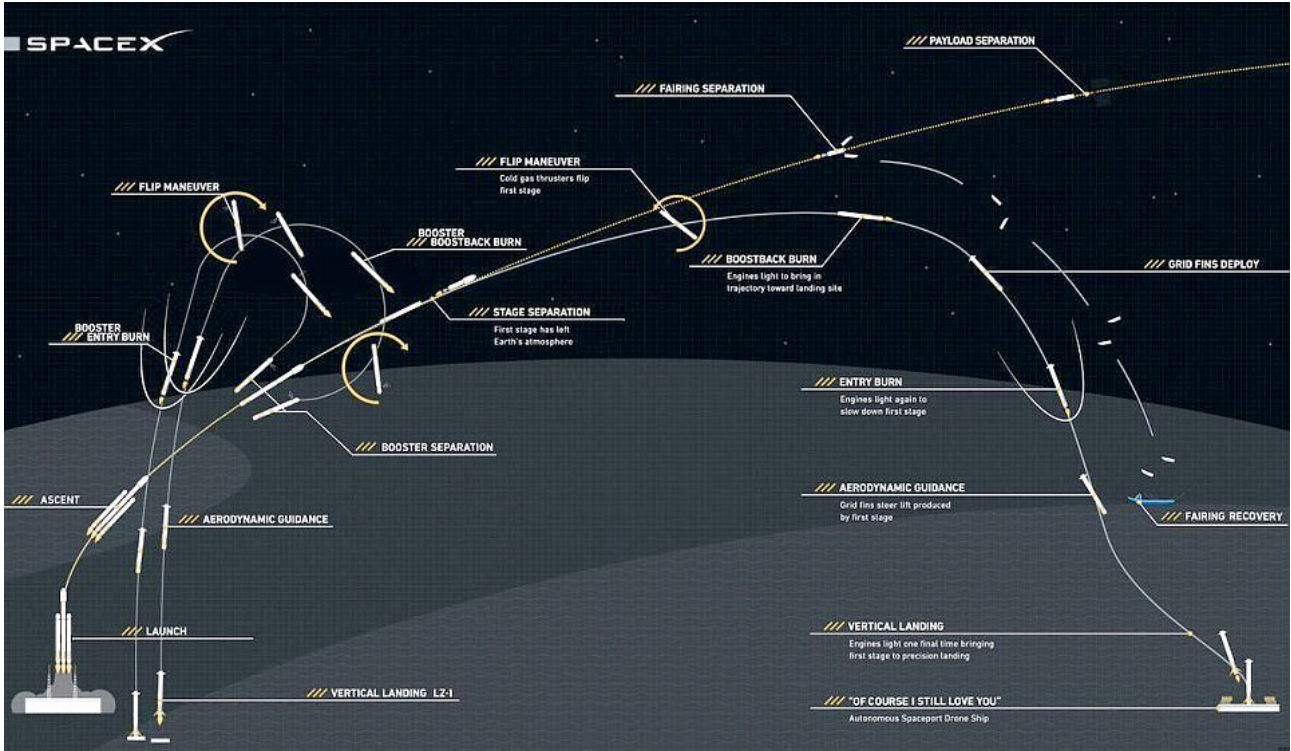


Figure 2.2: The trajectory of the Falcon Heavy[19].

Reusable launch technology has been possible for many years, in the form of the space shuttle. However, the space shuttle was weighed down by large launch costs and operational complexity, and was not a commercial success[20]. Recently, reusable launchers have become the focus of many of the largest private launch companies, as reusability becomes more achievable due to technological advances[21, 22]. The SpaceX Falcon 9 and Falcon Heavy have been demonstrated on multiple occasions, landing booster stages successfully, and re-flying reused boosters multiple times[21]. In the near future the Blue Origin New Glenn is planned[21], with potentially the Airbus Adeline to follow (to be used on the Ariane 6)[23]. The Falcon and New Glenn launchers are large rockets, and are shown in Figure 2.1 in a size comparison with other, expendable rocket systems, including the Ariane 5, which is projected to be similarly sized to the Ariane 6.

The purpose of reusing launch vehicles is to reduce the cost-over-time of the reused components drastically, which subsequently allows the cost of individual launches to be reduced[25]. Reducing costs lowers the barrier of entry for space launches, potentially improving the diversity of space-based enterprises. Reusing launch system components also allows faster turnaround times for launches, as refurbishment of stages is much faster than manufacturing stages from scratch. Reduced turnaround

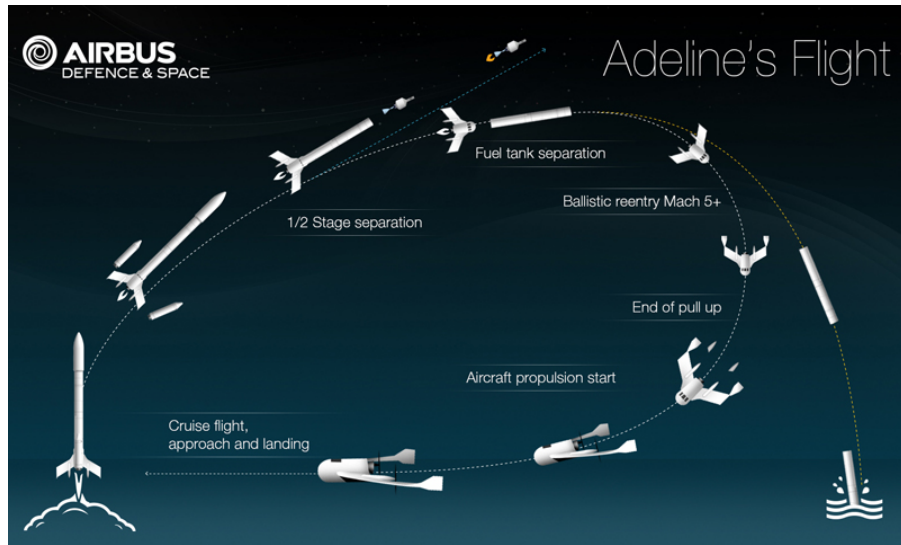


Figure 2.3: The trajectory of the Ariane featuring Adeline[24].

times are key for improving mission scheduling, allowing satellites to be launched more rapidly, on a more flexible time frame. For a launch vehicle to be reusable, it must necessarily have the ability to come back to Earth safely, without damage to major system components. In addition, it is preferable for the vehicle to return to its initial launch site, to reduce the cost and time necessary for transport. The trajectories of the Falcon Heavy and Adeline are shown in Figures 2.2 and 2.3, illustrating two radically different approaches to reusability; the exoatmospheric manoeuvre and booster-deceleration of the Falcon; and the in-atmospheric fly-back of the Adeline, which only recovers the engine component of the system. While these reusability approaches use different technologies, they are aiming to achieve the same thing: the recovery of a significant portion of the launch system, with as much of the launch system as possible returned to the initial launch location. These return flights require the addition of system components which allow the reusable stage to fly to a specified landing point. Control surfaces[26], structural components[27], additional fuel[27], and in the case of the Adeline, additional engines[23], must be incorporated within the reusable launch vehicle designs. The additional weight that these components contribute further increases the fuel and structural mass necessary to initially accelerate the reusable stage. The impact of reusability on the mass and cost of the vehicle is minimised when the velocity at the initiation of the return trajectory is decreased. Because of this mass increase on any stage which is to be designed to be reusable, most current reusable launch vehicle designs include only reusable first stages, with later stages being expendable.

2.1 Small Satellite Launchers

The vast improvements in computational technologies in recent years have allowed satellites to decrease in size and cost to a large degree. These factors have lowered the barrier of entry into small

Launcher	Company	Country	Payload Capacity	Cost/Kg (USD)	Availability	Stages & Propulsion	Reusability
Electron[29]	RocketLab	NZ/USA	150Kg to SSO	\$32,600	Available	Rocket-rocket	No
Bloostar[30]	Zero2Infinity	Spain	100kg to SSO	\$40,000	-	Balloon-rocket-rocket-rocket	No
Eris[28]	Gilmour Space Technologies	Aus/SG	380kg to LEO	\$23,000-38,000	Q4 2020		No
Intrepid-1[31]	Rocket Crafters	USA	376kg to SSO	\$23,936	Q1 2019	Rocket-rocket	No
KZ-1A[32]	CASIC	China	250kg to SSO	-	-	Rocket-rocket	No
Vector-H[33]	Vector Space Systems	USA	160kg to LEO	\$21,875	2018	Rocket-Rocket-(Third rocket optional)	No
SMILE[34]	NLR	EU	50kg	<\$50,000	-	-	-
Firefly α [35]	Firefly Aerospace	USA	630kg to SSO	-	2019	Rocket-Rocket	No
LauncherOne[36]	Virgin Orbit	UK	300kg to SSO	\$33,000	-	Aircraft-rocket-rocket	Aircraft
XS-1[37]	Boeing	USA	-	-	-	-	First Stage
500R[38]	Orbital Access	UK	500kg to SSO	-	-	Aircraft-Rocket	Fully Reusable

Table 2.1: A selection of the small satellite launchers which are operational or in development.

satellite manufacturing significantly, driving a surge in the demand for small satellite launches. Many private and public companies are currently developing small satellite launchers, that will allow small satellites to be launched into bespoke orbits on schedules determined by the customer[5]. The details of a selection of the most promising or innovative of the small satellite launchers currently in active development is shown in Table 2.1. Many of these launchers are projected to be available within the next few years, and will offer cost-per-kg comparable to piggybacking on larger launches. These small satellite launch systems are mostly expendable, aiming to reduce costs by creating a launch system which is as cost-efficient as possible to produce and launch[6]. This often entails making use of conventional, well-tested designs, combined with state of the art manufacturing techniques, such as 3-D printing[6, 28]. This method allows for rapid development, although it has an intrinsic cost limit due to the requirement of manufacturing a new launch system for each launch.

If small satellite systems are able to be designed to be reusable, the cost of launch would be able to be brought down further. However, designing a small satellite for reusability is more complex than for a larger rocket system. The systems used to manoeuvre exoatmospherically and decelerate like the Falcon or New Glenn or fly-back like the Adeline take a relatively higher mass margin as the size of the launcher decreases, in turn increasing the mass, and decreasing the cost efficiency of the launcher. If a cost efficient, reusable design for a small satellite launcher is to be produced, it is likely that a technology must be developed that is specifically geared towards small satellite launch. One of the most promising technologies currently under development, that may enable reusable small satellite launch systems, is high speed airbreathing engines[39], in particular the hypersonic scramjet engine.

2.2 Scramjets

-XXX have something about how sensitive scramjet engines are

A Scramjet, or supersonic combustion ramjet, is an airbreathing engine design which combusts air at supersonic speeds and is capable of high Mach number operation. Across their operating range, scramjets offer much higher specific impulse than rockets, the only other propulsion system capable of operating efficiently at hypersonic speeds[40, 41]. Scramjets compress air without moving parts, using geometry changes within the engine[42], as well as on the forebody of the vehicle to create inlet shocks which provide the compression required for combustion[43]. After combustion, the combustion products are expanded through a thrust nozzle, schematically shown in Figure 2.4. This is similar in operation to a ramjet engine, though a scramjet does not generate a normal shock, allowing supersonic air to enter the combustor. Maintaining supersonic speeds throughout the engine allows scramjets to operate efficiently at Mach numbers of 5 and greater. Scramjets were proposed in the 1940's[44] and found to be capable of positive net thrust in 1993[45], but have yet to be developed to a level which would allow for commercial application. Though scramjets are still in-development, the potential advantages which they offer over rockets for certain applications are driving their devel-

opment in a number of institutions[46].

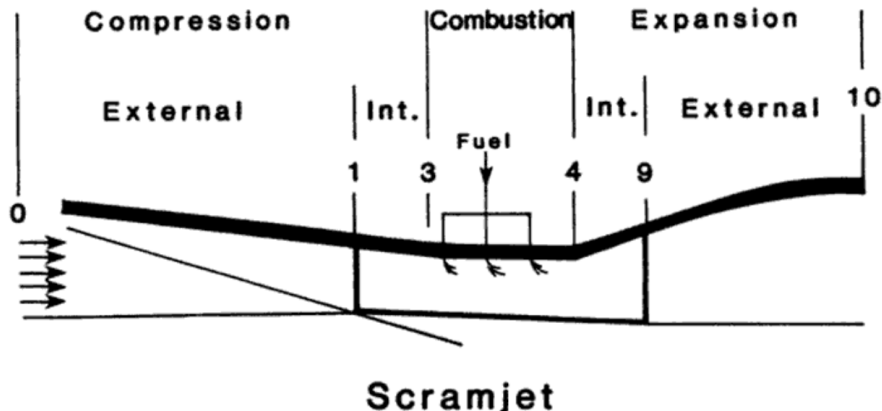


Figure 2.4: A simple schematic of a scramjet engine[47].

Scramjet engines are suitable for a number of applications where sustained flight or acceleration is desired at high Mach numbers. The high efficiency of scramjet engines means that significantly less propellant (fuel + oxidiser) is used during flight compared to rocket engines, and consequently, that a much smaller fraction of a scramjet-powered vehicle consists of propellant mass[10]. The smaller fuel mass fraction of a vehicle powered by scramjet engines mitigates the mass of the vehicle systems, allowing features such as wings, control surfaces, landing gear, and passenger transport capabilities to be included in the vehicle design[10].

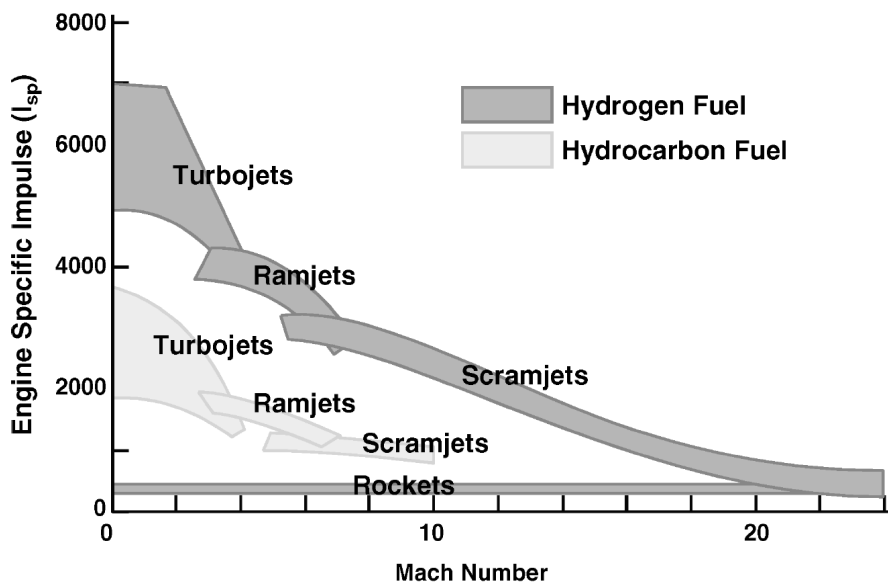


Figure 2.5: Characteristic performance for airbreathing and rocket engines with Mach number[48].

Theoretically, the operable range of scramjets is wide[49]; the specific impulse of a scramjet decreases with velocity, until it is equal to rockets around Mach 19[48], as shown in Figure 2.5.

However, in practical designs, the operating range for a scramjet engine is far more limited. For a fixed geometry scramjet, the operable region is constrained by the geometries of the forebody of the vehicle, the inlet, and the combustor of the scramjet engine[9]. The Mach number range of a scramjet engine varies by design, but Mach number ranges of 5-10[12], 7-11[50] and 6-10[51] have been suggested as appropriate operable regimes for scramjet-powered launch vehicles. The operable range of scramjet engines can be improved with mechanisms to vary the geometry of the inlet during flight[52]. However, the systems necessary for variable geometry inlets add weight and complexity to the scramjet engine, and can be detrimental to overall system performance[9].

The inclusion of scramjet engines for high efficiency operation in the hypersonic regime may be considerably advantageous for small satellite launch systems. However, the incorporation of these engines within a launch vehicle requires significant additional design complexity over tradition all-rocket systems, due to their unique operational constraint: the requirement to fly in-atmosphere for long periods, at hypersonic speeds. This means that a launch system incorporating scramjet engines must be designed to fly aerodynamically, balancing lift and drag with thrust and aerodynamic control. This is a significantly different design philosophy when compared to traditional all-rocket launch systems, that generally want to exit the atmosphere as quickly as possible, and minimise drag losses while doing so. Because of this significant difference in operation, the designs of airbreathing launch vehicles are likely to be radically different from traditional rocket systems. Novel designs must be developed for airbreathing launch systems, that take advantage of the unique advantages offered by airbreathing engines, while overcoming the challenges that they introduce.

2.3 The Launch System Design Process

The design of any launch system is a complex, multi-faceted process, that involves many areas of engineering and scientific expertise. Developing a trajectory for a launch system is simply a part of this process, although it is an integral step in the early launch vehicle design. The analysis of the trajectory of a launch system enables the designers to understand the performance characteristics of the launch system, and drives design decisions that are made throughout the development process.

Figure 2.6 illustrates the general design process flow for a launch system as defined by NASA[53], in which the design stages involve a repeated iterative process between the overall launch system design and compartmentalised design tasks. This compartmentalisation takes place firstly by separating the launch system into its hardware and software subsystems, and then into general areas that define the specifications of the subsystem design (design functions). These areas include;

- aerodynamics;
- trajectory, guidance and navigation;

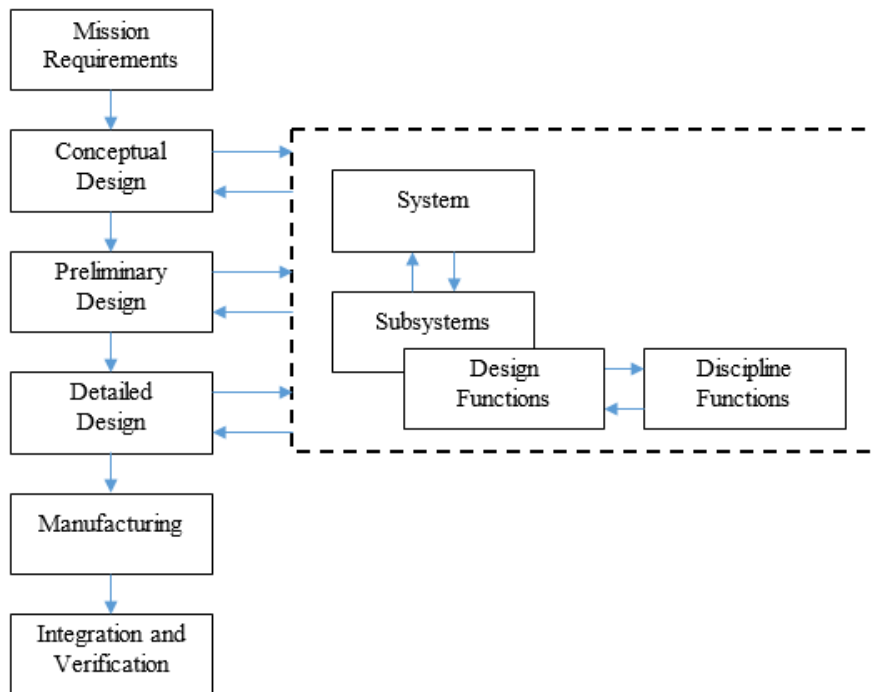


Figure 2.6: The general design process flow for a launch vehicle, adapted from Blair et al[53]

- control;
- structures;
- thermal;
- propulsion;
- avionics;
- materials;
- and manufacturing,

among others[53]. The design is then further compartmentalised into pertinent areas of specific speciality and expertise (discipline functions) that defines the problems that must be solved, and skills that are necessary for low level design. This process of compartmentalisation allows the effort associated with launch system design to be broken down into manageable amounts, and enables the efficient utilisation of discipline and industrial specialities. The design process is a continuous effort to compartmentalise the work that must be undertaken into manageable tasks, and then to reintegrate and synthesise the results in order to converge on a design that is able to satisfy the overarching mission requirements[53]. The trajectory design is simply one part of this design process, that can have significantly different levels of impact on the early design stages depending on the type of launcher being designed.

2.3. THE LAUNCH SYSTEM DESIGN PROCESS

The design of a traditional all-rocket launch system may use quite simplified trajectory models in the early stages, because the general shape of rocket launch system trajectories are well-known and relatively easily modelled. The primary goals of the trajectory of a rocket-powered launch system are to minimise drag while not exceeding structural and thermal limits, and in general this results in a vertically-launched pitching trajectory, that exits the atmosphere as rapidly as possible while managing velocity at points of maximum structural and thermal stress.

The trajectory of an airbreathing launch system is much more complex, because there is heavy dependencies and trade-offs between the way in which an airbreathing launch system is flown, and its performance characteristics. Relying on atmospheric air for oxidiser means that an airbreathing launch system requires sustained atmospheric flight, at relatively high densities to allow for efficient operation of the airbreathing engines. This atmospheric flight requires aircraft-style designs for control and stability, and results in complex trade-offs between the performance of the airbreathing engines, and the structural and thermal limitations of each stage. In addition, there is trade-offs between the performance of the various engines that are utilised by airbreathing launch systems, which generally mix airbreathing and rocket engines that have significantly different performance regimes. These trade-offs are specific to the types of engines and number of stages being employed by the launch system, and are closely dependent on the trajectory being flown. The determination of the ideal launch trajectory of an airbreathing launch system is an integral step in the early design process, allowing for the design of the launcher and its subsystems to be tailored to capitalise on the ideal flight profile, and for significant performance drivers to be identified early on. This is particularly true because many of the subsystems and technologies necessary to achieve airbreathing space access are in development at an academic level, and advances are necessary in multiple fields before the flight of an airbreathing launch vehicle becomes a reality. The investigation of the trajectory of an airbreathing launch system gives key insights into the design requirements of the launcher and its subsystems, that can drive academic study on the subsystems of airbreathing launchers, such as their propulsion and thermal protection systems, as well as their overall designs.

XXX here I need to include some more specifics - from ingos overall comments 1) that can be linked to the three stage launch system section of lit review

CHAPTER 3

LITERATURE REVIEW

The study of airbreathing access-to-space systems has been undertaken in some form since the early days of space flight. The prospect of the efficient, cost effective, and reusable space access that airbreathing launch may provide is enticing, and many man-hours and billions of dollars has been expended researching airbreathing launch vehicles. However, airbreathing launch is yet to be realised, due to the large scientific and engineering challenges involved in sending an object to space using airbreathing propulsion. Research is ongoing across many fields and disciplines to develop the designs of airbreathing launch vehicles, including the designs of subsystems such as engines, thermal protection systems, and control systems that can cope with the unique requirements of sustained hypersonic flight. The design of an airbreathing launch system must be determined with careful consideration of the trajectory that the launch system flies to orbit, because the trajectory of a launch system determines the structural and heating loads that are experienced, as well as the necessary control strategy that must be employed to achieve orbit. Accurate trajectory models are required to determine the performance metrics of the launch system, and these initial flight paths are used to guide the design of the launch system.

This section covers the literature available in the areas that are key to developing and analysing the trajectory for a rocket-scramjet-rocket launch system. Firstly, a study is conducted on the airbreathing launch systems that have previously been designed and analysed, along with an analysis of the trajectories of these launch systems that may offer valuable insights into the operations of rocket-scramjet-rocket launch systems. Of particular interest are the trajectories of multi-stage airbreathing launch systems, that give insights into the trajectory features that arise from effects of stage separations. After this, an overview is given of the optimal control methods that may be used to develop efficient trajectories, along with their applicability to launch vehicle trajectories. Lastly, a study is presented on the methods of aerodynamic modelling that may be used to develop dynamic models of the launch system, along with a focussed discussion on the Cart3D program, that is used in this work.

3.1 Hypersonic Airbreathing Launch Systems and Trajectories

Airbreathing access-to-space systems have been investigated in various forms including single-stage, two-stage, and three-stage designs. Of these design forms, single-stage and two-stage designs are by far the most common, with very few three-stage designs having been considered to date. This is partly due to the fact that nearly all of the airbreathing launch systems that have been designed are large launchers, designed to launch payloads on the order of thousands of kilograms to orbit. In large launchers, the additional structural mass that results from the addition of engines or subsystems can be mitigated more effectively than for small launcher form factors. For small satellite launchers, the mass penalties of the systems necessary for airbreathing launch and reusability become more significant, likely necessitating the division of the launcher into separate stages. For dedicated small satellite launch, which has become economically feasible only in recent years, a three-stage rocket-scramjet-rocket launcher system has been suggested as a feasible form factor for a small, airbreathing launcher[12].

For any airbreathing launch system, the design of a trajectory during the early design phases is particularly important. Airbreathing launch systems are typically designed using a combination of rocket and airbreathing engines, that have very different requirements for operation. Rocket engines in general perform well from atmospheric to vacuum conditions, while airbreathing engines require relatively high density air and sustained atmospheric flight for operation, which can cause the structural and thermal limits of the vehicle to come into play[12]. Figure 3.1 shows an example flight corridor for an airbreathing launch vehicle, illustrating the upper limits of dynamic pressure at which the structural limits of the launch vehicle are met, and the lower limit of dynamic pressure at which the airbreathing engines are no longer capable of operation. This brings unique complications, as sustained flight in-atmosphere requires a high lift coefficient and results in high structural and thermal loading over long periods, that must be considered during trajectory analysis. In addition, there are a number of design factors that must be considered during trajectory design including;

- the requirement for the airbreathing stages to fly in-atmosphere;
- the variable efficiency of the airbreathing engines;
- the relative efficiency of the different types of engines within the system;
- the aerodynamic performance of each vehicle or engine-mode of the system;
- and the structural limitations of the system.

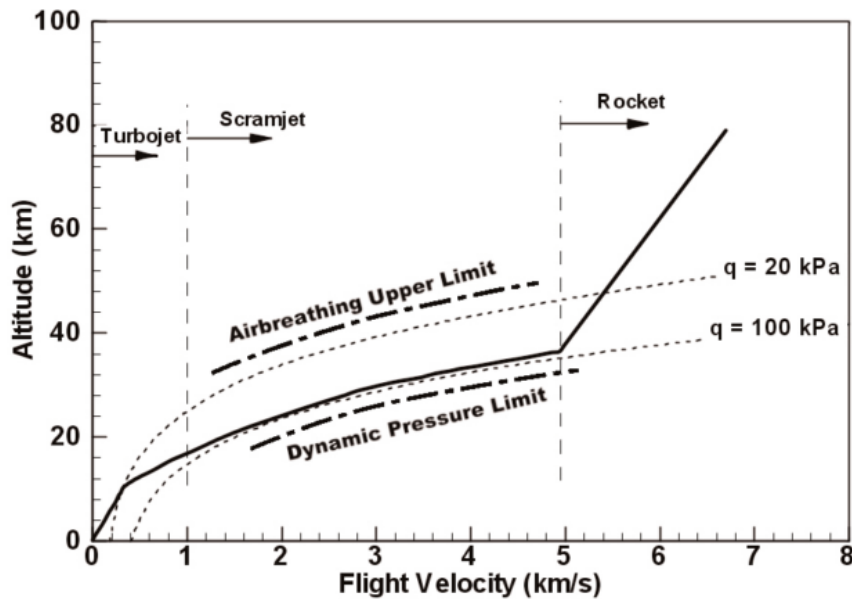
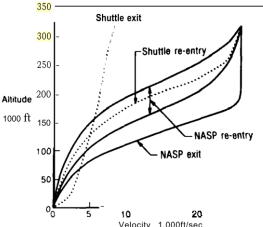
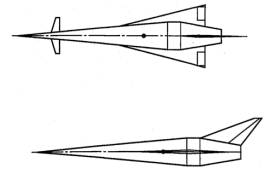
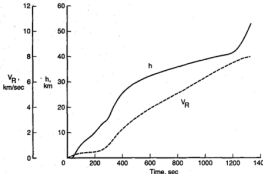


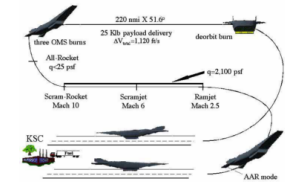
Figure 3.1: An example airbreathing flight corridor of an airbreathing launch vehicle[49].

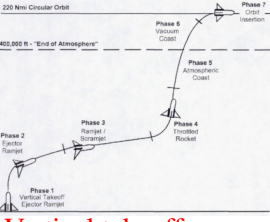
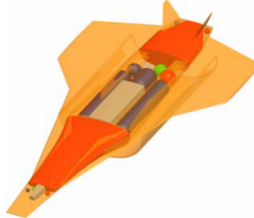
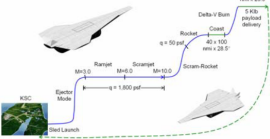
These factors cause trade-offs between the stages of the launch system[54], and limit the operational regime of the launch system.

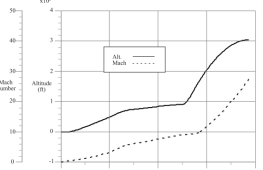
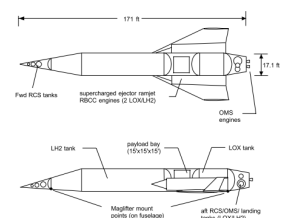
As well as complex trade-offs during ascent, the reduced fuel usage of airbreathing engines changes the mass distribution of airbreathing launch systems and generally have a high lift-to-drag ratio that allows for the fly-back and landing of some or all of the launch system in a similar manner to a conventional aircraft[12]. The return portion of the trajectory must be considered in the trajectory analysis and concurrent design for reusable launch systems, in order to develop a launch system design that is capable of being reused efficiently[55]. This brings additional considerations to the vehicle and trajectory design, because the vehicle must be designed to withstand the conditions of return as well as launch, and must be physically able to return and land at a suitable location[55]. The trajectory analysis of a reusable vehicle is particularly important, because the viability of returning the vehicle to a suitable landing location must be determined, and the impact of the return trajectory on the launch flight profile must be established. The fly-back can be a high-impact design driver, with the performance of the vehicle relying significantly on an efficient return flight[55, 56].

This study aims to understand the optimal trajectory of a rocket-scramjet-rocket multi-stage launch system, that may be considerably different to other configurations of airbreathing launchers. To this end, this section investigates the designs of all forms of airbreathing launch systems that have been developed, along with their trajectories. The manner in which the design and number of stages of the launch systems influences their trajectories is studied, allowing for some key features of airbreathing launch system trajectories to be identified.

Launcher	Design	Trajectory
X-30 (NASP)[57] <p>Conceived as a technology demonstrator for the NASP program, the X-30 would have been the first airbreathing launch system to be operationally demonstrated, but its program was cancelled prematurely. Many important aspects of the X-30 have not been made public[57] and so details on this vehicle are incomplete.</p>	 <ul style="list-style-type: none"> · Designs studied with weights 'less than 200000lbs and greater than 300000lbs'[57] (90718.5 - 136077.7kg). · Powered by scramjets with reusable rocket engines or RBCC engines. 	 <ul style="list-style-type: none"> · Horizontal launch.
Langley Accelerator (NASP)[58–60] <p>Developed as a standardised vehicle for single-stage-to-orbit airbreathing launcher studies, the Langley Accelerator was not intended to be an operational concept. The version developed by Powell et al.[59] is presented here.</p>	 <ul style="list-style-type: none"> · Nominally 136079kg weight, 61m length. · Fully airbreathing in-atmosphere, rockets for circularisation. · Forward canards are deployed at subsonic speeds. 	 <ul style="list-style-type: none"> · Horizontally launched. · Maximum dynamic pressure reached as rapidly as possible. · A pull-up is performed under the power of the scramjet engines. · Coast phase after scramjet shutdown until circularisation by rocket engines.

HOTOL[61] <p>The British HOTOL concept was a single-stage-to-orbit spaceplane developed initially as a proof-of-concept study in 1982, but later courted to the ESA as a major project and refused. Funding was withdrawn in 1982 before development could commence.</p>	 <ul style="list-style-type: none"> · 7-10t to payload to orbit. · Length of 62m. · Powered by four Swallow engines, operating in airbreathing mode until 26km altitude, and rocket mode thereafter. 	<ul style="list-style-type: none"> · No detailed trajectory information is readily available.
ABLV-GT (Hyper-X)[51, 62] <p>The ABLV-GT was developed by Georgia Tech Space Systems Design Lab as an extension of the ABLV (airbreathing launch vehicle) design study performed by NASA, aiming to develop a conceptual design for a realistic launch vehicle. This vehicle has strong links to the Next Generation Launch Technology Program, a successor to the NASP program, which produced the X-43 test vehicle, the first demonstrator of scramjet operation in free-flight.</p>	 <ul style="list-style-type: none"> · X-43A shown as a representative vehicle shape. · 13520000lbs mass and 190.5ft length. · Powered by turboramjet & RBCC engines. 	 <ul style="list-style-type: none"> · Horizontal takeoff. · Maximum dynamic pressure flight during majority of ram/scramjet operation. · Pull-up under rocket-augmented scramjet power.

<p>GTX (Trailblazer)[63, 64]</p> <p>The GTX (formerly Trailblazer) was another offshoot of the ABLV program.</p>	 <ul style="list-style-type: none"> · 1252617lbs total mass, 263.5ft length. · 25000lbs payload. · Ramjet-scramjet-rocket propulsion. 	 <ul style="list-style-type: none"> · Vertical takeoff. · Flight at maximum dynamic pressure of 2000psfa (95.76kPa). · Pull-up occurs under scramjet power, when the maximum Mach limit of the scramjet is reached. · Rocket power is used to accelerate to orbit.
<p>Lazarus[65]</p> <p>The Lazarus concept was developed at the Georgia Institute of Technology Space Systems Design Lab, as an SSTO concept for medium size payload launch, with a secondary purpose of use as a global strike platform.</p>	 <ul style="list-style-type: none"> · 180000lbs (81646.6kg) gross weight, 102.8ft (31.3m) length. · 5000lbs (2268.0kg) Payload. · RBCC engines with high energy density material fuel. · A sled is used for takeoff, that provides fuel to the RBCC engines. 	 <ul style="list-style-type: none"> · Horizontal takeoff using sled. · Maximum dynamic pressure flight during air-breathing operation at 1800psf (86.2kPa). · At Mach 10 a pull-up is initiated using combined scramjet-rocket propulsion. · At the minimum operable conditions of the scramjet engines, the rocket takes over to accelerate to orbit. · Return trajectory is not considered.

<p>Hyperion[66]</p> <p>The Hyperion was developed by Georgia Tech Space Systems Design Lab, as an assessment of the 'Vision Vehicle' design class, solicited by NASA as part of the Advanced Reusable Technologies Program. Hyperion was conceptualised to assess whether RBCC propulsion and other advanced technologies can significantly reduce the cost of space access.</p>	 <ul style="list-style-type: none"> · 800700lbs (363191.4kg) gross weight, 179ft (54.6m) length. · 20000lbs (9071.8kg) of payload to LEO. · Powered by 5 RBCC engines, with return flight supplemented by low-thrust H2 ducted fans. 	 <ul style="list-style-type: none"> · Horizontal takeoff. · Flight at maximum dynamic pressure of 2000psf (95.76kPa) during airbreathing operation. · Pull-up during scramjet operation, with transition to rocket mode during pull-up. · No Return trajectory considered.
<p>Argus[67]</p> <p>The Hyperion was developed by Georgia Tech Space Systems Design Lab, in support of NASA's Highly Reusable Space Transportation study. The Argus was a conceptual design intended to be investigated and compared to other classes of launchers to determine cost effective long term solutions to space access.</p>	 <ul style="list-style-type: none"> · 597250lbs (270908.0kg) gross takeoff mass, 171ft (52.1m) length. · 20000lbs (9071.8kg) payload. · Initially accelerated along a maglifter track. Afterwards powered by two RBCC ejector-ramjet engines, with OMS thrusters used for circularisation and manoeuvring on-orbit. 	<ul style="list-style-type: none"> · Horizontal launch on maglifter track. · After launch, accelerated using ejector ramjet so that maximum dynamic pressure of 1500psf (71.8kPa) is reached at transition to fan-ramjet mode. · At Mach 6, transition to rocket mode occurs for acceleration to parking orbit.

3.1.1 Single Stage Airbreathing Launch Systems

A single stage launch system design aims to achieve space launch with only one vehicle, and generally no separation of mass until payload deployment. Table XXX summarises the recent single-stage-to-orbit airbreathing launchers that have been developed as detailed designs, along with their key design and trajectory features.

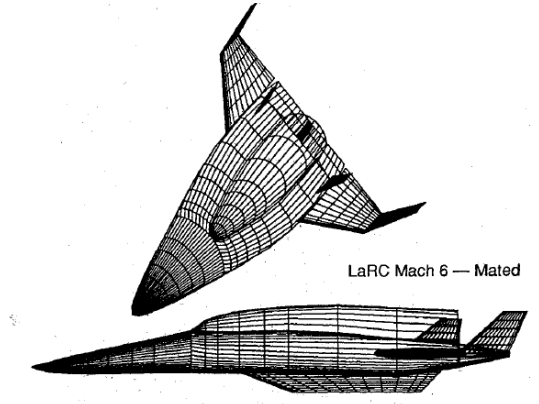
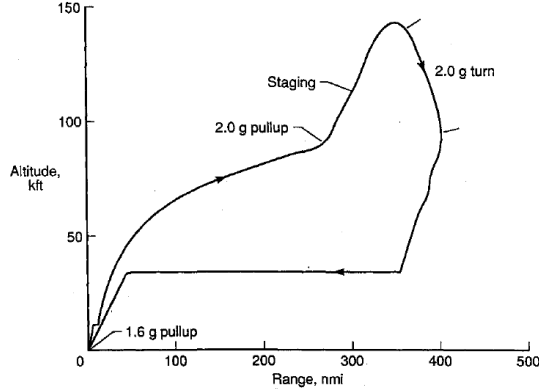
All of the single stage-to-orbit (SSTO) airbreathing launch vehicles that have been studied are designed to be fully reusable. Being fully reusable is the primary attraction of the SSTO spaceplane, and indeed is likely to be the only way in which a system of this type is able to be financially viable. The single-stage form factor is in general convenient for reusability, as the additional structural and subsystem complexity necessary to facilitate return is mitigated by having only one large vehicle. SSTO vehicles also have the advantage of not needing to stage, saving on the additional system weight and complexity required when staging in atmosphere. However, SSTO launch vehicles are required to accelerate the entire launch system to orbital or near-orbital speeds, and exit the atmosphere completely. This introduces significant complexity to the return flight and reuse of SSTO systems, which are required to re-enter the atmosphere at orbital speeds[57]. This reentry poses significant challenges to the thermal and structural protection and control subsystems of SSTO vehicles, particularly when a primary design driver is cost efficiency. Accelerating an entire launch system to orbit also results in a significant amount of 'dead-weight', ie. subsystems that are designed for use only in a specific part of a launch, that must nonetheless be transported to orbit and back. In particular for airbreathing SSTO systems, this 'dead-weight' derives from the need to carry multiple engines that are switched between during flight. This means that airbreathing SSTO launch systems are generally highly fuel efficient at all stages of flight, but carry heavy engines that are not used in all flight regimes. To mitigate this 'dead-weight', SSTO vehicles are generally powered by rocket-based combined cycle (RBCC) engines which are capable of operating in various airbreathing or air-assisted rocket modes using common engine components, sometimes augmented by turbojet engines for efficient power during launch or return flight. Despite this mitigation measure, the many subsystems required by SSTO launch systems are complex and heavy, and are likely to also be extremely costly. For this reason, all of the SSTO airbreathing launchers that have been investigated are designed for medium-to-large payload launch, and are large, heavy vehicles, with design profiles incorporating many aircraft-like features such as wings, tails and aerodynamic control surfaces.

Most SSTO airbreathing systems are designed to be horizontally launched, under turbojet or rocket-assisted power. The exception to this is the GTX, which launches vertically under rocket power[63, 64]. All of the SSTO vehicles examined follow a constant dynamic pressure trajectory during the majority of airbreathing hypersonic flight, with most vehicles performing a pull-up manoeuvre during airbreathing operation, before or during the transition to rocket-power. Constant dynamic pressure flight advantageous for an airbreathing accelerator due to the trade-off between

structural loading and engine performance[68]. As dynamic pressure increases so does the structural loading on the vehicle, however the performance of a ramjet or scramjet engine is directly reliant on dynamic pressure[68]. A constant dynamic pressure trajectory is viewed as being an acceptable compromise between these two factors when designing a launch vehicle, operating at the dynamic pressure limit of the launch vehicle. Although a constant dynamic pressure trajectory is likely to produce high efficiency flight for the high speed airbreathing portion of an ascent trajectory, there are a variety of factors that must be considered in designing the trajectory of a launch system. For example, a constant dynamic pressure flight may produce suboptimal conditions for the switch from airbreathing engines to rocket power for exoatmospheric flight, causing the pull-up manoeuvres that have been noted. At the end of airbreathing operation it is often more optimal for the vehicle to fly at less than maximum dynamic pressure for a time during airbreathing engine operation, allowing the trajectory angle and altitude to be raised before the rocket engines are powered-on. This trajectory shape trades off the performance of the airbreathing engines for altitude before the rocket engines are powered on fully, and has been shown to be the optimal trajectory throughout the studies of the vehicles covered in Table XXX[51, 59, 63–65, 69], as well as for generic trajectory optimisation studies that do not develop a detailed vehicle design[60, 69, 70]. A pull-up was found to be optimal for vehicles where the rocket engines are not ignited until circularization altitude[59, 60], vehicles where the rocket engine is ignited immediately after airbreathing engine cut-off[63, 64, 69] as well as for vehicles which operate in combined scramjet-rocket mode[51, 65]. For SSTO vehicles a pull-up manoeuvre is a trade-off between the altitude at airbreathing engine cut-off and the velocity achievable at cut-off. Due to the entire vehicle being lifted into orbit, this generally becomes a relatively simple problem of engine efficiency. The airbreathing engine is used for its high efficiency, until the dynamic pressure drops below the operable limit of the airbreathing engine, or until the thrust provided by the airbreathing engine is significantly counteracted by the effects of drag and gravity.

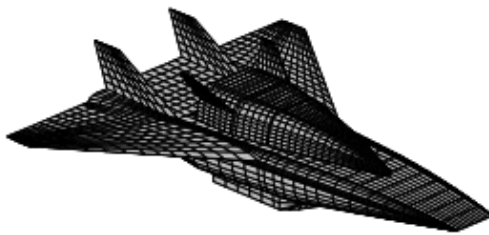
3.1.2 Two-Stage Launch Systems

The most studied alternative to single-stage-to-orbit for an airbreathing launch vehicle is the two-stage-to-orbit configuration. Table XXX provides a summary of the TSTO airbreathing launch systems that have gone through a detailed design process, along with their key design and trajectory features. The TSTO configuration generally separates the launch system into an airbreathing or airbreathing/rocket-powered 'booster' stage, and a rocket-powered 'orbiter' stage. This configuration allows for the separation of the booster stage after the airbreathing engines have ceased to be used. This separation removes a large fraction of the system mass, because airbreathing engines are generally complex and heavy systems. As a consequence of this mass reduction, the rocket engines used for the final acceleration to orbit may be considerably smaller, and therefore cheaper and lighter,

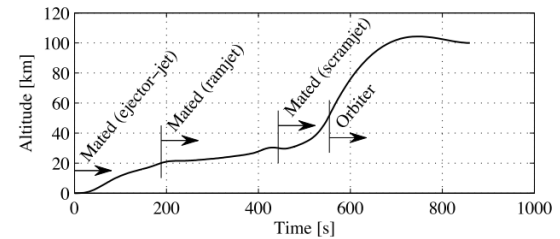
Launcher	Design	Trajectory
<p>LaRC Turboramjet[71]</p> <p>The LaRC boosters were developed by Wilhite et al.[71] in order to test the effects of staging Mach number on a two-stage system. These boosters were studied as part of the NASP program, and were intended only to be used as a representative vehicle for research purposes.</p>	 <ul style="list-style-type: none"> • Fully reusable. • Nominal gross takeoff weight of approximately 360klb (160Mg), although this varies with staging Mach number. • 10000lbs (4535.9kg) of payload to LEO. • First stage propulsion is rocket-turboramjet, second stage propulsion is rocket. 	 <ul style="list-style-type: none"> • Horizontal launch. • Trajectory constrained to maximum dynamic pressure of 1000psf (47.9kPa) until the staging Mach number of 5,6 or 7 is reached. • Pull-up occurs at nominal staging Mach number under ramjet power, to reach the prescribed staging dynamic pressure of 300psf (14.4kPa). Pull-up occurs at a 2g constrained rate. • The orbiter trajectory is undefined. • Booster return is achieved through an unpowered turn and deceleration, followed by a turbo-jet powered cruiseback.

JAXA TSTO Spaceplane[72]

Fujikawa et al.[73] have developed a spaceplane as a feasibility study on TSTO fully-reusable launch for JAXA.



- Fully-reusable.
- **Propulsion:** First stage RBCC, second stage rocket.
- **Payload:** 800kg.
- **Mass:** Booster 533.8t, orbiter 47.1t.
- **Length:** Booster 38.4m, orbiter 18.8m.



· **Launch:** Horizontal.

· **Airbreathing trajectory:** Flight at maximum dynamic pressure for periods, with manoeuvres performed to lower dynamic pressure in order to optimise the performance of the RBCC engines. Pull-up during scramjet operation, possibly to optimise separation point.

· **Return trajectory:** Not simulated.

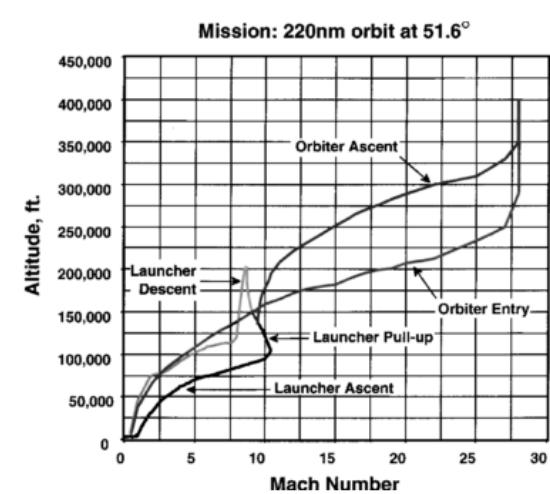
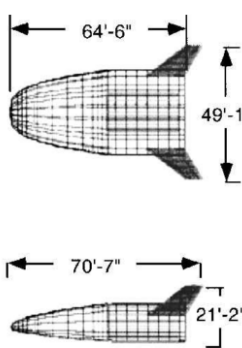
NASA Ames TSTO Spaceplane[74]

A TSTO spaceplane was conceptualised by Mehta and Bowles[74], based on a '93 design for the NASP program. This concept was designed to be economically viable launcher, with built-in growth potential.



Fully reusable.

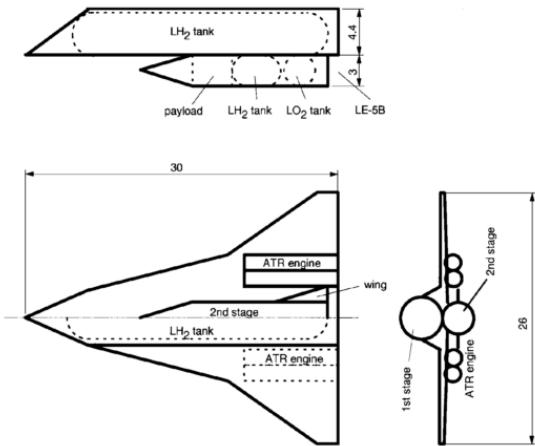
- 25000lbs (11339.8kg) of payload.
- Booster propulsion system is turbojet/ramjet/scramjet while orbiter has standard LOX/H₂ rocket propulsion.
- Booster mass is 602300lbs (273198kg) with a length of 224ft (68.3m), and orbiter mass is 199301lbs (90401kg) with a length of 64.5ft (19.7m).



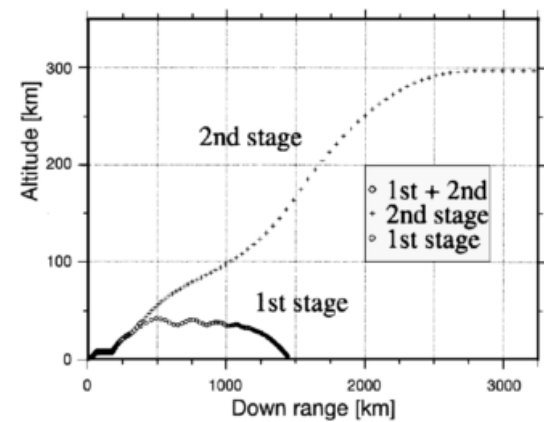
- Horizontal launch.
- Acceleration before the hypersonic regime is achieved steadily, with an increase in altitude at the transsonic 'pinch point' to reduce dynamic pressure.
- During the hypersonic regime, a constant dynamic pressure of 2100lb/ft² (100.5kPa) until Mach 10.
- At Mach 10, a 2g pull-up is initiated, to lower the dynamic pressure to 300lb/ft² (14.4kPa) for separation, and to improve the flight path angle at separation. The scramjet engines are cut off at the start of this pull-up.
- The booster flies to orbit under rocket power.
- The booster initiates a turn, and cruises back under turbojet power.
- The orbiter reenters and returns unpowered.

Tohoku University TSTO Launcher[75]

Developed by Takahashi et al.[75], a conceptual TSTO system was designed to investigate acceptable launch, landing and abort sites along the coast of the Japanese islands.



- Partially reusable, first stage only.
- 2000kg payload to LEO.
- The booster weighs 75.0ton, and is 30m long, while the orbiter weighs 19.7ton, and is 19m long.
- The booster uses the air-turbo-ramjet engine developed at Japan's Institute for Space and Astronautical Science. The orbiter uses the LE-5B rocket engine.



- Horizontal launch.
- Prescribed booster trajectory of flight at a maximum dynamic pressure of 50kpa.
- The rocket stage is separated at Mach 6 and 50kPa dynamic pressure, after which it pulls-up to orbit under rocket power.
- The booster stage glides downrange to a suitable landing site.

Sänger (Saenger)[61]

The Sänger was a German TSTO alternative to the HOTOL. Sänger was intended to drive studies and technology development within the German Hypersonic Technology Program (HTP).



- First stage reusable. Two alternative upper stages; a reusable, manned version for a crew of four and 3t payload, and an expendable cargo version for carrying 7-8t payload to LEO.
- First stage with a weight of 405t and length of 82.5m.
- First stage powered by tubojets and ramjets, with upper stages powered by conventional LOX/LH₂ rockets.

- No detailed trajectory information available beyond separation to second stage at Mach 6.6.

Dassault Aviation Star-H / HERMES [61]

Developed by Dassault, the STAR-H was the French study that sought to mirror the HOTOL and Sänger with the design of an aerospace plane capable of servicing the ISS. The STAR-H incorporates the Hermes, a European manned launcher concept, as 'payload' making it essentially a two-and-a-half stage vehicle.



- partially reusable. Reusable first stage, expendable second stage booster, 'payload' of a small spaceplane glider is also reusable.
- First stage weighing 299t, with a second stage weighing 101t, with the Hermes spaceplane as 'payload'.
- First stage powered by five combined cycle engines, second stage rocket powered.

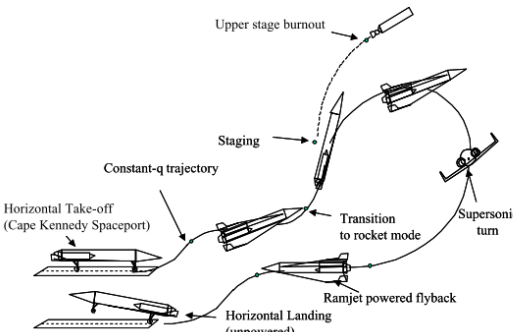
- No detailed trajectory information is available beyond separation to second stage at Mach 6.

Starsaber[76]

Starsaber was a conceptual design produced by the Georgia Institute of Technology Space Systems Design Lab, with the collaboration of NASA's Marshall Space Flight Centre. Starsaber was intended to investigate the feasibility of RBCC engines for small payload class missions.



- Partially reusable. First stage reusable, second stage expendable.
- 300lbs (136kg) payload.
- The reusable booster weighs 79150lbs (35902kg) and is 77ft (23.5m) long, and the expendable orbiter weighs 3400lbs (1542kg) and is 13.1ft (4.0m) long.
- The booster is powered by two RBCC (ejector-ramjet/ramjet/rocket) engines, while the orbiter is powered by rocket engines.



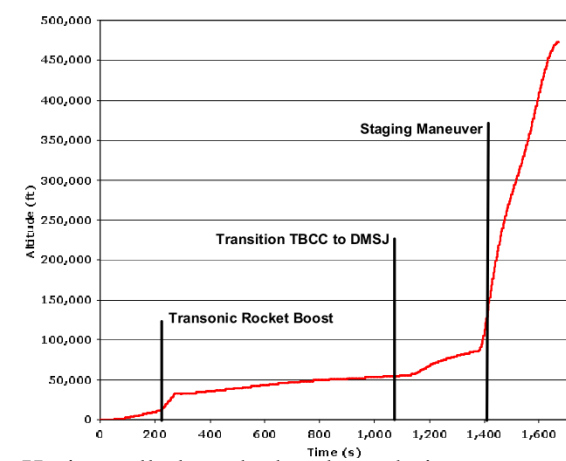
- Trajectory optimised in separate stages for minimum fuel, constrained to vehicle design and trajectory events.
- Horizontal launch.
- Takeoff occurs in ejector-ramjet mode, accelerating to the maximum dynamic pressure boundary of 1500psf (71.8kPa), at which point transition to ramjet mode occurs.
- Constant dynamic pressure is maintained throughout ramjet operation, before transition to all-rocket mode.
- The vehicle pulls-up in all-rocket mode, and separates the orbiter when the dynamic pressure falls below 1psf (0.05kPa), which continues to orbit under rocket power.
- The booster descends and returns to the launch site under ramjet power, choosing the altitude at which lift equals weight for a constant angle of attack.

QuickSat^[77]

Quicksat was designed by SpaceWorks Engineering and the Air Force Research Lab as a conceptual exploration of combined cycle propulsion systems for reusable space access. Quicksat was developed in support of a U.S. military initiative to investigate responsive space access for national security purposes. Quicksat is capable of both the orbital delivery of a Space Manoeuvre Vehicle, as well as hypersonic strike.



- Fully reusable.
- 500lbs (226.8kg) payload.
- The booster stage weighs 77125 (34983kg) and is 52.2ft (15.9m) long while the orbiter weighs 13090lbs (5937kg) and is 27.5ft (8.4m) long.
- The booster is powered by turbojets, dual-mode scramjets, and rockets, while the orbiter is rocket powered.



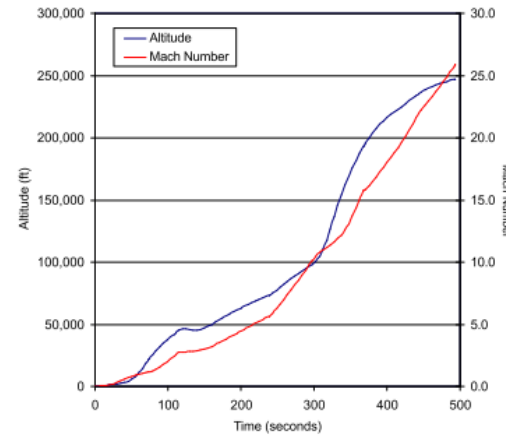
- Horizontally launched under turbojet power.
- Rockets are used through the transonic regime.
- Turbojets are again used along a dynamic pressure of 1600psf (76.6kPa).
- At Mach 3.75, the vehicle transitions to ramjet power, and flies at maximum dynamic pressure of 2000psf (95.7kPa), transitioning to scramjet power when necessary.
- At Mach 8, a pull-up is initiated, and the vehicle transitions to rocket power.
- At 250000ft, staging occurs, and the orbiter circularises under rocket power.
- The booster reenters, decelerates, and returns under turbojet power.

XCALIBUR[78]

XCALIBUR was designed by SpaceWorks Engineering in support of NASA Marshall Space Flight Centers Advanced Space Transportation Program (ASTP). The XCALIBUR design was intended to investigate the viability of RBCC engines for future reusable launch vehicles.



- Fully reusable.
- The booster stage is powered by four RBCC engines, while the orbiter is HEDM rocket powered.
- 20000lbs (9071kg) payload.
- The booster weighs 897790lbs (407231kg) and is 181.7ft (55.4m) long, and the orbiter weighs 103710lbs (47042kg) and is 42.4ft (12.9m) long.



- Vertical launch.
- The maximum dynamic pressure pf 1800psf (86.2kPa) is flown during ramjet and scramjet operation, for maximum engine performance.
- At Mach 10, pull-up occurs under scramjet power, in order to reach staging conditions of 95psf (4.5kPa) dynamic pressure.
- The upper stage injects into orbit using rocket boosters.

3.1. HYPERSONIC AIRBREATHING LAUNCH SYSTEMS AND TRAJECTORIES

while the inefficient mass scaling of the airbreathing engine systems may be mitigated. A variety array of engine architectures can be observed in the TSTO vehicles shown in Table XXX. The booster stages are universally powered, at least in part, by airbreathing engines. RBCC engines are common, however some designs eschew the use of rocket engines in the booster stage altogether. This is possible due to the lessened emphasis on mass efficiency, enabling the use of multiple efficient, but relatively low-speed engines. The separation of the booster stage in multi-stage launch systems also allows for a relatively simpler return and landing of the booster stage, when compared to single-stage launch systems. The booster stage is separated at significantly less than orbital velocity, decreasing the structural and heating loads that it experiences during return flight. This lessens the weight of the TPS systems necessary for the booster vehicle, and simplifies the return process. However, the opposite is true for the orbiter stage. The much smaller size of the orbiter stage means that the systems for its return will require a larger mass fraction of the orbiter vehicle, and the high speed entry and return will require significant TPS and control system complexity. For this reason, some of the TSTO systems shown in Table XXX opt for partial reusability, where the booster stage is reused, but the orbiter stage is discarded. This allows for the largest, most costly, and most easily reused portion of the launch system to be returned, while the orbiter stage may be designed to be low-cost and disposable, and in general designed to be more akin to a traditional rocket, and less like a 'spaceplane'.

The trajectories of TSTO airbreathing launch systems, where available, are relatively similar to those of SSTO launch systems. As shown in Table XXX, all of the TSTO systems that have gone through detailed design are launched horizontally, and most fly at the maximum dynamic pressure boundary for the majority of the duration of hypersonic airbreathing flight. The exception to this is the JAXA TSTO launcher, which flies at a higher altitude to increase the performance of its airbreathing engines. Near the end of airbreathing operation, a pull-up is generally performed, similarly to the pull-up observed in SSTO launchers, before stage separation. However, this pull-up is not universally performed, and when it is, it occurs to very different extents and generally is driven by the structural or thermal limits of the orbiter stage. This variety of staging points is due to the location of the staging point being determined by a multitude of factors stemming from the design and configuration of the launch system. The optimal separation point is determined by a trade-off between;

- the high efficiency of the scramjet engines;
- the thrust produced by the scramjet engines;
- the potential thrust of the rocket engines;
- the energy necessary to increase the altitude of the scramjet stage;
- and the aerodynamic efficiency when performing the required direction change.

All of these factors must be considered in order to generate an optimal trajectory. In addition, the staging point may be significantly limited by vehicle design factors. The structural or thermal requirements of the launch system, particularly of the upper-stage, can significantly limit the staging point. If the upper-stage is not designed to withstand significant dynamic pressures or thermal loads, then a separation in low-density air is necessary. There has been a number of studies which have identified a pull-up manoeuvre as being advantageous for a multi-stage system in order to decrease the dynamic pressure of the vehicle at airbreathing-rocket stage separation[71, 72, 74]. In the studies by Tsuchiya et al.[72] and Wilhite et al.[71], decreased dynamic pressure is necessary for the successful operation of the orbital rocket stages, of the systems under investigation. In these studies the airbreathing stages pull-up to the maximum allowable dynamic pressure for the rocket-powered orbital stages. When the orbital stages are able to operate, stage separation occurs. These pull-up manoeuvres demonstrate the advantages of a pull-up for the operation of the orbital stages, allowing the aerodynamic and thermal loading on the vehicle to be reduced. Another challenge inherent to multi-stage airbreathing launch systems is the dynamics of the stage separation itself. This stage separation often occurs in-atmosphere, at relatively low trajectory angles. This separation is a key factor in the design of each stage, particularly the time when the upper stage engine must be ignited to ensure appropriate control and speed after separation. This separation also results in vehicle-vehicle aerodynamic interactions between the stages of the launch system as they separate. Here vehicle shock-shock interactions can cause significant changes to aerodynamic forces and moments, requiring appropriate control approaches and vehicle shape design[79, 80]. These separation effects are not generally taken into account in the early stages of launch vehicle conceptualisation, as they can be considered as secondary to an overall trajectory design and optimisation in the early stages of design. However these separation effects are likely to be significant, and a multi-stage vehicle must be carefully analysed in the later stages of vehicle design using CFD and experimental analysis, along with an iterative design process, to ensure that appropriate control authority can be maintained during and after separation[79].

XXX I need to regrte this a bit, include that MDO trajectories are often simplistic, and make it sound less like MDOs are just too complex to analyse..

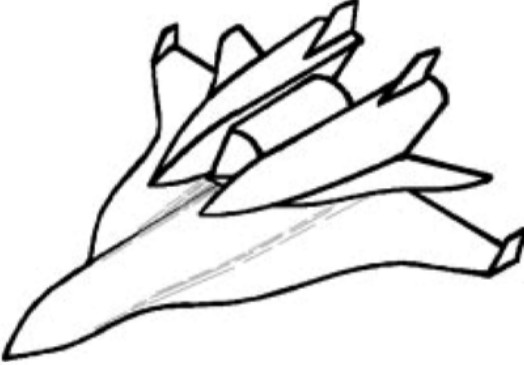
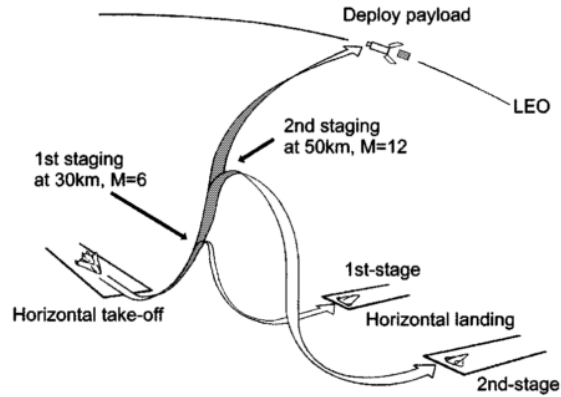
While the stage separation point of a multi-stage launch system is often considered to be determined by the design dependent constraints of the launch system, the design process is iterative, and the design of a launch vehicle must also be based upon the trajectory path that is considered most efficient. In the launch vehicles that have been studied, a pull-up is often considered the 'optimal' flight path. This is frequently determined during a multidisciplinary design optimisation, where the trajectory and vehicle design are optimised together, with a pull-up generally occurring to the aerothermal limits of the second stage vehicle. This makes it impractical to determine which features of the trajectory are optimal in isolation, and which are dependent on vehicle design. Mehta & Bowles[74] prescribe a 2g pull-up in order to "lower dynamic pressures and to achieve the optimal launching flight path angle

for the orbiter vehicle". This prescribed manoeuvre indicates that a pull-up before airbreathing-rocket transition is considered the optimal trajectory in isolation, although the specific optimal conditions are not investigated. The antithesis to the consideration of a pull-up as optimal is presented by launcher studies that do not perform a pull-up, where the maximum dynamic pressure flight during airbreathing operation of a TSTO launch system is considered to produce maximum efficiency. This is the case for the Tohoku University Launcher, as well as the Starsaber. The Tohoku University Launcher maintains constant dynamic pressure until separation, and the rocket stage is performs the pull-up to orbit under its own power, while the Starsaber transitions to rocket mode during constant dynamic pressure flight, and pulls up under rocket power. This may indicate that it is preferable for the booster vehicle to stay close to maximum dynamic pressure during airbreathing operation, when it is able to do so. This is supported by a study by Staufenbiel[54], which investigated the effects of staging conditions on a second stage rocket in isolation, and concluded that "higher Mach numbers are preferable to increasing the flight-path angle above values of a few degrees". However, this study did not include an airbreathing stage optimisation, and specifically stated that the airbreathing stage must be included to determine optimal separation conditions[54]. Clearly there is some discrepancy between whether a pull-up is considered optimal for a multi-stage launch system without consideration of vehicle design effects. These staging discrepancies, along with the varying trajectory shapes of TSTO launch systems in general, indicate that the trajectory of multi-stage airbreathing launch systems is heavily dependant on the general of the launch system, particularly the engines being used. It is certain that the trajectory and the design of multi-stage launch systems are heavily interlinked, and that both must be understood well before a detailed design is able to be achieved.

3.1.3 Three-Stage Launch Systems

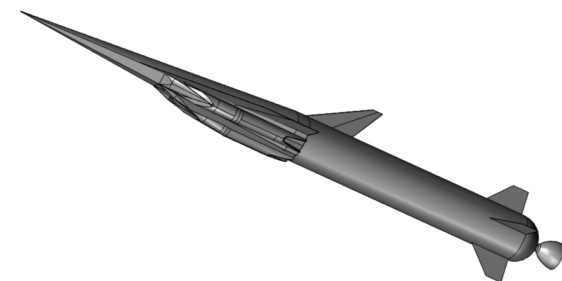
XXX here I need to link directly to background section, and outline explicitly how three stage launch systems are early in the design process, and why they might be considerably different to single and two-stage designs (including having much more segmented engines). then link more explicitly to the sections about return and the spartan

Three-stage-to-orbit (3STO) airbreathing launch systems have been advocated as an efficient configuration for dedicated small satellite launch, a payload profile that has recently garnered a large amount of interest. A three-stage configuration allows for cost-efficient partial-reusability in small launchers, enabling the acceleration of a small, disposable third stage, with reusable first and second stages. 3STO systems are likely to be most applicable to smaller launch systems, where any 'dead' weight from unused propulsion systems at hypersonic speeds carries relatively larger mass penalties when compared to more massive systems. The three-stage airbreathing launchers that have been or are being investigated are summarised in Table XXX. Only two such systems have been identified; the

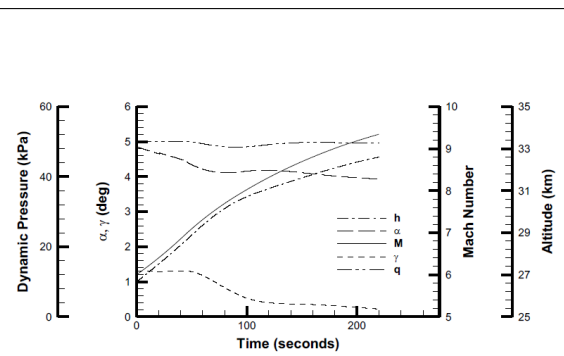
Launcher	Design	Trajectory
Tohoku University 3STO[81] Kimura and Sawada investigate a three-stage-to-orbit launch system with an expendable upper stage for responsive LEO launch.	 <ul style="list-style-type: none"> · 2t of payload to LEO. · Weight: First stage 123.42t, second stage 61.89t, third stage 11.27t. · Length: First stage 50m, second stage 26m, third stage 16m. · Propulsion: First stage four air-turboramjets, second stage scramjet, third stage rocket. 	 <ul style="list-style-type: none"> · Horizontal takeoff. · Trajectory is prescribed a priori. · First stage flies at a constant dynamic pressure of 20kPa, before staging at 30km altitude, at Mach 5-6. · The second stage ascends under scramjet power along a predefined trajectory that is designed to avoid violating maximum heating constraints, at a low trajectory angle, before staging at 50km altitude, at Mach 11-12. · The third stage ascends under rocket power. · The first and second stage land at a site down-range. The first stage cruises under turbojet power , while the second stage glides.

SPARTAN[82]

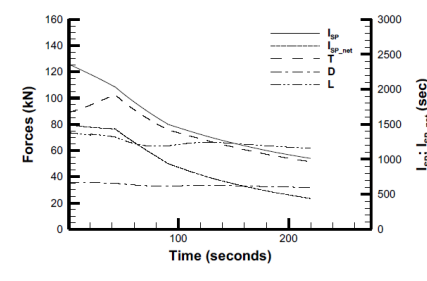
The SPARTAN is a three stage, partially reusable, access to space system under development at The University of Queensland[82, 83] and Hypersonix(CITEXXX). Designed for affordable small payload launch, The SPARTAN is partially reusable.



- Payload: 279.8kg
- Weight: First stage 11957.6kg, second stage 5905.1kg, third stage 2850kg.
- Length: Second stage 22.94m, third stage 11.8m.
- Propulsion: Rocket-scramjet-rocket



(a)



(b)

- Vertical launch.
- First stage performs a gravity turn.
- Trajectory constrained to scramjet stage flying a constant dynamic pressure of 50kPa.
- Third stage ascends under rocket power, held at 10° angle of attack.
- Return trajectory undefined.

Tohoku University 3STO launch system investigated by Kimura and Sawada in 1999[81], and The SPARTAN, a rocket-scramjet-rocket launch system currently under development by the University of Queensland and Hypersonix. Both of these systems are designed to be a cost effective near-term solution to airbreathing access to space, using a disposable third stage rocket along with reusable first and second stages. Both stages use second stages powered by scramjets, with The SPARTAN utilising a rocket-powered first stage along with vertical launch, while the Tohoku University launcher utilises turboramjets along with a horizontal launch and a large, winged first stage.

The flight paths of both of these launch systems are predefined, and designed around the physical limits of the launch systems and maximising the efficiency of the airbreathing engines. Both the Tohoku University launcher and the SPARTAN fly close to the maximum limits of the vehicle during airbreathing operation. While this is believed to be the most optimal or representative trajectory for these launch systems, no analysis has been undertaken to indicate that these trajectories are in fact the most efficient way of flying to orbit. This is particularly true for the SPARTAN, because the fly-back of the scramjet stage has not been modelled, even though it is an integral part of the cost effectiveness of the launch system. The vertical launch of The SPARTAN is considerably different to other multi-stage launch systems, and it remains to be seen whether a constant dynamic pressure airbreathing trajectory is in-fact the optimal way in which to constrain the system during launch. At the end of the airbreathing trajectory, when compared to the trajectories flown by two-stage-to-orbit airbreathing launch systems, it is evident that a pull-up during airbreathing operation, before the release of the third stage, may possibly improve the efficiency of a rocket-scramjet-rocket launch system. Although the extent of this pull-up, or indeed whether a pull-up is necessary at all, cannot be estimated from the previous studies of airbreathing launch systems. This study seeks to model the optimal trajectory of a rocket scramjet-rocket launch system, utilising a modified version of the SPARTAN launch system in order to gain insights into the most efficient way to fly a launch system of this type.

3.2 Hypersonic Vehicle Return and Glide Trajectories

There are three main methods that have been studied for potential hypersonic vehicle return; glide-back, cruise-back and boost-back. Glide-back involves the hypersonic vehicle returning to base and landing entirely using its aerodynamics. This requires sufficient lift to sustain the hypersonic vehicle over the entire return range, as well as the controllability to land the hypersonic vehicle in level flight. For a hypersonic trajectory a fully glide-back return flight is most likely unobtainable. This is due to the large downrange distance flown, and the large initial velocity at the beginning of the fly-back trajectory, when the vehicle is oriented away from the landing site. Multiple studies have investigated the maximum staging velocity allowable for the glide-back flight of a booster, and have found that the maximum separation velocity for glide-back to be feasible has been found to be between Mach 3-4 at 30km-120km downrange distance, with higher initial velocities or longer downrange distances

3.2. HYPERSONIC VEHICLE RETURN AND GLIDE TRAJECTORIES

requiring fly-back under power[55, 56].

Cruise-back involves the inclusion of subsonic engines, which are used to power the fly-back of the hypersonic vehicle until landing similar to a conventional aircraft. These engines may be included solely for the fly-back[55], or used in the acceleration phase for low velocity acceleration[56, 71, 74]. The addition of subsonic engines powering a constant velocity cruise-back phase allows the accelerator to return to base with a similar trajectory to that of traditional aircraft, allowing the velocity and altitude of the accelerator to be precisely controlled. However, the addition of subsonic engines necessary for cruise-back increases the mass of the vehicle significantly, leading to decreased mass efficiency and increased design complexity[55].

Another mode of powered fly-back is to use the existing hypersonic airbreathing engines during the return trajectory in a boost-back trajectory. Using the existing airbreathing engines allows for range to be added to a return trajectory, without the inclusion of additional engines, **saving on mass and space within the vehicle, and reducing the complexity of the design**. The hypersonic airbreathing engines can be operated at appropriate times during the fly-back, when they will be most impactful on the return trajectory range. However, the hypersonic airbreathing engines may only be used within their operating region, and vary in thrust and efficiency dependent on flight conditions. Hypersonic airbreathing engines have maximum efficiency at low Mach numbers[12], with the thrust produced depending on the dynamic pressure and inlet conditions, which vary with the trajectory path and angle of attack of the vehicle. The possibility of an airbreathing vehicle reigniting high speed airbreathing engines for short periods has been investigated by Tsuchiya and Mori[72], as described in table XXX. Tsuchiya and Mori investigate two conceptual launch vehicles; a vehicle powered solely by airbreathing propulsion returning after separation of an orbital stage at Mach 5.1, and an airbreathing/rocket vehicle returning after a separation at Mach 6.8[72]. Both vehicles use the high speed airbreathing engines during return flight. Both vehicles ignite the airbreathing engines at around Mach 3.5 for “several tens of seconds” to extend the range of the fly-back manoeuvres. After this, the vehicles descend and land at the launch site. These boosters fly to a downrange distance of 600-625km from the launch site, and less than 5% of the vehicles initial propellant was required to return the vehicles to the initial launch sites[72]. However, these boost-back trajectories were initiated at lower than Mach 7, and their feasibility at higher separation velocities is not clear. **Even at relatively low separation speeds it is evident that the additional fuel weight used during the return phase may significantly affect the performance of a launch system.** As such it is important to assess the effects of the fly-back of high-speed staging on the efficiency of a launch system, and to determine the functional implications of mandating return-to-launch-site capabilities.

In addition to investigating the trajectories of airbreathing launch vehicles, the maximum-range, minimum-fuel trajectories of hypersonic vehicles and lifting bodies that are not necessarily launch vehicles can also allow a better understanding of the maximum efficiency return trajectory shape. The maximum range trajectory of a hypersonic vehicle operating at high altitudes is often a ‘skipping’

trajectory, where the altitude of the vehicle is repeatedly raised and lowered to take advantage of the most efficient angle of attack of a vehicle while travelling through high density air[86–90]. A skipping trajectory has been shown to be range optimal for hypersonic gliding vehicles when range is desired to be maximised, from a wide range of release points and vehicle configurations[56, 86–88, 90, 91]. A skipping trajectory has also been shown to be optimal for an airbreathing hypersonic vehicle thrusting throughout the trajectory[89, 92], as shown in Figure 3.2. The range optimal operation of the scramjet engine is shown to be repeated ignitions at the trough of each skip[89]. The scramjets are ignited as the vehicle climbs after the trough, as the Mach number decreases to the minimum operable conditions of the scramjet engines[89]. Minimising the Mach number during operation in this way maximises the efficiency of the scramjet engines[89].

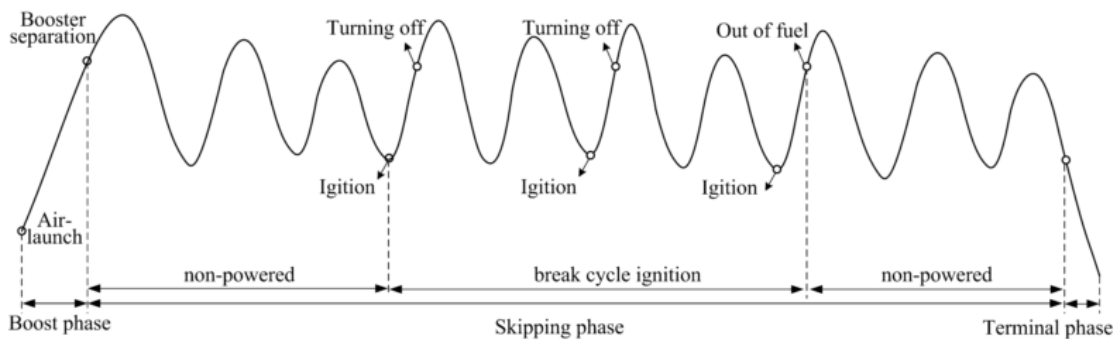


Figure 3.2: An illustration of the optimised maximum range trajectory of a hypersonic vehicle[89].

The complexity of the optimal return and maximum range trajectories for hypersonic vehicles require good aerodynamics and manoeuvrability to carry out properly, as well as potentially requiring multiple restarts from the airbreathing engines. A coupling of the ascent and return during trajectory design is clearly important, because there is a complex trade-off between both phases to produce an overall fuel-optimal trajectory, particularly if it is necessary for the airbreathing engines to be reignited during the return flight.

3.3 The SPARTAN

In order to investigate the optimal launch trajectory of a three stage, airbreathing launch system, a representative system design must be used to provide a general configuration, sizing, and design for an analysis. Only two three-stage launch systems were identified in Section XXX; the Tohoku University 3STO launcher, and The SPARTAN launch system. For this study, The SPARTAN launch system is chosen as the basis for a representative launch system, for multiple reasons:

- The SPARTAN is a small, partially returnable launch system, seeking to fill a reusability niche that cannot be satisfied by current rocket-powered launch system designs.

- The SPARTAN's design is relatively mature, having undergone significant study over the past years, and is still being actively developed.
- The SPARTAN is designed to utilise the REST engines, which are some of the most well validated scramjet engines together with airframe integration. Capturing the performance of the engines correctly is integral to developing a deeper understanding of the performance of airbreathing launch systems.

For these reasons The SPARTAN is assessed as an up-to-date design of a future rocket-scramjet-rocket launch system that is likely to be representative of future space launch systems of this type. Because of this, it is likely that a trajectory analysis performed on a SPARTAN-like launch system will be generally applicable to future rocket-scramjet-rocket launchers, and will progress the development of airbreathing launch systems as a whole.

The SPARTAN launch system is currently undergoing research and design, and is in the preliminary design phase. The SPARTAN has undergone an iterative design process over a number of years[12, 83] with a significant amount of resources dedicated to it by the University of Queensland's Centre for Hypersonics. The SPARTAN's design is based around the scramjet accelerator stage of the launch system (designated The SPARTAN in previous works, although this nomenclature has since changed), and this scramjet accelerator is the stage that has been designed in the most detail[12, 83], because the development and performance of the scramjet accelerator are likely to be the critical aspects of the launch system design.

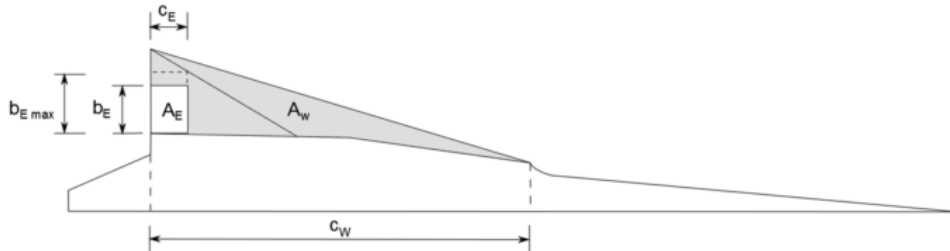


Figure 3.3: The elevons of the SPARTAN[12].

The scramjet accelerator stage of the SPARTAN was first designed by Jazra, Preller and Smart[83, 84], based on the winged-cone vehicle developed by Shaughnessy et al. as part of the NASP program[11]. The scramjet accelerator has been sized to be 22.94m long, with an 8.90m wingspan, and is powered by four rectangular-to-elliptical shape transition (REST) scramjet engines, developed at The University of Queensland, specifically designed to integrate smoothly with the conical forebody of the scramjet accelerator. Elevons are included on the wings of the scramjet accelerator for primary control, shown in Figure 3.3. These elevons were sized through variation of the width, b_E , to have an area equal to 15% of the area of the wing, and to have a cord length, c_E , of 15% of the cord length of the wing[82]. Three retractable landing gear assemblies are included on the scramjet accelerator,

shown in Figure 3.4, so that the scramjet stage may be returned and landed in the same manner as a traditional aircraft; horizontally on a specially purposed runway.

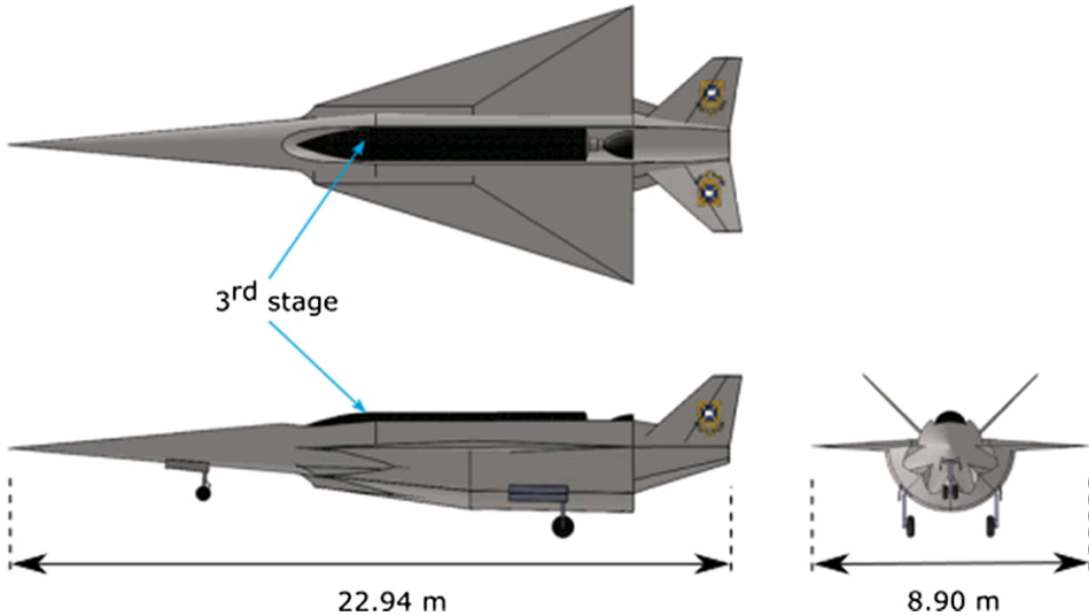


Figure 3.4: The scramjet accelerator of the SPARTAN, as designed by Preller[82].

To date, studies of the SPARTAN have assumed that the most efficient launch trajectory is achieved when the scramjet accelerator stage is constrained to fly at a constant dynamic pressure[12, 82]. Figure 3.5 shows the trajectory of the scramjet accelerator, simulated in three degrees of freedom to fly close to a constant 50kPa dynamic pressure, using a pole-placement angle of attack controller[12]. The ascent trajectory of the SPARTAN begins at Mach 6, and terminates at Mach 9.34, when the hydrogen fuel is exhausted[82]. The net specific impulse of the SPARTAN varies from 1492s at the beginning of the trajectory, to 439s by the time the fuel is depleted[12]. The SPARTAN is trimmed throughout the trajectory by ailerons on the wing, shown in Figure 3.3. Over the flight of the SPARTAN, the flap deflection changes from 10.6° to 12.2° [82]. The drag contribution of the flap varies from 14.3% to 14.5%, and the lift contribution from 18.8% to 21.0%[82]. However, this is calculated without a detailed analysis of the centre of gravity location, which is assumed to be located at 50% planform area. Past studies of the scramjet accelerator vehicle have assumed that a fly-back to launch site is possible after third stage separation[12, 82]. However, this fly-back has not yet been simulated.

The first stage rocket of The SPARTAN is launched vertically, accelerating the scramjet accelerator to its minimum operable Mach number. The first stage has not yet been modelled in detail, with only very representative aerodynamic models used for an analysis of a representative first stage rocket. It is eventually intended that the first stage of The SPARTAN be returnable to launch site under cruise-back power for reuse, however, a first stage capable of return flight has not been designed or modelled for a full scale SPARTAN system[12, 82]. Some preliminary work has been carried

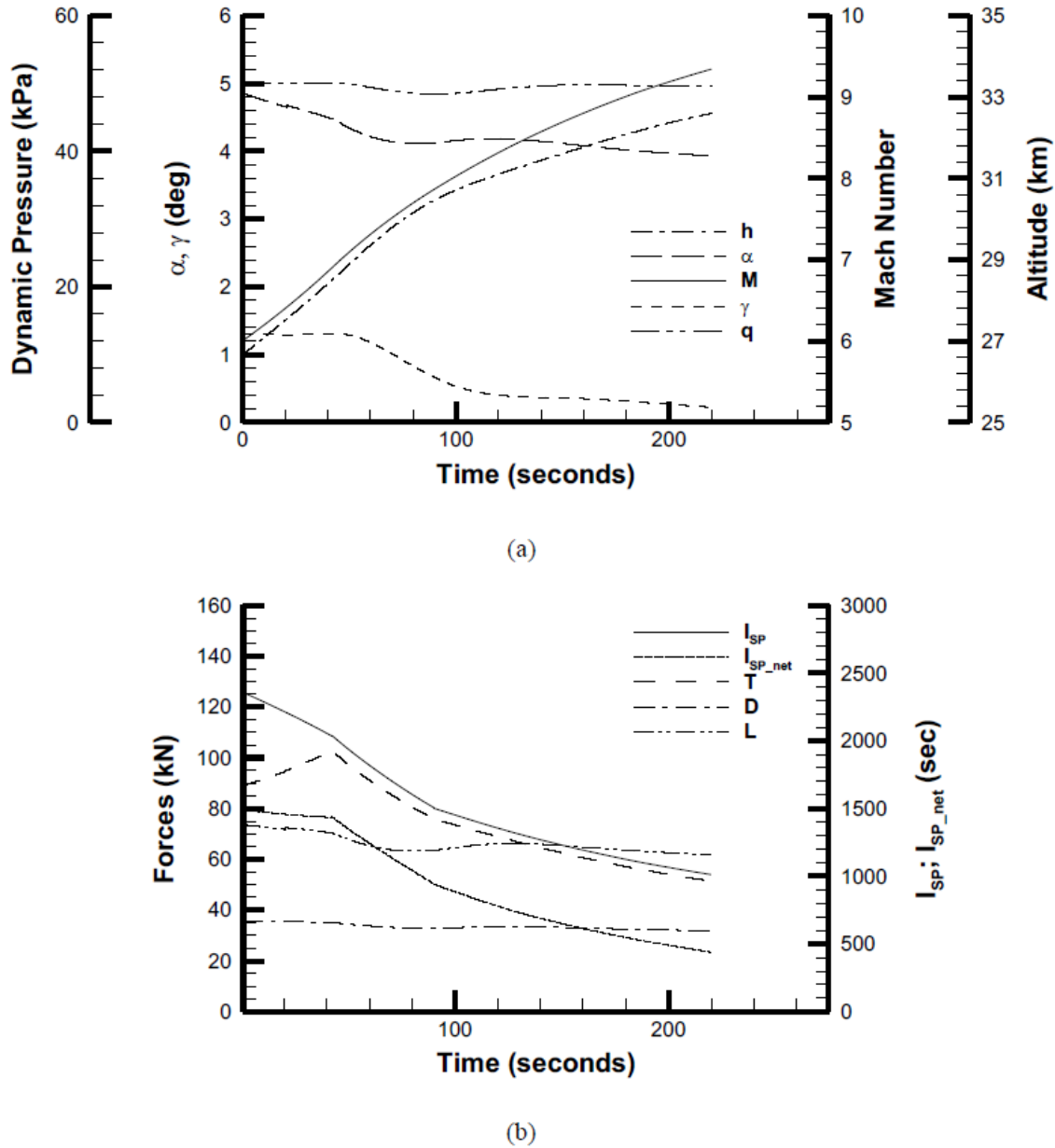


Figure 3.5: The flight trajectory of the SPARTAN. a) shows the physical trajectory and b) shows the forces on the vehicle and performance indicators.

out, exploring the reuse of the first stage boosters of The SPARTAN [4] for a modified, reduced size SPARTAN concept, however this work is still in its infancy, and the basic design of the booster or boosters is still to be determined[12, 82].

The third stage of The SPARTAN is an expendable rocket system, that consists of a rocket motor, fuel tanks, structure, payload and a thermal protection system[12], shown in Figure 3.6. The third stage has to this point been designed to be powered by the Pratt & Whitney RL-10-3A[12], and has exhibited good performance when powered by this engine. However, the RL-10-3A is a pump-fed

engine, and is likely to be prohibitively expensive for a small launch system. Initially, the third stage

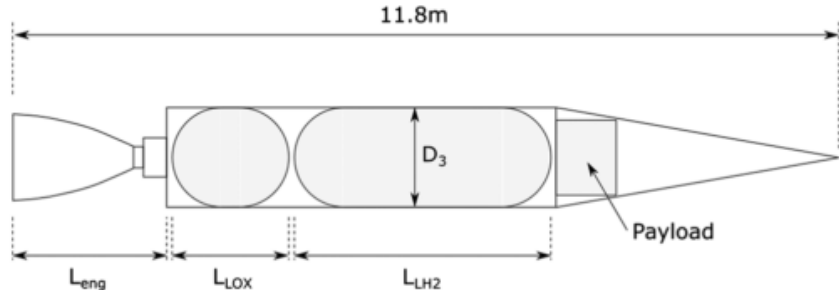


Figure 3.6: The third stage rocket of the rocket-scramjet-rocket launch system[12].

was designed to be situated within the fuselage of The SPARTAN's scramjet accelerator, in the nose cone[83]. This design was changed by Preller[12, 82], so that the rocket was situated in 'piggyback' position at the top of the fuselage as shown in Figure 3.4. Rather than being situated entirely within the fuselage, the third stage was designed to fit into a recess into the back of the vehicle, to aid in high dynamic pressure separation. However, the effect of this recess on the aerodynamics of the scramjet accelerator after separation has not been considered[12, 82]. It is likely that this recess would have a large effect on the aerodynamics and controllability of the vehicle, particularly at high Mach numbers, where large areas of separation and recirculation are likely to be present.

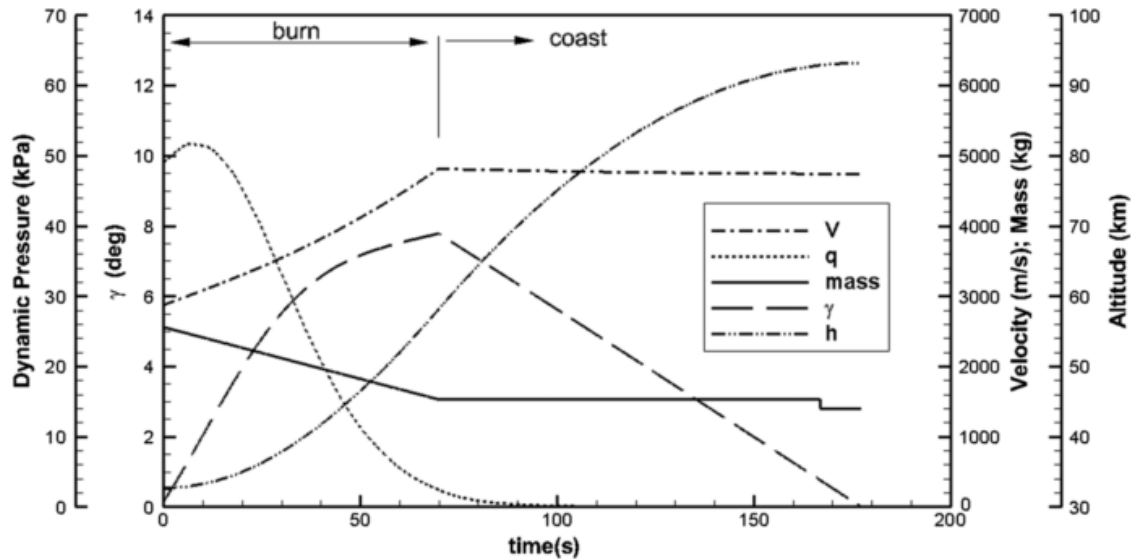


Figure 3.7: The third stage trajectory of The SPARTAN launch system[82].

The trajectory of the third stage has to date been constrained to the scramjet accelerator flying a constant dynamic pressure trajectory, releasing the third stage into a high dynamic pressure environment. This trajectory, shown in Figure 3.7, uses a constant 10° angle of attack throughout, enabling the third stage to pull-up out of the atmosphere. Once the density of the atmosphere is low enough, the

thermal protection system separated from the vehicle for mass efficiency, and once exoatmospheric, the third stage performs a Hohmann transfer to reach the desired orbit. This trajectory enables the delivery of 279.8kg[82] of payload to sun synchronous orbit when using a third stage powered by a Pratt & Whitney RL-10-3A[82].

Whilst the SPARTAN launch system is the most studied 3STO airbreathing system, it is evident that there is significant portions of the system left to design in detail, and significant design challenges to overcome. It is also apparent that the trajectory analysis of The SPARTAN, like all 3STO launch systems, and many 2STO launch systems, makes significant assumptions as to the most optimal flight path, notably constraining the scramjet accelerator to constant dynamic pressure flight. As previous studies have indicated[12], if the performance and designs of this launch system and 3STO airbreathing launch systems in general are to be improved, the development and analysis of an optimal launch trajectory is necessary.

3.4 Optimal Control

To investigate the best possible way of flying a rocket-scramjet-rocket launch system to orbit, a simulation must be developed that will calculate the optimal flight path, taking into account the trajectory of all of three stages of the launch system, including ascent trajectories, as well as the return to base of the scramjet accelerator stage. Calculating an optimal trajectory that combines all phases of a partially reusable, partially airbreathing, three-stage launch system is a complex task, that has not been carried out to-date. Defining the trajectory of a launch system with multiple stages and multiple modes of propulsion purely from an a priori vehicle analysis is unlikely to yield a trajectory that maximises the performance of the system, due to the highly nonlinear performance of a multi-stage, multi-propulsion mode launch system, and the complex trade-offs that are present between the stages. The effects of these trade-offs are extremely difficult to predict, particularly because of the high sensitivity of airbreathing engines to flight conditions, and the complex aerodynamics of an airbreathing launch system. A method of determining the optimal flight path is required, that is able to maximise the performance of the launch system with very few assumptions as to the shape of the trajectory.

Optimal control theory is used in situations where a control sequence must be found to produce an optimal trajectory with little prior knowledge of the form that the optimal trajectory will take. Optimal control theory is a general term for the mathematics of optimising a time variant dynamic system, that can be controlled. Optimal control theory is distinct from control theory in that it does not necessarily attempt to match a set reference or goal, as is generally the case for trajectories developed using control theory methods such as feedback control. Rather, a single global objective function is minimised by determining optimised control actions across the trajectory, subject to a set of user defined constraints. Optimal control theory has been widely used in aerospace applications, and has been successfully used to optimise the launch of airbreathing hypersonic launch vehicles[59, 60, 63–

65, 69], including some of the trajectories detailed in Section 3.1.

For an optimisation of a complex trajectory there are a variety of optimal control methods that are useful for specific problem types. These are separated into two categories: direct and indirect solution methods[15]. Indirect methods are based on the calculus of variations or minimum principle model, and generally result in high accuracy solutions to optimisation problems[93]. However indirect models suffer from the drawbacks of small radii of convergence and the fact that the equations to be solved often exhibit strong nonlinearity and discontinuities. This means that indirect methods will not be solvable unless the problem is very well defined with a minimum of nonlinearity, making indirect methods unsuitable for many complex optimisation problems, such as aerospace vehicle simulations which can exhibit strong nonlinear behaviour and have a wide solution space.

Direct methods transform an optimisation problem into a nonlinear programming (NLP) problem which can be solved computationally[94]. NLP solvers solve the optimisation problem defined as[95]:

$$\text{Minimise} \quad f(x) \quad (3.1)$$

$$\text{Subject to} \quad g_i(x) \leq 0 \quad \text{for } i = 1, \dots, m \quad (3.2)$$

$$\text{and} \quad h_j(x) = 0 \quad \text{for } j = 1, \dots, n \quad (3.3)$$

An optimisation problem that has been discretised in this form can thus be solved using any of a variety of NLP solvers. One of the most effective methods of solving twice differentiable NLP problems is sequential quadratic programming (SQP)[96] for which there is a variety of commercial solvers available such as NPSOL, SNOPT, and packages within MATLAB.

In order for these packages to be able to solve an optimisation problem it must be presented in discretised form, and as such must be transformed using transcription techniques[97]. The task of transcribing a continuous optimisation problem into discrete NLP solvable form is not simple. SQP solvers can very easily run into convergence issues when provided with an optimisation problem which has not been well defined. Also, any transcription must be carried out with care that the accuracy of the solution is not compromised. There are multiple ways to approximate a continuous optimisation problem directly as an NLP problem, the most common of which are shooting and collocation methods. The choice of discretisation method can affect the stability and accuracy of the solution as well as the solution time of the problem.

3.4.1 Shooting Methods

Shooting methods in optimal control are forward-time methods of discretisation[97]. Shooting methods explicitly enforce the dynamics of the system, and update the free conditions and system controls

to move towards an optimal solution from an initial guess[97]. Shooting methods are generally simple to apply, and require little specialised knowledge to use once they have been implemented.

The Single Shooting Method

The oldest and simplest method of approximating continuous optimisation problems as NLP problems is the direct single shooting method. Direct single shooting discretises the control function over the solution space, and solves this directly as an NLP by integrating the vehicle dynamics, or state variables, along the trajectory at each trajectory guess[14, 15, 97, 98]. **Figure 3.8 illustrates the single shooting method, with green points indicating the start and end points, and red dots indicating the discretisation of the trajectory path. The vehicle dynamics are solved over these discretised time points directly, with controls modified to minimise an end target.** Single shooting is simple to apply and has been used since the 1970s for rocket trajectory optimisation[99]. **Single shooting methods have also been used for the analysis of airbreathing launch trajectories, with some degree of success[51, 59, 66, 73, 78]. However,** single shooting methods suffer from nonlinearity problems, ie. an optimisation problem solved using the single shooting method will potentially struggle to solve if the problem exhibits even small nonlinearities, due to being unable to converge to an optimal solution. This makes the single shooting method unsuitable **for the in-depth trajectory analysis of complex problems such as a scramjet model, as there are many nonlinear factors inherent in atmosphere and airbreathing engine modelling. For this reason single shooting is not commonly used at the current time for the trajectory analysis of complex launch vehicles.**

The Multiple Shooting Method

Direct multiple shooting solves some of the instabilities of the single shooting method by splitting the trajectory into multiple shooting arcs, and collocating these at specific time points[14, 15, 97, 98]. This creates a system of discontinuities, illustrated in Figure 3.8, which are gradually minimised by the solver algorithm until the trajectory is continuous. These discontinuities allow greater flexibility for the solver than is afforded by the single shooting method.

The multiple shooting method has greatly improved convergence compared to the single shooting method, removing much of the susceptibility to instabilities resulting from nonlinear effects. For this reason, multiple shooting has been used successfully in a variety of applications, including the trajectory optimisation of reusable space vehicles[100]. However, the multiple shooting approach still suffers from a relatively small radius of convergence and slow computation times[98]. Radius of convergence is extremely important to this study as the optimal solution cannot be approximated to a great degree of accuracy. As such it is desirable to use a method with a large radius of convergence to apply to the optimisation problem being considered, to improve the robustness of the solution process.

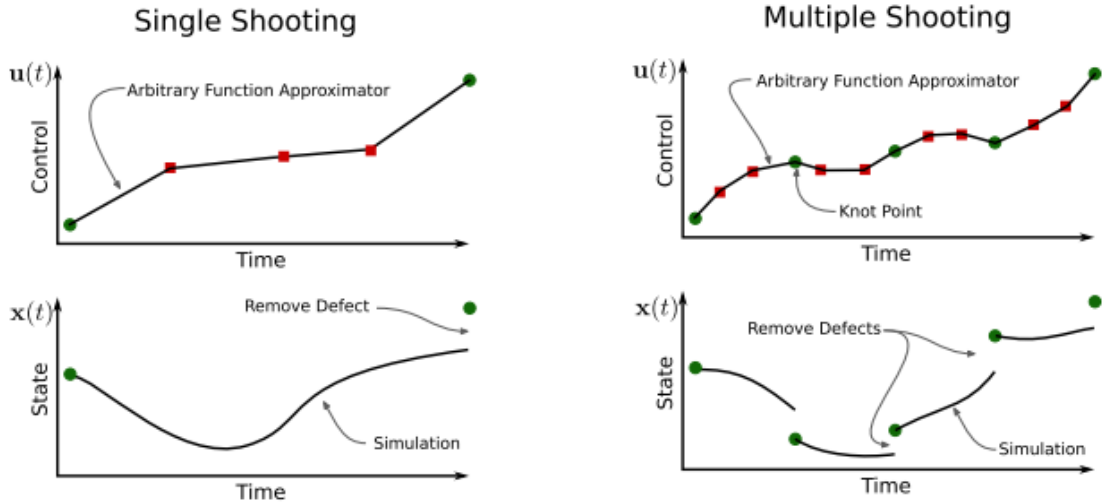


Figure 3.8: A comparison of single shooting and multiple shooting[97].

3.4.2 Collocation Methods

Collocation methods are arguably the most powerful methods for solving optimal control problems[14]. Collocation methods are simultaneous methods, where both the states and controls are approximated using a specific form of functional[14, 97]. In these methods, the dynamics of the system are not explicitly enforced, but instead are constrained at specified points along the trajectory, called collocation points, or nodes[97], with the trajectory often divided into multiple segments at specific nodes, called 'knot' points. These nodes and knot points are illustrated for a pseudospectral method of collocation in Figure 3.9, showing the relationship between the segments and nodes used, and the orthogonal polynomials that approximate the states and controls of the system being optimised. Constraining the dynamics in this way means that the derivative of the state functions become a constraint within the NLP, being equated to the polynomial approximation functions by the solver algorithm. Collocation methods provide larger radius of convergence, greater robustness, and smaller computational times compared to multiple shooting[98]. However, the solution accuracy of collocation methods is less than that of multiple shooting methods[98], although this can be improved through the choice of basis functions used for collocation[14].

Collocation methods can be represented in two ways; h and p schemes[97]. p schemes, or global methods, represent the entire trajectory as high order polynomials, and converge by increasing the order of these polynomial[97]. This method works well if the underlying solution is smooth, however, if there are discontinuities present, a p scheme will fail[97]. h schemes separate the trajectory into a series of medium order polynomials, stitched together at knot points using defect constraints, similarly to the multiple shooting method[14, 97, 101]. These joining points are called knot points[97, 101]. A comparison between h and p methods is shown in Figure 3.9.

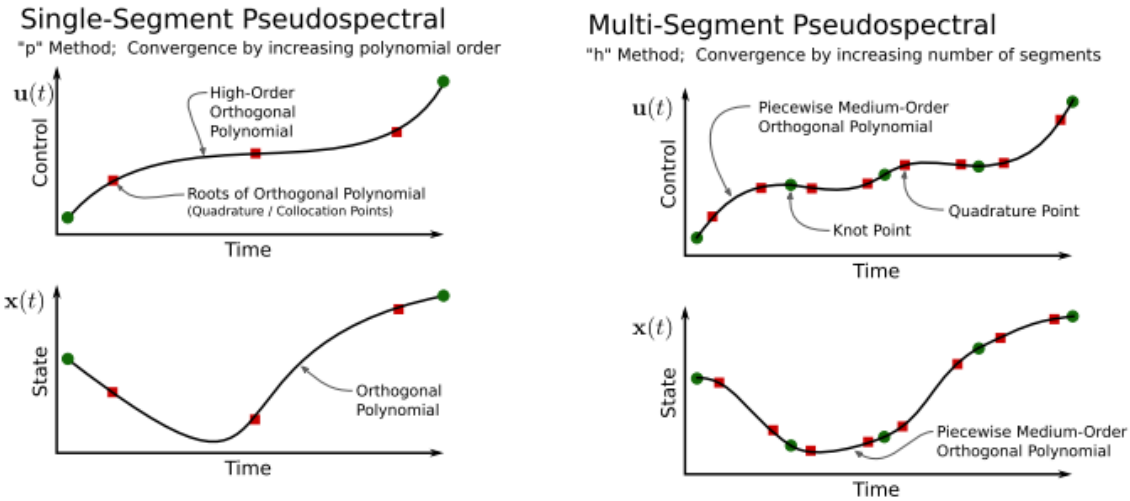


Figure 3.9: Examples of h and p collocation methods[97].

The Pseudospectral Method

The most accurate and effective type of collocation methods use orthogonal polynomials to approximate the state and control functionals[102]. In trajectory optimisation, this type of collocation is referred to as the pseudospectral method[97]. The pseudospectral method was first introduced in 1972 by Kreiss & Oliiger[103] as an efficient way to compute meteorology and oceanography problems. The pseudospectral method has recently garnered a large amount of attention for its ability to rapidly and accurately solve a wide variety of optimal control problems. When a solution is well behaved and smooth, the pseudospectral method converges at an exponential rate, with a high accuracy known as spectral accuracy[101, 104].

The pseudospectral method employs the use of orthogonal polynomials such as Legendre or Chebychev polynomials to approximate the state and control functions. This approximation is used to transcribe the optimal control problem into a nonlinear programming problem (NLP) through collocation. This process involves mapping the time domain of the system to the time interval $[-1, +1]$, and discretising the approximated dynamics at a specific set of points, obtained from Gaussian quadrature[14, 97, 102, 105, 106]. There are multiple types of pseudospectral methods, distinguished by the polynomial and collocation points used. Usually, these polynomials are Chebyshev or Lagrange polynomials[14, 102], and the collocation points are the roots of a Legendre polynomial[107]. Chebyshev polynomials have been used since the introduction of pseudospectral methods in optimal control, but have been superseded in many cases by Lagrange polynomials, which offer simpler collocation conditions[14]. There are many possible types of collocation nodes, although there are three most commonly used sets; Legendre-Gauss (LG); Legendre-Gauss-Radau (LGR); and Legendre-Gauss-Lobatto (LGL)[14, 107]. The choice of collocation type determines how the roots of the problem are calculated, and changes the formulation of the problem slightly[107]. Practically, there is very lit-

tle difference between these node sets[107]. Detailed information on the pseudospectral information may be found in Reference [105].

The pseudospectral method is usually employed as a p method, where a global polynomial is used, and convergence is achieved by increasing the order of this polynomial[14]. Recently, hp-adaptive pseudospectral methods have been introduced, which segment the mesh using an h method, whilst also having a variable polynomial degree, as in the p method[104]. These hp methods converge by varying the degree of the approximating polynomial as well as the number of segments simultaneously. Utilising both h and p methods improves the accuracy and robustness of the solution, as illustrated in Figure 3.10, from a study by Chai et al.[89] comparing the single shooting method to non-adaptive and hp-adaptive pseudospectral methods. **This figure illustrates a comparison of a boost-skip hypersonic vehicle optimised for maximum range.** All trajectories are relatively similar, however the hp-adaptive method is able to achieve slightly more range by redistributing nodes effectively. The hp-adaptive method also exhibits higher solution accuracy; in this problem the scramjet is limited to ignite at less than 1500m/s, and the hp-adaptive method ignites the scramjet at exactly 1500m/s, while the non-adaptive method ignited at 1499.256m/s, and the direct shooting at 1499.548m/s. This is a slight difference, but illustrates the improved capability of the hp-adaptive method to converge to specific optimal points. In addition to improved robustness and accuracy, the hp-adaptive method exhibits greater computational efficiency than the other methods, taking 5.3s in total to run this optimisation, compared to 12.7s for a non-adaptive method, and 268.2s for the direct shooting approach. In general the hp-adaptive method decreases the computational effort and memory usage necessary during the solution process by converging more rapidly to an optimal result[89, 104].

A secondary usability advantage of the pseudospectral method is the ability to generate Hamiltonian and costate values easily[14, 108, 109]. The Hamiltonian and costate values allow a solution to easily and quickly be checked to determine if some of the necessary conditions for optimality are being met. This is useful to determine if the optimal solution calculated by the pseudospectral solver is valid.

The pseudospectral method has been proven to be extremely effective for simulations in aerospace applications and has been proven in flight applications such as the zero propellant manoeuvre of the International Space Station in 2007, where the ISS was rotated 180 degrees without any propellant used following a pseudospectral method solution[110]. **The pseudospectral method has been used successfully in a multitude of studies for the trajectory analysis of hypersonic vehicles[86, 87, 89, 111–117], and has proved an extremely effective tool for solving the highly nonlinear trajectory optimisation problems that arise from complex aerodynamics.** These successful use cases indicate that the pseudospectral method is robust for complex, nonlinear systems, and that the pseudospectral method can be used to solve problems with many state variables and phases, such as is required by the aerodynamics and multi-stage nature of launch vehicles.

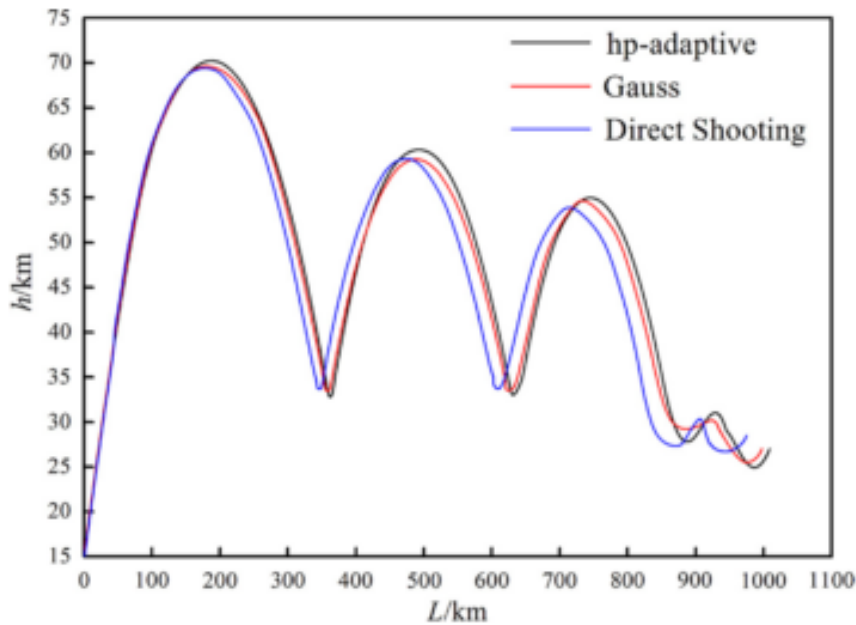


Figure 3.10: Comparison of optimisation techniques[89]. A hypersonic vehicle is optimised for maximum range. The hp-adaptive method can be observed to have produced the most optimal result.

3.5 Available Optimal Control Solvers

There are a number of optimal control solvers available, both commercially and open source, that represent well tested implementations of state of the art pseudospectral methods. A summary of the most prominent available solvers is shown in Table 3.1. These programs are mostly general solvers, and must be configured specifically in order to solve a particular optimal control problem. The exception is ASTOS[118], which is a standalone program designed for aerospace trajectory optimisation.

Functionally, most of the available solvers are similar in operation. The states and controls of the optimal control problem are defined to the program by the user, along with any constraints; continuous or endpoint. The cost function of the problem is input, and dynamic model of the system is defined. An initial guess is provided, and once activated, the solver will move toward an optimal solution from this initial guess. The most significant practical difference between the solvers lies in the robustness of the optimal solution, ie. how easily a particular solver is able to converge to the optimal solution. For a simple and continuous optimisation problem all solvers will be able to approach the same solution (though with varying efficiency). However, for a complex and nonlinear optimisation problem, some solvers will converge much more easily and rapidly than others. Generally, this stems from the underlying transcription method used. The most common form of discretisation used by these solvers is the pseudospectral method, although other forms of collocation, as well as multiple shooting, are also used. Of the methods used, hp-adaptive pseudospectral methods exhibit the best convergence and accuracy properties[89]. The readily available packages which utilise hp-adaptive pseudospectral

methods are GPOPS-2[119] and ICLOCS2[120]. Both ICLOCS2 and GPOPS-2 uses IPOPT[121], a widely used open source nonlinear optimisation package which utilises an interior point line search filter method.

ICLOCS2 is a software package in the alpha stages of development, which is based upon ICLOCS, a multiple shooting solver[120]. ICLOCS2 is able to implement a range of transcription methods, including a hp-adaptive Legendre-Gauss Pseudospectral method[120]. As ICLOCS2 is relatively new at the time of writing, it has not yet been implemented in any published works and documentation is limited.

GPOPS-2 is a proprietary hp-adaptive pseudospectral method solver, which implements a variety of hp-adaptive pseudospectral methods, so that the best method may be chosen for a given problem[119]. GPOPS-2 is specifically designed to be as flexible as possible, to accommodate for a wide range of problem formulations[119]. GPOPS-2 is well proven in aerospace applications, and has been used for spacecraft orbit optimisation as well as in-atmosphere trajectory optimisation[115, 122]. GPOPS-2 is well suited to solving multi-phase optimal control problems, which is necessary for efficient multi-stage launch optimisation[119]. GPOPS-2 represents the state of the art in trajectory optimisation software, and as such is used by a number of institutions around the world.

Software	Publisher	Platform	Optimisation Type
DIDO[123]	Elissar Global	MATLAB	Chebychev Pseudospectral
GPOPS II[119]	RP Optimization Research	MATLAB	hp-Adaptive Legendre-Gauss-Radau Pseudospectral
PROPT (IPOPT)[124]	TOMLAB	MATLAB	Legendre-Gauss Pseudospectral
ICLOCS2[120]	Imperial College	MATLAB	Multiple Shooting / hp-adaptive Legendre-Gauss Pseudospectral
POST2[125]	NASA	FORTRAN	Direct Shooting
OTIS[126]	NASA	Fortran	Pseudospectral + Various
TRANSWORHP[127]	ESA	Fortran/C++	Full Discretisation
ASTOS[118]	Astos Solutions	Standalone	Multiple Shooting/Collocation
ACADO[128]	Open Source	C++	Direct
JModelica[129]	Modelon AB, Open Source	Modelica/Python	Collocation/ Pseudospectral

Table 3.1: Summary of programs capable of pseudospectral optimisation.

Although many of these optimisation packages are relatively similar, and are appropriate for highly nonlinear hypersonic launch problems, GPOPS-2 is the most readily available package that

utilises a very high robustness and accuracy transcription method. However, GPOPS-2 is only a generic solver, requiring significant configuration to solve a launch problem. This configuration includes launch vehicle modelling, and design of the optimal control problem, so that a solution maybe achieved. These are no small tasks, as the configuration of an optimal control problem for a complex launch vehicle requires deep knowledge of both the vehicle design and performance, as well as the underlying optimal control processes.

XXX cite this last sentence

3.6 Aerodynamic Analysis

-XXX I should have here: previous studies have used low fidelity methods, particularly when doing an MDO, but I want to use a higher fidelity to allow better insights into the optimal trajectory shape

Optimising the trajectory of a space access vehicle using optimal control methods requires the input of a dynamic model of the launch vehicle. This dynamic model requires the aerodynamics of each stage of the launch system to be characterised at every flight condition experienced during launch. This is usually achieved either analytically for simple vehicle designs, or through the generation of large aerodynamic coefficient databases that cover the operable region of the vehicle. The generation of databases is generally necessary when it is desired to capture more complex and non-linear aerodynamics that must be pre-computed for efficiency.

There are a variety of tools available to calculate the aerodynamics of aerospace vehicles. These tools are primarily designed towards either accuracy or efficiency, as more accurate methods require more computational power, longer computational times and, usually, more man-hours to produce a solution. This trade off means a tool must be selected which best suits the requirements of a given problem. For a preliminary vehicle design, it is often desirable to select a tool which is as computationally efficient as possible, as the design of the vehicle is liable to change often. Whereas for more advanced stages of vehicle design, an accurate tool is desirable, to assess the design of the vehicle in detail.

The lowest fidelity, and highest efficiency methods include packages that use empirical relations derived from databases of existing vehicles, such as Missile Datcom[130], as well as panel method codes such as HYPAERO[12], cbaero[131] and HOTSOSE[132]. Low fidelity methods offer rapid solutions, with highly variable accuracy. For simple, standard vehicle shapes, low fidelity methods may be relatively accurate, as low fidelity solutions are usually calibrated to higher fidelity simulations or experiments. However, for complex vehicle geometries, for example geometries involving engine flow-paths, low fidelity models may be highly inaccurate[133].

Medium fidelity methods consist of inviscid Euler solvers such as Cart3D[134] and FUN3D[135], which are able to provide reasonable accuracy, with medium run times, by neglecting viscous effects within the solution. These solvers are often used in the later stages of preliminary design, or when

higher fidelity is necessary due to design features, but rapid solutions are still desired. Neglecting the viscous effects in the fluid flow means that the solution obtained from an inviscid solver will only be an approximation of the real flow, and that the accuracy of the solution varies depending on the type of problem being solved. For problems such as lift on a thin airfoil, inviscid Euler methods may be quite accurate, however for a problem such as boundary growth on a flat plate these methods will not accurately model the solution[136]. A particular advantage that many inviscid Euler codes provide is automatic adjoint mesh adaptation, the ability for the mesh to be automatically and rapidly generated, and updated sequentially throughout the solution process, refining areas of complex geometry or flow. This enables multiple solutions to be easily computed, without the need to regenerate meshes manually. In the early stages of vehicle design, inviscid-flow Euler CFD solvers are used extensively across industry and academia[137], as they are often able to capture **the trends in the aerodynamics of a launch vehicle sufficiently well for preliminary design purposes, while having relatively short run times that make the generation of aerodynamic databases practicable**. However, inviscid solvers naturally do not capture the aerodynamic forces on a vehicle due to viscous effects. This deficiency can be corrected using an approximation of the viscous forces, to improve the accuracy of the solution generated by an inviscid solver, while retaining the computational advantages of inviscid CFD[138].

High fidelity methods consist of Navier-Stokes CFD solvers such as Eilmer3/4[139], Fluent[140], CFX[141], COMSOL[142], TAU[143], and OpenFOAM[144]. These solvers will resolve the fluid flow and aerodynamic forces to a high level of accuracy, including viscous effects. However, the mesh for the problem must be generated prior to the calculation of the solution, which increases the working time significantly. Additionally, the computation times are much longer, and require more computational resources than lower fidelity methods. These factors make the generation of an aerodynamic database using high fidelity CFD an extremely time consuming process. As such, high fidelity CFD is suited for use on mature vehicle designs, or when accurate flow simulation is judged to be necessary to **capture the behaviour of all or part of a vehicle. This is generally applied when the behaviour of the flow is particularly complex, or when the accurate calculation of the flow properties is necessary to assess aerodynamics or engine performance.**

Cart3D

XXX Validate low mach no. paper and maybe discuss inviscid code at low mach numbers more (due to examiner comment) XXX Abenayake paper shows that cart is relatively accurate at high mach no.s but not so accurate at low M and doesnt have right trends at transsonic. Abenayake also estimates errors XXX line this section up with uncertainty section (also line missile datcom section up)
Cart3D is an inviscid Euler solver CFD package, designed for use during preliminary vehicle design and analysis[137]. Cart3D is computationally efficient and requires only a surface triangulation of the vehicle being analysed to initiate a simulation. Cart3D is utilised in this study due to its efficiency and

ease of use, along with its demonstrated accuracy for hypersonic flow calculations[146–149]. Cart3D features adjoint mesh adaptation, and uses cartesian ‘cut-cells’ which intersect the surface, allowing complex geometries to be analysed automatically. The mesh automatically refines as the simulation progresses, reducing error. The absence of a requirement for a user generated mesh allows Cart3D to be easily applied to complex launch vehicle designs, as well as allowing for simple modification of control surface deflections and flight conditions. Cart3D has been used extensively for aerodynamic simulations in preliminary design, including analysis of the plumes of the Sylon spaceplane[150], HIFIRE-5[151], and in low sonic boom shape optimisations[148]. Cart3D has shown good agreement

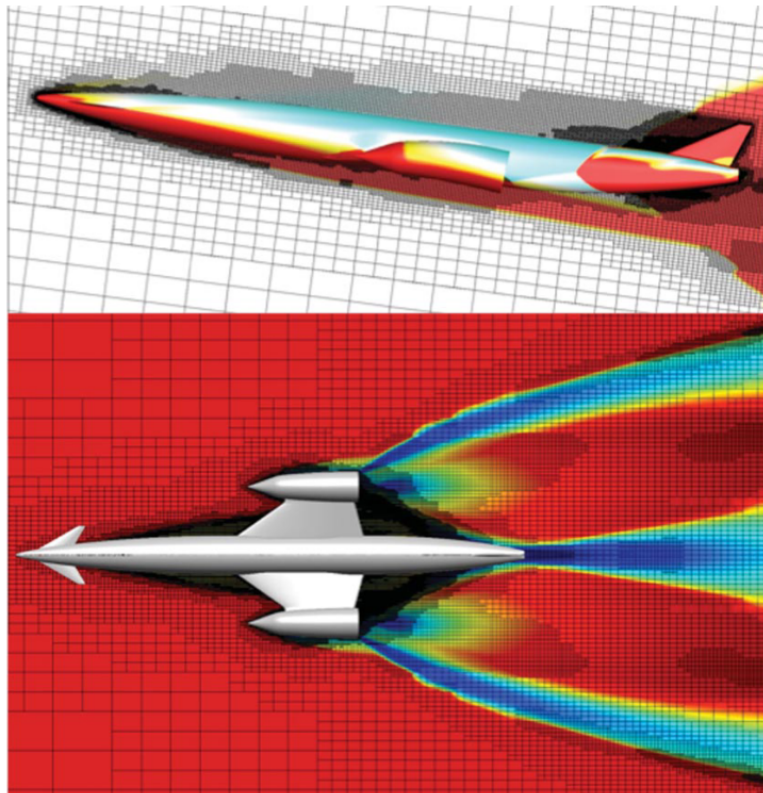


Figure 3.11: The Sylon spaceplane, simulated using Cart3D at Mach 12.189, $\alpha = 7.512^\circ$ [150]. Cell distribution produced by mesh adaptation is shown.

when compared to experimental results for winged boosters at hypersonic speeds[146], as well as supersonic missiles[147] and aircraft[148], and lifting bodies across wide Mach number ranges[149]. In addition, good agreement has been shown between Cart3D, experimental results, and full Navier-Stokes solutions for the HIFIRE-1 hypersonic test payload[146]. The model of the HIFIRE-1 and pressure coefficient results at each pressure tap are shown in Figure 3.12. Good agreement is shown between Cart3D and experimental results at all nearly all tested locations, with the exception at an identified area of shock-induced boundary layer separation, which an inviscid solution does not capture[146]. This indicates that Cart3D matches experimental results well in regions where the flow can be closely approximated by an inviscid analysis, however, regions of separation cause the accuracy of

Cart3D to diverge significantly. Finally, in a comparison between Cart3D and the Overflow-D Navier-Stokes solver, it was shown that both codes produce similar pressure distributions for simulations of the space shuttle fuel tanks at low Mach numbers[152]. The Overflow-D simulations were stated to require at least 20 times more CPU time than Cart3D[152], an example of the efficiency afforded by Cart3D.

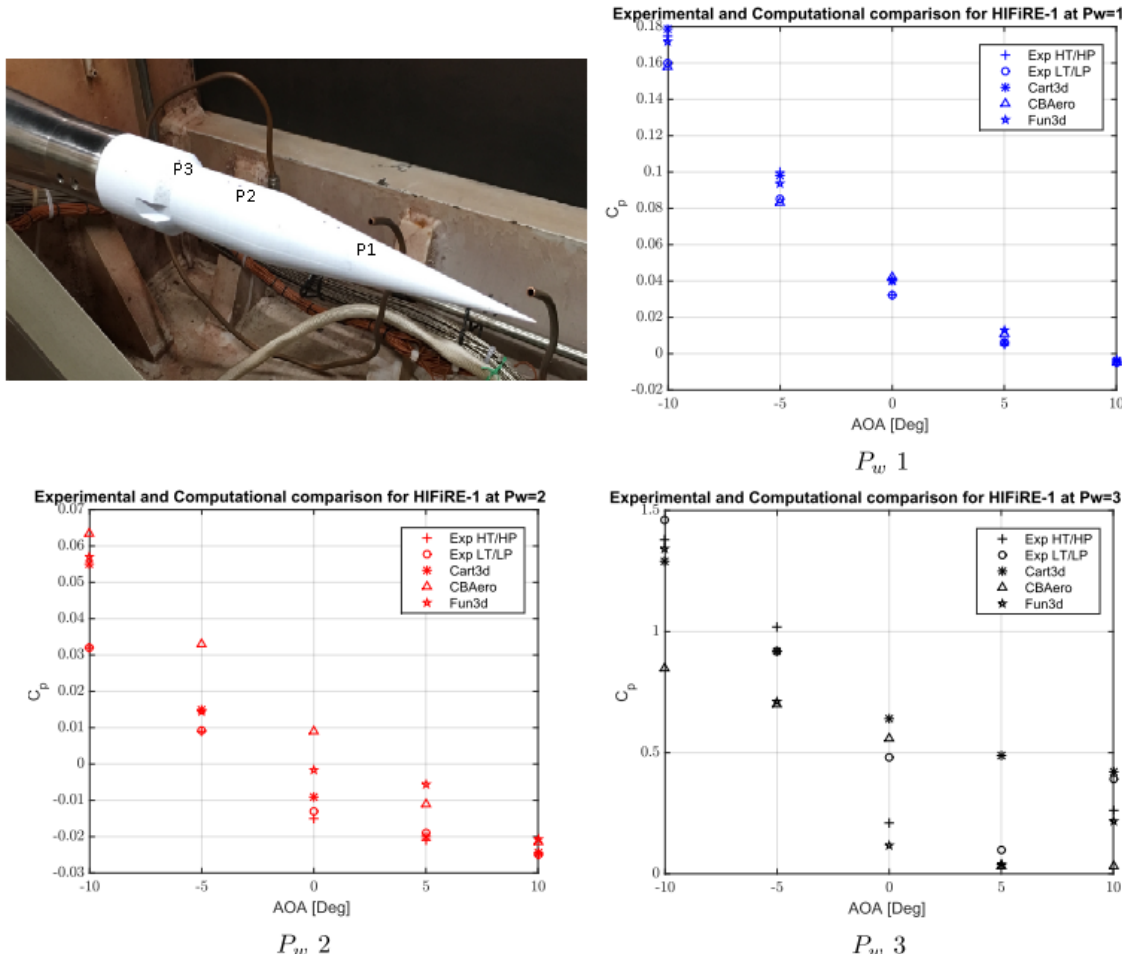


Figure 3.12: Comparisons of Cart3D with experimental data and the FUN3D Navier-Stokes CFD solver. P1, P2 and P3 indicate pressure tap locations. Modified from Sagerman et al.[146]. **XXX Change this picture to something more relevant**

3.7 Summary

XXX update summary after completion This section provided a review of available literature, pertaining to the design and trajectory optimisation of a rocket-scramjet-rocket launch system. Previous work on airbreathing launchers was detailed, and the launch trajectories of these launchers have been assessed. The SPARTAN rocket-scramjet-rocket launch system being developed at The University of

Queensland was detailed, along with the trajectory simulations performed to-date. Prior works suggest that the optimal trajectory for an airbreathing-rocket vehicle operating as a single stage involves flight at or close to maximum dynamic pressure, before a pull-up is initiated as the vehicle transitions from airbreathing to rocket power. This pull-up is also observed in some multi-stage vehicle trajectories, although in previous works this had generally been performed in order to satisfy operational requirements, rather than specifically improving the performance of the launch system. The return and maximum range trajectories of prior hypersonic vehicles have been investigated, and it was determined that a full glide-back of a vehicle is likely not possible without operation of the airbreathing engines. However, performing a ‘skipping’ manoeuvre may assist in maximising the glide range. The background of optimal control theory was outlined, and the specific optimal control techniques which are most applicable to trajectory optimisation were detailed, along with a survey of existing optimal control solvers. A survey into CFD solvers was conducted, and the specific details of Cart3D, which is utilised in this study, were examined.

CHAPTER 4

MODELLING OF LAUNCH SYSTEM DYNAMICS

In order to be competitive in the emerging small satellite market, a small satellite launcher must be cost-effective, reliable, and capable of launching on a flexible schedule. The inclusion of airbreathing engines within a small satellite launch system has the potential for improving cost effectiveness compared to disposable rocket-powered launchers, by allowing partial reusability of a launch system. The airbreathing engine most appropriate for small satellite launch systems is the scramjet engine, which operates efficiently within the hypersonic regime, with the capability to operate over a relatively large Mach number range compared to turbojet or ramjet engines. A launch system incorporating scramjets must necessarily include two rocket-powered flight phases: a rocket to accelerate the system from launch to the minimum operational Mach number of the scramjet engines, and a rocket to accelerate the payload at exoatmospheric conditions and place it into the correct orbit.

This chapter presents the design and modelling of a representative rocket-scramjet-rocket launch system, in which the scramjet stage is reusable for multiple launches. This rocket-scramjet-rocket launch system is designed to launch small satellites to a 567km altitude sun-synchronous orbit and is based on the SPARTAN launch system originally designed by Jazra, Preller & Smart[12, 83], and being developed by The University of Queensland and Hypersonix, to launch small satellites as part of a rocket-scramjet-rocket launch system. The SPARTAN launch system is used as the basis for representative launch system within this study as it is the only rocket-scramjet-rocket launch system that is currently undergoing research and design. The rocket-scramjet-rocket launch system described in this chapter is used as a representative model for a partially-airbreathing, partially-reusable, three-stage small satellite launcher.

The trajectory of a launch system involving scramjet propulsion is significantly different to that of a fully rocket-powered launch system, due to the requirement for the scramjet stage to fly within the atmosphere. Figure 4.1 shows a simplified representation of the launch trajectory for the vehicle simulated in this study. The launch system is launched vertically under rocket power, from a tradi-

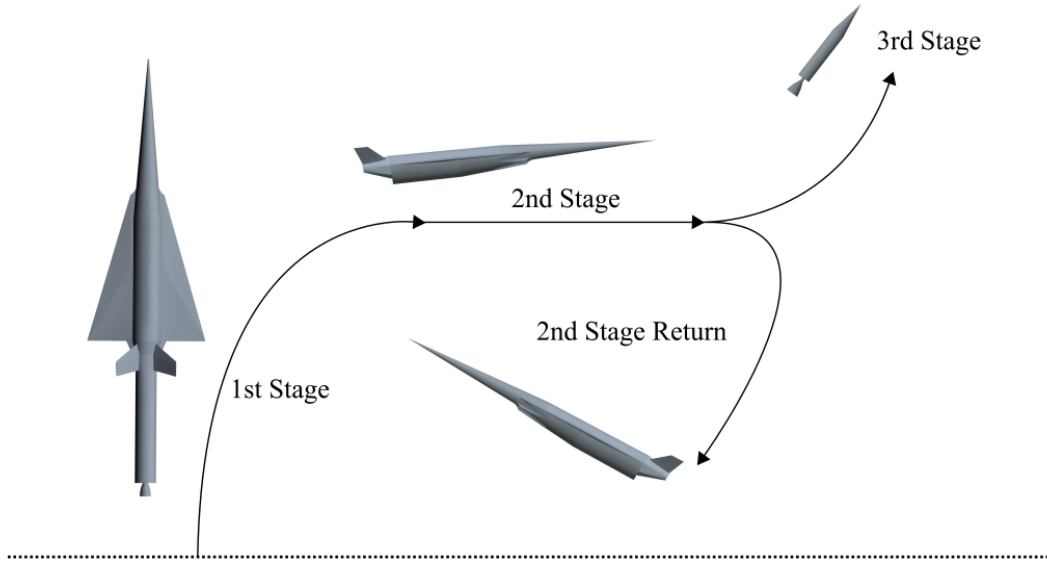


Figure 4.1: The launch process of the rocket-scramjet-rocket launch system, presented in simplified form.

tional small rocket launch facility. The scramjet accelerator is mounted to the front of the first stage rocket allowing the scramjet accelerator to take the brunt of the aerodynamic forces and heating, as well as allowing the use of the control surfaces of the scramjet accelerator. During first stage rocket operation, the launch system pitches rapidly, reaching close to horizontal flight to allow the scramjet accelerator to stay at high dynamic pressure conditions. The scramjet accelerator is accelerated to its minimum operating velocity of approximately Mach 5, at which point separation occurs. The scramjet accelerator's four scramjet engines are ignited, and the scramjet accelerator is accelerated through the atmosphere, reaching approximately Mach 9. At this point, the specific impulse of the scramjet engines, and thus the efficiency of the scramjet accelerator, have decreased, and the third stage rocket is separated. The third stage rocket accelerates and performs a pull-up, before cutting its engine and coasting out of the atmosphere. Once the rocket is exoatmospheric, the engine is reignited, performing first a circularisation burn, and then a Hohmann transfer to the intended orbit. Meanwhile, the scramjet accelerator banks and executes a fly-back manoeuvre to return to its initial launch site. The scramjet accelerator extends landing gear, and lands on a traditional runway in the style of a conventional aircraft. The scramjet accelerator is able to be rapidly refurbished and remounted for further launches. To fulfil the requirements of this trajectory, the scramjet accelerator must be able to fly and manoeuvre from velocities greater than Mach 9 to landing, as well as being able to withstand high structural and heating loads without significant deterioration.

The launch configuration of the SPARTAN is shown in Figures 4.2 & 4.3. The size and external

design of the scramjet accelerator are used exactly as defined for the Baseline vehicle designed by Preller & Smart[12]. Both the first and third stage rockets are designed in this study, and are sized around the Baseline vehicle. The first stage rocket has not previously been designed, and as such is created for this study, while the third stage is redesigned to use a SpaceX Kestrel engine. This third stage design replaces the third stage used in previous SPARTAN studies, which was powered by a Pratt & Whitney RL-10-3A engine[12]. The pump-fed RL-10-3A engine was deemed too costly, and it has been replaced by a significantly cheaper pressure-fed Kestrel engine in this study. The internal layout of the scramjet accelerator has been reconfigured around this redesigned third stage. This launch system weighs a total of ~~28355~~kg, and is 32.44m long.

The following sections present the detailed design of the launch system, along with the aerodynamic and propulsion modelling of each stage. The scramjet accelerator design is presented first, as the design of the scramjet accelerator drives the operational requirements and sizing of the launch system, and thus the design of the first and third stage rockets.

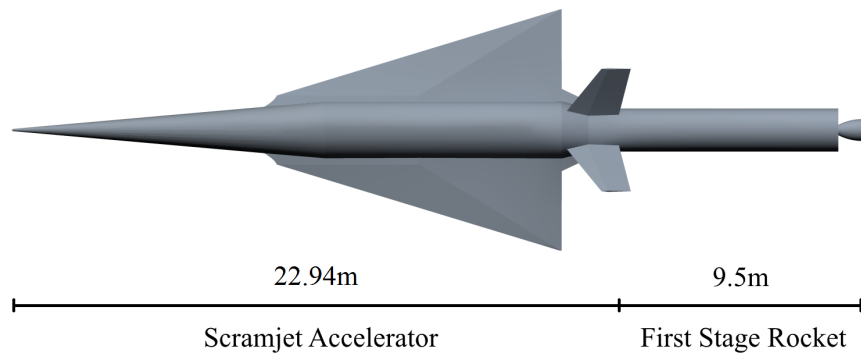


Figure 4.2: The SPARTAN launch system, top view, showing the scramjet accelerator and first stage.



Figure 4.3: The SPARTAN launch system, side view, showing the scramjet accelerator and fuel tanks, along with the third and first stages.

4.1 The Second Stage Scramjet Accelerator

4.1.1 The Scramjet Accelerator

The ~~representative scramjet-powered accelerator vehicle used in this study~~, shown in Figure 4.4, is based closely on the Baseline vehicle designed by Preller & Smart[12]. ~~The external geometry of the~~

scramjet accelerator is unchanged in this study, and is used to provide a baseline scale to the launch system. The scramjet accelerator is 22.94m long, with a frontal cone half angle of 5° [12]. A mass

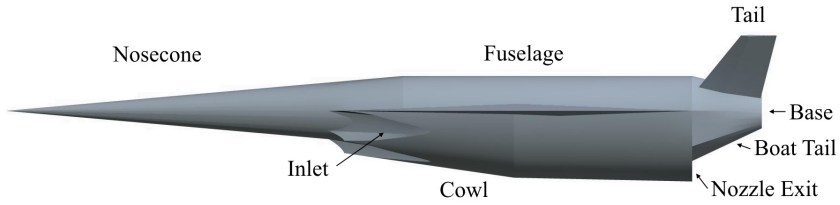


Figure 4.4: The external features of the scramjet accelerator.

breakdown of the scramjet accelerator is shown in Table 4.1, adapted from previous work by Preller & Smart[12]. The fuel mass of the scramjet accelerator has been modified for the representative launch system in this work, as the fuel tank sizes and total fuel mass are sized to accommodate the Kestrel-powered third stage, described in Section 4.3. This study assumes that the third stage is stored within

Part	Total	Fuselage	Wings	Tanks	Systems	Landing Gear	Scramjets	Fuel
Mass (kg)	6519.1	2861.6	350.7	179.4	707.5	188.9	669.0	1562.0

Table 4.1: Mass breakdown of the modified scramjet accelerator vehicle.

the fuselage of the scramjet accelerator for simplicity. It is assumed that the release mechanism for the third stage is able to be situated within the available space surrounding the third stage, however the release mechanism is not considered further in this study (see Section XXX).

The fuel tanks are sized to fit around the kestrel-powered third stage. There are three fuel tanks; two cylindrical tanks situated underneath the third stage; and a truncated conical tank in the nose. The conical fuel tank is designed to fit immediately forward of the third stage. This fuel tank is 8m long, leaving 1.47m^3 of space in the nose for cooling systems, frontal landing gear, and any additional systems or sensors which are necessary in the nose cone. The cylindrical tanks are positioned underneath and slightly to either side of the third stage, leaving space underneath for vehicle systems. The cylindrical fuel tanks are designed to be 8.5m long, with diameters of 0.87m, sized to give a nominal total tank volume of 22m^3 . The resized fuel tanks hold a total of 1562kg of LH2 fuel. This assumes an LH2 density of 71kg/m^3 , slightly denser than LH2 at phase transition point at 1 atm. The mass of the fuel tanks is scaled, by surface area, from Dawid Preller's Baseline vehicle model[12], giving a total fuel tank mass of 179.4kg.

4.1.2 Thermal Protection

The scramjet accelerator is thermally protected by a 11.3mm thick Carbon-Carbon aeroshell, with an alumina-borosilicate mat/ stainless steel multilayer insulator at the connection points between the aeroshell and the aluminium internal structure[82]. The nose tip of the scramjet accelerator is protected by 40mm thick tungsten, weighing 92kg, to provide rapid heat dissipation and sink in the area of greatest heating. For the purposes of this work it is assumed that the external shell is not connected to the internal structure close to points of large heating such as leading edges, and is structurally independent in these regions. In previous studies, a similar heat shielding has been assumed to provide adequate protection for the scramjet accelerator flying along a constant dynamic pressure trajectory[82], and this assumption is used in the main body of this work. The thermal properties of the launch system are investigated further in Section XXX and it is concluded that a more advanced thermal protection system may be necessary. However, the full redesign of the thermal protection system of the SPARTAN is beyond the scope of this report, particularly as this is currently an area of significant research effort, and there are many possibly viable options for the cooling of hypersonic systems.

4.1.3 Propulsion

The scramjet accelerator is powered by four underslung scramjet engines, fuelled by liquid hydrogen. These engines are Rectangular To Elliptical Shape Transition (REST) engines, configured to allow for a conical forebody (C-REST). REST engines have a rectangular to elliptical shape transition inlet, and an elliptical combustor, offering simplicity in design as well as reduced thermal loading and viscous drag compared to scramjets with planar geometries[153]. REST engines are also specifically designed to operate over a wide range of Mach numbers, and at off design conditions, making them particularly applicable to use on scramjet accelerator vehicles.

Propulsion Modelling

To deliver a payload to orbit, the SPARTAN's scramjet accelerator stage uses four Rectangular-to-Elliptical Shape Transition (REST) scramjet engines, with inlets configured to allow installation on a conical forebody (C-REST). The C-REST engines that the scramjet accelerator uses have been configured to fly between Mach 5 and 10. This type of engine is known as a C-RESTM10 engine[12]. The REST engine has been shown experimentally to operate successfully at off design conditions[7, 154], and has shown good agreements with numerical CFD models[7]. A C-RESTM10 propulsion database has been used in previous studies to model the scramjet engines of the scramjet accelerator[12]. The specific impulse profile of the C-RESTM10 engine, taken from the C-RESTM10 propulsion database, is shown in Figure 4.5. This database has been created through separate modelling of the compression within the inlet, combustion within the combustor, and expansion through the internal nozzle[82]. The inlet compression was modelled by performance curves based on a set of CFD solutions[82]. These performance curves are used to obtain the flow conditions at the end of the

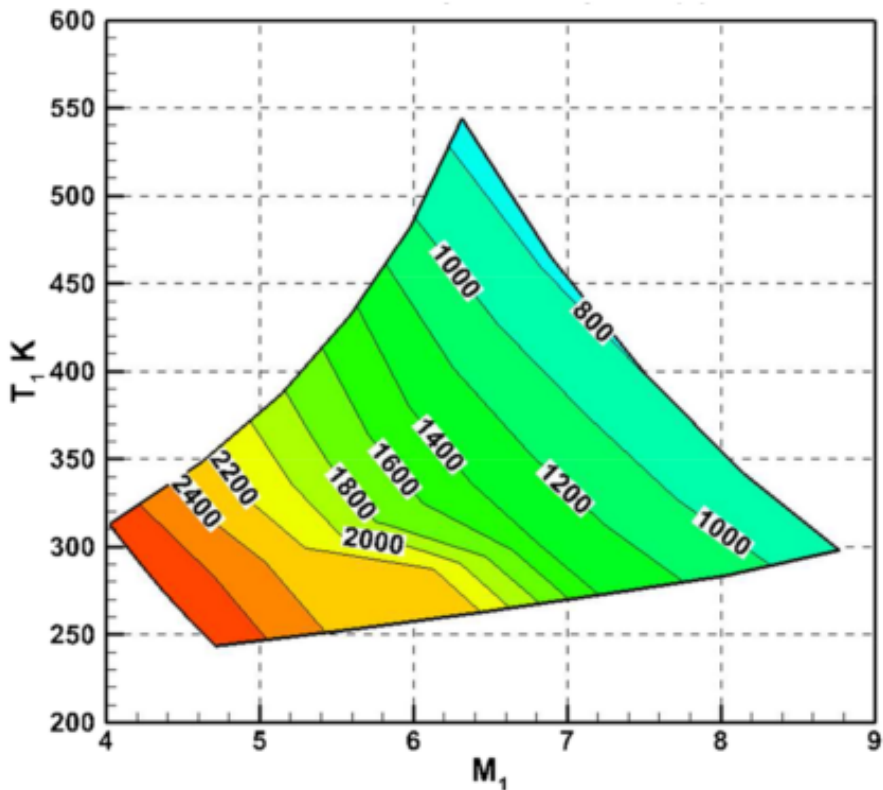


Figure 4.5: The C-RESTM10 propulsion database, specific impulse.

inlet. The combustor is modelled using quasi-one-dimentional cycle analysis, assuming a combustion efficiency of 80%[82]. Lastly, the properties at the end of the combustor are expanded assuming a nozzle efficiency of 90%[82]. The C-RESTM10 is designed for operation at $M_0 = 10$, and the contraction ratio and combustor divergence are not optimal for operation at low Mach numbers. At low Mach numbers, an equivalence ratio of 1 may cause the flow to choke and unstart. Consequently, an equivalence ratio of less than 1 was set at low Mach numbers, in order to avoid unstart[82]. At these Mach numbers, the C-REST engines are operating in dual-mode[82].

The C-REST engines are simulated separately to the aerodynamic simulations of the scramjet accelerator, using a combination of quasi-1D flow path analysis and performance curves based on high fidelity CFD simulations[12, 82]. The engine model takes the conditions at the inlet, and calculates the exit conditions and propulsive properties of the engine. The engine exit conditions are added into the aerodynamic simulations and the propulsive properties are used in the simulated vehicle model.

Before the flow enters the engine, it is affected by the conical shock generated by the forebody of the scramjet accelerator. Figure 4.6 shows the locations of the flow properties, which are necessary to calculate engine performance. The ambient atmospheric conditions are calculated by interpolation using the 1976 NASA Atmospheric properties[155]. The flow properties at the inlet of the engines is calculated using the Taylor-Maccoll analysis method for conical shocks[156]. This calculation is performed in the cone_shoot program provided for this study by Prof. Michael Smart. The flow

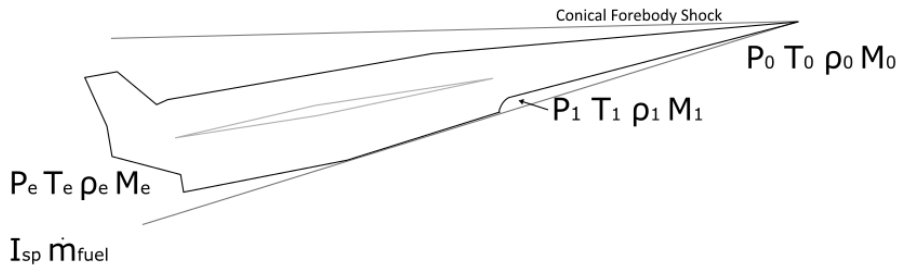


Figure 4.6: The locations of conditions relevant to C-REST engine simulation.

conditions as a function of flight conditions following the conical shock are shown in Figure 4.7.

The engine model used is based on the CRESTM10 database[12, 82], analysed using quasi-1D simulation and provided for this study by Prof. Michael Smart. This database has previously been used in simulations of the scramjet accelerator, as detailed in Section XXX. This database provides data points of engine performance over inlet conditions within the operational range, at 50kPa dynamic pressure equivalent conditions. The specific impulse data set is shown in Figure 4.8. This data is interpolated for the given inlet conditions, to calculate specific impulse produced by the engine. As the data points of the CRESTM10 database are unevenly distributed for inlet Mach and temperature, care must be taken in order to interpolate smoothly to allow the optimal control solver to converge successfully. To ensure that smooth interpolation is achieved, the CRESTM10 database is first interpolated using linear interpolation, for each ‘set’ of four nodes which form a square. A uniform grid is created using this linear interpolation, on which a cubic spline interpolation is applied using Matlab’s griddedInterpolant function. This is explained in detail in Appendix D. During flight the C-REST inlet conditions generally stay within the region bounded by the available data. However, for the purposes of the trajectory optimisation, it is necessary to provide data for a wide range of inlet conditions (T_1, M_1). To calculate I_{SP} and equivalence ratios outside of the modelled range of inlet conditions, the existing data is extrapolated. This extrapolation is performed in the same manner as the interpolation, a linear extrapolation, followed by a cubic spline interpolation of the extrapolated points. This allows for smooth continuity between the interpolated and extrapolated points, while ensuring that the extrapolated regions provide reasonable values.

For operation at high Mach numbers, the fuel mass flow rate is assumed to be stoichiometric, so that $m_f = 0.0291\dot{m}$. This ensures that the scramjet engines are performing at high efficiency throughout the acceleration of the scramjet stage. However, the C-REST engine is a fixed geometry engine, primarily designed for operability at high Mach numbers[12]. At lower Mach numbers, the addition of excessive fuel may cause the engine to choke and unstart, resulting in total loss of thrust[12]. To avoid unstart, an equivalence ratio (ϕ) of less than 1 is necessary at low Mach numbers. In this region the equivalence ratio is set to the maximum value which does not cause the engine to unstart. The equivalence ratio interpolation is linear, as the number of data points available for interpolation is low. The prescribed equivalence ratio over the range of scramjet engine operation is shown in Figure 4.9.

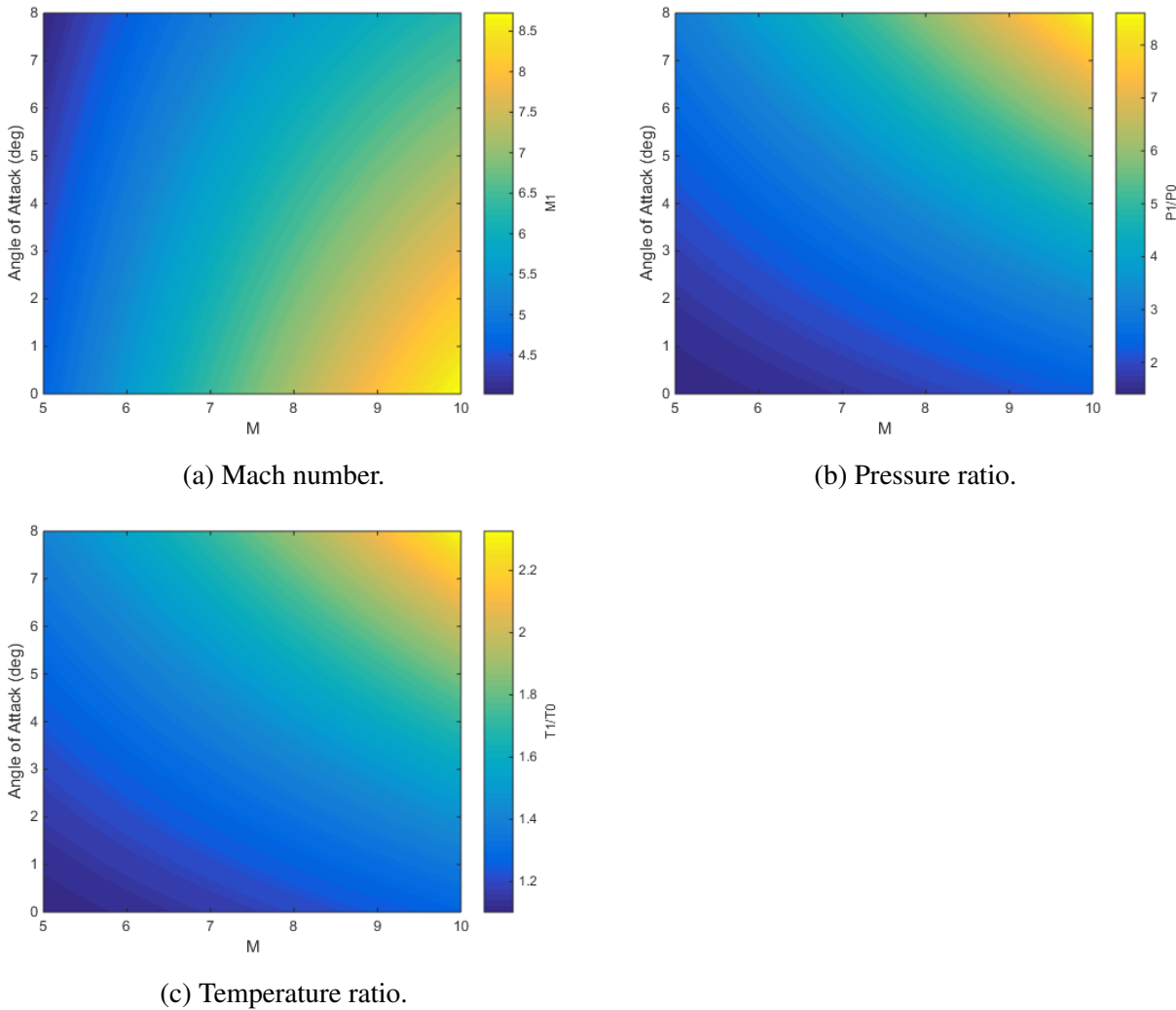


Figure 4.7: Flow conditions after the conical shock generated by the vehicle nose cone as a function of flight Mach number and angle of attack. Figure a) shows the Mach number, b) shows the pressure ratio, and c) shows the temperature ratio following the conical shock, at the engine inlet.

For these conditions, the fuel mass flow rate is determined by approximating the flow into the inlet as an ideal gas;

$$\dot{m} = 0.9 m_c A_{cap} P_0 M_0 \sqrt{\frac{\gamma_0}{R_{air} T_0}}, \quad (4.1)$$

$$\dot{m}_{fuel} = \left(\frac{m_{fuel}}{m_{ox}}\right)_{st} \phi \dot{m}. \quad (4.2)$$

The multiplier of 0.9 is an approximate term included to account for losses due to asymmetry within the engine[82]. The thrust for each engine, T , is obtained by inclusion of the interpolated specific impulse, ie.

$$T = g_0 \dot{m} I_{sp}. \quad (4.3)$$

In the available database, the C-REST engine was modelled to a nozzle exit area of 0.5586m^2 .

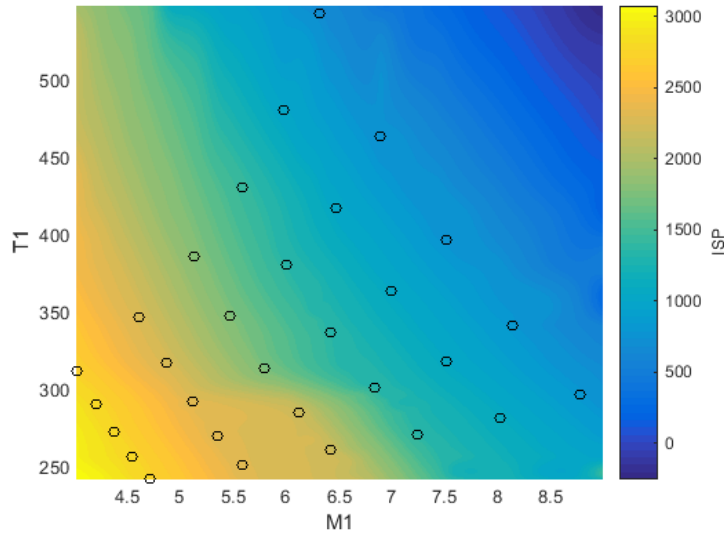


Figure 4.8: Specific impulse of the C-REST engines with input temperature and Mach number. Available data points are indicated.

This is smaller than the exit area modelled on the version of the scramjet accelerator used in this work, of 0.9719m^2 . For this reason, additional thrust is obtained from an additional nozzle segment, and the specific impulse of the C-REST engines will be higher than calculated in the database. The modelling of this additional nozzle segment and the thrust obtained are detailed in Section 4.1.4.

4.1.4 Aerodynamics

In order for the trajectory of the SPARTAN to be successfully simulated and optimised, the aerodynamics of the scramjet accelerator must be calculated for the large range of flight conditions experienced during its acceleration and return flights. The aerodynamics of the scramjet accelerator are calculated at set flight conditions covering the breadth of necessary conditions, and the results are tabulated in databases. During trajectory simulations, the aerodynamics of the scramjet accelerator are determined by interpolation over the aerodynamic databases using bivariate splines, and the drag and lift produced are calculated using the standard definition of the aerodynamic coefficients:

$$F_d = \frac{1}{2}\rho C_D v^2 A, \quad (4.4)$$

$$F_L = \frac{1}{2}\rho C_L v^2 A. \quad (4.5)$$

The trimmed aerodynamic databases of the scramjet accelerator are generated in full prior to trajectory simulation to improve the computational efficiency of the simulation. The aerodynamic coefficients of lift, drag and moment are tabulated, and these tables are interpolated during simula-

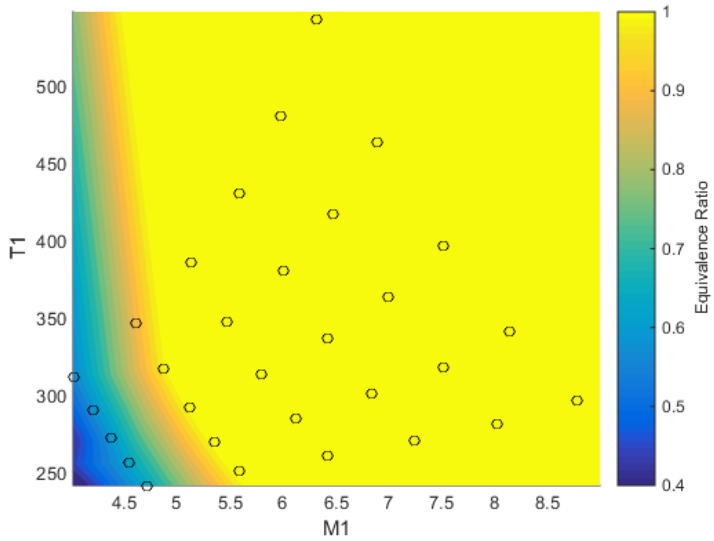


Figure 4.9: Operable equivalence ratio of the C-REST engines with input temperature and Mach number. Available data points are indicated.

tion. The aerodynamics are calculated for Mach numbers between 0-10, angles of attack between 0° and 10° , and for altitudes between 0-40km. Separate aerodynamic simulations are performed for engine-on and engine-off conditions, as the operation of the scramjet engines changes the aerodynamic characteristics of the scramjet accelerator significantly. When the engines are powered-on, the engines are generating thrust on the internal nozzle, as well as on the boat tail and base. When the scramjet engines are not operational air flows through the engine flowpath without fuel injection, generating a large amount of drag.

The process for generating the aerodynamic databases is shown in Figure 4.10. First, a CAD model of the scramjet accelerator is developed, providing the centre of gravity of the scramjet accelerator, as well as a geometry database which is used to create triangulated surface meshes. These surface meshes are then imported into the inviscid CFD solver Cart3D[134], which calculates flow solutions to determine the aerodynamics of the scramjet accelerator at various flight conditions. CFD solutions are generated for the scramjet accelerator with the scramjet engines turned off, with the scramjet engines operational, and for a range of flap deflections. The flap deflections necessary to trim the vehicle are calculated at every flight condition, by balancing the aerodynamic moment of the scramjet accelerator with the aerodynamic moment generated by the flaps. The additional lift and drag generated by the flaps are then added to the untrimmed aerodynamics to create a trimmed database. Finally, the viscous components of the aerodynamics of the scramjet accelerator are calculated, and added to the aerodynamic database. These processes are described in detail in the following sections.

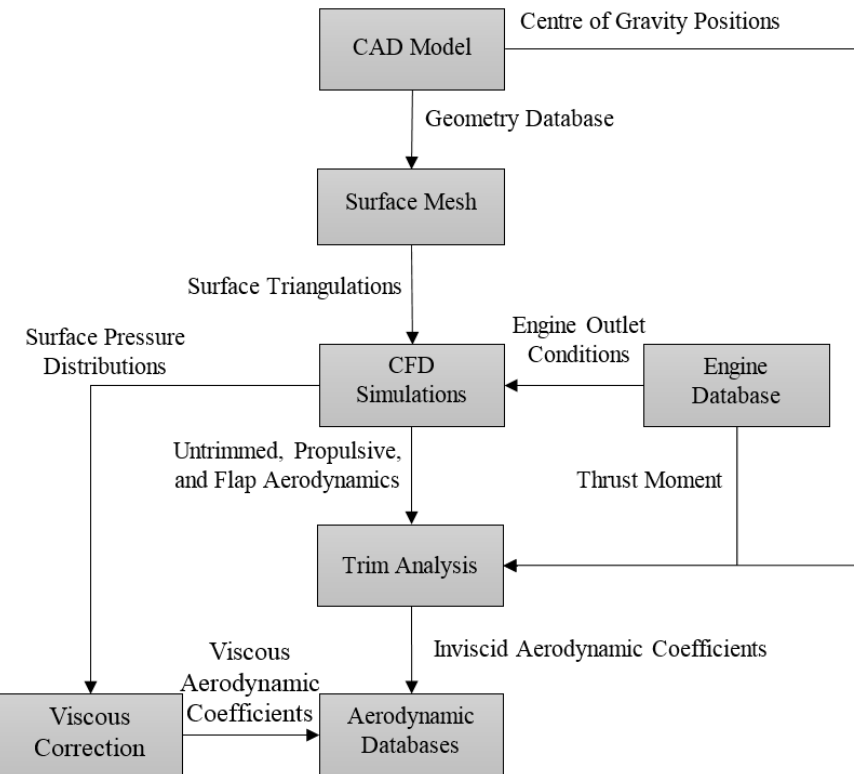


Figure 4.10: The process for generating aerodynamic databases.

Cart3D Simulations

The aerodynamics of the SPARTAN have been calculated using Cart3D, an inviscid CFD package used in the preliminary design of aerospace vehicles. Cart3D utilises adjoint mesh adaption with a Cartesian cut-cells approach to produce an iteratively refined mesh to fit a flow solution. Cart3D is used to generate the aerodynamic database of the SPARTAN due to its applicability in both the subsonic and supersonic regimes, and its robustness across multiple flow solutions[146–149, 152]. Cart3D has previously been used to analyse hypersonic vehicles, and has shown good agreement with experimental data across multiple studies[146–149], as described in Section 3.6.

Initially, a surface triangulation of the scramjet accelerator is created in Pointwise, shown in Figure 4.11. This is then imported into CART3D as a watertight surface. The Cart3D Meshes are then initiated with an outer boundary distance of 40 times the vehicle length. This boundary distance has been observed to produce suitable free stream conditions and good mesh convergence. Nine mesh adaption levels are used. Nine levels have been observed to generally produce good convergence, with moderate computation times of 1-3 hours per simulation. The convergence of the residuals and forces are investigated to ascertain if a solution has converged. Figure 4.12 shows an example solution validation for Mach 6, 2° angle of attack, engine-on conditions. Good convergence can be observed in the force functionals, with a corresponding decrease in the error estimate of the functional indicating

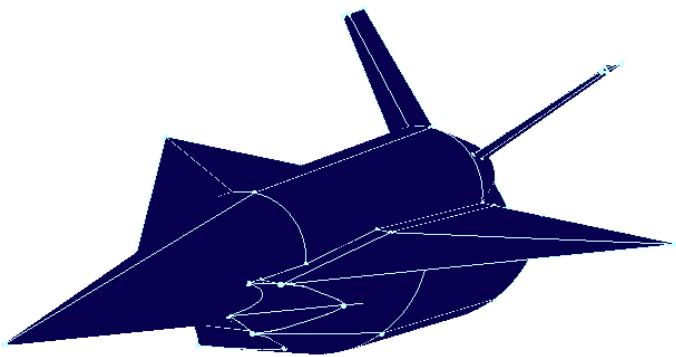


Figure 4.11: Surface triangulation of the scramjet accelerator, generated using Pointwise[157].

solution convergence.

Following simulation in CART3D over the required flight conditions, the aerodynamic coefficients are extracted. The simulation files are processed using Clic, a subprogram of CART3D used to calculate aerodynamic forces and moments, given surface pressure distributions. For engine-off aerodynamics, the aerodynamic coefficients of the entire scramjet accelerator are extracted. However, for the engine-on aerodynamics of the scramjet accelerator, the engine flowpath, boat tail and base of the scramjet accelerator are removed when the aerodynamic coefficients are extracted. The flowpath of the scramjet engines is assumed to be replaced by the conditions given by the CRESTM10 engine database, and a separate Cart3D simulation is used to calculate the aerodynamic forces on the boat tail and base.

Engine-On Aerodynamic Analysis

When the scramjet engines are turned on, the exhaust exits the nozzle of the engines and expands onto the boat tail of the scramjet accelerator. This changes the aerodynamics of the boat tail significantly, necessitating separate Cart3D simulations to calculate the varied aerodynamic coefficients of the boat tail. In addition, the scaled engine modelled in the CRESTM10 propulsion analysis has an exit area of 0.5586m^2 , smaller than the nozzle exit area on the scramjet accelerator, of 0.9719m^2 . The larger nozzle exit of the scramjet accelerator provides additional expansion area, and additional thrust, which must be modelled using Cart3D.

The exhaust of the C-REST engines is simulated using CART3D, using SurfBC boundary conditions, which produce outflow and inflow conditions at the inlet and exit of the scramjet engines[158]. The exit conditions calculated by the CRESTM10 database, as defined in Section 4.1.3, are set as the inflow conditions for the Cart3D surface. The inflow surfaces are positioned inside the nozzle on the scramjet accelerator model, scaled to match the exit area of the engines simulated for the CRESTM10 database, 0.5586m^2 . The surface triangulation of the scramjet accelerator with outflow

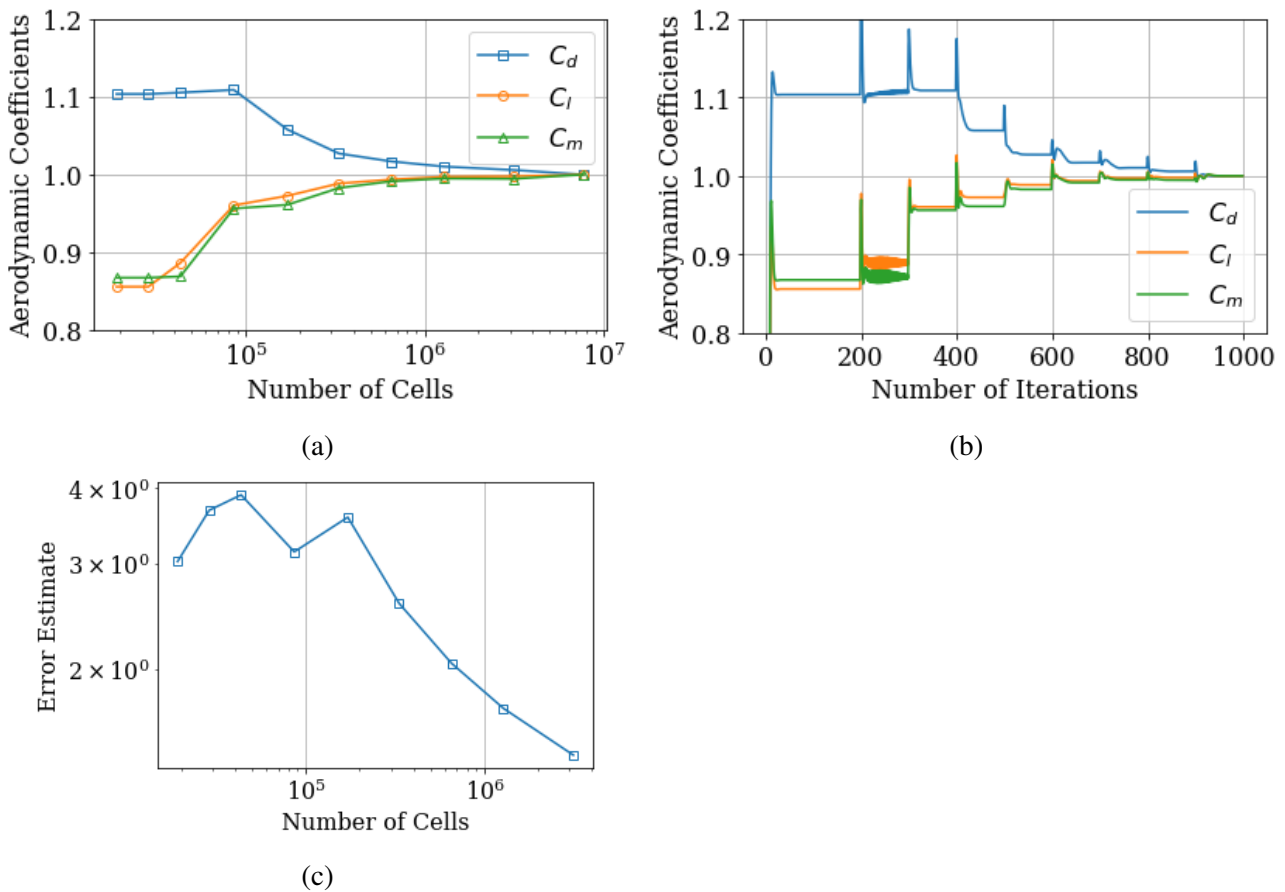


Figure 4.12: The convergence of a Cart3D simulation of the scramjet accelerator at Mach 6, 2° angle of attack.

surfaces is shown in Figure 4.13. Cart3D performs simulations nondimensionally, and requires the outflow conditions of a boundary to be normalised. The outflow conditions of P_e , ρ_e and M_e given by the CRESTM10 propulsion model are normalised to Cart3D nondimensionalised variables as follows[159, 160];

$$P_e^* = P_e / (\gamma_0 P_0), \quad (4.6)$$

$$\rho_e^* = \rho_e / \rho_0, \quad (4.7)$$

$$M_e^* = \sqrt{\gamma_e / \gamma_0} (M_e \sqrt{P_e^* / \rho_e^*})^2. \quad (4.8)$$

Where $*$ indicates the nondimensionalised input to Cart3D. This nondimensionalisation includes a correction on the Mach number to account for variation in the specific heat ratio, which is not possible to include directly in Cart3D[150]. The exhaust of the scramjet engines expands through the additional area of the scramjet accelerator's nozzle, and is further expanded onto the boat tail on the

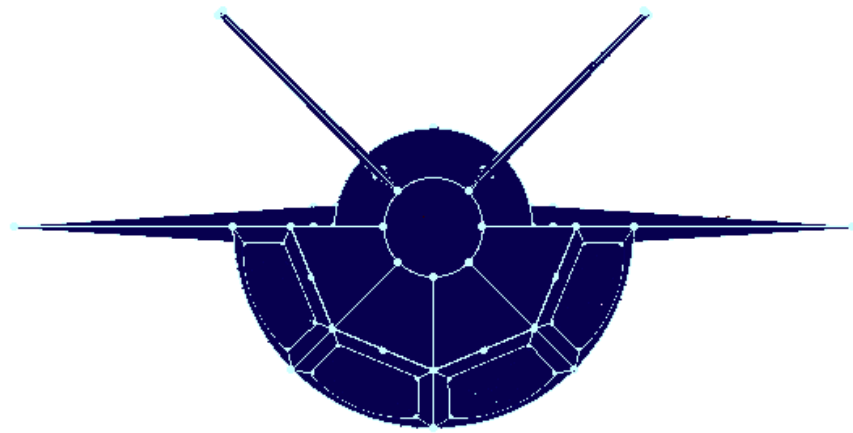


Figure 4.13: View of the scramjet accelerator surface triangulation showing engine outlet boundaries.

rear of the scramjet accelerator fuselage. This expansion causes significant force on the boat tail of the scramjet accelerator, generating additional lift, thrust, and moment forces. The total thrust generated by the scramjet accelerator, including the thrust generated by the additional nozzle expansion, and the forces on the boat tail, are shown in Figure 4.14, with the corresponding specific impulse shown in Figure 4.15.

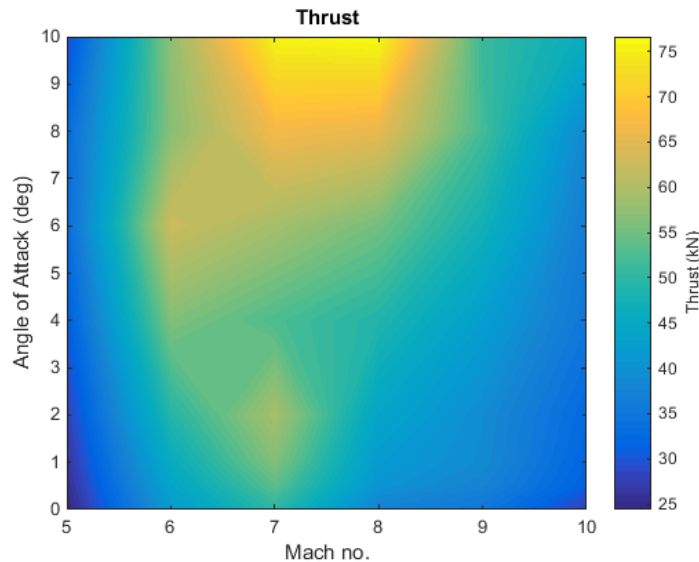


Figure 4.14: The total thrust output of the scramjet accelerator, including the CRESTM10 database, and Cart3D nozzle and boat tail simulations.

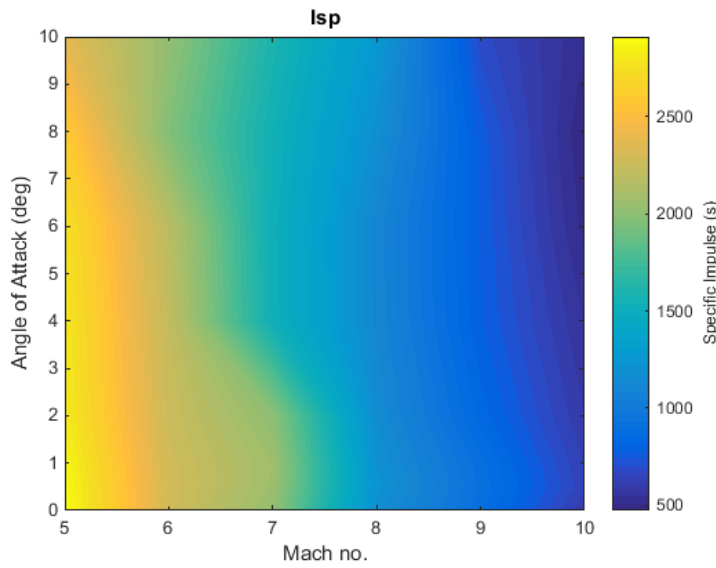


Figure 4.15: The specific impulse of the scramjet accelerator, including the C-rest database, and Cart3D nozzle and boat tail simulations.

Centre of Gravity Analysis

The centre of gravity locations of the SPARTAN are calculated using CREO. For simplicity, it is assumed that structural, systems and landing gear masses are homogeneously distributed throughout the centre fuselage of the scramjet accelerator. The calculated centre of gravity for the scramjet accelerator full of fuel and including the third stage rocket is **15.24m** along the body length. The centre of gravity varies as fuel is depleted throughout the acceleration phase, and at third stage release, changing the flap deflections required for trim. The cylindrical fuel tanks are depleted first, in order to shift the centre of gravity forward, and improve the aerodynamic stability of the scramjet accelerator during the majority of flight. Depleting fuel from the cylindrical fuel tanks first would likely also serve to reduce fuel slosh during flight, although the fuel slosh is not modelled in this study, and it is assumed that the centre of gravity of each individual tank remains constant. After the cylindrical tanks have been depleted, the fuel in the conical tank within the nose is used. The third stage is released at the end of acceleration, and the centre of gravity changes significantly. When the third stage is released there is still fuel stored in the conical tank for flyback, during which centre of gravity change must also be modelled. Consequently, aerodynamic databases are created for centre of gravity conditions of;

- full of fuel including third stage,
- conical fuel tank full of fuel, including third stage,
- empty of fuel including third stage,

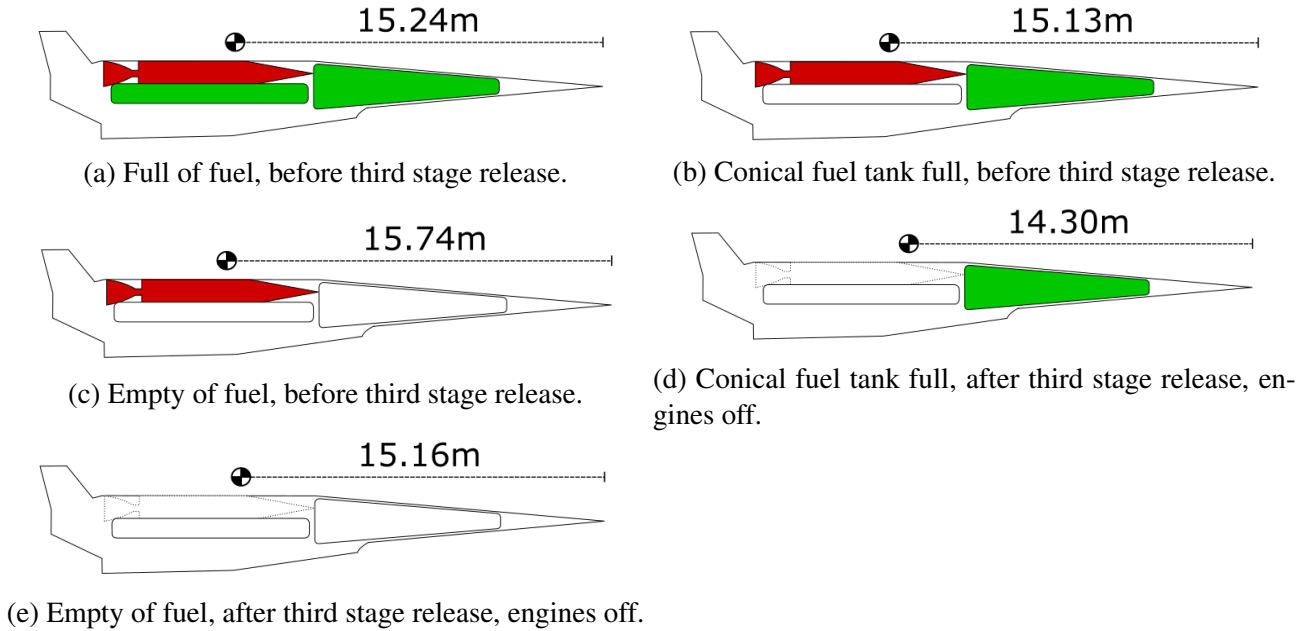


Figure 4.16: Centre of gravity positions throughout the flight of the scramjet accelerator.

- conical fuel tank full of fuel after third stage release,
- and empty of fuel after third stage release.

Each of these conditions, along with the corresponding centre of gravity, is shown in Figure 4.16. At each of the listed centre of gravity conditions, aerodynamic coefficients and flap deflections necessary for trim are calculated. As each fuel tank is depleted, and the centre of gravity shifts, the aerodynamics at the two closest centre of gravity conditions are interpolated to produce the aerodynamics of the scramjet accelerator.

Calculation of Trimmed Flap Deflections

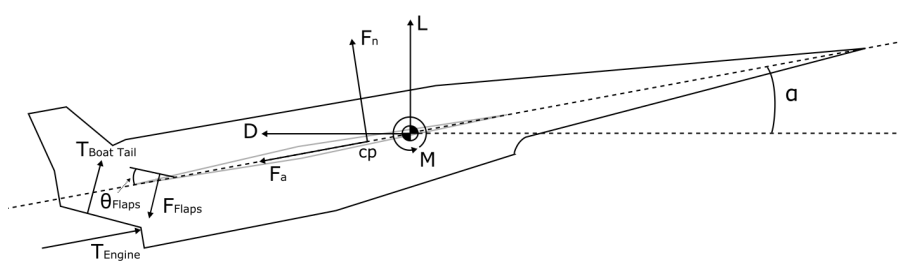


Figure 4.17: The forces on the scramjet accelerator during flight.

The scramjet accelerator as designed by Preller[12] is trimmed using control surfaces on the wings, shown in figure 4.18. The flaps of the scramjet accelerator are modelled at deflected states

of -20° , -10° , 10° , and 20° . The scramjet accelerator is modelled in CREO with the flaps at each of these deflected states, and a surface mesh is created in Pointwise. Cart3D is used to simulate each of these flap deflected states, and Clic is used to extract the aerodynamic coefficients, for Mach numbers between 0.2 and 10. These aerodynamic coefficients are tabulated, and interpolation splines fitted, so that the flight Mach number and the moment generated by the flaps are used to interpolate for the flap deflection, ie. $\theta_{Flaps} = f(M, M_{Flaps})$. Trim is determined by calculating the aerodynamic

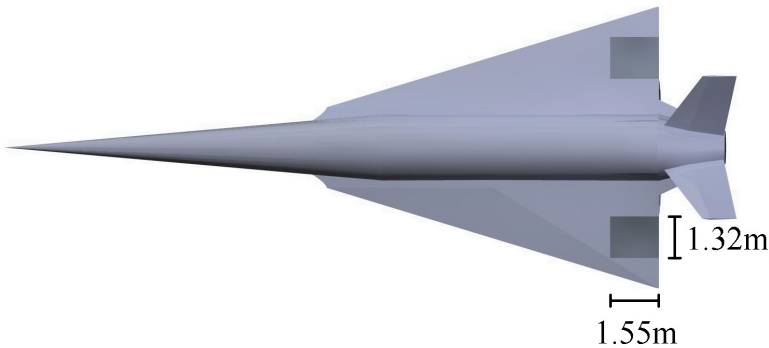
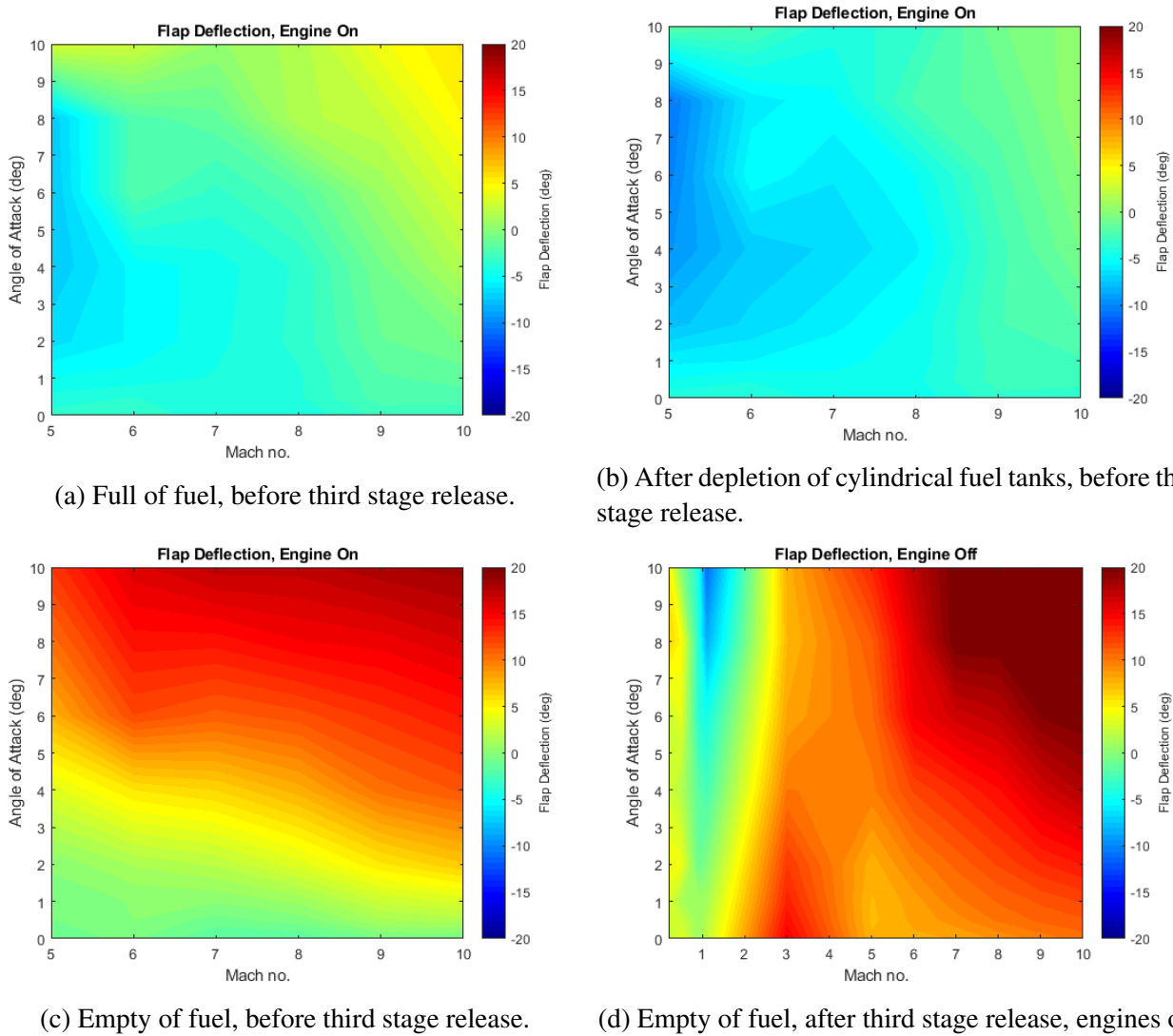


Figure 4.18: scramjet accelerator model showing control surfaces.

moment coefficient with zero flap deflection, then calculating the flap deflection necessary to balance the aerodynamic moments to zero. The moments generated by the untrimmed scramjet accelerator, as well as the thrust moments on the engines and boat tail when the C-REST engines are powered-on, are balanced by the moment generated by the flaps, so that:

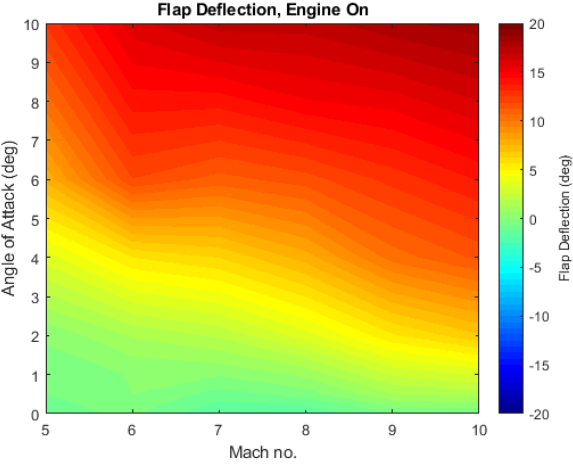
$$M_{Flap} = -M_{Untrimmed} \quad (4.9)$$

The flap deflections necessary for trim are shown in Figure 4.19, calculated for Mach numbers between 0.2 and 10, and at angles of attack from 0° to 10° . Engine-on flap deflections are shown at centre of gravity locations corresponding to full-fuel, full conical tank, and empty conditions with the third stage included, and engine-off flap deflections are shown at the centre of gravity corresponding to a fuel-empty condition after third stage release. The flap deflections are designated as negative up. Negative flap deflection necessary for trim indicates that the centre of pressure is aft of the centre of gravity, and that the vehicle has positive static margin. It can be observed that while the cylindrical fuel tanks are being used, the scramjet accelerator is generally stable at low angles of attack, and the static margin is close to 0, requiring only small flap deflections for trim. As the fuel in the conical tank is depleted, the centre of gravity moves aft, and the scramjet accelerator develops a negative static margin, requiring larger flap deflections to trim at high Mach numbers. These large flap deflections indicate that the scramjet accelerator may experience instability issues at the end of its acceleration, however, determining the controllability of the scramjet accelerator is outside the scope of this study.

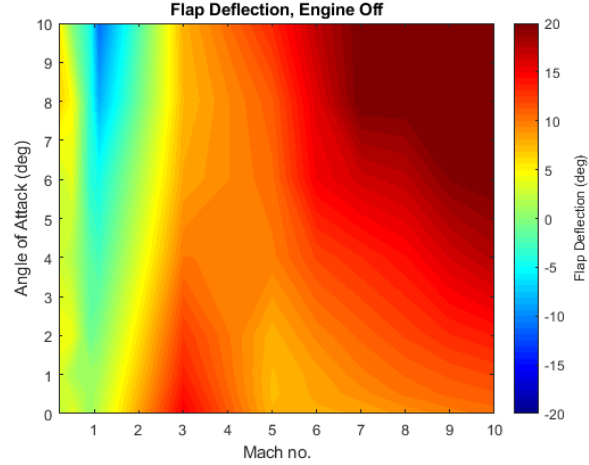


(a) Full of fuel, before third stage release.

(b) After depletion of cylindrical fuel tanks, before third stage release.



(c) Empty of fuel, before third stage release.



(d) Empty of fuel, after third stage release, engines off.

Figure 4.19: Flap deflection required for trim of the scramjet accelerator. Negative up.

Once the flap deflections necessary to trim the scramjet accelerator are calculated, the additional lift and drag produced by the flaps are added to the aerodynamic database, ensuring that the scramjet accelerator is trimmed at every flight condition. Trimmed aerodynamic databases are calculated for engine on and engine off conditions, as well as at all centre of gravity locations listed previously.

Viscous Correction

As Cart3D is an inviscid solver, the aerodynamic database generated by Cart3D lacks the forces generated by skin friction drag. In order for the aerodynamic model to more closely approximate realistic dynamics, a correction for the viscous forces on the scramjet accelerator is calculated, using the viscous correction solver VC3D[138]. VC3D utilises flat plate correlations for skin friction on each surface cell, employing a simplified running length based on the Euclidean distance to the respective

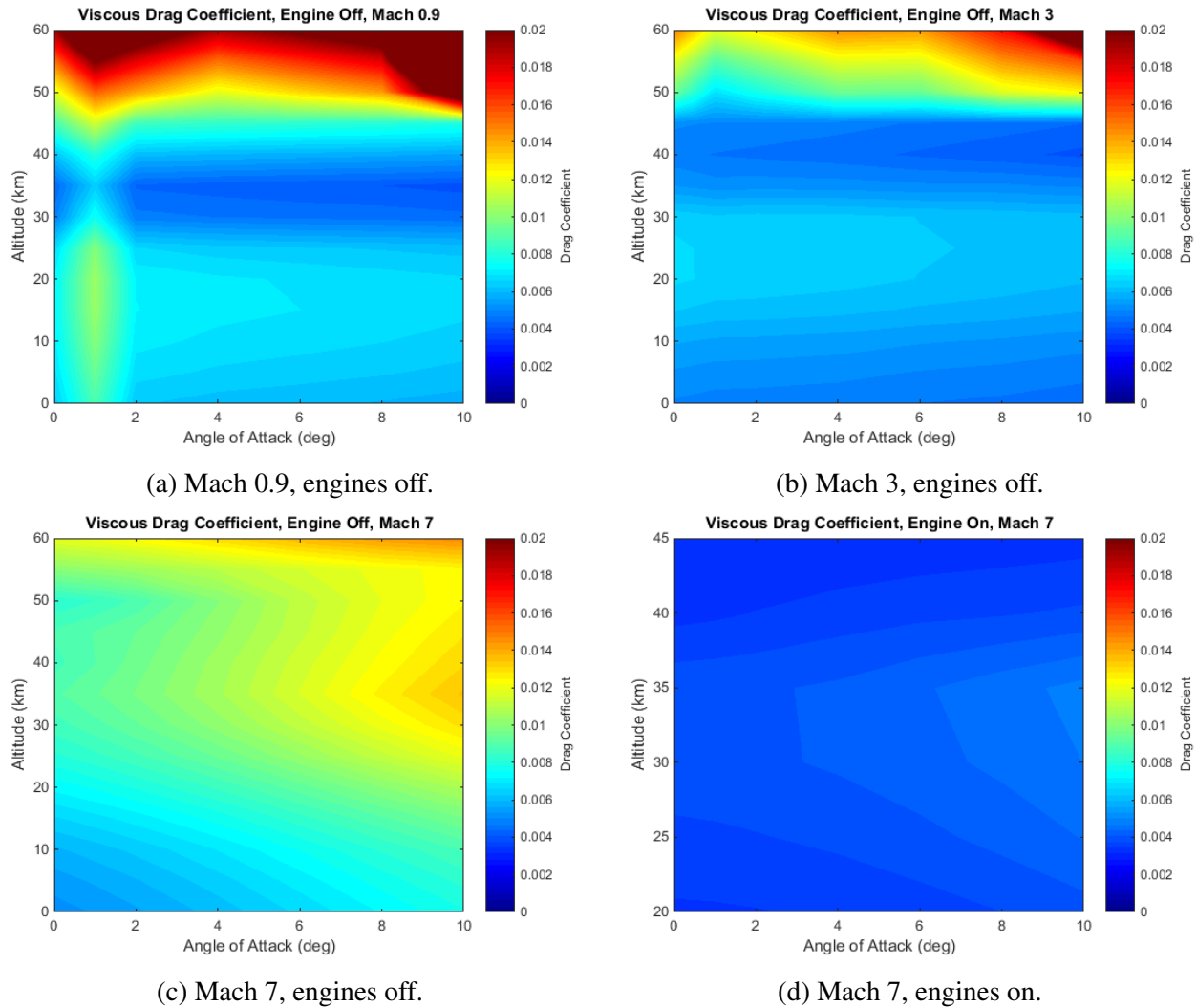


Figure 4.20: Viscous drag coefficient across various Mach numbers.

stagnation feature. Further details of this solver can be found in Reference[138]. This method has been shown to significantly improve upon the accuracy of the aerodynamic coefficients calculated by Cart3D for multiple test vehicles[138]. The additional viscous force and moment components from flap deflections are calculated using mean skin friction coefficient for computational efficiency, due to the very small contribution of this to the flap forces. The viscous drag coefficients are generated for the scramjet accelerator at every Mach number and angle of attack which are simulated in Cart3D. Viscous databases are generated for both engine-on and engine-off cases, for altitudes of 20-45km and 0-60km respectively. The viscous drag coefficients for selected flight conditions are shown in Figure 4.20.

4.1.5 Trimmed Aerodynamic Database of the Scramjet Accelerator with Engine-On

The engine-on aerodynamics of the scramjet accelerator are used during the simulation of the acceleration phase, when the C-REST engines are operational at all times, as well as during the fly-back phase, when the engines are operational for a short time to aid the scramjet accelerator in returning to its initial launch site. The external aerodynamics of the scramjet accelerator with the scramjet engines powered-on are calculated by removing the engine and boat tail from Cart3D simulations of the scramjet accelerator with engine flowpaths. Engine-on aerodynamic calculations are performed for Mach numbers 5, 7, 9 and 10. An example of a Cart3D solution of the nozzle exit and boat tail with the scramjet engines powered-on is shown in Figure 4.21, and the aerodynamics of the scramjet accelerator with engines powered-on are shown in Figure 4.22.

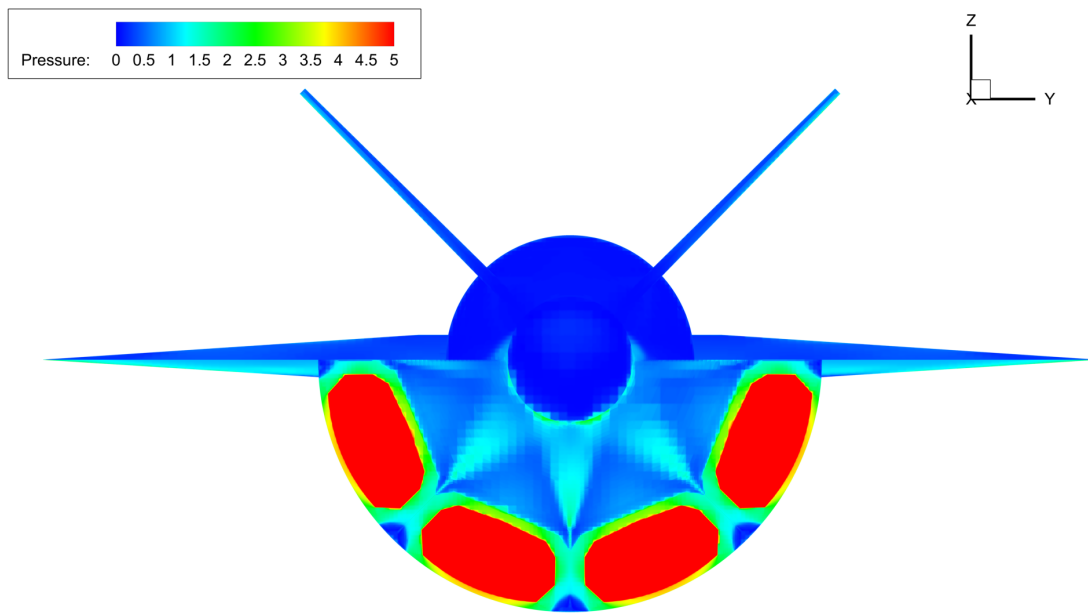


Figure 4.21: Engine-on Cart3D simulation at Mach 6, 2° angle of attack, and 25km altitude.

4.1.6 Trimmed Aerodynamic Database of the Scramjet Accelerator with Engine-Off

During the majority of the return flight, the scramjet engines are not operational, and the scramjet accelerator is gliding without power. The return phase takes the scramjet accelerator from third stage separation, at approximately Mach 9, to landing approach at low subsonic speeds. While the engines are not powered-on air flows through the flowpath without fuel injection, generating a large amount of drag. The aerodynamics of the scramjet accelerator are calculated using Cart3D for Mach numbers

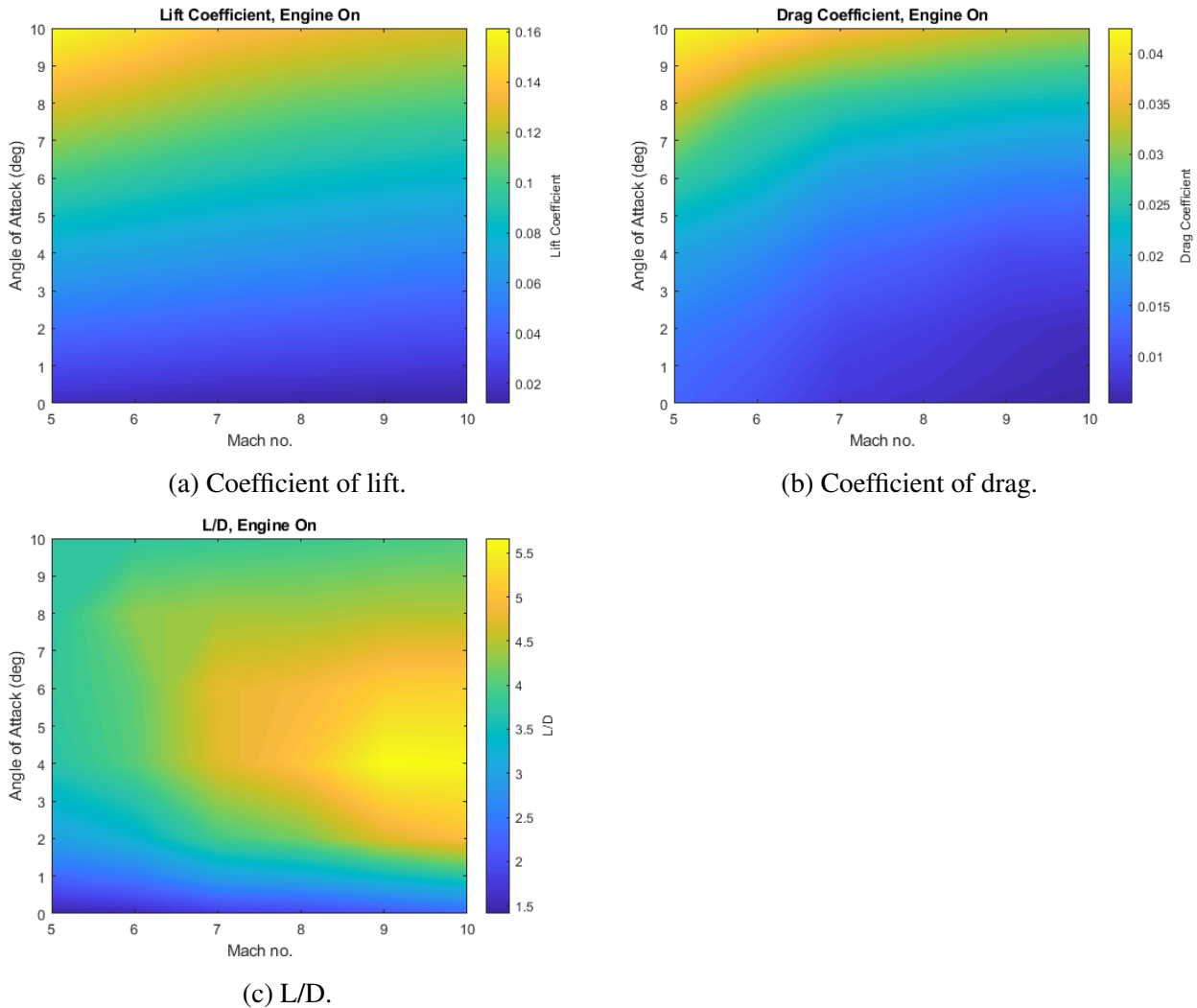


Figure 4.22: The aerodynamic coefficients of the scramjet accelerator with the C-REST engines powered-on at 30km altitude. Coefficients correspond to a reference area of 62.77m^2 and a centre of gravity of **15.24m** (full of fuel, with third stage).

from 0.2 to 10, and angle of attack values from 0° to 10° to cover the range of flight conditions experienced during the fly-back of the scramjet accelerator. An example Cart3D solution is shown for a Mach 7 engine off condition in Figure 4.23. A strong bow shock can be observed, as well as a large shock from the underside of the vehicle, generated by the engine cowl. It can be observed that the aerodynamic pressure is extremely high on the angled portion of the engine cowl, due to its high incident angle to the incoming flow. Significantly high pressure is also experienced by the nose cone and cowl underside, as well as on a section of the tail, where a small shock generated by the wings is incident on the tail. Figure 4.24 shows the engine off aerodynamic characteristics of the scramjet accelerator vehicle over the range of Mach numbers and angle of attack values analysed. These results show a distinct maximum region in the L/D of the scramjet accelerator at high Mach numbers, within the hypersonic regime. Below Mach 5, the L/D of the scramjet accelerator decreases

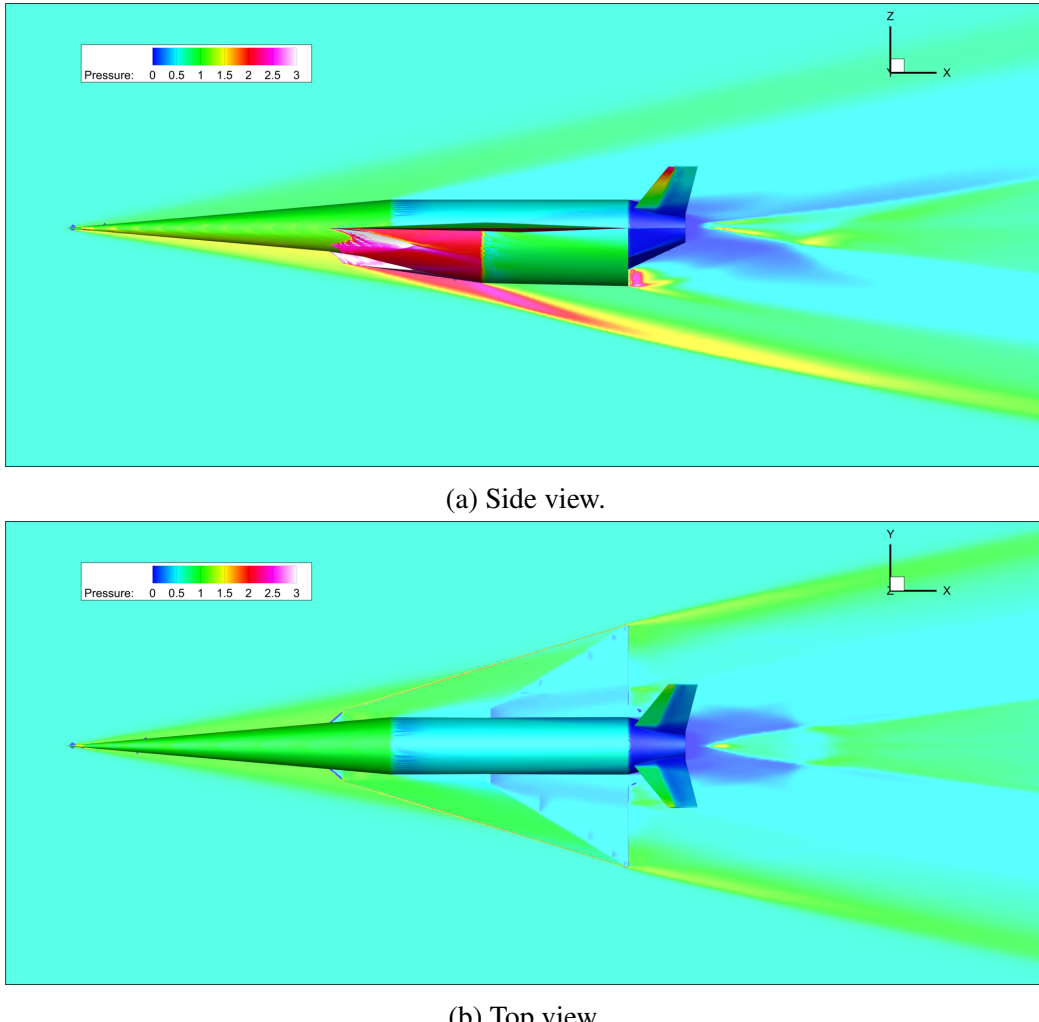
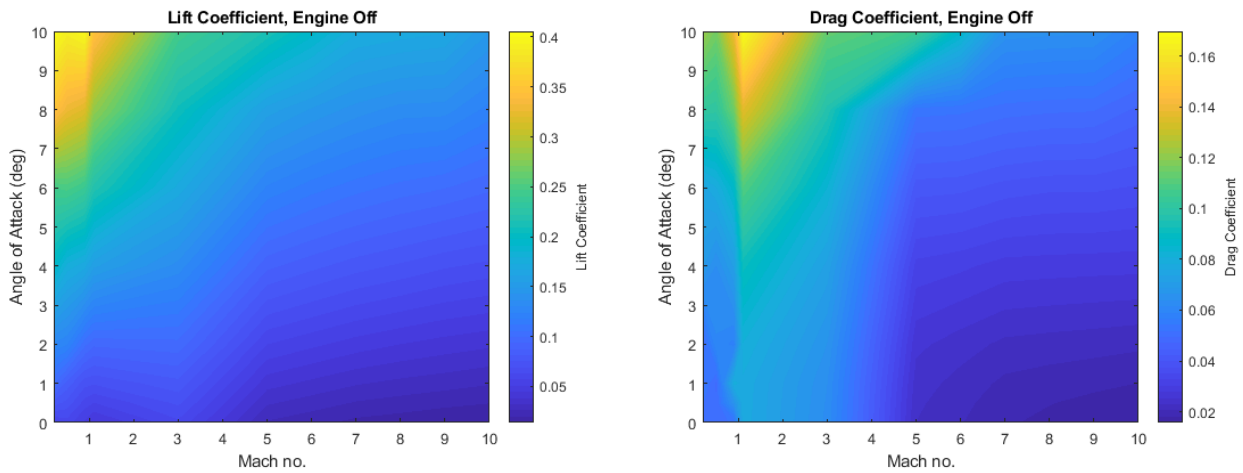


Figure 4.23: Cart3D flow result for the scramjet accelerator, at Mach 6, 2° angle of attack.

sharply. This is caused by the scramjet engines unstarting, generating significant drag. The unstarted scramjet engines are shown in Figure 4.25, where shocks within the inlet of the engine are evident, causing high pressures. Below Mach 3, the L/D shows a trend of general increase, except at very low angle of attack, as the effects of the unstarted engine lessen. Below Mach 1 the L/D of the scramjet accelerator increases significantly, in part due to not having the significant drag induced from the engines unstarting, as observed in the supersonic regime.

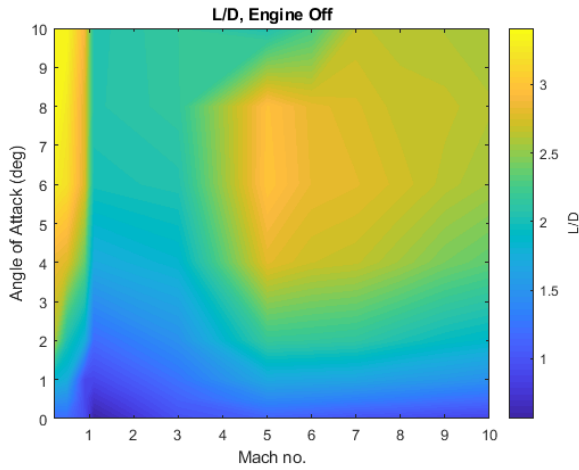
4.2 The First Stage Rocket

The first stage rocket is required to deliver the second stage to near horizontal flight at Mach 5.1 flight conditions, after which it is discarded. The representative first stage rocket in this study has been modelled as a Falcon-1e first stage scaled down lengthwise to 9.5m and to a mass of 1800kg, keeping the original diameter of 1.67m[161]. This scaling was based off a first principles design of



(a) Coefficients of lift of the scramjet accelerator, calculated using Cart3D.

(b) Coefficients of drag of the scramjet accelerator, calculated using Cart3D.



(c) L/D of the scramjet accelerator.

Figure 4.24: Aerodynamic Characteristics of the scramjet accelerator with C-REST engine powered-off at an altitude of 30km. Coefficients correspond to a reference area of 62.77m^2 and a centre of gravity of 15.16m (no third stage, no fuel).

the first stage mass and performance necessary to achieve the minimum operating conditions of the scramjet accelerator, performed by Preller & Smart[12], with some tuning due to the higher fidelity aerodynamics used in this study. The Falcon-1e has been chosen due to its appropriate scale, and the proven flightworthiness of the Falcon-1. The first stage is attached to the rear of the scramjet second stage and is powered by a single LOX-kerosene Merlin 1-C engine. A connecting cowl has been modelled between the first stage rocket and the scramjet accelerator to improve the aerodynamic profile. The first stage has a structural mass of 820.5kg, determined by scaling of the structural mass of the Falcon-1e. The engine mass of the Merlin 1-C is kept constant during scaling at 630kg[162]. The mass of the fuel in the first stage is scaled as part of the optimisation routine, as the dynamics of the vehicle, and its ability to reach a given separation point, are very closely coupled to the available

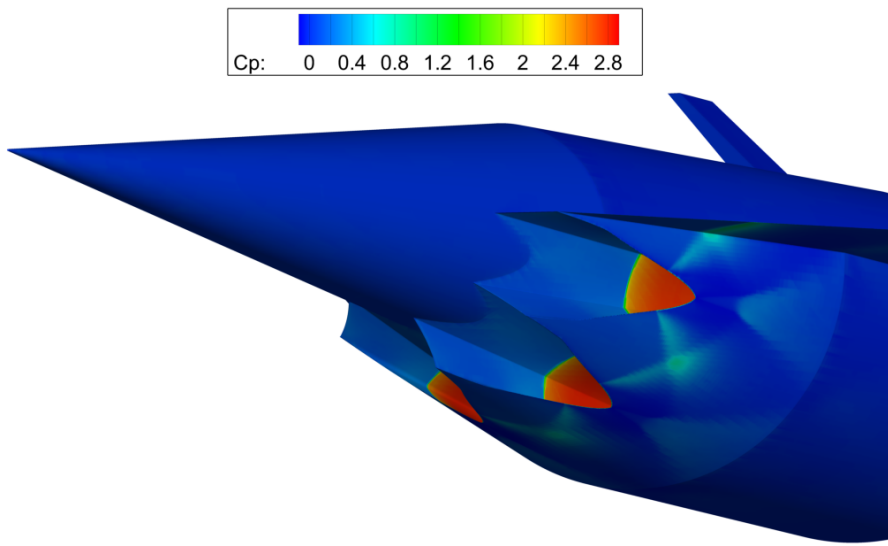


Figure 4.25: Unstarted scramjet engines at mach 3, 2° angle of attack.

fuel mass.

$I_{SP_{SL}}$	275s
$I_{SP_{vac}}$	304s
T_{SL}	555.9kN
A_e	$0.552m^2$

Table 4.2: First Stage Engine Properties[162].

The thrust and specific impulse of the Merlin 1-C are determined by interpolation between the sea level and vacuum specific impulse of the Merlin 1-C, shown in Table 4.2, with ambient pressure. Thrust scaling is determined by linear pressure scaling using nozzle exit area, $T = T_{SL} + (p_e - p_{SL})A_e$. The Merlin 1-C is throttled between 70% and 100%[163].

4.2.1 The Aerodynamics of the First Stage Rocket and Scramjet Accelerator

The aerodynamics of the launch system during first stage flight are calculated in a similar manner to those of the scramjet accelerator without the first stage rocket, as detailed in Section 4.1.4. The aerodynamics of the scramjet accelerator and first stage rocket are calculated using Cart3D and corrected for viscous effects. The first stage aerodynamics are modelled between angles of attack of 0° to -5° , as the first stage will be flying at negative angle of attack to induce faster pitch-over. Mach numbers from 0.2 to 5.1 (second stage separation velocity) are simulated. Figure 4.26 shows an example Cart3D simulation case, at Mach 2, -1° angle of attack. The coefficient of lift, drag and aerodynamic moment are tabulated for each simulation. Figure 4.27 shows the lift and drag coefficients of the first stage, as well as the lift-over-drag, across the simulated Mach Numbers and angles of attack. Above

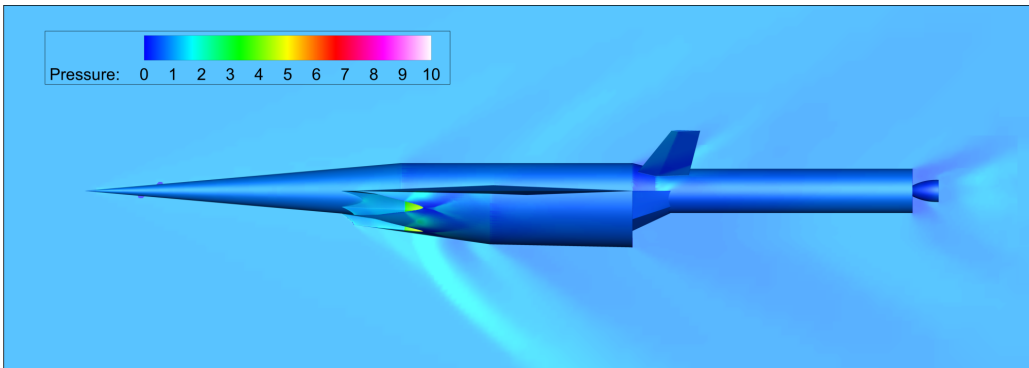


Figure 4.26: Cart3D result for the scramjet accelerator and first stage vehicles at Mach 2, -1° angle of attack.

-1° angle of attack, the L/D of the first stage is generally greater than 0, meaning that lift is being gained in the positive vertical direction, and that the angle of attack must be lower than 1° to assist pitching. At Mach numbers over Mach 2, the absolute magnitude of the L/D generally increases as the Mach number increases. This is caused by the decreased effects of the engines unstarting, in turn reducing the drag of the engines at higher Mach numbers, as observed in the aerodynamics of the scramjet accelerator in Section 4.1. Note that absolute magnitude is the metric used for ‘good’ L/D, as the angles of attack are negative.

The First stage is trimmed using thrust vectoring of the Merlin 1-C engine during flight. The centre of gravity of the launch system varies from 23.8m to 16.8m along the vehicle, as the fuel of the first stage is depleted. The thrust vector angle of the engine is adjusted so that the moment caused by the rocket engine is equal and opposite to the moment caused by the aerodynamics of the vehicle, as illustrated in Figure 4.28, ie. $M_T = -M_{Fn}$. This thrust vectoring is calculated as the trajectory is simulated, at every flight condition.

4.3 The Third Stage Rocket

The third stage rocket is an expendable portion of the launch system, tasked with delivering the payload to its final orbital position. The third stage is released from the scramjet accelerator at a flight speed of approximately Mach 9, after which it must fly within the atmosphere for a time, performing a significant altitude raising manoeuvre to achieve orbital flight[12]. In previous studies, the third stage of the SPARTAN was designed around a pump-fed RL-10-3A engine[12], and was designed to fit into a cavity on the back of the fuselage of the vehicle[12]. For the representative launch vehicle in this work a new third stage is designed, to reduce cost, and to integrate within the fuselage of the scramjet accelerator.

The third stage rocket in this study is designed around a modified version of the SpaceX Kestrel

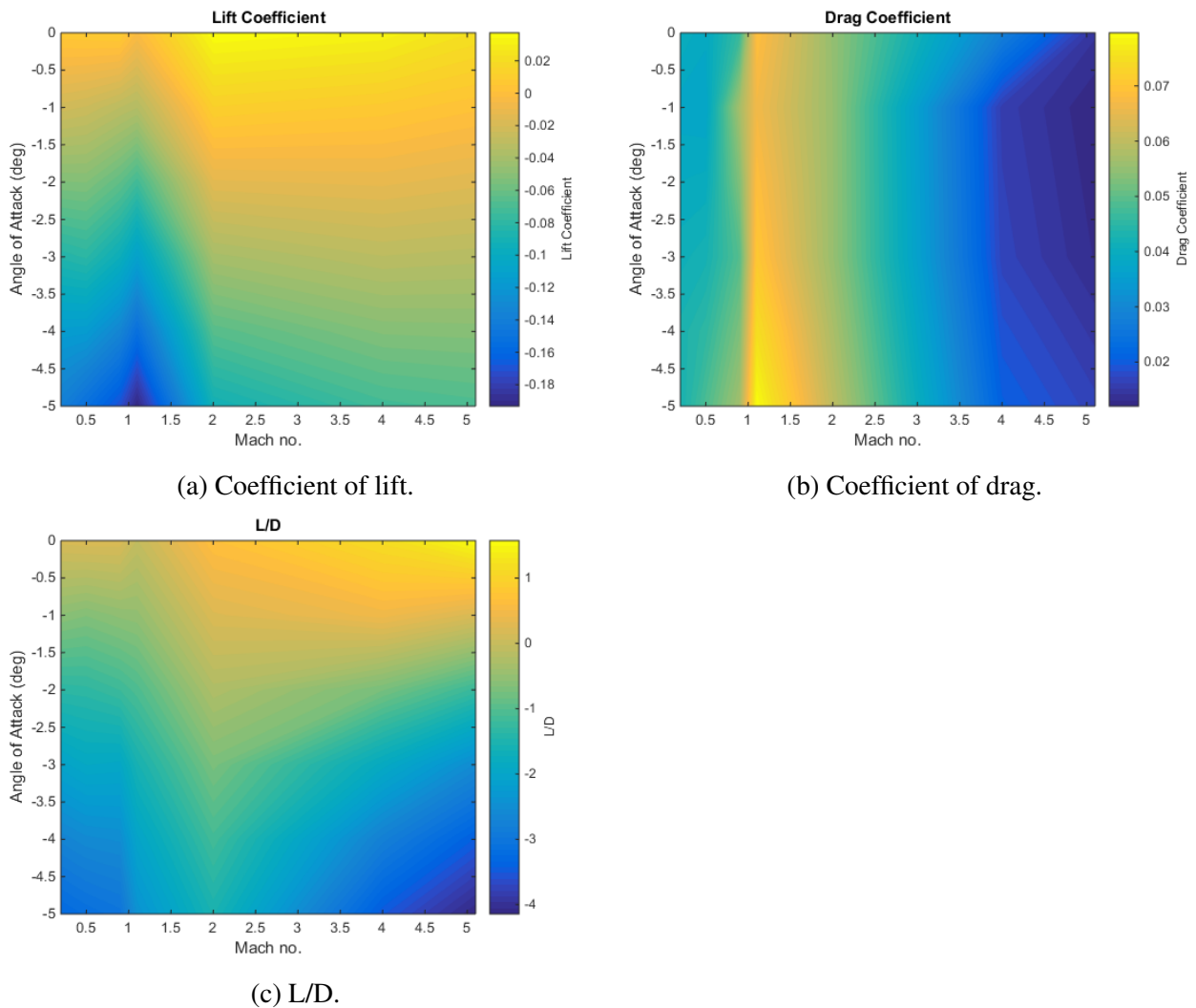


Figure 4.27: The aerodynamic characteristics of the SPARTAN stack. Coefficients correspond to a reference area of 62.77m^2 .

engine. The Kestrel is a pressure-fed engine, which was designed for launching small satellites to orbit as part of the now retired Falcon-1. The Kestrel is chosen primarily for its low cost, to ensure that the representative launch system in this study closely approximates a cost-effective future launch system. The third stage rocket in this study has a total length of 8.66m, and is sized so that it is able to fit within the main cylindrical fuselage section of the scramjet accelerator's geometry. This is done to reduce the heat loads present on the third stage during the second stage acceleration, as well as to improve the aerodynamics of the scramjet accelerator during ascent and fly-back. While the release mechanism of the third stage is not considered in this study, it is assumed that the release process will be simplified if the release mechanism is constrained to the cylindrical fuselage of the scramjet accelerator, rather than involving geometric variation of the nose cone of the scramjet accelerator, which receives a large amount of aerodynamic force as illustrated in Figure 4.23b.

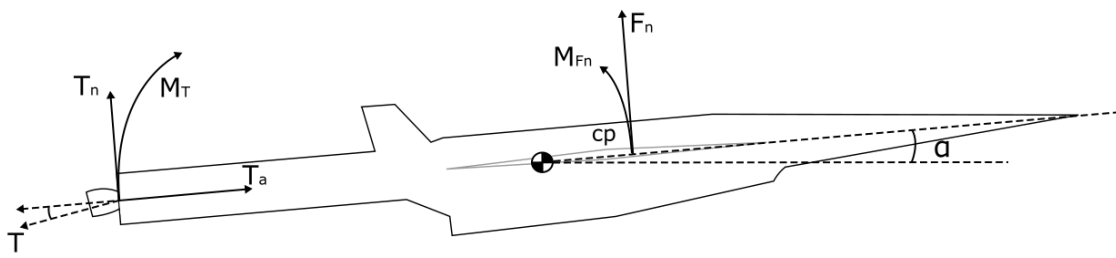


Figure 4.28: Thrust vectoring moment balancing of the first stage.



Figure 4.29: The third stage rocket, showing major internal features.

The third stage internals have been designed to weigh a total of 3300kg. This has been chosen as a nominal design weight, to satisfy the fuel necessary to achieve orbit with an acceptable payload, while also allowing for ample payload volume. The internal layout of the third stage rocket is shown in Figure 4.29, and a mass breakdown is given in Table 4.3. The third stage has a structural mass fraction of 0.079, to match the Falcon 1 second stage without the Kestrel engine or fairing included[161]. This gives a total structural mass of 236.3kg, without heat shield or engine.

Part	Total	Structural	Heat Shield	Engine	Fuel	Payload (est)
Mass (kg)	3300.0	236.3	124.6	78.0	2761.1	100.0

Table 4.3: Mass breakdown of the third stage rocket.

4.3.1 Geometry

The third stage has a total length of 9m, to fit within the main body fuselage of the scramjet accelerator. The third stage nose length is set at 3m, for a similar nose geometry to the third stage designed for previous analysis of the scramjet accelerator[12]. This nose geometry is chosen so that the heat shield in this study may be appropriately modelled after the heat shield designed for the RL-10-3A-powered third stage[12]. The third stage centrebody length has been set to 4.5m, giving a total length of 9m, with a 1.9m long Kestrel engine[161]. The diameter of the third stage has been set to 1.1m including heat shield, to match the diameter of the Kestrel engine, and to be close to half the diameter of the scramjet accelerator, a scale used to fix the third stage width of the RL-10-3A powered third stage[12].

4.3.2 Fuel Tank Sizing

The internal design of the third stage is allowed to be slightly variable as the trajectory is optimised. The third stage mass is fixed at 3300kg, and the calculated payload-to-orbit varies by exchanging leftover fuel mass for effective payload mass. The Kestrel engine utilises LOX/RP-1 propellants, with an oxidiser-to-fuel mixture ratio 2.56[164] and a density of 813kg/m³[165]. To calculate the dynamics of the third stage, the fuel tanks have been approximately sized, assuming 100kg of payload-to-orbit. Realistically the exchange between fuel and payload mass would cause the fuel tanks to be resized slightly, however, for the purposes of this study the fuel tanks are assumed to be of constant size for simplicity. Currently this is a reasonable assumption as the internals of the rocket are very simplified. With an assumed payload mass of 100kg, the third stage carries a total propellant mass of 2761.1kg. Table 4.4 breaks shows the component break-down of the LOX oxidiser and RP1 for this fuel weight. The total mass and volumes of these fuels will change slightly as the trajectory of the launch system is optimised, and fuel is traded for payload mass. However, the ratio between the fuel and oxidiser will stay constant.

	LOX	RP1
Ratio	2.56[164]	1
Density	1141kg/m ³	813kg/m ³ [165]
Volume	1.740m ³	0.954m ³
Mass	1985.5 kg	775.6 kg

Table 4.4: Third stage fuel distribution.

4.3.3 Heat Shield Sizing

XXX change cork density/thickness

The third stage rocket is separated from the scramjet accelerator at a high dynamic pressure, after which it spends some time accelerating in-atmosphere before reaching exoatmospheric conditions. The time spent within a high dynamic pressure environment creates a large amount of heat loading, which must be mitigated by heat shielding. The heat shielding must be capable of withstanding the extremely high heat and structural loading necessary to protect the third stage rocket internals and payload, as well as being lightweight, as the payload-to-orbit is extremely sensitive to the mass of the third stage, and cost effective, as increasing the cost of the third stage directly increases launch cost due to it being expendable.

The heat shield used to protect the third stage is constructed from a tungsten nose tip, a reinforced carbon-carbon nose cone, and a phenolic cork cylinder, weighing 124.6kg in total. This heat shield is designed to match the materials and thicknesses used by previous studies[12]. A mass breakdown is shown in Table 4.5. Tungsten is used at the tip of the nose cone, the area of maximum heat loading.

Tungsten has extremely high heat resistivity, and a very low coefficient of thermal expansion[166]. However, tungsten is costly and heavy, and conducts heat well, and so is only used on the very tip of the nose where it is absolutely necessary **to resist and distribute the large amount of heat generated by the stagnation region**. Reinforced carbon-carbon is used for the conical section of the heat shield, as this is an area that will be subject to high heat and structural loading. Carbon-carbon is able to withstand high temperatures, as well as being thermal shock resistant and having a low coefficient of thermal expansion[167]. Carbon-carbon is used in rocket and missile nose cones, as well as on aircraft leading edges due to its good heat resistant properties[167]. However, carbon-carbon is expensive, and is used only on the conical section of the heat shield to minimise cost. For the cylindrical section of the heat shield protecting the main body of the third stage, phenolic cork is used. Phenolic cork is a composite of ground cork and phenolic binders which is light and relatively cheap, with good heat resistivity. Phenolic cork has lower tensile strength and heat resistivity than carbon-carbon[167, 168], but is cheaper and lighter, making it appropriate for use on section of the heat shield which experiences lower heating and structural loads.

Part	Density	Geometry	mass
Tungsten Nose	$\rho_{Tungsten} = 19250 \text{ kg/m}^3$	50mm diameter cylinder, spherical tip	10.0kg
C-C Cone	$\rho_{CC} = 1593 \text{ kg/m}^3$	10.8mm thick, conical	89.7kg
Phenolic Cork Cylinder	$\rho_{PhenolicCork} = 320 \text{ kg/m}^3$	5mm thick, cylindrical	24.9kg

Table 4.5: Third stage heat shield breakdown.

4.3.4 Propulsion

The propulsion system for the third stage rocket in previous studies has been modelled after the RL-10-3A[82]. However, the RL-10-3A is an expensive, pump-fed engine designed for the upper stages of large launch vehicles. For the expendable upper stage of a small launch system, a cheap engine will be required, as the cost of this engine will have a large bearing on the cost efficiency of the launch system as a whole. This study redesigns the third stage rocket, so that it is more cost effective, and uses a more modern engine.

Exoatmospheric Rocket Engine Survey

The third stage requires a rocket engine with sufficient thrust to accelerate out of the atmosphere, and a diameter small enough to allow the rocket to fit within the fuselage of the scramjet accelerator. The major factors when choosing a rocket engine are efficiency and thrust-to-weight ratio, as well as cost. It is desirable to use a rocket engine which has already been developed and flight tested, to reduce the costs and potential complications of engine development. Table 4.6 shows a comparison study of

Engine	Fuel Supply	Fuel	Thrust	Isp	Mass	Diameter	Length	Thrust Vector Capability
R1-10A-3A	Pump-Fed	LOX/LH2	73.4kN	444s	141kg	1.01m	1.78m	Yes, Unknown limits
Aestus II	Pump-fed	MMH/NTO	46kN	337.5s	148	-	2.2m	6°
RS-72	Pump-fed	MMH/NTO	55.4kN	338s	154kg	-	2.286	6°
ATE	Pump-fed	MMH/NTO	20kN	345s	57.9kg	0.38m	1.4m	15°
Rutherford [169]	Pump-fed	LOX/RP-1	24kN	343s	35kg	-	-	-
AJ10-118K	Pressure-fed	A-50/NTO	43.3kN	320.5s	124.5kg	1.53m	2.7m	Fixed
Kestrel [161]	Pressure-fed	LOX/RP-1	30.7kN	317s	52kg	1.1m	1.9m	Yes, Unknown limits
Aestus	Pressure-fed	MMH/NTO	27.5kN	320s	110kg	1.27m	2.2m	4° & 4° by mechanical adjustment
OMS	Pressure-fed	MMH/NTO	26.7kN	316s	118kg	1.168m	1.956m	8°

Table 4.6: Comparison of upper stage rocket engines, sourced primarily from the Encyclopedia Astronautica reference website[162].

small sized upper stage rocket engines which are currently in use, or have been used, for commercial space flight. The pump-fed motors have significantly higher specific impulse than pressure fed motors, and while the masses of pressure-fed engines appear low compared to turbopump engines, this mass is generally made up for by the additional mass required by the pressurised propellant and pressurant tanks of pressure-fed engines.. However, while the cost of these engines is not generally published, pressure fed engines cost significantly less than pump-fed engines, due to the cost of the turbopump and the associated complexity of a pump-fed system. As such, it is desirable to use a pressure-fed rocket engine for a small satellite launch system if possible. Of the pressure-fed engines, the SpaceX Kestrel exhibits a significantly higher thrust/mass ratio than the other engines, with comparable specific impulse and size. Additionally, the Kestrel has been designed for a low cost, small satellite launcher, making the Kestrel engine likely to be fit-for-purpose for powering the third stage rocket.

Propulsion System Modelling

The Kestrel engine which powers the third stage is modified to have 50% increased propellant mass flow rate, giving a mass flow rate of 14.8kg/s. This is done to assist the rocket in exiting the atmosphere, as it was found during analysis that the third stage has difficulty exiting the atmosphere when powered by a standard Kestrel engine. A 50% increase in mass flow rate provides additional thrust such that the trajectory angle of the third stage does not decrease significantly after release from the scramjet accelerator flying a constant dynamic pressure trajectory. This was chosen as the indicative factor that the third stage is successfully able to pull-up out of the atmosphere. It is likely that this mass flow increase will necessitate a heavier combustion chamber as well as more heavy duty piping and valves, more or larger injectors, and a heavier nozzle and structure to transmit the higher thrust forces[164, 170]. To compensate for these factors, the mass of the Kestrel is increased by 50%, from 52kg[162] to 78kg, to approximate an increase in mass of the the thrust chamber as well as all feed systems, cooling systems, and the thrust transmission structure. This is estimated to be slightly conservative, as the surface area of the combustion chamber, and thus the mass and the cooling necessary, will not vary linearly with the increase in volume necessary to maintain a constant characteristic length as mass flow rate is increased[164, 170]. However, as the mass of the relative components of the Kestrel are not published, a conservative approach to mass modelling of the engine is most appropriate. The need to modify the Kestrel engine for this study highlights the potential necessity for the design of a cheap rocket engine with higher thrust than the Kestrel, Aestus or OMS, if a rocket-scramjet-rocket system is to be practical and cost-effective.

The nozzle exit of the Kestrel engine has been kept constant at 1.1m diameter. An increase in mass flow necessitates a corresponding increase in throat area. This increase in throat area decreases the area ratio of the nozzle. The initial area ratio is 60, measured from schematics in the Falcon-1

Users Guide. A 50% mass flow increase corresponds to a 50% throat area increase, which causes the area ratio to decrease to 40. This decrease in area ratio results in a 2% loss of efficiency from the nozzle, measured from the thrust coefficient relationships shown in Figure 4.30[164]. The modified specific impulse of the engine is 310.7s.

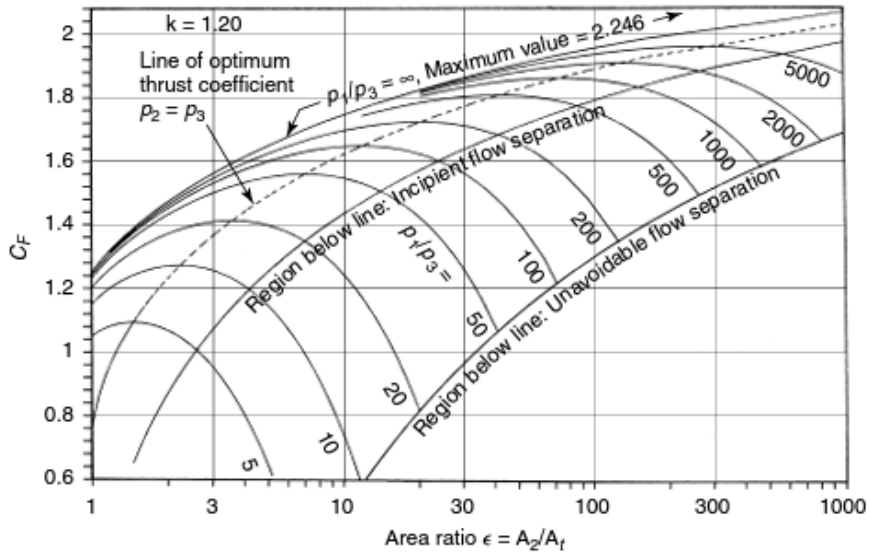


Figure 4.30: Variation in coefficient of thrust with area ratio[164].

4.3.5 Aerodynamics

The third stage aerodynamics have been calculated using Cart3D, in the same manner as for the scramjet accelerator and first stage, with a modification for viscous effects using VC3D. The aerodynamic coefficients of the third stage rocket are shown in Figure 4.31. These do not show any particular complexity, as is expected for a simple rocket shape, and the highest L/D is exhibited at the maximum angle of attack.

4.3.6 Thrust Vectoring

The third stage rocket is controlled via thrust vectoring. The centre of pressure is calculated using Missile Datcom. The thrust vector is set so that the moment generated by the engine matches the lift force acting at the centre of pressure, as shown in Figure 4.32, ie $M_T = -M_{F_n}$. This thrust vector is calculated at each flight condition during the trajectory simulations. The maximum thrust vector limit has been set to 8° . As no data on the maximum thrust vectoring capabilities of the kestrel engine was able to be found, this was set to the maximum gimbal range of the Aestus engine and Orbital Manoeuvring Engine (OME), which are similarly sized pressure-fed engines[162].

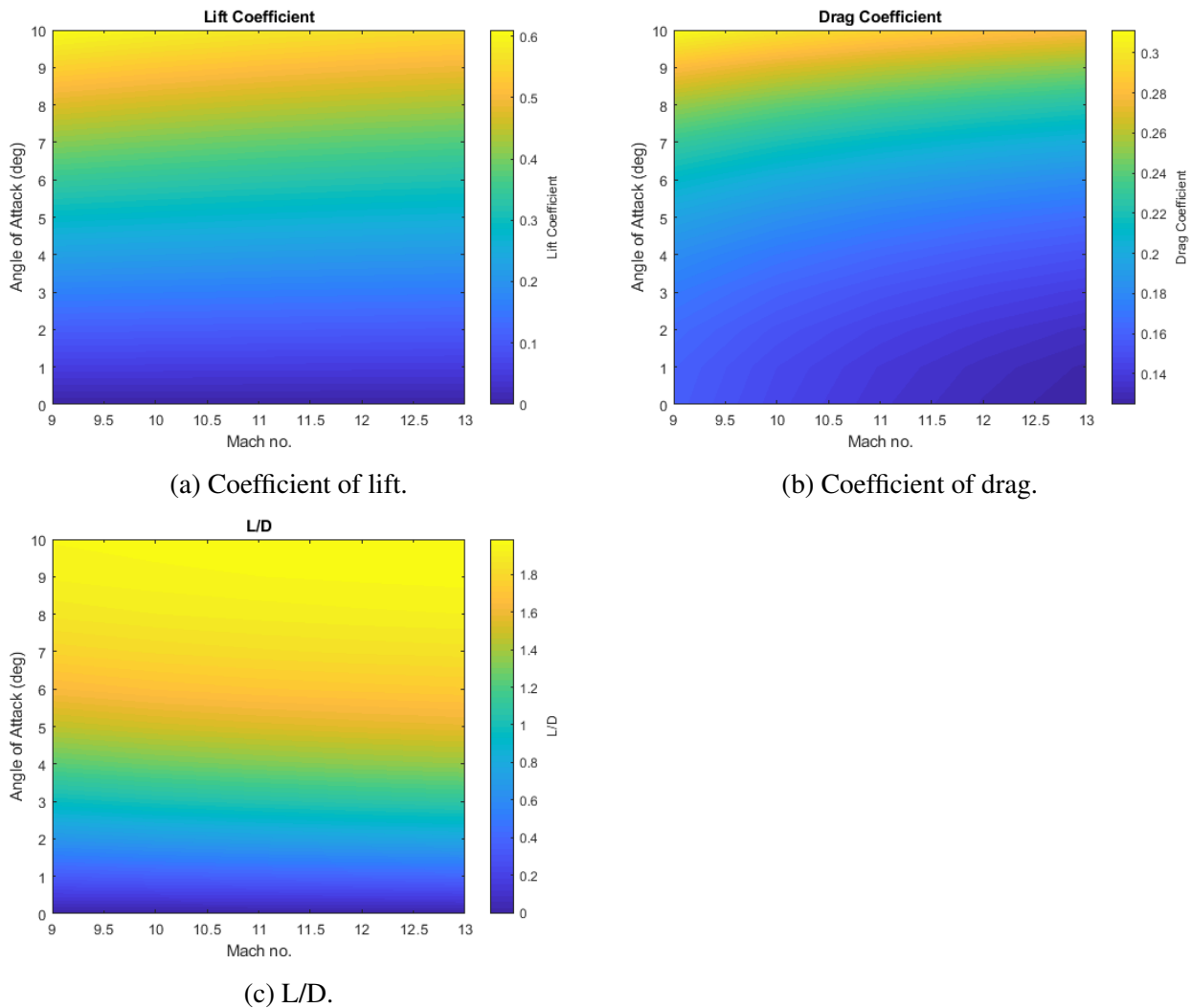


Figure 4.31: Aerodynamic characteristics of the third stage rocket, for a reference area of 0.95m^2 .

The centre of gravity is determined using CREO by creating a three dimensional model of the rocket with representative densities, illustrated in Figure 4.29. It is assumed that the mass of the structure of the rocket (excluding fuel tanks, heat shielding, engine and payload) is distributed homogeneously for simplicity. The Mass Properties tool within CREO is used to calculate the centre of gravity, which is located at 4.33m from the nose when the rocket is full of fuel, and 4.04m from the nose when the rocket is completely empty. The centre of gravity is interpolated linearly from these values as the fuel mass within the rocket decreases. These centre of gravity calculations are performed with the heat shield on, as the thrust vectoring is only calculated while the rocket is in-atmosphere, with the engine on. Note that the rocket will not become completely empty while in-atmosphere.

The third stage rocket is statically unstable. For the purposes of this study, it is assumed that the third stage rocket is controllable as long as the thrust vector limits of the vehicle are not exceeded. Flying this rocket at an angle of attack will require an advanced automatic controller, as the only

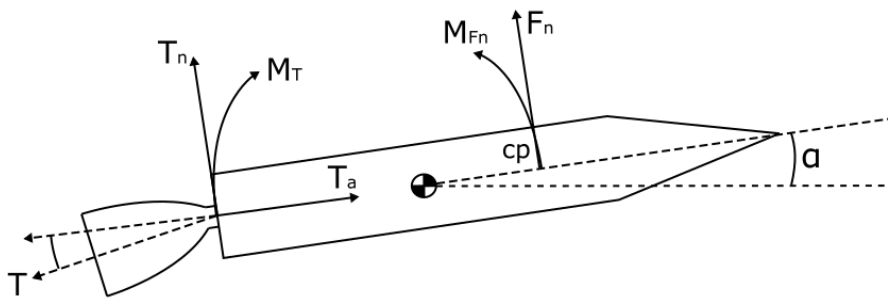


Figure 4.32: Thrust vector moment balancing of the third stage.

control available is produced by thrust vectoring. For the purposes of this study, the design of the third stage as presented is regarded to be sufficient as a representative third stage design. However, it is likely that in the future a highly detailed study of the third stage design and control strategy must be undertaken, to determine the practicality of thrust vector control.

4.4 Summary

In this chapter, the design and simulation of a rocket-scramjet-rocket launch system was presented, based on the SPARTAN launch system. The design of the first stage is based on the first stage of the Falcon-1e, scaled down to **9.5m**. The third stage is designed around the SpaceX Kestrel engine, with the fuel tanks of the scramjet accelerator resized to accommodate for the new third stage size. Mass breakdowns and key design features have been detailed for all three stages, including fuel ratios and structural mass fractions. The aerodynamic databases of all three stages were presented and analysed, and the process for generating these databases was detailed. The CFD simulations of each stage in Cart3D have been detailed, including the process of verifying the convergence of each solution. The propulsion modelling of the C-REST scramjet engines was presented, along with the schemes used to generate smooth, second order continuous interpolations of the engine data. The process for generating the trimmed aerodynamic databases for the scramjet accelerator has been presented, including the calculation of the control surface aerodynamics, and the calculation of the variable centre of gravity of the scramjet accelerator. The thrust vectoring control for the first and third stages was detailed.

CHAPTER 5

TRAJECTORY MODELLING AND OPTIMISATION

XXX I need to add that it is an oblate earth XXX I also need to ad the modifacitons to the first stage

This chapter presents the package LODESTAR (Launch Optimisation and Data Evaluation for Scramjet Trajectory Analysis Research), which has been developed to calculate the optimal trajectories of partially airbreathing satellite launch systems, as a general tool for this purpose is not currently widely available. LODESTAR has the capability to calculate optimal mission profiles for systems consisting of various combinations of rocket and airbreathing stages, using **accurate and robust** optimisation techniques. LODESTAR optimises a trajectory towards a user-defined objective function, such as maximum payload-to-orbit, subject to constraints that ensure that the launch system does not exceed its aerodynamic or structural limitations. LODESTAR calculates an optimal trajectory by simulating the dynamics of the launch system, and configuring an optimal control solver to define the launch trajectory optimisation problem being solved. The dynamics of the launch system are calculated in **three** degrees of freedom, with the performance of each vehicle calculated from aerodynamic and propulsion databases using precalculated interpolations, as described in Chapter 4. These interpolations are designed to be smooth and continuous in order to improve the robustness of the optimal control solver. LODESTAR separates a launch trajectory into multiple segments, to assist the solution process within the optimal control solver, improving robustness and accuracy. The segments with variable controls are solved within the optimal control solver, while the segments without control, or with prescribed control laws, are simulated directly in LODESTAR. The segments which are simulated directly in LODESTAR are evaluated during the solution process, and the information necessary for the optimisation is passed to the optimal control solver. Once the solution has been calculated, LODESTAR possesses the capability to verify the optimal control solution, an integral step when calculating an optimised trajectory with complex vehicle dynamics. LODESTAR is developed in MATLAB, and utilises GPOPS-2[171] as an optimal control solver. GPOPS-2 is a proprietary pseudospectral method optimisation package, which is based on an hp-adaptive version of the Radau

pseudospectral method, described in further detail in Section 3.5.

Within this chapter, the structure of LODESTAR is presented, as well as the set-up of LODESTAR for trajectory optimisation, and the verification methods used to determine if a solution has converged correctly. The configuration of LODESTAR presented in this chapter is designed specifically to calculate the maximum payload-to-orbit trajectory of a rocket-scramjet-rocket launch system, delivering a small satellite to sun synchronous orbit.

5.1 Mission Definition

The configuration of LODESTAR must be tailored towards the specific vehicle and mission profile which are being optimised. For this study, LODESTAR has been configured to simulate and optimise the launch of the rocket-scramjet-rocket vehicle, detailed in Chapter 4, for maximum payload-to-orbit. The nominal mission of the rocket-scramjet-rocket is presented here in order to provide a suitable reference for the configuration specifications, which are detailed in the following sections.

The mission chosen for the optimal trajectory calculation is a launch to sun synchronous orbit. A satellite in sun synchronous orbit is at close to polar inclination, regressing so that it keeps its orbital alignment to the sun. The sun synchronous orbit is one of the most commonly used types of orbit for space science missions, as it has many useful properties[172]. A sun synchronous orbit allows for global coverage, passing over each latitude at the same time each day, illustrated in Figure 5.1. It also allows for a satellite to either have full sun and have consistent power generation, or alternatively, allows for a satellite to have a consistent ‘dark side’ each day to alleviate thermal issues[172]. A sun synchronous orbit at 566km has been used in previous studies as the target orbit[12], and this orbit is also used for the current work.

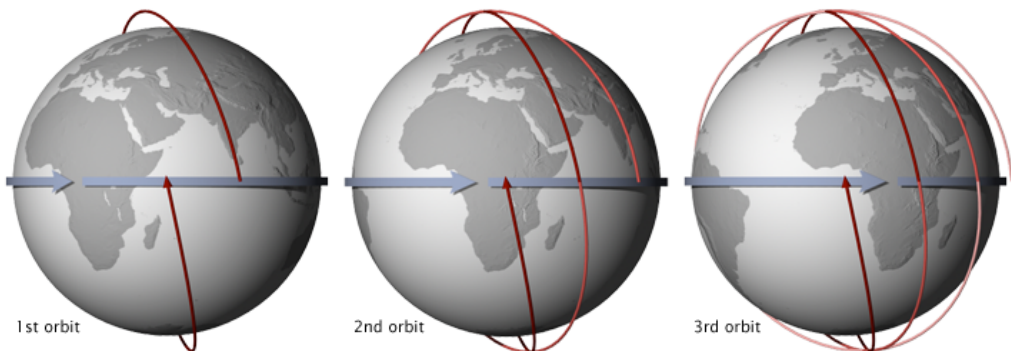


Figure 5.1: Sun synchronous orbit illustration, passing over the equator at the same time each day[173].

The launch site selected for the simulation is the proposed Equatorial Launch Australia launch site near Nhulunbuy in the Northern Territory, Australia[174]. This proposed launch site looks to

take advantage of the remoteness of northern Australia, as well as its close proximity to the equator. While the proximity to the equator of this launch site is slightly disadvantageous for launch to sun synchronous orbits, the possibility of other launch directions from this location, and its active development, make it an appropriate choice as a practical launch location within Australia. The site is ‘about 30km south of Nhulunbuy’[174] which places it within the approximate region indicated in Figure 5.2.



Figure 5.2: Approximate location of the ELA launch site. Image from Google maps.

5.2 Vehicle Simulation

LODESTAR simulates each of the vehicles within the rocket-scramjet-rocket launch system by establishing a set of dynamic equations that fully describe the motion of the vehicle in terms of the time, states (\mathbf{x}), and controls (\mathbf{u}) of the system;

$$\dot{\mathbf{x}}(t) = f[t, \mathbf{x}(t), \mathbf{u}(t)]. \quad (5.1)$$

The states and controls are the variables that define the time dependent physical characteristics of the system. The state variables are dependent on the controls and the system dynamics, while the control variables drive the behaviour of the system and can be varied independently [94]. The state

variables are defined by the coordinate system, and the outputs of each vehicle model [14]. These are nonlinear functions, that depend on the interpolation of data sets which supply the atmospheric, aerodynamic, and propulsion characteristics of each vehicle. The methods used to interpolate these data sets must be as smooth and continuous as possible, and cover the entire possible operational range of the vehicle. Even if the optimal solution is well within the range of all input data sets, the optimal control solver will potentially explore all regions within the user-defined bounds. If there are large discontinuities or inaccurate extrapolation effects within the possible solution space of a particular vehicle, the solver may be unable to converge, or converge to a physically invalid solution. Discontinuities within the aerodynamics or engine properties of a particular vehicle must be mitigated through the careful application of interpolation techniques. Discontinuities that are unable to be mitigated, such as stage separations, must be separated into distinct phases within the optimal control solution and connected by linkage constraints [15], as discussed further in Section 5.3.

5.2.1 Equations of Motion

The dynamics of the launch system are calculated in three degrees of freedom, in a geodetic rotational reference frame, illustrated in Figure 5.3. The Earth is modelled as an ablate spheroid using the World Geodetic System 1984[175] (WGS-84) shape and gravity model. In this reference frame, the dynamics of each vehicle are expressed in terms of the angle of attack α , bank angle η , radius from centre of Earth r , longitude ξ , latitude ϕ , flight path angle γ , velocity v and heading angle ζ . The equations of motion are given by[176, 177]:

$$\dot{r} = v \sin \gamma \quad (5.2)$$

$$\dot{\xi} = \frac{v \cos \gamma \cos \zeta}{r \cos \phi} \quad (5.3)$$

$$\dot{\phi} = \frac{v \cos \gamma \sin \zeta}{r} \quad (5.4)$$

$$\dot{\gamma} = \frac{(L + T \sin \alpha) \cos \eta}{mv} + \left(\frac{v}{r} - \frac{g_r}{v} \right) \cos \gamma - \frac{g_t}{v} \sin \gamma \cos \zeta + \cos \phi [2\omega_E \cos \zeta + \frac{\omega_E^2 r}{v} (\cos \phi \cos \gamma + \sin \phi \sin \gamma \sin \zeta)] \quad (5.5)$$

$$\dot{v} = \frac{T \cos \alpha - D}{m} - g_r \sin \gamma + g_t \cos \gamma \cos \zeta + \omega_E^2 r \cos \phi (\cos \phi \sin \gamma - \sin \phi \cos \gamma \sin \zeta) \quad (5.6)$$

$$\dot{\zeta} = \frac{(L + T \sin \alpha) \sin \eta}{mv \cos \gamma} - \frac{v}{r} \tan \phi \cos \gamma \cos \zeta + 2\omega_E \cos \phi \tan \gamma \sin \zeta - \frac{\omega_E^2 r}{v \cos \gamma} \sin \gamma \cos \phi \cos \zeta - 2\omega_E \sin \phi - g_t \sin \zeta \quad (5.7)$$

Where ω_E is the angular velocity of the Earth, and g_r and g_t are the gravity of the Earth in the

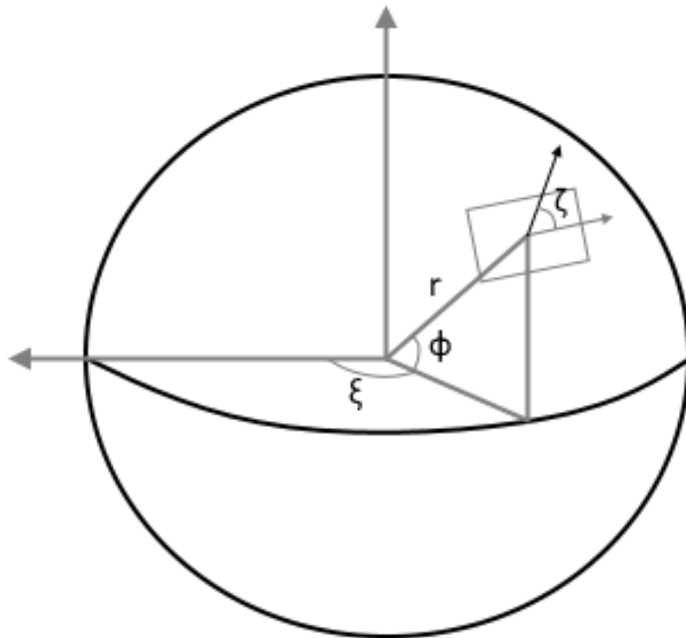


Figure 5.3: The Earth-fixed components of the geodetic rotational coordinate system.

radial and transverse directions. These dynamics are used as the dynamic constraints of the launch system, as shown in Equation 5.1, with each dynamic parameter implemented as a state variable (\mathbf{x}). The lift (L) and drag (D) forces are interpolated from the aerodynamic databases, described in Chapter 4.

5.3 Optimal Control Problem Structure

One of the primary functions of LODESTAR is to interface with the optimal control solver GPOPS-2. GPOPS-2 is a generic optimal control solver that utilises the pseudospectral method of optimal control, as well as the IPOPT nonlinear optimisation package. GPOPS-2 is described in detail in Section 3.5. Practically, the implementation of optimal control involves the specification of the dynamics of the system to be optimised, as well as the set of constraints and objectives that define the optimisation problem, described as follows:

Cost Function

The cost function, J , defines the target of the optimisation problem. This cost function may be any function which is defined by the states or controls of the optimisation problem. The cost function is

defined as follows:

$$J(t, \mathbf{x}(t), \mathbf{u}(t)) = M[t, \mathbf{x}(t_f), \mathbf{u}(t_f)] + \int_{t_0}^{t_f} P[\mathbf{x}(t), \mathbf{u}(t)] dt, \quad t \in [t_0, t_f], \quad (5.8)$$

where M is the terminal cost function and P is the time integrated cost.

Dynamic Constraints

The optimisation problem is subject to a set of dynamic constraints, which describe the behaviour of the system over the solution space:

$$\dot{\mathbf{x}}(t) - f[t, \mathbf{x}(t), \mathbf{u}(t)] = 0, \quad t \in [t_0, t_f]. \quad (5.9)$$

These dynamic constraints ensure that the polynomial approximations of the state variables, as described in Section 3.4.2, match the physical dynamics of the system. Implementing the dynamics as constraints in the manner of the pseudospectral method allows each state variable to be approximated separately, and gives the optimiser some freedom to explore each state variable independently, greatly increasing the robustness of the optimal control problem.

Bounds and Path Constraints

Inequality constraints define the bounds of each state, as well as any path constraints. The bounds directly confine the state and control variables to prescribed values. This serves the purpose of limiting the search space to the physically possible (eg. constraining altitude to be greater than ground level), constraining the vehicle within its performance limits (eg. limiting the angle of attack), and improving computational efficiency by ensuring that the optimiser is constrained to a reasonable solution space:

$$\mathbf{b}_{min} \leq \mathbf{x}(t), \mathbf{u}(t) \leq \mathbf{b}_{max}, \quad t \in [t_0, t_f]. \quad (5.10)$$

The path constraints are inequality constraints which consist of functions based on the states and controls of the system. Path constraints place adaptive bounds on the system, which vary over time with the state of the system:

$$\lambda[t, \mathbf{x}(t), \mathbf{u}(t)] \leq \mathbf{0}, \quad t \in [t_0, t_f]. \quad (5.11)$$

Path constraints are used by LODESTAR to impose physical limitations on the system such as structural, aerothermodynamic, pathing, and control limits.

Event Constraints

The event constraints constrain the states at the start and end points of a trajectory or phase:

$$\psi_0[\mathbf{x}(t_0), t_0] = \mathbf{0}, \quad (5.12)$$

$$\psi_f[\mathbf{x}(t_f), t_f] = \mathbf{0}. \quad (5.13)$$

These constraints determine the initial and terminal conditions of the optimisation problem, such as the initial location and velocity, and the starting fuel mass.

Together, these objectives, constraints, and variables describe the optimal control problem being solved, and form the inputs which LODESTAR provides to GPOPS-2. GPOPS-2 uses these inputs, along with a pseudospectral method transcription, to form the constrained optimisation problem that is solved using IPOPT.

5.3.1 Trajectory Connection Points

The optimisation of a large, multi-vehicle launch trajectory requires that the optimal control problem be broken down into multiple segments, or phases[171]. These phases are joined by event constraints, which couple the states and time of each phase to the preceding and following phases as follows:

$$\mathbf{x}_{f,1} - \mathbf{x}_{0,2} = 0, \quad (5.14)$$

$$t_{f,1} - t_{0,2} = 0. \quad (5.15)$$

This segmentation is performed in order to assist the convergence of the optimal control solver, by ensuring that the dynamics of the underlying model are as smooth and continuous as possible across each segment.

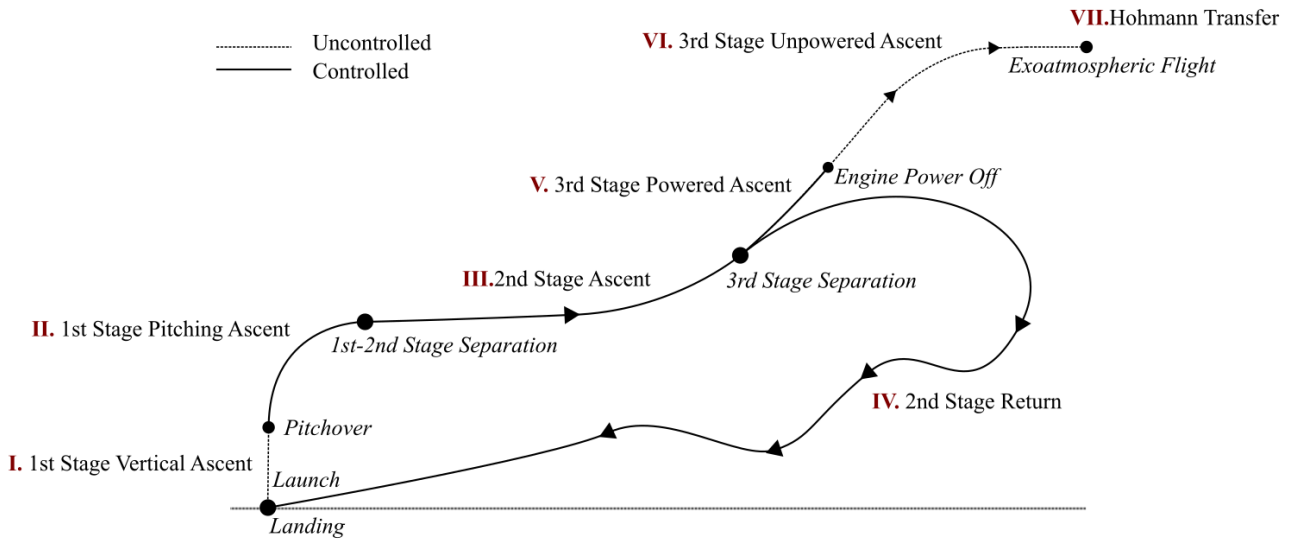


Figure 5.4: Illustration of the phases of the launch profile. Controlled and uncontrolled phases are distinguished.

For a launch system, discontinuities in the system dynamics generally arise when the aerodynam-

ics, mass or propulsion mode of a launch vehicle change significantly between stages or flight modes. If a vehicle model with large discontinuities is implemented directly into a single phase application of the pseudospectral method, it is likely to cause significant convergence issues, as the system dynamics will be unable to be approximated by the underlying polynomial of the pseudospectral method across these transition points[178].

To allow the trajectory profile to be formulated as an optimal control problem, the trajectory of the rocket-scramjet-rocket launch system is broken down into the seven segments shown in Figure 5.4. The segments are separated into two groups; controlled segments which take the form of phases within the optimal control problem; and segments without control which are either forward simulated at each iteration of the optimiser, or simulated externally to the optimal control problem. The unpowered segments of the third stage are simulated within the optimiser, and are included as a terminal cost, as described in Equation 5.8.

Segments II-V are controlled by various combinations of angle of attack, bank angle and throttle, and are implemented as the phases of the optimisation problem. These phases are: II, the 1st stage pitching ascent; III, the 2nd stage ascent; IV, the 2nd stage return flight; and V, the 3rd stage powered ascent. Segments I, VI and VII are segments without direct control, which are simulated using forward time stepping methods. These phases are: the pre-pitch segment of the first stage, the unpowered section of the third stage ascent, and the final Hohmann transfer to orbit. Each segment is connected through a set of continuity constraints. The optimal control problem phases are connected through the use of initial and end discontinuity constraints (Equations 5.14 and 5.15), while the forward simulated segments are simply initiated and terminated at set conditions. The segment coupling conditions are described in Table 5.1.

The following sections describe the setup of each individual phase of the optimal control problem, including the variables and constraints for the optimised phases. The bounds on the state dynamics are chosen to encompass the solution space, while not being overly expansive, to assist with the convergence and scaling of the optimal control solver. Across all optimised phases, the bounds on the latitude and longitude are chosen to cover the possible solution space, and are kept consistent across each phase to ensure that the position of the vehicle is not being unreasonably constrained between segments. The velocity constraints are chosen to cover the possible solution space, with the lower bound of 10m/s chosen to ensure that the velocity does not approach 0m/s, as this produces singularities within the system dynamics.

5.3.2 I. First Stage Vertical Ascent

LODESTAR optimises the ascent of the first stage rocket in two segments; pre and post-pitchover. These aerodynamics of flight during these segments are simulated using spline interpolation of the databases generated using the method described in Section 4.2.1, and the engine properties are deter-

Section	Initial Conditions	End Conditions	Controlled
I: 1 st Stage Vertical Ascent	Launches from rest, at the predefined launch site.	Fly until pitchover conditions are met.	no
II: 1 st Stage Pitching Ascent	Start at pitchover conditions	Terminates at end of fuel.	yes
III: 2 nd Stage Ascent	Must begin at 1 st stage pitching ascent end conditions.	Terminates at end of ascent fuel.	yes
IV: 2 nd Stage Return	Must begin at 2 nd stage ascent end conditions.	Must approach landing conditions at the initial launch site.	yes
V: 3 rd Stage Powered Ascent	Must begin at 2 nd stage ascent end conditions.	Must produce exoatmospheric flight at the termination of stage VI.	yes
VI: 3 rd Stage Unpowered Ascent	Must begin at 3 rd stage powered ascent end conditions.	Terminates when flight is parallel with Earth's surface.	no
VII: 3 rd Stage Hohmann Transfer	Must begin at 3 rd stage unpowered ascent end conditions.	Must attain prescribed orbit.	no

Table 5.1: Segment coupling conditions for combined trajectory optimisation.

mined using linear pressure scaling as described in Section 4.2.

The pre-pitchover phase is the segment of flight immediately after vertical launch. During this phase, the launch system continues vertically for a short time in order to clear the launch tower and stabilise the vehicle. The pre-pitchover section is prescribed, and is simulated externally to the optimisation to allow the dynamics of the system to behave appropriately during the pitching ascent. During vertical flight, the heading angle (Equation 5.7) is meaningless, and vertical flight is allowed during the pitching ascent, the heading angle change rate can tend towards infinity, causing mathematical and scaling errors. Simulating this segment after the optimisation has been completed makes the starting mass and altitude of the first stage slightly variable, but this variation is negligible. The pitchover is defined to occur at 30m altitude and 15m/s velocity. During the vertical launch the rocket is assumed to need no control, and is held at 0° angle of attack.

5.3.3 II. First Stage Pitching Ascent

At 30m altitude and 15m/s velocity, pitchover occurs. The pitchover is a very minor amount of instantaneous pitching (0.01°) which is introduced in order to begin the pitching ascent, allowing the heading angle of the vehicle to resolve correctly. The first stage pitching ascent trajectory is an angle of attack controlled phase in the optimisation routine, which is simulated from pitchover until second

Variable Group	Associated Variables	Value/Range
Initial Constraints	Velocity (v) Altitude (z) Latitude (ϕ) Longitude (ξ) Trajectory Angle (γ) Angle of Attack (α)	30m/s 30m -12.16° 136.75° 89.9° 0°
Terminal Constraints	$\mathbf{x}_{f,\text{II}} - \mathbf{x}_{0,\text{III}}$ $t_{f,\text{II}} - t_{0,\text{III}}$	0 0
Path Constraints	Dynamic Pressure (q)	0kPa - 50kPa
Control Variables	$\ddot{\alpha}$	$\pm 0.029^\circ/s^2$
State Variables	Altitude (z) Velocity (v) Trajectory Angle (γ) Latitude (ϕ) Longitude (ξ) Heading Angle (ζ) Total Mass (m) Angle of Attack (α) $\dot{\alpha}$	0 - 30km 10 - 3000m/s $-5.7^\circ - 89.9^\circ$ $\pm 28.6^\circ$ $114.6^\circ - 171.9^\circ$ $\pm 360^\circ$ 11453 - 29388kg $-5^\circ - 0^\circ$ $\pm 5.7^\circ/s$

Table 5.2: Optimisation setup of the first stage phase.

stage separation. Table 5.2 shows the optimisation setup of this phase. During this phase, the launch system is allowed to fly at negative angles of attack, to assist in pitching. The control for this phase is the second derivative of angle of attack, which is chosen as the control variable to assist in mitigating the first stage's sensitivity to angle of attack, ie. when the trajectory angle is near 90° and at low velocities, the effects of changes in angle of attack on the dynamics of the system are very large. This sensitivity can cause convergence issues, which are mitigated by using the second derivative of angle of attack as the control variable. The initial fuel mass of the first stage rocket is not fixed, as variations in the initial fuel mass can have an important effect on the capabilities of the first stage. The fuel mass can influence the velocity achievable at first to second stage separation, as well as the rate at which the rocket is able to pitch, and consequentially, the altitude and flight path angle range of the first stage. Allowing the initial fuel mass to vary increases the flexibility of the optimal control solver, and enables the optimal sizing of the first stage to be investigated.

5.3.4 III. Second Stage Ascent Trajectory

The second stage ascent phase consists of the acceleration of the SPARTAN scramjet-powered vehicle, controlled using the SPARTAN's angle of attack and bank angle. The optimisation setup of this phase is detailed in Table 5.3. The propulsion, lift, and drag of the vehicle are obtained from interpolation of the C-RESTM10 and trimmed aerodynamics databases described in Sections 4.1.3, 4.1.5,

Variable Group	Associated Variables	Value/Range
Initial Constraints	Fuel Mass (m_F)	1562kg
Terminal Constraints	$\mathbf{x}_{f,\text{II}} - \mathbf{x}_{0,\text{III}}$	0
	$t_{f,\text{II}} - t_{0,\text{III}}$	0
Terminal Constraints	Altitude (z)	0 - 45km
	Trajectory Angle (γ)	0 - 15°
	Bank Angle (η)	0°
	$\mathbf{x}_{f,\text{III}} - \mathbf{x}_{0,\text{IV}}$	0
	$t_{f,\text{III}} - t_{0,\text{IV}}$	0
	$\mathbf{x}_{f,\text{III}} - \mathbf{x}_{0,\text{V}}$	0
	$t_{f,\text{III}} - t_{0,\text{V}}$	0
Path Constraints	Dynamic Pressure	0 - 50kPa
Target Cost (Optional)	Dynamic Pressure*	$(q - 50000)^2 / 50000$
Control Variables	$\dot{\alpha}$	±0.5°/s
	$\dot{\eta}$	±1°/s
State Variables	Altitude (z)	0 - 50km
	Velocity (v)	10 - 3000m/s
	Trajectory Angle (γ)	-28.6° - 15°
	Latitude (ϕ)	±28.6°
	Longitude (ξ)	114.6° - 171.9°
	Heading Angle (ζ)	-240° - 360°
	Fuel Mass (m_F)	0 - 1562kg
	Angle of Attack (α)	0° - 10°
	Bank Angle η	-1° - 90°

Table 5.3: Optimisation setup of the second stage ascent. * This is only used in the constant dynamic pressure simulation. **XXX Check these, particularly traj angle**

and 4.1.6. During the ascent, the engines are assumed to be operating at the maximum thrust, corresponding to the maximum equivalence ratio at all times. This equivalence ratio is 1 in most sections of the trajectory, except at low Mach numbers where the possibility of unstart and choking necessitates a reduction in equivalence ratio. This trajectory is constrained by a maximum dynamic pressure of 50kPa, corresponding to the maximum structural limits of the vehicle. The control variables are set as the rate of change of angle of attack, and the rate of change of bank angle. Using the derivatives of the angle of attack and bank angle as the control variables serves to smooth the angle of attack and bank angle by constraining the change rates. The angle of attack is constrained to 10°, approximated as a reasonable upper bound to the angle of attack, and the limit to which the aerodynamic characteristics of the SPARTAN are modelled. The bank angle is constrained to a maximum of 90°, as it is assumed that the SPARTAN is not able to invert. The bank angle is also constrained to positive values only (ie. the heading angle may only increase) as the SPARTAN is launched from the ELA launch site at Nhulunbuy, and it is preferable to launch to the northeast or east to avoid overflying populated areas.

A cost function can be included during this phase, shown in Table 5.3, when flying a constant

dynamic pressure trajectory is desired. This cost function is smooth and approaches 0 at the target dynamic pressure, allowing the third stage cost function of payload mass to still be active, while prioritising flying at constant dynamic pressure.

5.3.5 IV. Second Stage Return Trajectory

Variable Group	Associated Variables	Value/Range
Initial Constraints	Bank Angle (η)	0°
	$\mathbf{x}_{f,\text{III}} - \mathbf{x}_{0,\text{IV}}$	0
	$t_{f,\text{III}} - t_{0,\text{IV}}$	0
Terminal Constraints	Latitude (ϕ)	-12.16°
	Longitude (ξ)	136.75°
Path Constraints	Dynamic Pressure (q)	0 - 50kPa
Control Variables	$\dot{\alpha}$	±0.5°/s
	$\dot{\eta}$	±1°/s
	Throttle	±0.2/s
State Variables	Altitude (z)	0 - 70km
	Velocity (v)	10 - 5000m/s
	Trajectory Angle (γ)	±80°
	Latitude (ϕ)	±28.6°
	Longitude (ξ)	114.6° - 171.9°
	Heading Angle (ζ)	60° - 500°
	Fuel Mass (m_F)	0kg - 500kg
	Angle of Attack (α)	0° - 10°
	Bank Angle (η)	0° - 90°
	Throttle	0 - 1

Table 5.4: Optimisation setup of the second stage return.

After releasing the third stage rocket, the scramjet-powered second stage must return back to the initial launch site. During this return flight, the SPARTAN is able to use its engines if necessary to ensure that it is able to return successfully. During the fly-back, the SPARTAN cannot exceed its dynamic pressure limit of 50kPa. The end state is constrained to a minimum of -20° trajectory angle, which is assumed to be an appropriate lower bound on the trajectory angle for approach to a landing strip. The altitude is constrained to less than 1km at the end point to ensure that the SPARTAN is approaching landing altitude. The velocity at the termination of the return trajectory is left variable. Constraining the end velocity may over-constrain the optimisation problem, and it is assumed that for a payload-to-orbit optimised trajectory the SPARTAN will end its return at a low velocity, so that the energy necessary for return is minimised.

The aerodynamics of the SPARTAN during fly-back are determined by interpolation of the engine-on and engine-off trimmed data sets described in Section 4.1.4. During the return, the C-REST

engines are able to be throttled on and off. As the scramjet engines are throttled on, the aerodynamics are assumed to vary linearly between the aerodynamics calculated by the engine-off and engine-on datasets. The throttle setting is defined as a state variable, with range between 0 and 1, where 1 represents the maximum equivalence ratio at that point. The corresponding fuel mass flow rate is scaled linearly with the throttle:

$$\dot{m}_{fuel} = \dot{m}_{fuel,max} \text{throttle}, \quad (5.16)$$

and the thrust of the engine is assumed to scale linearly with the fuel mass flow rate. A control variable of throttle change rate is added, to smooth the throttle in the same way as angle of attack and bank angle.

5.3.6 V. Third Stage Powered Ascent

Variable Group	Associated Variables	Value/Range
Initial Constraints	Total Mass (m)	3300kg
	$\mathbf{x}_{f,III} - \mathbf{x}_{0,V}$	0
	$t_{f,III} - t_{0,V}$	0
Terminal Constraints	$Alt_{f,VI}$	$\geq 90\text{km}$
	Heading Angle (ζ) VI	97.64°
	Angle of Attack (α)	0°
Path Constraints	Angle of Attack (α)	Maximum F_N
	Thrust Vector Angle	$\pm 8^\circ$
Target Cost	Payload-to-Orbit	Payload Calculated in Phase VII
Control Variables	$\dot{\alpha}$	$\pm 1^\circ$
State Variables	Altitude (z)	30 - 84km
	Velocity (v)	10 - 8000m/s
	Trajectory Angle (γ)	$-5^\circ - 30^\circ$
	Latitude (ϕ)	$\pm 28.6^\circ$
	Heading Angle (ζ)	$80^\circ - 120^\circ$
	Total Mass (m)	0kg - 3300kg
	Angle of Attack (α)	$-5^\circ - 0^\circ$

Table 5.5: Optimisation setup of the third stage powered ascent.

The trajectory of the third stage rocket is separated into the powered and unpowered phases of ascent. During the powered ascent phase, the third stage is manoeuvred out of the atmosphere using one continuous burn of the Kestrel engine. The powered ascent is an optimised phase, with optimisation properties described in Table 5.5. The powered phase is controlled using angle of attack, and trimmed using thrust vectoring of the engine, as described in Section 4.3.6. The aerodynamics of the third stage are determined using interpolation of the aerodynamic dataset developed as described in Section 4.3.5.

The third stage rocket is constrained to an angle of attack of less than 20° . This is assumed to be the maximum controllable angle of attack possible for the third stage rocket. Additionally, a maximum normal force restriction is placed on the third stage, to limit the angle of attack of the third stage by the normal force on the vehicle. However, as a detailed structural study of the third stage has not been conducted, the maximum allowable normal force on the third stage is not certain. For consistency, the maximum allowable normal force was calculated from the conditions of previous studies. Previous studies flew the third stage rocket at a constant 10° angle of attack, and initially released the rocket at 50kPa[12]. It is assumed that these release conditions produce the maximum allowable normal force on the third stage rocket. The maximum allowable normal force is calculated at the release Mach number, and is set as a path constraint.

The end angle of attack is constrained to 0° , as the angle of attack will not be able to be controlled during the unpowered ascent. The other terminal constraints of this phase correspond to end constraints imposed after the third stage unpowered ascent has been simulated. The altitude at the end of the unpowered ascent (Phase VI) is constrained to a lower limit of 90km, in order to ensure that the rocket is exoatmospheric. The final heading angle is also constrained at this point, so that the orbit of the third stage attains the correct inclination for sun synchronous orbit.

5.3.7 VI. Third Stage Unpowered Ascent

After the burn of the Kestrel engine is complete, at the end of phase V, the engine is cut and the third stage coasts to exoatmospheric conditions. The unpowered phase of the ascent is not controlled. After the engine is cut, the third stage does not have sufficient aerodynamic control to manoeuvre, and the trajectory of the third stage is a coast at 0° angle of attack. The trajectory of the third stage rocket is only directly optimised during the powered section of its trajectory, the unpowered section of the trajectory is simulated from the end of the controlled section of the trajectory, using a second order Taylor series approximation. This integration ceases when the flight path angle reaches 0° . During this phase, the heat shield is released once the rocket has reached a dynamic pressure of 10Pa, where it is assumed that atmospheric effects will have ceased to have a major thermal effect. As the third stage is required to deliver the payload into heliosynchronous orbit, the third stage must achieve an inclination of 97.63° at the end of this phase[172]. These terminal constraints are implemented in Phase V.

5.3.8 VII. Hohmann Transfer

After the rocket has attained exoatmospheric flight parallel to the Earth's surface, a circularisation burn is performed. This circularisation burn takes the third stage rocket into low orbit around the Earth. However, in order to reach a heliosynchronous orbit of 567km, the orbit of the third stage rocket must be raised. To this end, the final manoeuvre performed by the third stage rocket is a

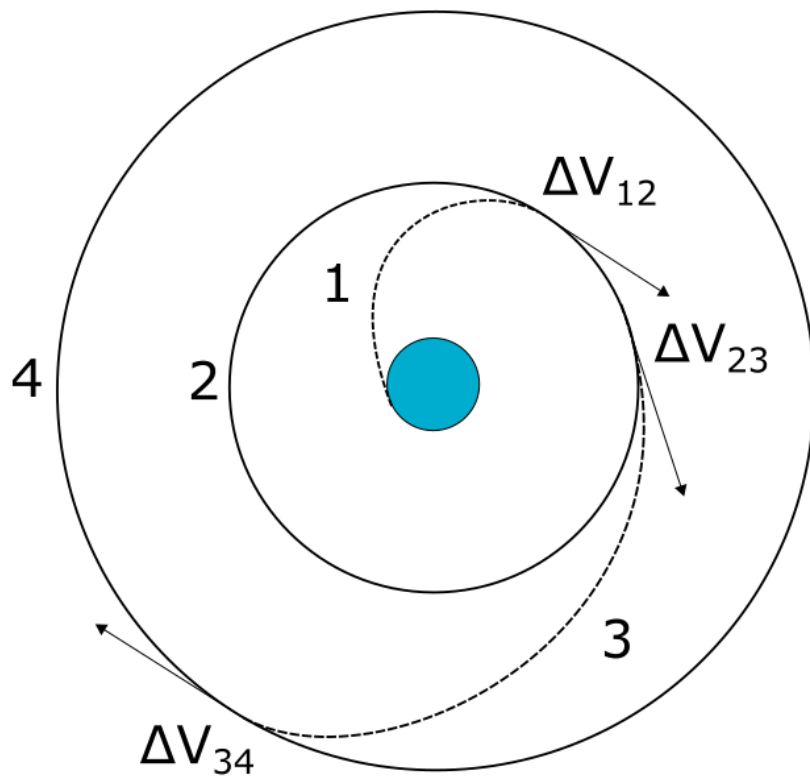


Figure 5.5: The Hohmann transfer manoeuvre. ΔV indicates a velocity change due to a burn.

Hohmann transfer. A Hohmann transfer is the most fuel efficient way to raise a spacecraft from one circular orbit to another[179]. The orbit of the third stage is first circularised into a low orbit through a velocity change due to a burn, ΔV_{12} :

$$\Delta V_{12} = \sqrt{\frac{\mu}{r_2}} - v_1, \quad (5.17)$$

where μ is the standard gravitational parameter, r is the distance from the centre of the Earth, and v_1 is the velocity before circularisation. Following circularisation, the third stage engine is reignited (or remains ignited) and the third stage manoeuvres into an appropriate elliptical orbit:

$$\Delta V_{23} = \sqrt{\frac{\mu}{r_2}} \left(\sqrt{\frac{2r_4}{r_2 + r_4}} - 1 \right). \quad (5.18)$$

At the apogee of the transfer orbit, corresponding to the desired orbital radius, an insertion burn is performed, and the orbit is circularised:

$$\Delta V_{34} = \sqrt{\frac{\mu}{r_4}} \left(1 - \sqrt{\frac{2r_2}{r_2 + r_4}} \right). \quad (5.19)$$

At this point, the payload is separated from the third stage rocket.

The mass of the third stage rocket after each burn is calculated using the Tsiolkovsky rocket equation:

$$m_2 = \frac{m_{1f}}{\exp^{\frac{V_{12}}{I_{SP} \cdot g_0}}} \quad (5.20)$$

$$m_3 = \frac{m_2}{\exp^{\frac{V_{23}}{I_{SP} \cdot g_0}}} \quad (5.21)$$

$$m_4 = \frac{m_3}{\exp^{\frac{V_{34}}{I_{SP} \cdot g_0}}} \quad (5.22)$$

Finally, the payload-to-orbit is determined by removing the structural mass from the total mass of the vehicle at the end of the Hohmann transfer. The remaining mass is taken to be the payload-to-orbit capability of the vehicle.

$$m_{payload} = m_4 - m_{struct} \quad (5.23)$$

5.4 Optimal Solution Analysis

Due to the nature of the pseudospectral method, it is possible that GPOPS-2 will not be able to converge to a physically valid or optimal solution. LODESTAR provides the capacity to analyse the optimal solution provided by the pseudospectral method solver to assist in determining whether the pseudospectral method solver has converged close to an optimal solution of the nonlinear programming problem. It is particularly useful to verify that the optimality and constraint tolerances that have been chosen are sufficiently small, or to check whether the pseudospectral method solver has approached an optimal solution in the case that the defined tolerances are not able to be reached. Checking the solution is achieved through the examination of five key parameters: the IPOPT constraint violation, and dual infeasibility parameters; the Hamiltonian necessary condition for optimality; the state derivatives; and finally, a forward simulation.

The first two metrics to be checked are the IPOPT constraint violation (*inf-pr*) and dual infeasibility parameter (*inf-du*)[180]. The constraint violation parameter is a measure of the infinity-norm (L_∞ -norm) of the constraints of the problem[180]. This factor must be suitably small in order to indicate that the constraints of the problem have been met. While the permissible magnitude of this factor changes with each individual problem, it is always desirable for this factor to be as small as possible. The dual infeasibility provides an indication of the optimality of the solution. A low dual infeasibility indicates that the solution is dual feasible and is likely to have approached an optimal solution. A dual feasible solution indicates that the dual problem is at least a lower bound on the optimal solution, $p^* \geq g(\lambda, v)$. For more details on duality see Reference[181]. Again, the magnitude of this value is variable with each problem, though as a problem becomes more complex, the ability to

converge towards an optimal solution diminishes. It should generally be observable that the $\inf-du$ term is decreasing by multiple orders of magnitude and is stable at the completion of optimisation for a solution to be approaching optimality.

The Hamiltonian of the optimal control problem is defined as:

$$H(x(t), u(t), \lambda(t), t) = \lambda^T(t) f(x(t), u(t)) + L(x(t), u(t)). \quad (5.24)$$

The Hamiltonian of the optimal control problem is calculated using LODESTAR, and investigated as a partial verification that the first order necessary conditions hold. Due to the unconstrained end time of the trajectory problems, the Hamiltonian necessary condition for an optimal solution is $H = 0$ [182]. A sufficiently small Hamiltonian indicates that the end solution is likely to have approached an optimal solution.

The pseudospectral method considers the dynamics of the system as constraints on the optimal control problem, and solves across the entire trajectory simultaneously. This causes the physical system dynamics to have an associated margin of error, ie. $\dot{x} = f(x)$ will only hold to a certain degree of accuracy. For a well-converged solution, this margin of error will be negligibly small, and the dynamics of the system will be consistent with the vehicle dynamics. However, when the problem has not converged, the dynamics of the system may have a large error. A check is performed on each state (dynamic variable) to affirm that the derivative of the approximated state is equal to the derivative supplied by the vehicle model. This checks that the solver has converged to a solution which satisfies the vehicle dynamics at each individual node (discretised time point). The state feasibility of the solution is checked through a verification of the state derivatives of each phase, $\dot{x} = f(x, u)$. \dot{x} is first determined through numerical differentiation of the state variables over the solution time, differentiated at the node points created by GPOPS-2. Then $f(x, u)$ is determined using the dynamics of the system and vehicle model, in the same way that $f(x, u)$ is input to the pseudospectral solver. Examination of the error between the ‘expected’ state derivatives, and the numerical approximation of the derivatives, $\dot{x} - f(x, u)$, allows the accuracy of the system dynamics to be assessed.

The final verification check is performing a full forward simulation. This forward simulation starts at the initial conditions of the optimal control problem, and propagates the dynamics of the system forward in time using the Runge-Kutta method, through Matlab’s ODE45 function. The forward simulation uses the optimised control variables as the only input. This checks that the flight path will follow the path computed by GPOPS-2, using only the calculated control inputs. This is the most complete test of the constraints of the optimal solution. However, in some cases calculating a forward solution may be problematic. The pseudospectral method has a limited number of nodes, potentially spread across relatively large time steps. Due to the high accuracy of the polynomial approximation, the pseudospectral method is able to maintain accuracy over large time steps[101, 104]. However, a forward simulation necessarily has less accuracy than the spectral method, and may interpolate

differently when applied to the optimal solution, causing minor deviations. These variations are usually negligibly small, however, this is problematic during the return phase, due to the way the throttling of the engines is modelled, ie. the specific impulse of the engines is set to 0 under Mach 5 or 20kPa inlet conditions during the optimisation process. As the engines are often throttled close to the minimum operable conditions, these restrictions can intensify the effects of otherwise minor deviations in the forward simulation. For this reason, the forward simulation of the return stage is split into three segments, with divisions at 1/6th and 1/3rd of the total trajectory length, chosen to separate the first major ‘skip’ and bank, and split the ‘skipping’ section of the trajectory. A forward simulation is initiated at each of these segments, mitigating some of the effects of the engines throttling on and off in the forward simulation. Splitting the forward simulation allows the forward simulation of the return stage to be assessed without the effects of the throttle model having an unreasonably large effect.

5.5 The Optimisation Process in LODESTAR

Figure 5.6 shows an illustration of the optimal control routine within LODESTAR. Each of the processes shown is described in more detail in the preceding sections, which are indicated in Figure 5.6. Initially, LODESTAR provides the initial guess and problem setup, configuring GPOPS-2 and defining the optimal control problem being solved. The iterative process begins with GPOPS-2 providing the current iteration of the trajectory solution to LODESTAR, along with a mesh of nodes that define the points in time at which the dynamics of the system are approximated. LODESTAR then calculates the aerodynamic and engine performance of the launch system at each node along the trajectory, as well as atmospheric and flight conditions. This data is used to calculate the dynamics of the vehicle along the trajectory. LODESTAR evaluates the trajectory, and simulates the unpowered third stage ascent and Hohmann transfer as forward simulations. LODESTAR uses the mass of the third stage fuel remaining at the end of its trajectory to calculate the payload-to-orbit, and passes this to GPOPS-2 as an endpoint cost function. The vehicle dynamics and payload-to-orbit are evaluated by GPOPS-2, which utilises the IPOPT nonlinear programming solver[121] to update the guess of the trajectory solution via an interior point method, at which point this updated guess is passed through to LODESTAR once more. The solution is evaluated by GPOPS-2 at each iteration to compute the feasibility and optimality of the solution. This process repeats until either a predefined tolerance of optimality, or a predefined number of iterations, is reached. The process repeats for a number of mesh iterations defined by the user, which further refine the trajectory. To aid in ensuring that an optimal solution is reached, GPOPS-2 is initiated from four separate initial guesses, with the final altitude guess varied by 1km between each initial trajectory. These iterations of GPOPS-2 are run in parallel, using Matlab’s Parfor function. After all the iterations of GPOPS-2 have completed, the solutions are evaluated, and the ‘best’ solution is chosen as the solution with the most accurately modelled

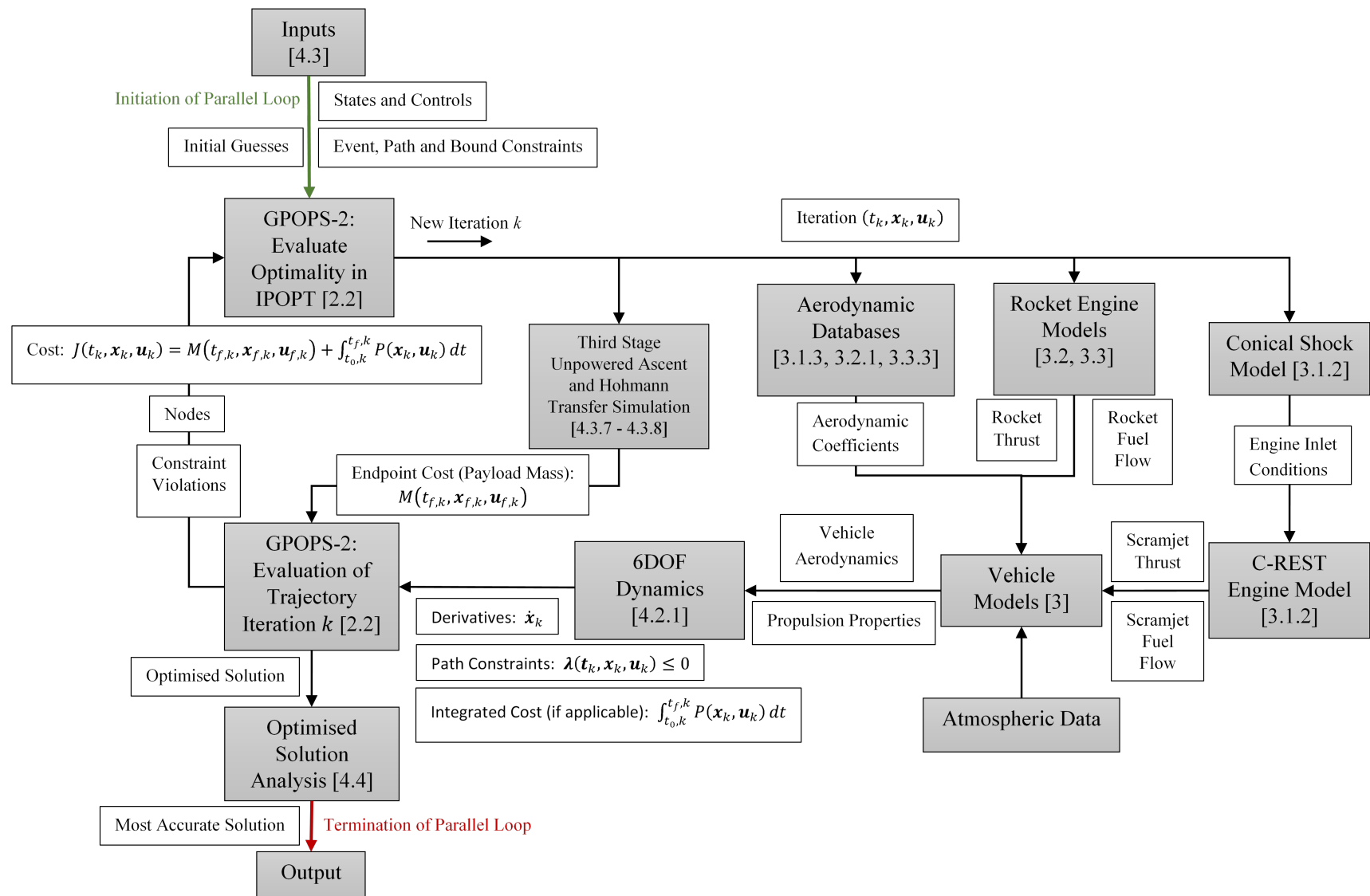


Figure 5.6: XXX Change 6DOF in this image! also check section no.s The process of the rocket-scramjet-rocket trajectory optimisation. Relevant sections are indicated in square brackets at each process step.

dynamics. This process is parallelised within LODESTAR, with green and red arrows in Figure 5.6 indicating the initiation and termination of the parallel loop respectively.

5.6 Trajectory and Performance Analysis

LODESTAR provides a range of plotting tools, which present the optimised trajectory graphically, along with various performance indicators of each vehicle, including L/D, net specific impulse, and control time histories. LODESTAR also possesses the capability to graphically show the aerodynamic and engine performance of the vehicle over the range of possible flight conditions, with overlays of the optimised trajectory path. These tools can be used to identify the performance region in which the vehicle is flying, in order to distinguish trends and trade-offs in the optimal flight path. In addition to graphical tools, LODESTAR also calculates an energy usage analysis of the launch system. This includes calculating the exergy efficiency of each vehicle, and the overall launch system, as well as individual sources of energy losses within each stage.

Exergy expresses how much useful work is available to a system, and exergy efficiency quantifies how well a system utilises the available work. Exergy efficiency can show how well each stage is using its available energy, and assist with quantifying the efficiency trade-offs between the stages. Exergy efficiency is an important parameter for analysing launch vehicles, allowing the relative efficiencies of each stage to be compared when the design or trajectory of a launch system is varied[183]. The exergy efficiency of a stage of a launch system is expressed as the fraction of the fuel combustion energy which is turned into ‘useful’ kinetic and potential energy during flight:

$$\eta_{exergy,stage} = 1 - \frac{\Delta m_{fuel} H_{fuel} - \Delta KE - \Delta PE + \Delta KE_{discarded} + \Delta PE_{discarded}}{\Delta m_{fuel} H_{fuel}}, \quad (5.25)$$

where H_{fuel} is the heating value of the fuel, ΔKE is the change in the kinetic energy of the stage, ΔPE is the change in the potential energy of the stage over its trajectory, and $\Delta KE_{discarded} + \Delta PE_{discarded}$ is the energy imparted to the mass discarded at staging. This exergy efficiency expresses how efficiently each stage utilises its available fuel over each individual trajectory. However, this stage-based exergy efficiency does not account for the effects of the unused mass of the successive stages on the performance of the launch system, ie. the exergy efficiency of each stage is a measure of how well it accelerates the next stage. The total exergy efficiency of the launch system is calculated as the fraction of the total available energy which goes directly into placing the payload into orbit:

$$\eta_{exergy} = \frac{\Delta KE_{payload} + \Delta PE_{payload}}{\sum_{stage} \Delta m_{fuel} H_{fuel}}. \quad (5.26)$$

This exergy efficiency expresses how efficiently the launch system as a whole is able to accelerate the payload to orbit. Within this work, exergy efficiency is expressed as the percentage of total exergy

utilised, $\% \eta$, ie. $\eta_{exergy} \times 100$.

5.7 Summary

This chapter presented a tool for optimising the trajectory of launch systems, designated LODESTAR. LODESTAR simulates each stage of a launch system, and interfaces with the optimal control solver GPOPS-2, to generate an optimised trajectory solution. The set-up of LODESTAR for the launch of a rocket-scramjet-rocket launch system, delivering a small satellite to sun synchronous orbit, has been detailed. Each stage of the launch system is simulated individually within LODESTAR, either as a separate phase of the optimal control problem, connected by event constraints, or as a forward simulation. The bounds of each stage have been chosen so as to provide suitable limits to the dynamics of the system, and the payload-to-orbit capability of the system has been set as the end cost function of the optimal control problem. The state and control variables of each stage were detailed, along with the state, event and path constraints. The capability of LODESTAR to verify the optimised solution was presented, including analysis using the necessary conditions of optimality, as well as forward simulation comparisons. Finally, the trajectory and performance analysis capabilities of LODESTAR were presented, including graphical tools and exergy efficiency calculations.

CHAPTER 6

OPTIMISED ASCENT TRAJECTORY

XXX NOTE First stage is not using less than full mass anymore, but is **THROTTLABLE**

XXX I need to make a point of the pull-up, compare with previous studies

XXX NOTE third stage has very small thrust vector angle, turns out that the force is pretty close to the CG

XXX check all sig figs after all results are done, and see what they need to be, and reduce some if necessary

This chapter presents a maximum payload-to-orbit trajectory optimisation for The SPARTAN launch system. This launch system is simulated as being launched from the Equatorial Launch Australia launch site in East Arnhem Land (Detailed in Section 5.1), and delivers a small satellite into sun synchronous orbit. LODESTAR is used to calculate the maximum payload-to-orbit trajectory solutions for this launch system. First, a trajectory solution is calculated in which the scramjet accelerator flies at constant dynamic pressure. This trajectory is calculated to serve as a baseline for comparisons, as previous studies have assumed that flying the scramjet accelerator at its maximum allowable dynamic pressure would produce the best overall system performance[12]. An optimal payload-to-orbit trajectory is then developed, and the trajectory shape compared and contrasted to the constant dynamic pressure trajectory. Lastly, a sensitivity study is performed, by varying key performance parameters of the launch system and investigating the effects of each parameter on the performance of the launch system.

The following trajectories are developed:

- Case 1: $q = 50\text{kPa}$ fixed scramjet accelerator trajectory.
→ This trajectory provides a baseline trajectory for comparison purposes.
- Case 2: Trajectory optimised for payload-to-orbit, $q_{max} = 50\text{kPa}$.
→ This trajectory demonstrates improved performance through trajectory optimisation.

- Case 3: Variation of maximum allowable dynamic pressure between $q_{max} = 45\text{kPa}$ & $q_{max} = 55\text{kPa}$.
→ Comparison of optimised trajectories allows the influence of the scramjet accelerator's ability to withstand aerodynamic forces on the launch system performance to be investigated.
- Case 4: Variation of the coefficient of drag of the scramjet accelerator between $C_d = 90\%$ & $C_d = 110\%$.
→ Comparison of optimised trajectories allows the effects of the scramjet accelerator's aerodynamic design on the launch system performance to be investigated.
- Case 5: Variation of the specific impulse of the scramjet accelerator's C-REST engines between $I_{SP} = 90\%$ & $I_{SP} = 110\%$.
→ Comparison of optimised trajectories allows the effects of the efficiency of the C-REST engines on the launch system performance to be investigated.
- Case 6: Variation of the mass of the scramjet accelerator between $m_2 = 90\%$ & $m_2 = 110\%$.
→ Comparison of optimised trajectories allows the effects of the internal design of the scramjet accelerator on the launch system performance to be investigated.
- Case 7: Variation of the fuel mass of the scramjet accelerator between $m_{fuel} = 90\%$ & $m_{fuel} = 110\%$.
→ Comparison of optimised trajectories allows the effects of the amount of fuel which the scramjet accelerator is able to carry on the launch system performance to be investigated.
- Case 8: Variation of the mass of the third stage rocket between $m_3 = 90\%$ & $m_3 = 110\%$.
→ Comparison of optimised trajectories allows the effects of the third stage internal design on the launch system performance to be investigated.
- Case 9: Variation of the specific impulse of the third stage rocket between $I_{SP,3} = 90\%$ & $I_{SP,3} = 110\%$.
→ Comparison of optimised trajectories allows the effects of the efficiency of the third stage engine on the launch system performance to be investigated.
- Case 10: Variation of the coefficient of drag of the third stage rocket between $C_d = 90\%$ & $C_d = 110\%$.
→ Comparison of optimised trajectories allows the effects of the aerodynamic design of the third stage on the launch system performance to be investigated.

These optimised trajectory cases allow the benefits of flying an optimised trajectory to be quantified, and allow the impact of key design parameters on the performance of the launch system to be characterised.

6.1 Case 1: Constant Dynamic Pressure Trajectory

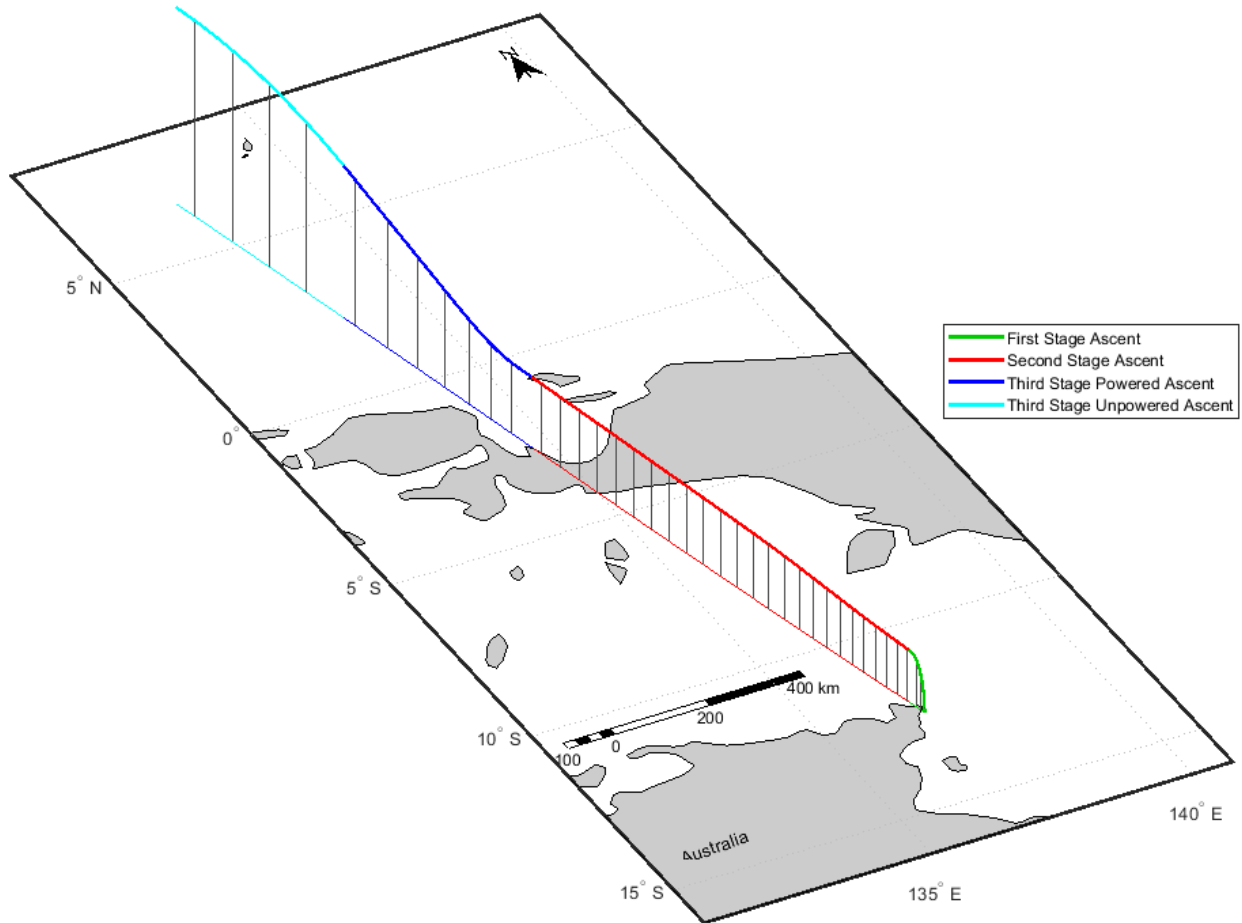


Figure 6.1: Maximum payload-to-orbit trajectory path with the scramjet accelerator flying at constant dynamic pressure (Case 1). Initial heading angle 91.4° .

The first trajectory that is produced using LODESTAR is a maximum payload-to-orbit trajectory in which the scramjet accelerator flies a constant dynamic pressure path, at its maximum allowable dynamic pressure of 50kPa. In order to drive the scramjet accelerator towards a constant dynamic pressure path, the cost function detailed in Table 5.3 is utilised. In addition to the dynamic pressure cost function, the maximum payload-to-orbit cost function is also active on the third stage phase, so that once the scramjet accelerator flies close to 50kPa, the third stage will fly a maximum payload-to-orbit trajectory from the termination of the scramjet accelerator's constant dynamic pressure path. Previous studies have assumed that flying the scramjet accelerator at constant dynamic pressure will produce the best possible system performance[12]. Because of this assumption, a constant dynamic pressure trajectory is produced to serve as a baseline for comparison with the maximum payload-to-

orbit optimised trajectory. Producing a constant dynamic pressure trajectory also serves to verify that LODESTAR is able to calculate a trajectory in which the scramjet accelerator flies at a fixed dynamic pressure for the duration of its flight. In addition, the designs and aerodynamic simulations of each vehicle of the launch system have been improved in this work, compared to previous studies[12]. In this work, the internal design of the scramjet accelerator has been modified (as described in Section 4.1), the third stage design has been modified significantly (as described in Section 4.3), the first stage is included (as described in Section 4.2), and Cart3D[134] is used for aerodynamic calculations (as detailed in Section 4.1.4). Simulating a constant dynamic pressure verifies that the first stage is able to reach the maximum dynamic pressure of the scramjet accelerator, and that the scramjet accelerator is able to fly at its maximum dynamic pressure within its control and aerodynamic limits. This verification ensures that any deviations from the scramjet accelerator’s maximum dynamic pressure when flying a maximum payload-to-orbit trajectory serve to improve the performance of the system, rather than being a result of the problem setup or design constraints.

Trajectory Condition	Value
Payload to Orbit (kg)	98.3
Total η_{exergy} (%)	1.155
1st Stage η_{exergy} (%)	6.252
Separation Alt, 1→2 (km)	23.84
Separation v, 1→2 (m/s)	1451
Separation γ, 1→2 (deg)	0.7
2nd Stage η_{exergy} (%)	5.120
Separation Alt, 2→3 (km)	32.16
Separation v, 2→3 (m/s)	2785
Separation γ, 2→3 (deg)	0.2
2nd Stage Distance Flown (km)	1084.9
3rd Stage η_{exergy} (%)	9.514
3rd Stage $t, q > 5\text{kpa}$ (s)	112.3
3rd Stage max α (deg)	10.0
3rd Stage Fuel Mass (kg)	2886.9

Table 6.1: Summary of the key results from a maximum payload-to-orbit trajectory with the scramjet accelerator constrained to 50kPa (Case 1). **XXX about sig figs: the high number of sig figs have been included to highlight trends in the variation section. I should potentially argue that a high number of significant figures are included for this, but make note that the results are still subject to significant sources of error?**

LODESTAR successfully computes the trajectory of the rocket-scramjet-rocket system, with the scramjet accelerator flying at constant dynamic pressure, achieving a payload-to-orbit of 98.3kg. Figure 6.1 shows the optimised trajectory path, Figures 6.2-6.4 show details of the optimised trajectory for each stage, and Table 6.1 provides a summary of the key parameters of the trajectory, including the exergy efficiency of each stage. The rocket-scramjet-rocket system launches vertically, flying a

6.1. CASE 1: CONSTANT DYNAMIC PRESSURE TRAJECTORY

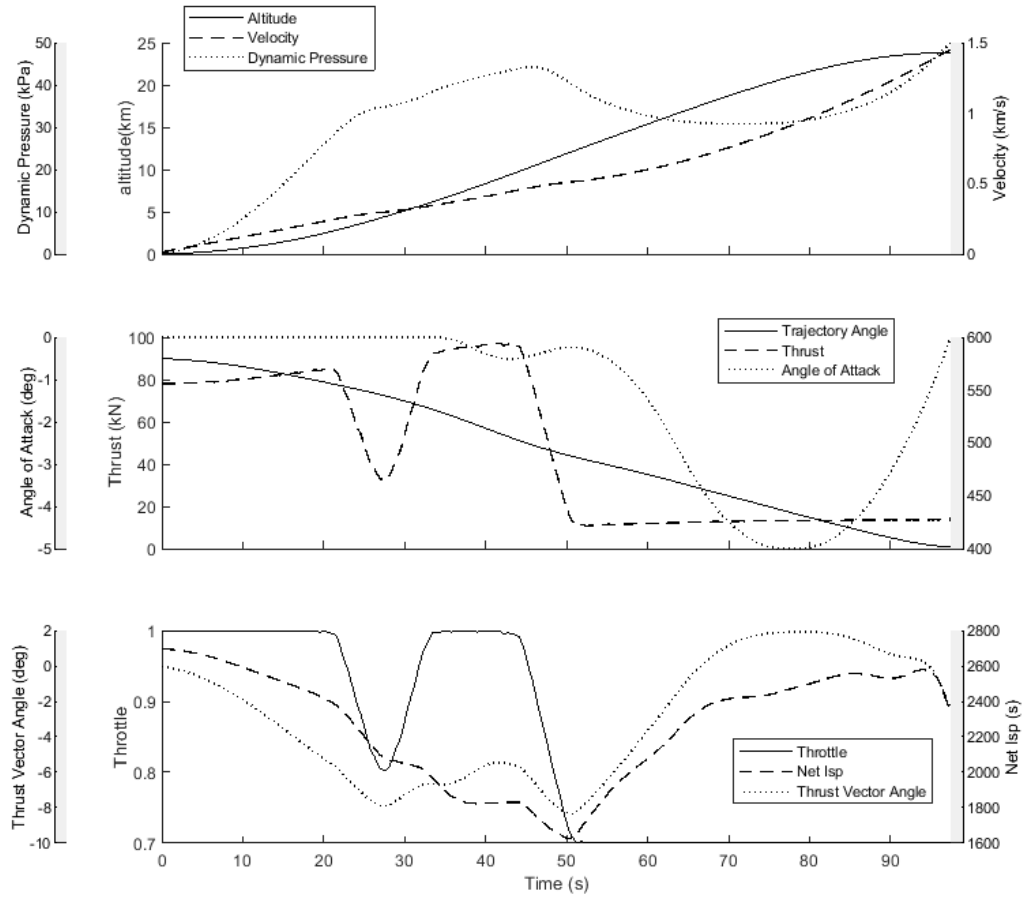


Figure 6.2: The first stage trajectory of the launch system, with the scramjet accelerator constrained to flight at constant dynamic pressure (Case 1).

fixed vertical trajectory for 3.9s, after which a pitchover is initiated. Under power of the first stage rocket, the launch system begins pitching, flying north-west, over the Arafura Sea. After pitchover the angle of attack stays constant at 0° for 99.9s, as shown in Figure 6.2. At this point, the angle of attack is reduced, reaching a minimum of -5.0° , before increasing back up to 0° for stage separation. The scramjet accelerator is separated at a trajectory angle of 0.7° at an altitude of 23.84km, at a flight time of 97.4s, with a total ground distance of 37.2km covered under power of the first stage rocket. In order to reach optimal first-second stage separation conditions, the first stage must launch with a lower-than-maximum fuel mass, to allow it to pitch in the correct manner. To achieve an optimal constant dynamic pressure trajectory, the first stage launches with a fuel mass of 17010kg, significantly lower than the full amount of allowable fuel mass, 17934kg. **XXX change this** The first stage rocket achieves an exergy efficiency of $6.252\% \eta$ when separating the scramjet accelerator onto a constant dynamic pressure trajectory.

The constant dynamic pressure trajectory for the scramjet accelerator stage is shown in Figure

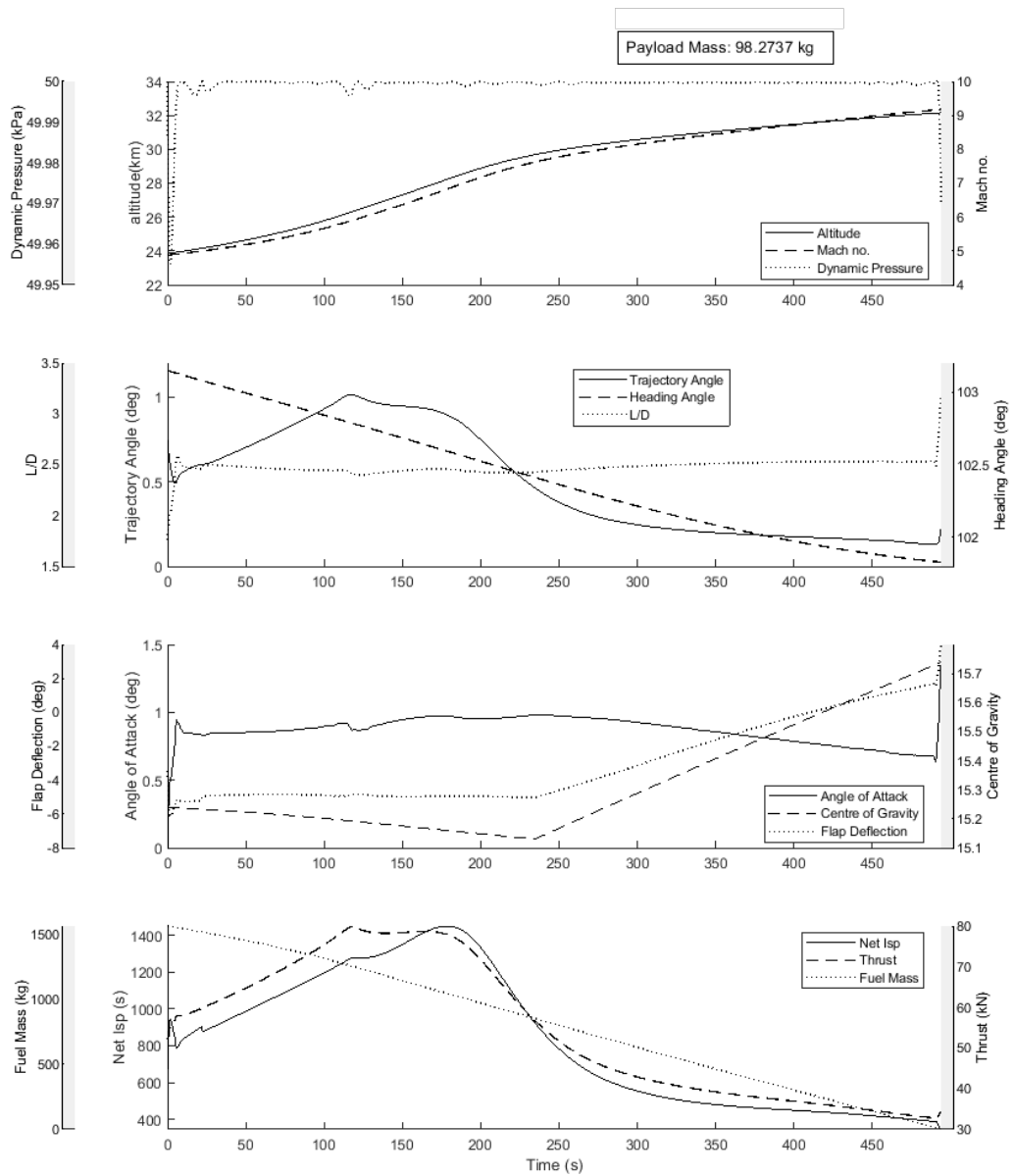


Figure 6.3: The constant dynamic pressure flight path of the scramjet accelerator (Case 1).

6.3, with key results summarised in Table 6.1. After the separation of the first stage rocket, the SPARTAN flies north west over the Arafura Sea, and crosses West Papua before releasing the third stage rocket. Due to the clear objective of a constant dynamic pressure trajectory, any deviations from the target dynamic pressure are readily apparent, allowing the efficacy of the optimiser to be verified. The constant dynamic pressure trajectory shows very close adherence to 50kPa dynamic pressure throughout the trajectory (maximum 0.2% deviation), indicating that scramjet accelerator flight at a constant dynamic pressure is able to be achieved by the SPARTAN. Over the trajectory, the

6.1. CASE 1: CONSTANT DYNAMIC PRESSURE TRAJECTORY

Mach number increases from **4.88** to **9.18**, the velocity increases from 1451m/s to 2785m/s, and the flap deflection increases from **-6.14°** to a maximum of **3.93°** during pull-up. The angles of attack of the scramjet accelerator are low across the trajectory, generally between **0.6-1.0°**, indicating that the lift of the scramjet accelerator is high for this mission profile. At the beginning of the trajectory the equivalence ratio increases, as the capture limitations are relaxed with increasing Mach number. This causes the net specific impulse ($I_{sp,net} = \frac{T-D}{\dot{m}_f g}$) to increase, to a maximum of **1448s**, during the first **180.4s** flight time. After this initial increase, the net specific impulse decreases over the trajectory, as the efficiency of the scramjet engines decreases. Third stage release occurs at **591.4s** flight time, at 32.16km altitude. Immediately before third stage separation, there is a slight increase in the angle of attack and flap deflection of the scramjet accelerator. This is done to increase the trajectory angle and improve the payload-to-orbit slightly, but does not have a significant effect on the performance of the launch system.

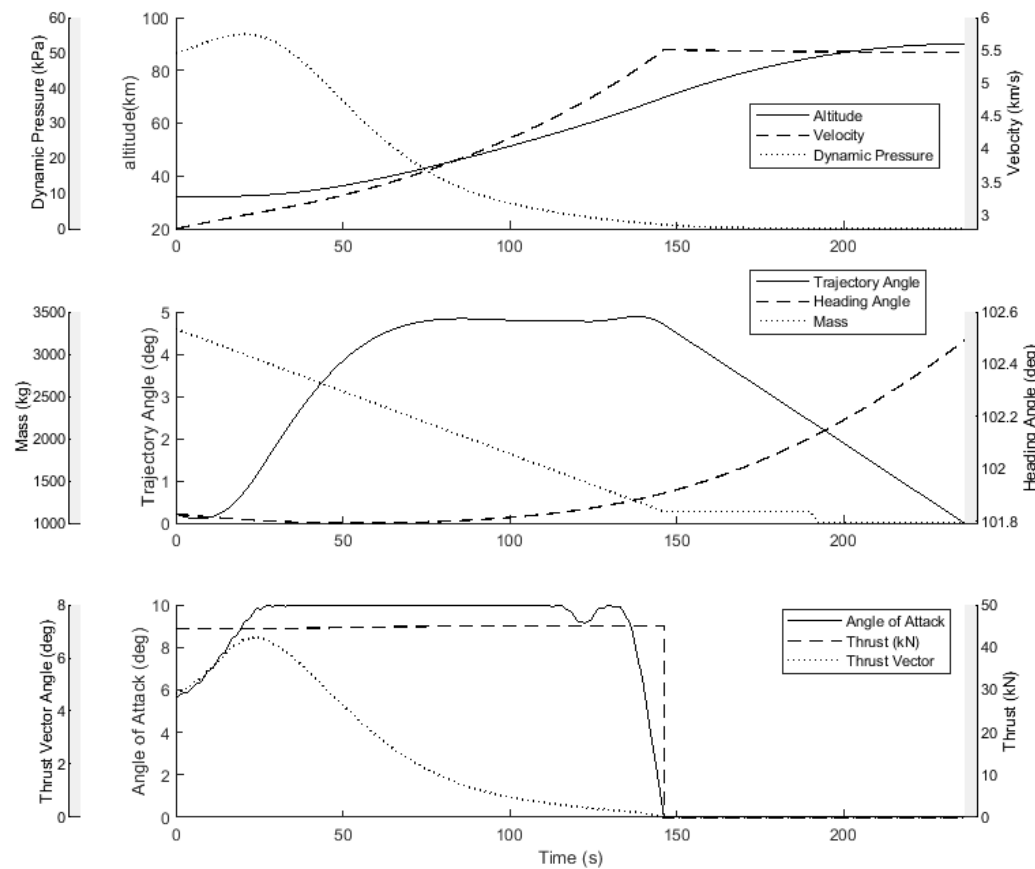


Figure 6.4: The third stage trajectory of the launch system, with the scramjet accelerator constrained to flight at constant dynamic pressure (Case 1).

Figure 6.4 shows the corresponding third stage atmospheric exit trajectory after release, evaluated

as described in Chapter 5. The third stage released from a constant dynamic pressure trajectory, shown in Figure 6.4, is limited by the maximum thrust vector angle for the first 37.3s of flight. **XXX change this** This places significant limitations on the maximum allowable angle of attack. This angle of attack limitation reduces the lift of the rocket, causing the flight path angle to stay close to horizontal for the first 12s of flight. This slow ascent leads to the rocket spending a large amount of time at low altitude, in a high drag environment, spending 112.3s at over 5kPa dynamic pressure. The angle of attack increases gradually to a maximum of 10° at 27.8s before decreasing until burnout at 130.4s **XXX change this**. The dynamic pressure of the third stage rocket reduces to 10kPa at 188.2s, at which point the heat shield is discarded. The rocket coasts to a trajectory angle of 0° , which is reached at a total flight time of 827.6s. The trajectory terminates at 90km, the lowest allowable altitude for circularisation. When this altitude is reached, the trajectory is circularised and a Hohmann transfer manoeuvre is performed to reach sun synchronous orbit.

6.2 Case 2: Optimised Ascent Trajectory

XXX If i havent already, I should point out that the small corrections being made during 50kPa flight probably indicate that the vehicle shape is not optimised for 50kPa flight, and that it wants to fly at max q but cant sustain an optimal aoa to do so, link to prior work that showed similar?

This section presents the maximum payload-to-orbit trajectory for the rocket-scramjet-rocket launch system, with the scramjet accelerator able to deviate from its maximum dynamic pressure. The optimal trajectory shape for a 50kPa dynamic pressure limited trajectory is shown in Figure 6.5, with detailed trajectory information for each stage shown in Figures 6.6 - 6.10, and key results summarised in Table 6.2. The maximum payload-to-orbit trajectory shape involves the scramjet accelerator performing altitude raising manoeuvres, where the dynamic pressure of the scramjet accelerator is lowered from its maximum of 50kPa. These manoeuvres serve either to increase the net specific impulse of the scramjet accelerator, or to trade-off the efficiency of the scramjet accelerator in order to increase the efficiency of the first and third stages. This payload-to-orbit optimised trajectory is able to deliver 156.4kg of payload to heliocentric orbit, an increase of **59.1%** over the constant, 50kPa dynamic pressure result (Case 1).

The first stage, shown in Figure 6.6, follows a very similar trajectory to that of the first stage releasing the scramjet accelerator onto a constant dynamic pressure trajectory. However, the trajectory angle at the separation of the scramjet accelerator is 10.8° , rather than the trajectory angle of 0.2° required for the scramjet accelerator to fly a constant dynamic pressure trajectory. Additionally, the altitude at first-second stage separation is raised to 24.52km, an increase of **0.68km** compared to the separation point of a scramjet accelerator flying at constant 50kPa dynamic pressure. This higher release angle and altitude causes the altitude of the scramjet accelerator to initially increase, and consequently for its dynamic pressure to decrease. This increased trajectory angle at separation is the

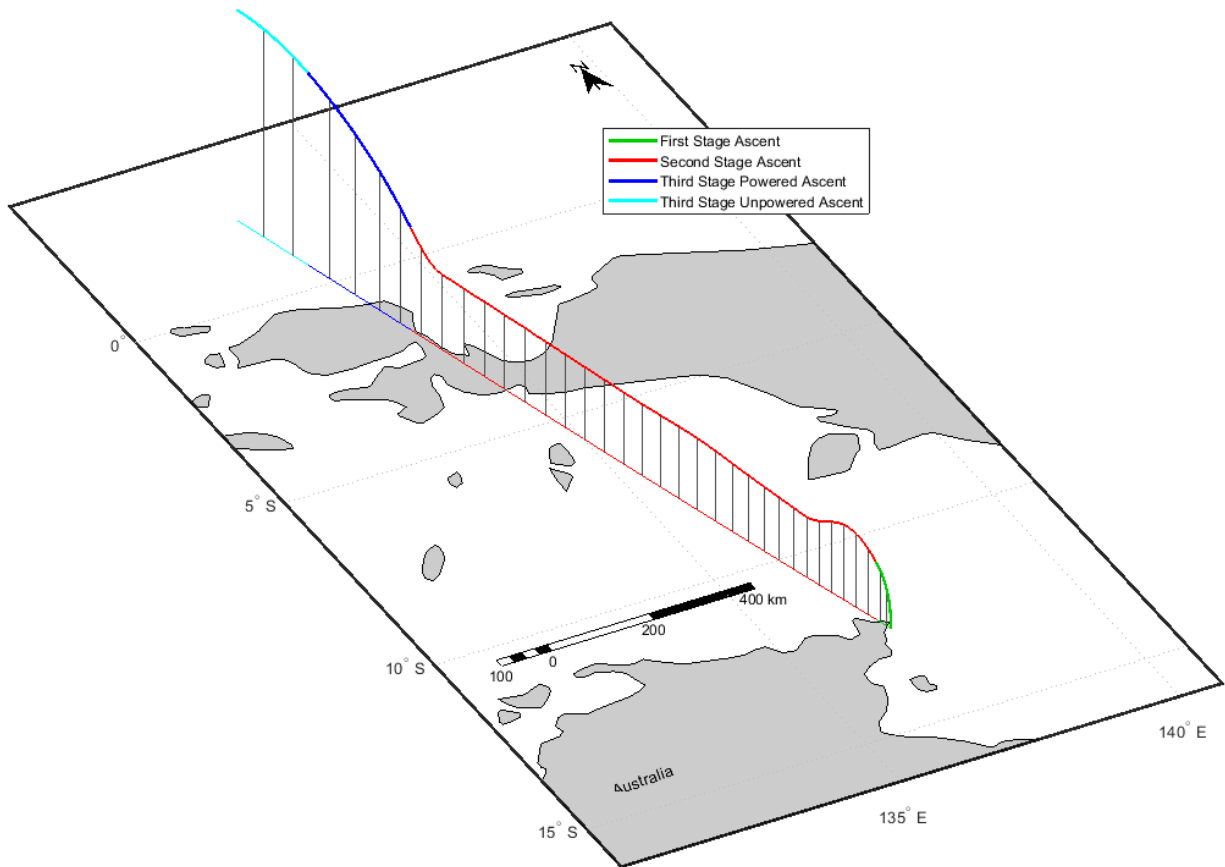


Figure 6.5: The optimised maximum payload-to-orbit trajectory of the launch system (Case 2).

consequence of a trade-off between the efficiency of the scramjet accelerator, and the efficiency and fuel mass of the first stage. In order to release the scramjet accelerator at a trajectory angle conducive to flying at a constant 50kPa dynamic pressure, the first stage must launch with a low fuel mass, to allow it to pitch in the correct manner. When the scramjet accelerator release angle and altitude are able to increase, the first stage is launched with a fuel mass of 17185kg, an increase of 1.0% compared to the constant dynamic pressure trajectory in Case 1. **XXX change this** This additional fuel and efficiency result in more energy being imparted upon the scramjet accelerator, 13.88GJ, compared to 12.62GJ when being released onto a 50kPa trajectory. In addition, the efficiency of the first stage is increased to $6.875\%\eta$ due to the increased acceleration, an overall improvement of $+0.148\%\eta$ (+2.4%) compared to the first stage separating the scramjet accelerator at 50kPa conditions. **XXX update this** During the maximum payload-to-orbit trajectory, the first stage rocket releases the scramjet accelerator at a velocity of 1533m/s, an increase of 5.7% compared to the first stage releasing the scramjet accelerator onto a constant dynamic pressure trajectory. Neither first stage utilises the full amount of allowable fuel mass, 17934kg, indicating that using the full fuel mass would necessitate separation

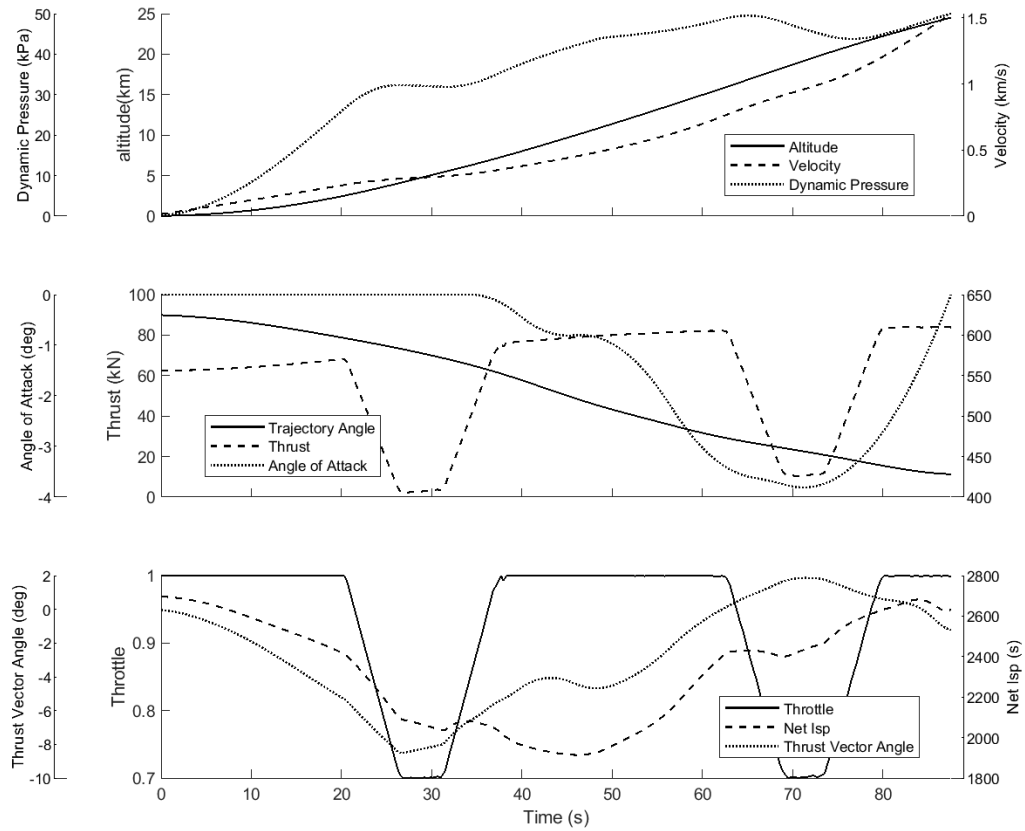


Figure 6.6: The optimised maximum payload-to-orbit trajectory of the launch system under power of the first stage rocket (Case 2).

conditions which would reduce the efficiency of the scramjet accelerator unfavourably. **XXX change this** These results indicate that the fuel mass utilised by the first stage has an optimal magnitude, and that including additional fuel past this amount does not increase the performance of the system. This implies that the size of the first stage is closely linked to the optimal trajectory of the system, and that future first stage designs should be sized so that optimal pitching is achieved.

After the initial deviation from the maximum dynamic pressure, the scramjet accelerator returns to 50kPa dynamic pressure for a time. At 184.9 seconds flight time, the altitude of the trajectory is again raised, and the dynamic pressure decreased, to a minimum of 43.0kPa. In this region the net specific impulse of the scramjet accelerator is relatively homogeneous with respect to changes in dynamic pressure, as can be observed in the specific impulse of the C-REST engines in Figure 6.9. The homogeneity between flight conditions means that the variation in engine performance with flight conditions is small and that flying at the maximum dynamic pressure in this region does not maximise the specific impulse from the C-REST engines. Figure 6.8 shows that while the optimised trajectory differs significantly from a constant dynamic pressure trajectory, both achieve similar net

Trajectory Condition	Value
Payload to Orbit (kg)	156.4
Total η_{exergy} (%)	1.685
1st Stage η_{exergy} (%)	6.875
Separation Alt, 1→2 (km)	24.52
Separation v, 1→2 (m/s)	1533
Separation γ, 1→2 (deg)	11.3
2nd Stage η_{exergy} (%)	4.401
Separation Alt, 2→3 (km)	43.81
Separation v, 2→3 (m/s)	2640
Separation γ, 2→3 (deg)	12.3
2nd Stage Distance Flown (km)	1195.6
3rd Stage η_{exergy} (%)	15.527
3rd Stage $t, q > 5\text{kPa}$ (s)	6.8
3rd Stage max α (deg)	10.0
3rd Stage Fuel Mass (kg)	2828.8

Table 6.2: A summary of key results from the maximum payload-to-orbit trajectory (Case 2).

specific impulses during the acceleration phase of flight, with the exception of the initial trajectory conditions at Mach 5, where the efficiency of the scramjet accelerator is traded for first stage rocket performance. Appendix E.3 details a maximum payload-to-orbit trajectory in which the scramjet accelerator is constrained to 50kPa between Mach 6-8, to prevent the altitude raising manoeuvre from taking place. This constrained trajectory allows for the magnitude of the performance gain from the altitude raising manoeuvre to be quantified. Overall, the altitude raising manoeuvre results in a slight increase in net specific impulse, compared to the trajectory constrained to maximum q , increasing the overall efficiency of the launch system from $1.690\%\eta$ to $1.685\%\eta$. This is a relatively minor variation, and the payload-to-orbit benefits of this altitude raising manoeuvre are correspondingly small; the optimised trajectory exhibits a payload-to-orbit increase of 0.4kg compared to the trajectory constrained to 50kPa between Mach 6-8, a difference of only 0.2%. **XXX update this with new constrained traj** However, it is important to note that, while its benefits are small, the altitude raising manoeuvre is consistently observed in all maximum payload-to-orbit optimised trajectories in which dynamic pressure is unconstrained. Also, despite its small benefit to payload-to-orbit, this altitude raising manoeuvre is significant as it reduces the heating and structural loading on the scramjet accelerator, though it is beyond the scope of this study to quantify these benefits. **XXX link to other studies that showed off max q flight**

At **319.4**s, the scramjet accelerator returns to flight at close to 50kPa dynamic pressure until **511.1**s, at which point a pull-up manoeuvre is performed, gaining altitude until the third stage rocket is released at **543.7**s of scramjet accelerator flight time. The point at which the pull-up manoeuvre begins is the location that takes into account the best combination of velocity, altitude and release

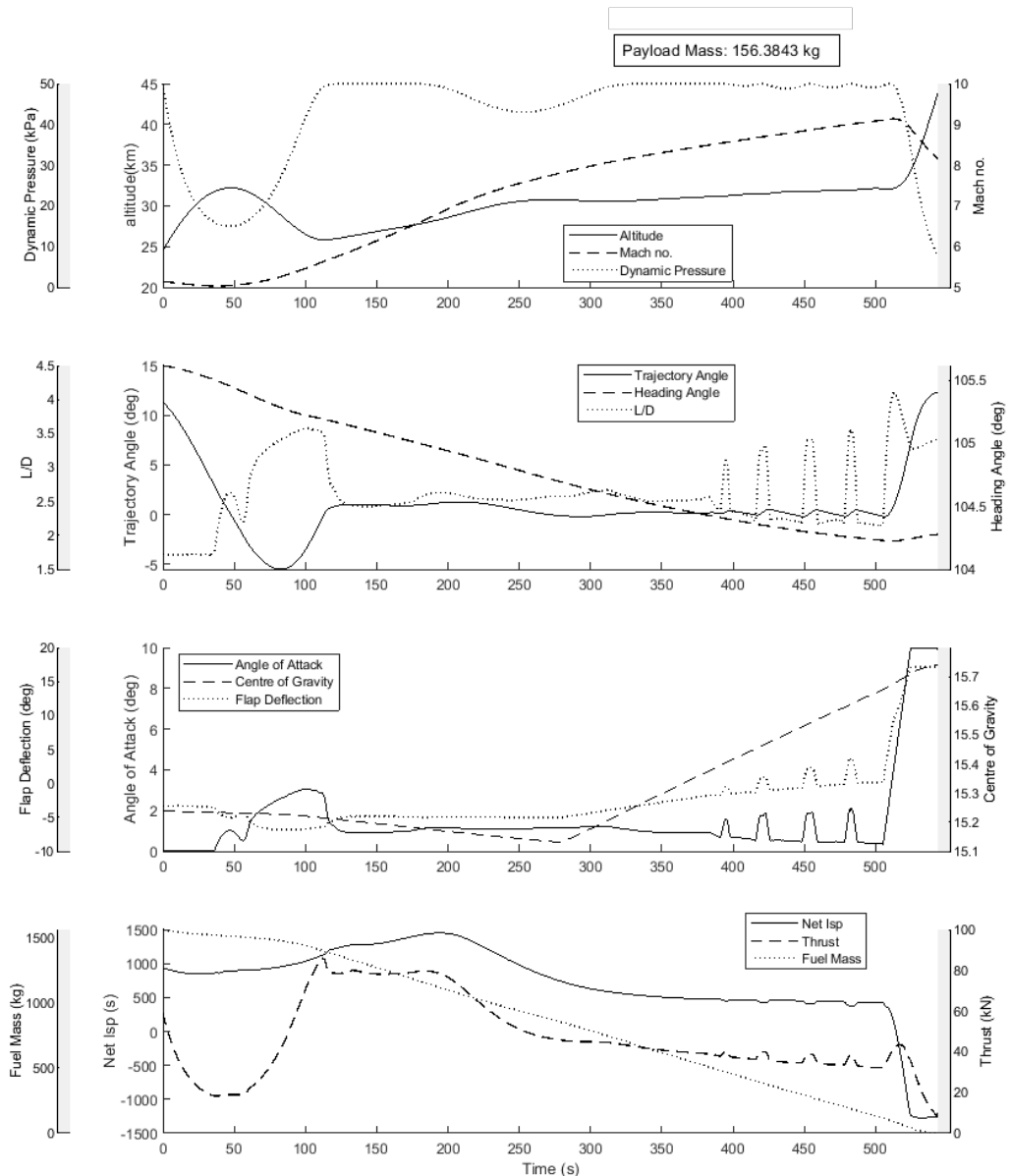


Figure 6.7: The optimised maximum payload-to-orbit trajectory of the scramjet accelerator (Case 2).

angle for the trade-off between the scramjet stage performance and the release of the third stage rocket. This pull-up indicates the region at which increasing altitude and release angle becomes more important than extracting maximum thrust from the scramjet (which is generally attained at high q and low flight angle at an equivalence ratio of 1). At high Mach numbers, flight in a lower dynamic pressure environment results in less thrust output from the scramjet engines, as well as an increase in angle of attack and flap deflection angle to compensate for the additional lift required. Due to this, less overall acceleration is obtained compared to the fixed dynamic pressure result. Separation occurs

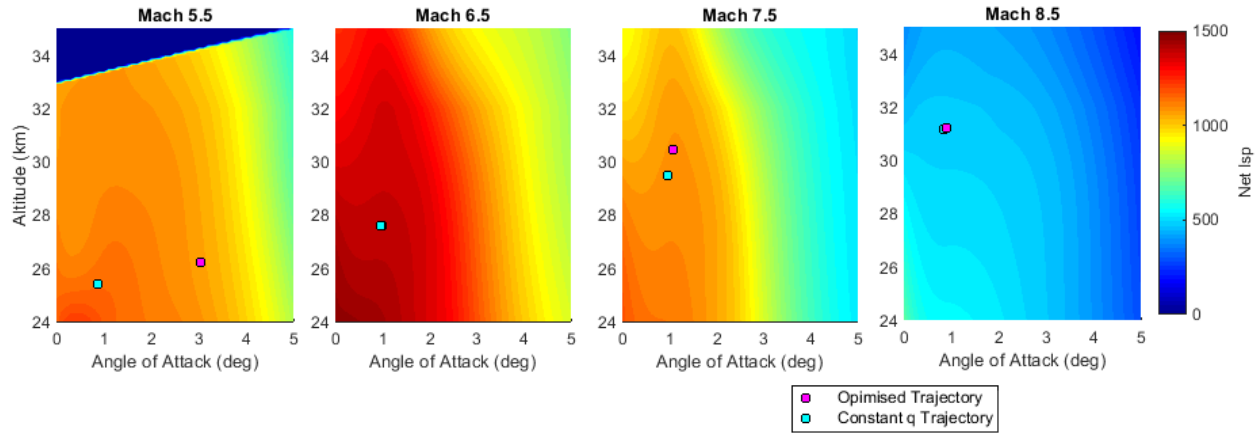


Figure 6.8: Net Isp contours for the scramjet accelerator at Mach numbers from 5-9, showing flight conditions for an optimised trajectory with no constraints (Case 2) and a constant dynamic pressure trajectory (Case 1).

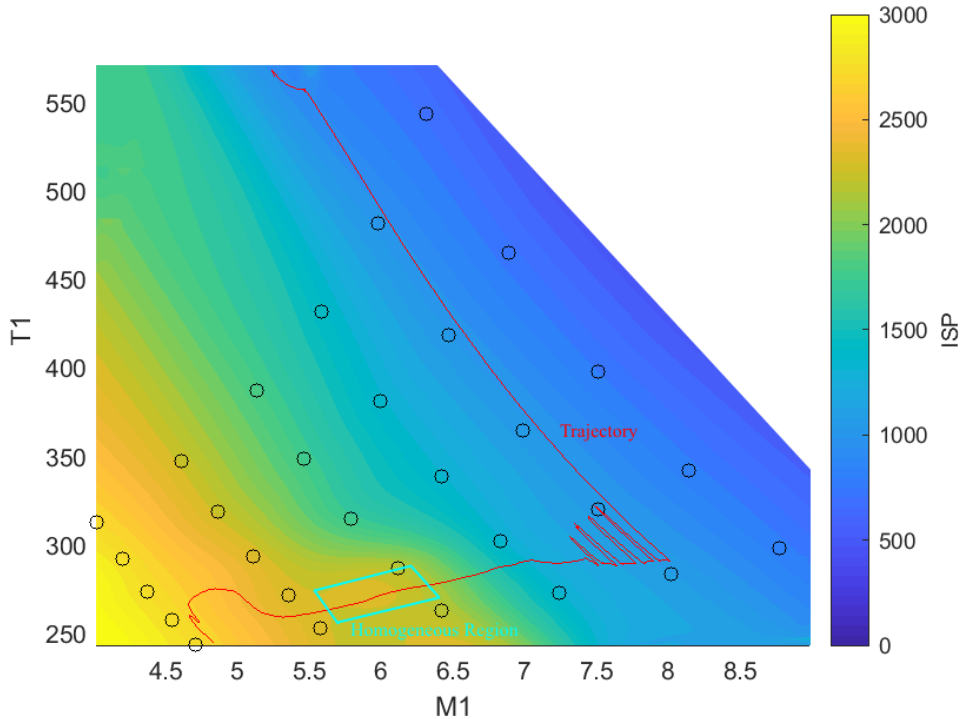


Figure 6.9: The specific impulse of the C-REST engines, plotted for inlet temperature (T1) and inlet Mach number (M1). Data points are shown in black.

at a velocity of 2640m/s, a decrease of 145.0m/s (-5.2%). However, at the same time separation altitude increases by 11.65km (+36.2%) to 41.73km, resulting in a decrease in separation dynamic pressure to 7.8kPa. The scramjet stage pull-up assists the rocket in manoeuvring to exoatmospheric

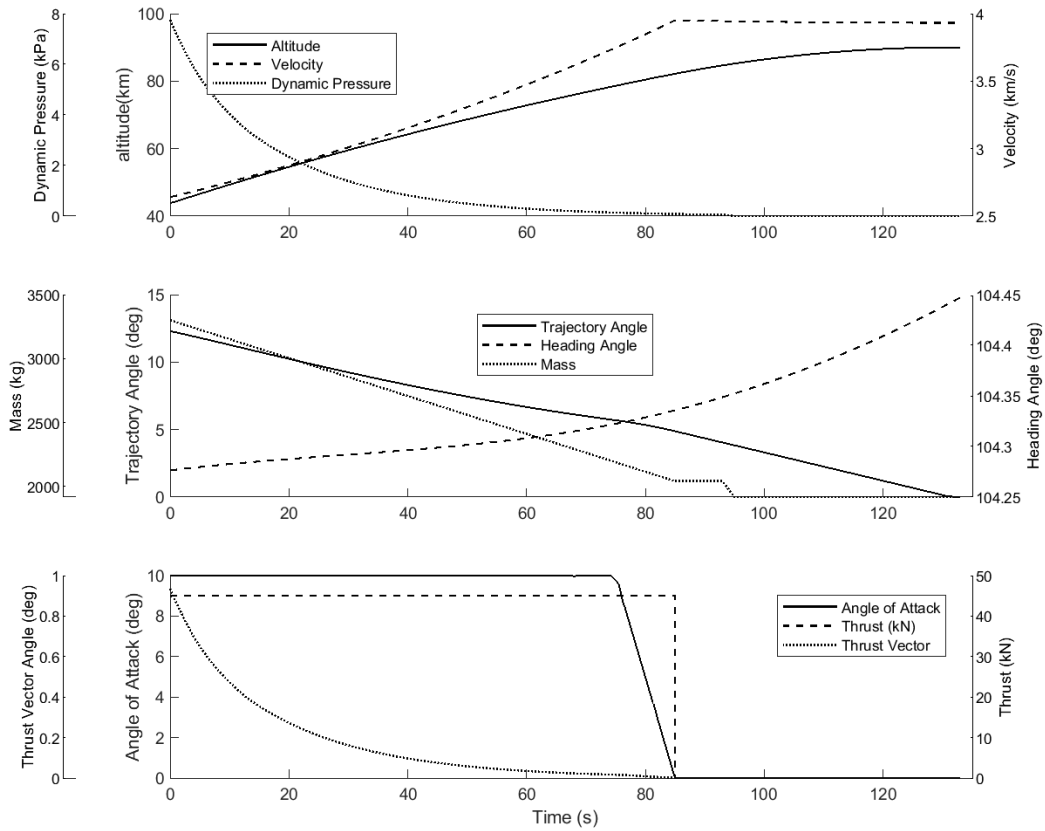


Figure 6.10: The third stage trajectory of the launch system flying the maximum payload-to-orbit trajectory (Case 2).

altitude by increasing the altitude and angle at separation, utilising the superior aerodynamics and manoeuvrability of the scramjet accelerator. The increase in release angle, to the optimal angle of 12.3° , significantly reduces the turning that is required by the rocket as evident from comparing Fig 6.4 and 6.10. Overall, the altitude raising manoeuvres which the scramjet accelerator performs result in a decrease in the exergy efficiency of the scramjet accelerator to $4.401\%\eta$, a total decrease of $-0.719\%\eta$ (-14.04%) compared to the scramjet accelerator flying at a constant dynamic pressure. However, the optimised trajectory drastically increases the exergy efficiency of the third stage, to $15.527\%\eta$, an overall increase of $+6.013\%\eta$ ($+63.20\%$) compared to the third stage released from the scramjet accelerator flying a fixed dynamic pressure trajectory. Along with the increased efficiency of the first stage, this exergy trade-off leads to the total exergy efficiency of the launch system increasing, from $1.155\%\eta$ to $1.685\%\eta$.

The trajectory of the third stage rocket after release from an optimised scramjet trajectory is shown in Figure 6.10. Release at a higher, more optimal angle, reduces the aerodynamic moment necessary to trim the vehicle. In turn, this reduced moment reduces the necessary thrust vector angle, so that

the thrust vector limit is not reached. The third stage rocket is released at a high trajectory angle, and continuously gains altitude, avoiding the close-to-horizontal flight required by the fixed dynamic pressure release (Case 1). Due to the higher altitude and release angle, the third stage rocket is released at a lower dynamic pressure, 7.8kPa compared to 50.0kPa, and spends much less time flying in a high dynamic pressure environment, 7.7s at over 5kPa dynamic pressure rather than 112.3s. The reduced time that the rocket must spend in a high dynamic pressure environment, and the decrease in the maximum dynamic pressure that the rocket stage experiences, may allow the structural mass and heat shielding necessary to achieve exoatmospheric flight to be decreased. This reduced mass may enable higher payload to orbit, though it is beyond the scope of this study to investigate these design changes. **XXX link to section where I do this**

XXX update this para Previous studies considering the optimised trajectory of vehicles with multiple propulsion methods within a single stage show airbreathing-rocket transitions at, or close to, exoatmospheric flight, at altitudes from 56-130km[51, 60, 64]. Compared to these studies, the maximum payload to orbit trajectory of the multi-stage system shows a scramjet-rocket transition point at much lower altitudes. This lower transition point is a consequence of the stage separation creating an energy trade-off between the stages, which does not occur in a single stage vehicle. Single-stage vehicles must necessarily transport all components to exoatmosphere, and so utilise the scramjet engines until higher altitude to take advantage of their high efficiency. A multi-stage vehicle is able to separate the scramjet stage. This separation occurs when the performance benefits provided by the superior aerodynamics and engine efficiency of the scramjet stage are offset by the energy required to lift the extra mass to higher altitude. The beneficial ability to separate the scramjet stage results in a lower altitude scramjet-rocket transition point, when compared to single stage vehicle designs.

6.3 Energy Usage Analysis

An energy usage analysis is conducted on the maximum payload-to-orbit launch trajectories, both with, and without the scramjet accelerator constrained to constant dynamic pressure flight (Cases 1 & 2). This is performed in order to understand the primary sources of energy loss for each stage, and to compare the trajectories optimised with, and without the scramjet accelerator constrained to constant dynamic pressure. An energy usage breakdown of each of each stage is compared in Table 6.3. The energy usage breakdown compares: the energy used to accelerate the payload, $\Delta KE_{payload} + \Delta PE_{payload}$; the energy imparted to the successive stages, $\Delta KE_{nextstage} + \Delta PE_{nextstage}$; the energy used overcoming drag, $\int_{t_0}^{t_f} v D dt$; the energy used imparting energy to the structural mass of each stage, which is separated, $\Delta KE_{discarded} + \Delta PE_{discarded}$; and the energy lost due to propulsion inefficiency.

The efficiency of the first stage rocket increases when the first-second stage separation altitude and trajectory angle are raised, in the trajectory with no dynamic pressure constraint. This is due to the lower propulsive efficiency of rockets at low speeds, illustrated by the equation for the propulsive

Trajectory Condition	50kpa Constant q	No q Constraint
First Stage Fuel Exergy	201.91 GJ	201.91 GJ
KE + PE of Payload	0.063% (0.13 GJ)	0.109% (0.22 GJ)
KE + PE of 2 nd & 3 rd Stage	6.190% (12.50 GJ)	6.765% (13.66 GJ)
Overcoming Drag	2.76% (5.57 GJ)	2.49% (5.03 GJ)
KE + PE of 1 st Stage Structural Mass	0.92% (1.86 GJ)	1.01% (2.04 GJ)
Propulsion Inefficiency	90.06(181.84 GJ) %	89.62% (180.95 GJ)
scramjet accelerator Fuel Exergy	187.38 GJ	187.38 GJ
KE + PE of Payload	0.152% (0.28 GJ)	0.209% (0.39 GJ)
KE + PE of 3 rd Stage	4.968% (9.31 GJ)	4.192% (7.85 GJ)
Overcoming Drag	18.68% (35.00 GJ)	20.42% (38.26 GJ)
KE + PE of scramjet accelerator Structural Mass	7.69% (14.40 GJ)	6.61% (12.39 GJ)
Propulsion Inefficiency	68.51% (128.37 GJ)	68.57% (128.49 GJ)
Third Stage Fuel Exergy	35.03 GJ	34.33 GJ
KE + PE of Payload	9.514% (3.33 GJ)	15.527% (5.33 GJ)
Overcoming Drag	8.52% (2.98 GJ)	0.33% (0.11 GJ)
KE + PE of 3 rd Stage Structural Mass	29.96% (10.49 GJ)	30.85% (10.59 GJ)
KE + PE of Heat Shield	8.46% (2.96 GJ)	3.56% (1.22 GJ)
Propulsion Inefficiency	43.54% (15.25 GJ)	49.73% (17.07 GJ)

Table 6.3: An energy usage breakdown of the ascent trajectories, both with, and without, the scramjet accelerator constrained to constant dynamic pressure (Cases 1 & 2). Blue indicates a 'productive' energy usage, whereas red indicates energy 'wastage'. XXX fix all to be same s.f.

efficiency of a rocket[164]:

$$\eta_P = \frac{2v_0/v_g}{1 + (v_0/v_g)^2}, \quad (6.1)$$

where v_g is the exhaust velocity, and v_0 is the velocity of the vehicle. At low rocket velocities there is a large difference between the flight speed of the vehicle, and the exhaust velocity of the rocket engine, resulting in low propulsion efficiencies, and consequently high propulsive inefficiency losses. The propulsive losses of the first stage rocket decrease when the scramjet accelerator is not constrained to a constant dynamic pressure trajectory, as a consequence of the additional acceleration obtained from the larger fuel exergy. However, due to the first stage rocket starting from rest, the first stage rocket always loses a large portion of its exergy to propulsive inefficiency.

The energy imparted upon the payload and third stage rocket during the scramjet accelerator's acceleration is decreased significantly when the scramjet accelerator is allowed to deviate from 50kPa dynamic pressure, reducing from 9.31GJ to 7.85GJ, a decrease of -15.7%. This energy is traded-off during the pull-up manoeuvre, by utilising the superior aerodynamics of the scramjet accelerator to manoeuvre into flight conditions that are favourable for the separation of the third stage, improving the efficiency of the third stage ascent. Even though less energy is imparted upon the third stage before separation, a release from the end of a scramjet accelerator pull-up enables the third stage to impart significantly more energy onto the payload, at 5.33GJ, compared to 3.33GJ when released

from 50kPa, an increase of **+60.1%**, with a significantly increased exergy efficiency of 15.527%.

The additional energy efficiency of the third stage comes from a decrease in the energy lost due to drag, as well as a decrease in the energy imparted upon the heat shield. The energy lost from the third stage overcoming drag is dependent on the amount of time that the rocket spends in the atmosphere, and comprises 8.52% of the fuel exergy when released at 50kPa, and 0.33% when released after a pull-up of the scramjet accelerator. The energy lost accelerating the heat shield is also significantly larger when released from the scramjet accelerator flying a constant dynamic pressure trajectory, at 8.46% of the fuel exergy, compared to only 3.56% when the third stage is released after a pull-up of the scramjet accelerator. This is due to the third stage spending considerably more time in a high dynamic pressure environment when released from a constant dynamic pressure trajectory, requiring the heat shield for longer, so that more kinetic and potential energy is imparted upon the heat shield during acceleration. However, the energy losses due to the propulsion inefficiency of the third stage are higher when released from the end of a scramjet accelerator pull-up, compared to the trajectory constrained to constant dynamic pressure. This is due to the third stage being released at lower velocity, from the end of a scramjet accelerator pull-up manoeuvre, resulting in a lower efficiency as illustrated in Equation 6.1. This indicates that there is a trade-off between the propulsion inefficiencies of the third stage, and the drag and heat shield energy losses.

The propulsion inefficiency losses of the scramjet accelerator are relatively low, compared to those of the first stage. These lowered propulsion losses are due to the scramjet accelerator's engines utilising atmospheric oxygen as an oxidiser, resulting in a higher propulsion system efficiency. However, the scramjet accelerator loses a large amount of its exergy to overcoming drag. These high drag losses are due to the scramjet accelerator accelerating at high speeds within the atmosphere, at high dynamic pressures, and serve to partially offset the reduced energy losses due to the high propulsive efficiency of the scramjet accelerator. The drag losses of the scramjet accelerator flying a trajectory with no dynamic pressure constraint are higher than those of the scramjet accelerator flying a constant dynamic pressure trajectory, at 20.42%, compared to 18.68%. This is due to the additional manoeuvring of the scramjet accelerator during the pull-up before third stage release when the dynamic pressure is not constrained, which requires high angles of attack, and increases drag significantly.

The propulsive energy losses of the third stage are also low, compared to the first stage rocket. This is due to the larger velocity of the third stage, compared to the first stage, which increases the propulsive efficiency of the third stage rocket.

6.4 Sensitivity Analysis

XXX add first stage thrust and mass variation? ... maybe if i think its worth it

XXX I need more justification and estimation of variance (can maybe look at dawids and other shape optimisation papers to get an idea?) I also need to focus this partly in terms of uncertainties

XXX I need to make it clear that the sensitivity study is an important contribution, that gives useful insights into the interplay between the stages

XXX I need to make clear that this analysis isn't just 'what are the number differences' but mostly 'is the trajectory optimisation valid across vehicle designs'

XXX remove max aoa form tables

The launch system studied in this work is intended to be representative of a three stage, rocket-scramjet-rocket, small satellite launch system, to be used to inform future vehicle designs. It is anticipated that the design of the launch system will change significantly before an optimal, or even practically feasible, iteration is reached. Additionally, this study models the launch system using medium and low fidelity methods, which may be significant sources of error on the final optimised trajectory. To quantify how variations in the design of a stage or variations in the performance of a stage due to modelling error may affect the performance of the launch system, it is useful to conduct a sensitivity analysis on the launch system. A sensitivity analysis is conducted, in which selected design parameters of the launch system are varied, and the effects on the optimised maximum payload-to-orbit trajectory of the launch system are investigated. Appendix F shows comparison plots of the scramjet accelerator and third stage trajectories for each parameter variation study, however, the first stage rocket trajectories are very similar and are not compared graphically. Key results including performance factors of each stage and separation conditions are summarised within this section. This study is performed in order to determine the relative importance of the design parameters on the efficiency of the system, as well as investigating changes in the maximum payload-to-orbit trajectory as the performance of the launch system is varied. The investigation of the key design parameters of the launch system provides a comparative metric, which is used to quantify the relative impact of the vehicle design on the performance of the launch system. The performance trade-offs between the stages are investigated by studying the variation in the optimised trajectory, particularly the stage separation conditions, as the parameters of the launch system design are changed. Trends are developed for each parameter study, quantifying how much the performance factors of the launch system vary per percentage of variation of each design parameter ($\Delta/\Delta\%$). This percentage variation gives a general metric for how much each design parameter effects the performance factors of the launch system. However, the relative magnitude of one percent variation of each individual design parameter must be taken into account when making comparisons.

The information obtained from this parameter variation study can be used to inform future launch system designs. In addition, this sensitivity study serves to verify the ability of LODESTAR to generate optimal trajectories with varied vehicle designs, as well as investigating the robustness of the optimised solution with respect to uncertainties in the vehicle design and performance. When necessary for the trajectory simulations within this section, it is assumed that the scramjet engines are operable at velocities slightly under Mach 5. This assumption is made in order to allow meaningful assessment of parameters which effect the first-second stage separation velocity, without modifica-

tion of the first stage rocket. All optimised trajectories within this section use the full amount of fuel available to the scramjet accelerator vehicle.

6.4.1 Case 3: Maximum Dynamic Pressure Sensitivity

Trajectory Condition	q_{max} :	40kPa	45kPa	50kPa	55kPa	60kPa	$\Delta/\Delta\%q$
Payload to Orbit (kg)	181.4	185.7	189.2	192.8	196.4	0.4	
Payload Variation (%)	-4.11	-1.82	0.00	1.90	3.82	0.2	
Total η_{exergy} (%)	1.624	1.662	1.693	1.726	1.757	3e-05	
1st Stage η_{exergy} (%)	6.334	6.315	6.292	6.258	6.244	-0.002	
Separation Alt, 1→2 (km)	25.49	24.77	24.12	23.51	23.00	-0.06	
Separation v, 1→2 (m/s)	1480	1483	1484	1483	1485	-	
Separation γ, 1→2 (deg)	5.5	4.4	3.1	1.1	0.8	-0.13	
2nd Stage η_{exergy} (%)	4.571	4.647	4.718	4.808	4.887	0.008	
Separation Alt, 2→3 (km)	42.00	41.90	41.73	41.61	41.39	-0.02	
Separation v, 2→3 (m/s)	2657	2673	2687	2703	2720	1.56	
Separation γ, 2→3 (deg)	10.1	10.5	10.8	11.0	11.2	0.03	
2nd Stage Distance Flown (km)	1363.9	1267.2	1190.1	1116.9	1069.3	-7.4	
3rd Stage η_{exergy} (%)	17.956	18.390	18.733	19.090	19.448	0.037	
3rd Stage $t, q > 5\text{kpa}$ (s)	12.7	12.4	14.2	12.6	13.3	-	
3rd Stage max α (deg)	17.8	16.6	16.2	15.5	14.7	0	
3rd Stage Fuel Mass (kg)	2833.4	2829.1	2825.6	2822.0	2818.4	-0.37	

Table 6.4: Comparison of key trajectory parameters with variation in the maximum dynamic pressure of the scramjet accelerator (Case 3).

To investigate the sensitivity of the vehicle to changes in q_{max} , the maximum permissible dynamic pressure is varied by $\pm 10\text{kPa}$ in 5kPa increments, and the flight trajectory optimised, with results shown in Table 6.4, and comparison plots shown in Appendix F.1.1. The variation in maximum dynamic pressure has only a small effect on the total exergy efficiency of the system, and hence only a small effect on the payload mass delivered to sun synchronous orbit. Varying the maximum dynamic pressure by $\pm 20\%$ causes a variation of only $+0.064\%\eta$ or $-0.069\%\eta$ in the exergy efficiency of the launch system and a corresponding $+7.2\text{kg}$ ($+3.82\%$) or -7.8kg (-4.11%) variation in the payload to orbit. The scramjet accelerator pull-up manoeuvres of all cases are similar, with a slight trend of decreasing altitude as the maximum dynamic pressure is increased. Altitudes of 42.00km and 41.39km are reached for the 40kPa and 60kPa limited cases respectively, with separation velocities of 2657m/s and 2720m/s . The 40kPa limited case flies for 612.1s , significantly longer than the 60kPa limited case, which flies for 468.1s . As the dynamic pressure decreases, the size of the altitude raising manoeuvre in the middle of the trajectory decreases. This is due to the increased altitude and angle of attack moving the flight conditions into a region where the specific impulse of the C-REST engines is not homogeneous, so that it is beneficial to fly at maximum dynamic pressure. All trajectories pull-up

to similar altitudes, with a relatively small variation in separation velocity of +33m/s (+1.2%) and -30m/s (-1.1%). This small variation in velocity is despite the increase in air density and decrease in angle of attack required for flight at higher dynamic pressures, both of which increase the mass flow into the engine. Although the thrust output of the C-REST engines increases with dynamic pressure, so does the drag on the vehicle, and the net increase in performance is relatively small ($0.008 \frac{\Delta\% \eta_{exergy}}{\Delta\% q}$). The trade-off between the exergy efficiency of the first and second stages shifts as the dynamic pressure limit is increased, with the first stage rocket becoming less efficient (varying $6.334\%\eta$ at 40kPa to $6.244\%\eta$ at 60kPa), while the exergy efficiency of the scramjet accelerator increases (varying from an η_{exergy} of $4.571\%\eta$ at 40kPa to $4.887\%\eta$ at 60kPa). The decreased altitude of first-second stage separation required for flight close to 60kPa dynamic pressure causes the first stage to pitch more to reach the optimal staging conditions, increasing the drag losses of the first stage from 1.57% at 40kPa maximum dynamic pressure, to 1.73% at 60kPa maximum dynamic pressure. These increased drag losses result in a less efficient first stage trajectory, which partially offsets some of the increased scramjet accelerator performance gained from the flight at higher dynamic pressure.

6.4.2 Case 4: Scramjet Accelerator Drag Sensitivity

XXX I should link the number of small skips with what was said previously, these reduce as the drag increases, lending credence to my arguments that they are due to the SPRTAn not being optimised for max q flight

To investigate the effect of the vehicle design and uncertainty in aerodynamic performance on the optimal trajectory, the drag of the scramjet accelerator is varied by $\pm 10\%$, and an optimised trajectory calculated with dynamic pressure limited to 50kpa. The drag of the scramjet accelerator is varied during both the first stage ascent, as well as the acceleration of the scramjet accelerator. Results are compared to the 100% drag result in Table 6.5 with a trajectory path comparison shown in Appendix F.1.2.

The drag of the scramjet accelerator has a significant effect on the overall exergy efficiency of the system ($+0.207\%\eta$ at 90% drag, and $-0.170\%\eta$ at 110% drag) and correspondingly, on the maximum payload-to-orbit, $+22.6\text{kg}$ at 90% drag, a variation of $+14.5\%$ and -18.6kg at 110% drag, a variation of -11.2% . The exergy efficiencies of the first stage rocket and the scramjet accelerator are decreased significantly as the drag is increased, from $7.287\%\eta$ and $4.910\%\eta$ respectively at 90% drag, to $6.457\%\eta$ and $4.032\%\eta$ respectively at 110% drag. This reduction in efficiency is due to the increase in energy which must be used to overcome the added drag. The altitude and trajectory angle at the first-second stage separation decrease significantly as the drag is increased. This indicates that the first stage is able to pitch more during its trajectory, as a consequence of accelerating more slowly, as the drag increases. XXX traj angle doesnt The scramjet accelerator trajectory results show that when drag is varied, the optimal trajectories do not change shape significantly, and have similarly sized pull-ups,

Trajectory Condition	$C_{d,2}$:	90%	95%	100%	105%	110%	$\Delta/\Delta\%C_{d,2}$
Payload to Orbit (kg)		179.0	165.8	156.4	147.2	137.8	-2
Payload Variation (%)		14.49	6.04	0.00	-5.89	-11.90	-1.29
Total η_{exergy} (%)		1.892	1.772	1.685	1.601	1.515	-0.00018
1st Stage η_{exergy} (%)		7.287	7.082	6.875	6.665	6.457	-0.042
Separation Alt, 1→2 (km)		24.94	24.74	24.52	24.30	24.07	-0.04
Separation v, 1→2 (m/s)		1584	1559	1533	1506	1478	-5.3
Separation γ, 1→2 (deg)		11.2	11.2	11.3	11.4	11.5	0.02
2nd Stage η_{exergy} (%)		4.910	4.603	4.401	4.217	4.032	-0.043
Separation Alt, 2→3 (km)		43.20	43.54	43.81	43.51	43.15	-
Separation v, 2→3 (m/s)		2780	2700	2640	2585	2529	-12.38
Separation γ, 2→3 (deg)		11.6	12.0	12.3	12.6	12.9	0.06
2nd Stage Flight Time (s)		629.9	630.4	631.2	637.9	649.3	0.93
2nd Stage Distance Flown (km)		1246.1	1221.5	1195.6	1176.4	1159.3	-4.37
3rd Stage η_{exergy} (%)		17.728	16.447	15.527	14.628	13.706	-0.197
3rd Stage $t, q > 5\text{kpa}$ (s)		9.7	8.1	6.8	6.8	7.5	-
3rd Stage max α (deg)		10.0	10.0	10.0	10.0	10.0	-
3rd Stage Fuel Mass (kg)		2806.2	2819.4	2828.8	2838.0	2847.4	2.02

Table 6.5: Comparison of key trajectory parameters with variation in the drag of the scramjet accelerator (Case 4).

though as the drag is increased (ie. L/D is decreased), the second stage follows a slightly slower and hence lower flight path, and the scramjet accelerator pulls-up to a higher trajectory angle. The similar shape of the optimal trajectory with variation in the aerodynamics of the scramjet accelerator suggests that sacrificing velocity to increase separation altitude in a pull-up manoeuvre is optimal for multiple vehicle designs, and that the size of this pull-up is consistent with variation in the aerodynamics of the scramjet accelerator. **XXX maybe change pull up stuff to 'no clear trend' rather than 'similarly sized'** As the drag of the scramjet accelerator increases, the exergy efficiency of the third stage shows a corresponding decrease, from 17.728% η at 90% drag, to 13.706% η at 110% drag. This is primarily due to the lower velocity of scramjet accelerator-third stage separation at higher drag, which results in a decreased third stage propulsive efficiency (illustrated by Equation 6.1). This decreased propulsive efficiency in turn increases the losses due to propulsive inefficiency during the operation of the third stage, from 47.39% at $C_D=90\%$, to 51.53% at $C_D=110\%$.

6.4.3 Case 5: C-REST Specific Impulse Sensitivity

The specific impulse of the C-REST scramjet engines is varied by $\pm 10\%$ to directly investigate the effects of the efficiency of the scramjet engines on the performance of the launch vehicle. A comparison of key trajectory parameters is shown in Table 6.6, with comparison plots presented in Appendix F.1.3. The maximum payload-to-orbit varies by +25.3kg (+16.2%) to -19.2kg (-12.3%), and the to-

Trajectory Condition	$I_{SP,2}$:	90%	95%	100%	105%	110%	$\Delta/\Delta\%I_{SP,2}$
Payload to Orbit (kg)		137.2	146.8	156.4	167.9	181.7	2.2
Payload Variation (%)	-12.30	-6.12	0.00	7.35	16.19	1.41	
Total η_{exergy} (%)	1.510	1.598	1.685	1.790	1.917	0.0002	
1st Stage η_{exergy} (%)	6.872	6.882	6.875	6.882	6.875	-	
Separation Alt, 1→2 (km)	24.52	24.53	24.52	24.53	24.52	-	
Separation v, 1→2 (m/s)	1532	1534	1533	1534	1533	-	
Separation γ, 1→2 (deg)	11.3	11.3	11.3	11.4	11.5	-	
2nd Stage η_{exergy} (%)	3.846	4.122	4.401	4.744	5.159	0.065	
Separation Alt, 2→3 (km)	43.32	43.45	43.81	43.21	43.85	-	
Separation v, 2→3 (m/s)	2520	2582	2640	2716	2799	13.83	
Separation γ, 2→3 (deg)	13.1	12.7	12.3	11.9	11.3	-0.08	
2nd Stage Flight Time (s)	638.9	633.2	631.2	628.7	637.3	-	
2nd Stage Distance Flown (km)	1157.2	1174.4	1195.6	1218.9	1254.6	4.78	
3rd Stage η_{exergy} (%)	13.648	14.593	15.527	16.643	17.981	0.214	
3rd Stage $t, q > 5\text{kpa}$ (s)	6.5	6.7	6.8	9.6	8.4	-	
3rd Stage max α (deg)	10.0	10.0	10.0	10.0	10.0	-	
3rd Stage Fuel Mass (kg)	2848.0	2838.4	2828.8	2817.3	2803.5	-2.2	

Table 6.6: Comparison of key trajectory parameters with variations in the specific impulse of the C-REST engines (Case 5).

tal exergy efficiency varies by $+0.232\%\eta$ to $-0.175\%\eta$, at 110% I_{SP} and 90% I_{SP} respectively. The increased C-REST specific impulse does not vary the first stage performance significantly, and the first-second stage separation point stays relatively constant for all cases, except the 110% I_{SP} case, where the altitude and trajectory angle of the first-second stage separation increase. The lack of a clear trend in the first stage release point indicates that the efficiency trade-off between the first stage and the scramjet accelerator is not significantly affected by the efficiency of the scramjet accelerator, and is primarily driven by the capabilities of the first stage rocket.

Varying the specific impulse of the C-REST engines has a considerable effect on the exergy efficiency of the scramjet accelerator, causing the efficiency to increase by $+0.758\%\eta$ ($+14.7\%$) at 110% I_{SP} and decrease by $-0.555\%\eta$ (-12.6%) at 90% I_{SP} . Increasing the specific impulse of the C-REST engines allows the scramjet accelerator to accelerate more over the flight time, increasing the velocity at second-third stage separation significantly. The propulsive inefficiency losses of the scramjet accelerator decrease from 70.37% at 90% I_{SP} , to 66.35% at 110% I_{SP} . However, the drag losses, and the energy needed to accelerate the structural mass of the third stage, increase from 20.01% and 5.78% at 90% I_{SP} , to 20.74% and 7.75% of the scramjet accelerator's total exergy at 110% I_{SP} , partially offsetting the increased performance. These increased losses are due to the additional velocity at the end of the trajectory causing increased drag, and requiring more kinetic energy to be imparted upon the structural mass of the scramjet accelerator. Varying the specific impulse does not change the optimal second-third stage separation altitude significantly, however the increased velocity allows

this altitude to be reached by the scramjet accelerator with less trajectory angle variation during the pull-up. Increasing the specific impulse allows the third stage to successfully reach orbit from a lower trajectory angle release point, as low as 11.3° at 110% I_{SP} , while decreasing the specific impulse requires a higher release point, up to 13.1° at 90% I_{SP} . The exergy efficiency of the third stage is increased as the specific impulse of the scramjet accelerator increases, increasing by $+2.454\%\eta$ at 110% I_{SP} , and decreasing by $-1.879\%\eta$ at 90% I_{SP} . This is due to the significantly decreased propulsive losses of the third stage when released at a higher velocity, 46.90% (**15.90 GJ**) at 110% I_{SP} , compared to 51.76% (**17.89 GJ**) at 90% I_{SP} .

6.4.4 Case 6: scramjet accelerator Mass Sensitivity

XXX change to 10%

Trajectory Condition	m_2 :	95%	97.5%	100%	102.5%	105%	$\Delta/\Delta\%q$
Payload to Orbit (kg)	162.7	159.5	156.4	153.0	149.7	-1.3	
Payload Variation (%)	4.06	2.00	0.00	-2.16	-4.29	-0.83	
Total η_{exergy} (%)	1.743	1.714	1.685	1.654	1.624	-0.00012	
1st Stage η_{exergy} (%)	6.973	6.924	6.875	6.820	6.766	-0.021	
Separation Alt, 1→2 (km)	24.81	24.66	24.52	24.37	24.23	-0.06	
Separation v, 1→2 (m/s)	1568	1550	1533	1515	1497	-7.07	
Separation γ, 1→2 (deg)	11.0	11.2	11.3	11.5	11.6	0.05	
2nd Stage η_{exergy} (%)	4.457	4.424	4.401	4.371	4.340	-0.011	
Separation Alt, 2→3 (km)	43.90	43.90	43.81	43.41	43.40	-0.06	
Separation v, 2→3 (m/s)	2674	2656	2640	2625	2607	-6.56	
Separation γ, 2→3 (deg)	12.3	12.3	12.3	12.3	12.3	-	
2nd Stage Flight Time (s)	634.6	631.8	631.2	633.0	633.1	-	
2nd Stage Distance Flown (km)	1228.5	1209.8	1195.6	1184.1	1169.7	-5.74	
3rd Stage η_{exergy} (%)	16.150	15.835	15.527	15.196	14.867	-0.128	
3rd Stage $t, q > 5\text{kpa}$ (s)	7.3	6.6	6.8	7.9	7.5	-	
3rd Stage max α (deg)	10.0	10.0	10.0	10.0	10.0	-	
3rd Stage Fuel Mass (kg)	2822.5	2825.7	2828.8	2832.2	2835.5	1.31	

Table 6.7: Comparison of key trajectory parameters with variation in the structural mass of the scramjet accelerator (Case 6).

The mass of the scramjet accelerator is varied by $\pm 5\%$ ($\pm 247.9\text{kg}$), to investigate the effects of the structural, thermal shielding, and system mass of the scramjet accelerator on the performance of the launch system. A mass variation of only 5% is investigated, in order to prevent the first-second stage separation velocity from dropping unacceptably low. A summary of the key parameters of each trajectory is detailed in Table 6.7, with comparison plots shown in Appendix F.1.4. Variation in the mass of the scramjet accelerator causes the maximum payload-to-orbit of the launch system to vary by +7.4kg (+3.95%) at 95% structural mass and by -7.9kg (-4.16%) at 105% structural mass. The ex-

ergy efficiency of the first stage rocket decreases as the mass of the scramjet accelerator is increased ($-0.224\%\eta$ at 105% structural mass) and increases as the mass of the scramjet accelerator is decreased ($+0.215\%\eta$ at 95% structural mass). As the mass of the scramjet accelerator increases, the acceleration of the first stage decreases, and the propulsive inefficiency losses of the first stage increase, from 89.48% at 95% structural mass to 89.76% at 105% structural mass. Additionally, the altitude and trajectory angle at first-second stage separation are decreased significantly. This causes the drag losses of the first stage to increase as the mass of the scramjet accelerator is increased, from 2.49% at 95% structural mass to 2.50% at 105% structural mass. This increase in drag losses is despite the acceleration of the first stage decreasing, and is due to the first stage using its aerodynamics to manoeuvre more, at higher scramjet accelerator mass values. This increased manoeuvring indicates that as the mass of the scramjet accelerator increases, and the performance of the rocket decreases, it becomes beneficial to trade-off more of the exergy efficiency of the first stage, to benefit the performance of the scramjet accelerator.

A higher scramjet accelerator structural mass causes the scramjet accelerator to stay at relatively lower velocities over its trajectory, which results in a higher specific impulse throughout. Varying the structural mass of the scramjet accelerator does not significantly affect the altitude at the end of the pull-up manoeuvre. However, as the mass of the scramjet accelerator is varied, the velocity at scramjet accelerator-third stage separation does change significantly, by +46m/s (+17.1%) at 95% structural mass, and -50m/s (-18.6%) at 105% structural mass. In order to reach similar altitudes at the end of pull-up, the trajectory angle at the second-third stage separation increases as the structural mass is increased, by $+0.3^\circ$ (+2.8%) at 105% structural mass, and decreases as the structural mass is decreased, by -0.2° (-1.9%), at 95% structural mass. As the mass of the scramjet accelerator increases, the exergy efficiency of the third stage is decreased, varying by $-0.76\%\eta$ at 105% structural mass, and as the scramjet accelerator mass is decreased, the exergy efficiency of the third stage is increased, varying by $+0.722\%\eta$ at 95% structural mass, due to increased propulsive efficiency from being released at a higher velocity.

6.4.5 Case 7: Scramjet Accelerator Fuel Mass Sensitivity

The available fuel mass of the scramjet accelerator is varied by $\pm 10\%$, to investigate the effects of variations of the fuel tank size within the scramjet accelerator. Comparison plots are shown in Appendix F.1.5, with a summary of key trajectory parameters detailed in Table 6.8. The fuel mass causes the maximum payload to orbit to vary by **+7.3kg (+4.67%)** at 110% fuel mass, and by **-7.5kg (-4.80%)** at 90% fuel mass. In every case, the scramjet accelerator utilises the full amount of fuel available to it, so that the addition of extra fuel mass allows the scramjet accelerator to accelerate for longer.

As was observed in Case 6, the addition of extra mass to the scramjet accelerator causes the

Trajectory Condition	$m_{f,2}:$	90%	95%	100%	105%	110%	$\Delta/\Delta\%m_{F,2}$
Payload to Orbit (kg)		148.9	152.6	156.4	160.0	163.7	0.7
Payload Variation (%)		-4.75	-2.39	0.00	2.33	4.67	0.47
Total η_{exergy} (%)		1.692	1.688	1.685	1.681	1.678	-1e-05
1st Stage η_{exergy} (%)		6.937	6.908	6.875	6.845	6.806	-0.006
Separation Alt, 1→2 (km)		24.70	24.61	24.52	24.43	24.34	-0.02
Separation v, 1→2 (m/s)		1555	1544	1533	1522	1510	-2.22
Separation γ, 1→2 (deg)		11.1	11.2	11.3	11.4	11.5	0.02
2nd Stage η_{exergy} (%)		4.576	4.481	4.401	4.319	4.253	-0.016
Separation Alt, 2→3 (km)		43.67	43.79	43.81	43.81	43.59	-
Separation v, 2→3 (m/s)		2593	2616	2640	2663	2687	4.66
Separation γ, 2→3 (deg)		12.6	12.5	12.3	12.2	12.0	-0.03
2nd Stage Flight Time (s)		583.1	607.6	631.2	656.3	682.2	4.94
2nd Stage Distance Flown (km)		1077.1	1137.2	1195.6	1256.3	1319.4	12.07
3rd Stage η_{exergy} (%)		14.802	15.162	15.527	15.883	16.237	0.072
3rd Stage $t, q > 5\text{kpa}$ (s)		6.2	6.3	6.8	6.8	7.7	0.07
3rd Stage max α (deg)		10.0	10.0	10.0	10.0	10.0	-
3rd Stage Fuel Mass (kg)		2836.3	2832.6	2828.8	2825.2	2821.5	-0.74

Table 6.8: Comparison of key trajectory parameters with variation in the fuel mass of the scramjet accelerator (Case 7).

first stage separation altitude and velocity to decrease, and also for the first stage exergy efficiency to decrease. At 110% fuel mass, the first-second stage separation altitude decreases by **-0.18km (-0.7%)**, the separation velocity decreases by **-23m/s (-1.5%)** and the exergy efficiency of the first stage decreases by **-0.069% η (-1.0%)**, while at 90% fuel mass, the first-second stage separation altitude increases by **+0.18km (+0.7%)**, the separation velocity increases by **+22m/s (+1.4%)** and the exergy efficiency of the first stage increases by **+0.007% η (+0.4%)**. All cases exhibit similar trajectory shapes, with the scramjet accelerator pulling-up to similar altitudes, so that increasing the fuel mass directly increases the velocity at second-third stage separation and requires slightly less pull-up angle. The second-third stage separation velocity is increased by **+47m/s (+1.8%)** and the trajectory angle is decreased by **-0.3° (-2.4%)** at 110% fuel mass, while the velocity is decreased by **-47m/s (-1.8%)** and the trajectory angle is increased by **+0.3° (+2.4%)** at 90% fuel mass. As the increased fuel mass directly increases the velocity at the end of the scramjet accelerator's trajectory, the beneficial effects of additional fuel exhibit diminishing returns as the velocity at the end of the scramjet accelerator's trajectory increases, and Isp decreases. This diminishing specific impulse causes the exergy efficiency of the scramjet accelerator to decrease by **-0.148% η (-3.4%)** at 110% fuel mass, and to increase by **+0.175% η (+4.0%)** at 90% fuel mass. However, the addition of extra fuel mass means that there is more total energy available to the scramjet accelerator (**206.1 GJ** at 110% fuel mass, compared to **168.6 GJ** at 90% fuel mass), and so the scramjet accelerator is able to accelerate more over its trajectory. For this reason, the addition of fuel mass to the scramjet accelerator is beneficial, although

the benefits to the payload-to-orbit exhibit diminishing returns. One again, as the second-third stage release velocity increases, the exergy efficiency of the third stage increases due to increased propulsive efficiency.

6.4.6 Case 8: Third Stage Mass Sensitivity

XXX relate this to increase of third stage thrust and its associated increase in engine mass, as per examiners comment... cant really do this because this includes fuel, maybe just put a note where I increase the engine mass that it directly subtracts from payload mass

XXX I need to completely redo this, because there is no clear trend in payload...

XXX the decrease in payload with increased mass is probably due to the 10 degree limit on aoa, in addition to the way that the engine was sized

Trajectory Condition	$m_3:$	90%	95%	100%	105%	110%	$\Delta/\Delta\%m_3$
Payload to Orbit (kg)	141.9	149.5	156.4	140.5	108.0	-	
Payload Variation (%)	-9.29	-4.43	0.00	-10.13	-30.94	-	
Total η_{exergy} (%)	1.599	1.645	1.685	1.517	1.200	-	
1st Stage η_{exergy} (%)	7.008	6.941	6.875	6.800	6.731	-0.014	
Separation Alt, 1→2 (km)	24.91	24.71	24.52	24.32	24.13	-0.04	
Separation v, 1→2 (m/s)	1580	1556	1533	1509	1486	-4.72	
Separation γ, 1→2 (deg)	11.0	11.2	11.3	11.5	11.6	0.03	
2nd Stage η_{exergy} (%)	4.065	4.228	4.401	4.789	5.402	0.065	
Separation Alt, 2→3 (km)	43.70	43.64	43.81	36.58	33.15	-	
Separation v, 2→3 (m/s)	2695	2666	2640	2686	2758	-	
Separation γ, 2→3 (deg)	11.9	12.2	12.3	10.0	3.0	-	
2nd Stage Flight Time (s)	635.3	633.3	631.2	627.9	630.5	-	
2nd Stage Distance Flown (km)	1239.0	1217.1	1195.6	1167.6	1154.5	-4.37	
3rd Stage η_{exergy} (%)	15.620	15.607	15.527	13.198	9.521	-0.292	
3rd Stage $t, q > 5\text{kpa}$ (s)	7.9	7.1	6.8	28.0	152.2	-	
3rd Stage max α (deg)	10.0	10.0	10.0	10.0	10.0	-	
3rd Stage Fuel Mass (kg)	2539.4	2683.8	2828.8	2996.6	3181.1	31.92	

Table 6.9: Comparison of key trajectory parameters with variation in the mass of the third stage (Case 8).

The total mass of the third stage rocket is varied by $\pm 10\%$, to investigate the effects of changing the internal mass density of the third stage rocket on the performance of the launch system. Table 6.9 details key trajectory parameters, and Appendix F.1.6 presents comparison plots of each trajectory. The mass of the heat shield is unchanged at 124.6kg, and the structural mass is assumed to contribute to 9% of the remaining mass (so that the structural mass varies by $\pm 10\%$). The remaining mass which is varied consists of a flexible combination of fuel and payload mass, in the same manner as all other cases. This mass variation investigates the effects of the third stage internal layout on the trajectory

of the launch system, quantifying the consequences of fitting additional fuel, payload and structure within the available space.

Varying the mass of the third stage rocket by $\pm 10\%$ varies the maximum payload-to-orbit by +7.4kg (3.96%) and -10.2kg (-5.36%). The majority of the additional mass is used for fuel and structural mass, with only 2.1% of the added third stage mass utilised for payload. The payload mass percentage of the additional mass is less than the payload mass percentage of the standard third stage, without heat shield, 6.0%, indicating that as mass is added to the internals of the third stage, the payload efficiency of the third stage decreases. As the mass of the third stage increases, the altitude and trajectory angle of the first-second stage separation point decrease, as was observed previously when the mass of the scramjet accelerator is increased. The scramjet accelerator pulls-up to similar altitudes as the third stage mass is varied, however, the velocity at the second-third stage separation is decreased by -75m/s (-2.8%) at 110% third stage mass, and increased by +65m/s (+2.4%) at 90% third stage mass. Consequently, a larger trajectory angle is required during the scramjet accelerator's pull-up manoeuvre as the third stage mass is increased, increasing by $+0.9^\circ$ (+8.3%) at 110% third stage mass, and decreasing by -0.4° (-3.7%) at 90% third stage mass. As the mass of the third stage is varied by $\pm 10\%$, the exergy efficiency of the scramjet accelerator varies by $+0.340\%\eta$ (+7.2%) and $-0.414\%\eta$ (-8.8%) respectively, and the exergy efficiency of the third stage varies by $-0.986\%\eta$ (-5.3%) and $+0.927\%\eta$ (+4.9%) respectively. The increase in the exergy efficiency of the scramjet accelerator at higher third stage masses is due to the scramjet accelerator flying at lower velocities when the third stage mass is higher, resulting in higher specific impulse from the scramjet engines. The decrease in the exergy efficiency of the third stage rocket, as its mass increases, is due to a combination of the additional energy which is needed to accelerate the added structural mass, and the decreased velocity at separation, which decreases the propulsive efficiency of the third stage.

6.4.7 Case 9: Third Stage Specific Impulse Sensitivity

XXX change to 10%

The specific impulse of the third stage rocket is varied between 95-105% in order to investigate the effect of the rocket engine efficiency on the payload-to-orbit. Appendix F.1.7 presents comparison plots of the optimised trajectories, and Table 6.10 details key trajectory parameters. The specific impulse variation has a significant effect on the trajectory of the system, and the payload-to-orbit, increasing the payload by +45.9kg (+24.29%) at 105% I_{sp} , and decreasing the payload by -45.9kg (-24.22%) at 95% I_{sp} .

Though the effect of the specific impulse of the third stage on the maximum payload-to-orbit is large, the majority of the improved efficiency comes from the circularisation and Hohmann transfer manoeuvres, where increasing the specific impulse results in significantly less fuel mass usage, which directly translates to additional payload. Varying the specific impulse of the third stage only changes

Trajectory Condition	$I_{SP,3}$:	95%	97.5%	100%	102.5%	105%	$\Delta/\Delta\%I_{SP,3}$
Payload to Orbit (kg)	143.3	166.4	189.2	212.3	235.1	4.6	
Payload Variation (%)	-24.22	-12.02	0.00	12.25	24.29	2.43	
Total η_{exergy} (%)	1.281	1.488	1.693	1.901	2.107	0.00041	
1st Stage η_{exergy} (%)	6.291	6.296	6.292	6.299	6.291		-
Separation Alt, 1→2 (km)	24.12	24.13	24.12	24.13	24.12		-
Separation v, 1→2 (m/s)	1484	1485	1484	1486	1484		-
Separation γ, 1→2 (deg)	3.2	3.3	3.1	3.2	3.1		-
2nd Stage η_{exergy} (%)	4.704	4.710	4.718	4.721	4.749	0.002	
Separation Alt, 2→3 (km)	41.75	41.64	41.73	41.60	41.38		-
Separation v, 2→3 (m/s)	2684	2686	2687	2689	2694	0.48	
Separation γ, 2→3 (deg)	11.0	10.9	10.8	10.8	10.6		-
2nd Stage Distance Flown (km)	1188.2	1190.3	1190.1	1189.6	1188.3		-
3rd Stage η_{exergy} (%)	13.973	16.351	18.733	21.200	23.659	0.484	
3rd Stage $t, q > 5\text{kpa}$ (s)	11.9	14.3	14.2	13.2	13.6		-
3rd Stage max α (deg)	16.1	16.0	16.2	15.8	15.9		-
3rd Stage Fuel Mass (kg)	2871.4	2848.4	2825.6	2802.5	2779.7		-4.59

Table 6.10: Comparison of key trajectory parameters with variation in the third stage specific impulse (Case 9).

the in-atmosphere trajectory of the third stage slightly, varying the velocity of the third stage before circularisation by only +55.7m/s (+1.5%) at 105% I_{sp} and -28.1m/s (-0.7%) at 95% I_{sp} . The third stage specific impulse variation has no direct influence on the trajectory of the first stage rocket, and the first-second stage separation conditions are relatively consistent across the thrust levels simulated. As the specific impulse of the third stage is varied, the size and shape of the scramjet accelerator's trajectory and pull-up manoeuvre are only slightly affected by the specific impulse of the third stage rocket engine, with no consistent trend. However, the exergy efficiency and velocity of the scramjet accelerator increase as the third stage specific impulse is increased, by +0.031% η (+0.66%) and +7m/s (+0.26%) respectively at 105% I_{SP} , and decrease as the third stage specific impulse is decreased, by -0.014% η (-0.30%) and -3m/s (-0.11%) respectively at 95% I_{SP} . In addition, the energy losses due to propulsive inefficiency of the third stage are decreased as the specific impulse is increased, to 44.24% at 105% I_{SP} , compared to 55.17% at 95% I_{SP} , due to the more rapid acceleration of the third stage. This trend indicates that as the specific impulse, and propulsion efficiency, of the third stage increase, it is beneficial to fly a trajectory with a slightly smaller pull-up manoeuvre ('smaller' indicating a lower combined altitude and trajectory angle).

6.4.8 Case 10: Third Stage Drag Sensitivity

I should potentially change lift instead of drag here, or change to 10% (i think i should keep it as drag, the small effect of drag is pretty useful to know..)

Trajectory Condition	$C_{d,3}$:	90%	95%	100%	105%	110%	$\Delta/\Delta\%C_{d,3}$
Payload to Orbit (kg)	156.5	156.4	156.3	156.1	156.0	0	
Payload Variation (%)	0.15	0.04	0.00	-0.13	-0.19	-0.01	
Total η_{exergy} (%)	1.686	1.685	1.684	1.683	1.682	0	
1st Stage η_{exergy} (%)	6.870	6.875	6.873	6.872	6.873	-	
Separation Alt, 1→2 (km)	24.52	24.52	24.52	24.52	24.52	-	
Separation v, 1→2 (m/s)	1532	1533	1532	1532	1532	-	
Separation γ, 1→2 (deg)	11.3	11.3	11.4	11.3	11.3	-	
2nd Stage η_{exergy} (%)	4.404	4.398	4.398	4.393	4.398	-	
Separation Alt, 2→3 (km)	43.38	43.48	43.60	43.86	43.73	-	
Separation v, 2→3 (m/s)	2642	2641	2640	2638	2640	-	
Separation γ, 2→3 (deg)	12.3	12.3	12.3	12.3	12.3	-	
2nd Stage Flight Time (s)	631.1	632.2	634.4	632.6	632.4	-	
2nd Stage Distance Flown (km)	1194.2	1196.8	1201.3	1198.2	1198.0	-	
3rd Stage η_{exergy} (%)	15.542	15.525	15.519	15.499	15.488	-0.001	
3rd Stage $t, q > 5\text{kpa}$ (s)	8.2	7.6	7.3	7.0	6.8	-0.03	
3rd Stage max α (deg)	10.0	10.0	10.0	10.0	10.0	-	
3rd Stage Fuel Mass (kg)	2828.7	2828.8	2828.9	2829.1	2829.2	0.01	

Table 6.11: Comparison of key trajectory parameters with variation in the drag of the third stage (Case 10).

The coefficient of drag of the third stage rocket is varied by $\pm 20\%$ to investigate the effects of the third stage design and sizing on the performance of the launch system. Table 6.11 details the key trajectory parameters of each optimised trajectory, and Appendix F.1.8 shows trajectory comparison plots. The third stage drag is found to have only a very small effect on the performance of the launch system, varying the payload to orbit by only +0.9kg (+0.50%) at 120% C_d and -0.8kg (-0.40%) at 80% C_d . This indicates that the aerodynamic properties of the third stage rocket do not contribute significantly to the performance of the system.

The first stage trajectory is not affected by variations in the drag of the third stage. The scramjet accelerator exhibits a slightly higher pull-up as the drag of the third stage is increased by 20%, increasing altitude by +0.51km (+1.2%), and trajectory angle at separation by +0.4° (+3.7%) trajectory angle, while decreasing the separation velocity by -10.0m/s (-0.37%). Conversely, decreasing the drag of the third stage by 20% decreases the altitude at second-third stage separation by -1.0km (-2.5%), decreases the trajectory angle at separation by -0.6° (-5.6%), and increases the velocity by +17m/s (+0.6%). Increasing the drag of the third stage by 20% causes a decrease in the exergy efficiency of the scramjet accelerator of -0.036% η (-0.76%), and a decrease in the efficiency of the third stage of -0.068% η (-0.36%), while decreasing the drag of the third stage by 20% causes an increase in the exergy efficiency of the scramjet accelerator of +0.060% η (+1.27%), and an increase in the third stage efficiency of +0.082% η (+0.44%). As the drag of the third stage increases, the scramjet accelerator pulls-up to a higher altitude so that the third stage spends less time in a high dynamic pressure

environment, where the increased drag has a significant effect, mitigating the energy loss due to the increased drag. The higher pull-up of the scramjet accelerator with the third stage drag increased by 20%, decreases the time that the third stage spends above 5kPa dynamic pressure by -2.4s (-16.9%), resulting in drag losses of 0.37% (0.19 GJ), while the lower pull-up of the scramjet accelerator when the third stage drag is decreased by 20% increases the time spent at greater than 5kPa dynamic pressure by +2.5s (+17.6%), resulting in drag losses of 0.31% (0.22 GJ). This indicates that as the drag of the third stage is increased, the optimal pull-up manoeuvre is increased so as to more than compensate for the additional energy losses, trading off the efficiency of the scramjet accelerator to do so.

6.5 Comparison of Design Parameters

Payload Variation (kg) per % Parameter Variation

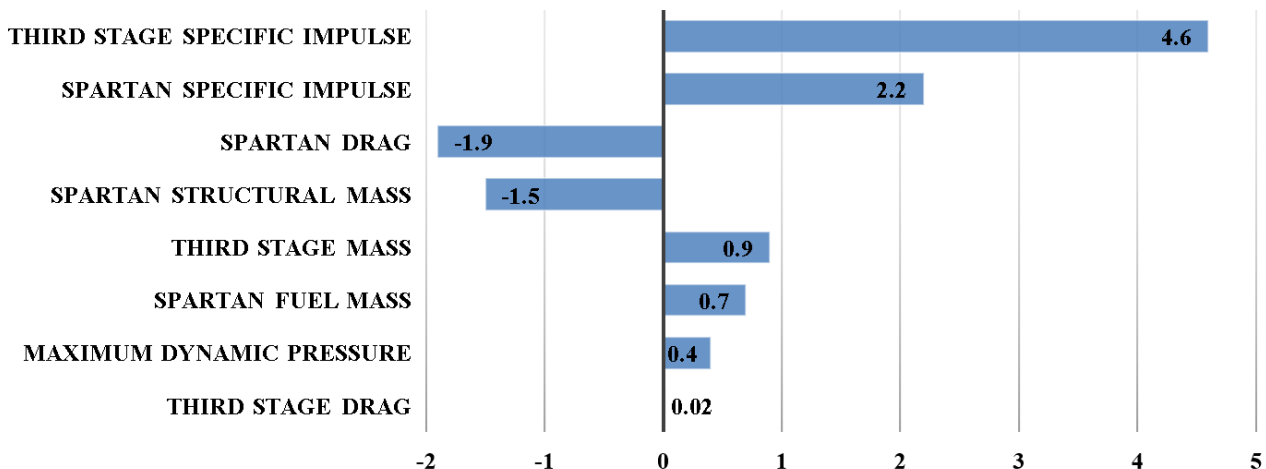


Figure 6.11: The sensitivity of the key design parameters of the launch system.

XXX I should be clear about why I am doing this - to inform future design decisions

The preceding sections calculate the relative sensitivity of the launch system performance to a variety of design parameters. Comparing and contrasting the sensitivity of the launch system to each design parameter allows for the relative impact of each design parameter to be assessed. Figure 6.11 shows the change in payload mass per percentage point variation of each design parameter. This change per percentage variation indicates the magnitude by which the payload-to-orbit varies as each design parameter is varied by $\pm 1\%$ (signs are shown for positive parameter variations, with negative signs indicating a decrease in performance), and is measure of the sensitivity of the launch system to variations in each design parameter. However, a 1% variation has a significantly different implication in the context of each individual design parameter, as certain parameters can be adjusted more easily.

As such, the change per percentage is most useful when directly assessing each design parameter, and taking into account the associated effects on other, coupled design parameters.

The influence of the maximum dynamic pressure of the scramjet accelerator on the performance of the launch system is low, particularly when compared to the influence of the closely linked scramjet accelerator mass parameter. These parameters are coupled directly, because the scramjet accelerator's thermal protective properties and structural strength define the maximum dynamic pressure. This means that the low variance in performance with maximum dynamic pressure may be offset by the variation in the mass of the scramjet accelerator, ie. a lower maximum dynamic pressure requires less structural and thermal protection system mass. The relative sensitivities of the launch system to dynamic pressure ($0.4 \frac{\Delta kg}{\Delta \% q_{max}}$), and scramjet accelerator mass ($1.5 \frac{\Delta kg}{\Delta \% m_{scramjetaccelerator}}$), and their absolute magnitudes (50kPa and 4957kg respectively), allow the sensitivities of these coupled effects to be directly quantified. Comparing these sensitivities implies that so long as decreasing the dynamic pressure by 1kPa allows for a reduction in structural and TPS mass of greater than -26.5kg, then operating the scramjet accelerator at lower dynamic pressures may be preferable.

The influence of the fuel mass of the scramjet accelerator on the performance of the launch system is also low, per percentage variation. However, the fuel mass is only a fraction of the total mass of the scramjet accelerator. This means that relatively small mass changes, by kg, in fuel mass are still significant. When the fuel mass of the scramjet accelerator is increased, the structural mass of the tanks will require a corresponding increase. Comparing the impact of the fuel mass and structural mass of the scramjet accelerator along with their relative magnitudes (1562kg of fuel mass and 4957kg of structural mass), the absolute impact of each is $0.044 \frac{\Delta kg_{payload}}{\Delta kg}$ and $-0.030 \frac{\Delta kg_{payload}}{\Delta kg}$ respectively. This means that so long as fuel mass can be added to the scramjet accelerator with less than 1.47kg of structural mass incorporated for each 1kg of fuel mass, adding additional fuel mass will be beneficial. However, the fuel mass is constrained considerably by the available internal space within the scramjet accelerator, which is likely to be the main limiting factor. If the size of the fuselage of the scramjet accelerator is increased, the aerodynamic performance of the scramjet accelerator will be altered proportionally. The sensitivity of the launch system to the drag of the scramjet accelerator, $-1.9 \frac{\Delta kg}{\Delta \% C_d}$, means that so long as 1kg of fuel can be added to the scramjet accelerator with a drag increase of less than 0.024%, then the maximum payload-to-orbit will increase.

The payload-to-orbit is sensitive to the specific impulse of the C-REST engines, varying at a rate of $2.2 \frac{\Delta kg}{\Delta \% I_{SP}}$. Increasing the specific impulse of the scramjet engines is likely to require the addition of extra systems within the scramjet engines, adding weight to the scramjet accelerator, or a change in the shape of the scramjet engines, adding drag to the scramjet accelerator. The slightly lower sensitivity of the launch system to the scramjet accelerator mass ($1.5 \frac{\Delta kg}{\Delta \% m_{scramjetaccelerator}}$) compared to the sensitivity to the specific impulse, means that so long as increasing the I_{SP} of the scramjet accelerator by 1% causes a corresponding increase in the structural mass of the scramjet accelerator of less than 1.47% (72.9kg), the performance of the launch system will improve. The sensitivity of the launch system

to variation of the scramjet accelerator drag ($1.9 \frac{\Delta kg}{\Delta \% C_d, \text{scramjetaccelerator}}$) is similar in magnitude to the sensitivity to specific impulse. If a variation in the shape of the scramjet engines or forebody increases the I_{SP} of the scramjet accelerator by 1%, while increasing the drag of the scramjet accelerator by less than 1.16%, then the efficiency of the launch system will be improved.

The specific impulse of the third stage rocket has the highest percentage payload variation effect on the launch system of any of the design parameters tested, at $4.6 \frac{\Delta kg}{\Delta \% I_{SP,3}}$. Increasing the specific impulse of the third stage is likely to involve modifications to the engine, increasing the pressure within the fuel tanks, or adding a turbopump to assist fuel flow, all of which involve increasing the mass of the third stage rocket. This additional mass is subtracted directly from the available payload mass of the system. This implies that so long as the specific impulse of the third stage can be increased by 1% for less than 4.6kg additional engine and system mass, that the performance of the launch system will improve. However, increasing the specific impulse of the rocket engine is likely to add a large amount of cost to the third stage rocket, which is particularly detrimental, as the third stage is not reusable. This additional cost factor is likely to be the limiting factor on the specific impulse of the third stage rocket.

The aerodynamic performance of the third stage is shown to have only a very small impact on the performance of the launch system, with a drag sensitivity of only $0.02 \frac{\Delta kg}{\Delta \% C_{d,3}}$. This means that for any third stage shape variations, the aerodynamic sensitivity is small. However, variations in the size of the third stage rocket are likely to require modifications in the size of the scramjet accelerator's fuselage. The sensitivity of the scramjet accelerator to drag, $1.9 \frac{\Delta kg}{\Delta \% C_d, \text{scramjetaccelerator}}$, means that if the third stage can be enlarged so that the third stage mass increases by 1kg, with a corresponding enlargement of the fuselage of the scramjet accelerator so that the increase in scramjet accelerator drag is less than 0.014%, the maximum payload-to-orbit will increase.

6.6 Summary

In this chapter, LODESTAR was used to design the trajectory of the SPARTAN rocket-scramjet-rocket multi-stage launch system. A trajectory was simulated in which the scramjet accelerator stage flies at a constant dynamic pressure, producing 98.3kg of payload-to-orbit. This trajectory served to verify LODESTAR and the simulation of the launch system, as well as providing a baseline trajectory for comparison. A trajectory optimised for maximum payload-to-orbit was then calculated, which increased the payload mass to sun synchronous orbit to 156.4kg (an increase of 19.5%) compared to the constant dynamic pressure trajectory. The optimal flight path indicates that the optimal scramjet flight path for a system transitioning between separate airbreathing and rocket-powered stages involves the scramjet accelerator flying at less than its maximum dynamic pressure at three separate points along the trajectory. Initially, the first-second stage separation occurs at a higher trajectory angle than in the constant dynamic pressure trajectory, causing the scramjet accelerator to fly at lower dynamic

pressure, and trading off the exergy efficiency of the scramjet accelerator for an increase in the exergy efficiency and fuel mass of the first stage, for an overall performance gain. The optimal flight path then exhibits an altitude raising manoeuvre in the middle of the trajectory, which improves the exergy efficiency of the scramjet accelerator by a very minor $+0.003\%\eta$ ($+0.03\%$). Finally, the scramjet accelerator executes a pull-up manoeuvre before the second-third stage separation. This optimal pull-up manoeuvre trades off velocity (a decrease of 116.2m/s) for altitude (an increase of 9.48km) and improved flight path angle (an increase of 10.45°). This pull-up manoeuvre, along with the higher first-second stage separation, decreases the exergy efficiency of the scramjet accelerator by $-0.508\%\eta$ (-9.7%) when compared to the constant dynamic pressure case. However, these conditions improve the exergy efficiency of the third stage rocket significantly, by $+3.286\%\eta$, an increase of $+21.3\%$ over the third stage released from a constant dynamic pressure trajectory. The pull up manoeuvre in the payload-to-orbit optimised trajectory also reduces the maximum dynamic pressure experienced by the third stage to 10.8kPa, a decrease of 43.4kPa compared to a trajectory with minimum pull-up, which allows future design benefits due to heat shield and structural mass reduction.

A sensitivity study was conducted, to determine the relative effects of key vehicle design parameters on the optimised trajectory. The maximum dynamic pressure, specific impulse, aerodynamic performance, structural mass, and fuel mass of the scramjet accelerator were modified, along with the specific impulse, mass and aerodynamic performance of the third stage, and the magnitudes of their payload-to-orbit sensitivities compared. It was observed that the efficiency trade-off between the first stage and the scramjet accelerator depends primarily on the pitching ability of the first stage, so that when the first stage is capable of pitching more rapidly, the trade-off shifts in favour of the scramjet accelerator. The specific impulse of the third stage rocket was found to produce the most overall effect on the payload-to-orbit, increasing the payload by $+45.9\text{kg}$ ($+24.26\%$) at $105\% I_{sp}$, and decreasing the payload by -45.9kg (-24.26%) at $95\% I_{sp}$. However, increasing the specific impulse of the third stage rocket is likely to come at a high cost premium, which may be undesirable as the third stage is non-reusable. The most easily variable design factor, the maximum dynamic pressure of the scramjet accelerator, was found to have a relatively small effect on the payload-to-orbit performance of the launch system, varying the payload-to-orbit by only $+24.2\text{kg}$ ($+12.8\%$) at 60kPa and -20.5kg (-10.8%) at 40kPa. The negative effect on the payload-to-orbit when flying at 40kPa is likely to be offset by the lower TPS and structural mass required by lower dynamic pressure flight. It was determined that if the TPS and structural mass decrease is greater than -26.5kg for every 1kPa reduction in the maximum dynamic pressure, then flying at lower dynamic pressure is potentially preferable.

CHAPTER 7

OPTIMISED TRAJECTORY INCLUDING FLY-BACK

XXXI should be clear that the method of calculating the payload mass to orbit does not affect the optimised trajectory XXX Its interesting if the SPARTAN is flying close to its min q at first hump

XXX sort out SPARTAN nomenclature

This chapter presents the maximum payload-to-orbit trajectory of the rocket-scramjet-rocket launch system, with the fly-back of the scramjet accelerator included within the optimal trajectory calculation performed by LODESTAR. Flying back the scramjet accelerator for landing at the initial launch site is one of the primary enabling factors in the cost efficient operation of the launch system. If the scramjet accelerator is launched onto a trajectory from which it is not able to fly-back, it must perform a downrange landing, likely at an Indonesian airfield when launched northerly from north Australia. This would necessitate transporting the scramjet accelerator back to Australia, a costly and time consuming process, and would require for international landing facilities to be available. Flying back the scramjet accelerator during the launch process removes the need for costly transportation from a downrange launch site, and allows for rapid refurbishment and re-use. In addition, if a launch site is used from which there is no downrange landing site, the scramjet accelerator must necessarily fly-back to the initial launch site.

The fly-back of the scramjet accelerator requires turning-around the scramjet accelerator after third stage separation, covering the necessary ground distance for return, and decelerating to reduce the speed of the scramjet accelerator to landing approach velocity, while maintaining a suitable descent angle to allow for a controlled approach. The return of the scramjet accelerator to the initial launch site is included in the optimisation process to assess whether it is possible for the fly-back of the scramjet accelerator to be achieved as a part of the launch process, and to maximise the overall payload-to-orbit efficiency of the launch system. This is compared to the optimised, maximum payload-to-orbit trajectory without fly-back (detailed in Chapter 6) to assess the detrimental effects of the fly-back on the performance of the launch system. A sensitivity analysis is conducted, in a similar

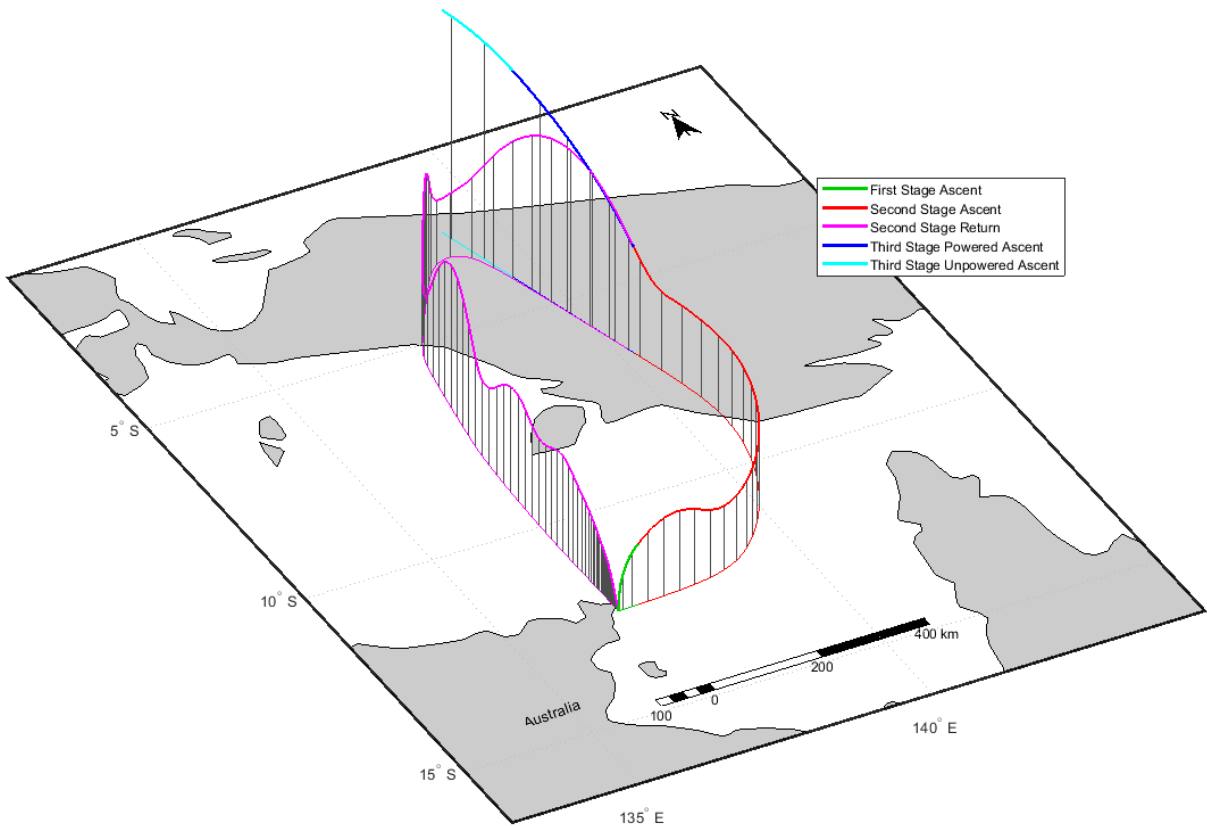


Figure 7.1: Maximum payload-to-orbit trajectory path with the inclusion of scramjet accelerator fly-back (Case 11). Initial heading angle of 3.3° .

fashion to Chapter 6. This sensitivity analysis allows the influence of the fly-back of the scramjet accelerator on the design sensitivities of the launch system to be analysed.

7.1 Case 11: SPARTAN Trajectory with Scramjet Accelerator Return

LODESTAR is used to optimise the trajectory of the rocket-scramjet-rocket launch system, including the return of the scramjet accelerator to its initial launch site. The optimised trajectory is shown in Figure 7.1. The rocket-scramjet-rocket launch system is shown to be able to successfully launch a small satellite to sun synchronous orbit, while flying-back the scramjet accelerator to the initial launch site location, and approaching the landing site at appropriately low altitude and velocity to allow for landing. The optimised trajectory attains a payload mass to SSO of 132.1kg, a **-24.3kg (-15.5%)** reduction in payload mass compared to the optimised ascent-only trajectory, detailed in Chapter 6. The benefits of flying back the scramjet accelerator to its initial launch site, compared to the alternative

Trajectory Condition	Value
Payload to Orbit (kg)	132.1
Total η_{exergy} (%)	1.578
1st Stage η_{exergy} (%)	6.923
Separation Alt, 1→2 (km)	24.57
Separation v, 1→2 (m/s)	1539
Separation γ, 1→2 (deg)	11.1
2nd Stage η_{exergy} (%)	3.758
Separation Alt, 2→3 (km)	42.87
Separation v, 2→3 (m/s)	2506
Separation γ, 2→3 (deg)	12.7
2nd Stage Distance Flown (km)	869.6
2nd Stage Return Fuel (kg)	257.8
2nd Stage Return Distance (km)	1522.3
3rd Stage η_{exergy} (%)	13.141
3rd Stage $t, q > 5\text{kpa}$ (s)	7.7
3rd Stage max α (deg)	10.0
3rd Stage Fuel Mass (kg)	2853.1

Table 7.1: Selected trajectory conditions for a maximum payload-to-orbit trajectory including scramjet accelerator fly-back (Case 11).

of transporting the scramjet accelerator back to the launch site from a remote landing, are likely to far outweigh this associated reduction in payload.

7.2 Ascent Trajectory

When the fly-back of the scramjet accelerator is included in the trajectory optimisation, the shape of the ascent trajectory of the launch system is altered significantly, compared to the ascent-only trajectory, detailed in Chapter 6. The first stage initially pitches towards the east, beginning at a heading angle of -12.45° . After pitchover, the first stage gradually reduces the angle of attack to a minimum of -0.47° at 30.9s flight time, in order to make small adjustments to the pitch profile while the velocity is low. After this, the first stage angle of attack returns to 0° at 42.9s flight time, and is maintained for 16.4s. **XXX update all this first stage stuff** The angle of attack is then reduced, to a minimum of -3.58° in order to adjust the altitude and trajectory angle, before increasing back to 0° at first-second stage separation. The scramjet accelerator is released in an easterly direction, at a heading angle of 2.16° , an altitude of 24.57km, and a trajectory angle of 11.1° . The altitude of first-second stage separation is 3.02km (+12.5%) higher than the first-second stage separation point with no fly-back, with a trajectory angle at separation which is $+2.5^\circ$ (+80.6%) higher. This higher release point requires less aerodynamic manoeuvring of the first stage, and enables the first stage to be efficiently launched with a higher fuel mass of 17943kg, an increase of +758kg (+4.4%) compared to

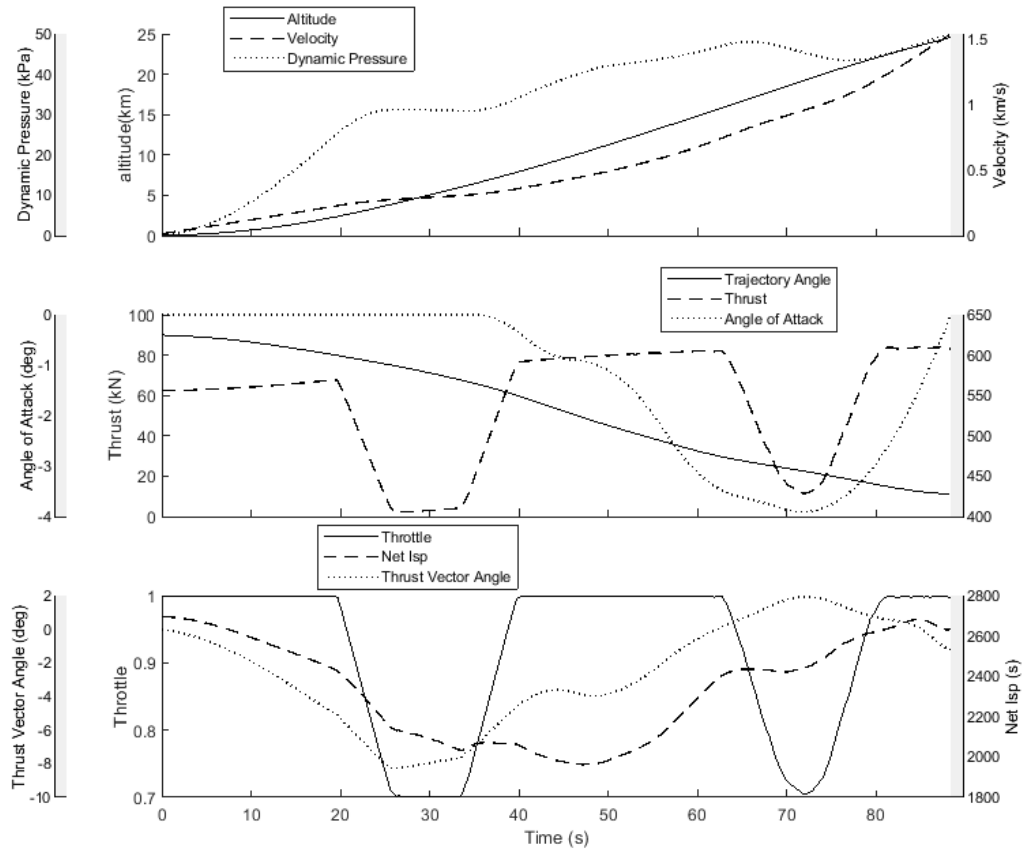


Figure 7.2: The first stage of the optimised maximum payload-to-orbit trajectory with scramjet accelerator fly-back (Case 11).

the trajectory without fly-back. This additional fuel increases the total acceleration of the first stage, **XXX change all this too** in turn increasing the exergy efficiency of the first stage rocket by $+0.308\% \eta$ (+4.9%) due to a higher propulsion efficiency, and allowing the first stage to achieve a higher velocity at separation (an increase of +64m/s, +4.3%).

XXX change the first part of this The higher altitude, larger trajectory angle, and increased velocity at the first-second stage separation point causes an altitude raising manoeuvre at the beginning of the scramjet accelerator's acceleration, which is significantly higher than the altitude raising manoeuvre with no fly-back. This altitude raising manoeuvre takes the scramjet accelerator to an altitude of 32.3km at 47.1s, and decreases the dynamic pressure of the scramjet accelerator to 14.9kPa, allowing time for the bank angle of the scramjet accelerator to be increased. After the first-second stage separation, the bank angle is increased, at the maximum change rate, to 52.2°, which aids the scramjet accelerator in decreasing its altitude. As the altitude of the scramjet accelerator begins to reduce, the bank angle **reduces** and the angle of attack is raised to 3.9° to increase lift, slowing the descent of the scramjet accelerator. The bank angle then begins to increase once more, and as the scramjet acceler-

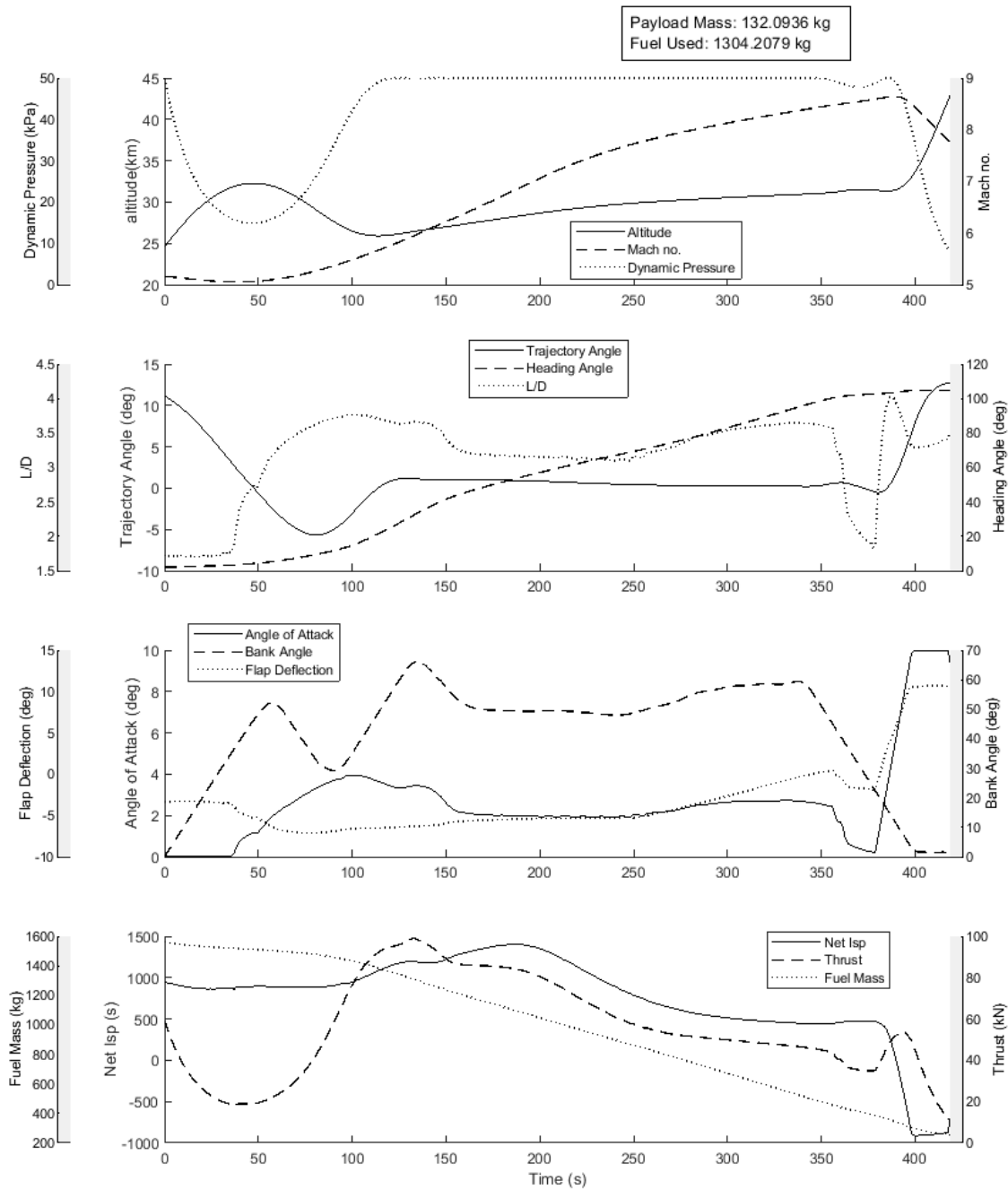


Figure 7.3: The acceleration of the scramjet accelerator flying an optimised maximum payload-to-orbit trajectory with scramjet accelerator fly-back (Case 11).

ator reaches close to its maximum dynamic pressure at 122.5s, the bank angle reaches its maximum of 66.2° .

After this point, the bank angle of the scramjet accelerator is maintained between 48.0° and 52.5° ,

exhibiting higher bank angles towards the latter part of the ascent. At the end of the scramjet accelerator's ascent, the bank angle is reduced, so that the third stage is released at 0° bank angle. This 0° bank angle is defined as a constraint on the end of the trajectory, to ensure that the third stage rocket is released in the vertical plane, and is able to manoeuvre to orbit.

The angle of attack of the scramjet accelerator is significantly higher over the course of the maximum payload-to-orbit trajectory with fly-back inclusion, compared to maximum payload-to-orbit trajectory with no fly-back, detailed in Section 6.2. These significantly higher angles of attack are a result of the high bank angle of the scramjet accelerator throughout its trajectory, which cause the lift of the scramjet accelerator to be partially used for changing the heading of the scramjet accelerator, rather than providing vertical force. The higher angles of attack result in the optimal trajectory of the scramjet accelerator following a close to maximum dynamic pressure path for most of the duration of its trajectory, without the altitude raising manoeuvre observed in Section 6.2. The increase in angle of attack means that the scramjet accelerator no longer flies within the homogeneous region of the specific impulse of the C-REST engines. instead the flight conditions are close to a region where an increase in angle of attack causes a sharp decrease in specific impulse, illustrated in Figure 7.4. This indicates that the angle of attack, and consequently the allowable bank angle, of the scramjet accelerator is being limited by the performance of the C-REST engines. The scramjet accelerator stays close to its maximum dynamic pressure until a pull-up is performed at **386.6s** flight time.

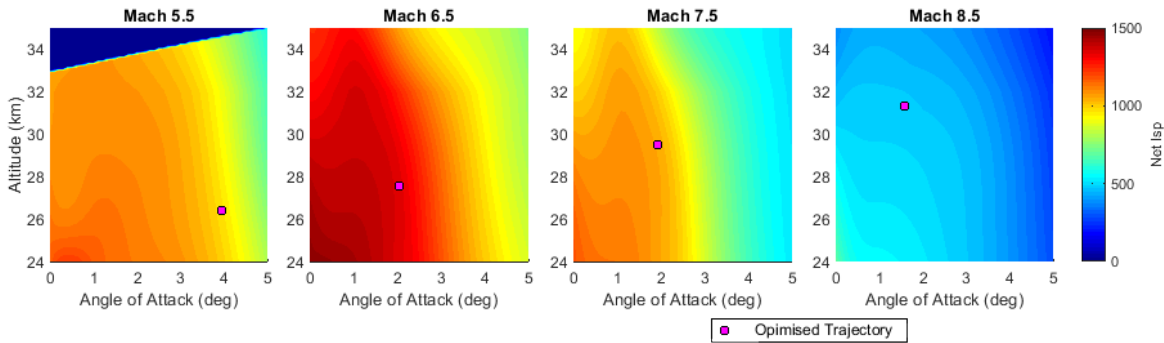


Figure 7.4: Net I_{SP} contours for the scramjet accelerator at Mach numbers between 5.5 and 8.5, showing the optimised trajectory path (Case 11).

The higher angles of attack flown by the scramjet accelerator also have the consequence of decreasing the net specific impulse of the scramjet accelerator during its acceleration, with the maximum specific impulse being decreased by **-3.4%**. The overall exergy efficiency of the scramjet accelerator is decreased, to $3.758\%\eta$, a decrease of **-0.643%\eta** (**-14.6%**) compared to the maximum payload-to-orbit trajectory with no fly-back. This exergy efficiency decrease is due partially to the decrease in the specific impulse of the scramjet engines, but more significantly is attributed to the fuel necessary for the return flight resulting in less fuel being available for the ascent of the scramjet accelerator, and thus less 'useful' work being attained from the total fuel mass. A total fuel mass of **1304.2kg** is

used during the scramjet accelerator's acceleration, out of a total of 1562kg of available fuel. This reduction in fuel mass used, along with the reduction in net specific impulse due to the higher angle of attack values, reduces the velocity at second-third stage separation by **-134.0m/s (-5.1%)** compared to the maximum payload-to-orbit case with no scramjet accelerator fly-back. The scramjet accelerator pulls up to 42.87km altitude and 12.7° trajectory angle before the second-third stage separation, a difference of only **-0.94km (-2.1%)** and **+0.4° (+3.3%)** compared to the maximum payload-to-orbit trajectory without fly-back, indicating that the inclusion of fly-back does not have a large effect on the magnitude of the pull-up manoeuvre.

The exergy efficiency of the third stage is decreased by **-2.386% η (-15.4%)** when compared to the maximum payload-to-orbit trajectory with no scramjet accelerator fly-back. This lowered efficiency is primarily due to the lower velocity of the third stage release, which increases the losses of the third stage due to propulsive inefficiencies.

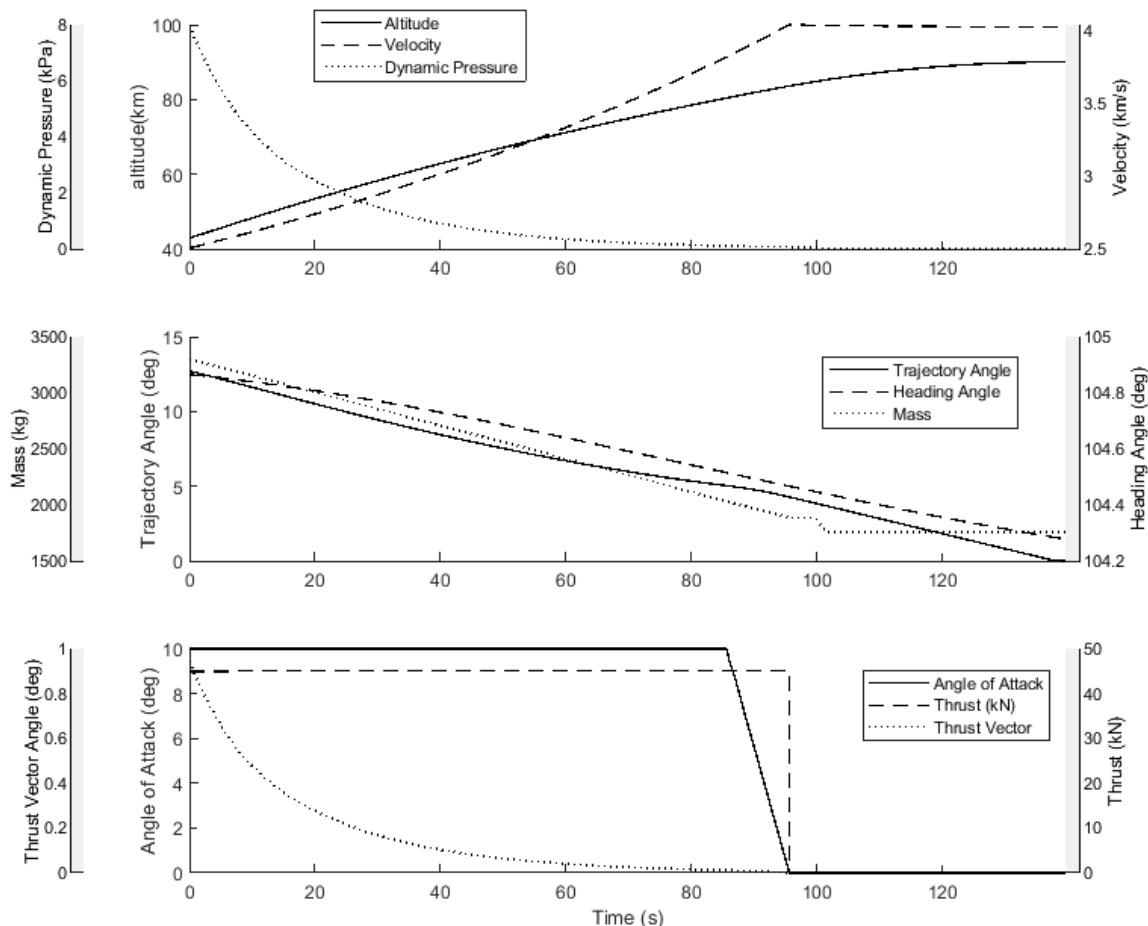


Figure 7.5: The third stage trajectory of an optimised maximum payload-to-orbit trajectory with scramjet accelerator fly-back (Case 11).

7.3 Fly-Back Trajectory

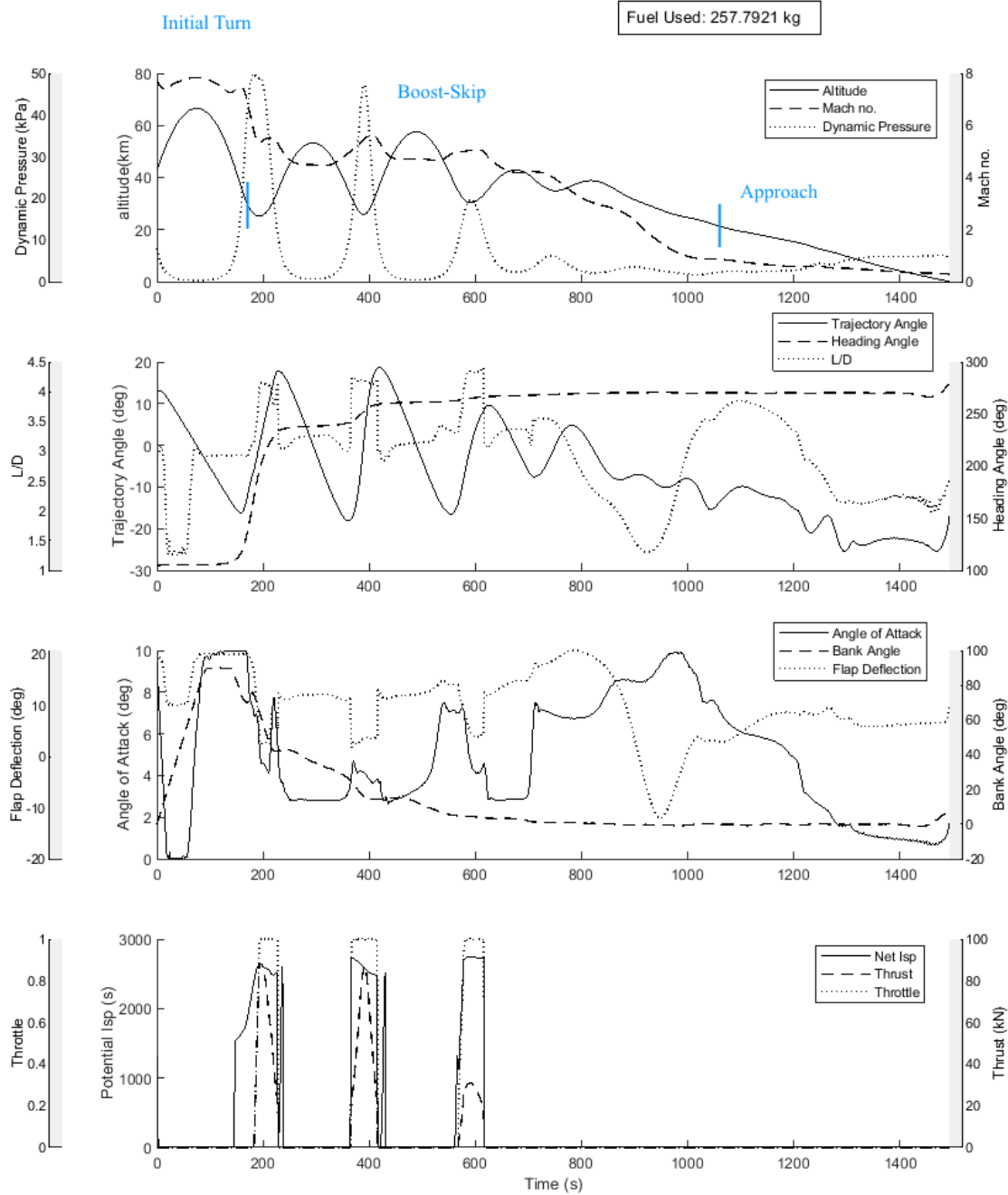


Figure 7.6: The fly-back trajectory of the scramjet accelerator flying an optimised maximum payload-to-orbit trajectory (Case 11).

The optimised fly-back trajectory is shown in Figure 7.6. The scramjet accelerator is shown to

be capable of fly-back, using 257.8kg of fuel, 16.5% of the total fuel. Throughout its fly-back the scramjet accelerator performs distinct skipping manoeuvres, and ignites the scramjet engines a total of three times. These skips are consistent with previous research which has shown that a periodic skipping trajectory increases the downrange distance achievable by hypersonic vehicles both during powered and unpowered flight[56, 86–89, 91, 92], and serve to reduce the fuel necessary for the return flight.

It is observed that the optimised trajectory exhibits characteristics which can be separated into three distinct segments; 1. initial turn, 2. boost-skip, and 3. approach, as indicated in Figure 7.6.

Initial Turn

The scramjet accelerator separates from the third stage rocket at a bank angle of 0°, and then increases its bank angle at close to the maximum change rate until 94.5s return flight time, at which point the maximum of 90.0° bank angle is reached. This high bank angle serves to rapidly change the heading of the scramjet accelerator, in order to minimise the down-range distance flown, and reduce the fuel necessary for fly-back. The angle of attack is kept low during this time, in order to minimise the size of the initial skip. As the scramjet accelerator reaches the zenith of its initial skip, at 73.6s flight time and 66.5km altitude, the angle of attack is rapidly increased, up to the maximum of 10.0°. This increase in angle of attack generates additional lift to slow the descent of the scramjet accelerator into the trough of the first skip, ensuring that the dynamic pressure limit is not exceeded.

Boost-Skip

At 194.1s flight time, the scramjet engines are ignited. The C-REST engines are powered-on in the trough between the first and second skips, at a point of high potential specific impulse, and initially burn for 33.8s. During the initial burn, the L/D of the scramjet accelerator increases significantly, due to the scramjet engine flow paths of the scramjet accelerator generating thrust, rather than drag. This increase in L/D raises the altitude of the scramjet accelerator and, along with heavy banking, changes the heading of the scramjet accelerator significantly. The burn is limited by the lower inlet dynamic pressure limit of the C-REST engines, of 20kPa, and terminates at 227.9s flight time. After the initial burn ends, the angle of attack of the scramjet accelerator is decreased to 3.2°, and the scramjet accelerator executes its second skip. Once the scramjet accelerator is descending again, and as soon as the dynamic pressure is high enough for C-REST engine operation at 369.0s return flight time, the scramjet engines are once again ignited. During the second burn, the angle of attack of the scramjet accelerator is increased, to modify the temperature and Mach number at the inlet of the C-REST engines so that the maximum specific impulse is obtained from the C-REST engines during the burn. The angle of attack varies between 4.7° to 3.7° during the second burn, and the L/D is once again raised significantly, initiating the third skip. This skip raises the altitude of the scramjet

accelerator to 53.3km, before it decreases once again. The third and last burn is initiated at 581.7s and lasts until 615.9s, when the remaining fuel has been depleted. Before the third burn, the angle of attack is first increased up to 7.5°, and then decreased at the beginning of the burn, to a minimum of 4.1° during the burn. The angle of attack values observed are similar to those observed during the second burn, indicating that these angle of attack values obtain a high specific impulse from the C-REST engines, this can be observed in Figure D.6, which shows the specific impulse profile of the return flight during the boost-skip phase.

After the third burn phase, the angle of attack is initially controlled so that the skipping trajectory of the scramjet accelerator is damped. Immediately after the third burn phase, the angle of attack is reduced, to 2.84°. This reduction coincides with the ascent portion of the fourth skip, reducing the lift, and the amount of altitude gained. As the zenith of the forth skip is reached, the angle of attack is increased to 7.5°, increasing the lift, and once again slowing the descent. This high angle of attack is increased until 984.9s, in stages corresponding with the descent of the last two small skips. It is notable that the angle of attack is controlled in this way during the unpowered portion of the trajectory, as it indicates that the skips are being damped. This implies that some degree of skipping is desirable after the final scramjet burn, but that the angle of attack is being controlled to produce optimally sized skips.

Approach

After the final small skip, at 1046.0s flight time, the angle of attack is adjusted, so that a gradual, controlled descent is initiated. After the skip phase, as the vehicle is approaching Mach 1, the angle of attack is reduced gradually to bring the scramjet accelerator down below 1km altitude, in a controlled manner. At 1455.0s, the bank angle is increased, in order to perform a final adjustment of the heading angle, to bring the scramjet accelerator to the desired end location. The scramjet accelerator drops below 1km altitude at -17.0° trajectory angle and 95.2m/s velocity (Mach 0.28). It is assumed that the scramjet accelerator is able to perform a landing manoeuvre after this point.

7.4 Energy Usage Analysis

An energy usage analysis is conducted for a maximum payload-to-orbit trajectory, including the fly-back of the scramjet accelerator. This is compared to the energy usage breakdown of the optimised trajectory without the fly-back of the scramjet accelerator in Table 7.2. Similarly to Section 6.3, the energy used to accelerate the payload is shown, along with the energy imparted to the successive stages; the energy used overcoming drag; the energy used imparting energy to the structural mass of each stage, which is separated; and the energy lost due to propulsion inefficiency.

The fly-back of the scramjet accelerator reduces the fuel, and thus the fuel exergy, available to

Trajectory Condition	No Fly-Back	With Fly-Back
First Stage Fuel Exergy	201.91 GJ	201.91 GJ
KE + PE of Payload	0.109% (0.22 GJ)	0.093% (0.19 GJ)
KE + PE of 2 nd & 3 rd Stage	6.765% (13.66 GJ)	6.829% (13.79 GJ)
Overcoming Drag	2.49% (5.03 GJ)	2.41% (4.87 GJ)
KE + PE of 1 st Stage Structural Mass	1.01% (2.04 GJ)	1.02% (2.06 GJ)
Propulsion Inefficiency	89.62% (180.95 GJ)	89.64% (181.00 GJ)
Scramjet Accelerator Fuel Exergy	187.38 GJ	156.45 GJ
KE + PE of Payload	0.209% (0.39 GJ)	0.180% (0.28J)
KE + PE of 3 rd Stage	4.192% (7.85 GJ)	4.321% (6.76 GJ)
Overcoming Drag	20.42% (38.26 GJ)	21.45% (33.56 GJ)
KE + PE of Scramjet Accelerator Structural Mass	6.61% (12.39 GJ)	6.76% (10.58 GJ)
Propulsion Inefficiency	68.57% (128.49 GJ)	67.29% (105.27 GJ)
Return Fuel Exergy	-	30.92 GJ
KE + PE of Scramjet Accelerator Structural Mass	-	-56.94% (-17.61 GJ)
Overcoming Drag	-	95.30% (29.47 GJ)
Propulsion Inefficiency	-	61.64% (19.06 GJ)
Third Stage Fuel Exergy	34.33 GJ	34.62 GJ
KE + PE of Payload	15.527% (5.33 GJ)	13.141% (4.55 GJ)
Overcoming Drag	0.33% (0.11 GJ)	0.34% (0.12 GJ)
KE + PE of 3 rd Stage Structural Mass	30.85% (10.59 GJ)	30.91% (10.70 GJ)
KE + PE of Heat Shield	3.56% (1.22 GJ)	4.07% (1.41 GJ)
Propulsion Inefficiency	49.73% (17.07 GJ)	51.55% (17.85 GJ)

Table 7.2: An energy usage breakdown of the ascent trajectories, both with, and without, scramjet accelerator fly-back (Cases 11 & 2). Blue indicates a 'productive' energy usage, whereas red indicates energy 'wastage'. Negative energy indicates energy being supplied.

the scramjet accelerator during ascent. This lower exergy, along with the altered manoeuvrability needs of the scramjet accelerator when the fly-back is included, causes the altitude and trajectory angle at the first-second stage separation to be raised. The increased altitude and trajectory angle at separation increases the fuel mass that the first stage rocket is able to use efficiently, and also increases the exergy efficiency of the first stage, partly compensating for the decrease in the efficiency of the scramjet accelerator due to fly-back. Overall, when the fly-back is included, more of the exergy of the first stage is utilised imparting energy upon the combination of the payload and the successive stages, at **6.922% (13.98GJ)**, compared to **6.874% (13.88GJ)** without scramjet accelerator fly-back. This is due to the rocket flying a more efficient trajectory, with lower drag and propulsive losses, terminating at a higher altitude and velocity.

When the fly-back is included, the second-third stage separation occurs at a lower altitude and velocity, and the lower fuel exergy of the scramjet accelerator during its ascent results in less energy being imparted upon the payload and third stage by the scramjet accelerator (**7.04GJ**), compared to the trajectory without fly-back (**8.24GJ**). The lower, slower separation point when fly-back is included

causes the losses of the third stage to increase from all sources. The propulsive inefficiency losses are particularly affected, increasing from 49.73% (17.07 GJ) without fly-back to 51.55% (17.85 GJ) with fly-back, due to the lower velocity of the separation point, which decreases the propulsive efficiency of the third stage (illustrated by Equation 6.1). When flying a trajectory where the scramjet accelerator's fly-back is included, the drag losses during the ascent of the scramjet accelerator consist of a larger percentage of the ascent fuel exergy usage (21.45%, compared to 20.42% without fly-back). This is despite the lower velocity range over which the scramjet accelerator is accelerating when fly-back is included, and is due to the less favourable first-second stage separation conditions, as well as the high banking throughout the acceleration.

The energy necessary to return the scramjet accelerator to its initial launch location is provided by both the fuel used during the return (30.92GJ), as well as the kinetic and potential energy imparted upon the scramjet accelerator during its ascent (10.58GJ). Significantly more energy is required to overcome drag during the return (29.47GJ) than is available from the kinetic and potential energy of the scramjet accelerator (17.61GJ), illustrating the necessity for igniting the scramjet engines during the return flight.

7.5 Design Sensitivity Analysis

XXX make the argument that these parameters are for trajectory studies and to inform designers on criticality of coefficients

It has been shown that the fly-back of the scramjet accelerator has a significant effect on the performance of the rocket-scramjet-rocket launch system, and that the maximum payload-to-orbit optimised trajectory changes significantly to compensate for the additional requirement of successfully returning the scramjet accelerator stage. This section investigates the sensitivity of the launch system to changes in the vehicle design, with the fly-back of the scramjet accelerator included. This sensitivity study varies the following:

- Case 12: Dynamic Pressure,
- Case 13: Specific Impulse,
- Case 14: Scramjet Accelerator Drag,
- Case 15: Scramjet Accelerator Mass,
- Case 16: Scramjet Accelerator Fuel Mass,
- Case 17: Third Stage Mass,
- Case 18: Third Stage Thrust.

As in Section 6.4, the effect of third stage drag is negligible. For this reason, variation in the third stage drag is omitted from this study.

The launch system is able to successfully place a small satellite in orbit for every performance condition which has been tested, while returning the scramjet accelerator to its initial launch location for landing. Every maximum payload-to-orbit optimised trajectory exhibits considerable banking during the scramjet accelerator's ascent trajectory, as well as a pull-up of the scramjet accelerator before third stage release. In every case the optimised return flight path exhibits initial turn, boost-skip and approach phases. However, the height, and duration of the second skip of the return phase varies between cases, exhibiting no clear trend across the majority of the sensitivity studies which have been performed.

The first-second stage separation angle and altitude show no clear trend in any of the sensitivity studies performed, except for the third stage mass variation, in contrast to the sensitivity studies with no fly-back, detailed in Section 6.4, in which the scramjet accelerator mass and drag parameters change the first stage separation point significantly. All of the optimised trajectory solutions show a distinct initial altitude raising manoeuvre performed by the scramjet accelerator, however, the size is inconsistent across optimised trajectory solutions, indicating that this manoeuvre is no longer solely a product of an efficiency trade-off between the first stage pitching and scramjet accelerator engine efficiency. In the maximum payload-to-orbit optimised trajectories calculated during the sensitivity analysis, it is observed that the trajectory angle at the first-second stage separation varies significantly between the optimised trajectories, with no discernible trend. When the scramjet accelerator is released at a high trajectory angle, the first stage is able to use more fuel, and fly a more efficient trajectory. In contrast to the trajectory with no fly-back, releasing the scramjet accelerator at a higher trajectory angle and altitude causes it to spend a significant amount of time in a low dynamic pressure environment, giving time for the bank angle to increase. The high bank angle is utilised during the descent of the scramjet accelerator onto the maximum dynamic pressure path, to rapidly change the heading of the scramjet accelerator. This mitigates some of the reduction in efficiency caused by a higher first-second separation point. A lower release angle results in the first stage flying a slightly less efficient trajectory. However, a lower release angle also results in the scramjet accelerator using its fuel more rapidly, and manoeuvring more at the beginning of its trajectory, which results in the fly-back requiring less fuel. The trade-off between first stage efficiency and the initial operational efficiency of the scramjet accelerator appears to be close, and for each particular trajectory optimisation one or the other is favoured with no clear trend.

It is also observed that there are two distinct return trajectory shapes for the return trajectory of the scramjet accelerator. The more common return trajectory shape has been shown in the preceding section, and consists of three or more large skips to begin the return trajectory. The second trajectory shape exhibits a small second skip, with the first two burns very closely spaced, or combined into one longer burn. An example of this second type of return trajectory is shown in Figure F.25. During the

first two burns, a higher bank angle is maintained when compared to the large skip trajectory shape, however, after the first two burns are completed, the bank angle is reduced more rapidly. During simulations, it was observed that on occasion, the optimal return trajectory type would change as the initial guess or problem setup was altered, with no significant change in the payload-to-orbit capabilities of the launch system. This variability suggests that there is minimal difference between the two shapes of return trajectory, and that both can potentially lead to efficient return flights.

7.5.1 Case 12: Maximum Dynamic Pressure Sensitivity with Fly-Back

Trajectory Condition	q_{max} :	45kPa	47.5kPa	50kPa	52.5kPa	55kPa	$\Delta/\Delta\%q_{max}$
Payload to Orbit (kg)	109.9	118.6	132.1	135.5	137.6	0.7	
Payload Variation (%)	-16.82	-10.24	0.00	2.55	4.13	0.55	
Total η_{exergy} (%)	1.351	1.458	1.576	1.606	1.627	7e-05	
1st Stage η_{exergy} (%)	7.073	6.695	6.925	6.924	6.930		-
Separation Alt, 1→2 (km)	25.90	25.05	24.58	24.28	24.01		-0.05
Separation v, 1→2 (m/s)	1550	1505	1539	1541	1543		-
Separation γ, 1→2 (deg)	16.9	9.9	11.3	11.2	11.4		-
2nd Stage η_{exergy} (%)	3.648	3.517	3.758	3.796	3.815		-
Separation Alt, 2→3 (km)	37.46	41.07	42.52	42.82	42.73		-
Separation v, 2→3 (m/s)	2514	2439	2507	2515	2520		-
Separation γ, 2→3 (deg)	10.9	12.9	12.7	13.0	13.3		-
2nd Stage Flight Time (s)	597.5	552.9	508.8	493.7	483.8		-2.87
2nd Stage Distance Flown (km)	997.7	913.1	872.3	845.0	823.5		-4.17
2nd Stage Return Fuel (kg)	237.2	286.4	252.4	246.7	247.4		-
2nd Stage Return Distance (km)	1461.0	1495.8	1520.4	1507.0	1503.8		-
3rd Stage η_{exergy} (%)	10.883	11.806	13.142	13.480	13.689	0.073	
3rd Stage $t, q > 5\text{kPa}$ (s)	24.4	10.3	9.1	6.9	7.7		-
3rd Stage max α (deg)	10.0	10.0	10.0	10.0	10.0		-
3rd Stage Fuel Mass (kg)	2875.3	2866.6	2853.1	2849.7	2847.6		-0.72

Table 7.3: Comparison of key trajectory parameters with variation in the maximum dynamic pressure of the scramjet accelerator, with fly-back (Case 12).

The maximum dynamic pressure allowable during flight is varied by $\pm 20\%$ in order to determine the sensitivity of the launch system to the structural and thermal limitations of the scramjet accelerator. Table 7.3 shows a summary of the key parameters of each optimised trajectory, and trajectory comparison plots are shown in Appendix F.2.1. The variation in each trajectory parameter per % of the dynamic pressure is shown, if there is a clear trend. The payload-to-orbit of the launch system improves by **+5.5kg (+4.2%)** at 55kPa, and decreases by **-22.2kg (-16.8%)** at 45kPa. The overall exergy efficiency of the system increases as the maximum dynamic pressure increases, by **+0.051% η** at 55kPa, and decreases as the maximum dynamic pressure decreases, by **-0.225% η** at 45kpa. No

significant variation is observed between sensitivity studies with or without the fly-back included in the sensitivity of the launch system to the maximum dynamic pressure of the scramjet accelerator, by percentage.

When fly-back is included, no trends are observed in the exergy efficiencies of the first stage or scramjet accelerator, due to maximum dynamic pressure variation. Compared to the sensitivity study with no fly-back, the trade-offs between the efficiencies of the stages include the manoeuvrability of the scramjet accelerator, which dictates the fuel used during the return flight. This additional factor produces more complicated energy trade-offs, resulting in differing optimal trajectory shapes. This can particularly be observed in the 45kPa maximum dynamic pressure trajectory, which exhibits significantly different trade-offs between each stage, when compared to the other cases. **XXX this is old, change this whole section, as well as below** The 45kPa maximum dynamic pressure simulation shows a low exergy efficiency for the first stage than would be suggested by the general exergy efficiency trends. However, the 45kPa simulation trades the performance of the first stage to achieve greater manoeuvrability at the beginning of the scramjet accelerator's trajectory, resulting in less fuel being used during fly-back, and a higher overall exergy efficiency for the scramjet accelerator. The first-second separation occurs at a lower altitude and trajectory angle compared to the other simulations, allowing the acceleration to be achieved more quickly at the start of the trajectory, and enabling the scramjet accelerator to manoeuvre more effectively at the beginning of its trajectory. As a consequence, the 45kPa simulation uses only 257.0kg of fuel during the fly-back, against the general trend of the return fuel usage.

The exergy efficiency of the scramjet accelerator exhibits a higher general sensitivity to variations in the maximum dynamic pressure, when fly back is included. Increasing the maximum dynamic pressure improves the manoeuvring capabilities of the scramjet accelerator and increases the acceleration rate during ascent, which leads to a smaller flight time, and less ground coverage, generally reducing the amount of fuel necessary for fly-back, once more with the exception of the 45kPa case. This is a factor not present in the sensitivity study without fly-back, however, this does not significantly impact on the overall payload-to-orbit sensitivity of the launch system.

7.5.2 Case 13: Scramjet Accelerator Drag Sensitivity with Fly-Back

The coefficient of drag is varied by $\pm 10\%$ to investigate the effect of variation in the aerodynamic design of the scramjet accelerator on the performance of the launch system, when the fly-back of the scramjet accelerator is included. Appendix F.2.2 presents trajectory comparison plots, and Table 7.4 compares key parameters of each trajectory. Increasing the drag of the scramjet accelerator by 10% decreases the payload-to-orbit by **-18.5kg (-14.0%)**, while decreasing the drag by 10% increases the payload-to-orbit by **+17.3kg (+13.1%)**. The sensitivity to variations in the scramjet accelerator's aerodynamics is decreased when compared to the sensitivity study with no fly-back, down to $-1.5 \frac{\Delta kg}{\Delta \% C_d}$

Trajectory Condition	$C_{d,2}$:	90%	95%	100%	105%	110%	$\Delta/\Delta\%C_{d,2}$
Payload to Orbit (kg)		149.4	140.1	132.1	123.3	113.6	-1.8
Payload Variation (%)		13.11	6.08	0.00	-6.67	-13.98	-1.34
Total η_{exergy} (%)		1.733	1.653	1.578	1.490	1.371	-0.00018
1st Stage η_{exergy} (%)		7.291	7.102	6.923	6.739	6.676	-0.032
Separation Alt, 1→2 (km)		25.01	24.77	24.57	24.39	24.66	-
Separation v, 1→2 (m/s)		1584	1561	1539	1515	1505	-4.1
Separation γ, 1→2 (deg)		10.3	10.8	11.1	11.5	15.7	0.23
2nd Stage η_{exergy} (%)		4.107	3.921	3.758	3.580	3.311	-0.039
Separation Alt, 2→3 (km)		43.14	42.99	42.87	42.42	41.89	-0.06
Separation v, 2→3 (m/s)		2612	2557	2506	2452	2385	-11.17
Separation γ, 2→3 (deg)		12.2	12.4	12.7	13.0	13.6	0.07
2nd Stage Flight Time (s)		504.9	505.9	506.9	511.6	586.2	3.37
2nd Stage Distance Flown (km)		910.3	889.1	869.6	849.5	917.7	-
2nd Stage Return Fuel (kg)		228.1	249.0	257.8	253.6	196.5	-
2nd Stage Return Distance (km)		1642.5	1591.5	1522.3	1390.4	1161.2	-23.27
3rd Stage η_{exergy} (%)		14.837	13.929	13.141	12.275	11.327	-0.173
3rd Stage $t, q > 5\text{kpa}$ (s)		8.9	7.6	7.7	7.7	7.5	-
3rd Stage max α (deg)		10.0	10.0	10.0	10.0	10.0	-
3rd Stage Fuel Mass (kg)		2835.8	2845.1	2853.1	2861.9	2871.6	1.77

Table 7.4: Comparison of key trajectory parameters with variation in the drag of the scramjet accelerator, with fly-back (Case 13).

($-0.9 \frac{\Delta\%}{\Delta\%C_d}$) compared to $-1.9 \frac{\Delta kg}{\Delta\%C_d}$ ($-0.99 \frac{\Delta\%}{\Delta\%C_d}$). **XXX update this** This is due to the increased drag decreasing the total acceleration, which in turn generally decreases the ground distance necessary to cover during the fly-back, partially offsetting the detrimental effects of the increased drag on the performance of the launch system. The 95% drag case is the exception to the trend in fly-back distance. This case exhibits different trade-offs between the ascent and fly-back of the scramjet accelerator, manoeuvring less so that a more efficient ascent trajectory is flown, while requiring a longer, and less fuel efficient fly-back. **XXX check**

The exergy efficiencies of all three stages are decreased significantly as the drag of the scramjet accelerator is increased. This decrease in efficiency is due to the increased drag losses of the first stage and scramjet accelerator, 2.48% and 24.45% respectively at 110% C_D , compared to 2.27% and 19.98% respectively at 90% C_D , and the increased propulsive inefficiency losses of the third stage when released from a lower velocity, 53.55% at 110% C_D , compared to 49.89% at 90% C_D . As was observed in the drag sensitivity study with no fly-back in Section 6.4.2, the second-third stage separation angle shows an increase as the drag is increased, by $+0.9^\circ$ ($+7.1\%$) at 110% drag, and decreasing by -0.5° (-3.9%) at 90% drag. In addition, the altitude of the second-third stage separation shows a clear trend, decreasing as the drag of the scramjet accelerator is increased, by -0.98km (-2.29%) at 110% drag, and increasing slightly as the drag is decreased, by $+0.27\text{km}$ ($+0.63\%$) at 90% drag.

The release altitude and trajectory angle serve to initiate the first skip of the return trajectory in a consistent manner, so that the shape of the initial skip is very similar with drag variation. In all cases the angle of attack is reduced to 0° immediately during return to lessen the size of the initial skip, and is then raised to close to the maximum of 10° to prevent the dynamic pressure limit being exceeded. This consistency indicates that the initial skip of the return flight is driving the conditions at second-third stage release, and that it is primarily the control and structural limitations, rather than the aerodynamics of the scramjet accelerator, which determine the shape of this skip. **XXX check this**

7.5.3 Case 14: C-REST Specific Impulse Sensitivity with Fly-Back

Trajectory Condition	$I_{SP,2}$:	90%	95%	100%	105%	110%	$\Delta/\Delta\%I_{SP,2}$
Payload to Orbit (kg)	114.6	123.4	132.1	139.6	148.3	1.7	
Payload Variation (%)	-13.24	-6.59	0.00	5.69	12.28	1.27	
Total η_{exergy} (%)	1.414	1.498	1.578	1.651	1.733	0.00016	
1st Stage η_{exergy} (%)	6.927	6.930	6.923	6.899	6.896	-	
Separation Alt, 1→2 (km)	24.58	24.58	24.57	24.57	24.56	-	
Separation v, 1→2 (m/s)	1539	1540	1539	1536	1535	-	
Separation γ, 1→2 (deg)	11.2	11.3	11.1	11.1	11.0	-	
2nd Stage η_{exergy} (%)	3.265	3.506	3.758	3.990	4.240	0.049	
Separation Alt, 2→3 (km)	42.62	42.31	42.87	42.68	42.85	-	
Separation v, 2→3 (m/s)	2393	2451	2506	2557	2611	10.83	
Separation γ, 2→3 (deg)	13.4	13.1	12.7	12.4	12.1	-0.06	
2nd Stage Flight Time (s)	507.4	507.5	506.9	509.0	509.9	-	
2nd Stage Distance Flown (km)	827.4	849.2	869.6	888.6	908.6	4.04	
2nd Stage Return Fuel (kg)	275.2	268.8	257.8	255.6	247.0	-1.39	
2nd Stage Return Distance (km)	1419.2	1476.9	1522.3	1590.0	1645.2	11.3	
3rd Stage η_{exergy} (%)	11.422	12.287	13.141	13.876	14.727	0.164	
3rd Stage $t, q > 5\text{kpa}$ (s)	7.7	7.6	7.7	9.2	9.2	-	
3rd Stage max α (deg)	10.0	10.0	10.0	10.0	10.0	-	
3rd Stage Fuel Mass (kg)	2870.6	2861.8	2853.1	2845.6	2836.9	-1.67	

Table 7.5: Comparison of key trajectory parameters with variation in the specific impulse of the C-REST engines, with fly-back (Case 14).

The specific impulse of the scramjet accelerator is varied by $\pm 10\%$ in order to assess the sensitivity of the optimised trajectory to the performance of the scramjet engines. Key parameters of the trajectories are summarised in Table 7.5, and comparison plots are shown in Appendix F.2.3. Raising the specific impulse of the C-REST engines increases the payload-to-orbit, by **+16.2kg (+12.3%)** at 110% I_{SP} , while lowering the specific impulse decreases the payload-to-orbit, by **-17.5kg (-13.2%)** at 90% I_{SP} . This produces a general trend in the payload-to-orbit of $1.7 \frac{\Delta kg}{\Delta \% I_{SP}}$, lower than the trend of $2.2 \frac{\Delta kg}{\Delta \% I_{SP}}$ observed in the sensitivity study without fly-back, in Section 6.4.3. **XXX change this and**

below This lowered sensitivity in the payload-to-orbit is due to a correspondingly lowered sensitivity in the exergy efficiency of the scramjet accelerator, of $0.051 \frac{\Delta\% \eta}{\Delta\% I_{SP}}$, compared to $0.065 \frac{\Delta\% \eta}{\Delta\% I_{SP}}$ in the sensitivity study without fly-back. This lowered sensitivity is due to the modified I_{SP} having no effect on the performance of the scramjet accelerator during the unpowered portions of the fly-back trajectory, which serve to offset the overall variation in exergy efficiency.

Similarly to the specific impulse sensitivity study without fly-back conducted in Section 6.4.3, the first-second separation conditions, as well as the exergy efficiency of the first stage, exhibit no clear trends. Following first-second separation, the shape of the trajectory path of the scramjet accelerator does not change significantly with specific impulse variation, including the the pull-up altitude. As with the optimised trajectories with no fly-back, increasing the specific impulse of the scramjet engines by 10% increases the velocity at separation (by +105m/s, +4.2%) and decreases the trajectory angle (by -0.6°, -4.7%), while decreasing the specific impulse of the scramjet engines by 10% decreases the velocity at second-third stage separation (by -113m/s, -4.5%), and increases the trajectory angle (by 0.7°, +5.5%). The exergy efficiency of the third stage rocket increases as the exergy efficiency of the scramjet accelerator increases. This is in line with the trend which has been observed in all previous cases, that the increased separation velocity increases the propulsive efficiency of the third stage, increasing its performance.

7.5.4 Case 15: Scramjet Accelerator Mass Sensitivity with Fly-Back

The mass of the scramjet accelerator is varied by ±5% to investigate the sensitivity of the launch system performance to the structural mass of the second stage, with the inclusion of scramjet accelerator fly-back. As in Section 6.4.4, the mass is varied by only ±5% in order to limit the variation in the velocity of the first-second separation. Table 7.6 details key parameters of each trajectory, and Appendix F.2.4 shows comparison plots. Varying the structural mass of the scramjet accelerator yields a change in maximum payload-mass to orbit of +7.2kg (+4.22%) at 95% mass, and -6.0kg (-3.56%) at 105% mass.

The first-second separation conditions show no significant trend with variation in the mass of the scramjet accelerator, except for differing velocities due to the first stage accelerating a varied total mass. As observed in Section 6.4.4, the structural mass of the scramjet accelerator is increased, the exergy efficiency of the first stage decreases, from 8.780% η at 95% structural mass, to 8.356% η at 105% structural mass. This is due to the first stage rocket not accelerating as quickly as the mass of the scramjet accelerator is increased, causing the propulsive efficiency of the first stage to decrease (illustrated by Equation 6.1). However, the sensitivity of the exergy efficiency of the first stage rocket to variation in the mass of the scramjet accelerator is lower when compared to the sensitivity study with no fly-back (described in Section 6.4.4), at $-0.028 \frac{\Delta\% \eta}{\Delta\% m_{scramjetaccelerator}}$, compared to $-0.043 \frac{\Delta\% \eta}{\Delta\% m_{scramjetaccelerator}}$ with no fly-back. Additionally, this exergy efficiency variation is solely due to vari-

Trajectory Condition	m_2 :	95%	97.5%	100%	102.5%	105%	$\Delta/\Delta\%m_2$
Payload to Orbit (kg)		177.4	174.9	170.2	167.4	164.2	-1.4
Payload Variation (%)		4.22	2.72	0.00	-1.66	-3.56	-0.8
Total η_{exergy} (%)		1.674	1.645	1.609	1.588	1.558	-0.00012
1st Stage η_{exergy} (%)		6.722	6.645	6.600	6.511	6.440	-0.028
Separation Alt, 1→2 (km)		27.22	26.34	27.14	25.93	25.61	-
Separation v, 1→2 (m/s)		1590	1572	1548	1532	1512	-7.84
Separation γ, 1→2 (deg)		5.1	4.0	5.6	3.8	3.6	-
2nd Stage η_{exergy} (%)		4.079	4.054	3.989	3.955	3.930	-0.016
Separation Alt, 2→3 (km)		41.38	41.02	40.93	40.93	40.66	-0.06
Separation v, 2→3 (m/s)		2624	2606	2581	2559	2541	-8.52
Separation γ, 2→3 (deg)		10.8	11.0	11.0	11.3	11.3	-
2nd Stage Distance Flown (km)		890.3	859.9	868.4	834.2	821.2	-
2nd Stage Return Fuel (kg)		260.8	251.6	268.0	281.3	282.6	-
2nd Stage Return Distance (km)		1562.2	1518.2	1535.7	1555.0	1505.5	-
3rd Stage η_{exergy} (%)		17.585	17.343	16.888	16.617	16.301	-0.132
3rd Stage $t, q > 5\text{kpa}$ (s)		13.6	13.8	13.3	13.0	13.7	-
3rd Stage max α (deg)		17.7	16.0	16.7	16.5	16.6	-
3rd Stage Fuel Mass (kg)		2837.4	2839.9	2844.5	2847.4	2850.6	1.36

Table 7.6: Comparison of key trajectory parameters with variation in the structural mass of the scramjet accelerator, with fly-back (Case 15).

ations in the propulsive efficiency of the first stage, with no consistent variation in drag losses. This indicates that the mass of the scramjet accelerator does not cause an efficiency trade-off between the first stage and the scramjet accelerator, when the fly-back of the scramjet accelerator is included. This is in contrast to the trade-off observed in the sensitivity study without fly-back, in Section 6.4.4, and is due to the first-second separation conditions being partly determined by the requirement of the scramjet accelerator to bank when the fly-back is included.

As was observed in Section 6.4.4, the lower velocity of first-second separation means that when the scramjet accelerator mass is increased, the velocity range over which the scramjet accelerator is accelerating is lower. This is beneficial for the specific impulse of the C-REST engines, which exhibit higher I_{SP} at lower velocities. For this reason, when the scramjet accelerator mass is increased, the specific impulse of the scramjet accelerator stays high for longer, above 500s I_{SP} for 278.8s of its trajectory at 105% mass, compared to 254.4s above 500s I_{SP} at 95% mass. However, the higher scramjet accelerator mass decreases the overall acceleration of the scramjet accelerator, in turn decreasing the efficiency of the third stage due to increased propulsive losses. In contrast to the mass sensitivity study without fly-back, the second-third stage separation point shows a trend of decreasing altitude, of $-0.06 \frac{\Delta km}{\Delta \% m_{scramjetaccelerator}}$. As was observed when the drag of the scramjet accelerator was varied in Section 7.5.2, this is in order to maintain a consistently sized initial skip during the return trajectory.

7.5.5 Case 16: Scramjet Accelerator Fuel Mass Sensitivity with Fly-Back

Trajectory Condition	$m_{f,2}$:	90%	95%	100%	105%	110%	$\Delta/\Delta\%m_{F,2}$
Payload to Orbit (kg)	126.0	128.5	132.1	134.8	138.5	0.6	
Payload Variation (%)	-4.62	-2.71	0.00	2.04	4.85	0.47	
Total η_{exergy} (%)	1.597	1.578	1.578	1.565	1.564	-	
1st Stage η_{exergy} (%)	6.961	6.936	6.923	6.884	6.866	-0.005	
Separation Alt, 1→2 (km)	24.73	24.65	24.57	24.48	24.40	-0.02	
Separation v, 1→2 (m/s)	1558	1547	1539	1527	1518	-2.01	
Separation γ, 1→2 (deg)	10.8	10.8	11.1	11.1	11.3	-	
2nd Stage η_{exergy} (%)	3.917	3.821	3.758	3.690	3.646	-0.013	
Separation Alt, 2→3 (km)	42.63	43.01	42.87	43.09	43.04	-	
Separation v, 2→3 (m/s)	2466	2482	2506	2524	2549	4.14	
Separation γ, 2→3 (deg)	13.0	12.8	12.7	12.6	12.4	-0.03	
2nd Stage Flight Time (s)	463.5	483.8	506.9	526.9	551.1	4.37	
2nd Stage Distance Flown (km)	773.2	816.0	869.6	914.4	971.2	9.89	
2nd Stage Return Fuel (kg)	263.4	252.7	257.8	253.2	250.6	-	
2nd Stage Return Distance (km)	1520.8	1477.6	1522.3	1511.8	1526.5	-	
3rd Stage η_{exergy} (%)	12.542	12.790	13.141	13.404	13.767	0.061	
3rd Stage $t, q > 5\text{kpa}$ (s)	7.6	7.6	7.7	7.7	8.8	0.05	
3rd Stage max α (deg)	10.0	10.0	10.0	10.0	10.0	-	
3rd Stage Fuel Mass (kg)	2859.2	2856.7	2853.1	2850.4	2846.7	-0.63	

Table 7.7: Comparison of key trajectory parameters with variation in the fuel mass of the scramjet accelerator, with fly-back (Case 16).

The fuel mass of the scramjet accelerator is varied by $\pm 10\%$, to investigate the sensitivity of the performance of the launch system to variations in the size of the fuel tanks within the scramjet accelerator. Appendix F.2.5 shows plots comparing each trajectory, and Table 7.7 details comparisons of key trajectory parameters. When the fuel mass within the scramjet accelerator is increased by 10%, the payload to orbit increases by **+6.4kg (+4.8%)** and when the fuel mass is decreased by 10%, the payload mass reduces by **-6.1g (-4.6%)**. The magnitude of the payload-to-orbit sensitivity is very similar to the sensitivity observed without fly-back, in Section 6.4.5, indicating that the addition of fly-back does not have a significant effect on the sensitivity of the launch system to variations in the fuel mass of the scramjet accelerator.

The first stage shows no significant trend in its trajectory when the fuel mass of the scramjet accelerator is varied, besides a decrease in the overall acceleration due to the additional mass. This is in contrast to the trends observed in Section 6.4.5, and is due to the additional factor of the banking of the scramjet accelerator driving the first-second separation conditions, as observed in Section 7.5.4. As in Section 6.4.5, increasing the fuel mass of the scramjet accelerator decreases the exergy efficiency of the scramjet accelerator, by **-0.112% η (-2.98%)** at 110% fuel mass, and decreasing the fuel mass of the scramjet accelerator increases its exergy efficiency, by **+0.159% η (+4.23%)** at 90%

fuel mass. Once again, the overall exergy efficiency of the system shows no distinct trend. As in Section 6.4.5, this is due to the increased period of acceleration causing the specific impulse of the C-REST engines to decrease. However, the overall energy availability is increased by the additional fuel mass, resulting in more overall exergy. This results in the overall energy imparted upon the third stage by the scramjet accelerator increasing, from 6.606GJ at 90% m_f , to 7.516GJ at 110% m_f , in turn increasing the payload-to-orbit.

7.5.6 Case 17: Third Stage Mass Sensitivity with Fly-Back

XXX this is weird, redo? but the no-flyback case has the same trend... its probably because I have a 10 degree limit on aoa

Trajectory Condition	m_3 :	90%	95%	100%	105%	110%	$\Delta/\Delta\%m_3$
Payload to Orbit (kg)		119.9	126.4	132.1	114.8	86.9	-
Payload Variation (%)		-9.23	-4.33	0.00	-13.08	-34.20	-
Total η_{exergy} (%)		1.506	1.546	1.578	1.377	1.068	-
1st Stage η_{exergy} (%)		7.039	6.978	6.923	6.860	6.798	-0.012
Separation Alt, 1→2 (km)		24.94	24.75	24.57	24.39	24.20	-0.04
Separation v, 1→2 (m/s)		1584	1561	1539	1516	1494	-4.48
Separation γ, 1→2 (deg)		10.6	10.8	11.1	11.4	11.5	0.05
2nd Stage η_{exergy} (%)		3.451	3.605	3.758	4.105	4.744	0.062
Separation Alt, 2→3 (km)		42.92	42.94	42.87	36.67	32.93	-
Separation v, 2→3 (m/s)		2552	2528	2506	2550	2638	-
Separation γ, 2→3 (deg)		12.5	12.6	12.7	10.7	3.3	-
2nd Stage Flight Time (s)		501.8	503.6	506.9	505.2	526.0	-
2nd Stage Distance Flown (km)		886.3	876.0	869.6	853.5	888.2	-
2nd Stage Return Fuel (kg)		254.1	255.2	257.8	240.7	192.8	-
2nd Stage Return Distance (km)		1545.7	1534.4	1522.3	1447.2	1175.0	-16.57
3rd Stage η_{exergy} (%)		13.235	13.226	13.141	10.804	7.683	-0.271
3rd Stage $t, q > 5\text{kpa}$ (s)		9.0	8.0	7.7	28.1	155.4	-
3rd Stage max α (deg)		10.0	10.0	10.0	10.0	10.0	-
3rd Stage Fuel Mass (kg)		2561.4	2706.9	2853.1	3022.4	3202.2	31.94

Table 7.8: Comparison of key trajectory parameters with variation in the mass of the third stage, with fly-back (Case 17).

The mass of the third stage rocket is varied by $\pm 10\%$, to investigate the effects of the internal mass density of the third stage rocket, when the fly-back of the scramjet accelerator is included. Table 7.8 details key trajectory parameters, and Appendix F.2.6 shows trajectory comparison plots. As in Section 6.4.6, the varied mass is a combination of the fuel and structural mass of the third stage, and payload mass, representing the density of the components within the third stage. As previously, the heat shield mass is not varied, the structural mass held at 9% of the total, non-heat shield mass, and the remaining mass variation is a combination of fuel and payload mass.

Increasing the third stage mass by 10% causes a corresponding increase in the payload-to-orbit of +9.9kg (+5.76%), while decreasing the third stage mass by 10% causes a decrease in payload-to-orbit of -9.4kg (-5.54%). This payload-to-orbit mass sensitivity is slightly higher than the third stage mass sensitivity without fly-back, detailed in Section 6.4.6. In addition, the payload-to-orbit is lower when the fly-back of the scramjet accelerator is included, resulting in a significantly higher percentage payload increase, at $0.56 \frac{\Delta m_{payload}}{\Delta \% m_3}$, compared to $0.47 \frac{\Delta m_{payload}}{\Delta \% m_3}$ without fly-back. Similarly to the sensitivity study without fly-back, in Section 6.4.6, the exergy efficiency of the scramjet accelerator increases as the mass of the third stage increases, by $+0.337\% \eta$ (+8.4%) at 110% m_3 , and decreases when the third stage mass is decreased, by $-0.236\% \eta$ (-5.9%) at 90% m_3 . This trend is caused by the higher third stage mass decreasing the acceleration of the scramjet accelerator, so that overall, the specific impulse of the scramjet accelerator stays higher. The sensitivity of the exergy efficiency of the scramjet accelerator is lower when fly-back is included, at $0.029 \frac{\Delta \% \eta}{\Delta \% m_3}$, compared to $0.037 \frac{\Delta \% \eta}{\Delta \% m_3}$ without fly-back. This lowered sensitivity is due to the efficiency of the fly-back relying on the performance of the scramjet accelerator alone, which is not directly affected by variations in the third stage mass. The exergy efficiency sensitivity of the third stage is also decreased to $-0.071 \frac{\Delta \% \eta}{\Delta \% m_3}$ when fly-back is included, compared to $-0.095 \frac{\Delta \% \eta}{\Delta \% m_3}$ without fly-back. However, this lowered efficiency trend still results in an increased payload mass-to-orbit sensitivity compared to the trajectory case without fly-back. This is due to the lower payload-to-orbit when fly-back is included, which results in more fuel within the third stage, and consequently that each percentage of exergy efficiency gained or lost results in a larger total payload mass change.

7.5.7 Case 18: Third Stage Specific Impulse Sensitivity with Fly-Back

XXX I should probably keep this as 5% variation

The specific impulse of the third stage rocket is varied by $\pm 5\%$ to investigate the sensitivity of the launch system to the performance of the third stage rocket, when the fly-back of the scramjet accelerator is included. Table 7.9 shows selected performance indicators, while Appendix F.2.7 shows comparison plots of the maximum payload-to-orbit trajectory at each third stage specific impulse.

The sensitivity of the optimal trajectory to the third stage specific impulse with scramjet accelerator fly-back is very similar to that observed in the sensitivity study with no scramjet accelerator fly-back, in Section 6.4.7, with a sensitivity of $4.6 \frac{\Delta m_{payload}}{\Delta \% I_{SP,3}}$ variation. These similar sensitivities indicate that the fly-back does not considerably effect the sensitivity of the launch system to variations in the third stage specific impulse, and that the third stage specific impulse has a consistent magnitude of effect at lower separation velocities. The trajectory of the first stage does not change significantly as the specific impulse of the third stage is varied. The exergy efficiency of the first stage shows a slight trend, however, this is very small. The trajectory scramjet accelerator shows no distinct trends as the specific impulse of the third stage is varied, except for a general decrease in the third stage

Trajectory Condition	$I_{SP,3}$:	90%	95%	100%	105%	110%	$\Delta/\Delta\%I_{SP,3}$
Payload to Orbit (kg)		-5.6	84.2	132.1	176.8	222.5	11
Payload Variation (%)		-104.27	-36.27	0.00	33.84	68.41	8.31
Total η_{exergy} (%)		0.226	1.075	1.576	2.020	2.470	0.00109
1st Stage η_{exergy} (%)		6.921	7.108	6.925	6.904	6.913	-
Separation Alt, 1→2 (km)		24.57	26.34	24.58	24.56	24.56	-
Separation v, 1→2 (m/s)		1538	1552	1539	1536	1537	-
Separation γ, 1→2 (deg)		11.1	18.6	11.3	11.1	11.0	-
2nd Stage η_{exergy} (%)		4.373	3.562	3.758	3.761	3.787	-
Separation Alt, 2→3 (km)		32.53	42.02	42.52	42.06	42.56	-
Separation v, 2→3 (m/s)		2679	2480	2507	2508	2513	-
Separation γ, 2→3 (deg)		2.6	13.3	12.7	12.6	12.5	-
2nd Stage Flight Time (s)		514.0	606.2	508.8	505.5	505.3	-
2nd Stage Distance Flown (km)		892.4	996.8	872.3	863.7	866.5	-
2nd Stage Return Fuel (kg)		225.6	159.1	252.4	258.5	256.4	-
2nd Stage Return Distance (km)		1288.3	1230.9	1520.4	1514.5	1507.9	-
3rd Stage η_{exergy} (%)		-0.532	8.253	13.142	17.868	22.842	1.127
3rd Stage $t, q > 5\text{kpa}$ (s)		132.3	9.3	9.1	8.9	8.0	-4.98
3rd Stage max α (deg)		10.0	10.0	10.0	10.0	10.0	-
3rd Stage Fuel Mass (kg)		2990.8	2901.0	2853.1	2808.4	2762.7	-10.98

Table 7.9: Comparison of key trajectory parameters with variation in the specific impulse of the third stage, with fly-back (Case 18).

separation angle. As the specific impulse of the third stage is increased, second-third stage separation angle and the angle of attack schedule of the third stage are modified, so that 90km altitude is reached at circularisation conditions in all cases. This causes an increase in specific impulse to result in more time spent in-atmosphere, with the third stage spending 14.9s at dynamic pressures greater than 5kPa at 105% I_{SP} , compared to 12.1s at 95% I_{SP} .

7.6 Comparison of Sensitivities with Fly-Back

The sensitivities of the performance of the launch system, including the fly-back of the scramjet accelerator, to a variety of design parameters have been presented in the preceding sections. Figure 7.7 shows a relative comparison of the payload-to-orbit sensitivity for each design parameter, by percentage. The magnitude of each sensitivity is also compared with the sensitivity of the launch system performance without fly-back, detailed in Section 6.5.

The sensitivity of the launch system to the maximum dynamic pressure is unchanged when fly-back is included. However, the slight decrease in the sensitivity of the launch system to the structural mass of the scramjet accelerator, to $-1.4 \frac{\Delta k_g}{\Delta \% m_{scramjetaccelerator}}$, means that the potential beneficial effects of reducing the maximum dynamic pressure of the scramjet accelerator are reduced slightly. So long

Payload Variation (kg) per % Parameter Variation

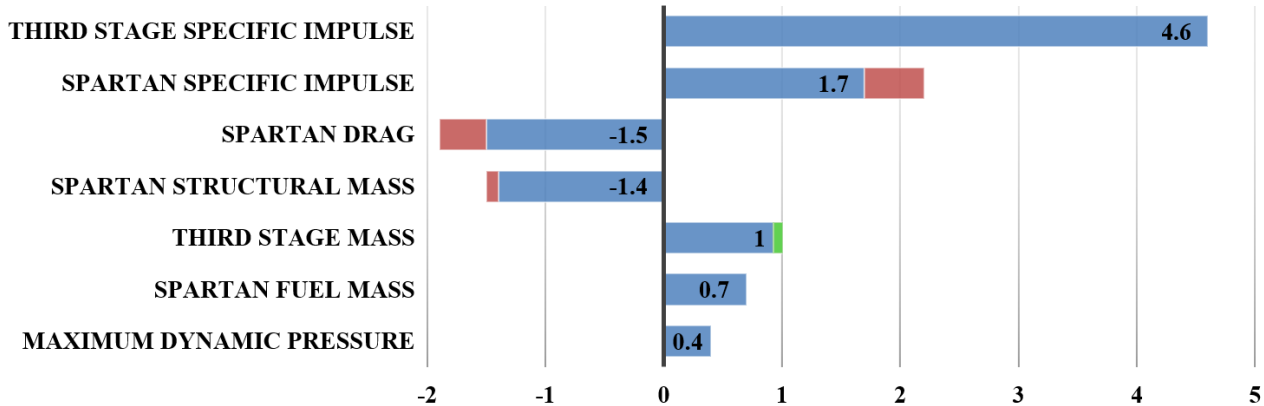


Figure 7.7: The sensitivity of the key design parameters of the launch system, including scramjet accelerator fly-back. Red and green coloured areas indicate decreases or increases in the magnitude of sensitivity respectively, compared to the sensitivity study without scramjet accelerator fly-back in Section 6.5.

as the mass of the scramjet accelerator reduces by 28.3kg for each 1kPa reduction in the maximum dynamic pressure, the performance of the launch system will improve. The sensitivity of the launch system to the specific impulse of the scramjet accelerator is decreased significantly when the fly-back of the scramjet accelerator is included, to $1.7 \frac{\Delta kg}{\Delta \% I_{SP,scramjetaccelerator}}$, a decrease of $-0.5 \frac{\Delta kg}{\Delta \% I_{SP,scramjetaccelerator}}$ (-22.7%) compared to the sensitivity without fly-back. The sensitivity of the launch system to the scramjet accelerator's structural mass is also decreased, to $-1.4 \frac{\Delta kg}{\Delta \% m_{scramjetaccelerator}}$. Comparing these sensitivities, it is apparent that if the specific impulse of the scramjet accelerator can be increased by 1% with less than 1.21% (60.0kg) increase in the total mass of the scramjet accelerator, then the overall performance of the launch system will be improved. Similarly, the sensitivity of the launch system to variation in the drag of the scramjet accelerator is reduced, to $-1.5 \frac{\Delta kg}{\Delta \% C_{d,scramjetaccelerator}}$. Comparing this sensitivity with the sensitivity to the structural mass of the scramjet accelerator, the specific impulse of the C-REST engines must be improved by 1% while increasing the drag of the scramjet accelerator by less than 1.13% due to shape variation, in order for the overall performance change to be beneficial.

The decreased sensitivity of the launch system performance to the structural mass of the scramjet accelerator, along with the unchanged fuel mass sensitivity, means that so long as 1kg of fuel mass can be added with less than 1.59kg of structural mass added, the performance of the launch system will improve. Additionally, the decreased sensitivity of the launch system to the drag of the scramjet accelerator means that so long as 1kg of fuel can be added to the scramjet accelerator, with a drag increase of less than 0.030% due to increased size, then the maximum payload-to-orbit will increase.

Lastly, comparing the increased third stage mass sensitivity, of $1\frac{\Delta kg}{\Delta \% m_3}$, with the decreased scramjet accelerator drag sensitivity, shows that if the size of the third stage can be increased so that the third stage mass increases by 1kg, while the size of the scramjet accelerator's fuselage is varied so that the increase in scramjet accelerator drag is less than 0.020%, the maximum payload-to-orbit will be improved.

7.7 Summary

In this chapter, the maximum payload-to-orbit trajectory for The SPARTAN rocket-scramjet-rocket system has been calculated, with the inclusion of the fly-back of the scramjet accelerator stage. It was found that this launch system is able to deliver 132.1kg of payload to sun synchronous orbit, while successfully returning the scramjet-powered stage to the initial launch site. This return flight decreases the payload-to-orbit by -19.0kg (-10%), but removes the need for the costly and time consuming transportation of the scramjet accelerator after launch, which would be necessary if landing at a downrange location. During the return flight, the scramjet engines are powered on three times, in total using 257.8kg of fuel for the return flight, 17.2% of the scramjet accelerator's total fuel.

It was found that when the fly-back of the scramjet accelerator is included in the optimal trajectory calculation, the first stage of the launch system pitches in an easterly direction. The launch system exhibits a first-second separation point of 24.57km, an increase of 3.0km when compared to the maximum payload-to-orbit trajectory with no fly-back, and a trajectory angle of 11.1° , an increase of 2.5° . This higher separation point allows the first stage to efficiently use 17943kg of fuel, as well as increasing its exergy efficiency to $6.923\%\eta$, increases of +758kg (+4.4%) and +0.308% η (+4.9%) respectively when compared to the maximum payload-to-orbit trajectory with no fly-back. In addition to increasing the fuel and exergy efficiency of the first stage, the higher first-second separation serves to increase the altitude of the scramjet accelerator at the beginning of its trajectory. This allows the scramjet accelerator time to increase its bank angle, so that when the scramjet accelerator descends it is able to change its heading angle rapidly. The scramjet accelerator maintains a high bank angle throughout its trajectory, executing a banking manoeuvre, and staying close to its maximum dynamic pressure. This banking manoeuvre requires higher angles of attack, increasing the drag of the scramjet accelerator, but also reduces the ground distance necessary for the return of the scramjet accelerator, decreasing the amount of fuel necessary for fly-back and increasing the overall efficiency of the scramjet accelerator. At the end of its acceleration, the scramjet accelerator was found to exhibit a pull-up manoeuvre before the separation of the third stage, in a similar fashion to the maximum payload-to-orbit trajectory with no fly-back.

The fly-back of the scramjet accelerator is found to be separated into three stages; an initial turn, a boost phase, and an approach. The initial turn takes place immediately after separation, and consists of the scramjet accelerator banking heavily in order to manoeuvre the heading angle back towards the

initial launch site. During the boost-skip phase the scramjet accelerator exhibits multiple ‘skipping’ manoeuvres. These skipping manoeuvres have been shown in previous literature to extend the flight range of hypersonic vehicles[56, 86–89, 91, 92], and serve to reduce the amount of fuel used during the fly-back. In addition, the skipping manoeuvres allow the scramjet engines to be powered on at the points where the specific impulse of the C-REST engines are highest, maximising the performance of the scramjet accelerator, and minimising the fuel necessary for return. During the approach phase, the trajectory of the scramjet accelerator is smoothed, and the scramjet accelerator glides to the landing point. The optimal trajectory terminates when scramjet accelerator reaches 1km altitude at a velocity of 120m/s. After this point, it is assumed that the scramjet accelerator lands on a traditional runway. This result indicates that it is feasible to return a hypersonic launch vehicle separated at a high Mach number to its initial launch site, and that a cost efficient mission profile for a rocket-scramjet-rocket launch system is attainable.

The sensitivity of the launch system to various design parameters has been investigated. The payload-to-orbit sensitivity of the launch system to variations in the specific impulse, drag and structural mass of the scramjet accelerator was found to decrease when fly-back is included, compared to the sensitivity study with no fly-back. This decreased sensitivity indicates that the fly-back of the scramjet accelerator offsets some of the payload-to-orbit variation due to changes in these parameters. It was found that the first-second separation conditions do not exhibit clear trends with scramjet accelerator performance when fly-back is included, in contrast to the trade-offs observed in Section 6.4. The disappearance of these trends indicates that when the fly-back of the scramjet accelerator is included, the first-second separation point is determined by a more complex trade-off. This trade-off involves the banking and manoeuvrability of the scramjet accelerator at the start of its acceleration, which affects the efficiency of the return flight.

CHAPTER 8

CONCLUSIONS

The purpose of this work was to design and investigate the launch trajectory of a partially-reusable, rocket-scramjet-rocket, small satellite launch system. The trajectory of this launch system was optimised for maximum payload-to-orbit, and characterised in order to determine the key performance parameters of the launch system. This aim was achieved through the completion of the set of objectives detailed as follows:

Development of a detailed design and aerodynamic simulation for a rocket-scramjet-rocket launch system.

In order to create a representative model for a trajectory simulation, the design of a rocket-scramjet-rocket launch system was developed. This launch system was designed around the SPARTAN scramjet-powered accelerator, which is in development at The University of Queensland. A first stage rocket was designed, to accelerate the SPARTAN to its minimum operating speed of Mach 5. This first stage was based upon the Falcon-1e, scaled down lengthwise to 8.5m and throttled down to a constant 70% to assist in pitching. A third stage rocket was designed, based around the Kestrel upper stage rocket motor for cost effectiveness. This third stage was sized to fit within the fuselage of the SPARTAN, to be 9m long, and 1.5m wide. The heat shield necessary for atmospheric flight, and the internal fuel tanks of the third stage were sized, resulting in a total mass of 3300kg. The fuel tanks of the SPARTAN were resized, to accommodate this redesigned third stage.

The aerodynamics of the first stage and the SPARTAN were calculated using Cart3D, an inviscid CFD package, and the aerodynamics of the SPARTAN were modified using a viscous correction for accuracy. The aerodynamics of the launch system were calculated across the operable regimes of the vehicles, which for the SPARTAN included both engine-on and engine-off conditions, across a range of Mach numbers from 0.2 to 10. The control surfaces of the SPARTAN were modelled, and the aerodynamics of the SPARTAN simulated with flaps deployed. A variable centre of gravity model

CHAPTER 8. CONCLUSIONS

was created for the SPARTAN, to model the changes in the vehicle dynamics during flight. The aerodynamics of the SPARTAN were calculated at multiple centre of gravity positions, and a trimmed aerodynamic database was created. The aerodynamics of the third stage were modelled using Missile Datcom, a partially empirical tool for estimating the aerodynamics of missile and rocket vehicles, with the aerodynamic control of the third stage attained through thrust vectoring.

Calculation of the maximum payload-to-orbit trajectory for a rocket-scramjet-rocket launch system using optimal control, with and without fly-back.

In order to calculate the maximum payload-to-orbit trajectory of the launch system, a software package was created to simulate and optimise launch system trajectories, designated LODESTAR. LODESTAR utilises GPOPS-2, a pseudospectral method optimal control solver, and simulates the trajectory of each stage of the launch system in a geodetic rotational reference frame. LODESTAR optimises the entire trajectory of the launch system simultaneously, so that the performance trade-offs between the stages are captured accurately.

A mission profile has been developed for the SPARTAN-based rocket-scramjet-rocket launch system, launching a satellite to sun synchronous orbit from the Northern Territory, Australia. Initially, the trajectory of the launch system was developed with the assumption that the SPARTAN lands at a location downrange. A mission case was developed in which the scramjet stage of the launch vehicle was constrained to flight at its maximum dynamic pressure, providing a baseline trajectory case for comparison. This constant dynamic pressure trajectory was found to be capable of delivering 98.3kg to sun synchronous orbit. The maximum payload-to-orbit trajectory of the launch system was then calculated. It was found that, when flying the payload-optimised trajectory, the launch system is capable of delivering 156.4kg of payload to sun synchronous orbit, an increase of 19.5% over the simulation with the SPARTAN constrained to constant dynamic pressure. Three key features were observed in the trajectory; a higher first stage-SPARTAN separation point, an altitude raising manoeuvre in the centre of the SPARTAN's trajectory, and a pull-up before SPARTAN-third stage separation. The altitude raising manoeuvre in the centre of the SPARTAN's trajectory was observed occur in a region of homogeneity in the performance of the SPARTAN, increasing the efficiency of the SPARTAN by +0.53%. The improvement in payload-to-orbit was found to result primarily from the stage separation conditions, as a consequence of favourable trade-offs between the efficiencies of the stages of the launch system. The higher first stage-SPARTAN separation point was found to decrease the amount of turning which the first stage must perform, allowing the first stage to launch with more fuel while maintaining manoeuvrability. This larger amount of fuel was found to increase the total energy imparted to the SPARTAN, as well as increasing the acceleration, and consequently the propulsive efficiency of the first stage. Similarly, a pull-up before the SPARTAN-third stage separation decreases the amount of turning which the third stage must perform, and enables the third stage to gain altitude much more rapidly, causing it to spend significantly less flight time at high dynamic pressure. This

reduced exposure to high dynamic pressure reduces the energy losses due to the aerodynamic drag of the third stage, as well as reducing the amount of energy imparted upon the heat shield, by allowing it to be jettisoned earlier. The altitude increasing manoeuvres at the stage separations were found to result in the exergy efficiency of the SPARTAN decreasing by $-0.508\%\eta$ (-9.7%). However, this reduction in the efficiency of the SPARTAN is a trade-off for increases in the exergy efficiencies of the first and third stages, of $+0.148\%\eta$ (+2.4%) and $+3.286\%\eta$ (+21.3%) respectively, resulting in a significantly higher overall efficiency.

The mission definition was adjusted, to include a constraint of the SPARTAN flying back to the initial launch site after the separation of the third stage. The optimised maximum payload-to-orbit trajectory profile was calculated, and it was found that the launch system is capable of delivering 132.1kg of payload to sun synchronous orbit, while returning the SPARTAN to the initial launch site. This result shows that it is feasible to return a scramjet-powered accelerator to its initial launch site, with only a -19kg (-10.0%) reduction in the payload mass-to-orbit. The inclusion of the fly-back of the SPARTAN was found to alter the shape of the ascent trajectory significantly. When the fly-back was included, the first stage was found to initially pitch towards the east, exhibiting a significantly higher first stage-SPARTAN separation point than the optimised trajectory with no fly-back. The SPARTAN was then observed to bank heavily, executing a heading angle change manoeuvre during its acceleration. No altitude raising manoeuvre was observed during this banking acceleration, due to the higher angles of attack while banking resulting in flight at the SPARTAN's maximum dynamic pressure being optimal. When the fly-back was included, the SPARTAN was still observed to perform a pull-up manoeuvre before third stage separation, of a similar magnitude to the pull-up manoeuvre performed with no fly-back. The optimal fly-back of the SPARTAN was found to require the ignition of the scramjet engines, and was observed to exhibit three distinct phases, an initial turn, a boost-skip, and an approach. During the initial turn, the bank angle of the SPARTAN is increased rapidly, in order to manoeuvre the heading angle of the SPARTAN back towards its initial launch site. After this initial turn, the boost-skip phase is initiated, consisting of multiple skipping manoeuvres. These skipping manoeuvres serve both to increase the range of the SPARTAN during its return, minimising the fuel necessary for the fly-back, as well as to improve the specific impulse of the scramjet engines. The scramjet engines were observed to be ignited at the trough of each skip, as soon as the SPARTAN accelerates above the minimum operable Mach number of the C-REST engines. At this point of the skipping manoeuvres, the specific impulse of the scramjet engines is highest, so that igniting the scramjet engines at this point minimises the fuel necessary for the return flight. After the scramjets were ignited a total of three times, three unpowered skips were performed, decreasing in size sequentially. Finally, the skips ceased entirely, beginning a steady descent and approach to the landing site. In total, 257.8kg of fuel was used during the fly-back, 17.2% of the SPARTAN's total fuel mass.

These maximum payload-to-orbit trajectory profiles, which have been calculated using LODESTAR, are non-intuitive, and involve complex trade-offs between the efficiencies of each stage of the launch

CHAPTER 8. CONCLUSIONS

system, as well as the fly-back of the SPARTAN. The design of these optimised flight paths is made possible through the use of the pseudospectral method of optimal control, coupled with accurate propulsion and aerodynamic modelling. These trajectory profiles improve the performance of the launch system, and can assist in directing future design decisions for partially-airbreathing, multi-stage launch systems. Particularly of interest is the optimal pull-up of the SPARTAN, before the release of the third stage. This pull-up, as well as increasing payload-to-orbit, significantly lowers the dynamic pressures experienced by the third stage rocket, an important factor when designing the thermal protection and structure of the third stage.

Analysis of the sensitivity of the maximum payload-to-orbit trajectory to variations in key design parameters of the launch system.

Eight key design parameters of the launch system were modified, and the sensitivities of the maximum payload-to-orbit trajectory were studied. The parameters varied were: the maximum dynamic pressure of the SPARTAN, the fuel mass within the SPARTAN, the drag of the SPARTAN, the specific impulse of the SPARTAN, the mass of the SPARTAN, the drag of the third stage, the specific impulse of the third stage, and the mass of the third stage. These parameters were varied for trajectories both with, and without, SPARTAN fly-back. It was found that in the cases with no fly-back, the ability of the first stage to pitch, determined by the acceleration of the launch system, is the primary driver of the first stage-SPARTAN separation conditions. The first stage-SPARTAN separation altitude was observed to decrease when the first stage accelerated more slowly, due to the better pitching ability of the first stage. However, this trend was not generally observed when the fly-back of the SPARTAN was included. The disappearance of this trend indicates that when the fly-back of the SPARTAN is included, the first stage-SPARTAN separation point is determined by a more complex trade-off, involving the banking and manoeuvrability of the SPARTAN. When the efficiency of the SPARTAN was increased, the efficiency of the third stage was also observed to increase. This increased efficiency trend was due to the increased velocity at the SPARTAN-third stage separation point, which improves the propulsive efficiency of the third stage rocket. Variations in the efficiency of the third stage were found to produce no significant variation in the trajectory of the SPARTAN.

Out of the modified design parameters, it was found that the specific impulse of the third stage had by far the largest effect on the performance of the launch system, varying the payload-to-orbit by 4.6kg for each percent of additional specific impulse. This large sensitivity is due to the particular importance of the specific impulse during the Hohmann transfer, which is significant in determining the final payload mass. The sensitivities of all significantly coupled design parameters were compared, and their relative quantities assessed to provide meaningful insights into the design of the launch system. Of these comparisons, the relationship between the maximum dynamic pressure and the structural mass of the SPARTAN was found to be of particular interest. It was found that the sensitivity of the launch system to the maximum dynamic pressure of the SPARTAN is relatively low,

indicating that it may be advantageous to fly the SPARTAN at a lower maximum dynamic pressure, in order to reduce heat shielding and structural mass. It was found that if the mass of the SPARTAN can be reduced by greater than -26.5kg per -1kPa reduction in maximum dynamic pressure (or -28.4kg per 1kPa when fly-back is included) then a larger payload-to-orbit will be achieved.

This investigation into the sensitivity of the optimised trajectory to variations in the design parameters of the launch system has provided insights into the shape of the optimised trajectory, and allowed the effects of the modified design parameters to be quantified. These findings can be used to predict the maximum payload-to-orbit trajectories of future launch systems, as well as how design changes may affect the performance of the launch system utilised in this study.

CHAPTER 9

RECOMMENDATIONS FOR FUTURE WORK

**XXX I should get way more specific here, will help to clarify why I havent done a full design study
XXX add cavity simulations**

This work on the calculation of a maximum payload-to-orbit trajectory for a rocket-scramjet-rocket launch system was carried out to determine the behaviour and sensitivities of such a launch system, in order to inform future launch vehicle designs. In addition to improvements in the design of the launch system, a number of outstanding research questions were identified during the course of this work. In order to build upon this work and advance our knowledge of reusable, partially-airbreathing launch systems, the following research directions are suggested:

Controllability studies of all three vehicles of the launch system.

During this work, the controls of the vehicles within the launch system were constrained to values which were estimated to represent the realistic control limits of each vehicle. A controllability study of all three stages would improve the accuracy of the vehicle simulation models, and introduce more realistic control limits to the trajectory optimisation. **XXX expand this with more specifics, eg MPC as mentioned in control uncertainty appendix**

Design of a fly-back first stage booster.

During this work, the first stage booster is assumed to be expendable, to enable a simple design process. However, in the future it is likely that the first stage of the launch system will be required to be reusable for the launch system to be economically feasible. As such, a first stage booster must be designed and sized which is capable of accelerating the SPARTAN to operational speeds, as well as returning to the initial launch site after separation at Mach 5.

Cost analysis of the launch system.

A primary driver for a realistic launch system is its overall performance, as a function of payload-

to-orbit, launch flexibility, and launch cost. In order for a new style of launch system to be properly characterised, a bottom-up cost model estimate is necessary. A bottom-up cost model estimate would allow for the primary cost drivers to be identified, down to a subsystem level. This should include an in-depth analysis of the operational needs and economics of running a launch service provider.

Multi-disciplinary design optimisation sizing of the launch system.

During this work, the first and third stages of the launch system were designed around the previously sized SPARTAN vehicle, and the dimensions and performance of the SPARTAN were kept fixed (apart from during sensitivity studies). The development and characterisation of the maximum payload-to-orbit trajectory of the rocket-scramjet-rocket launch system paves the way for a multi-disciplinary design optimisation, of all three stages concurrently. A multi-disciplinary design optimisation of the system would allow the sizing, design, and relative performance of the three stages to be optimised, taking into account the variation in the maximum payload-to-orbit trajectory path.

REFERENCES

- [1] S. O. Forbes-Spyratos, M. P. Kearney, M. K. Smart, and I. H. Jahn. “Trajectory Design of a Rocket-Scramjet-Rocket Multi-Stage Launch System”. In: *Journal of Spacecraft and Rockets* (2018). DOI: [10.2514/1.A34107](https://doi.org/10.2514/1.A34107).
- [2] S. Forbes-Spyratos, M. Kearney, M. Smart, and I. Jahn. “Trajectory design of a rocket-scramjet-rocket multi-stage launch system”. In: *21st AIAA International Space Planes and Hypersonics Technologies Conference, Hypersonics 2017*. Xiamen, China, 2017. ISBN: 9781624104633.
- [3] S. O. Forbes-Spyratos, M. P. Kearney, M. K. Smart, and I. H. Jahn. “Fly-back of a scramjet-powered accelerator”. In: *AIAA Scitech, 2018*. Orlando, FL, 2018. ISBN: 9781624105241. DOI: [10.2514/6.2018-2177](https://doi.org/10.2514/6.2018-2177).
- [4] J. Chai, M. Smart, S. Forbes-Spyratos, and M. Kearney. “Fly Back Booster Design for Mach 5 Scramjet Launch”. In: *68th International Astronautical Congress*. Aelade, Australia, 2017.
- [5] Federal Aviation Administration. *The Annual Compendium of Commercial Space Transportation: 2018*. Tech. rep. January. Washington, DC, 2018, p. 255. URL: https://www.faa.gov/about/office_org/headquarters_offices/ast/media/2018_AST_Compendium.pdf.
- [6] C. Niederstrasser and W. Frick. “Small Launch Vehicles A 2015 State of the Industry Survey”. In: *Proceedings of the 29th Annual AIAA/USU Conference on Small Satellites*. Logan, UT, 2015.
- [7] M. K. Smart and M. R. Tetlow. “Orbital Delivery of Small Payloads Using Hypersonic Air-breathing Propulsion”. In: *Journal of Spacecraft and Rockets* 46.1 (2009), pp. 117–125. ISSN: 0022-4650. DOI: [10.2514/1.38784](https://doi.org/10.2514/1.38784).

REFERENCES

- [8] A. D. Ketsdever, M. P. Young, J. B. Mossman, and A. P. Pancotti. “Overview of Advanced Concepts for Space Access”. In: *Journal of Spacecraft and Rockets* 47.2 (2010), pp. 238–250. ISSN: 0022-4650. DOI: [10.2514/1.46148](https://doi.org/10.2514/1.46148).
- [9] M. Smart. *Scramjet Inlets*. Tech. rep. 9. Defense Technical Information Center, 2010. DOI: [10.2514/5.9781600866609.0447.0511](https://doi.org/10.2514/5.9781600866609.0447.0511).
- [10] F. Curran, J. Hunt, N. Lovell, G. Maggio, and V. Bilardo. “The Benefits of Hypersonic Airbreathing Launch Systems for Access to Space”. In: *39th AIAA/ASME/SAE/ASEE Joint Propulsion Conference and Exhibit* July (2003), pp. 1–14. DOI: [10.2514/6.2003-5265](https://doi.org/10.2514/6.2003-5265). URL: <http://arc.aiaa.org/doi/10.2514/6.2003-5265>.
- [11] J. D. Shaughnessy, S. Z. Pinckney, and J. D. McMinn. “Hypersonic Vehicle Simulation Configuration Model : Winged-Cone Configuration”. In: (1990).
- [12] D. Preller and M. K. Smart. “Reusable Launch of Small Satellites Using Scramjets”. In: *Journal of Spacecraft and Rockets* 54.6 (2017), pp. 1–13. ISSN: 0022-4650. DOI: [10.2514/1.A33610](https://doi.org/10.2514/1.A33610). URL: <https://doi.org/10.2514/1.A33610>.
- [13] Heiser H. H. and D. T. Pratt. *Hypersonic Airbreathing Propulsion*. Washington, D.C: American Institute of Aeronautics and Astronautics, 1994, p. 11. ISBN: 1-56347-035-7. DOI: [10.2514/4.470356](https://doi.org/10.2514/4.470356).
- [14] A. Rao. “A survey of numerical methods for optimal control”. In: *Advances in the Astronautical Sciences* 135 (2009), pp. 497–528. URL: <http://vdol.mae.ufl.edu/ConferencePublications/trajectorySurveyAAS.pdf>.
- [15] J. T. Betts. “Survey of Numerical Methods for Trajectory Optimization”. In: *Journal of Guidance, Control, and Dynamics* 21.2 (1998), pp. 193–207. ISSN: 0731-5090. DOI: [10.2514/2.4231](https://doi.org/10.2514/2.4231).
- [16] *Australia's hypersonic plane for a new space race*. URL: <http://www.bbc.com/future/story/20161117-australias-hypersonic-spaceplane-for-a-new-space-race> (visited on 06/21/2018).
- [17] S. Lewin. *Blue Origin Announces Big 'New Glenn' Rocket for Satellite & Crew Launches*. 2016. URL: <https://www.space.com/34034-blue-origin-new-glenn-rocket-for-satellites-people.html> (visited on 06/21/2018).
- [18] R. Kendall and P. Portanova. *Launch Vehicles Then and Now: 50 Years of Evolution*. 2010. URL: <http://www.aerospace.org/crosslinkmag/spring-2010/launch-vehicles-then-and-now-50-years-of-evolution/> (visited on 06/21/2018).

- [19] H. Pettit. *The galaxy's fastest car*. 2018. URL: <http://www.dailymail.co.uk/sciencetech/article-5361789/Ride-Elon-Musks-Starman-travels-space.html> (visited on 06/21/2018).
- [20] R. D. Launius. "Assessing the legacy of the Space Shuttle". In: *Space Policy* 22.4 (2006), pp. 226–234. ISSN: 02659646. DOI: [10.1016/j.spacepol.2006.08.008](https://doi.org/10.1016/j.spacepol.2006.08.008).
- [21] J. Foust. *SpaceX achievements generate growing interest in reusable launchers*. 2018. URL: <http://spacenews.com/spacex-achievements-generate-growing-interest-in-reusable-launchers/> (visited on 06/21/2018).
- [22] D. Mosher. *SpaceX faces a growing list of competitors in the new space race*. 2018. URL: <https://www.businessinsider.com.au/spacex-elon-musk-competition-companies-rockets-2018-3> (visited on 06/21/2018).
- [23] S. Clark. *Ariane 6 Rocket Holding to Schedule for 2020 Maiden Flight*. 2016. URL: <https://spaceflightnow.com/2016/08/13/ariane-6-rocket-holding-to-schedule-for-2020-maiden-flight/> (visited on 10/06/2018).
- [24] To Challenge SpaceX, Rockets Get Wings. 2016. URL: <http://www.spacesafetymagazine.com/news/to-challenge-spacex-rockets-get-wings/> (visited on 06/21/2018).
- [25] Richard Webb. "Is It Worth It? The Economics of Reusable Space Transportation". In: *ICEAA 2016 International Training Symposium, Bristol, UK* (2016), pp. 1–19.
- [26] S. Clark. *Falcon 9 rocket launching Sunday sports fin upgrade*. 2018. URL: <https://spaceflightnow.com/2017/06/25/falcon-9-rocket-launching-sunday-sports-fin-upgrade/> (visited on 06/21/2018).
- [27] M. Sarigul-Klijn and N. Sarigul-Klijn. "Flight Mechanics of Manned Sub-Orbital Reusable Launch Vehicles with Recommendations for Launch and Recovery". In: *41st Aerospace Sciences Meeting and Exhibit, Aerospace Sciences Meetings*. Reno, NV, 2003.
- [28] M. Gilmour. *Gilmour Space Secures AUD 19 Million to Launch Next-Generation Hybrid Rockets to Space*. 2018. URL: <https://www.gspacetech.com/single-post/2018/09/28/Gilmour-Space-secures-AUD-19-million-to-launch-next-gen-hybrid-rockets> (visited on 10/06/2018).
- [29] Rocket Lab. *Electron*. 2016. URL: <https://www.rocketlabusa.com/electron/> (visited on 11/30/2017).
- [30] Zero2Infinity. *Bloostar*. 2016. URL: <http://www.zero2infinity.space/bloostar/> (visited on 11/30/2017).
- [31] RocketCrafters. *Intrepid-1*. 2017. URL: <http://rocketcrafters.space/products-services/intrepid-launcher-family/intrepid-1/> (visited on 12/01/2017).

REFERENCES

- [32] *China Launches New Rocket*. 2018. URL: <http://www.spacelaunchreport.com/kz.html> (visited on 10/06/2018).
- [33] Vector Space. *Vector Launch Vehicle Family*. 2017. URL: <https://vectorspacesystems.com/technology/> (visited on 12/01/2017).
- [34] M. Kuhn, I. Müller, I. Petkov, B. Oving, A. J. van Kleef, C. J. Verberne, B. Haemmerli, and A. Boiron. “Innovative European Launcher Concept SMILE”. In: *21st AIAA International Space Planes and Hypersonics Technologies Conference* March (2017), pp. 1–14. DOI: [10.2514/6.2017-2441](https://arc.aiaa.org/doi/10.2514/6.2017-2441). URL: <https://arc.aiaa.org/doi/10.2514/6.2017-2441>.
- [35] Firefly. *Firefly*. 2017. URL: <http://www.fireflyspace.com/> (visited on 11/30/2017).
- [36] VirginOrbit. *LauncherOne*. 2017. URL: <https://virginorbit.com/> (visited on 11/30/2017).
- [37] D. Outreach. *DARPA Picks Design for Next-Generation Spaceplane*. 2017. URL: <https://www.darpa.mil/news-events/2017-05-24> (visited on 11/16/2017).
- [38] Orbital Access. *The Orbital 500R*. 2017. URL: <http://www.orbital-access.com/the-orbital-500/> (visited on 12/01/2017).
- [39] M. K. Smart and M. R. Tetlow. “Orbital Delivery of Small Payloads Using Hypersonic Air-breathing Propulsion”. In: *Journal of Spacecraft and Rockets* 46.1 (2009), pp. 117–125. ISSN: 0022-4650. DOI: [10.2514/1.38784](https://arc.aiaa.org/doi/abs/10.2514/1.38784). URL: [http://arc.aiaa.org/doi/abs/10.2514/1.38784](https://arc.aiaa.org/doi/abs/10.2514/1.38784).
- [40] F. S. Billig. “Research on supersonic combustion”. In: *Journal of Propulsion and Power* 9.4 (1993), pp. 499–514. ISSN: 0748-4658. DOI: [10.2514/3.23652](https://arc.aiaa.org/doi/10.2514/3.23652).
- [41] S. Cook and U. Hueter. “NASA’s Integrated Space Transportation Plan 3rd generation reusable launch vehicle technology update”. In: *Acta Astronautica* 53.4-10 (2003), pp. 719–728. ISSN: 00945765. DOI: [10.1016/S0094-5765\(03\)00113-9](https://arc.aiaa.org/doi/10.1016/S0094-5765(03)00113-9).
- [42] E. T. Curran. “Scramjet Engines: The First Forty Years”. In: *Journal of Propulsion and Power* 17.6 (2001), pp. 1138–1148. ISSN: 0748-4658. DOI: [10.2514/2.5875](https://arc.aiaa.org/doi/10.2514/2.5875). URL: [http://arc.aiaa.org/doi/10.2514/2.5875](https://arc.aiaa.org/doi/10.2514/2.5875).
- [43] M. K. Smart. “How Much Compression Should a Scramjet Inlet Do?” In: *AIAA Journal* 50.3 (2012), pp. 610–619. ISSN: 0001-1452. DOI: [10.2514/1.J051281](https://arc.aiaa.org/doi/10.2514/1.J051281). URL: [http://arc.aiaa.org/doi/10.2514/1.J051281](https://arc.aiaa.org/doi/10.2514/1.J051281).
- [44] E. T. Curran. “Scramjet Engines: The First Forty Years”. In: *Journal of Propulsion and Power* 17.6 (2001), pp. 1138–1148. ISSN: 0748-4658. DOI: [10.2514/2.5875](https://arc.aiaa.org/doi/10.2514/2.5875).
- [45] A Paull, R. Stalker, and D Mee. “Thrust Measurements of a Complete Axisymmetric Scramjet in an Impulse Facility”. In: *5th International Space Planes and Hypersonics Conference*. Munich, Germany, 1993.

- [46] E. Curran. *Scramjet Propulsion*. Progress in Astronautics and Aeronautics, 2001. ISBN: 978-1-60086-660-9.
- [47] W. Heiser, D. Pratt, D. Daley, and U. Mehta. *Hypersonic Airbreathing Propulsion*. the American Institute of Aeronautics and Astronautics, 1994. ISBN: 978-1-56347-035-6.
- [48] R. S. Fry. “A Century of Ramjet Propulsion Technology Evolution”. In: *Journal of Propulsion and Power* 20.1 (2004), pp. 27–58. ISSN: 0748-4658. DOI: [10.2514/1.9178](https://doi.org/10.2514/1.9178). URL: <http://arc.aiaa.org/doi/10.2514/1.9178>.
- [49] M Smart. “Scramjets”. In: 3219 (2007).
- [50] D. J. Dalle, S. M. Torrez, J. F. Driscoll, M. a. Bolender, and K. G. Bowcutt. “Minimum-Fuel Ascent of a Hypersonic Vehicle Using Surrogate Optimization”. In: *Journal of Aircraft* 51.6 (2014), pp. 1973–1986. ISSN: 0021-8669. DOI: [10.2514/1.C032617](https://doi.org/10.2514/1.C032617). URL: <http://arc.aiaa.org/doi/10.2514/1.C032617>.
- [51] J. Bradford, J. Olds, R. Bechtel, T. Cormier, and D. Messitt. “Exploration of the design space for the ABLV-GT SSTO reusable launch vehicle”. In: *Space 2000 Conference and Exposition* September (2000). DOI: [doi:10.2514/6.2000-5136](https://doi.org/10.2514/6.2000-5136). URL: <http://dx.doi.org/10.2514/6.2000-5136>.
- [52] D. Dalle, S. Torrez, and J. Driscoll. “Turn Performance of an Air-Breathing Hypersonic Vehicle”. In: *AIAA Atmospheric Flight Mechanics Conference* August (2011). DOI: [10.2514/6.2011-6300](https://doi.org/10.2514/6.2011-6300). URL: <http://arc.aiaa.org/doi/10.2514/6.2011-6300>.
- [53] J. C. Blair, R. S. Ryan, L. a. Schutzenhofer, and W. R. Humphries. *Launch Vehicle Design Process : Integration , Technical and Lessons Learned*. Tech. rep. May. NASA STI Program Office, 2001.
- [54] R. W. Staufenbiel. “Second-Stage Trajectories of Air-Breathing Space Planes”. In: 27.6 (2000), pp. 618–622.
- [55] B. M. Hellman. *Comparison of Return to Launch Site Options for a Reusable Booster Stage*. Tech. rep. Space Sytems Design Lab, Georgia Institute of technology, 2005, pp. 1–18.
- [56] M. R. Tetlow, U. M. Sch-ograve, Ttle, and G. M. Schneider. “Comparison of Glideback and Flyback Boosters”. In: *Journal of Spacecraft and Rockets* 38.5 (1992), pp. 752–758. ISSN: 0022-4650. DOI: [10.2514/2.3742](https://doi.org/10.2514/2.3742). URL: <http://dx.doi.org/10.2514/2.3742>.
- [57] N. A.-s. Plane. “The National Aero-Space Plane”. In: () .
- [58] J. D. Shaughnessy, S. Z. Pinckney, and J. D. McMinn. “NASA Technical Memorandum Hypersonic Vehicle Simulation Configuration Model :” in: *Simulation* (1990).

REFERENCES

- [59] R. W. Powell, J. D. Shaughnessy, C. I. Cruz, and J. C. Naftel. “Ascent performance of an air-breathing horizontal-takeoff launch vehicle”. In: *Journal of Guidance, Control, and Dynamics* 14.4 (1991), pp. 834–839. ISSN: 0731-5090. DOI: [10.2514/3.20719](https://doi.org/10.2514/3.20719).
- [60] P. Lu. “Inverse dynamics approach to trajectory optimization for an aerospace plane”. In: *Journal of Guidance, Control, and Dynamics* 16.4 (1993), pp. 726–732. ISSN: 0731-5090. DOI: [10.2514/3.21073](https://doi.org/10.2514/3.21073). URL: <http://arc.aiaa.org/doi/abs/10.2514/3.21073>.
- [61] L. van den Aberleen. *Spaceplane HERMES: Europe's Dream of Independent Manned Spaceflight Luc van den Abeelen*. Cham, Switzerland: Springer, 2017, pp. 176–179. ISBN: 9783319444703.
- [62] C. R. McClinton, V. L. Rausch, R. J. Shaw, U. Metha, and C. Naftel. “Hyper-X: Foundation for future hypersonic launch vehicles”. In: *Acta Astronautica* 57.2-8 (2005), pp. 614–622. ISSN: 00945765. DOI: [10.1016/j.actaastro.2005.03.061](https://doi.org/10.1016/j.actaastro.2005.03.061).
- [63] J. M. Roche and D. N. Kosareo. *Structural Sizing of a 25000-Lb Payload , Air-Breathing Launch Vehicle for Single-Stage-To-Orbit*. Tech. rep. January 2001. 2000.
- [64] C. Trefny. “An Air-Breathing Concept Launch Vehicle for Single-Stage-to-Orbit”. In: *35th Joint Propulsion Conference and Exhibit*. May. Los Angeles, CA, 1999. DOI: [10.2514/6.1999-2730](https://doi.org/10.2514/6.1999-2730).
- [65] D. Young, T. Kokan, C. Tanner, I. Clark, C. Tanner, and A. Wilhite. “Lazarus: A SSTO Hypersonic Vehicle Concept Utilizing RBCC and HEDM Propulsion Technologies”. In: *14th AIAA/AHI Space Planes and Hypersonic Systems and Technologies Conference*. 2006, pp. 1–15. ISBN: 978-1-62410-050-5. DOI: [10.2514/6.2006-8099](https://doi.org/10.2514/6.2006-8099). URL: <http://arc.aiaa.org/doi/10.2514/6.2006-8099>.
- [66] J. Olds, J. Bradford, A. Charania, L. Ledsinger, D. McCormick, and K. Sorensen. “Hyperion - An SSTO vision vehicle concept utilizing rocket-based combined cycle propulsion”. In: (2013). DOI: [10.2514/6.1999-4944](https://doi.org/10.2514/6.1999-4944).
- [67] J. R. Olds and P. X. Bellini. “AIAA 98-1557 Argus , a Highly Reusable SSTO Rocket- Based Combined Cycle Launch Vehicle with Maglifter Launch Assist Georgia Institute of Technology Atlanta , GA AIAA 8th International Space Planes and Hypersonic Systems and Technologies Conference April ”. In: (1998).
- [68] J. Olds and I. Budianto. “Constant Dynamic Pressure Trajectory Simulation with POST”. In: *Aerospace Sciences Meeting & Exhibit*. Reno, NV, 1998, pp. 1–13. DOI: [10.2514/6.1998-302](https://doi.org/10.2514/6.1998-302). URL: <http://citeseerx.ist.psu.edu/viewdoc/download?doi=10.1.1.25.6506&rep=rep1&type=pdf>.

- [69] F. Pescetelli, E. Minisci, C. Maddock, I. Taylor, and R. Brown. “Ascent Trajectory Optimisation for a Single-Stage-to-Orbit Vehicle with Hybrid Propulsion”. In: *18th AIAA/3AF International Space Planes and Hypersonic Systems and Technologies Conference*. September. 2012, pp. 1–18. ISBN: 978-1-60086-931-0. DOI: [10.2514/6.2012-5828](https://doi.org/10.2514/6.2012-5828). URL: <http://arc.aiaa.org/doi/abs/10.2514/6.2012-5828>.
- [70] E. Mooij. *Modeling and Optimization in Space Engineering*. Springer, 2019.
- [71] A. W. Wilhite, W. C. Engelund, D. O. Stanley, and J. C. Naftel. “Technology and staging effects on two-stage-to-orbit systems”. In: *Journal of Spacecraft and Rockets* 31.1 (1991), pp. 31–39. ISSN: 0022-4650. DOI: [10.2514/3.26399](https://doi.org/10.2514/3.26399).
- [72] T. Tsuchiya and T. Mori. “Optimal Design of Two-Stage-To-Orbit Space Planes with Air-breathing Engines”. In: *Journal of Spacecraft and Rockets* 42.1 (2005), pp. 90–97. ISSN: 0022-4650. DOI: [10.2514/1.8012](https://doi.org/10.2514/1.8012).
- [73] T. Fujikawa, T. Tsuchiya, and S. Tomioka. “Multidisciplinary Design Optimization of a Two-Stage-to-Orbit Reusable Launch Vehicle with Ethanol-Fueled Rocket-Based Combined Cycle Engines”. In: *Transactions of the Japan Society for Aeronautical and Space Sciences* 60.5 (2017), pp. 265–275. ISSN: 0549-3811. DOI: [10.2322/tjsass.60.265](https://doi.org/10.2322/tjsass.60.265).
- [74] U. B. Mehta and J. V. Bowles. “Two-Stage-to-Orbit Spaceplane Concept with Growth Potential”. In: *Journal of Propulsion and Power* 17.6 (2001), pp. 1149–1161. ISSN: 0748-4658. DOI: [10.2514/2.5886](https://doi.org/10.2514/2.5886).
- [75] S. Takahashi, K. Mizobata, and K. Sawada. “Conceptual Study of a Two-Stage, Air-Breathing Reusable Launch Vehicle”. In: *Journal of Spacecraft and Rockets* 34.5 (1997), pp. 628–635. ISSN: 0022-4650. DOI: [10.2514/2.3280](https://doi.org/10.2514/2.3280).
- [76] B. S. Germain, J. R. Olds, J. McIntire, D. Nelson, J. Weglian, and L. Ledsinger. “AIAA 2001-3516 Starsaber : A Small Payload-Class TSTO Vehicle Concept Utilizing Rocket-Based Combined Cycle Propulsion Georgia Institute of Technology 37 th AIAA / ASME / SAE / ASEE Joint Propulsion Conference And Exhibit Salt Lake City , Utah”. In: *Earth* July (2001).
- [77] D. Eklund. “Quicksat: A Two Stage to Orbit Reusable Launch Vehicle Utilizing Air Breathing Propulsion for Responsive Space Access”. In: September (2012), pp. 1–20. DOI: [10.2514/6.2004-5950](https://doi.org/10.2514/6.2004-5950).
- [78] J. E. Bradford, a Charania, J. R. Olds, M. Graham, S. Engineering, and U. S. a. Ga. “XCALIBUR : A VERTICAL TAKEOFF TSTO RLV CONCEPT WITH A HEDM UPPERSTAGE AND A SCRAM-ROCKET BOOSTER 53rd International Astronautical Congress The World Space Congress - 2002 10-19 Oct 2002 / Houston , Texas”. In: *Director* (2002).

REFERENCES

- [79] F. Space and T. Systems. “Stage Separation Aerodynamics of Future Space Transport Systems Stage Separation Aerodynamics of Future Space Transport Systems”. PhD thesis. Technischen Universität München, 2006.
- [80] K. Kudo and T. Kanda. “Staging of Two-Stage-to-Orbit Aerospace Plane”. In: *Transactions of the Japan Society for Aeronautical and Space Sciences* 48.161 (2005), pp. 129–134. ISSN: 0549-3811. DOI: [10.2322/tjsass.48.129](https://doi.org/10.2322/tjsass.48.129).
- [81] T Kimura and K Sawada. “Three-Stage Launch System with Scramjets”. In: *Journal of Spacecraft and Rockets* 36.5 (1999), pp. 675–680. ISSN: 00224650. DOI: [10.2514/2.3500](https://doi.org/10.2514/2.3500).
- [82] D. Preller. “Multidisciplinary Design and Optimisation of a Pitch Trimmed Hypersonic Airbreathing Accelerating Vehicle”. Ph.D Dissertation. The University of Queensland, 2018.
- [83] T. Jazra, D. Preller, and M. K. Smart. “Design of an Airbreathing Second Stage for a Rocket-Scramjet-Rocket Launch Vehicle”. In: *Journal of Spacecraft and Rockets* 50.2 (2013), pp. 411–422. ISSN: 0022-4650. DOI: [10.2514/1.A32381](https://doi.org/10.2514/1.A32381). URL: <http://arc.aiaa.org/doi/abs/10.2514/1.A32381>.
- [84] T. Jazra. “Optimisation of Hypersonic Vehicles for Airbreathing Propulsion”. In: November (2010).
- [85] T. Ferguson. “Small Satellite Separation from a Hypersonic Airbreathing Vehicle”. PhD thesis. The University of Queensland, 2009.
- [86] N. D. Moshman and R. J. Proulx. “Range Improvements in Gliding Reentry Vehicles from Thrust Capability”. In: *Journal of Spacecraft and Rockets* 51.5 (2014), pp. 1681–1694. ISSN: 0022-4650. DOI: [10.2514/1.A32764](https://doi.org/10.2514/1.A32764). URL: <http://arc.aiaa.org/doi/10.2514/1.A32764>.
- [87] C. L. Darby, W. W. Hager, and A. V. Rao. “Direct Trajectory Optimization Using a Variable Low-Order Adaptive Pseudospectral Method”. In: *Journal of Spacecraft and Rockets* 48.3 (2011), pp. 433–445. ISSN: 0022-4650. DOI: [10.2514/1.52136](https://doi.org/10.2514/1.52136).
- [88] F. Toso, A. Riccardi, E. Minisci, C. Maddock, and Ristie. “Optimisation of ascent and descent trajectories for lifting body space access vehicles”. In: *66th International Astronautical Congress*. Jerusalem, 2015.
- [89] D. Chai, Y. W. Fang, Y. L. Wu, and S. H. Xu. “Boost-skipping trajectory optimization for air-breathing hypersonic missile”. In: *Aerospace Science and Technology* 46 (2015), pp. 506–513. ISSN: 12709638. DOI: [10.1016/j.ast.2015.09.004](https://doi.org/10.1016/j.ast.2015.09.004). URL: <http://dx.doi.org/10.1016/j.ast.2015.09.004>.

- [90] H. J. Pesch. “Neighboring Optimum Guidance of a Space-Shuttle-Orbiter-Type Vehicle”. In: *Journal of Guidance, Control, and Dynamics* 3.5 (1980), pp. 386–391. ISSN: 0731-5090. DOI: [10.2514/3.56011](https://doi.org/10.2514/3.56011). URL: <http://arc.aiaa.org/doi/abs/10.2514/3.56011>.
- [91] B. A. J. Eggers, H. J. Allen, and S. E. Neice. *A Comparative Analysis of the Performance of Long-Range Hypervelocity Vehicles*. Tech. rep. October. Ames Aeronautical Society, 1957.
- [92] T. Kanda and T. Hiraiwa. “Evaluation of Effectiveness of Periodic Flight by a Hypersonic Vehicle”. In: *Journal of Aircraft* 44.6 (2007), pp. 2076–2077. ISSN: 0021-8669. DOI: [10.2514/1.31143](https://doi.org/10.2514/1.31143).
- [93] R Bulirsch, E Nerz, H. J. Pesch, and O von Stryk. “Combining direct and indirect methods in optimal control: Range maximization of a hang glider”. In: *Optimal Control (Calculus of Variations, Optimal Control Theory and Numerical Methods)* 111 (1993), pp. 273–288.
- [94] O. Stryk and R. Bulirsch. “Direct and indirect methods for trajectory optimization”. In: *Annals of Operations Research* 37 (1992), pp. 357–373. ISSN: 0254-5330. DOI: [10.1007/BF02071065](https://doi.org/10.1007/BF02071065).
- [95] M. S. Bazaraa, H. D. Sherali, and C. M. Shetty. *Nonlinear Programming: Theory and Algorithms*. John Wiley & Sons, 2013.
- [96] P. Boggs and J. Tolle. “Sequential quadratic programming for large-scale nonlinear optimization”. In: *Journal of Computational and Applied Mathematics* 124.1-2 (2000), pp. 123–137. ISSN: 03770427. DOI: [10.1016/S0377-0427\(00\)00429-5](https://doi.org/10.1016/S0377-0427(00)00429-5). URL: <http://linkinghub.elsevier.com/retrieve/pii/S0377042700004295> \$ \backslash backslash \\$ n http://www.sciencedirect.com/science/article/pii/S0377042700004295.
- [97] M. P. Kelly. “Transcription Methods for Trajectory Optimization A beginners tutorial”. In: *Arxiv* (2015), pp. 1–14.
- [98] G. Fasano and J. Pinter. *Modelling and Optimisation in Space Engineering*. New York, NY: Springer, 2013. DOI: [10.1007/978-1-4614-4469-5](https://doi.org/10.1007/978-1-4614-4469-5).
- [99] D. Jezewski. “An Optimal, Analytic Solution to the Linear-Gravity, Constant-Thrust Trajectory Problem”. In: *Journal of Spacecraft and Rockets* July (1971), pp. 793–796.
- [100] C. A. Maddock, L. Ricciardi, M. West, J. West, K. Kontis, S. Rengarajan, D. Evans, A. Milne, and S. McIntyre. “Conceptual design analysis for a two-stage-to-orbit semi-reusable launch system for small satellites”. In: *Acta Astronautica* 152.August (2018), pp. 782–792. ISSN: 00945765. DOI: [10.1016/j.actaastro.2018.08.021](https://doi.org/10.1016/j.actaastro.2018.08.021). URL: <https://doi.org/10.1016/j.actaastro.2018.08.021>.

REFERENCES

- [101] I. M. Ross and F. Fahroo. “Pseudospectral Knotting Methods for Solving Nonsmooth Optimal Control Problems”. In: *Journal of Guidance, Control, and Dynamics* 27.3 (2004), pp. 397–405. ISSN: 0731-5090. DOI: [10.2514/1.3426](https://doi.org/10.2514/1.3426).
- [102] F. Fahroo and I. Ross. “Direct trajectory optimization by a Chebyshev pseudospectral method”. In: *Proceedings of the 2000 American Control Conference*. Chicago, IL, 2000, pp. 3860–3864. ISBN: 0-7803-5519-9. DOI: [10.1109/ACC.2000.876945](https://doi.org/10.1109/ACC.2000.876945).
- [103] H.-O. Kreiss and J. Oliger. “Comparison of accurate methods for the integration of hyperbolic equations”. In: *Tellus A* 1971 (1972). ISSN: 0280-6495. DOI: [10.3402/tellusa.v24i3.10634](https://doi.org/10.3402/tellusa.v24i3.10634).
- [104] C. L. Darby, W. W. Hager, and A. V. Rao. “An hp-adaptive pseudospectral method for solving optimal control problems”. In: *Optimal Control Applications and Methods* 32.3 (2011), pp. 476–502. DOI: [10.1002/oca.957](https://doi.wiley.com/10.1002/oca.957). URL: <http://doi.wiley.com/10.1002/oca.957>.
- [105] G. Huntington, D. Benson, and A. Rao. “A Comparison of Accuracy and Computational Efficiency of Three Pseudospectral Methods”. In: *AIAA Guidance, Navigation and Control Conference and Exhibit* (2007), pp. 1–43. DOI: [10.2514/6.2007-6405](https://doi.org/10.2514/6.2007-6405). URL: <http://arc.aiaa.org/doi/abs/10.2514/6.2007-6405> <http://arc.aiaa.org/doi/pdf/10.2514/6.2007-6405>.
- [106] D. Garg, W. W. Hager, and A. V. Rao. “Pseudospectral Methods for Solving Infnite-Horizon Optimal Control Problems”. In: *Automatica* 47.4 (2011), pp. 829–837.
- [107] D Garg, M. Patterson, and W. Hager. “An Overview of Three Pseudospectral Methods for the Numerical Solution of Optimal Control Problems”. In: *Advances in thAstronautical Sciences* 135 (2009), pp. 1–17. URL: <http://vdol.mae.ufl.edu/ConferencePublications/unifiedFrameworkAAS.pdf>.
- [108] Q. Gong, I. M. Ross, and F. Fahroo. “Costate Computation by a Chebyshev Pseudospectral Method”. In: *Journal of Guidance, Control, and Dynamics* 33.2 (2010), pp. 623–628. ISSN: 0731-5090. DOI: [10.2514/1.45154](https://doi.org/10.2514/1.45154).
- [109] F. Fahroo and I. M. Ross. “Costate Estimation by a Legendre Pseudospectral Method”. In: *Journal of Guidance, Control, and Dynamics* 24.2 (2001), pp. 270–277. ISSN: 0731-5090. DOI: [10.2514/2.4709](https://doi.org/10.2514/2.4709).
- [110] N. Bedrossian, B. Technologies, and L. N. Nasa. “Zero Propellant Maneuvre Flight Results For 180 Degree ISS Rotation”. In: *20th International Symposium on Space Flight Dynamics*. Annapolis, MD, 2007.

- [111] H. Li, R. Zhang, Z. Li, and R. Zhang. “Footprint problem with angle of attack optimization for high lifting reentry vehicle”. In: *Chinese Journal of Aeronautics* 25.2 (2012), pp. 243–251. ISSN: 10009361. DOI: [10.1016/S1000-9361\(11\)60384-1](https://doi.org/10.1016/S1000-9361(11)60384-1). URL: [http://dx.doi.org/10.1016/S1000-9361\(11\)60384-1](http://dx.doi.org/10.1016/S1000-9361(11)60384-1).
- [112] S. Josselyn and I. M. Ross. “Rapid Verification Method for the Trajectory Optimization of Reentry Vehicles”. In: *Notes* 26.3 (2002), pp. 505–508. ISSN: 0731-5090. DOI: [10.2514/2.5074](https://doi.org/10.2514/2.5074).
- [113] J. Zhao and R. Zhou. “Reentry trajectory optimization for hypersonic vehicle satisfying complex constraints”. In: *Chinese Journal of Aeronautics* 26.6 (2013), pp. 1544–1553. ISSN: 10009361. DOI: [10.1016/j.cja.2013.10.009](https://doi.org/10.1016/j.cja.2013.10.009). URL: <http://dx.doi.org/10.1016/j.cja.2013.10.009>.
- [114] B. Tian and Q. Zong. “Optimal guidance for reentry vehicles based on indirect Legendre pseudospectral method”. In: *Acta Astronautica* 68.7-8 (2011), pp. 1176–1184. ISSN: 00945765. DOI: [10.1016/j.actaastro.2010.10.010](https://doi.org/10.1016/j.actaastro.2010.10.010). URL: <http://linkinghub.elsevier.com/retrieve/pii/S0094576510003899>.
- [115] S. T.U. I. Rizvi, L. S. He, and D. J. Xu. “Optimal trajectory and heat load analysis of different shape lifting reentry vehicles for medium range application”. In: *Defence Technology* 11.4 (2015), pp. 350–361. ISSN: 22149147. DOI: [10.1016/j.dt.2015.06.003](https://doi.org/10.1016/j.dt.2015.06.003). URL: <http://dx.doi.org/10.1016/j.dt.2015.06.003>.
- [116] S. Yang, T. Cui, X. Hao, and D. Yu. “Trajectory optimization for a ramjet-powered vehicle in ascent phase via the Gauss pseudospectral method”. In: *Aerospace Science and Technology* 67 (2017), pp. 88–95. ISSN: 12709638. DOI: [10.1016/j.ast.2017.04.001](https://doi.org/10.1016/j.ast.2017.04.001). URL: <http://dx.doi.org/10.1016/j.ast.2017.04.001>.
- [117] M. Kodera, H. Ogawa, S. Tomioka, and S. Ueda. “Multi-Objective Design and Trajectory Optimization of Space Transport Systems with RBCC Propulsion via Evolutionary Algorithms and Pseudospectral Methods”. In: *52nd Aerospace Sciences Meeting January* (2014), pp. 1–14. DOI: [10.2514/6.2014-0629](https://doi.org/10.2514/6.2014-0629). URL: <http://arc.aiaa.org/doi/10.2514/6.2014-0629>.
- [118] Astos Solutions. *Astos Solutions*. 2018. URL: <https://www.astos.de/> (visited on 07/24/2018).
- [119] A. V. Rao, D. a. Benson, C. Darby, M. a. Patterson, C. Francolin, I. Sanders, and G. T. Huntington. “Algorithm 902”. In: *ACM Transactions on Mathematical Software* 37.2 (2010), pp. 1–39. ISSN: 00983500. DOI: [10.1145/1731022.1731032](https://doi.org/10.1145/1731022.1731032).
- [120] Y. Nie, O. Faqir, and E. Kerrigan. *ICLOCS2*. 2018. URL: <http://www.ee.ic.ac.uk/ICLOCS/> (visited on 07/24/2018).

REFERENCES

- [121] a Wächter and L. T. Biegler. *On the Implementation of a Primal-Dual Interior Point Filter Line Search Algorithm for Large-Scale Nonlinear Programming*. Vol. 106. 1. 2006, pp. 25–57. ISBN: 1010700405.
- [122] T. Lipp and S. Boyd. “Minimum-time speed optimisation over a fixed path”. In: *International Journal of Control* 87.January 2015 (2014), pp. 1297–1311. ISSN: 0020-7179. DOI: [10.1080/00207179.2013.875224](https://doi.org/10.1080/00207179.2013.875224). URL: <http://www.tandfonline.com/doi/abs/10.1080/00207179.2013.875224>.
- [123] I. M. Ross and F Fahroo. “A direct method for solving nonsmooth optimal control problems”. In: *Proceedings of the 2002 {IFAC World Congress}* (2002).
- [124] P. E. Rutquist and M. M. Edvall. “PROPT - Matlab Optimal Control Software”. In: *Tomlab Optimization Inc* 260 (2010), pp. –.
- [125] W. Colson. *Program to Optimize Simulated Trajectories 2*. 2017. URL: <https://post2.larc.nasa.gov/> (visited on 07/24/2018).
- [126] R. Falck. *OTIS*. 2016. URL: <https://otis.grc.nasa.gov/index.html> (visited on 07/24/2018).
- [127] D. Wassel, F. Wolff, J. Vogelsang, and C. Büskens. “the Esa Nlp-Solver Worhp Recent Developments and Applications”. In: *Modeling and Optimization in Space Engineering* (2013).
- [128] B Houska, H. Ferrau, and M. Diehl. “ACADO Toolkit – An Open Source Framework for Automatic Control and Dynamic Optimization”. In: *Optimal Control Applications and Methods* 32.3 (2011), pp. 298–312.
- [129] *JModelica.org*. URL: <https://jmodelica.org/> (visited on 07/24/2018).
- [130] C. Rosema, J. Doyle, L. Auman, M. Underwood, and W. B. Blake. *Missile DATCOM User’s Manual - 2011 Revision*. Tech. rep. Army Aviation and Missile Research Development, 2011. DOI: [10.21236/ad1000581](https://doi.org/10.21236/ad1000581).
- [131] D. Kinney. “Aero-Thermodynamics for Conceptual Design”. In: *42nd AIAA Aerospace Sciences Meeting and Exhibit*. January. Reno, NV, 2004, pp. 1–11. ISBN: 978-1-62410-078-9. DOI: [10.2514/6.2004-31](https://doi.org/10.2514/6.2004-31). URL: <http://www.aric.or.kr/treatise/journal/content.asp?idx=53932>.
- [132] U Reisch and Y Anseaume. *Validation of the Approximate Calculation Procedure HOTSOSE For Aerodynamic and Thermal Loads in Hypersonic Flow with Existing Experimental and Numerical Results*. Tech. rep. DLR-Forschungsbericht, 1998.
- [133] T. Eggers. “Aerodynamic Analysis of the Dual-Mode Ramjet Vehicle JAPHAR”. In: *Notes on Numerical Fluid Mechanics and Multidisciplinary Design*. Vol. 115. 2011, pp. 137–140. ISBN: 9783642177699.

- [134] M. J. Aftosmis, M. J., Berger and G. Adomavicius. “A Parallel Multilevel Method for Adaptively Refined Cartesian Grids with Embedded Boundaries”. In: *38th Aerospace Sciences Meeting and Exhibit*. Reno NV, 2000. DOI: [10.2514/6.2000-808](https://doi.org/10.2514/6.2000-808).
- [135] F. Manual, R. T. Biedron, J. M. Derlaga, P. A. Gnoffo, D. P. Hammond, W. T. Jones, B. Kleb, E. M. Lee-rausch, E. J. Nielsen, M. A. Park, C. L. Rumsey, J. L. Thomas, and W. A. Wood. *FUN3D Manual: 13.3*. Tech. rep. February. Langley Research Center, Hampton, Virginia: NASA, 2018.
- [136] NASA Glenn Research Center. *Euler Equations*. URL: <https://www.grc.nasa.gov/WWW/k-12/airplane/eulereqs.html> (visited on 07/24/2018).
- [137] D. Almosnino. “A Low Subsonic Study of the NASA N2A Hybrid Wing-Body Using an Inviscid Euler-Adjoint Solver”. In: *34th AIAA Applied Aerodynamics Conference* June (2016), pp. 1–18. DOI: [doi:10.2514/6.2016-3267](https://doi.org/10.2514/6.2016-3267). URL: <http://dx.doi.org/10.2514/6.2016-3267>.
- [138] A. D. Ward, M. K. Smart, and R. J. Gollan. “Development of a Rapid Inviscid/Boundary-Layer Aerodynamics Tool”. In: *22nd AIAA International Space Planes and Hypersonics Systems and Technologies Conference*. September. Orlando, FL, 2018, pp. 1–14. ISBN: 978-1-62410-577-7. DOI: [10.2514/6.2018-5270](https://doi.org/10.2514/6.2018-5270). URL: <https://arc.aiaa.org/doi/10.2514/6.2018-5270>.
- [139] R Gollan and P Jacobs. “About the formulation, verification and validation of the hypersonic flow solver Eilmser”. In: *International Journal for Numerical Methods in Fluids* 73 (2013). ISSN: 02712091. DOI: [10.1002/fld](https://doi.org/10.1002/fld). arXiv: [fld.1 \[DOI: 10.1002\]](https://arxiv.org/abs/1307.0001).
- [140] Ansys. *Fluent Bruchure*. Tech. rep. Ansys, 2014, p. 2. URL: <http://ansys.com/staticassets/ANSYS/staticassets/resourcelibrary/brochure/ansys-fluent-brochure-14.0.pdf>.
- [141] AEA Technology. *Itroduction to CFX-TASCflow*. URL: <http://hmf.enseeiht.fr/travaux/CD0102/travaux/optmfn/micp/reports/s19cfx2/pages/frame2.htm> (visited on 10/05/2018).
- [142] COMSOL. *Product: CFD Module*. URL: <https://www.comsol.com/cfd-module\#cfds-software> (visited on 10/05/2018).
- [143] D. Schwamborn, T. Gerhold, and R. Heinrich. “The DLR TAU-Code: Recent Applications in Research and Industry”. In: *European Conference on Computational Fluid Dynamics, EC-COMAS CFD 2006* (2006), pp. 1–25.
- [144] The OpenFOAM Foundation. *OpenFOAM*. URL: <https://openfoam.org/> (visited on 10/06/2018).

REFERENCES

- [145] C. Segal. *The Scramjet Engine: Processes and Characteristics*. Cambridge, UK: Cambridge University Press, 2009, p. 229. ISBN: 9780521838153.
- [146] D. G. Sagerman, M. P. Rumpfkeil, B. M. Hellman, and N. Dasque. “Comparisons of Measured and Modeled Aero-thermal Distributions for Complex Hypersonic Configurations”. In: *55th AIAA Aerospace Sciences Meeting January* (2017), pp. 1–22. DOI: [10.2514/6.2017-0264](https://doi.org/10.2514/6.2017-0264). URL: <http://arc.aiaa.org/doi/10.2514/6.2017-0264>.
- [147] D. Abeynayake and A. Agon. “Comparison of computational and semi-empirical aerodynamics tools for making fit-for-purpose modelling decisions”. In: *20th International Congress on Modelling and Simulation*. Adelaide, Australia, 2013, pp. 1–6.
- [148] M. J. Aftosmis, M. Nemec, and S. E. Cliff. “Adjoint-based low-boom design with Cart3D”. In: *29th AIAA Applied Aerodynamics Conference 2011*. June. 2011, pp. 1–17. ISBN: 9781624101458. DOI: [doi:10.2514/6.2011-3500](https://doi.org/10.2514/6.2011-3500). URL: <http://www.scopus.com/inward/record.url?eid=2-s2.0-84872373928&partnerID=tZ0tx3y1>.
- [149] D Almosnino. “Assessment of an inviscid euler-adjoint solver for prediction of aerodynamic characteristics of the NASA HL-20 lifting body”. In: *34th AIAA Applied Aerodynamics Conference, 2016 June* (2016). DOI: [10.2514/6.2016-3266](https://doi.org/10.2514/6.2016-3266). URL: <https://www.scopus.com/inward/record.uri?eid=2-s2.0-84980371959&partnerID=40&md5=1b304aabaaad2976daf4d0742d5bdc6ba>.
- [150] U. Mehta, M. Aftosmis, J. Bowles, and S. Pandya. “Skylon Aerospace Plane and Its Aerodynamics and Plumes”. In: *Journal of Spacecraft and Rockets* 53.2 (2016), pp. 340–353. ISSN: 0022-4650. DOI: [10.2514/1.A33408](https://doi.org/10.2514/1.A33408). URL: <http://arc.aiaa.org/doi/10.2514/1.A33408>.
- [151] R. Kimmel, D. Adamczak, K Berger, and M Choudhari. “HIFiRE-5 flight vehicle design”. In: *AIAA paper July* (2010), pp. 1–17. DOI: [10.2514/6.2010-4985](https://doi.org/10.2514/6.2010-4985). URL: <http://arc.aiaa.org/doi/pdf/10.2514/6.2010-4985>.
- [152] R. Gomez, D. Vicker, S. Rogers, M. Aftosmis, W. Chan, R. Meakin, S. Murman, and S. Murman. “STS-107 Investigation Ascent CFD Support”. In: *34th AIAA Fluid Dynamics Conference and Exhibit* (2004), pp. 1–15. DOI: [10.2514/6.2004-2226](https://doi.org/10.2514/6.2004-2226). URL: <http://arc.aiaa.org/doi/10.2514/6.2004-2226>.
- [153] M Suraweera and M. K. Smart. “Shock Tunnel Experiments with a Mach 12 {REST} Scramjet at Off-Design Conditions”. In: *Journal of Propulsion and Power* 25.3 (2009), pp. 555–564. ISSN: 0748-4658. DOI: [10.2514/1.37946](https://doi.org/10.2514/1.37946).

- [154] M. K. Smart and E. G. Ruf. “Free-jet testing of a {REST} scramjet at off-design conditions”. In: *Collection of Technical Papers - 25th AIAA Aerodynamic Measurement Technology and Ground Testing Conference* AIAA 2006-2955 (2006), pp. 190–201. DOI: [doi:10.2514/6.2006-2955](https://doi.org/10.2514/6.2006-2955).
- [155] NASA. *U.S. Standard Atmosphere, 1976*. U.S. Government Printing Office, Washington, D.C., 1976, pp. 1–243. URL: <http://ntrs.nasa.gov/archive/nasa/casi.ntrs.nasa.gov/19770009539.pdf>.
- [156] J. W. MacColl. “The Conical Shock Wave Formed by a Cone Moving at a High Speed”. In: *Proceedings of the Royal Society A: Mathematical, Physical and Engineering Sciences* 159.898 (1937), pp. 459–472. ISSN: 1364-5021. DOI: [10.1098/rspa.1937.0083](https://doi.org/10.1098/rspa.1937.0083). URL: <http://rspa.royalsocietypublishing.org/cgi/doi/10.1098/rspa.1937.0083>.
- [157] Pointwise. www.pointwise.com. 2017. URL: <http://www.pointwise.com/> (visited on 02/01/2017).
- [158] S. Pandya, S. Murman, and M. Aftosmis. “Validation of Inlet and Exhaust Boundary Conditions for a Cartesian Method”. In: *22nd Applied Aerodynamics Conference and Exhibit* January (2004), pp. 1–16. ISSN: 10485953. DOI: [10.2514/6.2004-4837](https://doi.org/10.2514/6.2004-4837). URL: <http://arc.aiaa.org/doi/10.2514/6.2004-4837>.
- [159] Desktop Aeronautics. *Specifying Power BCs for Rocket Plumes*. Tech. rep. NASA, pp. 9–11. URL: <https://www.nas.nasa.gov/publications/software/docs/cart3d/pages/howto/howTo_RocketPlumes_08.11.pdf>.
- [160] U. Mehta, M. Aftosmis, J. Bowles, and S. Pandya. “Skylon Aerodynamics and SABRE Plumes”. In: *20th AIAA International Space Planes and Hypersonic Systems and Technologies Conference*. July. Glasgow, Scotland, 2015, pp. 1–21. ISBN: 9781624103209. DOI: [10.2514/6.2015-3605](https://doi.org/10.2514/6.2015-3605).
- [161] Space Exploration technologies. *Falcon 1 Launch Vehicle Payload Users Guide*. Tech. rep. Hawthorne, CA: Space Exploration Technologies, 2008, p. 65.
- [162] M. Wade. *Encyclopedia Astronautica*. 2017. URL: <http://www.astronautix.com/> (visited on 07/24/2018).
- [163] G. Norris. *SpaceX Unveils Plans To Be Worlds Top Rocket Maker*. 2011. URL: <https://web.archive.org/web/20150621134912/http://aviationweek.com/awin/spacex-unveils-plans-be-world-s-top-rocket-maker> (visited on 03/17/2019).
- [164] G. Sutton and O. Biblarz. *Rocket propulsion Elements*. 8th. John Wiley & Sons, 2010, p. 67. ISBN: 978-0470080245. DOI: [10.1017/S0001924000034308](https://doi.org/10.1017/S0001924000034308).

REFERENCES

- [165] J. W. Magee Bruno, T.J., Friend, D. G., Huber, M.L., Laesecke, A., Lemmon, E.W., McLinden, M.O., Perkins, R.A., Baranski, J., Widegren, J.A. *Thermophysical Properties Measurements and Models for Rocket Propellant RP-1: Phase I, NIST- IR 6644, National Institute of Standards and Technology (U.S.)* Tech. rep. 2006.
- [166] International Tungsten Industry Association. *Tungsten Properties*. URL: <https://www.itia.info/tungsten-properties.html> (visited on 10/05/2018).
- [167] E. Fitzer and L. Manocha. *Carbon Reinforcements and Carbon/Carbon Composites*. Berlin, Heidelberg: Springer Berlin Heidelberg, 1998. ISBN: 3-642-58745-3.
- [168] Amorim. *Reinventing Thermal Protection*. Tech. rep. Regency Park SA: Amorim Cork Composites, 2018. URL: <http://pdf.nauticexpo.com/pdf/amorim-cork-composites/tps/39162-105388.html>.
- [169] Rocket lab USA. *Rocket Lab reaches 500 Rutherford engine test fires*. 2018. URL: <https://www.rocketlabusa.com/news/updates/rocket-lab-reaches-500-rutherford-engine-test-fires/>.
- [170] D Huzel and D Huang. *Design of Liquid Propellant Rocket Engines*. American Institute of Aeronautics and Astronautics, 1992, pp. 1–472. ISBN: 1563470136.
- [171] M. a. Patterson, D Ph, A. V. Rao, and D Ph. *GPOPS-II manul: A General-Purpose MATLAB Software for Solving Multiple-Phase Optimal Control Problems Version 2 . 1*. Tech. rep. October. 2015, pp. 1–72.
- [172] R. J. Boain. “A-B-Cs of Sun-Synchronous Orbit Mission Design 14 AAS / AIAA Space Flight Mechanics Conference”. In: *14th AAS/AIAA Space Flight Mechanics Conference* (2004), pp. 1–19.
- [173] R. Simmon. *Three Classes of Orbit*. 2009. URL: <https://earthobservatory.nasa.gov/Features/OrbitsCatalog/page2.php> (visited on 08/22/2018).
- [174] M. Palin. *Australias first commercial space base to launch rockets within a year*. 2017. URL: <https://www.news.com.technology/science/space/australias-first-commercial-space-base-to-launch-rockets-within-a-year/news-story/eb7841c5b39e04fd31302e8b1056e3ab> (visited on 10/05/2018).
- [175] Icao. “World Geodetic System - 1984 (WGS-84) Manual”. In: 1984 (2002), pp. 21–23.
- [176] C. Maddock, F. Toso, L. Ricciardi, A. Mogavero, K. H. Lo, S. Rengarajan, K. Kontis, A. Milne, D. Evans, M. West, and S. McIntyre. “Vehicle and Mission Design of a Future Small Payload Launcher”. In: *21st AIAA International Space Planes and Hypersonics Technologies Conference* March (2017), pp. 1–20. DOI: [10.2514/6.2017-2224](https://arc.aiaa.org/doi/10.2514/6.2017-2224). URL: <https://arc.aiaa.org/doi/10.2514/6.2017-2224>.

- [177] A. Tewari. *Atmospheric and Space Flight Dynamics*. 2007. ISBN: 978-0-8176-4437-6. DOI: [10.1007/978-0-8176-4438-3](https://doi.org/10.1007/978-0-8176-4438-3). URL: <http://link.springer.com/10.1007/978-0-8176-4438-3>.
- [178] J. T. Betts. *Practical Methods for Optimal Control and Estimation Using Nonlinear Programming*. 2nd. New York, NY: Cambridge University Press, 2009. ISBN: 0898716888 9780898716887.
- [179] B Barrar. *An Analytic Proof That the Hohmann-Type Transfer is the True Minimum Tro-Impulse Transfer*. Tech. rep. Fort Belvoir, VA: Defense Technical Information Center, 1962.
- [180] Y. Kawajir, C. D. Laird, and A. Waechter. “Introduction to IPOPT: A tutorial for downloading, installing, and using IPOPT .” In: *Most* (2010), pp. 1–68. ISSN: 00981354. DOI: http://web.mit.edu/ipopt_v3.8/doc/documentation.pdf. arXiv: [arXiv:1011.1669v3](https://arxiv.org/abs/1011.1669v3).
- [181] H. Hindi. “A tutorial on convex optimization II: duality and interior point methods”. In: *2006 American Control Conference 1* (2006), 11 pp. ISSN: 07431619. DOI: [10.1109/ACC.2006.1655436](https://doi.org/10.1109/ACC.2006.1655436). URL: <http://ieeexplore.ieee.org/document/1655436/>.
- [182] P. Pucci and J. B. Serrin. *The maximum principle*. Vol. 73. Springer, 2007, pp. 80–104. ISBN: 978-3-7643-8145-5.
- [183] A. Gilbert, B. Mesmer, and M. D. Watson. “Exergy analysis of rocket systems”. In: *9th Annual IEEE International Systems Conference, SysCon 2015*. Vancouver, British Columbia, Canada, 2015, pp. 283–288. ISBN: 9781479959273. DOI: [10.1109/SYSCON.2015.7116765](https://doi.org/10.1109/SYSCON.2015.7116765).
- [184] J. Anderson. *Hypersonic and high Temperature Gas Dynamics: Second Edition*. American Institute of Aeronautics and Astronautics, 2000.
- [185] D. Dirkx and E. Mooj. *Conceptual Shape Optimization of Entry Vehicles Applied to Capsules and Winged Fuselage Vehicles*. 1st ed. Cham, Switzerland: Springer, 2017, pp. 65–67.
- [186] M. E. Tauber, G. P. Menees, and H. G. Adelman. “Aerothermodynamics of transatmospheric vehicles”. In: *Journal of Aircraft* 24.9 (2008), pp. 594–602. ISSN: 0021-8669. DOI: [10.2514/3.45483](https://doi.org/10.2514/3.45483).
- [187] D. a. Kourtides, W. C. Pitts, M. Araujo, and R. S. Zimmerman. “High-Temperature Properties of Ceramic Fibers and Insulations for Thermal Protection of Atmospheric Entry and Hypersonic Cruise Vehicles”. In: *Journal of Fire Sciences* 6.5 (1988), pp. 313–332. ISSN: 15308049. DOI: [10.1177/073490418800600501](https://doi.org/10.1177/073490418800600501).
- [188] M. Marini. “Analysis of hypersonic compression ramp laminar flows under sharp leading edge conditions”. In: *Aerospace Science and Technology* 5.4 (2001), pp. 257–271. ISSN: 12709638. DOI: [10.1016/S1270-9638\(01\)01109-9](https://doi.org/10.1016/S1270-9638(01)01109-9).

REFERENCES

- [189] C. Gong, B. Chen, and L. Gu. “Design and Optimization of RBCC Powered Suborbital Reusable Launch Vehicle”. In: *19th AIAA International Space Planes and Hypersonic Systems and Technologies Conference* June (2014), pp. 1–20. DOI: [10.2514/6.2014-2361](https://doi.org/10.2514/6.2014-2361). URL: <http://arc.aiaa.org/doi/abs/10.2514/6.2014-2361>.
- [190] D. Preller. “Multidisciplinary Design and Optimisation of a Pitch Trimmed Hypersonic Air-breathing Accelerating Vehicle”. PhD thesis. University of Queensland, 2018.
- [191] D. Abeynayake and A. Agon. “Comparison of computational and semi-empirical aerodynamics tools for making fit-for-purpose modelling decisions”. In: December (2013), pp. 1–6.
- [192] K. J. Davidian, R. H. Dieck, and I. Chuang. “A detailed description of the uncertainty analysis for high area ratio rocket nozzle tests at the NASA Lewis Research Center”. In: *NASA Technical Memorandum* (1987). ISSN: 04999320.
- [193] H. W. Carlson and D. J. Maglieri. “Review of Sonic Boom Generation Theory and Prediction Methods”. In: *The Journal of the Acoustical Society of America* 51.2C (1972), pp. 675–685. ISSN: 0001-4966. DOI: [10.1121/1.1912901](https://doi.org/10.1121/1.1912901). URL: <http://asa.scitation.org/doi/10.1121/1.1912901>.
- [194] R. L. Hershey and T. H. Higgins. *Statistical Model of Sonic Boom Structural Damage*. Tech. rep. July. U.S. Department of Transportation, 1976.
- [195] J. Hentschke. *Ordinary Meeting Agenda*. Streaky Bay, SA, Australia, 2017. URL: <https://www.streakybay.sa.gov.au/webdata/resources/minutesAgendas/CouncilAgenda-Report-October2017.pdf> (visited on 10/06/2018).

APPENDIX A

THERMAL ANALYSIS

XXX note: layers might be at different temps, tested temps may not be exceeded. XXXI should be clear that it is close to max operating conditions

The thermal protection of a hypersonic launch vehicle is essential to its operation, and is one of the most significant challenges that must be overcome before airbreathing launch systems can become a reality. The SPARTAN-based launch system in this study includes nearly the same thermal protection that is used in previous SPARTAN studies, that has been assumed to be able to protect the SPARTAN throughout its launch trajectory[82]. However, no detailed thermal analysis of the SPARTAN has been carried out to date. This section aims to analyse the thermal protection system of the SPARTAN, in order to determine whether it is sufficient for operation to a first approximation. While the purpose of this work is not to significantly redesign a launch vehicle, the design of the SPARTAN's TPS is investigated to analyse the level of thermal protection that may be necessary for future operation.

During launch, the launch system is exposed to large aerothermal loading that must be resisted using passive thermal protection systems. The heat flux over the trajectory is modelled at various locations on the SPARTAN and third stage, and integrated over the trajectory using 1-D heat conduction analysis to determine the efficacy of the thermal protection system. For the body, the criteria for thermal protection system effectiveness is that the temperature at the internal surface of the thermal protection system must be under 1000°C, corresponding to the operable limit of the internal insulation. For the nose tip and the wing leading edge it is assumed that the thermal protection system will not be directly attached to the internal insulation, so that the criteria for thermal protection system success is that the temperature at these points is maintained below the operable limit of the thermal protection system material.

The heat transfer coefficients on the body of the vehicle are computed using Reynolds analogy:

$$c_h = \frac{c_f}{2s}, \quad (\text{A.1})$$

APPENDIX A. THERMAL ANALYSIS

where c_f is the coefficient of friction and s is the Reynold's analogy factor, assumed to be 1.16[138]. This solution is performed within the viscous solver VC3D, at specific locations around the body of the scramjet accelerator and third stage, as shown in Figure A.1. On the scramjet accelerator, the nose stagnation point (1) and wing leading edges (2) are examined, along with a point midway along the nose (3), as well as midway along the cowl front (4), one-quarter of the length along the wing (5), and on the tip of the tail (6) on the windward side. On the third stage, the stagnation point on the nose (1) is examined, along with a point half way along the nose cone (2), and a point half way along the cylindrical cowl (3) on the windward side. These points are judged to be locations of potential high heat loads on the vehicles, and are examined as worst-case examples for thermal analysis.

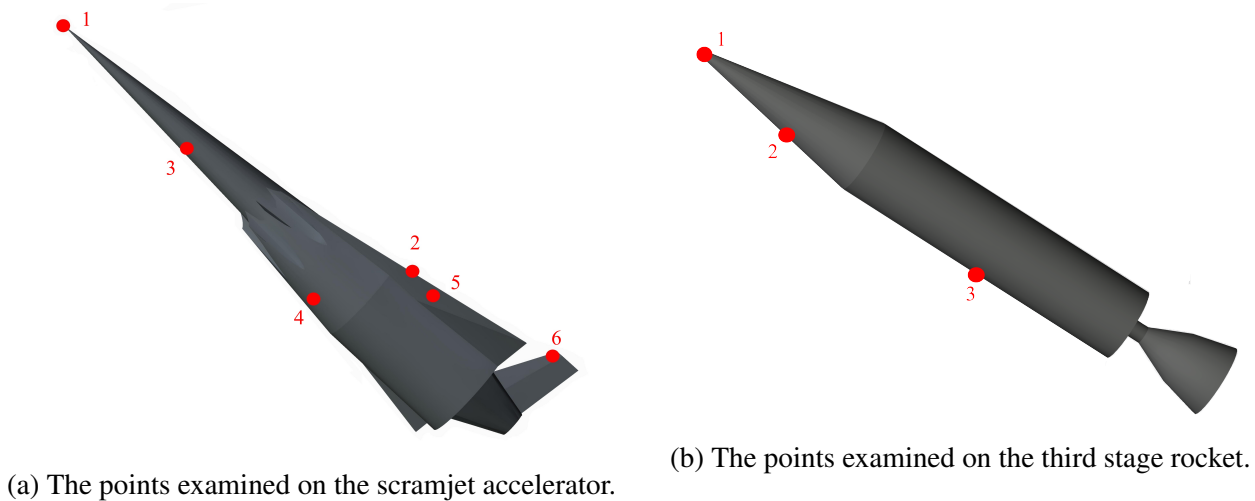


Figure A.1: The points chosen for thermal analysis, selected for the potential of high heat loading.

The heat transfer at the stagnation point and leading edge of the wings, where the simple Reynold's analogy is not valid due to large pressure gradients in the flow[184], is estimated using semi-empirical correlations[185]. At the stagnation point, the heat transfer is given by[185]:

$$q_s = k_1 \rho^{N_1} V^{N_2}, \quad (\text{A.2})$$

where $N_1 = 0.5$ and $N_2 = 3$, and the constant k is[185]:

$$k_1 = \frac{1.83 \times 10^{-4}}{\sqrt{R_n}} \left(1 - \frac{T_w}{T_{aw}}\right), \quad (\text{A.3})$$

where R_n is the nose radius, T_w is the wall temperature, and T_{aw} is the adiabatic wall temperature.

The heating at the leading edge is given by a weighted average correlation between a stagnation point and a flat plate[185, 186]:

$$q_{LE} = \left(\frac{1}{2} q_s^2 \cos^2(\Lambda) + q_{FP}^2 \sin^2(\Lambda)\right)^{1/2}, \quad (\text{A.4})$$

where Λ is the wing sweep angle, and the equation for a flat plate is calculated assuming turbulent flow under 2962m/s as:

$$q_{FP} = k_2 \rho^{N_3} V^{N_4}, \quad (\text{A.5})$$

where $N_3 = 3.37$, $N_4 = 0.8$ and

$$k_2 = 3.35 \times 10^{-4} \cos^{1.78}(\theta) \sin^{1.6}(\theta) x_T^{-1/5} \left(\frac{T_w}{556} \right)^{-1/4} \left(1 - 1.11 \frac{T_w}{T_{aw}} \right), \quad (\text{A.6})$$

where θ is the flow incidence angle and x_T is the distance along the body from the transition point[185, 186]. For the purposes of the leading edge heating the transition point is assumed to be half the distance along the nose cone, and the transitional boundary layer length is assumed to be equal to the preceding laminar flow distance. Along with this assumption, the aeroheating is calculated at the start of the wing, providing an overall worst case scenario for the heating rate. Results for both best case and worst case transition points are provided in Appendix XXX and are shown to exhibit only XXX% difference. As this is comparatively small and acknowledging the preliminary design nature (and associated design uncertainties) of the current project, we have opted to use the worst case assumption for estimating heat-transfer.

A.1 Thermal Analysis of the Standard Trajectory

To determine the effectiveness of the SPARTAN's TPS system, a 1-D heat analysis is conducted. This heating calculation is implemented through the uqTurbine software package for 1-D heat transfer calculation, using the heat transfer calculated as defined in the previous section at each point along the trajectory. This gives an indication of the temperature at the specified points around the SPARTAN throughout its trajectory. Figures A.2 and A.3 show the heat responses at the specified locations on the vehicles over the ascent trajectory of The SPARTAN. At the nose and leading edge it is assumed that there is no direct thermal connection to the internal insulation by the structure or TPS at the regions of maximum heat loads. The maximum heating in this area is therefore assumed to be limited by the properties of the TPS itself. The tungsten nose reaches 1947.6K, and the Carbon-Carbon wing leading edge reaches 1697.2K, well within the operational regimes of the materials. The primary challenge foreseen in the design of the stagnation region and leading edges is the design of appropriate structural support so that the regions of high heat loads are able to be supported, while not exceeding the maximum operational temperature of the internal insulation close to the areas of high heat loads.

On the body of the scramjet accelerator, the nose reaches a maximum of 1355.9K, the cowl 1340.5K, the wing XXXK, and the tail 1113.3K on the vehicle-facing edge. These temperatures are within the operational regime of the multilayer internal insulation, at which the back face of the insulation has been shown experimentally to keep temperatures under 400°C[187], significantly less

than the melting temperature of Aluminium, which is used for the internal structure. However, these temperatures are still significantly high, and potentially liable to produce enhanced deformation in the internal structure of the scramjet accelerator or the insulation material. In this work it is assumed that the internal structure and insulation of the scramjet accelerator has been designed appropriately to account for regions of high heat load.

A.2 Heating limited Trajectory

- heating calculated in-loop using adiabatic wall (?) ?

A.3 TPS Design Exploration

A.4 Scramjet Accelerator

-TPS thickness exploration

XXX currently not converging

-TPS thermal conductivity / density exploration

-possibly layers of different materials or new materials entirely

-active cooling exploration

17kW of cooling on the inner wall, activated during the scramjet accelerator stage, brings the internal nose temperature down to 1275.8K.

A.5 Third Stage

– heat shield reduction due to pull-up

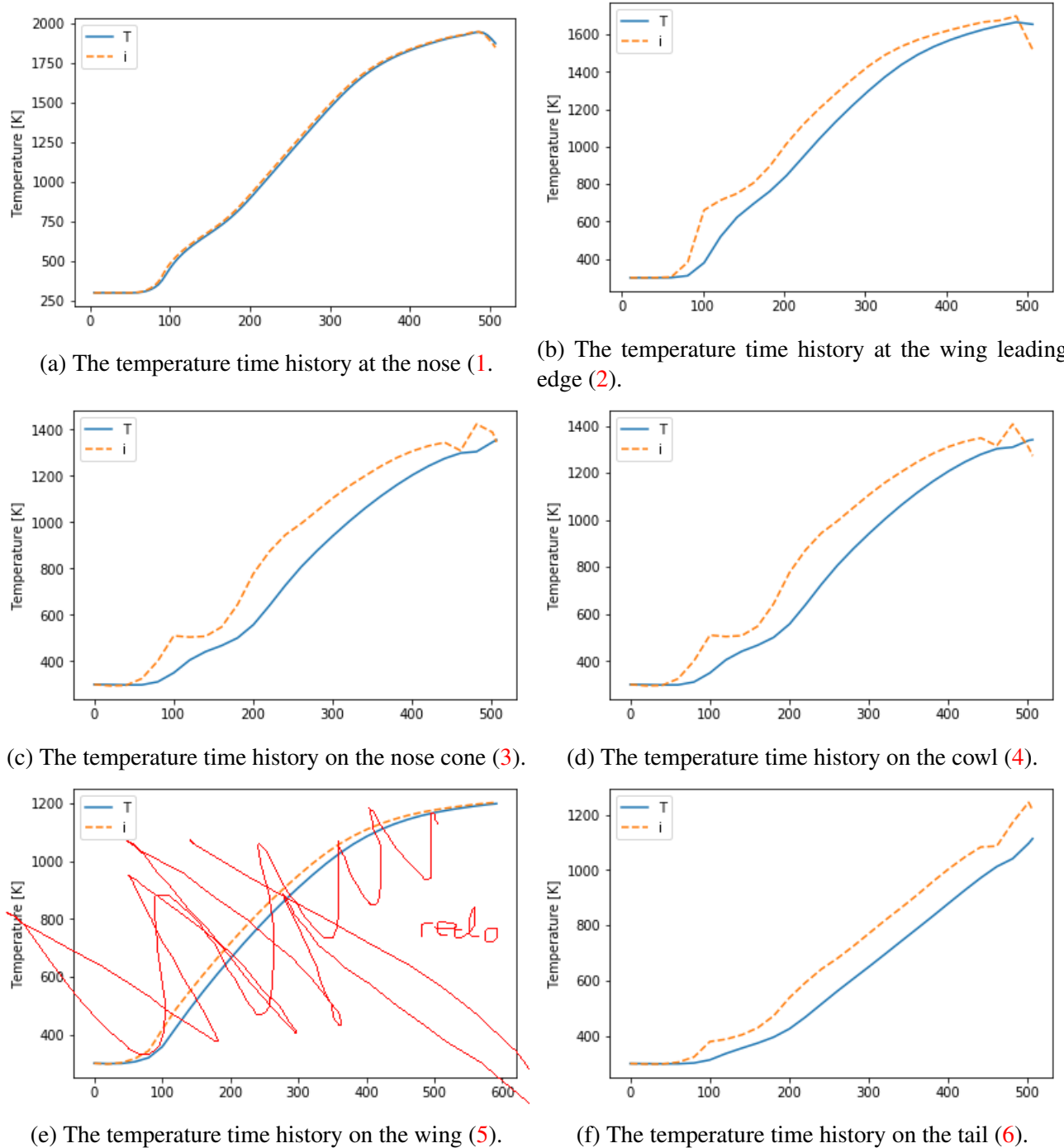
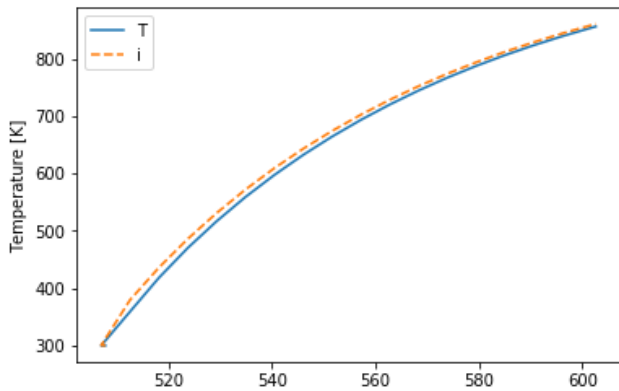


Figure A.2: Temperature time histories on the scramjet accelerator.

APPENDIX A. THERMAL ANALYSIS



(a) The temperature time history at the nose (1).

Figure A.3: Temperature time histories on the third stage rocket with time.

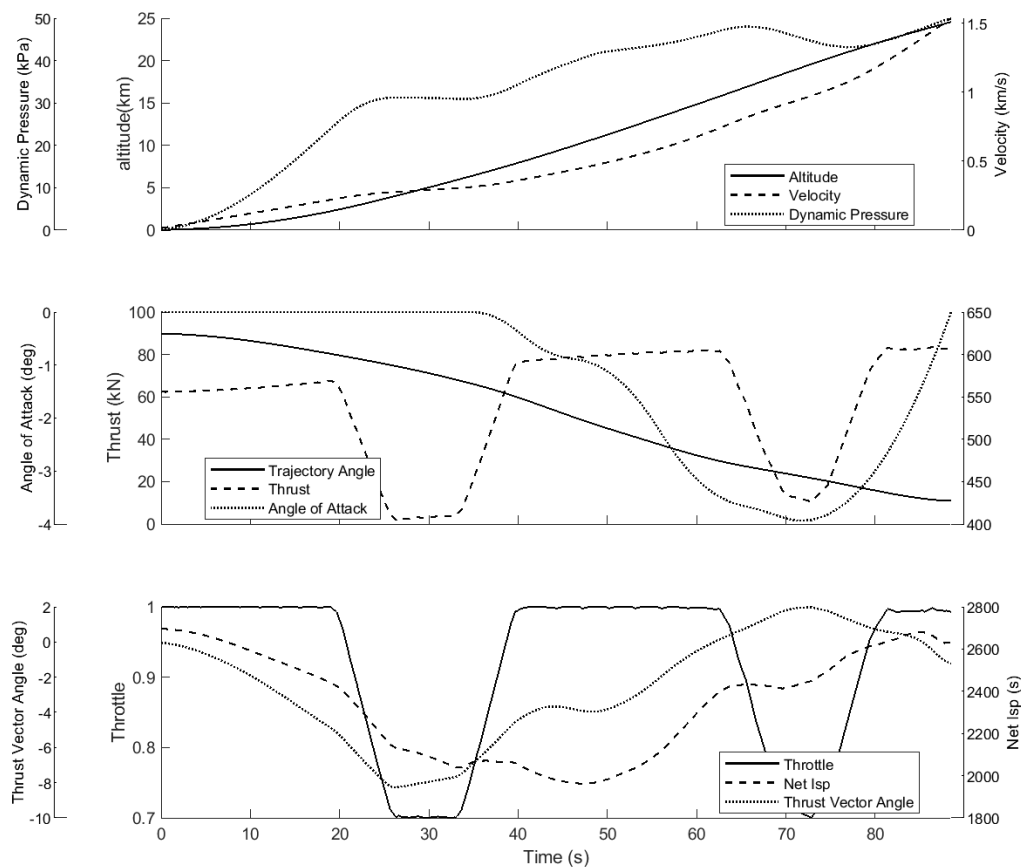


Figure A.4

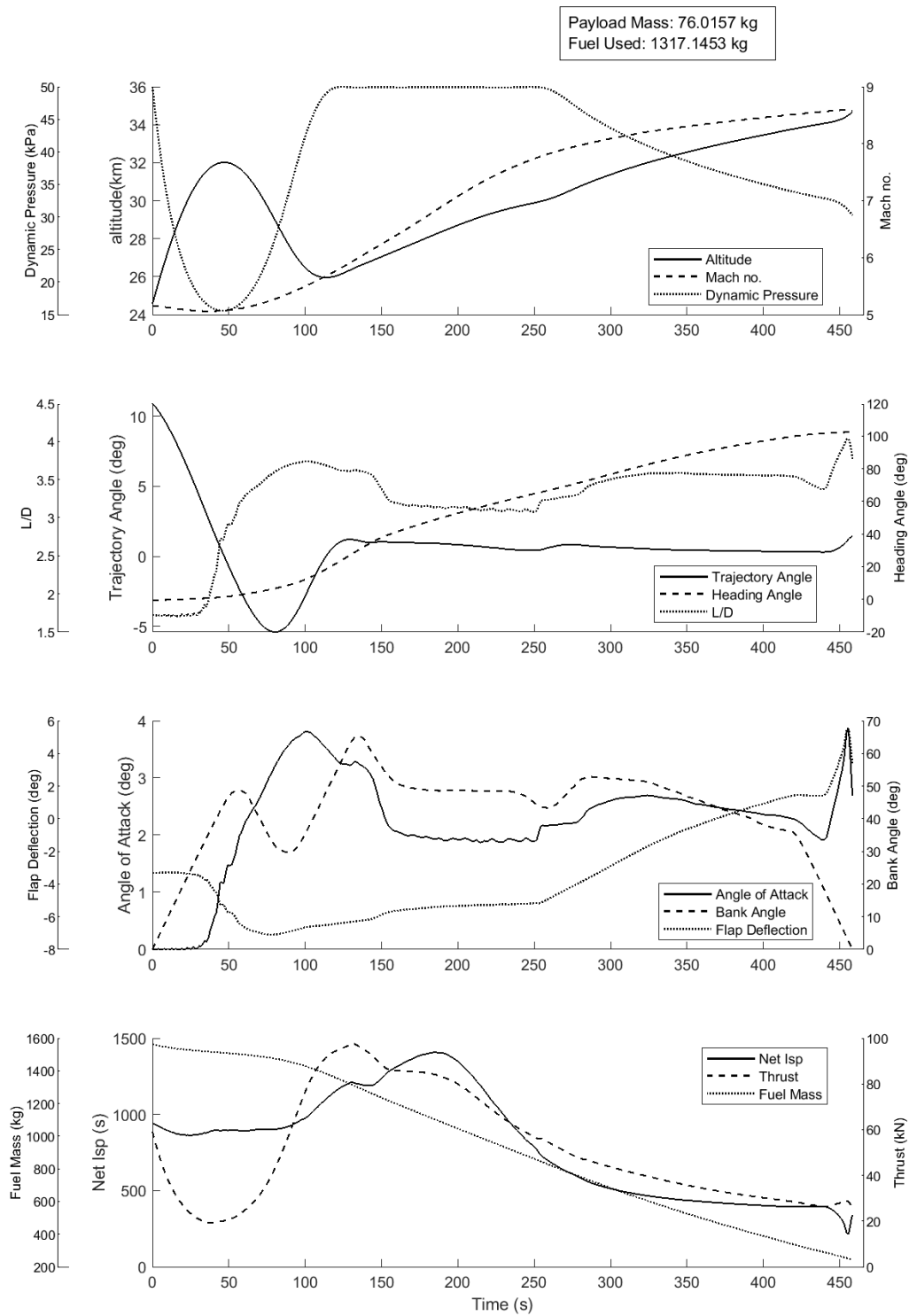


Figure A.5

APPENDIX A. THERMAL ANALYSIS

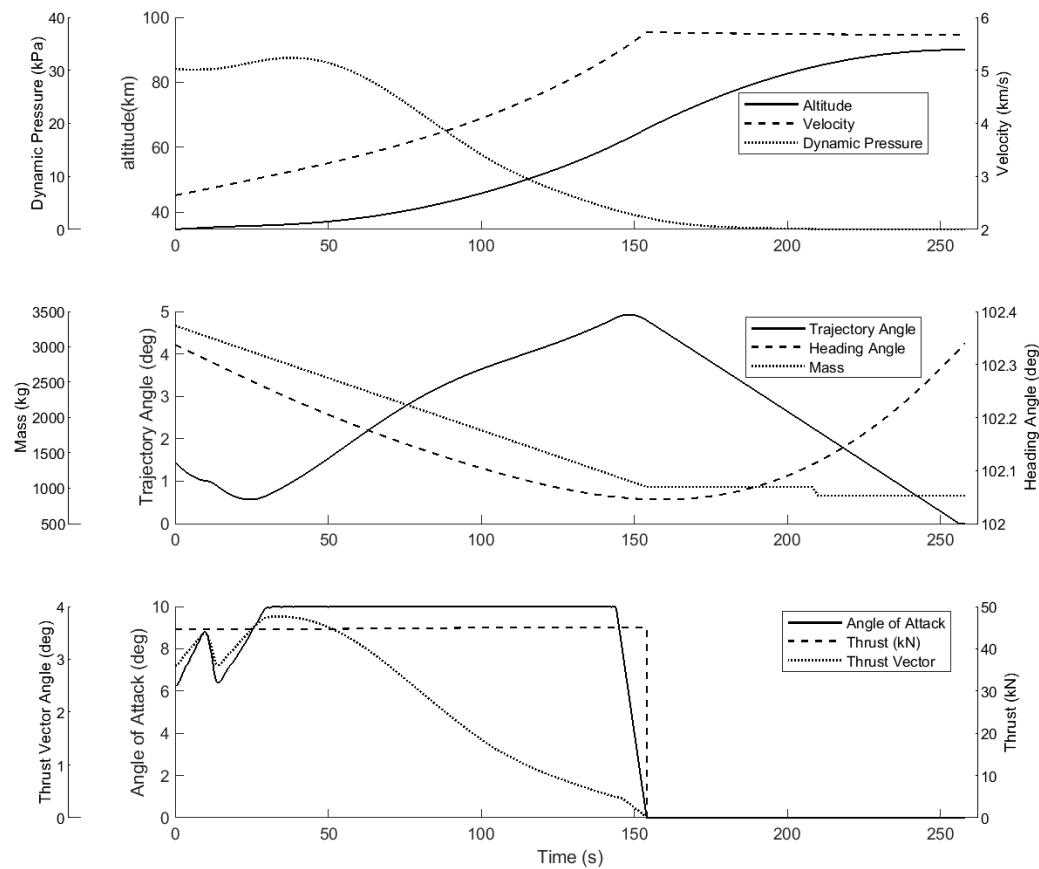


Figure A.6

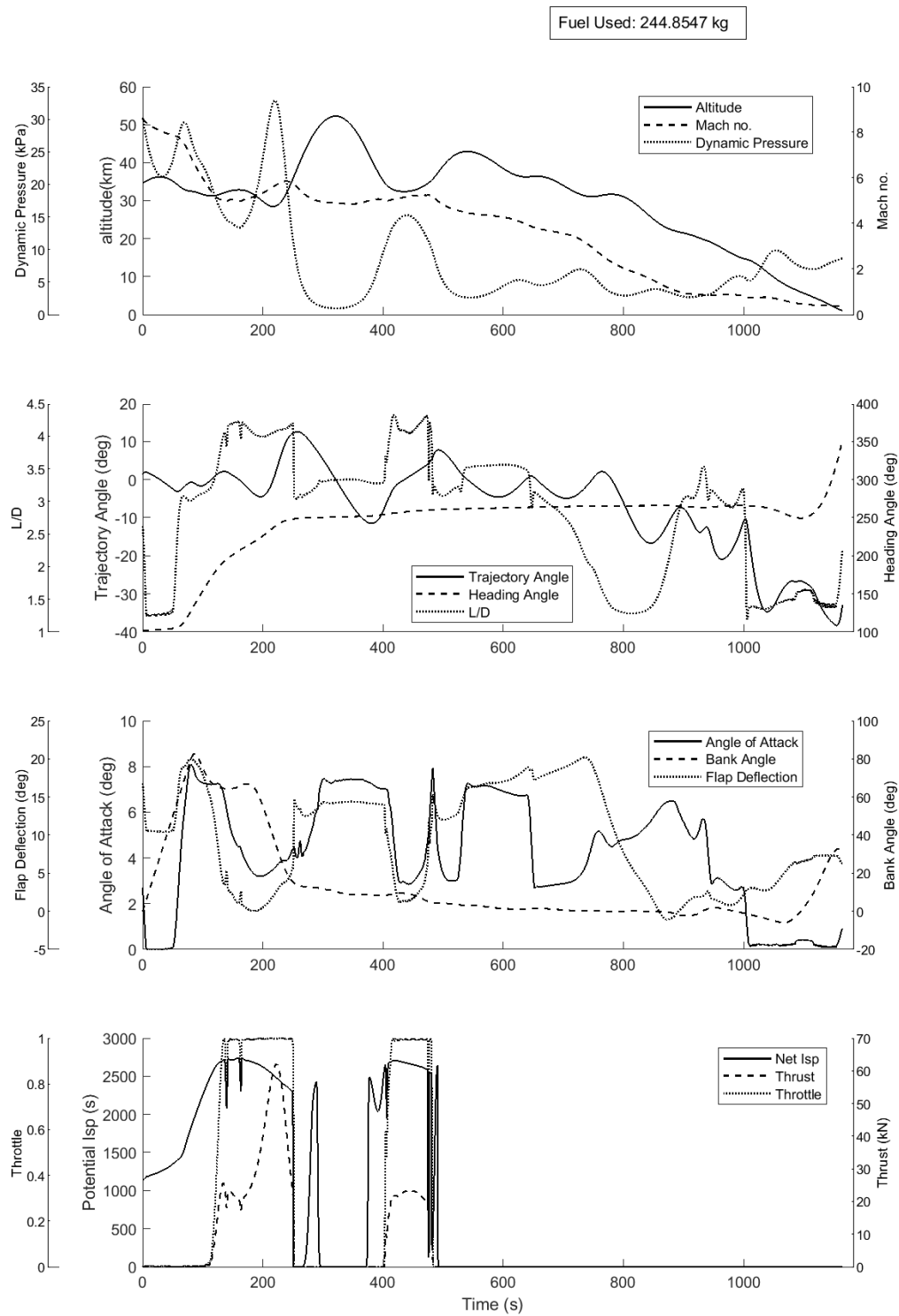


Figure A.7

APPENDIX A. THERMAL ANALYSIS

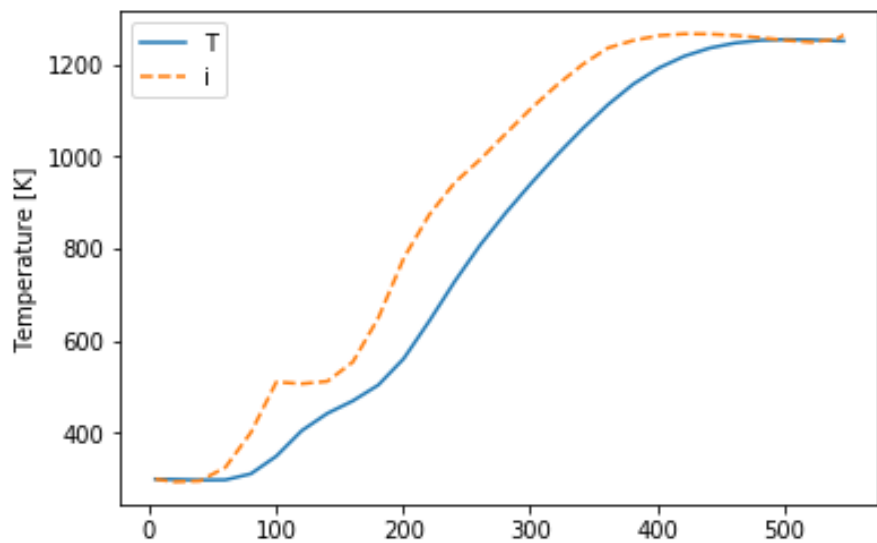


Figure A.8

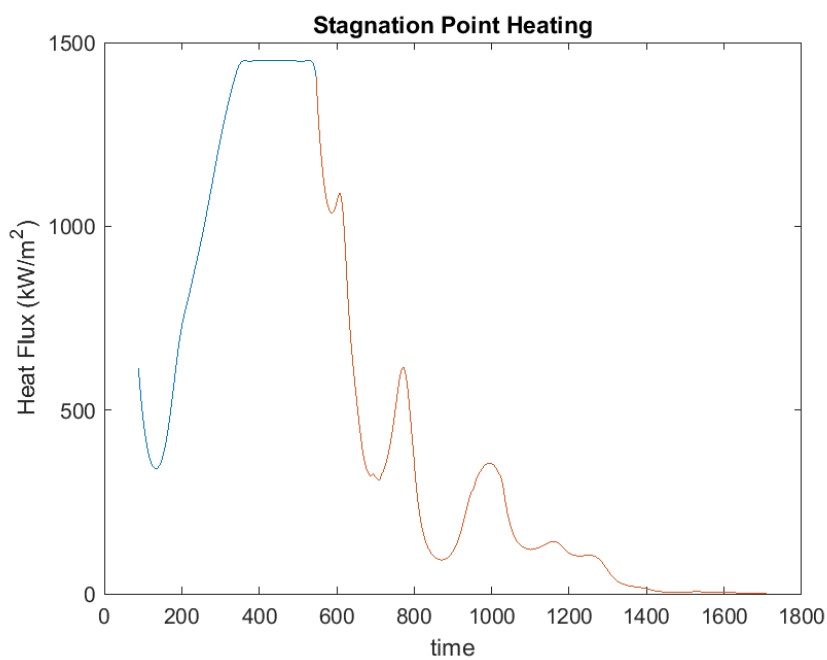


Figure A.9

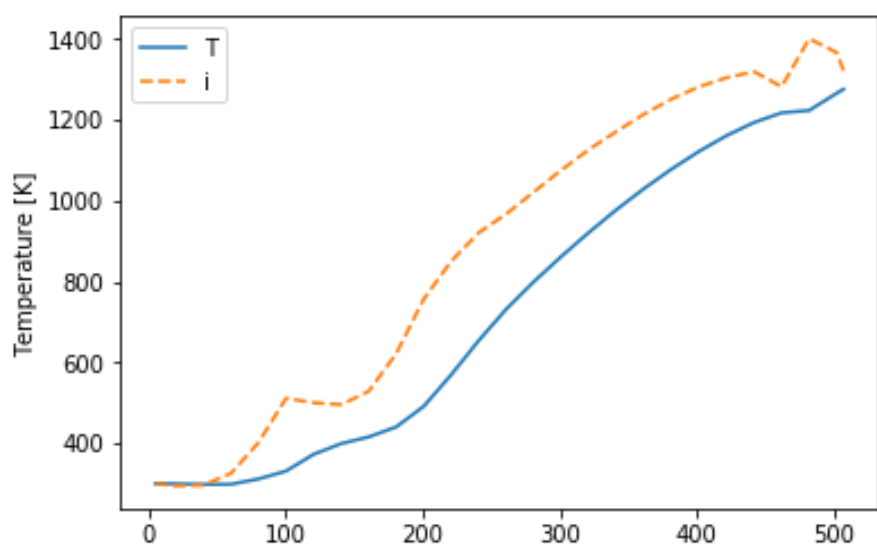


Figure A.10

APPENDIX B

UNCERTAINTIES AND SIMPLIFICATIONS

This thesis aims to provide new insight into the operability and feasibility of multi-stage launch systems incorporating an air-breathing stage. No such launch systems currently exist, and several of the sub-systems necessary for the successful their operation are in the research stage of development. This means that that reliable performance data is not available, and the predicted performance (i.e. payload to orbit) will be affected by design and modelling error, resulting in a variation of achievable performance. The aim of this chapter is to apply a systematic approach to develop an understanding of how these variations may affect the performance of the launch system. These variations have been separated into two categories; design choices, variability that can be controlled by a designer; and modelling accuracy, ie. uncertainty introduced by modelling assumptions and simplifications. To explore these we need to consider firstly what a realistic design process would look like and secondly how the vehicle flight simulations are different to realistic flight.

The design process is considered in this analysis as the stage where the vehicle designers set the vehicle geometry, structure, and internal layout, defining the mass, mass-distribution, and the nominal aerodynamic performance of the vehicle. In this work the design process is necessarily simplified, and it is assumed that by making appropriate design choices the nominal vehicle can be constructed (i.e. it is assumed that the designer can achieve the nominal design by selecting appropriate materials and layouts), and that the nominal vehicle is capable of flying an appropriate launch trajectory. For this stage a parameter by parameter sensitivity study is conducted, to provide an understanding of how the design factors of the launch system impact on the performance of the launch system and the shape of the optimised trajectory.

The second aspect to consider is the difference between the actual launch system and the “as-designed” nominal launch system. These uncertainties are due to uncertainties inherent to the modelling assumptions in the aerodynamics and propulsion modelling of the launch system, in effect, even the most detailed designs will still suffer from many of the same modelling uncertainties as analysed

(though with reduced margins). As the designer has no direct control over these variations between the “as-designed” and actual vehicle, we need to rely on a-priori experience and a stochastic approach to quantify how the variations may affect the ultimate performance of the vehicle. To consider this effect we conduct a reduced Monte-Carlo simulation (using Latin Hypercube sampling) to characterise how the modelling errors and simplifications affect the performance of an otherwise “known” vehicle.

Using this two stage approach we can indicate the effects of design choices, that will evolve as partially-airbreathing, multi-stage access to space systems move from the preliminary to detailed design, and delineate these from uncertainties that arise due to errors/simplifications inherent to modelling vs real flight.

B.1 Modelling and Design Simplifications

The representative launch system in this study is based on the launch system designed to accommodate the SPARTAN[12]. This launch system is in the preliminary design phases, and has not yet been designed or modelled to an accurate subsystem level. This work aims to model a modified version of this launch system to a fidelity where a trajectory may be optimised and analysed with significant results, and it is assumed that the representative launch system utilised in this work is appropriate for successfully launching to orbit. However, there are necessarily some simplifications that occur in the design and modelling of the launch system, that may have significant effects on the trajectory of the launch system. Some of the effects of the design simplifications are captured in the sensitivity study carried out in Sections [XXX](#), for example mass variations, however some of the simplifications may be limiting factors to the trajectories that are able to be flown, particularly control and staging effects. These limiting factors are not considered in this study, because they are heavily dependent on the vehicle design, and it is assumed that future design studies will be carried out that will investigate the ability of this type of launch system to fly a practical launch trajectory, along with an interconnected design study. This section discusses some of the significant design and modelling factors that are not explicitly addressed in the current work.

B.1.1 Control

Control Modelling

This work assumes a point mass vehicle in all phases of simulation, with the control surface deflections or thrust vector of each stage modified throughout the trajectory to trim the vehicle, assuming that the entire aerodynamics performance is known prior to flight. This is done in order to effectively apply the Pseudospectral method of optimal control for the purposes of this work. Practically however, an actual control system must respond to the performance of the system on the fly. Complex controller designs will likely be necessary to fly a launch system of this type, and the trajectories that

a launch system of this type is able to fly may be limited by the controllability of the stages of the launch system. The controllability will be heavily interdependent on the vehicle design, and will require the high fidelity modelling of each vehicle throughout the trajectory, as well as modelling of the control scheme. In particular, the portions of the trajectory during which the vehicles of the launch system have been determined to be aerodynamically unstable may be difficult to control in a practical manner, and should be considered carefully for future designs of launch systems of this type. It is expected that much of the discrepancy between the assumptions in this work and practical control system design could be compensated through applying Model Predictive Control to re-evaluate the optimal trajectory during the flight. Exploring this further is one of the items identified under future work.

Control Surface Design

The control surfaces of the representative SPARTAN in this study are based on previous iterations of the SPARTAN[12], and are modelled as large rectangular flaps. These flaps trim the vehicle during flight, and deflect significantly. These flaps experience large forces, and will need strong and resilient actuators to be able to hold deflection for long periods of time. In future iterations of a launch systems of this type, it may be necessary to design any aerodynamically controlled stages so that the necessary deflections of the control surfaces are minimised, through careful design of the aerodynamic profile and centre of gravity location.

In addition to the possible limitations arising from the actuation mechanism, the control surfaces of the vehicle may experience design limitations due to the design and placement of the control surface. A control surface deflected in a supersonic flow acts as a compression ramp, with an incidence angle that changes rapidly at the flap hinge. Depending on the flow conditions, wall temperature adverse pressure gradient and boundary layer stability, the shock at the flap may cause the boundary layer to separate, causing a recirculation bubble, along with a separation shock that reattaches on the control surface[188]. This recirculation bubble decreases the pressure in the region that it is present on the control surface, while the separation shock increases the shear stress directly downstream of its reattachment[188]. These effects may reduce the effectiveness of the control surfaces at higher deflection angles, changing the deflection necessary to achieve trim. In addition, the reattachment of the shock will cause a high temperature region on the control surface, that may need to be accounted for during the design of the thermal protection system of the control surface.

B.1.2 Staging Effects

A rocket-scramjet-rocket multi-stage launch system will require stage separations at high Mach numbers, into high dynamic pressure conditions. These stage separations may induce aerodynamic forces and moments on the stages of the launch system that are significantly different to the nominal flight

regime of each stage, and will need to be carefully studied and mitigated for a launch system of this type to be feasible. It is possible that the design of the launch system may be significantly driven by the ability of the launch system to stage successfully at high dynamic pressure conditions.

During the first-second stage separation the first stage and cowling will require separation while flying at low trajectory angles, at high dynamic pressure. For the first and second stages to separate cleanly, the first stage and cowling must decelerate more rapidly than the second stage scramjet. This manoeuvre must be executed in a controlled manner, for there must be no risk of adverse contact between the stages. Clean separation may be challenging, and is likely to require ignition of the scramjet engines prior to the release of the first stage.

The separation of the third stage rocket is particularly challenging, requiring separating the third stage from the scramjet-powered accelerator while retaining control authority over both vehicles, and ensuring that there is no significant risk of contact between the vehicles. This work assumes that the third stage is contained within the airbreathing stage, similar to some previous designs of the SPARTAN launch system[83]. However, other design strategies of multi-stage airbreathing launchers support the upper stage on top of[72, 189] or below[75] the airbreathing stage, or contain upper stages within a cavity on the back of the vehicle[12, 71, 74]. Each of these methods has positives, as well as drawbacks that must be considered throughout the design process. The storage of the third stage within the main body of the scramjet-powered accelerator during the ascent phase, necessitating a release mechanism such as retractable panels or a hinged fuselage section. This method of release is also likely to require an ejection mechanism, to impart a force onto the third stage and create distance between the stages. Additionally, it is possible that it would be necessary to ignite the third stage before it is fully released from the SPARTAN, due to the lack of a control mechanism for the third stage without the rocket engine ignited. Storing the third stage outside the body of the airbreathing stage would necessitate the third stage being designed for additional thermal protection and possibly structural strength, and would likely reduce the aerodynamic performance of the airbreathing stage. Storing the upper stage in a cavity on the back of the airbreathing vehicle mitigates some of the aerodynamic and thermal drawbacks, but introduces complications during fly-back, when the cavity on the upper side of the airbreathing vehicle is open. This cavity may have significant impact on the aerodynamics of the vehicle during fly-back, potentially increasing the drag and changing the aerodynamic moments of the vehicle significantly. The methods of staging of a launch system of this type must be considered carefully in future design studies, taking into account the controllability of the launch system, along with the aerodynamic and aerothermal properties of each stage.

B.1.3 Mass Model Simplifications

This study uses a simplified mass model of the representative launch system, utilising design studies of the SPARTAN vehicle[12] that are based on statistical models and models of a representative winged-

cone vehicle[190], and a scaled model of the Falcon 1e[161]. In addition, the mass model distribution of the launch system in this study assumes a homogeneous distribution of subsystem and structural masses when calculating centre of gravity, and the rotational inertia of the launch system are not modelled. These mass models carry with them some uncertainty margin, however these uncertainty margins are not directly estimated in this work due to the lack of data or reference studies available for launch systems of this type and size. In future design studies, the subsystems of the vehicles and interface mechanisms will need to be modelled in detail, and positioned so that good control characteristics are obtained. The relationship between the control characteristics of the vehicle and its internal design will need to be investigated, and this will be thoroughly coupled with the separation dynamics of the launch system.

B.2 Aerodynamic and Propulsion Simulation Uncertainties

Because of the large number of simulations necessary to cover the possible flight regimes of the launch system, the launch system in this study is analysed using medium and low fidelity modelling techniques chosen for their fitness-for-purpose for optimal trajectory analysis, with an emphasis on computational efficiency as well as accuracy. The uncertainties in the propulsive and aerodynamic properties of the launch system modelled in this work must be estimated, as there are no flight test or experimental results available for the representative launch system analysed in this study. In this section an estimate of the aerodynamic and propulsive uncertainties associated with the trajectory optimisations in this work is provided, and a Latin hypercube analysis is carried out to determine the variance in a sample trajectory optimisation.

B.2.1 Aerodynamic Uncertainty

The aerodynamic coefficients of the SPARTAN in this work are calculated using an inviscid Euler solver, Cart3D, with a flat plate correction for the viscous forces. This is a medium fidelity method, which brings with it a significant associated uncertainty in the aerodynamics of the vehicle, particularly at subsonic and transonic conditions. Although the aerodynamics of the vehicle in this work are not experimentally validated, studies have previously compared Cart3D with experimental data for a number of geometries at various flight conditions. These experimental comparisons are utilised to estimate the uncertainty arising in the aerodynamic coefficients due to the use of Cart3D. These comparison studies do not usually correct for viscous forces, and so underpredict drag in almost all cases.

Abeynayake & Agon assess two missile geometries; a conventional missile at transonic and supersonic speeds, and a non-conventional missile that has a cruise missile profile and includes small wings at subsonic speeds[191]. The study by Abeynayake and Agon estimates the magnitude of the uncer-

tainty of Cart3D in a comparison to experimental results, although no viscous correction is included, and so the lack of a viscous component significantly affects the aerodynamic coefficients, particularly drag. The uncertainty magnitudes are estimated in relative error, normalised by the average value of data points between 0° and 10° angle of attack for drag, or the value at 10° angle of attack in the case of the lift and pitching moment coefficients[191]. It is noted that these relative errors only give an indication of the accuracy of a specific tool[191]. It is found that when compared to experimental results, Cart3D has a mean error in drag of 31.3% for subsonic, 23.5% for supersonic, and 18.0% for transonic cases[191] when compared to wind tunnel data for the non-conventional missile at angle of attack values between -10° and 10° in the subsonic regime, and the conventional missile at angles of attack of 0° to 10° in the transonic and supersonic regimes. The mean relative error in lift was found to be 16.5% for subsonic, 1.3% for supersonic, and 28.7% for transonic cases[191], and the error in pitching moment 22.0% for supersonic and 67.1% for transonic cases, with no subsonic error given[191]. In this comparison study Cart3D was not able to match experimental trends closely in the subsonic and transonic regimes. Errors of up to 80.2% in drag are observed in the subsonic regime for an unconventional missile geometry[191], although the drag error diminishes significantly at angle of attack values between -5° and 5° . In the supersonic regime, Cart3D appears to closely match the experimental lift and drag trends, with an underprediction in the magnitude of the drag forces due to the absence of viscous forces. Cart3D had poor results when computing pitching moment, although it was occasionally able to match the magnitude of the pitching moment well Cart3D was not able to match the experimental pitching moment trends for either vehicle[191]. The work by Abeynayake & Agon indicates that the uncertainties associated with Cart3D are significant, particularly at angle of attack values greater than 5 in the subsonic and transonic regimes, and that it does not estimate pitching moment trends well. However, a portion of the uncertainty magnitudes are associated with the inviscid nature of Cart3D, particularly in the drag forces.

A study by Ward et al.[138] compares Cart3D results to experimental results for a blunt body at hypersonic speeds, a lifting body vehicle at subsonic and supersonic speeds, and a hypersonic accelerator test geometry at hypersonic speeds. Ward et al. provide a method for viscous correction of the Cart3D results, and also compare this with experimental results, focusing on the amount that drag error is able to be corrected. In this study Cart3D was found to predict trends drag coefficients well for all tested cases both subsonic and supersonic, although with a consistent underprediction of 15-25% in drag coefficient due to a lack of viscous effects[138]. When corrected for viscous effects, the drag coefficient was found to agree closely with the experimental results at supersonic and hypersonic speeds, with error reducing to less than 10% for the hypersonic accelerator test vehicle, and less than 11% for the lifting body at supersonic speed[138]. Drag error at high angles of attack at subsonic speeds was still found to be large, at 38%, however, at angles of attack under 5° the error reduced significantly, matching the experimental results to within 16%. The Euclidean correction method outlined by A. Ward was utilised to correct the inviscid aerodynamic coefficients in this study, with

viscous aerodynamics provided by A. Ward for this work.

These two studies are used to inform the uncertainty margins in the aerodynamics of the first and second stages of the representative launch system. Note that while the values reported by Abeynayake & Agon[191] are non-dimensionalised relative accuracies, it is assumed here that the values reported somewhat indicate the accuracy of Cart3D. For the lift uncertainties and the pitching moment at in the transonic and supersonic regimes, the uncertainty values are taken directly from the mean relative accuracies reported by Abeynayake & Agon[191]. The pitching moment error in the subsonic regime is not stated, so the average relative error for all Cart3D coefficients at subsonic speeds, 23%, is used. The subsonic uncertainty in the drag is estimated at a nominal value of 20%, accounting for reduced uncertainty due to the low angle of attack of the launch system at subsonic speeds, which is shown to reduce error significantly. This value is based primarily on the uncertainty determined by Ward et al.[138] in the low subsonic regime at low angles of attack, with a slight increase due to the high uncertainties that are observed by Abeynayake & Agon[191], which do not show evidence of a consistent trend due to a lack of viscous effects, though are again significantly reduced at low angles of attack. In the transonic case, Abenayake and Agon find that Cart3D is not capable of predicting the trends of the aerodynamic data well[191]. For this reason, the drag uncertainty in the transonic regime is set to 18%, to match the mean value reported by Abenayake and Agon[191], as it is not evident that the lack of a viscous drag component produces a clear trend, and no corrected transonic cases are available. In the supersonic regime the ability of Cart3D to predict drag improves, and the lack of viscous effects causes an underprediction in drag while still matching experimental trends when uncorrected[138, 191]. The uncertainty in drag in the supersonic regime is set to 11%, to match the maximum error observed after viscous correction by Ward et al.[138], assuming that the consistent underprediction observed by Abeynayake & Agon[191] is primarily due to a lack of viscous effects.

B.2.2 Propulsion System Uncertainties

The Rocket Engines

The propulsive properties of the rocket engines that power the first and third stages of the launch system are taken from the Falcon 1 Launch Vehicle Payload User's Guide[161], a document released by SpaceX that does not contain detailed information as to how the engine properties are calculated. It is assumed that the properties of the engines presented by SpaceX have been measured experimentally, and that the primary uncertainties associated with the rocket engine properties are experimental uncertainties. With no knowledge of the experimental facilities or processes used, it is necessary to estimate the experimental uncertainty through analysis of other experimental facilities, information that is generally sparse. Davidian, Diek and Chuang[192] assess the specific impulse uncertainty associated with high area ratio rocket tests at NASA Lewis Research centre, by propagating an "exhaustive" list of possible error sources. The test facility was found to be capable of measuring specific

Uncertainty	Subsonic	Transonic	Supersonic/Hypersonic
1 st & 3 rd Stage I_{SP}	1.3%	1.3%	1.3%
Scramjet I_{SP}	-	-	25%
C_L	16.5%	28.7%	1.3%
C_D	20%	18%	11%
C_M	23%	67.1%	22.0%

Table B.1: The uncertainty margins associated with the aerodynamic and propulsive modelling of The SPARTAN.

impulse to within 1.30%, thrust to within 1.12%, and mass flow rate to within 0.72%. These propagated uncertainty values assumed that there was no bias errors, and that calibration had no error prior to testing. The uncertainty in the specific impulse of 1.30% is used as the rocket engine performance uncertainty for the purposes of this study, assuming that the testing that has been carried out on the Merlin 1-C and Kestrel engines has the same error margins as the NASA Lewis Research Centre facilities.

The Scramjet Engine

The C-REST engines are modelled in this work using a dataset developed using a combination of high-fidelity CFD, and quasi 1-D analysis, tuned using experimental results. Estimating the error in this model in comparison to a realistic, flight capable scramjet is not feasible, due to the lack of flight test data or full-scale engine ground testing for scramjet engines in the public domain. For the purposes of this study a nominal uncertainty of 25% is associated with the specific impulse of the scramjet engines based on the experience of the Author's colleagues and supervisors at The University of Queensland's Centre for Hypersonics. This is an estimated uncertainty margin, and it is possible that the uncertainty margin may be higher than this estimated value. However it is probable that if there are errors larger than 25% in the performance modelling of the scramjet engines, then the design of the system may have to change considerably to be feasible. For this reason, the uncertainty margin of the scramjet specific impulse is kept at 25% for payload-to-orbit uncertainty margin calculations, although it is acknowledged that major unforeseen modelling or experimental errors may cause design changes to be necessary or lead to the infeasibility of the system as a whole.

B.2.3 Quantification of Aerodynamic and Propulsion Uncertainty Effects

Quantification of Uncertainty Magnitudes

The uncertainty margins of the aerodynamic and propulsive data for the representative launch system analysed in this study are shown in Table B.1. These uncertainty margins have been applied based on the errors described in the studies analysed Sections B.2.1 & B.2.2.

Variation Study

In order to quantify the effects of the uncertainty in the aerodynamic and propulsion models, a variation study is carried out using a Latin Hypercube Sampling technique. **XXX LHC variation study to be added here**

B.2.4 Atmospheric Variations

The Earth's atmosphere varies significantly depending on location, and over time. As such, the atmosphere into which the SPARTAn is launched may be considerably different to the atmosphere that is being modelled in this work. The variations in the properties of the atmosphere with geography or time may affect the aerodynamic and engine performance of the launch system significantly, and change the altitude at which maximum dynamic pressure is reached. These variations may have significant impact on the aerodynamic and aero-thermal performance of the launch system at a particular altitude, as well as the performance of the propulsion systems of the launch system, particularly the scramjet engines. This study uses the U.S Standard Atmosphere 1976 model[155] to calculate the properties of the atmosphere during simulations. The U.S Standard Atmosphere 1976 is based on a collection of data from sites across America, Brazil, Australia, and Russia, with values calculated for annual mean properties at an interpolated latitude of 45° [155]. The properties that are calculated using this atmosphere are subject to seasonal variability, as well as variability due to geographic position. Figure B.1 shows the variation in temperature and pressure in the 1976 U.S Standard Atmosphere model with altitude. In the higher latitudes maximum and minimum temperatures at altitudes below 25km are seasonal, however at higher altitudes semi-annual and biennial oscillations have a large influence[155]. The variations shown do not occur at the same time in the same envelopes of the atmosphere; warm temperatures at the surface are associated with cold temperatures near the tropopause, and temperatures near the stratopause are negatively correlated with temperatures near the mesopause[155]. These oscillations are particularly important in the equatorial regions, where the seasonal variation in temperature is smallest.

The effects of atmospheric variation are quantified by modelling the 1976 U.S Standard Atmosphere model to take into account the maximum and minimum variations shown in Figure B.1. It is assumed that the conditions at the surface compared to the tropopause vary inversely, as well as the conditions of the stratopause compared to the mesopause, as indicated in B.1. The conditions in the stratosphere are assumed to vary linearly between the conditions at the tropopause and stratopause. It is also assumed that density varies inversely to temperature, so that maximum temperature conditions correspond to minimum density. As such, there are two conditions at ground level, and two conditions at stratopause to be investigated.

XXX need to add standard traj to this

APPENDIX B. UNCERTAINTIES AND SIMPLIFICATIONS

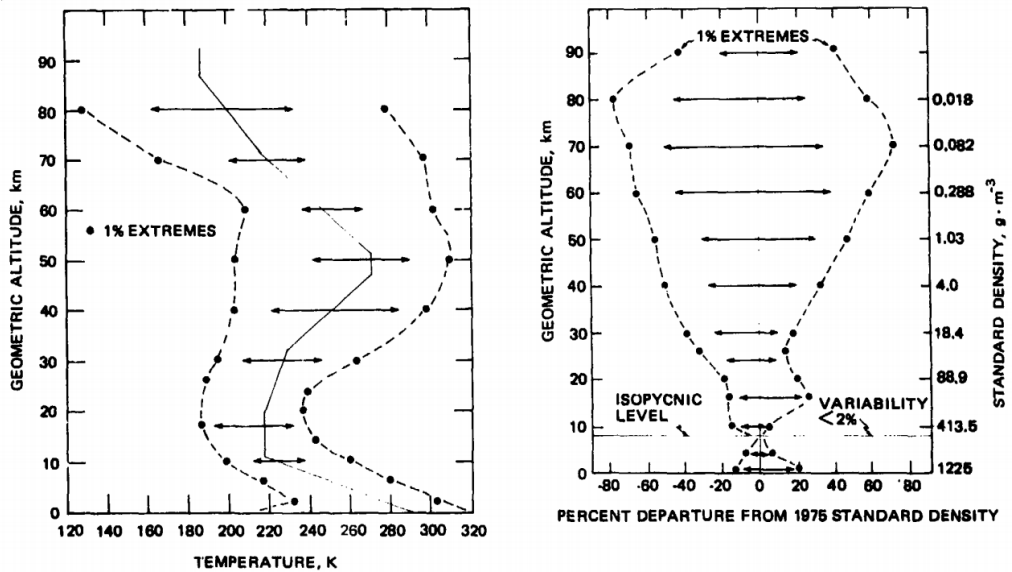


Figure B.1: Variation in temperature and density in the 1976 U.S Standard Atmosphere Model[155]. Arrows indicate lowest and highest mean monthly values obtained at any location, and dashed lines indicate one-percent extremes.

Trajectory Condition	MinTGround	MinTStrat	MaxTGround	MinTStrat	MinTGround	MaxTGround
Payload to Orbit (kg)	132.7		145.2		115.3	
Payload Variation (%)	15.07		25.94		0.00	
Total η_{exergy} (%)	1.592		1.713		1.357	
1st Stage η_{exergy} (%)	6.785		6.888		6.943	
Separation Alt, 1→2 (km)	23.92		25.01		24.95	
Separation v, 1→2 (m/s)	1524		1531		1539	
Separation γ, 1→2 (deg)	11.3		10.0		17.1	
2nd Stage η_{exergy} (%)	3.730		4.092		3.276	
Separation Alt, 2→3 (km)	43.93		44.46		40.89	
Separation v, 2→3 (m/s)	2484		2572		2404	
Separation γ, 2→3 (deg)	13.3		12.5		13.5	
2nd Stage Flight Time (s)	508.6		477.1		674.0	
2nd Stage Distance Flown (km)	862.7		827.1		1074.4	
2nd Stage Return Fuel (kg)	273.2		266.4		121.0	
2nd Stage Return Distance (km)	1530.3		1559.0		1042.3	
3rd Stage η_{exergy} (%)	13.213		14.436		11.494	
3rd Stage $t, q > 5\text{kpa}$ (s)	8.0		8.3		5.8	
3rd Stage max α (deg)	10.0		10.0		10.0	
3rd Stage Fuel Mass (kg)	2852.5		2840.0		2869.9	

APPENDIX C

EXAMPLES AND VERIFICATION

C.1 Example - Brachistochrone Problem

This section describes a short example of an optimal control problem solved in GPOPS-II. The purpose of this example is to demonstrate the effectiveness of the pseudospectral method and GPOPS-II, and to provide a simple example case to establish the terminology of an optimal control problem.

The brachistochrone (from the Greek for 'shortest time') problem is a simple optimal control problem, which describes a ball rolling in two dimensions under gravity. The objective is to find the curve of descent which will minimise the time from point a , where the ball is at rest, to point b . It is assumed that gravity is constant and that there is no forces other than gravity acting on the ball. The analytical solution of this problem can be computed using the Euler-Lagrange equation as the equations describing a cycloid:

$$x = A(\theta + \sin \theta),$$

$$y = A(1 - \cos \theta)$$

This problem is included within GPOPS-2 as an example problem, and has been solved to illustrate the GPOPS-2 solution set-up[119]. Table C.1 describes the set-up of the optimal control problem in GPOPS-2. The dynamic equations for the Brachistochrone problem are:

$$\dot{x} = v * \cos(u),$$

$$\dot{y} = v * \sin(u),$$

$$\dot{v} = g * \sin(u).$$

These equations are provided to GPOPS-2 as the time-variant system model in this form. The control variable is set to be the descent angle. The initial constraints are defined to initiate the ball at rest at the origin, and the terminal constraints are defined to terminate the problem at coordinates of [2,2]. The cost is set to minimum time, so that the solution will be the descent angle which minimises the

Primal Variables	x Position y Position Velocity
Control Variables	Angle of Descent
Initial Constraints	Velocity x Position y Position
Terminal Constraints	x Position y Position
Path Constraints	None
Target Cost	Minimum Time

Table C.1: Optimisation setup of the Brachistochrone problem.

time to get from the initial position, to the end position.

The GPOPS-2 solution to the Brachistochrone problem is shown in Figure C.1, matching the analytical solution almost exactly. This is expected in this case, as the dynamics of the basic Brachistochrone problem are very simple. As the dynamics become more complex, it is no longer possible to obtain an analytical solution.

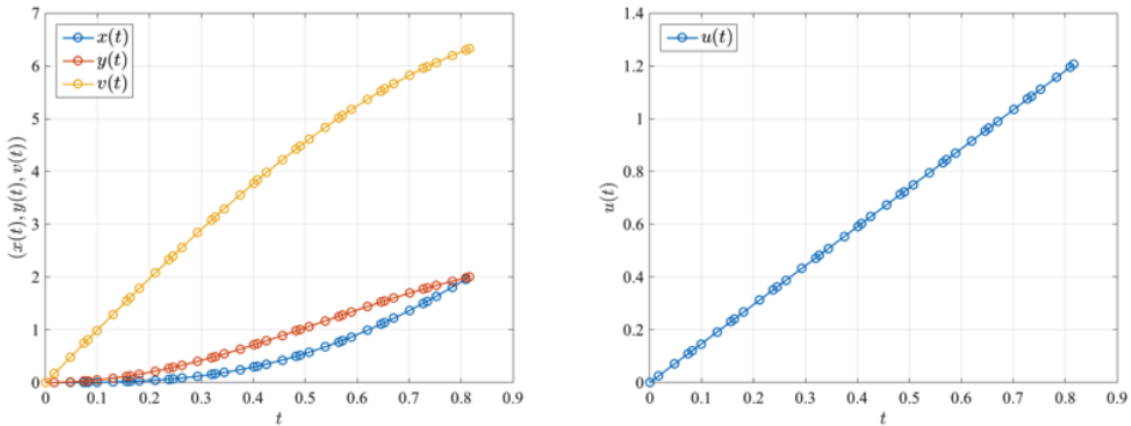


Figure C.1: The solution to the Brachistochrone problem, solved in GPOPS-2[119].

C.2 Example - Space Shuttle Reentry

XXX I havent been able to find any good trajectories for comparison, that offer me the ability to recreate them. XXX this is not quite the same as the GPOPS example, more similar to my dynamics

This section describes an optimised shuttle reentry trajectory problem, taken from the textbook 'Practical Methods for Optimal Control and Estimation Using Nonlinear Programming' by Betts[178],

which has been simulated in GPOPS-2 to illustrate the capabilities of GPOPS-2 when applied to a complex aerodynamic problem of an existing vehicle. The optimisation of the space shuttle reentry is relevant due to the large flight regime and long time period being simulated, which leads to a complex, extremely sensitive optimal control problem[178], similar in a simplified manner to the problem being solved in this work. The shuttle reentry problem is highly nonlinear and intractable to simple optimisation methods[178], making it suitable for illustrating the robustness of GPOPS-2 for aerospace problems of this type. The space shuttle reentry problem aims to maximise crossrange during reentry, with two cases; unconstrained, and limited by a simple heating rate constraint. The example in this section uses the vehicle model exactly as defined by Betts[178] for comparison purposes, however the problem is formulated in a simplified version of the coordinate system that is used in the rest of this work.

C.2.1 Problem Formulation

The dynamics of the space shuttle are defined exactly similarly to those in the problem designed by Betts[178], using a simplified model that neglects the rotation of the Earth and the tangential component of gravity:

$$\dot{r} = v \sin \gamma, \quad (\text{C.1})$$

$$\dot{\xi} = \frac{v \cos \gamma \cos \zeta}{r \cos \phi}, \quad (\text{C.2})$$

$$\dot{\phi} = \frac{v \cos \gamma \sin \zeta}{r}, \quad (\text{C.3})$$

$$\dot{\gamma} = \frac{L \cos \eta}{mv} + \left(\frac{v}{r} - \frac{g}{v} \right) \cos \gamma, \quad (\text{C.4})$$

$$\dot{v} = \frac{D}{m} - g \sin \gamma, \quad (\text{C.5})$$

$$\dot{\zeta} = \frac{L \sin \eta}{mv \cos \gamma} - \frac{v}{r} \tan \phi \cos \gamma \cos \zeta. \quad (\text{C.6})$$

The aerodynamics of the vehicle are modelled using simple correlations, where $C_L = 0.20704 + 0.029244\alpha$, and $C_D = 0.07854 - 0.61592 \times 10^{-2}\alpha^2 + 0.621408 \times 10^{-3}\alpha^3$. The density is modelled as exponentially decaying, $\rho = 1.2255708354e^{-h/7254}$, and the gravity is modelled by an inverse square law, $g = \frac{\mu}{r^2}$. The space shuttle initial conditions are set as follows[178], to simulate the entry of the shuttle into the upper atmosphere:

$$\begin{aligned} h_0 &= 79248\text{m}, & v_0 &= 7803\text{m/s}, \\ \gamma_0 &= -1^\circ, & \phi_0 &= 0^\circ, \\ \xi_0 &= 0^\circ, & \zeta_0 &= 0^\circ, \end{aligned}$$

and the end conditions are set as follows[178], to match the terminal area energy management interface:

$$h_f = 24384\text{m}, \quad v_f = 762\text{m/s}, \quad \gamma_f = -5^\circ.$$

The problem is set to maximise crossrange from the initial point, which in this case is equivalent to maximising latitude:

$$J = -\phi_f. \quad (\text{C.7})$$

C.2.2 Unconstrained Result

The shuttle reentry crossrange maximisation problem is optimised in GPOPS-2, with result time histories shown in Figures C.2 and C.3. The shuttle follows a 'skipping' trajectory, with an initially large bank angle that changes the heading of the vehicle rapidly in the early stages of reentry. The skips serve to maximise the range of the space shuttle's flight, and they are controlled by the angle of attack of the vehicle. The solution computed in GPOPS-2 matches the result computed by Betts[178], with the shape of the trajectories being close to identical. A maximum crossrange of 34.18° is achieved, a difference of 0.11% when compared to the solution computed by Betts[178]. This result is indicative of the ability of GPOPS-2 to compute highly sensitive optimal control problems for aerospace vehicles.

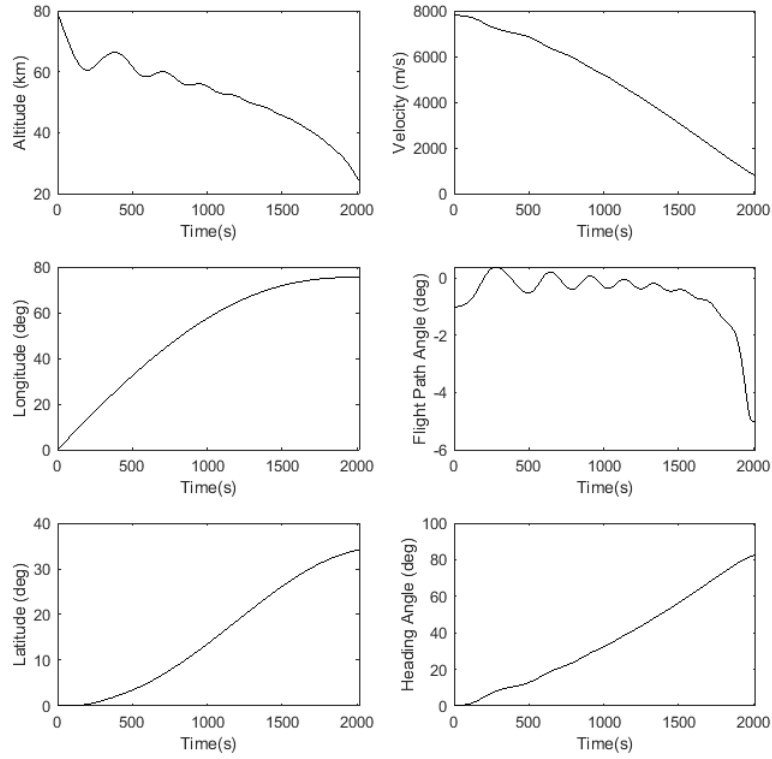


Figure C.2

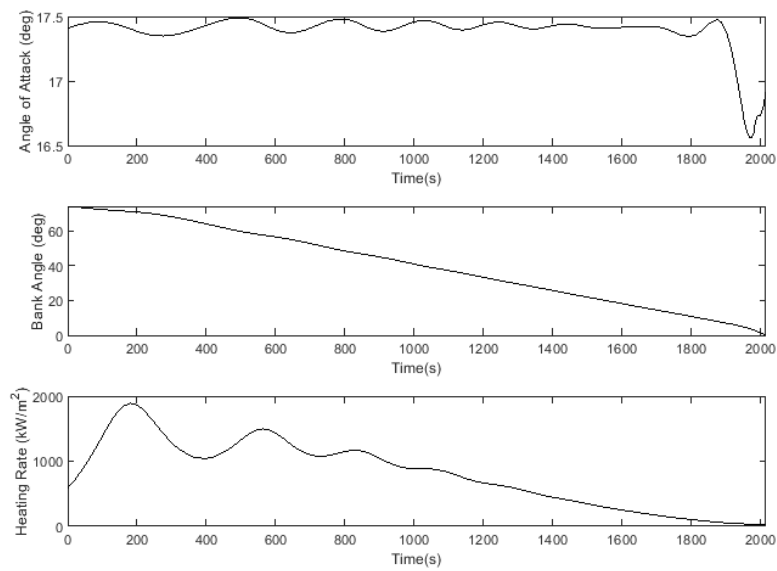


Figure C.3

C.2.3 Heating Rate Limited Result

The heating rate of the space shuttle is limited during descent, to illustrate the ability of GPOPS-2 to deal with complex inequality constraints. The leading edge heating is approximated using a simplified empirical model, so that $q = q_a q_r$, where $q_r = 17700\sqrt{\rho}(0.0001v)^{3.07}$ and $q_a = 1.0672181 - 0.19213774 \times 10^{-1}\alpha + 0.21286289 \times 10^{-3}\alpha^2 - 0.10117249 \times 10^{-5}\alpha^3$. The trajectory is successfully optimised in the presence of this complex inequality, once again showing a near identical trajectory to the optimised solution calculated by Betts[178]. The maximum crossrange is reduced to 30.70° , a difference of 0.25% to the solution calculated by Betts[178].

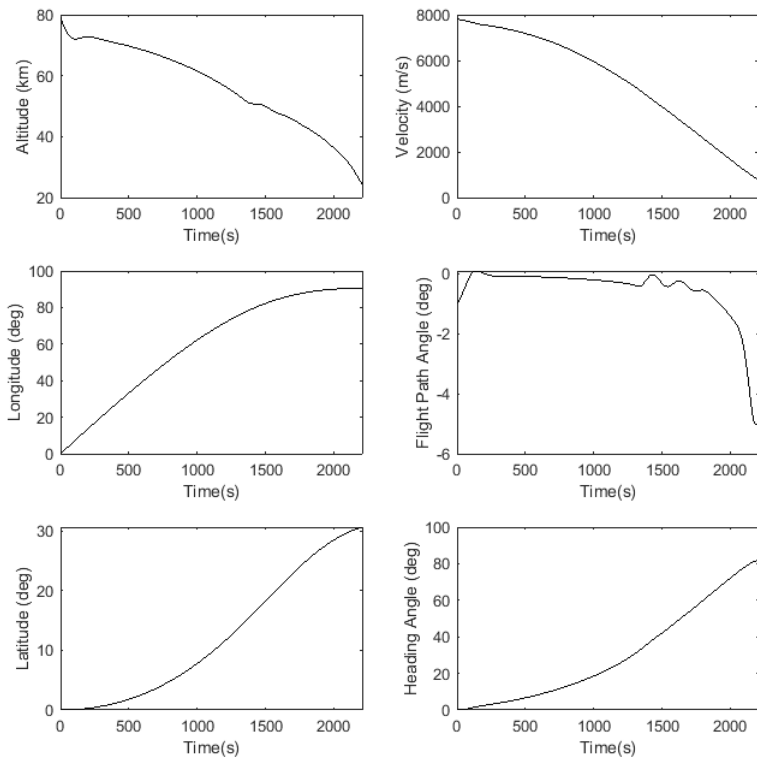


Figure C.4

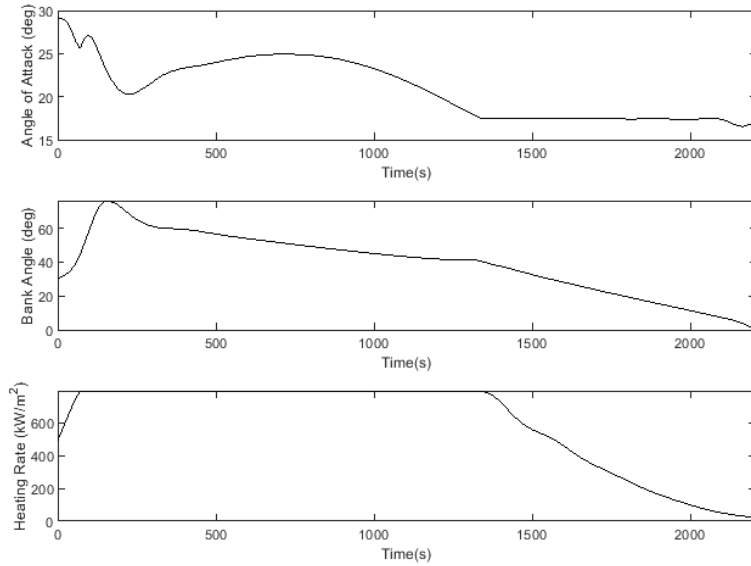


Figure C.5

C.3 Optimised Trajectory Verification

XXX Add verification here (possibly with one of maddocks works, or a single stage to orbit, or space shuttle) XXX this is the section that describes the error in 'timestep' as requested by reviewer, though there are multiple other factors. 'A Comparison of Accuracy and Computational Efficiency of Three Pseudospectral Methods' also uses matlab's ODE45 for error comparison.

C.4 Optimised Trajectory Analysis

This section presents an example of the convergence and verification of a trajectory optimised using GPOPS-2, within LODESTAR. The convergence and verification of a maximum payload-to-orbit trajectory solution, with SPARTAN fly-back (Case 11) is shown.

C.4.1 Mesh History

The mesh history of the optimal trajectory solution is shown in Figure C.6. The mesh is updated by GPOPS-2 in each iteration of the optimal solution. It can be observed that the meshes of the first and third stage rockets contain significantly less node points at the final iteration than the meshes of the SPARTAN's acceleration and return. This is due to the relatively simple dynamics and shorter flight time of the first and third stages. The first stage shows a cluster of nodes at the beginning of its trajectory, in the subsonic, transonic and low Mach regimes. In this region, the aerodynamics are changing

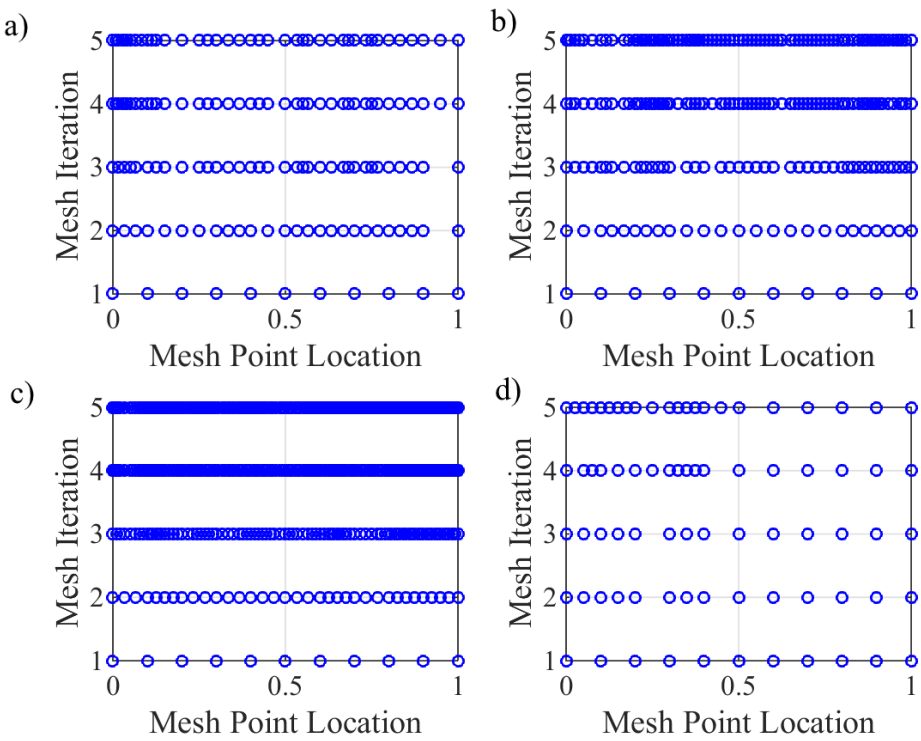


Figure C.6: The mesh history of each phase of the optimised, maximum payload-to-orbit trajectory with SPARTAN fly-back (Case 11). the phases are shown in each subfigure as follows: a) first stage rocket, b) SPARTAN acceleration, c) SPARTAN fly-back and d) third stage.

rapidly, and the nodes are clustered to accurately capture the dynamic behaviour of the vehicle. After transition occurs to supersonic flight, the aerodynamics and engine performance of the vehicle change more slowly, and the nodes become more widely spaced. In contrast, the acceleration of the SPARTAN shows significant node density throughout. The operation of the SPARTAN is complex, as the dynamics of the vehicle and the performance of the scramjet engines vary significantly, even during relatively level flight. For this reason, the nodes of the return flight show even greater density. The trajectory conditions change significantly as the SPARTAN performs skipping manoeuvres, and transitions through the various return phases, necessitating high node density to capture the vehicle dynamics, particularly between powered and unpowered flight. The trajectories of the SPARTAN also last for a significantly longer time than the rocket trajectories, requiring more total nodes to accurately capture the vehicle dynamics. The third stage shows the least nodes at the final mesh iteration, as the dynamics of the third stage are relatively simple. Some node clustering is observed in the first part of the trajectory, where the atmospheric density is still significant.

C.4.2 Verification

After a trajectory has been calculated, it must be verified to ensure that the optimal control solver has converged correctly. Details on this verification are provided in Section 5.4. Figure C.7 shows the Hamiltonian time history for the optimised trajectory solution of Case 11. For an optimal solution to be found, the Hamiltonian should be equal to 0 at all points over every phase. In a practical solution, a Hamiltonian close to 0 is acceptable, which is observable over all phases in the optimised solution. The Hamiltonian is close to 0 at all points of the trajectory, indicating that an optimal solution has been found.

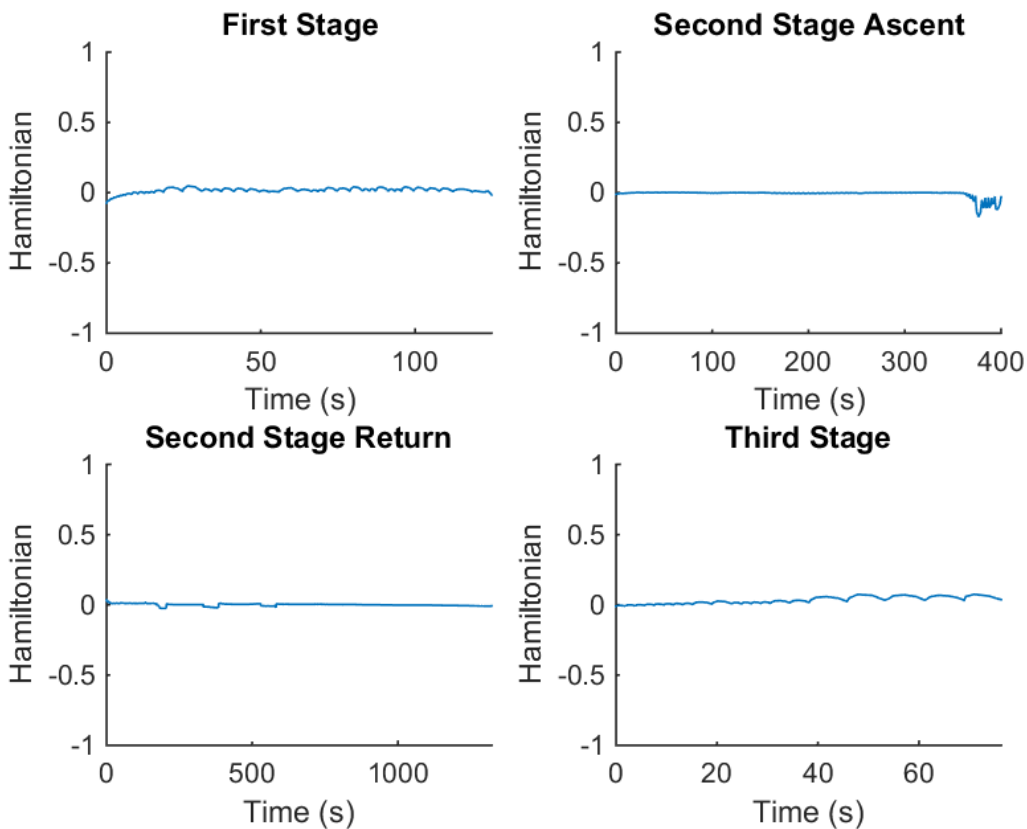


Figure C.7: The Hamiltonian time history of each phase of the maximum payload-to-orbit optimised trajectory, with SPARTAN fly-back (Case 11).

The next step in the verification process is to ensure that the dynamic constraints of the optimal control problem holds across the entire solution, ie. $\dot{\mathbf{x}}(t) = f[t, \mathbf{x}(t), \mathbf{u}(t)]$. This is the most important step in the verification process, which checks that the optimal control solver has converged correctly, so that the physical dynamics of the vehicle are being correctly represented by the polynomial approximations within GPOPS-2. The dynamic constraints are tested by first calculating the dynamics of each vehicle at every node of the solution, using the vehicle simulations. These dynamics are then integrated over time using trapezoidal integration, starting at the initial conditions of each phase.

The integrated dynamics are then compared to the states of the optimised solution. If the dynamic constraints have been satisfied, then the integrated dynamics of the system will be equal to the state variables of the solution. The error in the dynamic constraints of each state are shown in Figure C.8, calculated as the difference between the integrated dynamics and each state variable, normalised to the range of the state variable. It can be observed that all errors in the dynamic constraints are very small. The error that is present is likely to be due to the inaccuracies of the trapezoidal method, which is significantly less accurate than the approximating polynomials of the pseudospectral method.

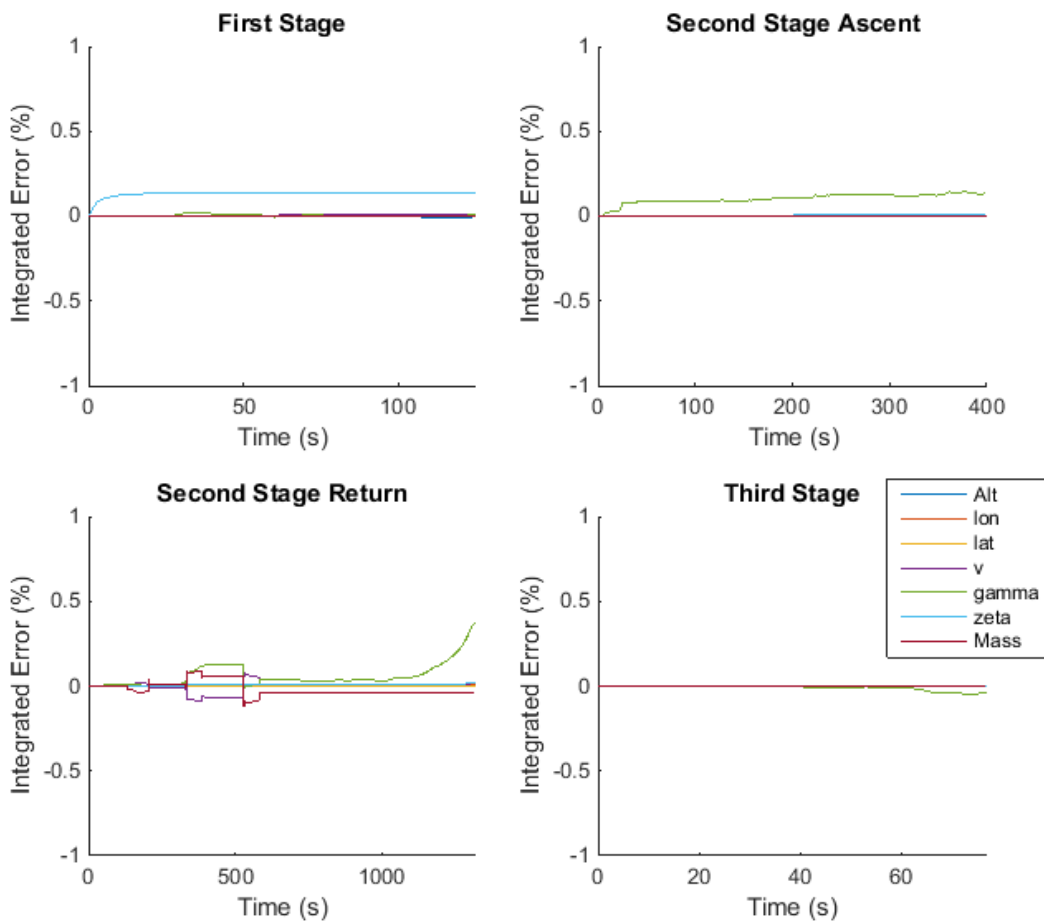


Figure C.8: The error between the integrated dynamics of the system, and the solution states of each phase of the maximum payload-to-orbit optimised trajectory, with SPARTAN fly-back (Case 11). Normalised to the range of each state.

The final verification step is a forward simulation of each phase. This forward simulation compares the solution state with a simulation which is forward integrated using only the controls of each stage. This is the most stringent method of checking the validity of the solution dynamics. However, it is expected that this verification will have significantly higher errors than the check which verifies the dynamics of each state independently, as the interdependencies of each state come into play, and

small errors are compounded. Figure C.9 shows the error between the forward simulation and the solution states. As described in Section 5.4, the forward simulation of the return flight is separated into three segments, at 1/6th and 1/3rd of the flight time. The errors in the forward simulation of each stage are observed to be acceptably small, significantly under 1% in all cases, and it is evident that compounding errors are the cause of the most extreme deviations.

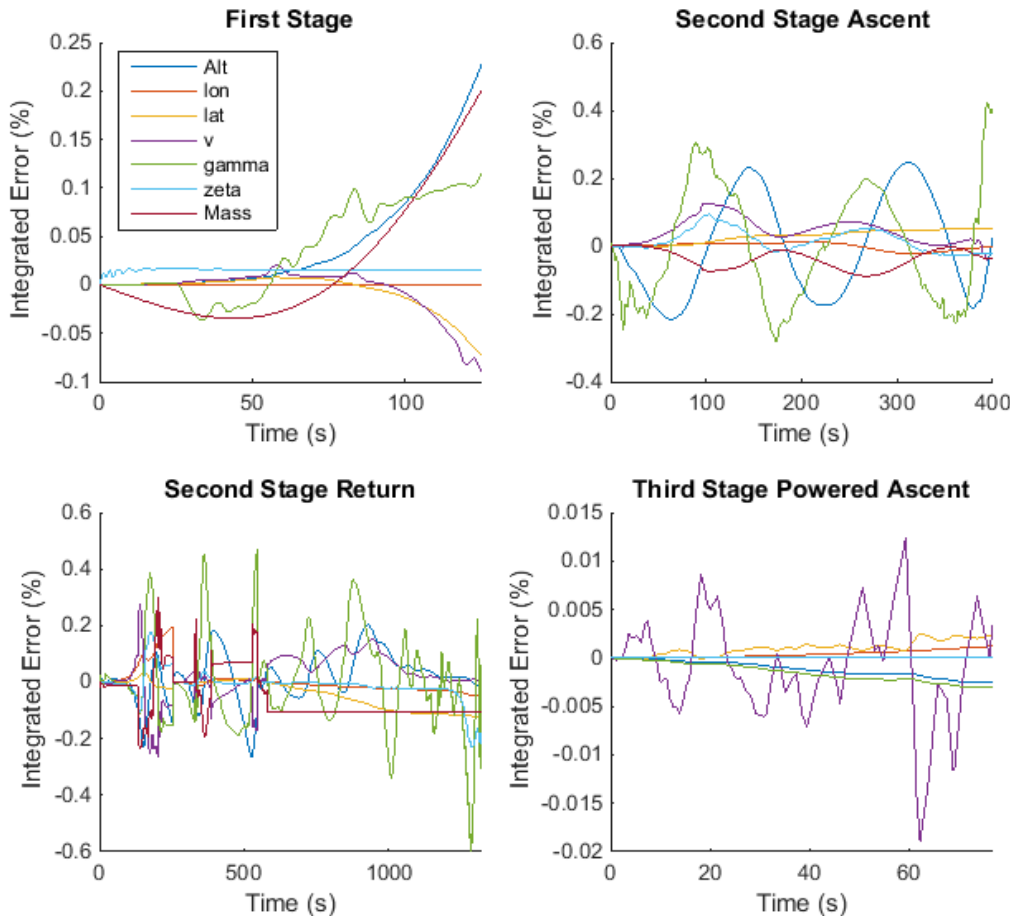


Figure C.9: The error between the forward simulated states, and the solution states of each phase of the maximum payload-to-orbit optimised trajectory, with SPARTAN fly-back (Case 11). Normalised to the range of each state.

APPENDIX D

MODELLING AND SIMULATION

D.1 Propulsion Interpolation Scheme

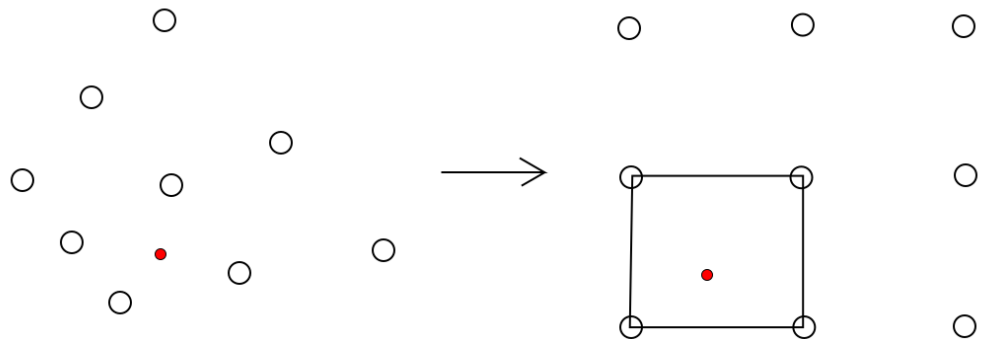


Figure D.1: The transformation to a normalised interpolation scheme.

This section describes the interpolation scheme used for the C-RESTM10 database to determine specific impulse. The C-RESTM10 engine database consists of a set of engine conditions, including specific impulse, ordered by the inlet Mach number and temperature. This data set must be interpolated, to calculate the performance of the engine at each flight condition. However, no inlet Mach number and temperature values are repeated between any of the C-RESTM10 data points. This makes for a scattered data set which complicates the process of interpolating for specific impulse. It was observed that when interpolating for specific impulse, a scattered interpolation produces particularly poor results, and that fitting splines to the data set is the only way to produce an appropriate interpolation scheme. However, even when splines were fit, and the general trends of the specific impulse

were matched, minuscule oscillations were still present in the interpolated values. These oscillations do not significantly affect a forward simulation, however, when using the vehicle model as part of an optimal control calculation, they can affect the convergence process. Consequently, it was necessary to craft a bespoke interpolation scheme in order to accurately interpolate the specific impulse of the vehicle.

This interpolation begins by designating a new coordinate system, normalised to [0 1], running from data point with the lowest inlet temperature [0,0], to the data point with the highest inlet temperature [1,1]. Each data point is then given a set of normalised coordinates, and a cubic spline is fit to this set of normalised points using MATLAB's `griddedInterpolant` function. The normalised, ordered, data set ensures that this cubic spline is smooth, with no oscillations present. In order to interpolate at a specific location, each data point bounding the interpolation region is set as the corner of a square of data points in normalised coordinates. This is illustrated in Figure D.1. The distance to each of these bounding data points is calculated, and the location to be interpolated is assigned a set of normalised coordinates. This set of normalised coordinates is used to interpolate for specific impulse.

This process is accurate, but computationally time consuming, and would increase the computation time of the optimisation process significantly if implemented directly within the vehicle model. In order to expedite the interpolation process, interpolations are performed for the specific impulse for every combination of inlet Mach number and temperature present in the C-RESM10 database. This creates a grid of interpolated data points, which includes all of the data points present in the C-RESTM10 database. This grid of interpolated specific impulse values is then used as a new data set, which is now in meshgrid form, by which the specific impulse is interpolated. A bivariate spline is fitted to this grid of data points, using MATLAB's `griddedInterpolant` function, which is accessed by the vehicle model to determine specific impulse during flight.

D.2 SPARTAN Flow Results

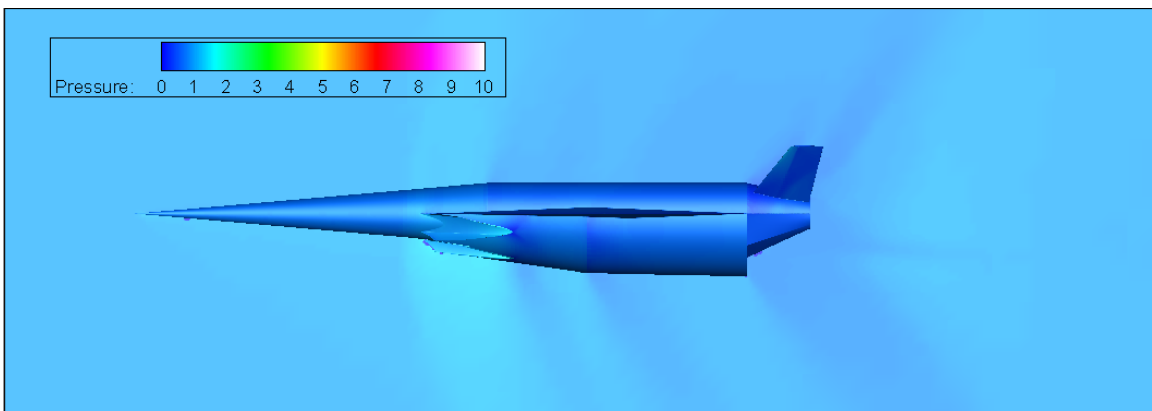


Figure D.2: CART3D flow result for the SPARTAN, at Mach 1.1, 6° angle of attack.

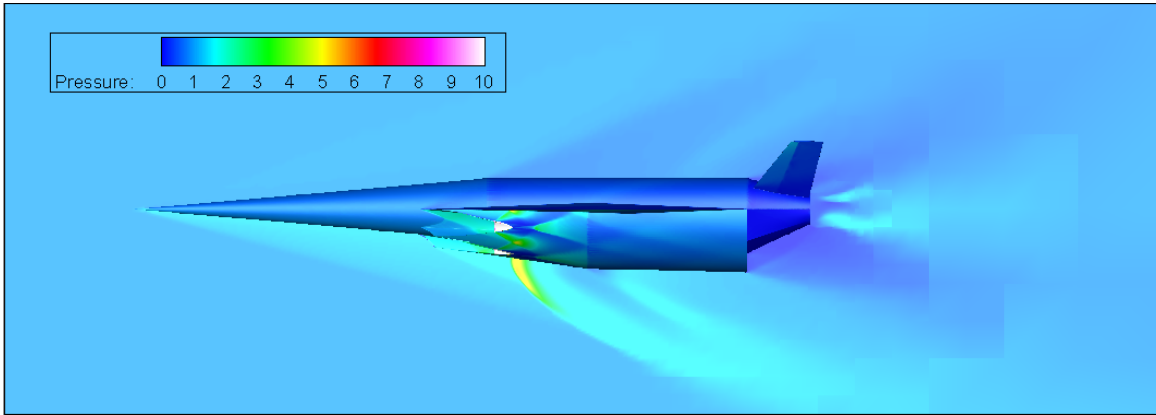


Figure D.3: CART3D flow result for the SPARTAN, at Mach 3, 6° angle of attack.

This section shows additional flow results for the SPARTAN, calculated using Cart3D. Figures D.2 and D.3 show flow results for the SPARTAN, at Mach numbers of 1.1 and 3 respectively. It can be observed that at Mach 1.1, the bow shock is not significant, and the shock structure that is evident at higher speeds has not yet formed. At Mach 3, the unstalled C-REST engines are evident, causing significant amounts of the air entering the inlet to be expelled. Shock-shock interaction structures are evident on the cowl of the engines, causing areas of localised high pressure.

D.3 Cart3D Mesh

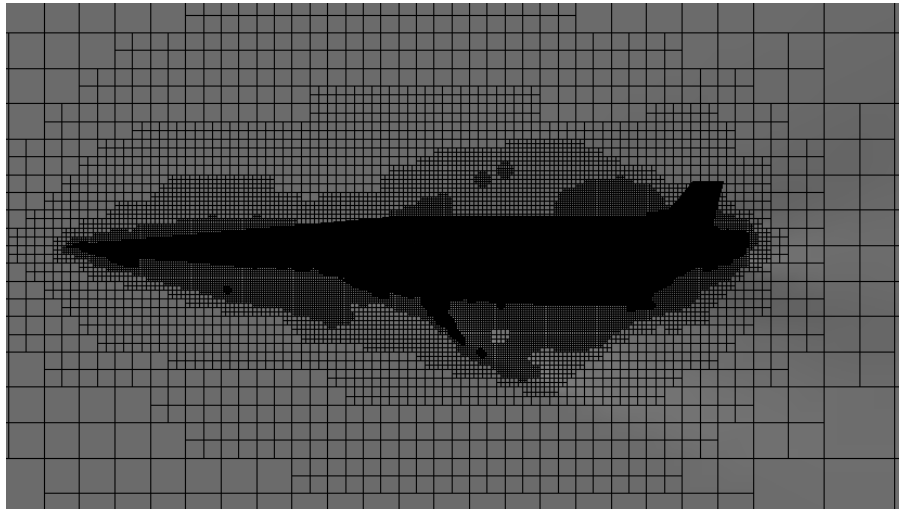


Figure D.4: Adapted mesh of the SPARTAN at Mach 6 3° angle of attack.

This section illustrates the converged meshes used by Cart3D. Figures D.4 and D.5 show adapted meshes for Cart3D solutions of the SPARTAN, and the SPARTAN and first stage. These meshes have been generated adaptively by Cart3D during the solution process. It can be observed that the mesh

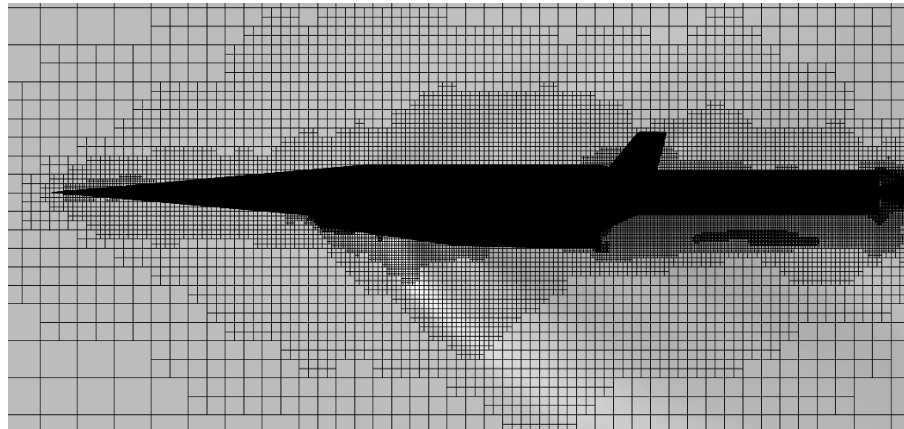


Figure D.5: Adapted mesh around the SPARTAN and first stage vehicles, flying at Mach 2, -1° angle of attack.

clusters around the vehicle, particularly in regions where strong shocks are present, where the mesh clusters at the shock front.

D.4 Performance of the SPARTAN During Fly-Back

Figure D.6 shows the performance of the SPARTAN during the boost phase, described in Section 7.3.

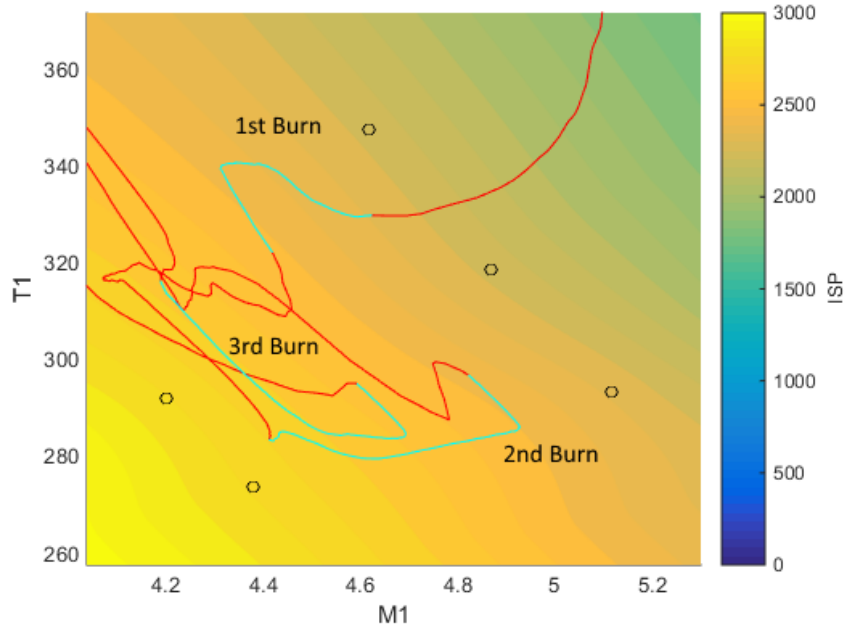


Figure D.6: The performance of the SPARTAN during the boost phase. Light blue indicates that the scramjet engines are turned on.

APPENDIX E

ALTERNATE TRAJECTORY CASES

E.1 Trajectory With Decreased Third Stage TPS Mass

XXX Add here as a design variation for reviewer

E.2 Trajectory With Variation in Return Drag

I should maybe do a variation of just the return drag - "the performance of the launch system may be significantly different on the ascent and return trajectories (in addition to the engine flowpaths)"

E.3 Maximum Payload-To-Orbit Trajectory With Dynamic Pressure Constraint

XXX update this, make sure to update values too, used in ascent section The maximum payload-to-orbit trajectory of the launch system with no SPARTAN fly-back (Case 2) was found to involve a significant altitude raising manoeuvre in the middle of the acceleration trajectory of the SPARTAN. Discerning the benefits of this altitude raising manoeuvre proved complex, requiring a trajectory to be calculated in which the altitude raising manoeuvre is prevented from occurring. This section describes an optimised trajectory in which the middle section of the SPARTAN's acceleration is constrained to flight at maximum dynamic pressure.

This trajectory was optimised for maximum payload-to-orbit, with a 50kPa dynamic constraint between Mach numbers of 6 and 8, the region in which the altitude raising manoeuvre was observed to occur. This constraint successfully removed the altitude raising manoeuvre from the maximum

payload-to-orbit optimised trajectory, allowing for a comparison to be made to quantify the benefits of the altitude raising manoeuvre. This comparison is made in Section 6.2. Figures E.1, E.2 and E.3 show the maximum payload-to-orbit trajectory constrained to 50kPa between Mach numbers 6 to 8, and Table E.1 details key parameters of the trajectory.

Trajectory Condition	Value
Payload to Orbit (kg)	188.8
Total η_{exergy} (%)	1.690
1st Stage η_{exergy} (%)	6.295
Separation Alt, 1→2 (km)	24.12
Separation v, 1→2 (m/s)	1485
Separation γ, 1→2 (deg)	3.2
2nd Stage η_{exergy} (%)	4.693
Separation Alt, 2→3 (km)	42.44
Separation v, 2→3 (m/s)	2679
Separation γ, 2→3 (deg)	10.9
2nd Stage Flight Time (s)	629.8
2nd Stage Distance Flown (km)	1145.7
3rd Stage η_{exergy} (%)	18.706
3rd Stage t, $q > 5\text{kpa}$ (s)	10.8
3rd Stage max α (deg)	16.0
3rd Stage Fuel Mass (kg)	2826.0

Table E.1: A summary of key results from the maximum payload-to-orbit trajectory, constrained to 50kPa between Mach numbers 6 to 8.

E.4 Sonic Boom Ground Effects

The flight of a hypersonic vehicle has the potential to create significant overpressures on the ground due to sonic booms. This section describes the effects of the sonic booms generated by the SPARTAN.

Even when a hypersonic vehicle is flying at high altitudes, the overpressures on the ground may still be large enough to have detrimental effects on any populated areas being overflown. The overpressure from sonic booms can cause significant annoyance to the populace, or in more extreme cases, long term damage to building structures or peoples health. When the SPARTAN is launched to a sun synchronous orbit from the Equatorial Launch Australia launch site, it flies over a significant portion of Papua. Fortunately, Papua is sparsely populated, and the number of towns flown over by the SPARTAN will be low. However the effects on these population centres may still be significant. In order to assess the impact of the SPARTAN’s flight, the magnitude of the overpressure from its sonic booms must be calculated.

The sonic boom overpressures are estimated using the ‘first cut’ estimation technique [193]. This

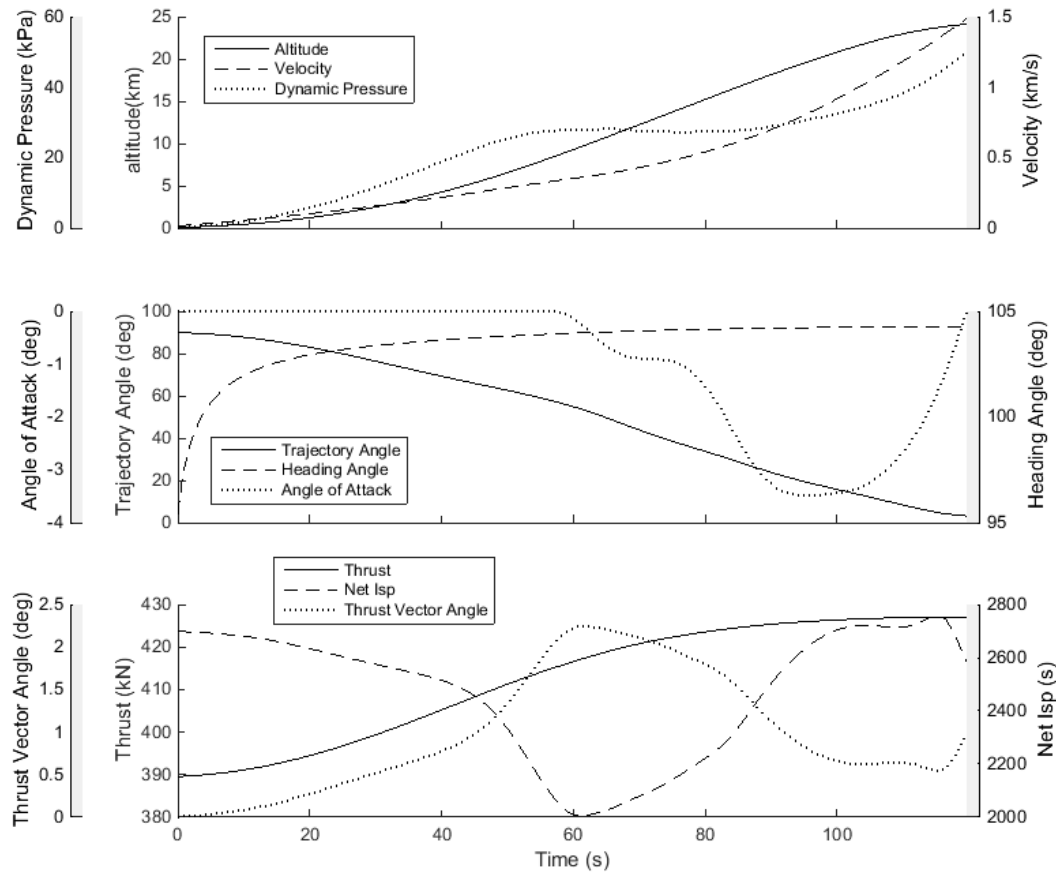


Figure E.1: The optimised maximum payload-to-orbit trajectory of the launch system constrained to 50kPa between Mach numbers 6 to 8, under power of the first stage rocket.

estimation technique can approximate sonic boom overpressures moderately well, and is useful as a first approximation to the sonic boom overpressures generated by an aerospace vehicle. The overpressures generated by the SPARTAN are calculated over its trajectory, shown in Figure E.5. It is found that overpressures of up to 375.3Pa occur during flight over land during the maximum payload-to-orbit trajectory of the SPARTAN. These overpressures have a low but significant probability of causing cosmetic damage to structures (1.5% for plaster and 0.4% for glass)[194]. In addition, overpressures of these magnitudes have been rated as unacceptably annoying to the majority populace being overflowed, as shown in Figure E.4. These overpressures indicate that overflight of populated areas may not be reasonable for the SPARTAN flying its maximum payload-to-orbit trajectory path, with fly-back (Case 11).

Trajectory Condition	Value
Payload to Orbit (kg)	175.2
Total η_{exergy} (%)	1.662
1st Stage η_{exergy} (%)	6.559
Separation Alt, 1→2 (km)	25.64
Separation v, 1→2 (m/s)	1552
Separation γ, 1→2 (deg)	3.4
2nd Stage η_{exergy} (%)	4.014
Separation Alt, 2→3 (km)	41.30
Separation v, 2→3 (m/s)	2581
Separation γ, 2→3 (deg)	11.1
2nd Stage Flight Time (s)	500.8
2nd Stage Distance Flown (km)	835.0
2nd Stage Return Fuel (kg)	280.9
2nd Stage Return Distance (km)	1595.4
3rd Stage η_{exergy} (%)	17.352
3rd Stage $t, q > 5\text{kpa}$ (s)	12.1
3rd Stage max α (deg)	16.4
3rd Stage Fuel Mass (kg)	2839.6

Table E.2: A summary of key trajectory parameters of the maximum payload-to-orbit trajectory launched in a southerly direction.

E.5 Alternate Launch Location

In this section, an alternate southerly launch is investigated for the rocket-scramjet-rocket launch system, in the case that flight over Papua is not possible. This launch occurs from Streaky Bay, the possible location of a launch site being developed by Southern Launch Australia[195]. The maximum payload-to-orbit has been calculated from this launch site using LODESTAR. Figure E.6 shows the ground track of this optimised trajectory, and Table E.2 details a summary of the key trajectory parameters. The shape of this optimised trajectory is very similar to the optimal trajectory of the launch system launched from the Northern Territory (Case 11). The first stage initially pitches towards the west, separating the SPARTAN in a westerly direction. The SPARTAN then performs a banking manoeuvre to the south, and a pull-up before third stage release. After separation, the SPARTAN exhibits initial turn, boost-skip and approach phases during fly-back, with the scramjet engine igniting three times at the troughs of the first three skips, in the same manner as when launching northerly. A higher payload to orbit is achieved when launching from a southerly location, attaining a total of 175.2kg of payload-to-orbit, an increase of +2.9% compared to northerly launch. This payload increase is caused by the rotation of the Earth hindering, rather than assisting, when launching into a retrograde orbit, making launch from a more southerly point desirable.

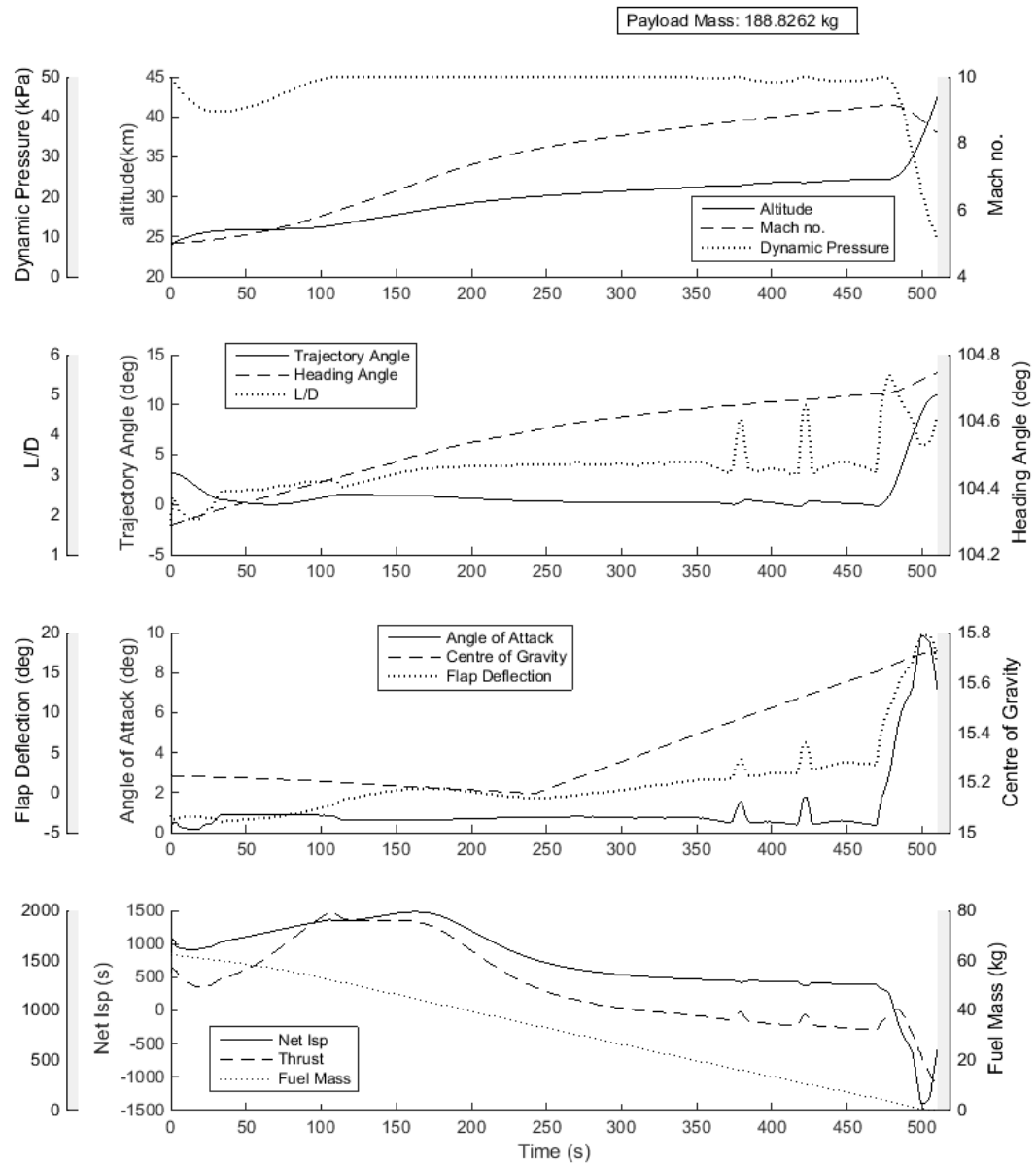


Figure E.2: The optimised maximum payload-to-orbit trajectory of the SPARTAN, constrained to 50kPa between Mach numbers 6 to 8.

APPENDIX E. ALTERNATE TRAJECTORY CASES

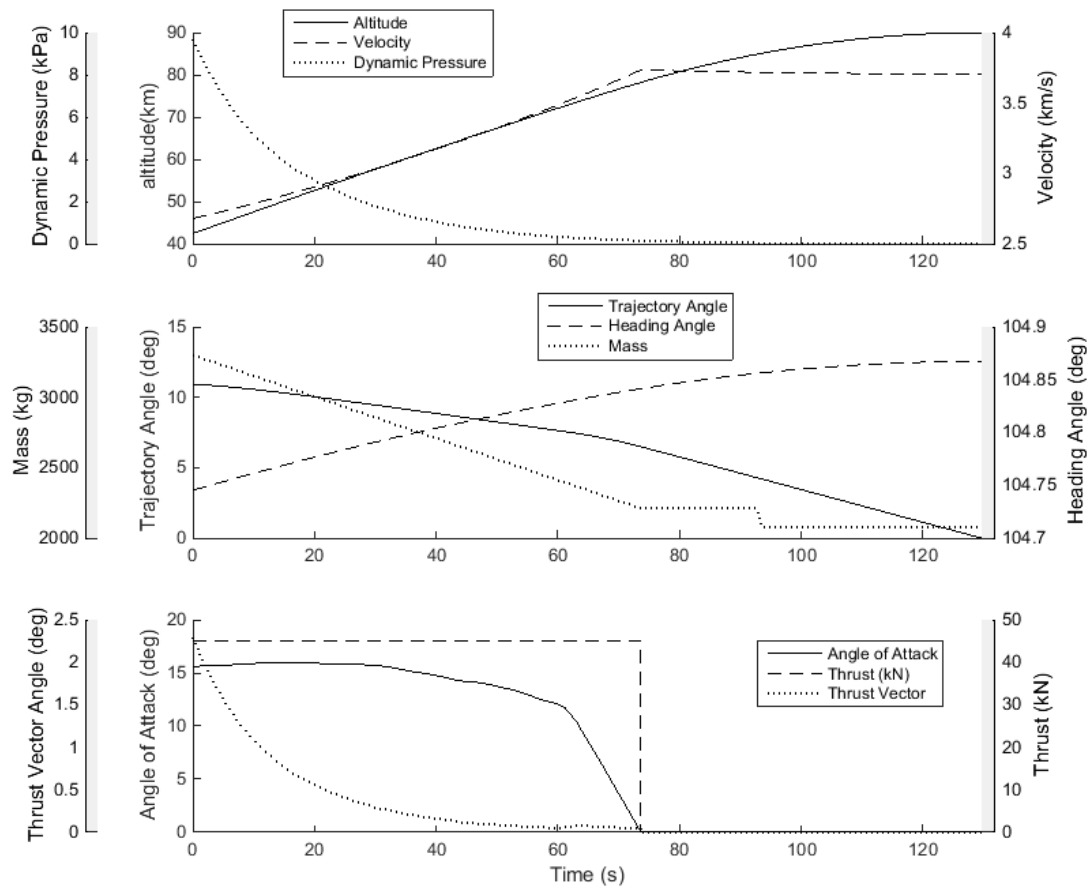


Figure E.3: The third stage trajectory of the launch system flying the maximum payload-to-orbit trajectory, constrained to 50kPa between Mach numbers 6 to 8.

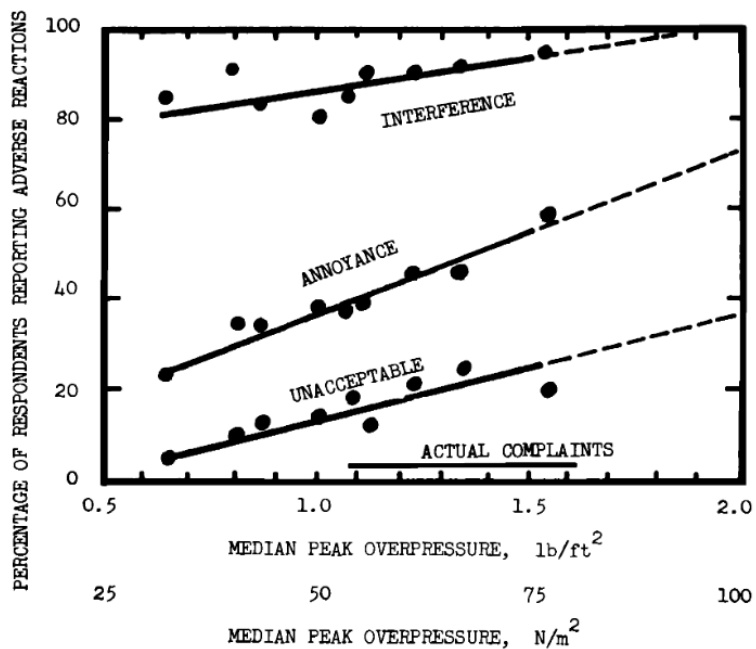


Figure E.4: The level of population annoyance with increasing overpressure.

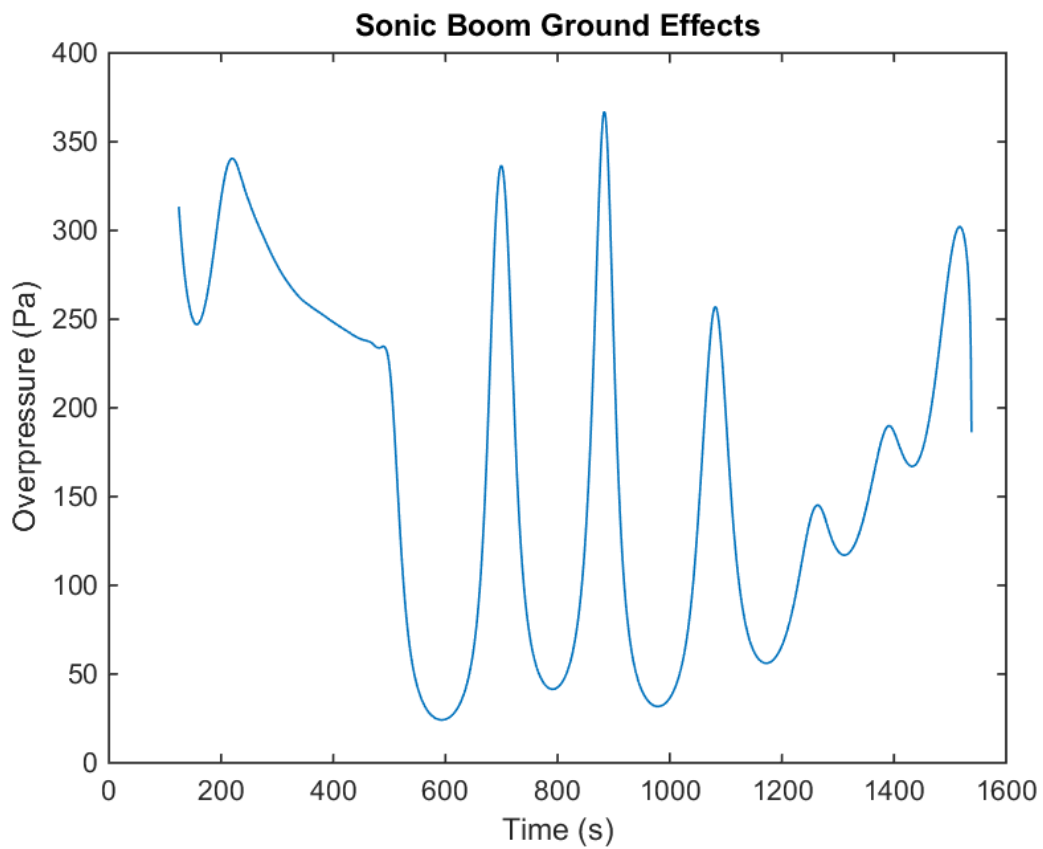


Figure E.5: The sonic boom overpressure on the ground, for the optimised trajectory path (Case 11).

APPENDIX E. ALTERNATE TRAJECTORY CASES

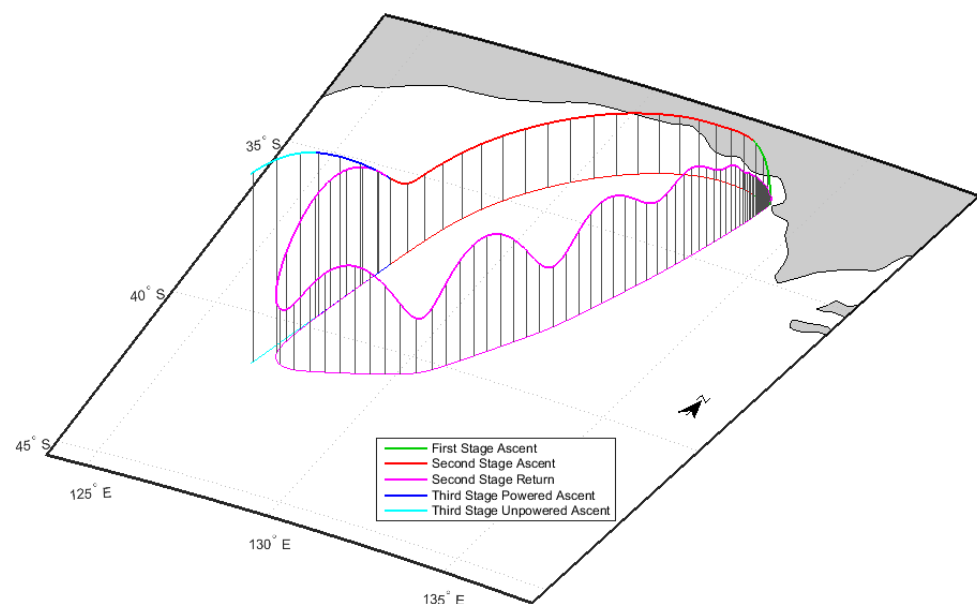


Figure E.6: The optimised maximum payload-to-orbit trajectory of the launch system launching onto a southerly orbit, from Streaky Bay.

APPENDIX F

TRAJECTORY PLOT COMPARISONS

XXX update these

This section contains trajectory plot comparisons for the sensitivity studies performed in Section 6.4 and 7.5. Comparisons and analyses between these trajectories are performed in the relevant sections.

F.1 Optimised Ascent Trajectory Comparisons With No Fly-Back

F.1.1 Case 3: Maximum Dynamic Pressure Sensitivity Comparison

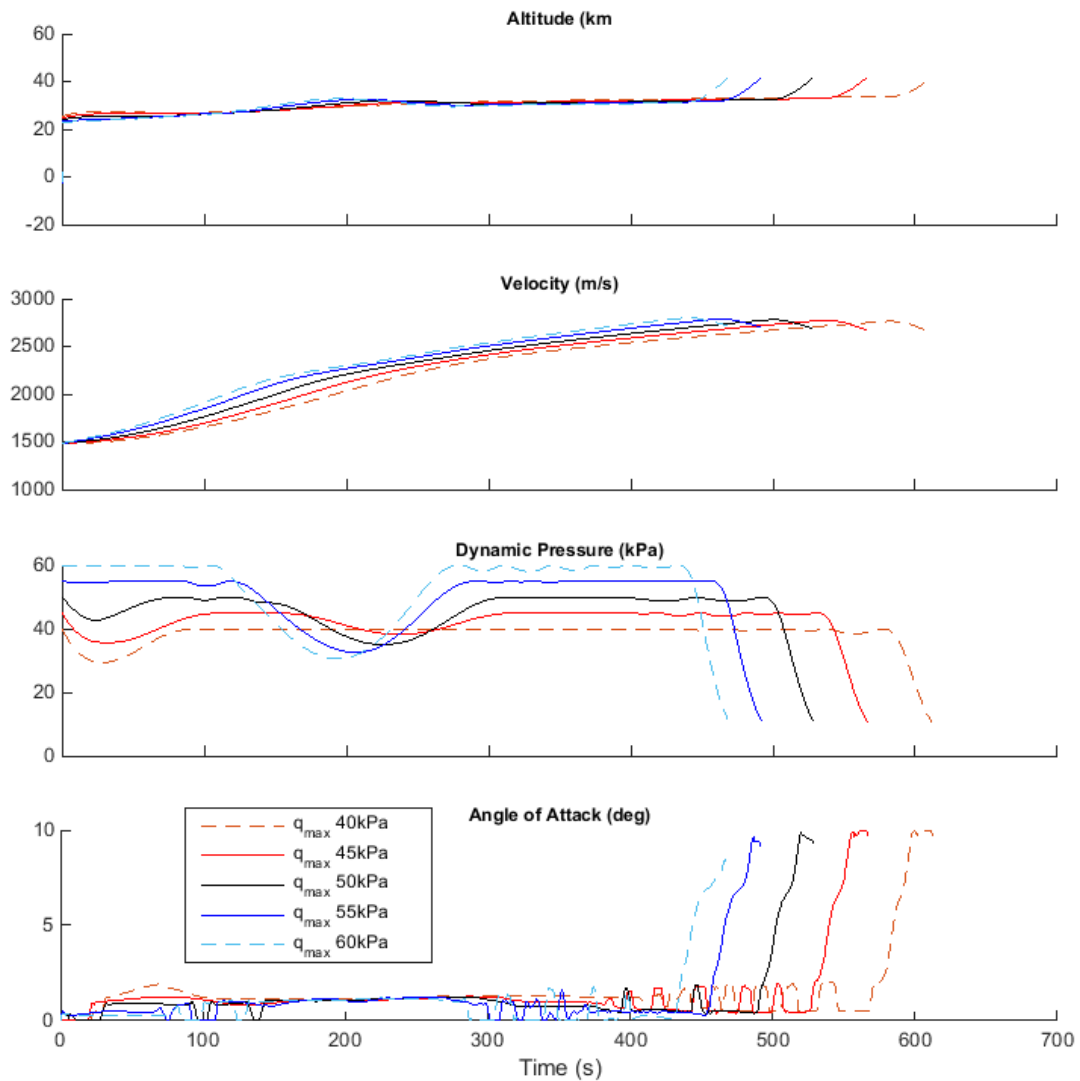


Figure F.1: Comparison of SPARTAN ascent trajectories with variation in the maximum dynamic pressure of the SPARTAN.

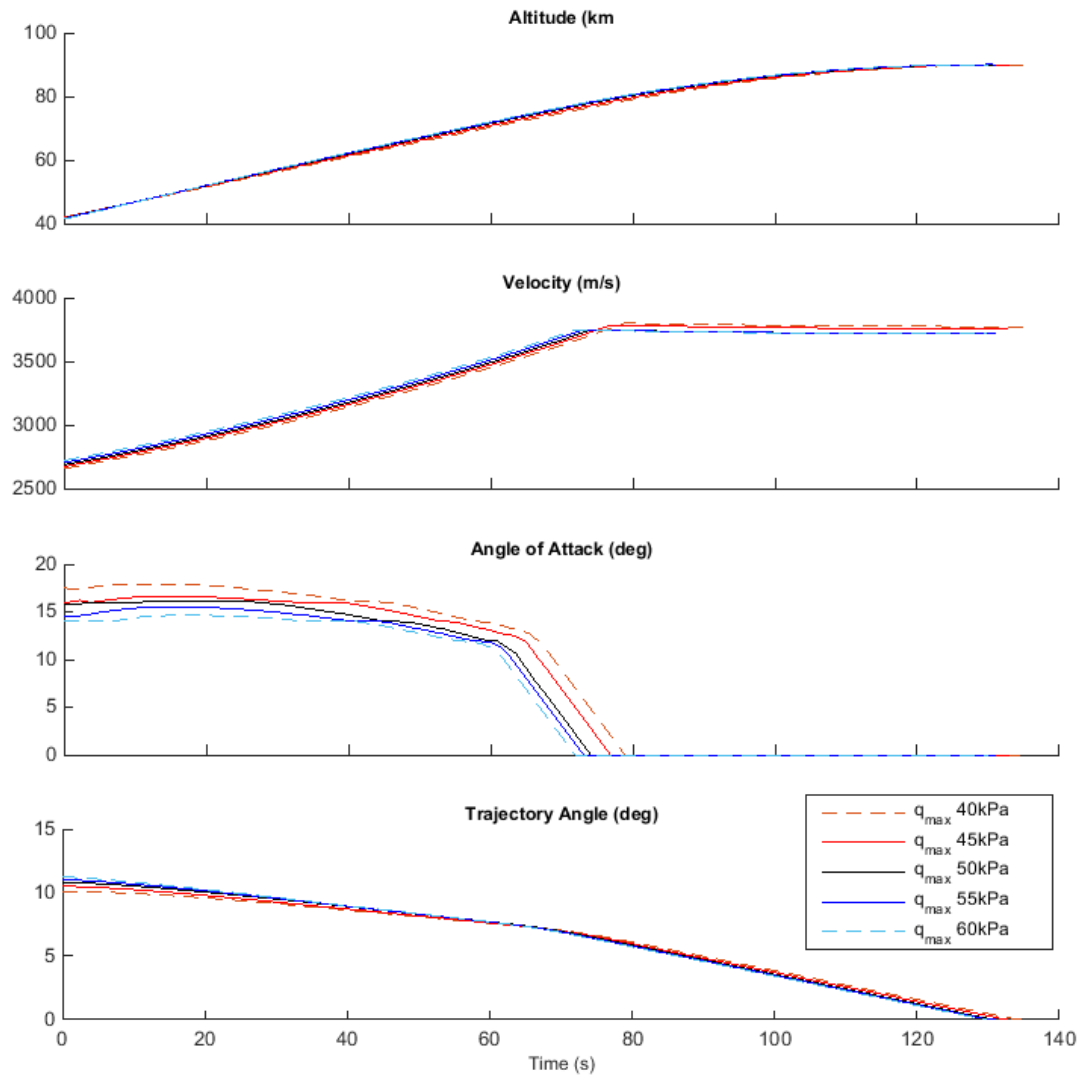


Figure F.2: Comparison of third stage rocket ascent trajectories with variation in the maximum dynamic pressure of the SPARTAN.

F.1.2 Case 4: SPARTAN Drag Sensitivity Comparison

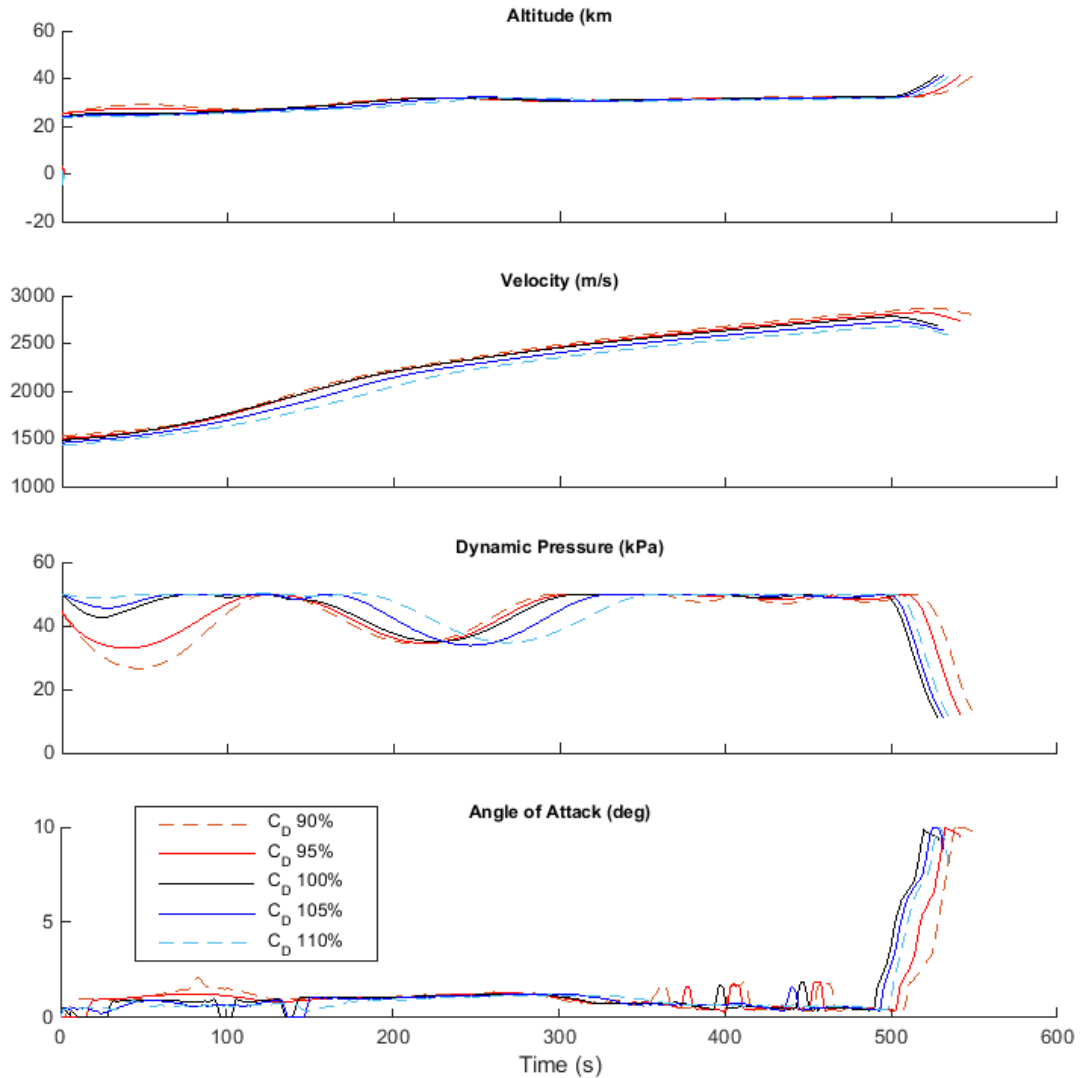


Figure F.3: Comparison of SPARTAN ascent trajectories with variation in the drag of the SPARTAN.

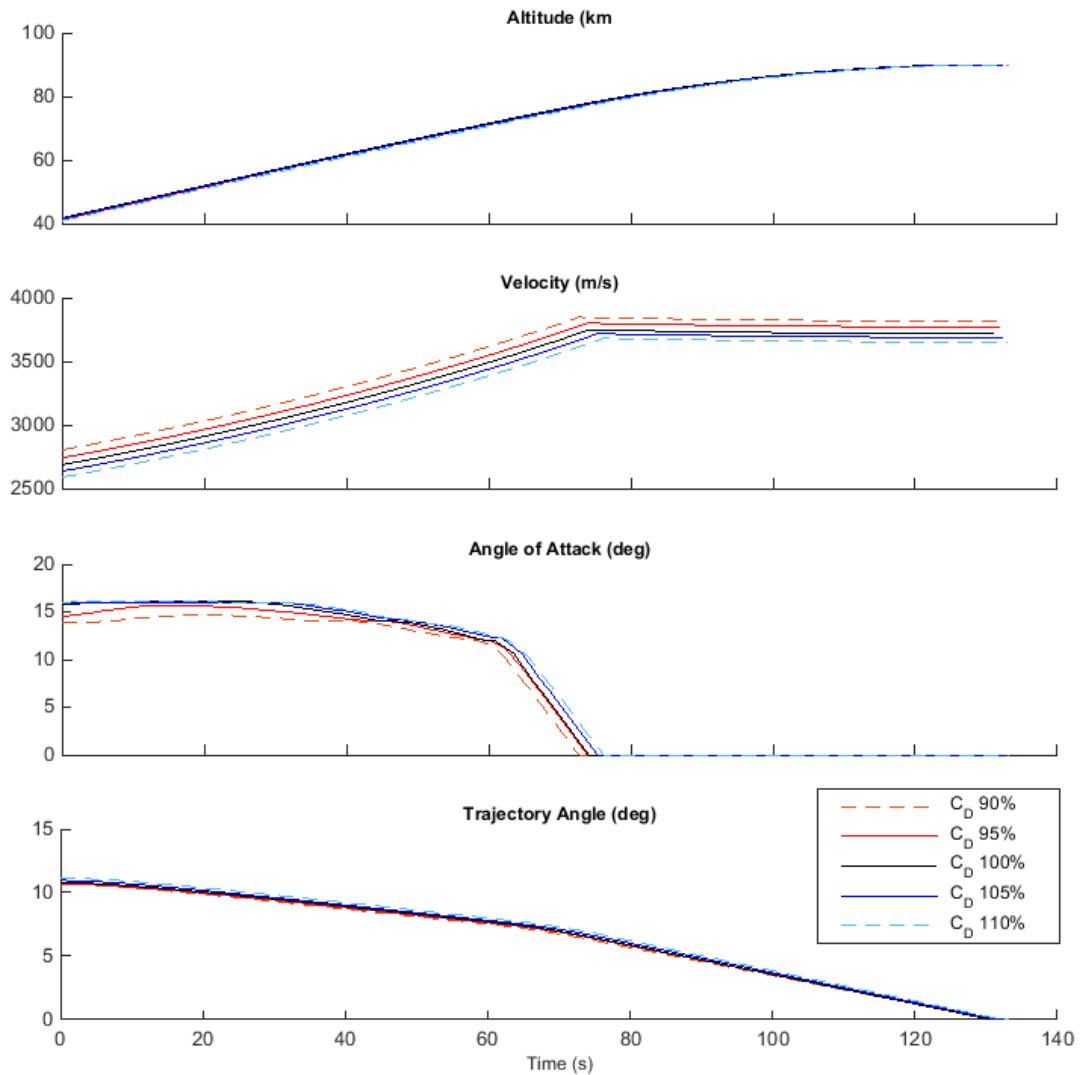


Figure F.4: Comparison of third stage rocket ascent trajectories with variation in the drag of the SPARTAN.

F.1.3 Case 5: SPARTAN Specific Impulse Sensitivity Comparison

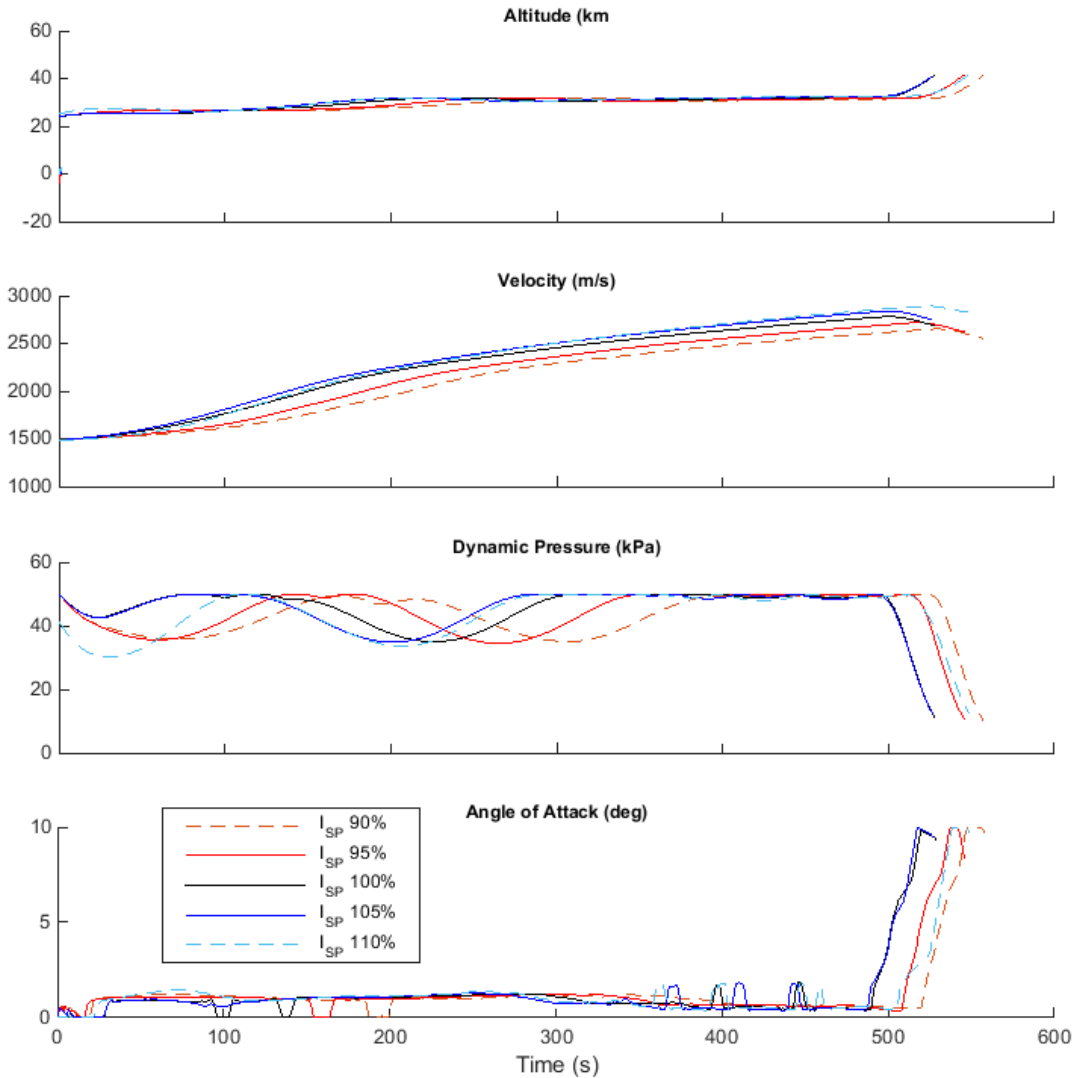


Figure F.5: Comparison of SPARTAN ascent trajectories with variation in the specific impulse of the SPARTAN.

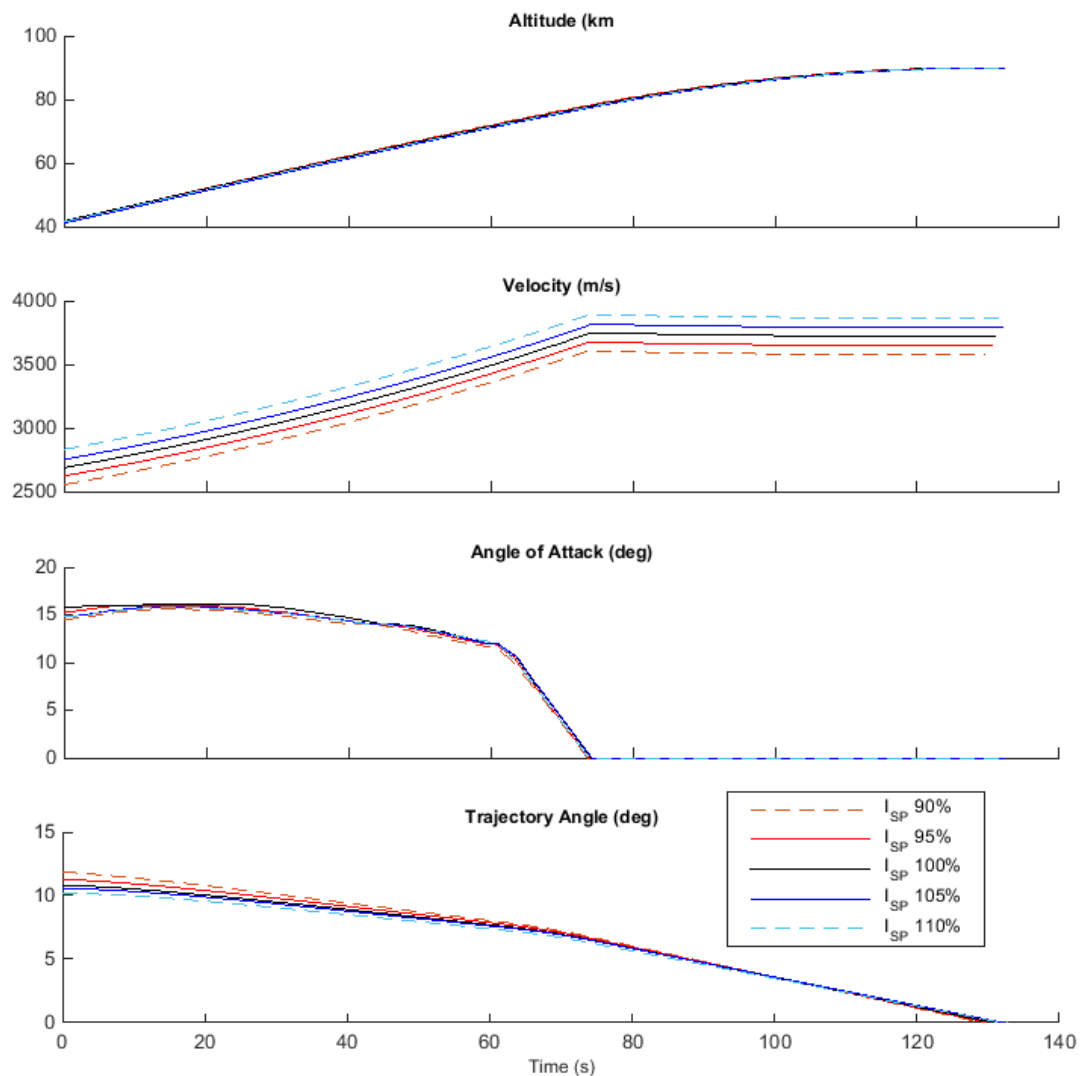


Figure F.6: Comparison of third stage rocket ascent trajectories with variation in the specific impulse of the SPARTAN.

F.1.4 Case 6: SPARTAN Mass Sensitivity Comparison

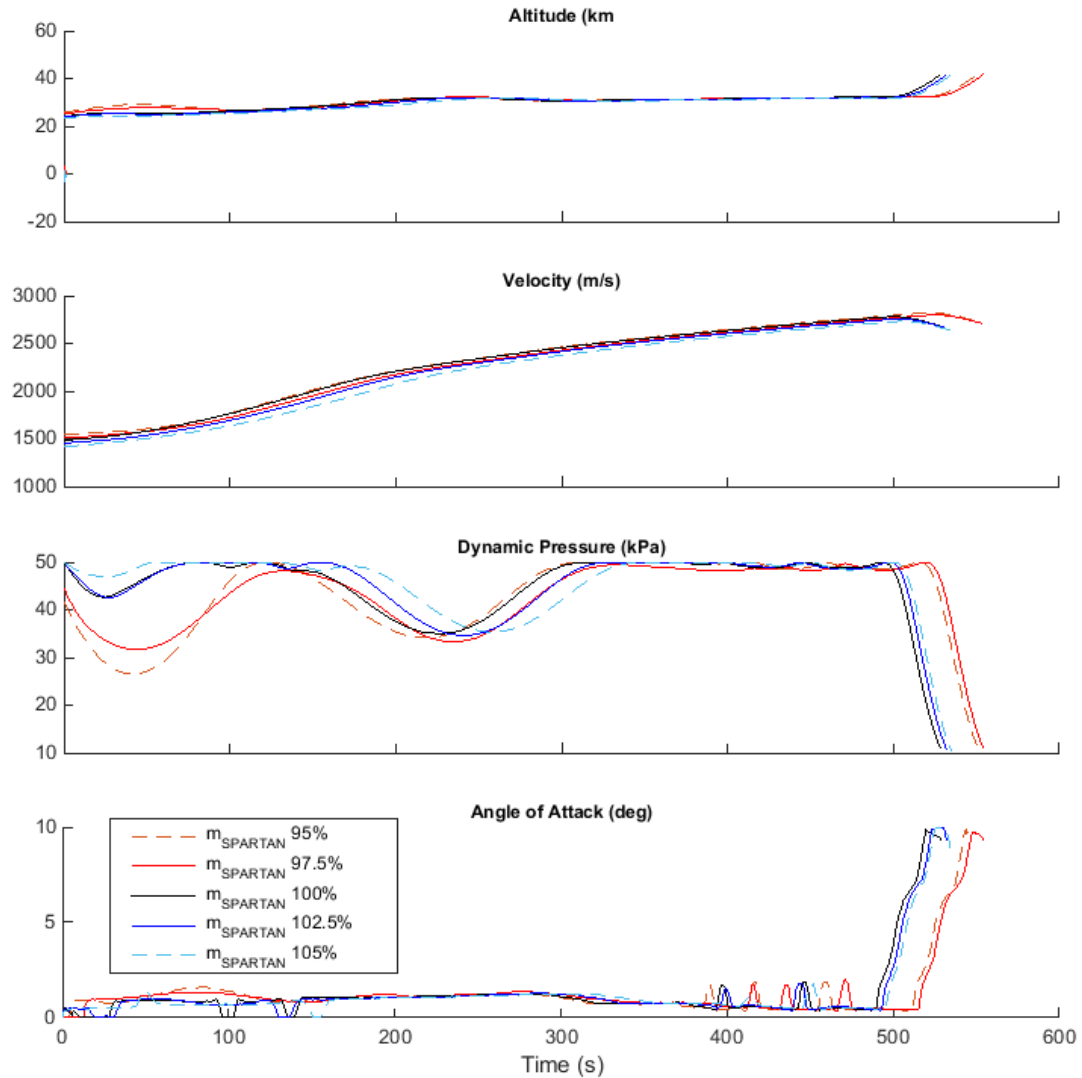


Figure F.7: Comparison of SPARTAN ascent trajectories with variation in the mass of the SPARTAN.

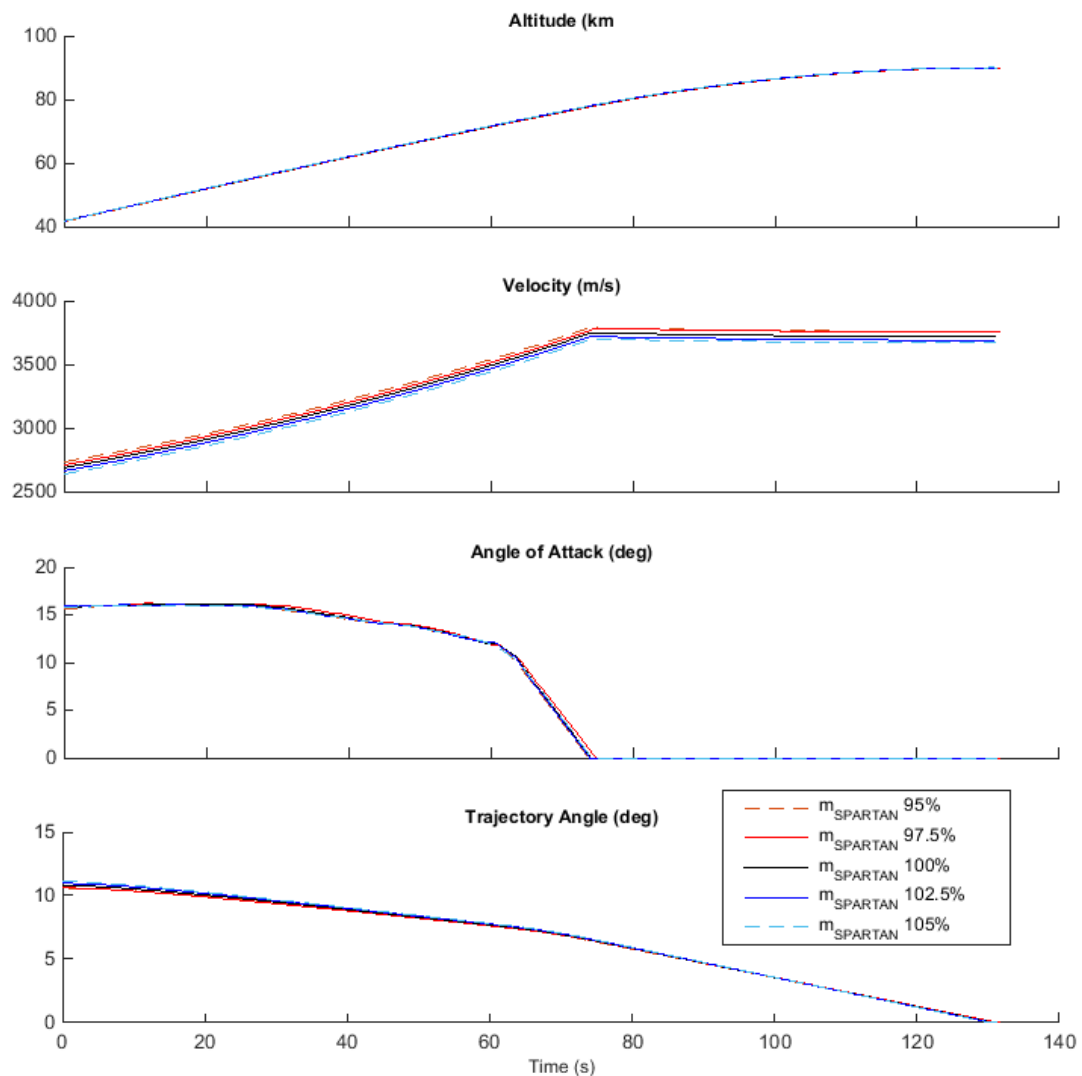


Figure F.8: Comparison of third stage rocket ascent trajectories with variation in the mass of the SPARTAN.

F.1.5 Case 7: SPARTAN Fuel Mass Sensitivity Comparison

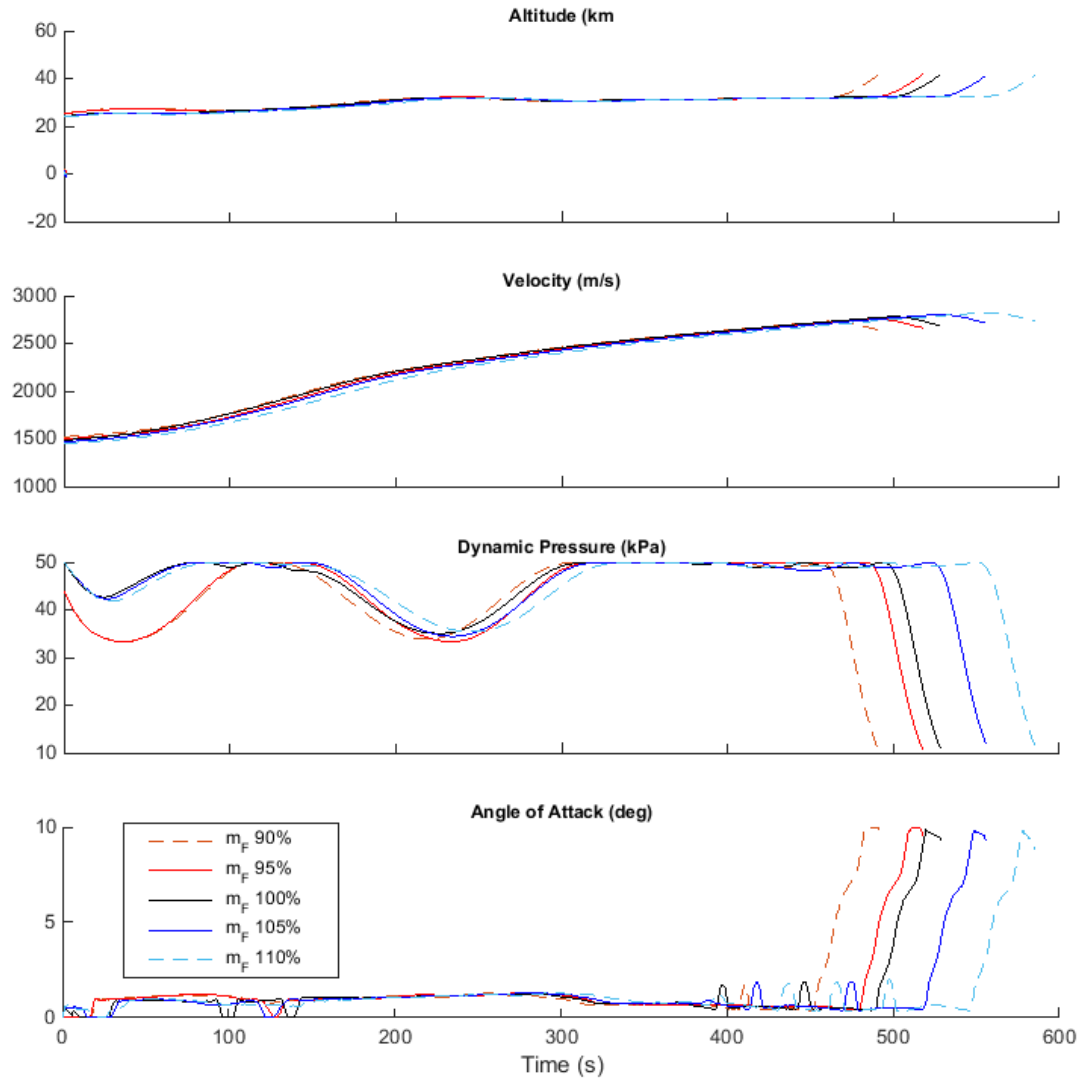


Figure F.9: Comparison of SPARTAN ascent trajectories with variation in the fuel mass of the SPARTAN.

F.1. OPTIMISED ASCENT TRAJECTORY COMPARISONS WITH NO FLY-BACK

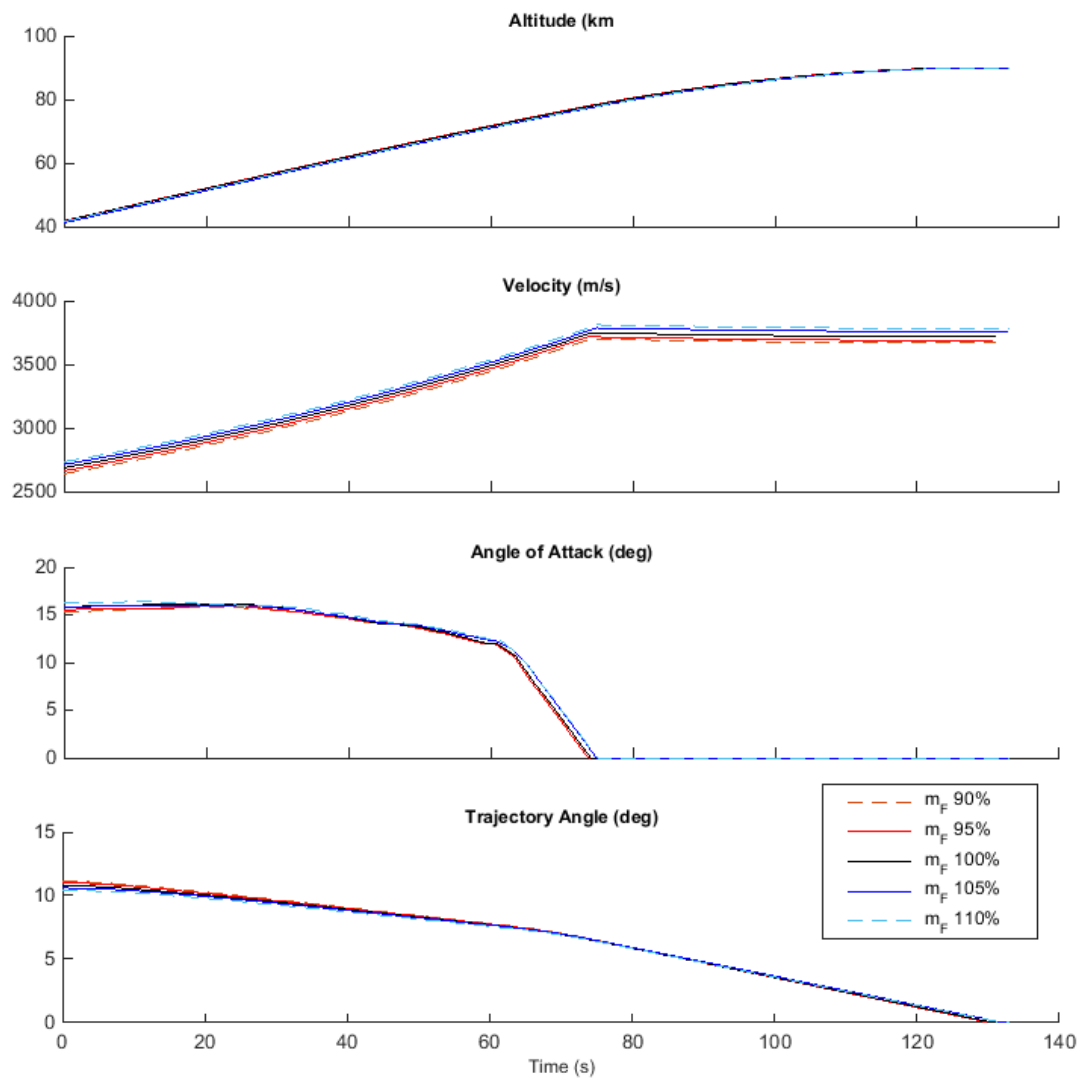


Figure F.10: Comparison of third stage rocket ascent trajectories with variation in the fuel mass of the SPARTAN.

F.1.6 Case 8: Third Stage Mass Sensitivity Comparison

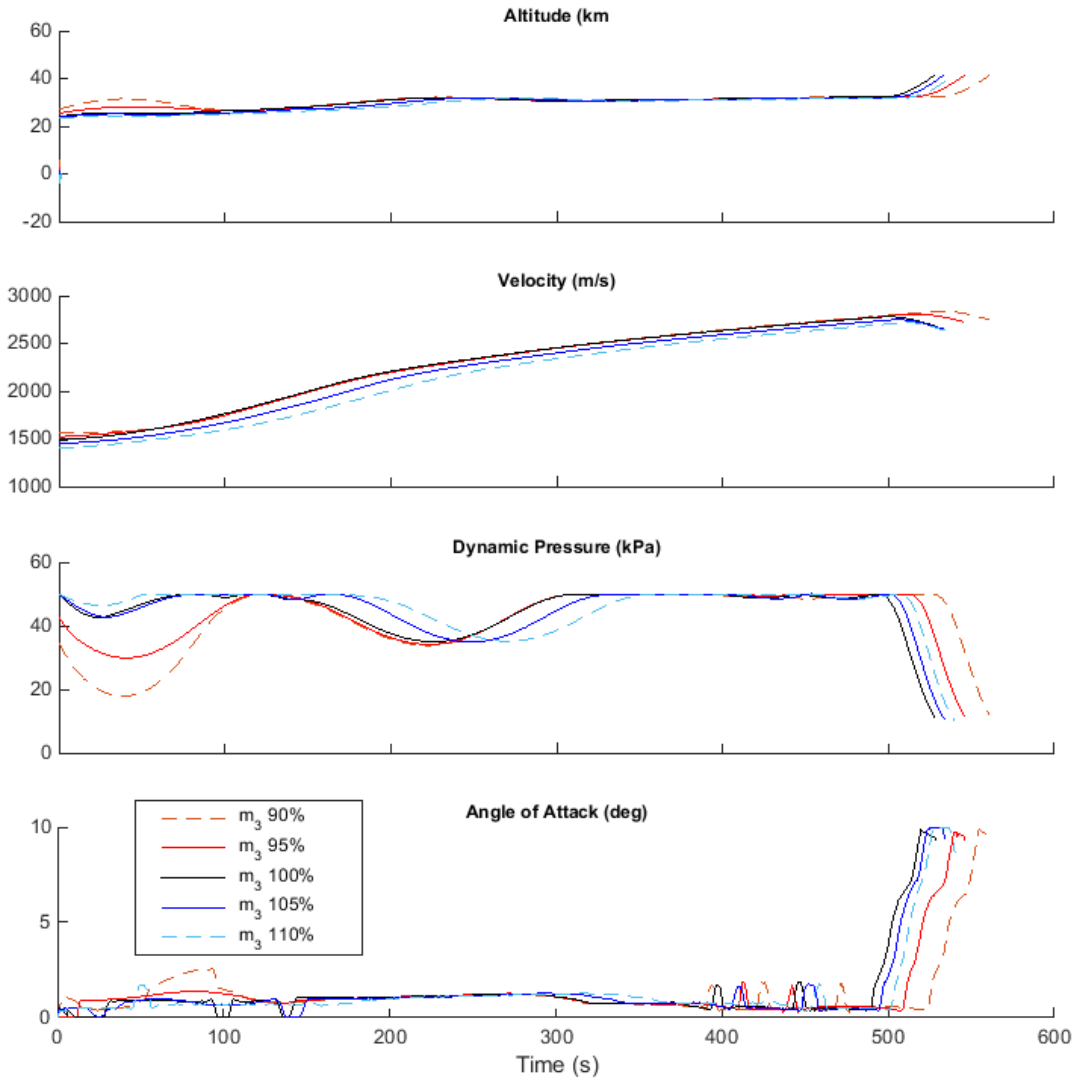


Figure F.11: Comparison of SPARTAN ascent trajectories with variation in the mass of the third stage.

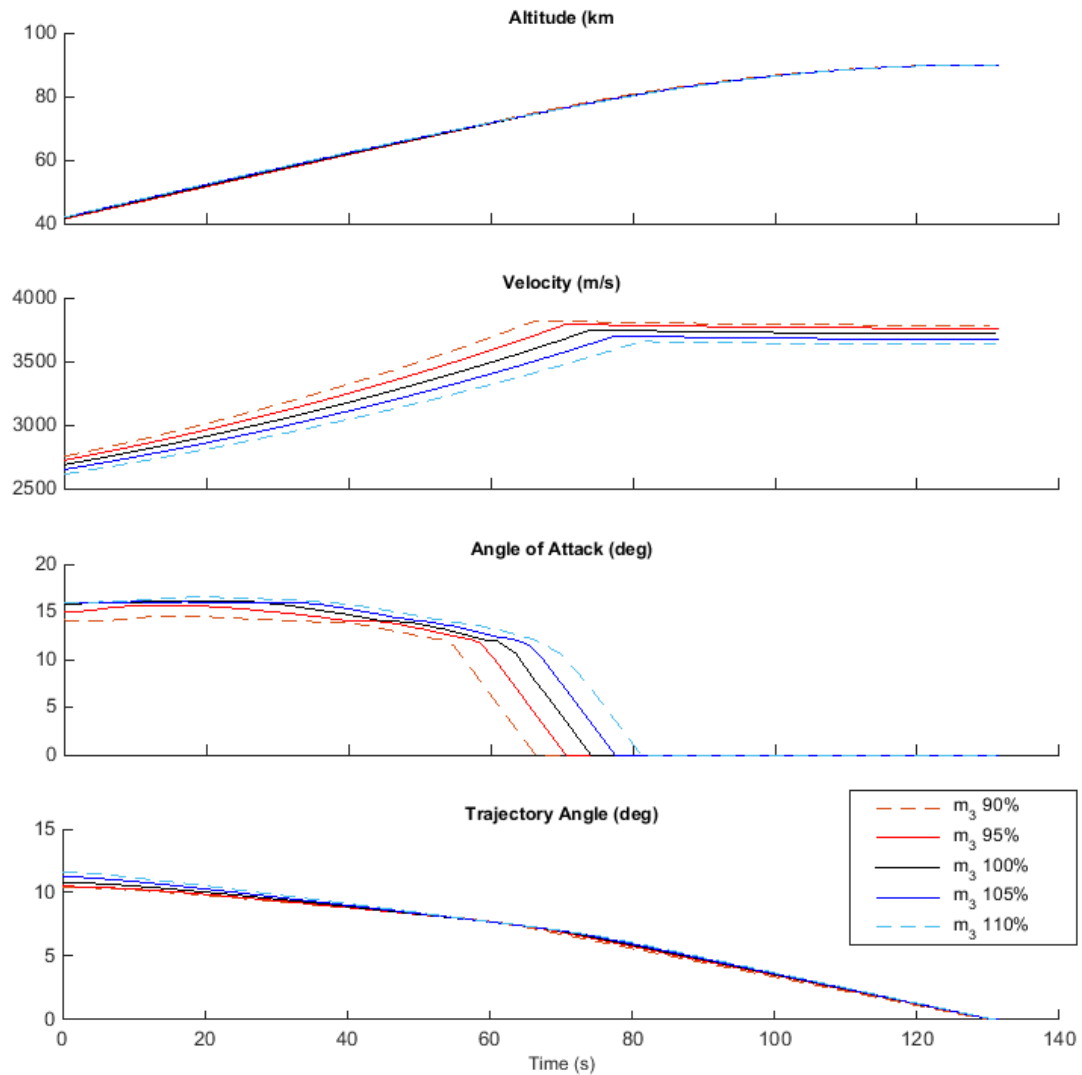


Figure F.12: Comparison of third stage rocket ascent trajectories with variation in the mass of the third stage.

F.1.7 Case 9: Third Stage Specific Impulse Sensitivity Comparison

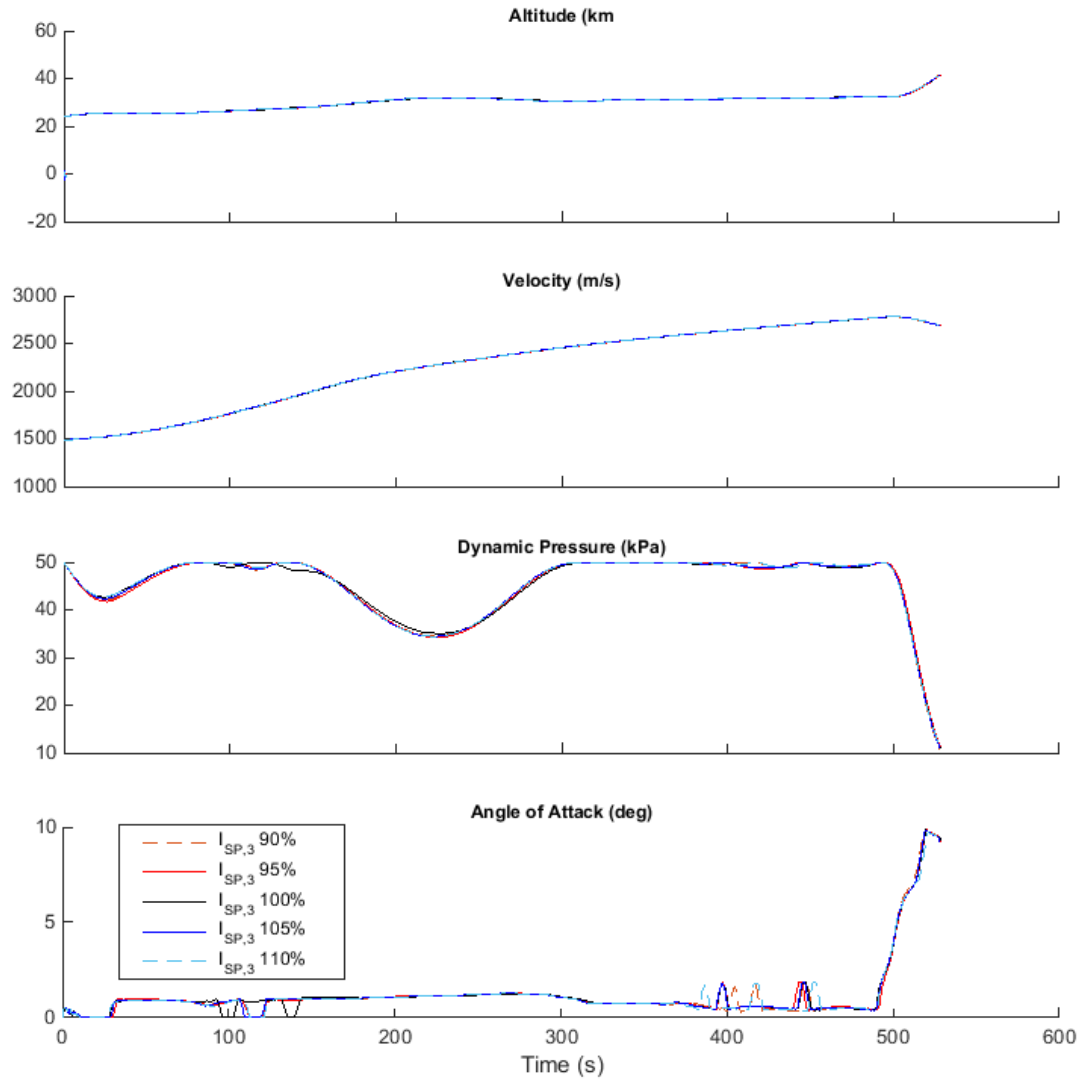


Figure F.13: Comparison of SPARTAN ascent trajectories with variation in the specific impulse of the third stage.

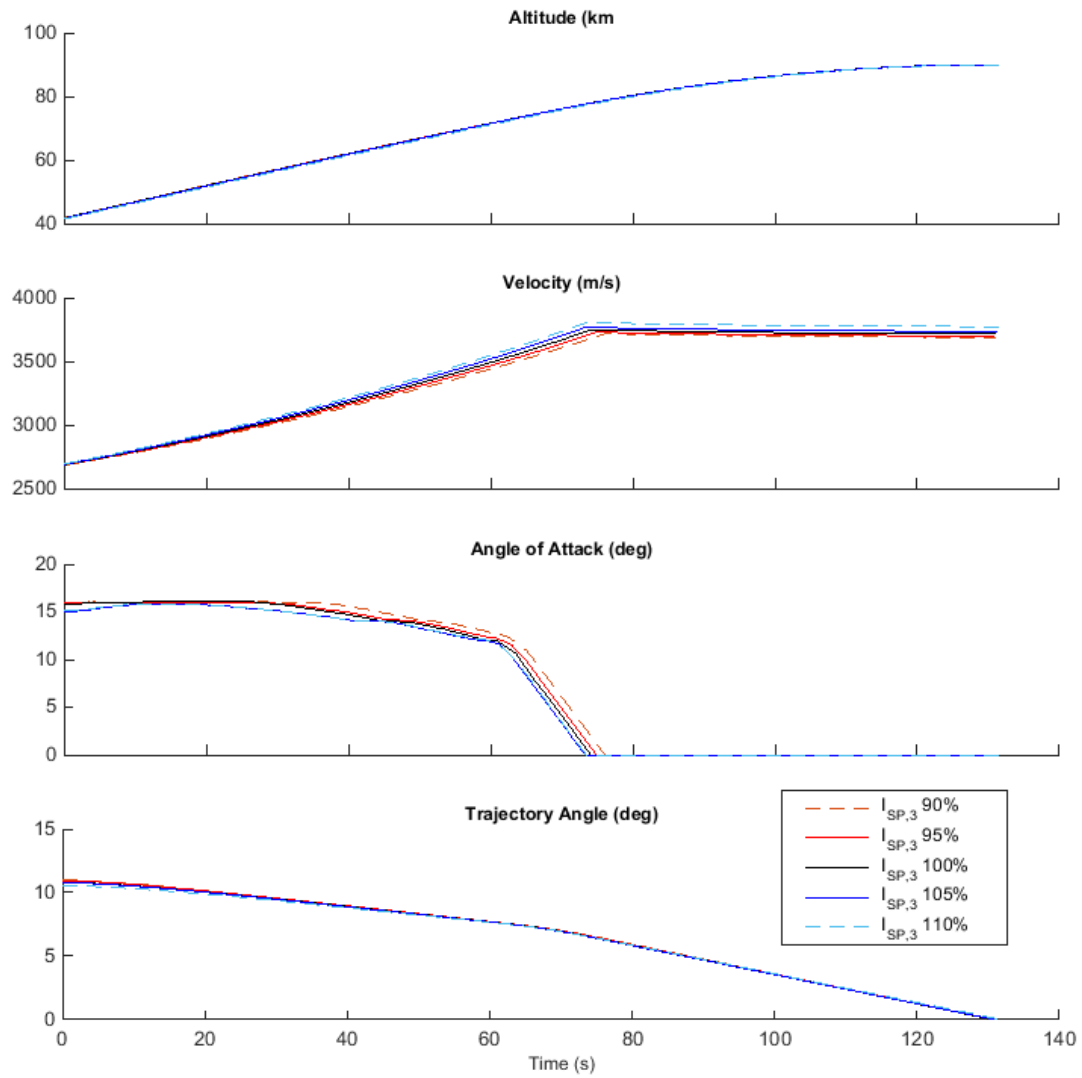


Figure F.14: Comparison of third stage rocket ascent trajectories with variation in the specific impulse of the third stage.

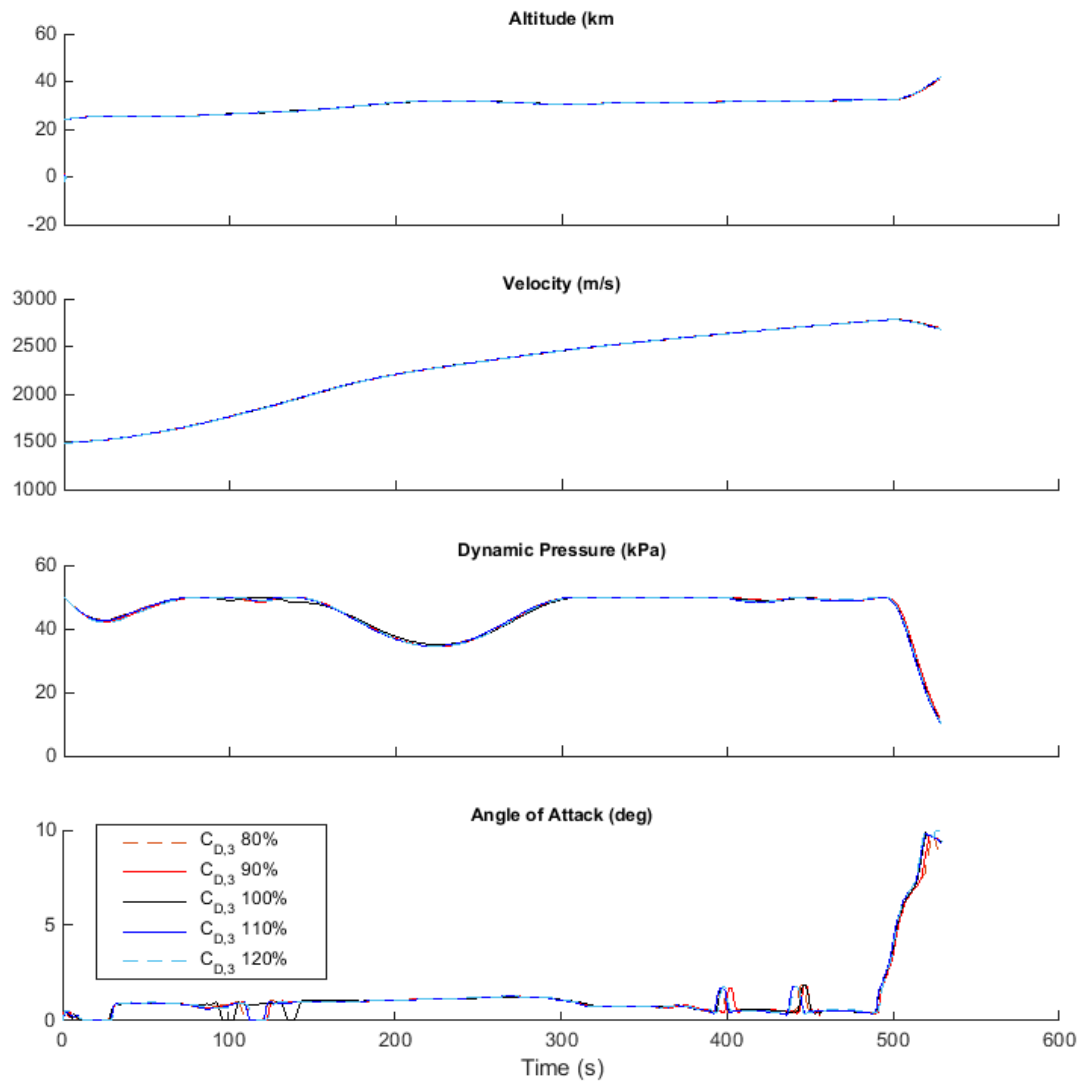
F.1.8 Case 10: Third Stage Drag Sensitivity Comparison

Figure F.15: Comparison of SPARTAN ascent trajectories with variation in the drag of the third stage.

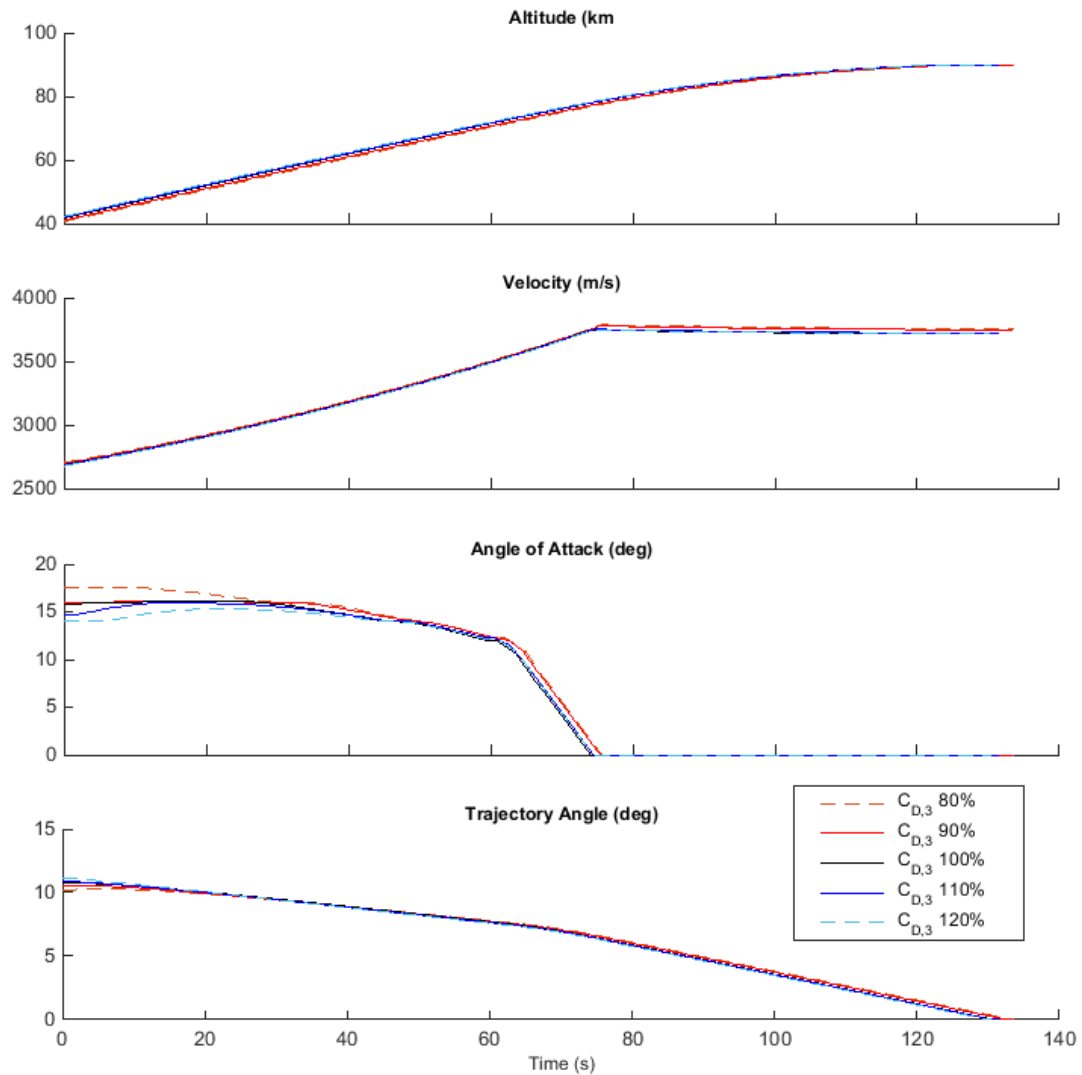


Figure F.16: Comparison of third stage rocket ascent trajectories with variation in the drag of the third stage.

F.2 Optimised Ascent Trajectory Comparisons With Fly-Back

F.2.1 Case 12: Dynamic Pressure Sensitivity Comparison

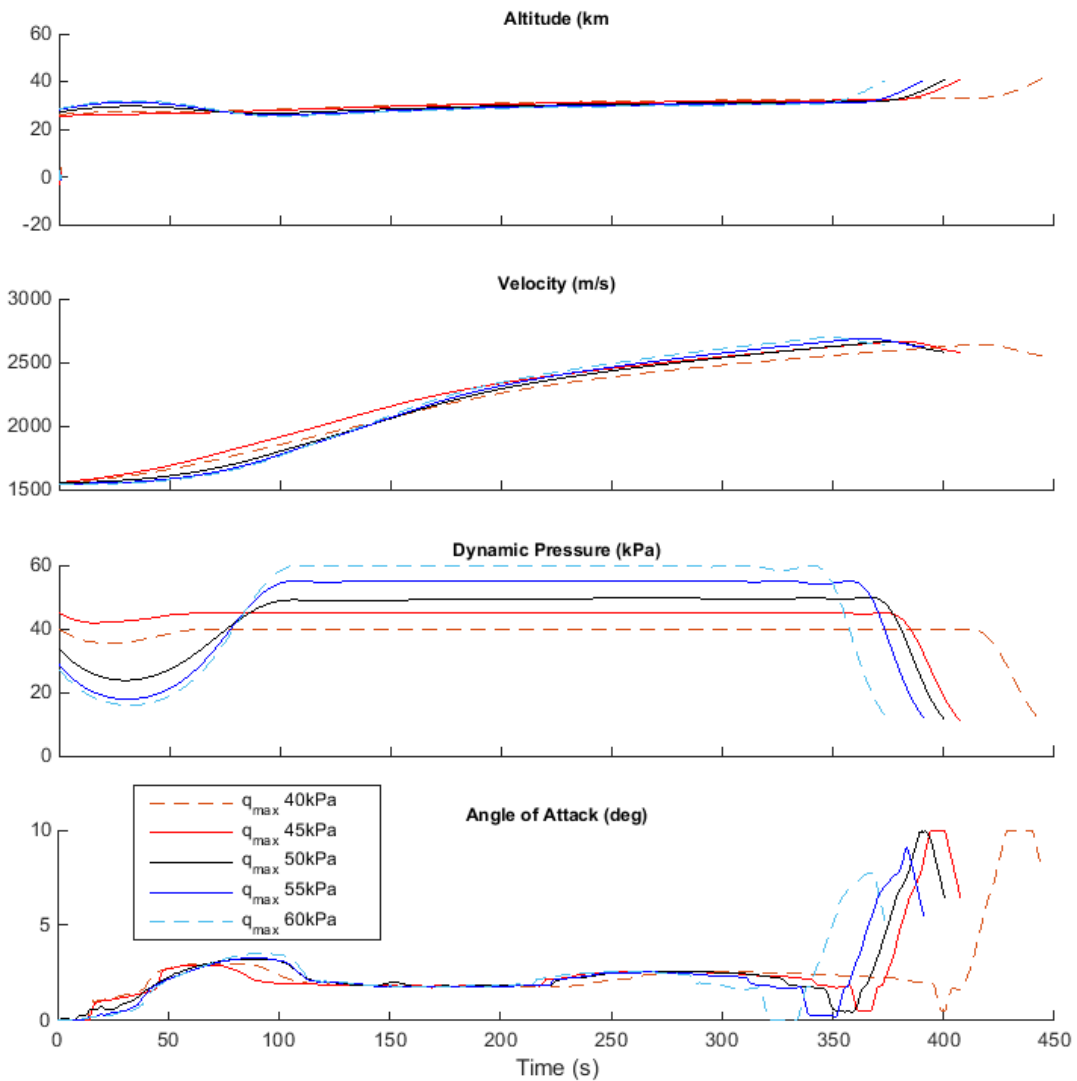


Figure F.17: Comparison of SPARTAN ascent trajectories with variation in the maximum dynamic pressure of the SPARTAN.

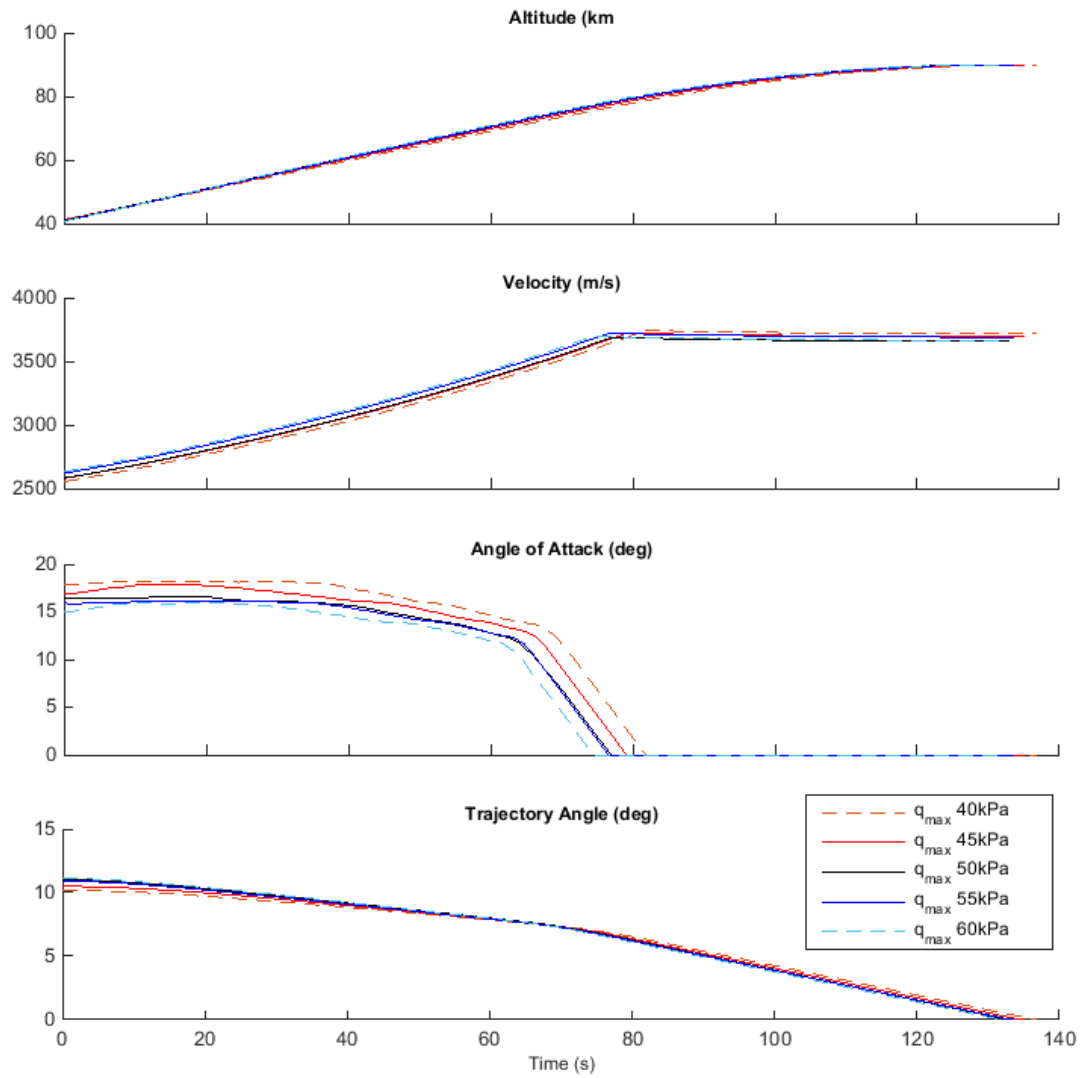


Figure F.18: Comparison of third stage rocket ascent trajectories with variation in the maximum dynamic pressure of the SPARTAN.

APPENDIX F. TRAJECTORY PLOT COMPARISONS

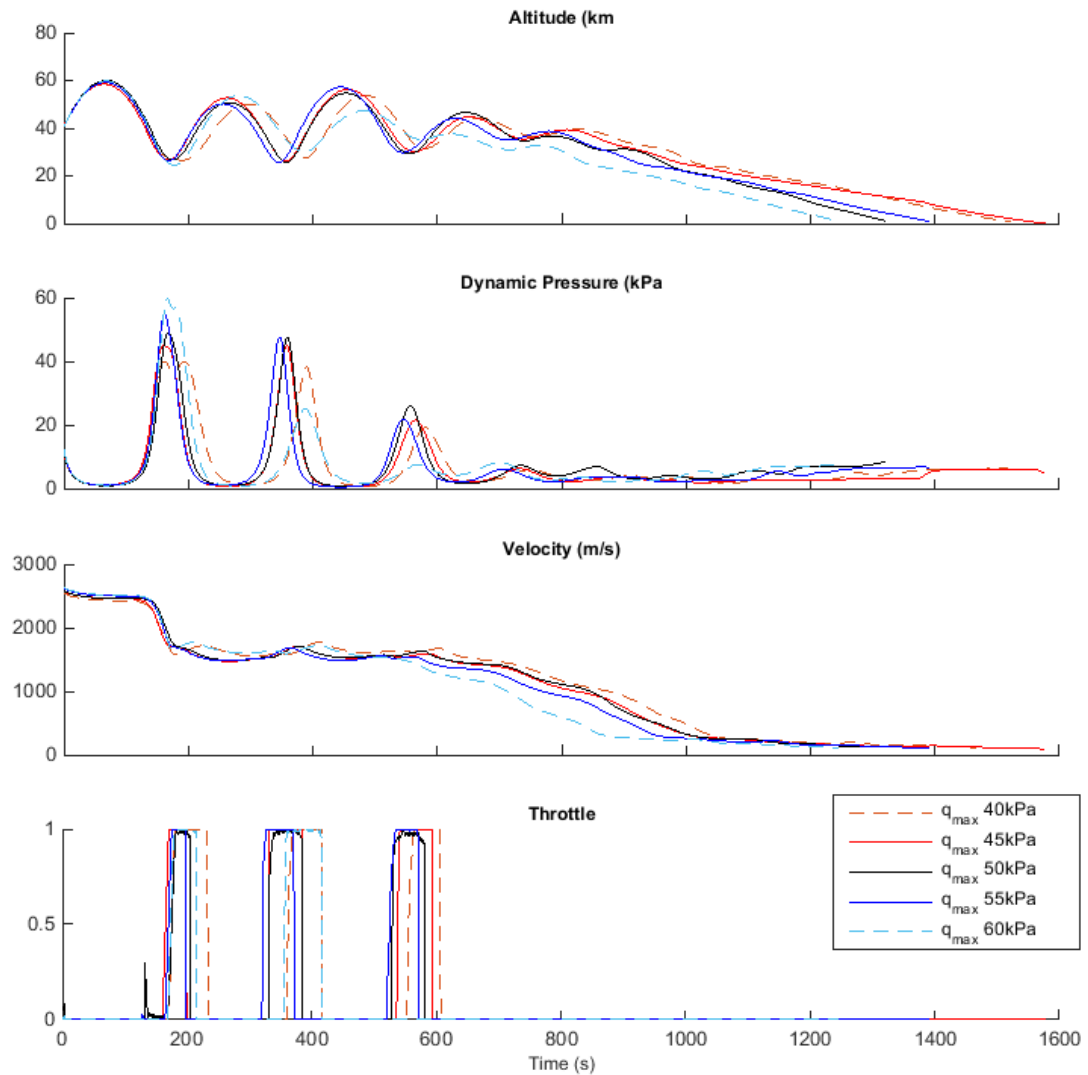


Figure F.19: Comparison of SPARTAN return trajectories with variation in the maximum dynamic pressure of the SPARTAN.

F.2.2 Case 13: SPARTAN Drag Sensitivity Comparison

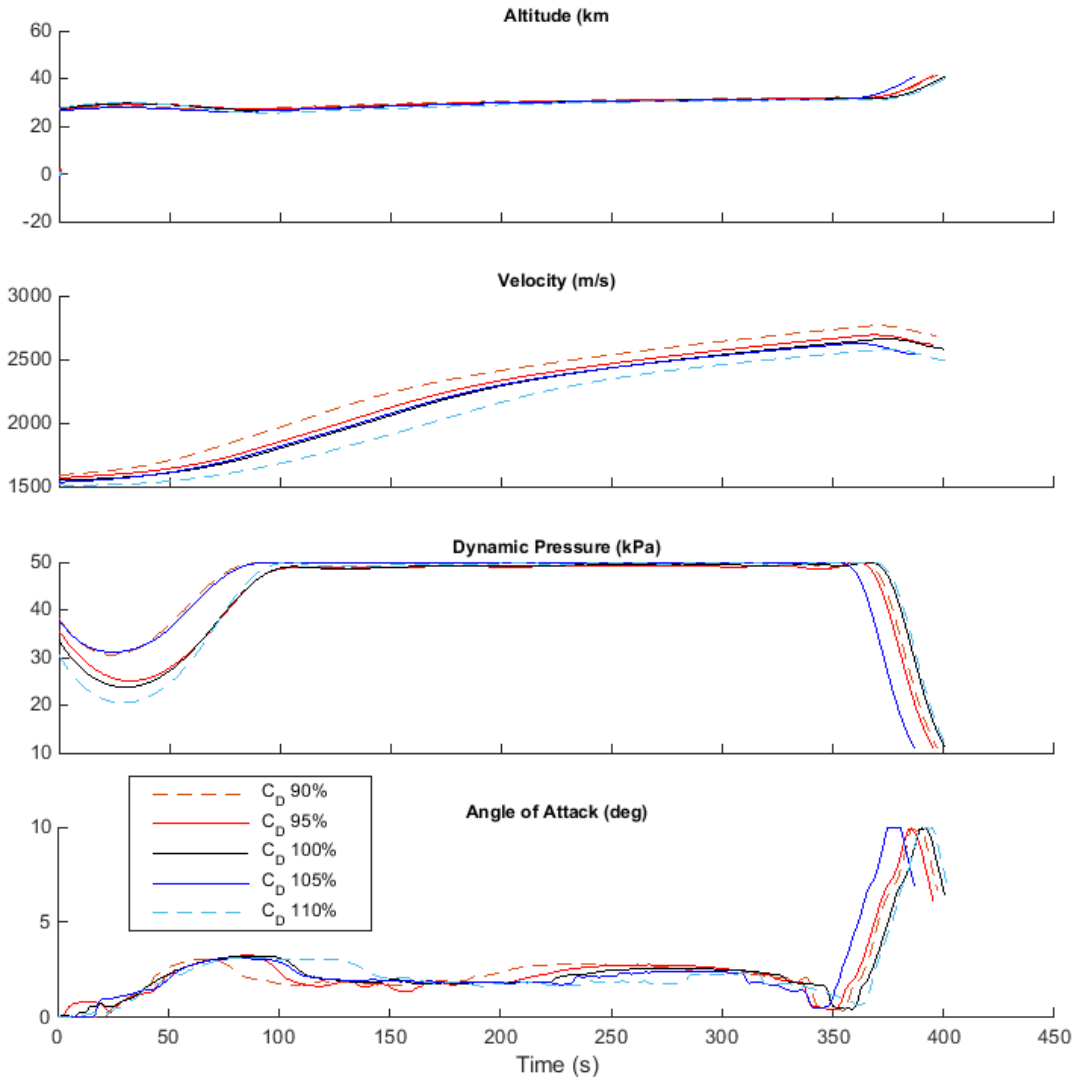


Figure F.20: Comparison of SPARTAN ascent trajectories with variation in the drag of the SPARTAN.

APPENDIX F. TRAJECTORY PLOT COMPARISONS

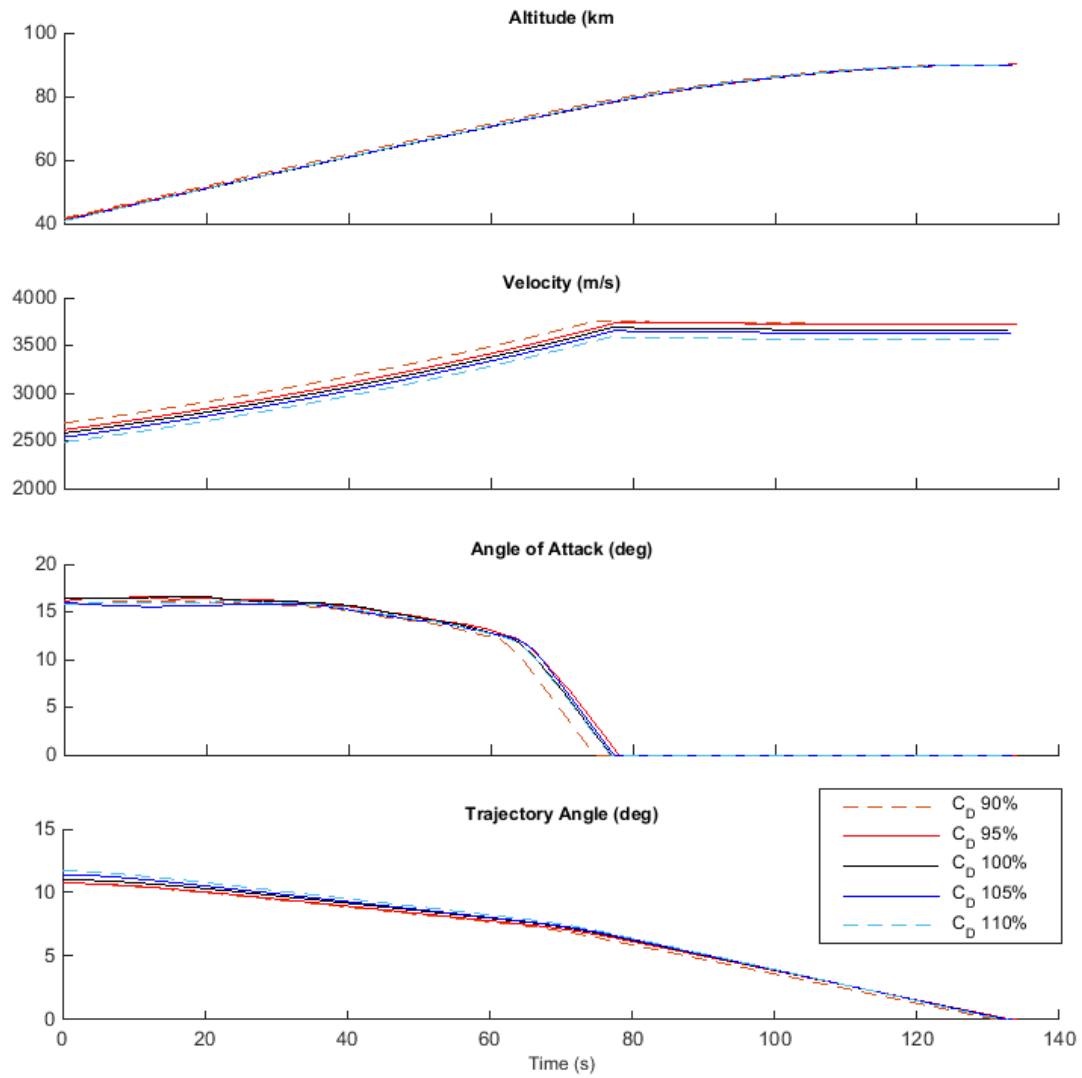


Figure F.21: Comparison of third stage rocket ascent trajectories with variation in the drag of the SPARTAN.

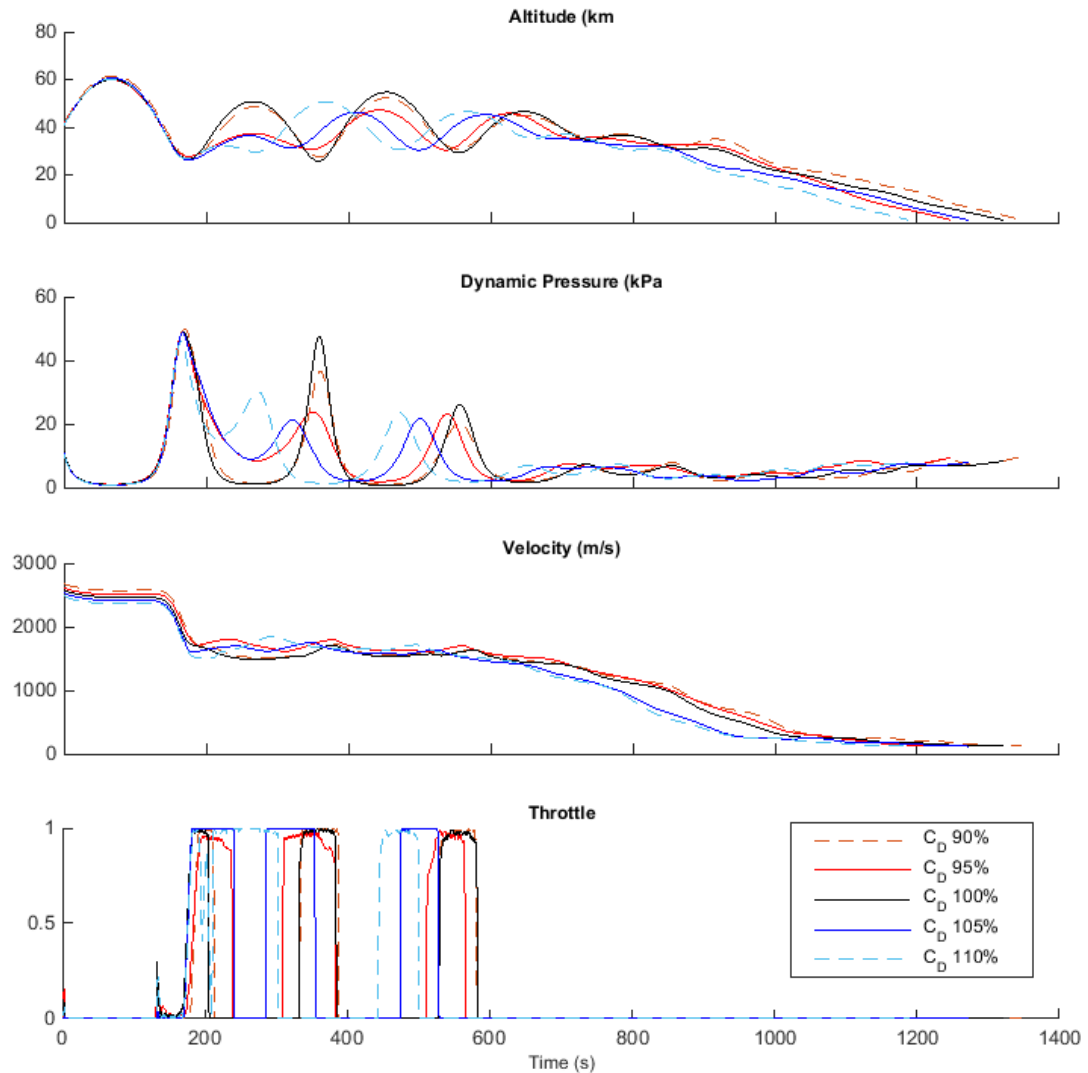


Figure F.22: Comparison of SPARTAN return trajectories with variation in the drag of the SPARTAN.

F.2.3 Case 14: SPARTAN Specific Impulse Sensitivity Comparison

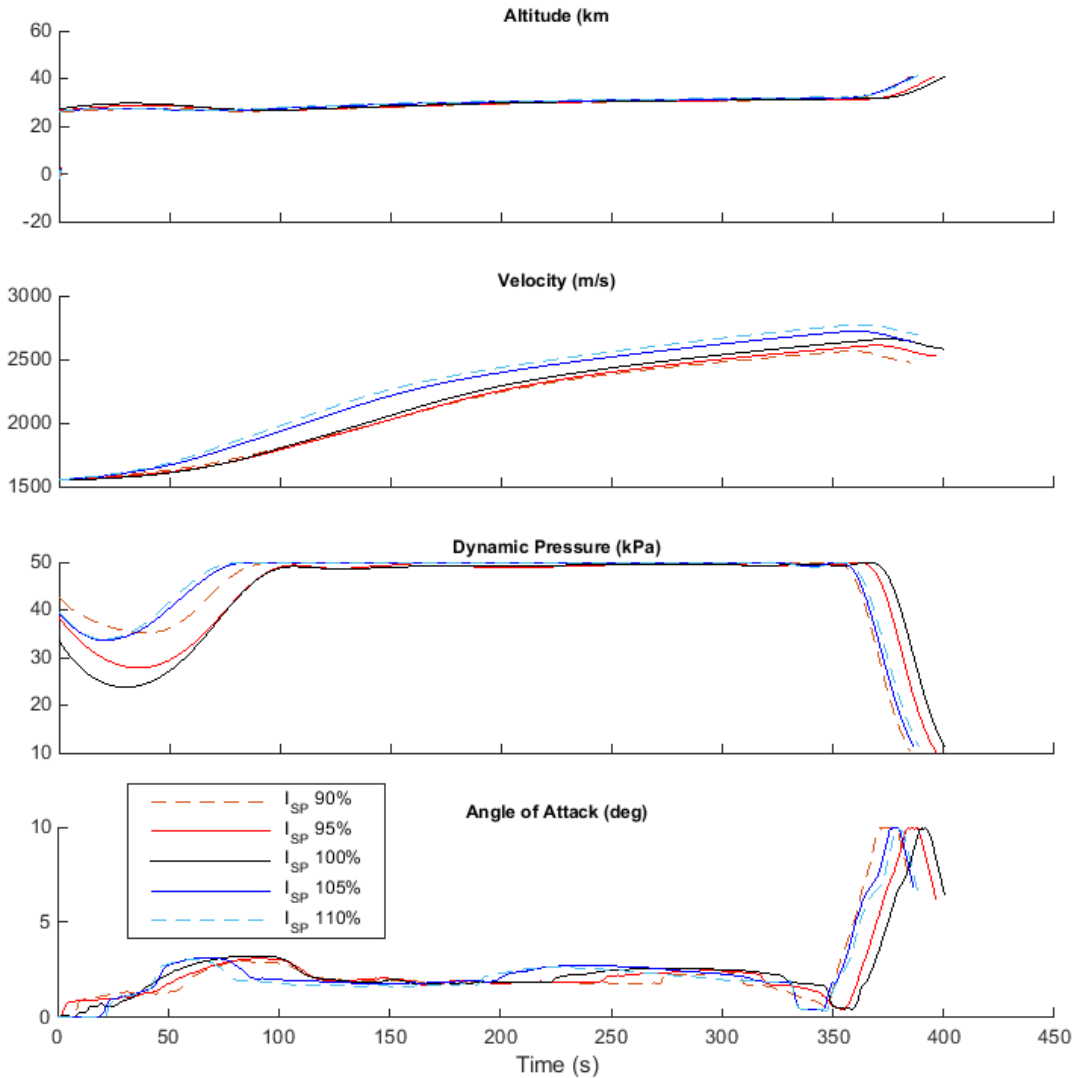


Figure F.23: Comparison of SPARTAN ascent trajectories with variation in the specific impulse of the SPARTAN.

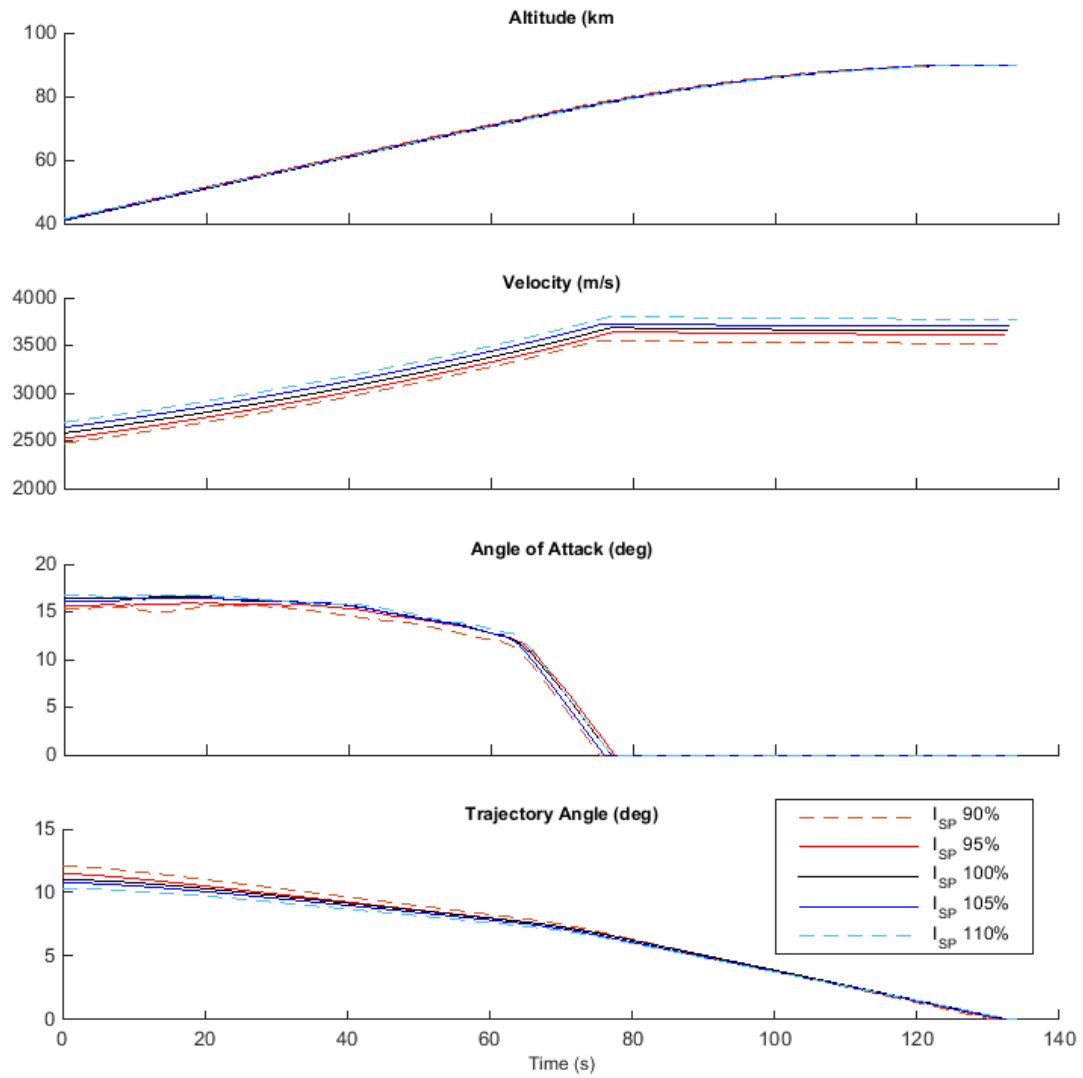


Figure F.24: Comparison of third stage rocket ascent trajectories with variation in the specific impulse of the SPARTAN.

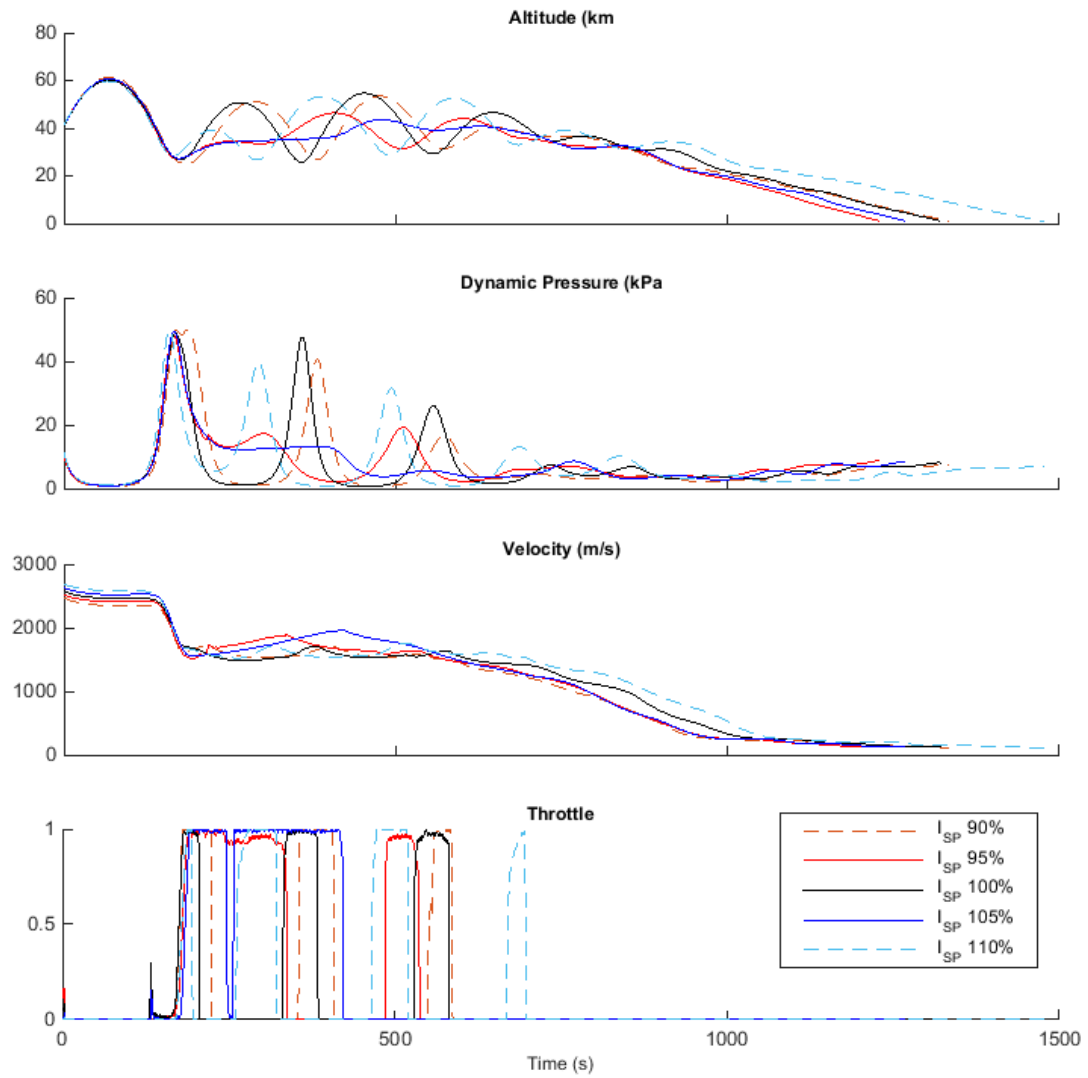


Figure F.25: Comparison of SPARTAN return trajectories with variation in the specific impulse of the SPARTAN.

F.2.4 Case 15: SPARTAN Mass Sensitivity Comparison

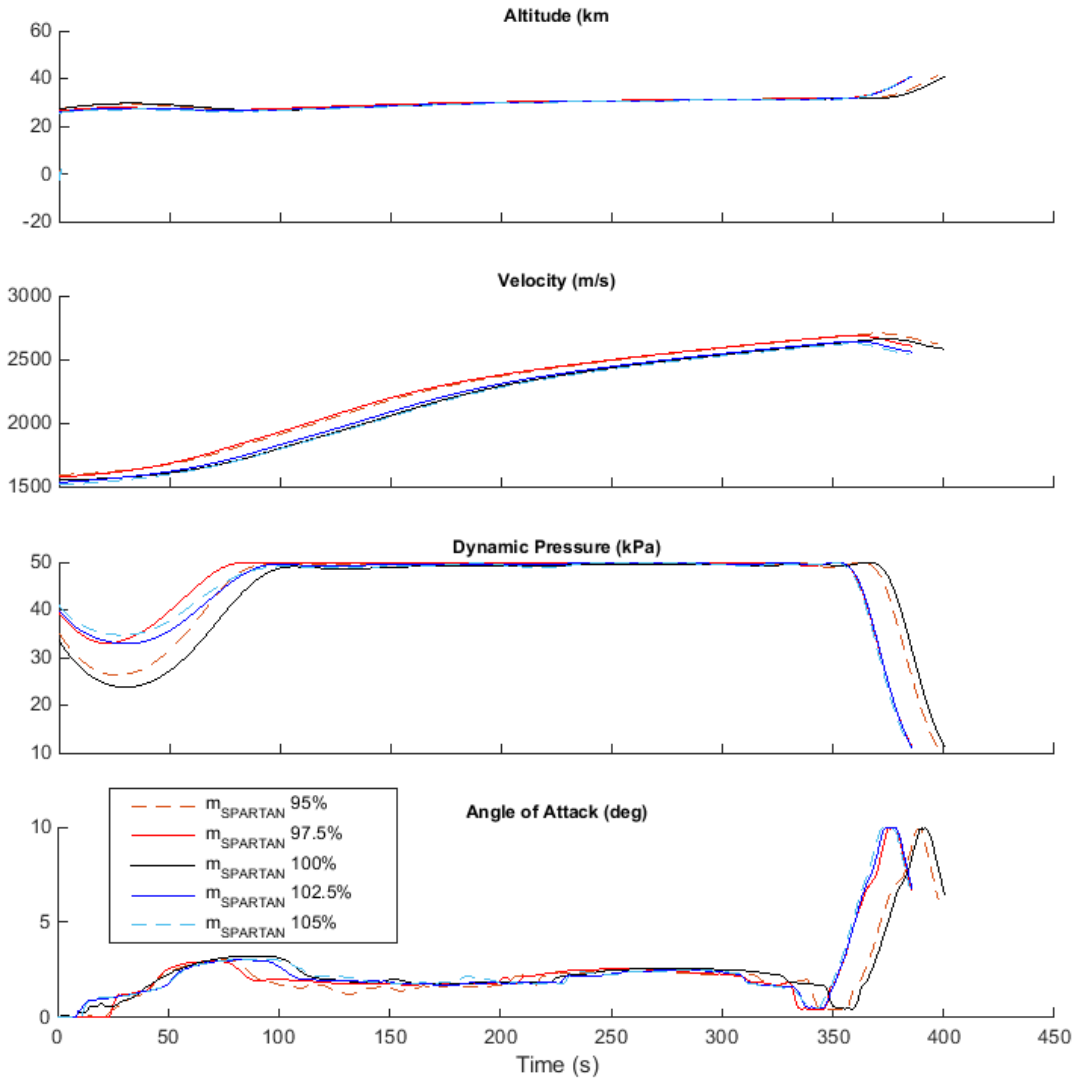


Figure F.26: Comparison of SPARTAN ascent trajectories with variation in the mass of the SPARTAN.

APPENDIX F. TRAJECTORY PLOT COMPARISONS

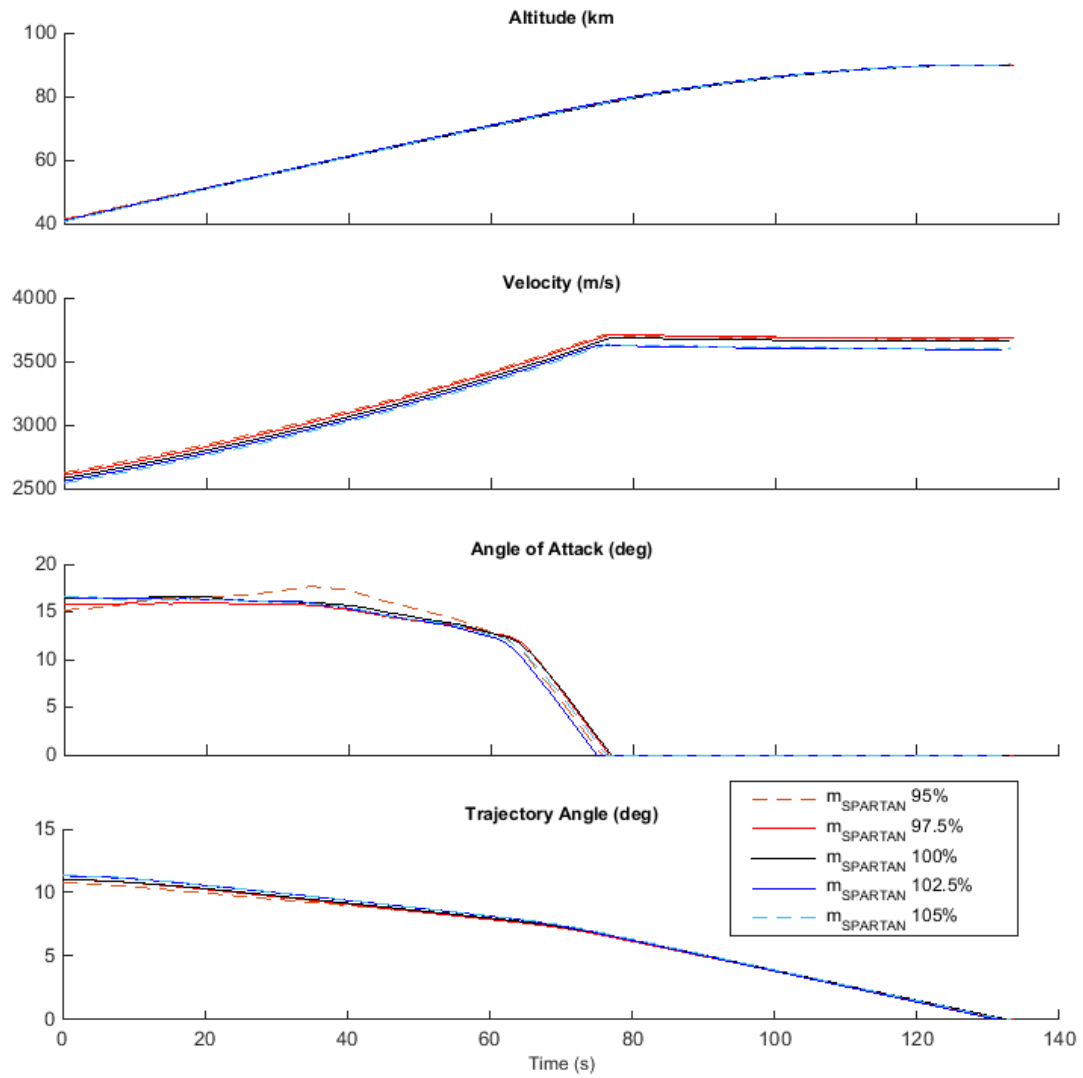


Figure F.27: Comparison of third stage rocket ascent trajectories with variation in the mass of the SPARTAN.

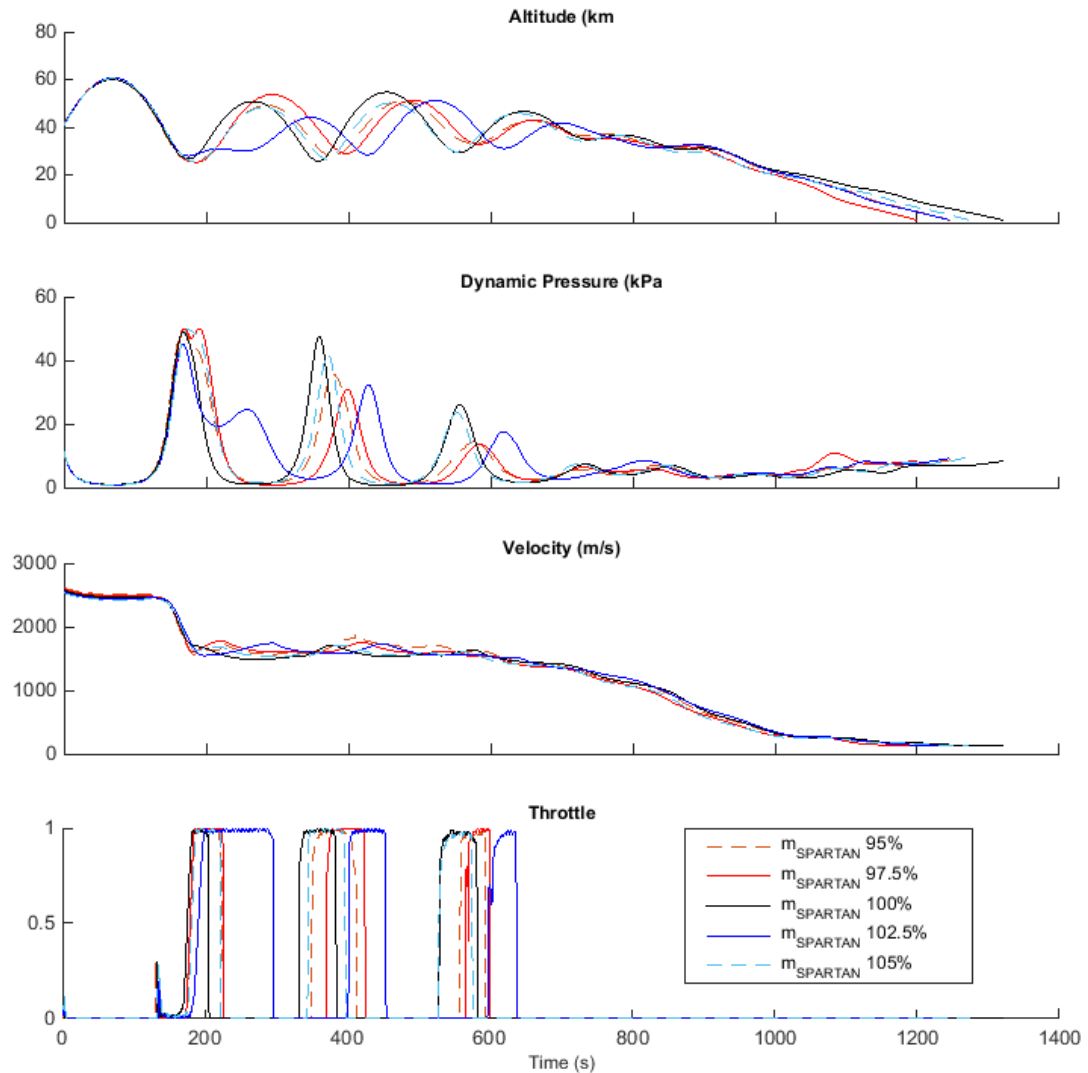


Figure F.28: Comparison of SPARTAN return trajectories with variation in the mass of the SPARTAN.

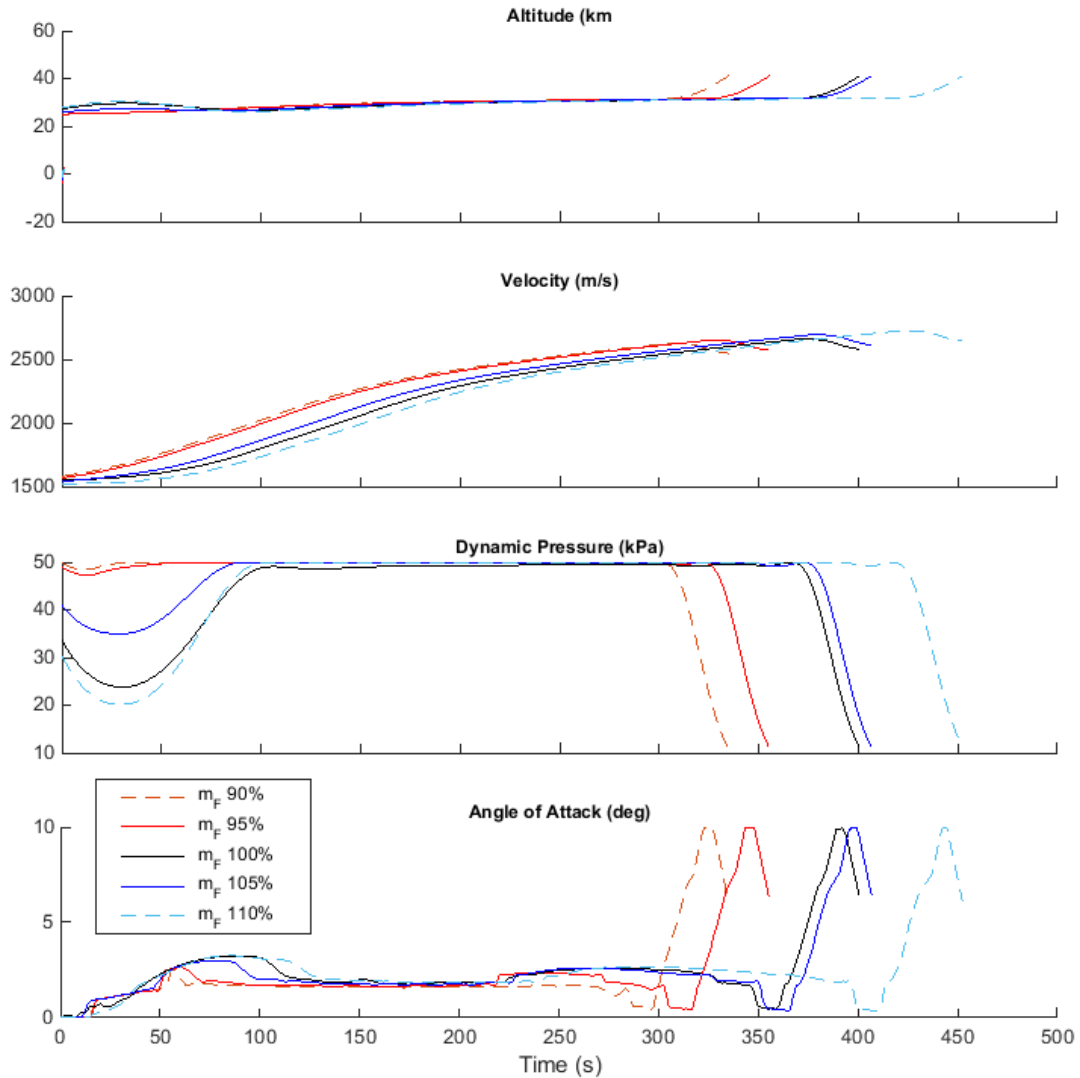
F.2.5 Case 16: SPARTAN Fuel Mass Sensitivity Comparison

Figure F.29: Comparison of SPARTAN ascent trajectories with variation in the fuel mass of the SPARTAN.

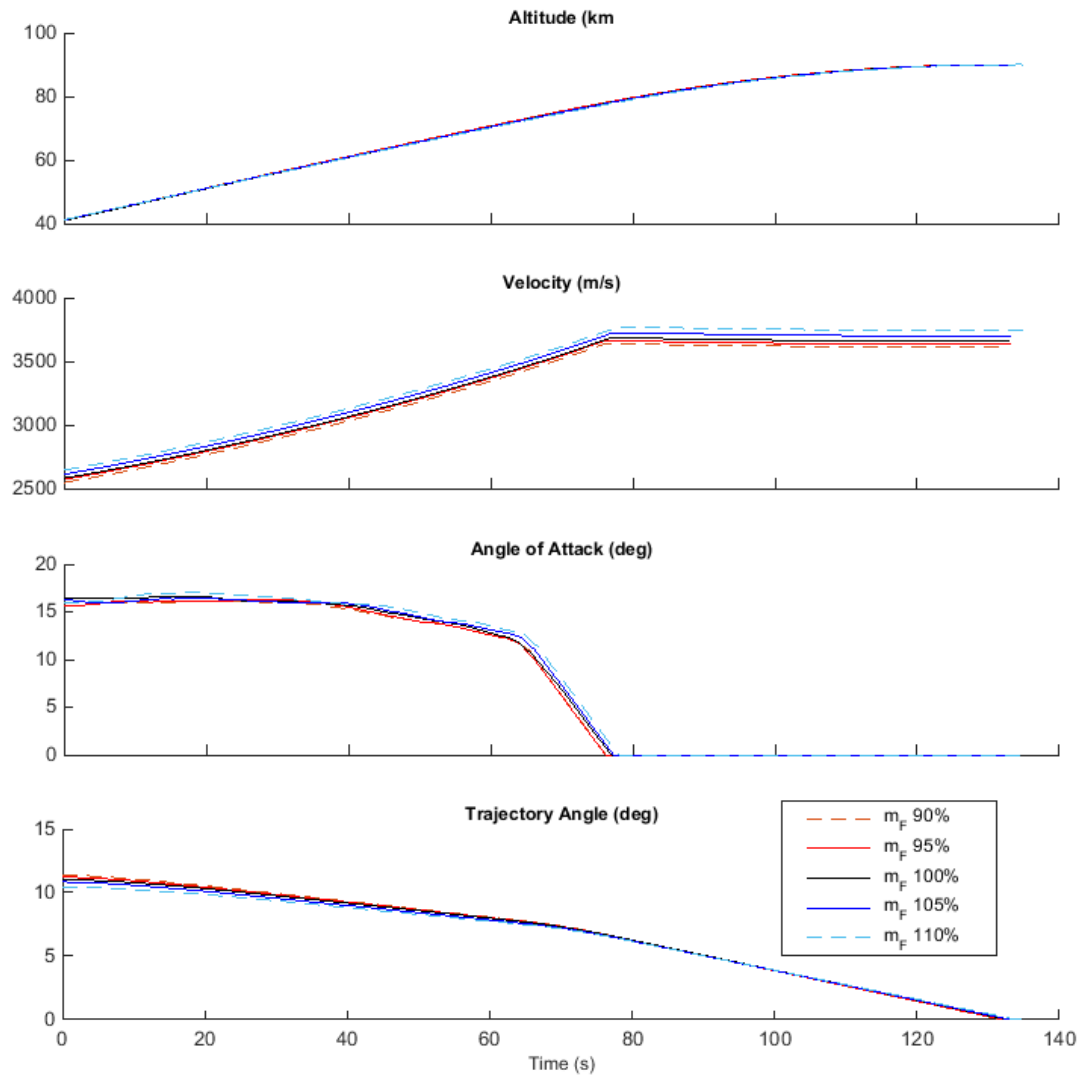


Figure F.30: Comparison of third stage rocket ascent trajectories with variation in the fuel mass of the SPARTAN.

APPENDIX F. TRAJECTORY PLOT COMPARISONS

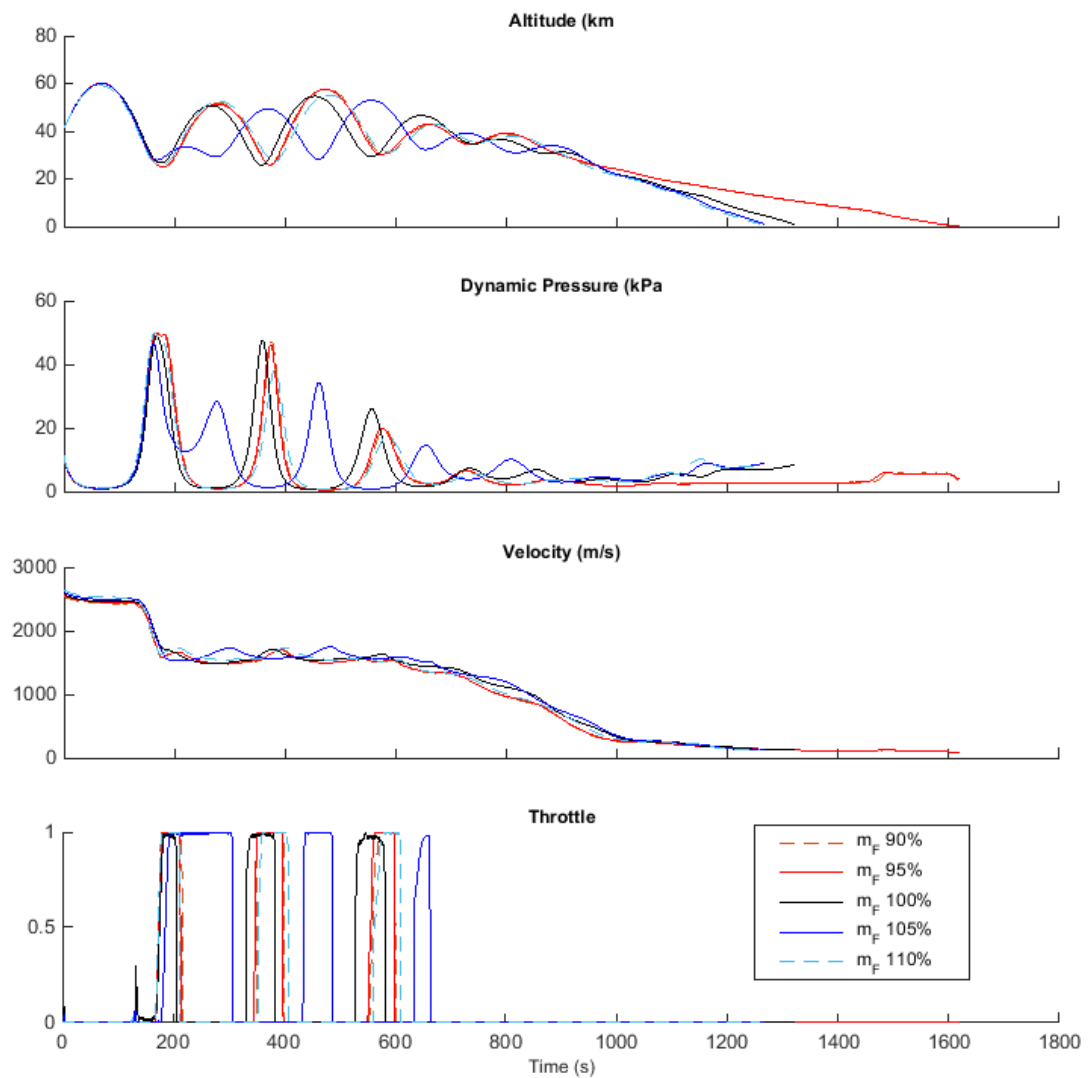


Figure F.31: Comparison of SPARTAN return trajectories with variation in the fuel mass of the SPARTAN.

F.2.6 Case 17: Third Stage Mass Sensitivity Comparison

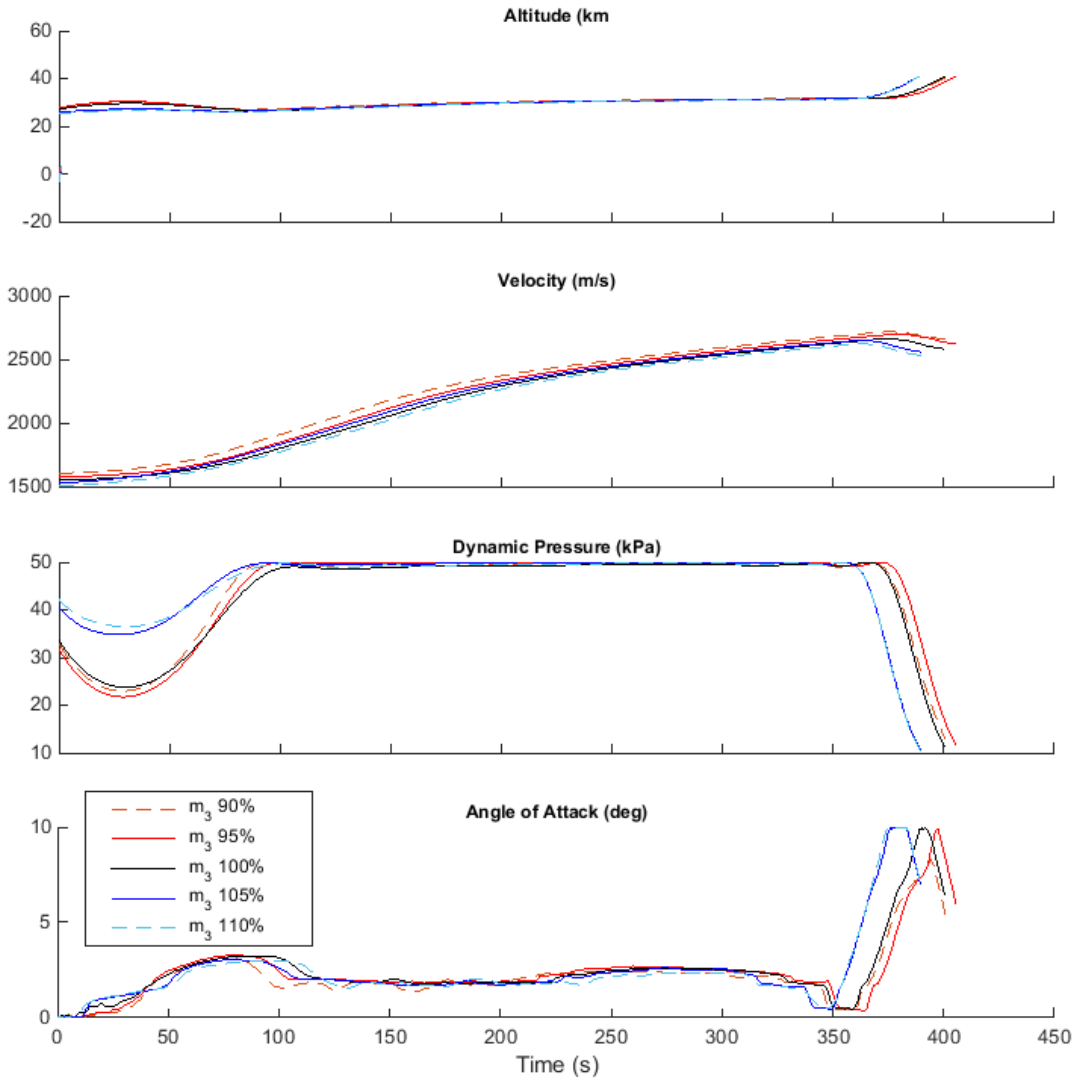


Figure F.32: Comparison of SPARTAN ascent trajectories with variation in the mass of the third stage.

APPENDIX F. TRAJECTORY PLOT COMPARISONS

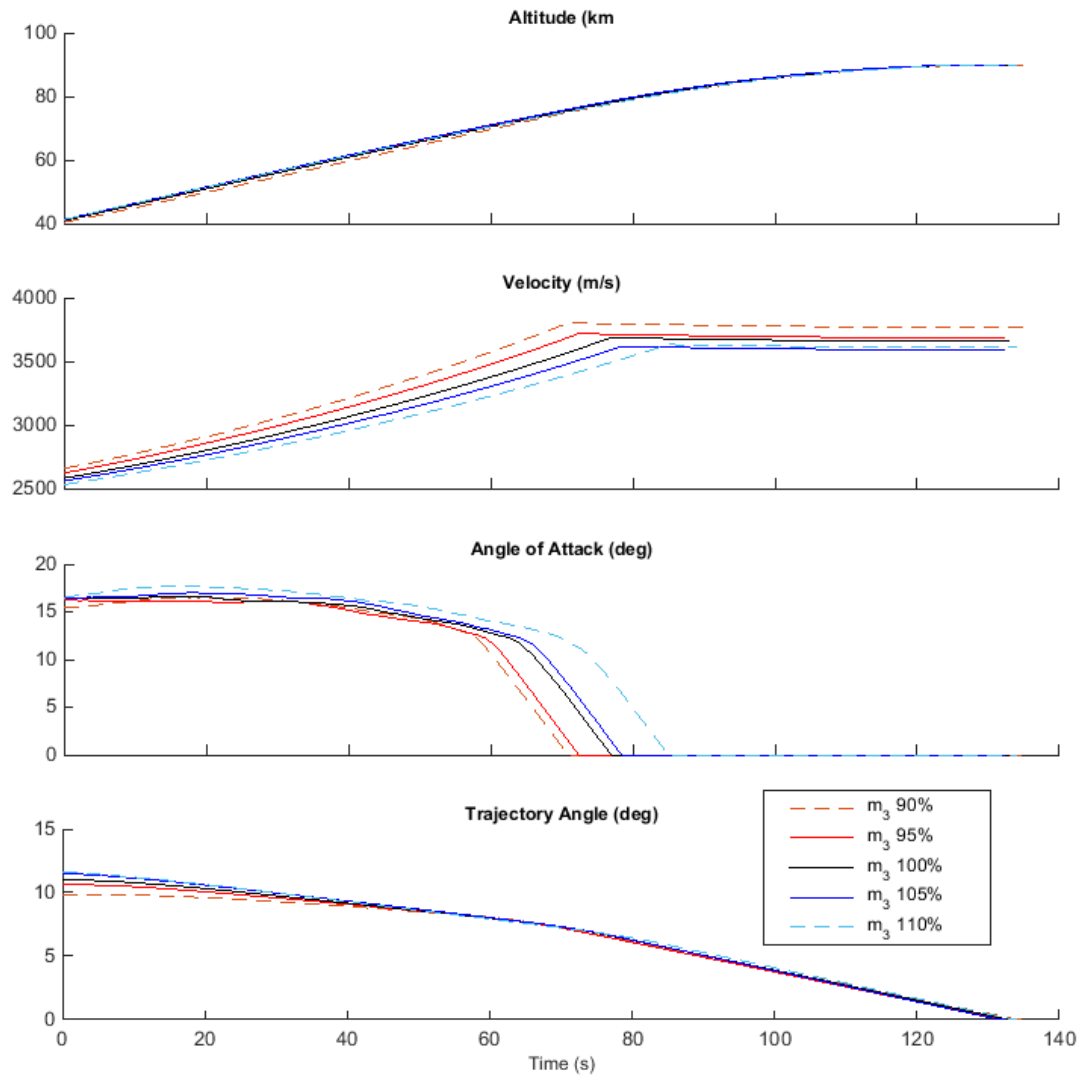


Figure F.33: Comparison of third stage rocket ascent trajectories with variation in the mass of the third stage.

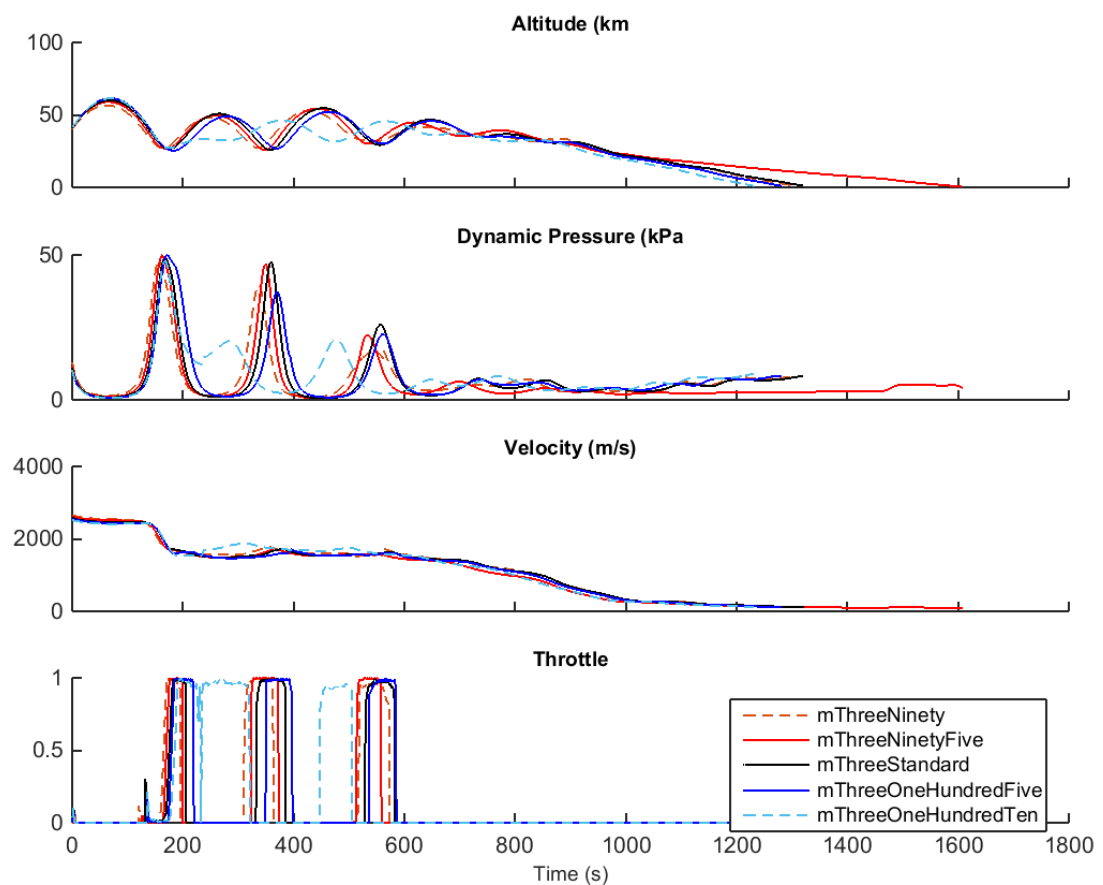


Figure F.34: Comparison of SPARTAN return trajectories with variation in the mass of the third stage.

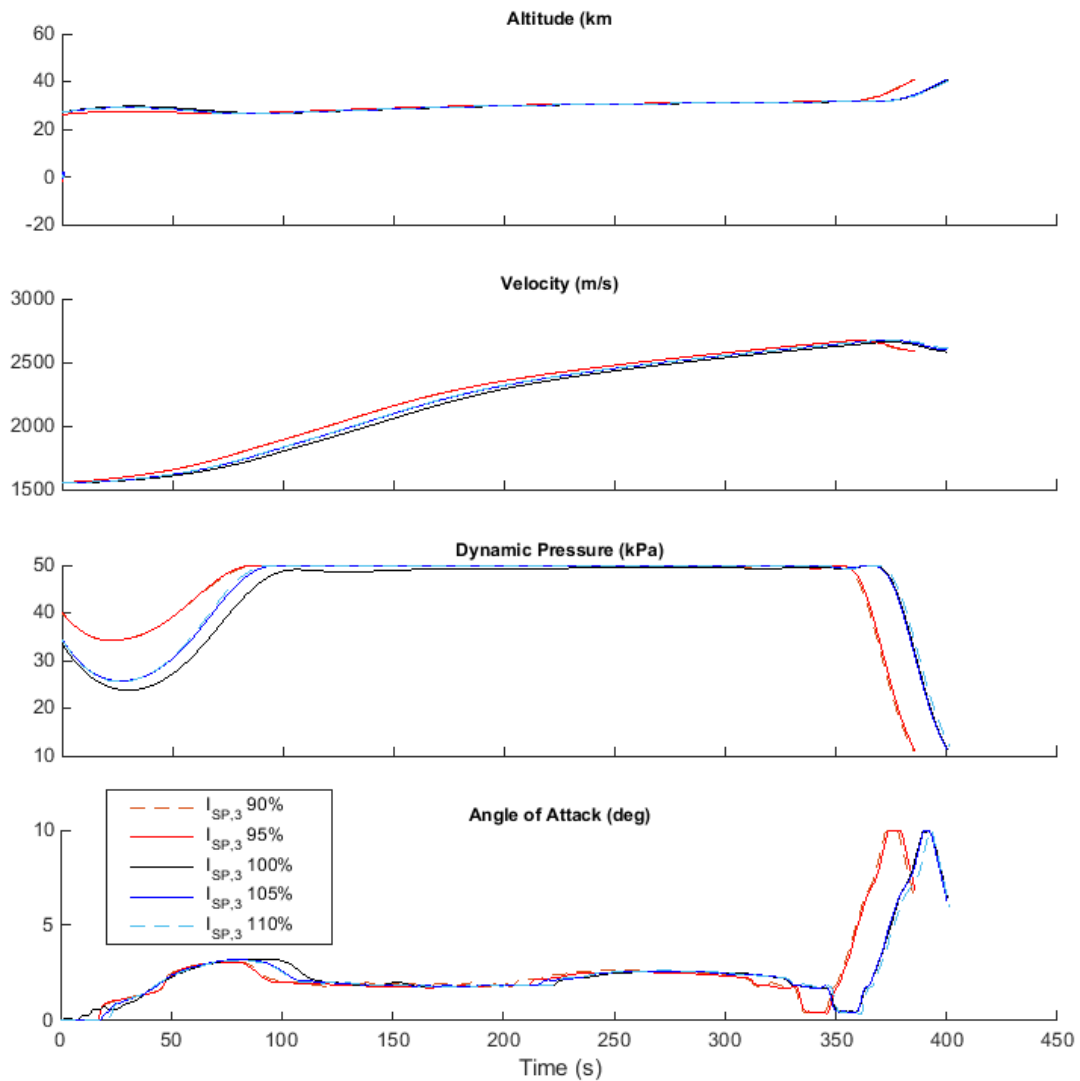
F.2.7 Case 18: Third Stage Specific Impulse Sensitivity Comparison

Figure F.35: Comparison of SPARTAN ascent trajectories with variation in the specific impulse of the third stage.

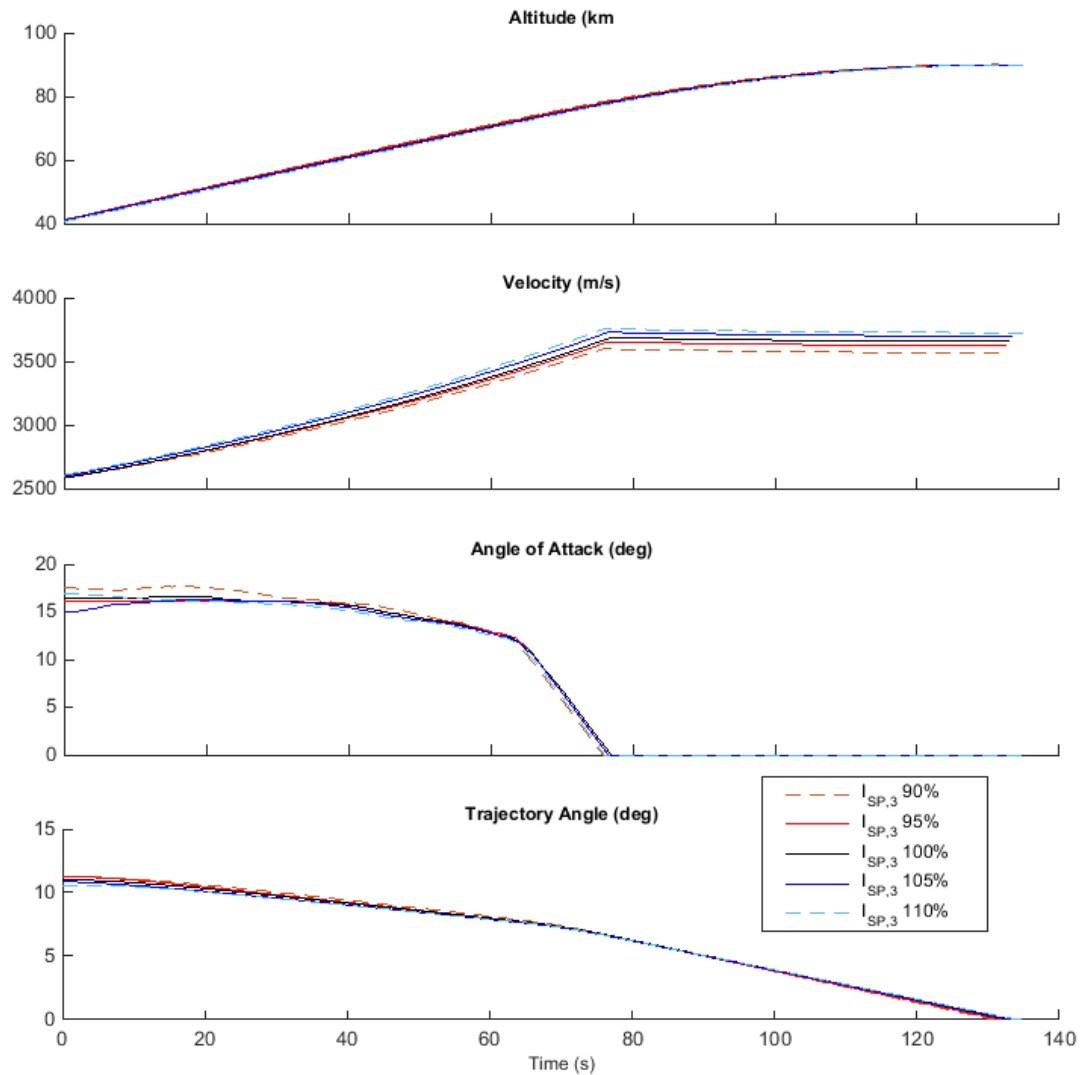


Figure F.36: Comparison of third stage rocket ascent trajectories with variation in the specific impulse of the third stage.

APPENDIX F. TRAJECTORY PLOT COMPARISONS

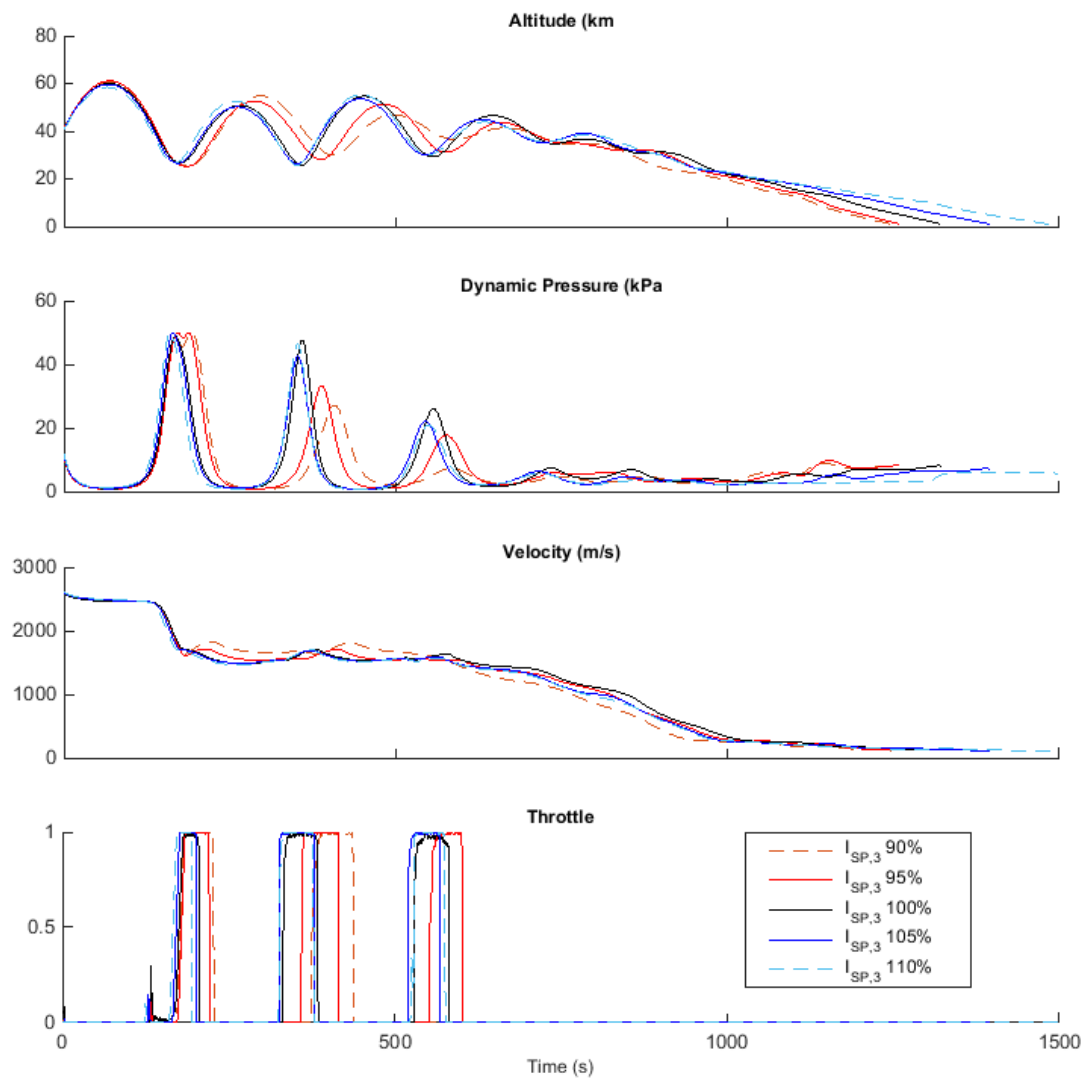


Figure F.37: Comparison of SPARTAN return trajectories with variation in the specific impulse of the third stage.

APPENDIX G

VISCOUS DRAG VARIATION

XXX Will need to redo this with variation for all stages

This section presents the sensitivity of the launch system performance to variations in the viscous drag of the SPARTAN. This sensitivity analysis is intended as a reference, to indicate the magnitude of variations in the viscous drag of the SPARTAN due to variations in modelling methods, and is unlikely to be indicative of any physical design variations. The viscous drag component of the SPARTAN's aerodynamics is calculated using flat plate correlations, which require an estimation of the laminar to turbulent transition point on the body of the SPARTAN[138]. This transition point is difficult to estimate to a high degree of accuracy, and can have a significant effect on the viscous drag of an aircraft[138]. The viscous drag component of the SPARTAN's aerodynamics is varied, in order to assess the impact of the viscous drag model used. Optimal trajectories are calculated with the viscous drag set at levels of 20%, 50%, 107% and 115% of the baseline, which correspond to the possible viscous drag range due to transition point variation. Table G.1 details key trajectory parameters of the optimised trajectories, and Figures G.1, G.2 and G.3 show comparison plots of the optimised trajectories. The sensitivity of the launch system to the viscous drag of the SPARTAN is shown to be relatively low, as the deviations in the viscous drag model are expected to be small, relative to the range tested. This low sensitivity indicating that the modelling process of the viscous drag is unlikely to have a large effect on the accuracy of the maximum payload-to-orbit solution.

Trajectory Condition	vC _D :	20%	50%	100%	107%	115%	$\Delta/\Delta\%vC_D$
Payload to Orbit (kg)	212.9	196.0	170.2	166.5	166.2	-2.5	
Payload Variation (%)	25.09	15.12	0.00	-2.19	-2.36	-0.31	
Total η_{exergy} (%)	1.983	1.839	1.609	1.581	1.561	-0.00024	
1st Stage η_{exergy} (%)	6.540	6.571	6.600	6.592	6.618		-
Separation Alt, 1→2 (km)	24.84	25.95	27.14	26.89	27.61		-
Separation v, 1→2 (m/s)	1554	1552	1548	1549	1548		-
Separation γ, 1→2 (deg)	2.1	3.7	5.6	5.1	6.4		-
2nd Stage η_{exergy} (%)	5.366	4.792	3.989	3.871	3.843	-0.064	
Separation Alt, 2→3 (km)	40.88	40.66	40.93	41.09	41.24		-
Separation v, 2→3 (m/s)	2863	2750	2581	2553	2549		-33.84
Separation γ, 2→3 (deg)	8.8	9.8	11.0	11.3	11.4		-0.1
2nd Stage Flight Time (s)	517.0	516.8	525.4	517.5	532.1		-
2nd Stage Distance Flown (km)	937.0	901.3	868.4	847.0	876.3		-
2nd Stage Return Fuel (kg)	212.2	239.9	268.0	283.7	245.3		-
2nd Stage Return Distance (km)	1783.4	1722.9	1535.7	1523.9	1483.4		-21.35
3rd Stage η_{exergy} (%)	20.979	19.369	16.888	16.530	16.504	-0.249	
3rd Stage $t, q > 5\text{kpa}$ (s)	21.0	16.7	13.3	12.7	12.1		-0.24
3rd Stage max α (deg)	17.6	16.7	16.7	15.8	16.3		-
3rd Stage Fuel Mass (kg)	2801.8	2818.8	2844.5	2848.3	2848.6		-32.96

Table G.1: Summary of key trajectory parameters with SPARTAN viscous drag variation.

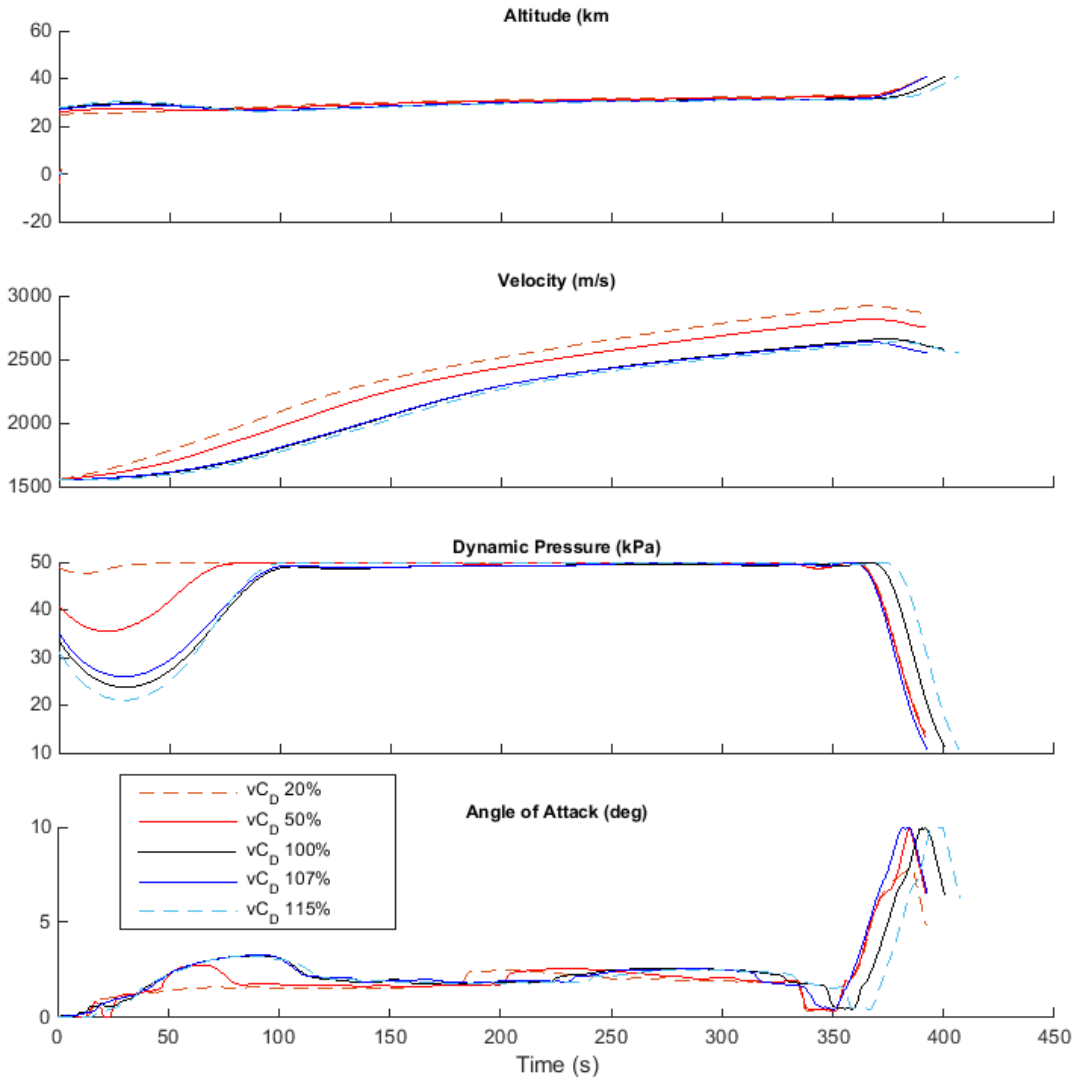


Figure G.1: Comparison of SPARTAN ascent trajectories with variation in the viscous drag of the SPARTAN.

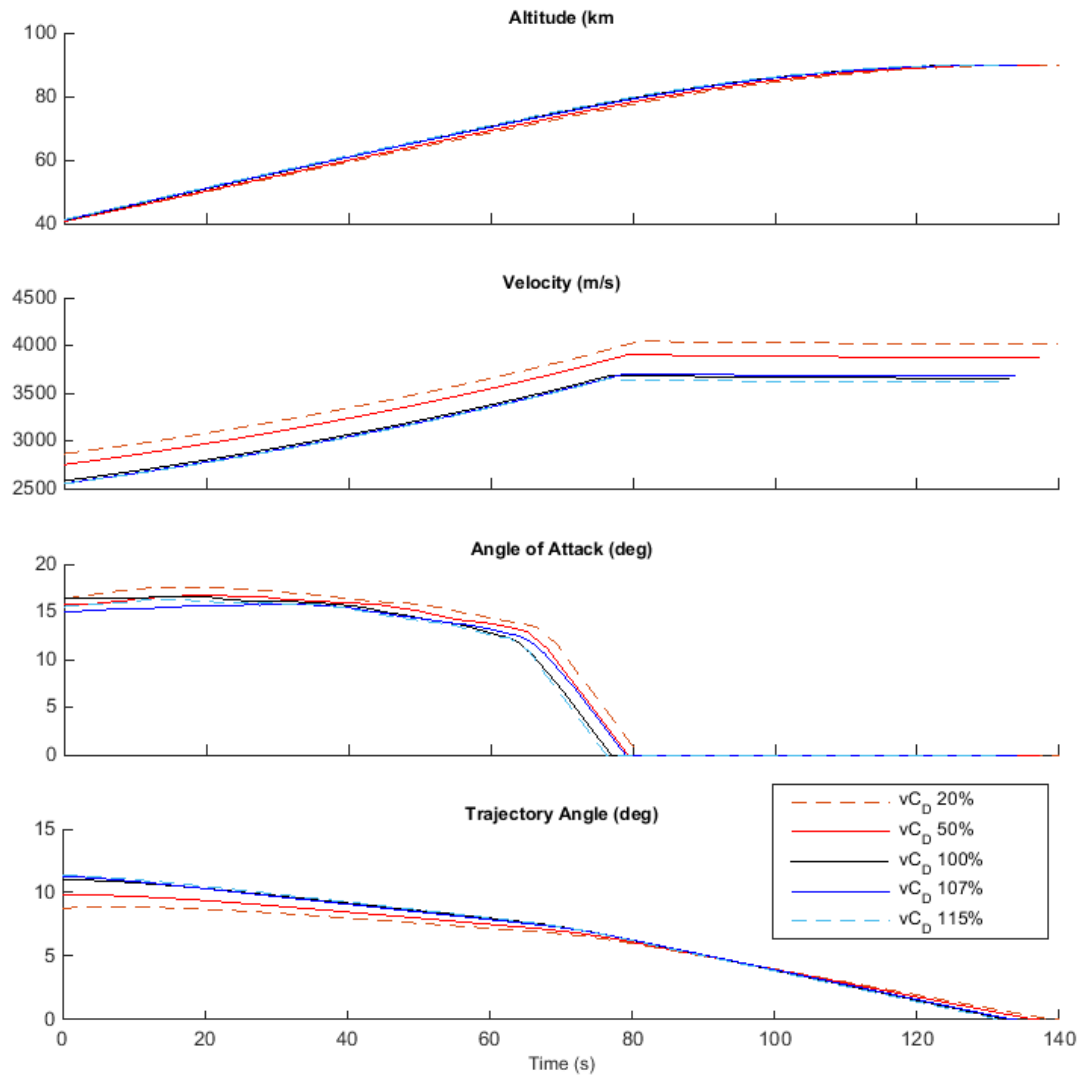


Figure G.2: Comparison of third stage ascent trajectories with variation in the viscous drag of the SPARTAN.

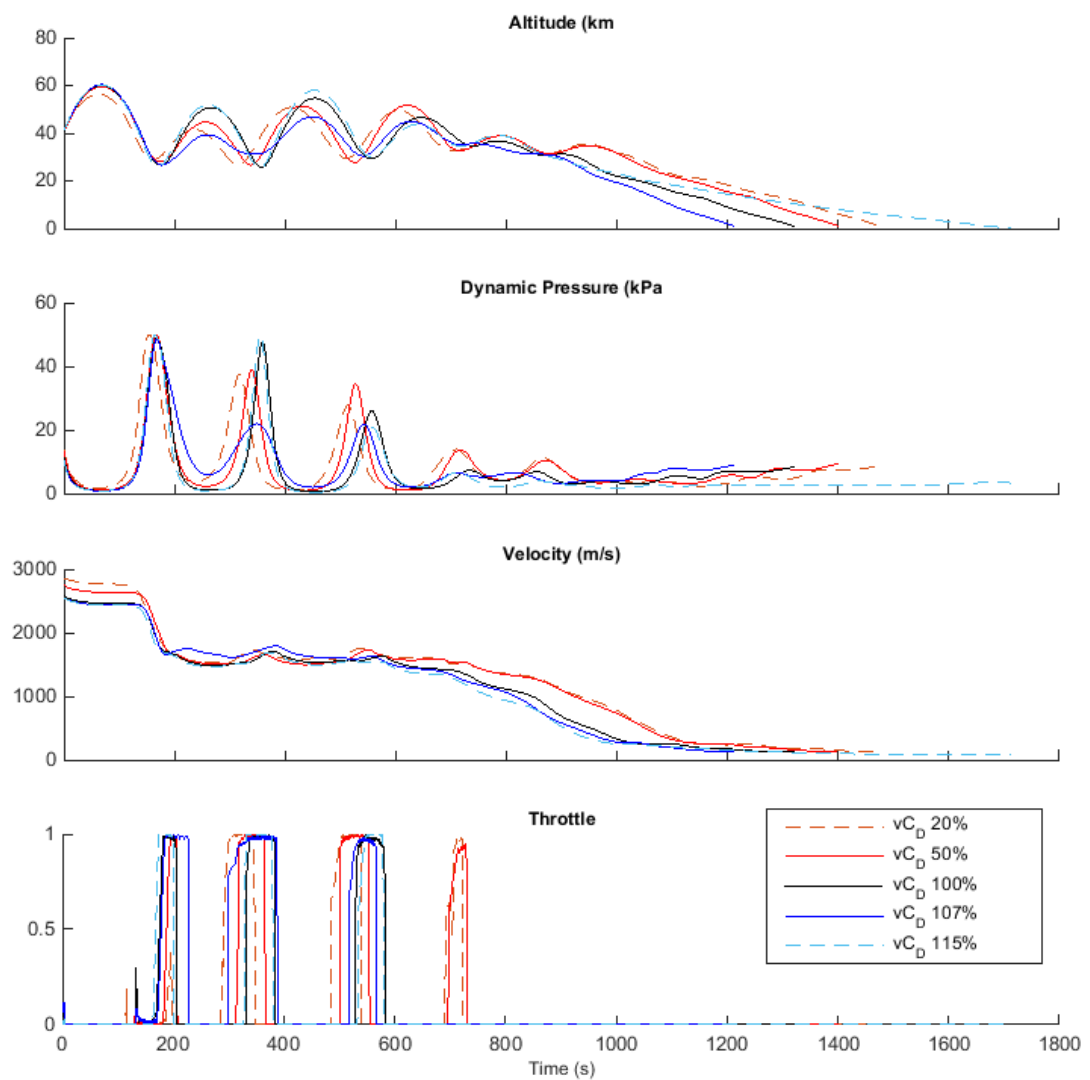


Figure G.3: Comparison of SPARTAN return trajectories with variation in the viscous drag of the SPARTAN.